FINAL REPORT

University Research Initiative

Contract No.: N00014-92-J-1808
May 1996 - September 1997

Mechanism-Based Design for High-Temperature, High-Performance Composites

by

A.G. Evans & F.A. Leckie
University of California,
Santa Barbara, CA

and

J.W. Hutchinson
Harvard University,
Cambridge, MA

Cambridge University
Harvard University
Washington State University
University of Pennsylvania
University of Virginia

19980721 081

DISTRIBUTION STATEMENT A
Approved for public release;
Distribution Unlimited

DTIC QUALITY INSPECTED 3

Book 4 of 4:
MEASURMENT AND MICRO-MECHANISMS

SUMMARY

OF

TABLE OF CONTENTS

EXECUTIVE SUMMARY

BOOK 1: CONSTITUENT PROPERTIES AND MACROSCOPIC PERFORMANCE OF CMC - I

BOOK 2: CONSTITUENT PROPERTIES AND MACROSCOPIC PERFORMANCE OF CMC - II

BOOK 3:

- **Section A:** CONSTITUENT PROPERTIES AND MACROSCOPIC PERFORMANCE OF MMC
- **Section B:** CONSTITUTIVE LAWS AND DESIGN

BOOK 4: MEASUREMENT AND MICRO-MECHANISMS

BOOK 4

MEASUREMENT AND MICRO-MECHANISMS

A Photothermal Technique for the Determination of the Thermal Conductance of Interfaces and Cracks	J.R. Dryden K.R. McDonald A. Majumdar F.W. Zok	1
Determination of Fibre Strength Distributions from Bundle Tests Using Optical Luminescence Spectroscopy	J. He D.R. Clarke	41
Polarization Dependence of the Cr^{3+} R-Line Fluorescence from Sapphire and Its Application to Crystal Orientation and Piezospectroscopic Measurement	J. He D.R. Clarke	63
Residual Stresses in Dielectrics Caused by Metallization Lines and Pads	M.Y. He J. Lipkin D.R. Clarke A.G. Evans M. Tenhover	73
Convergent Debonding of Films and Fibers	M.Y. He A.G. Evans J.W. Hutchinson	81
A Model of Evolving Damage Bands in Materials	Y. Huang X.Y. Gong Z. Suo Z.Q. Jiang	91
Effect of Interfacial Carbon on Adhesion and Fracture Toughness of Gold-Sapphire Interfaces	D.M. Lipkin D.R. Clarke A.G. Evans	103
Estimating the Metal-Ceramic van der Waals Adhesion Energy	D.M. Lipkin J.N. Israelachvili D.R. Clarke	139
Laser-Utrasonic Evaluation of Damage Unidirectional Ceramic Matrix Composites	Y.-M. Liu T.E. Mitchell H.N.G. Wadley	153
Fiber Optic Measurement of Residual Stress in Ti-6Al-4V/SiC Fiber Composites Using Cr^{3+} Doped Sapphire Fibers	G.T. Munger H.N.G. Wadley	163
Motions of Microscopic Surfaces in Materials	Z. Suo	179

Damage Evolution and Acoustic Emission Mechanisms in $\alpha_2\beta$/SCS-6 Titanium Matrix Composites	D.J. Sypeck H.N.G. Wadley	281
Acoustic Emission Analysis of SCS-6 Fiber Fracture in Titanium Matrix Composites	D.J. Sypeck H.N.G. Wadley	313

A PHOTOTHERMAL TECHNIQUE FOR THE DETERMINATION OF THE THERMAL CONDUCTANCE OF INTERFACES AND CRACKS

J.R. Dryden*, K.R. McDonald, A. Majumdar‡ and F.W. Zok

Materials Department
University of California
Santa Barbara, California 93106

* On sabbatical leave from:
Department of Mechanical and Materials Engineering
University of Western Ontario
London, Ontario N6A 5B9
Canada

‡ Presently at:
Department of Mechanical Engineering
University of California
Berkeley, California 94720

Submitted to
Reviews of Scientific Instruments

Revised January, 1998

ABSTRACT

The paper describes a phase-sensitive photothermal technique for the determination of the thermal conductance of a crack or interface embedded within a plate of finite thickness. The technique involves sinusoidally-modulated heating at one point on the surface using a focused laser beam and measurement of the phase shift of the thermal wave at some other point. An analysis is presented for the relationship between the phase lag, the modulation frequency, the specimen geometry, and the thermal properties of both the interface and the solid. The technique is demonstrated using a model system comprising two stainless steel disks, with the "interfaces" between them being formed either by simply placing the two disks in contact with each another, or by placing thin layers of polyethylene sheets between the disks. The trends are rationalized on the basis of the thermal properties of the constituents.

1. INTRODUCTION

The present article describes a photothermal technique and the associated analysis for the determination of the thermal conductance of a crack or interface embedded within a plate of finite thickness. The technique is based on periodic heating at a point on one surface, using, for example, a focused laser beam, and measurement of the phase lag of the thermal wave at some other point. In the absence of an interface, the technique can be used to determine the thermal diffusivity of the material. The work is motivated by concurrent studies on the thermal conductance of delamination cracks in fiber-reinforced ceramic matrix composites (CMCs) and its effect on failure in the presence of a temperature gradient. An example of such a crack is shown in Fig. 1. Although the technique is being developed mainly to study CMCs, it can be applied readily to other problems involving interfaces or cracks in multilayered or coated systems.

Photothermal techniques have been used extensively to study the thermal properties of materials [1-12]. A recent summary of these can be found in [12]. The techniques have been used also as nondestructive tools for detecting sub-surface defects [12-18]. The focus of the present work is on one specific subgroup of these techniques, notably, that based upon periodic heating and phase lag measurement. The main advantage of the present technique is that it provides *quantitative* information about the thermal conductance of cracks and interfaces, rather than simply identifying regions where such defects are present. This information is crucial for failure prediction in a broad range of technological systems, including delamination of thermally-loaded CMC structures, multilayered power electronic devices and thermal barrier coatings.

In the past, thermal conductances have been measured predominantly by dc techniques [19-22]. These techniques require a heat flux, q, to flow through the interface as well as through the bulk of the two contacting solids. The temperature distribution in the bulk solid is measured and extrapolated to the interface to estimate the interfacial temperature jump, ΔT_i. The contact conductance is then estimated by the relation, $h = q/\Delta T_i$. Although this technique is widely used, it suffers from several drawbacks. First, the heat flux must be constant over the bulk of both contacting solids which requires insulation material to be placed around the specimen. Second, it requires a cooling unit to remove the heat from the system; otherwise, the temperature of the sample increases monotonically with time. Finally, since the temperature distribution needs to be measured in the bulk, the samples must be sufficiently thick for at least three thermocouples to be inserted. Consequently, the technique is not easily adapted for measurement in small scale specimens or structures. The ac technique described in the present paper has several advantages over the existing dc techniques. Notably, it does not require insulation of the system from the surroundings nor of a cooling unit to extract heat. Moreover, it can be performed relatively quickly on both large and small specimens.

The paper is organized in the following way. Section 2 describes an analysis for the temperature distribution and phase lag in a finite plate containing an interface parallel to the plate surfaces and heated periodically at one point on the surface. The approach used to solve the problem is based on standard concepts of heat flow through solids and across interfaces [23]. Both generic solutions and specific numerical results for the phase lag are presented and used in guiding the experimental program. Section 3 describes an experimental demonstration of the use of the technique for determining both the thermal diffusivity of a steel alloy with known thermal properties as well as the interface conductance in a series of model systems comprising steel disks with several different types of interfaces. Section 4 provides some concluding remarks. The use of the technique to determine the thermal conductance of delamination cracks in CMCs is presented elsewhere [24].

2. ANALYSIS

2.1 Preliminaries

A schematic of the specimen geometry to be analyzed is shown in Fig. 2. The specimen is considered to be infinite in the x-y plane and of thickness A in the z-direction. An interface (or crack) is situated parallel to the top and bottom surfaces at $z = B$, with z being measured from the top surface. (This geometry closely resembles the one of the CMC panel with a centrally-located delamination crack, illustrated in Fig. 1.) The thermal diffusivity and conductivity of the material outside of the interface are denoted α and k, and the thermal conductance of the interface is denoted h. A useful normalized form of these parameters is given by

$$\rho = \frac{k}{2Ah} \tag{1}$$

(This parameter is essentially the inverse of the corresponding Biot number, b; the two are related through $\rho=1/2b$.) The limiting case of $\rho = 0$ can be viewed either as one in which there is no interface or, equivalently, one in which the interface is perfectly conducting.

A periodic heat source is input at $(r, z) = (0, 0)$ at a frequency, $\omega = 2\pi f$, with f being the frequency in Hz. The corresponding wave number, β, is given by

$$\beta = \sqrt{\omega/2\alpha} = \sqrt{\pi f/\alpha} \tag{2}$$

The top and bottom surfaces are taken to be perfectly insulating. In the following analysis, expressions are obtained for the temperature and the phase lag relative to the heat input at various positions within the specimen.

2.2 Solution of the Diffusion Equation

With regard to the sketch in Fig. 2, the problem is axisymmetric, so that the temperature depends on the radial distance r from the z-axis. The temperatures in the regions B > z > 0 and A > z > B are denoted v (r, z, t) and u (r, z, t), respectively; they are required to satisfy the heat flow equations [19]

$$\frac{\partial^2 u}{\partial r^2} + \frac{1}{r}\frac{\partial u}{\partial r} + \frac{\partial^2 u}{\partial z^2} - \frac{1}{\alpha}\frac{\partial u}{\partial t} = 0 \tag{3a}$$

$$\frac{\partial^2 v}{\partial r^2} + \frac{1}{r}\frac{\partial v}{\partial r} + \frac{\partial^2 v}{\partial z^2} - \frac{1}{\alpha}\frac{\partial v}{\partial t} = 0 \tag{3b}$$

Across the interface, z = B, there is a heat flow balance and the discontinuous temperature jump is proportional to the flux so that the two equations

$$\frac{\partial u}{\partial z} = \frac{\partial v}{\partial z} \tag{4a}$$

$$= \frac{h}{k}(u - v) \tag{4b}$$

must be satisfied.

The flux condition on the top surface is given by

$$-k\frac{\partial v}{\partial z} = \frac{Q}{\pi a^2} H(a - r) \cos \omega t$$

where H (a-r) is the step function, Q is the power, a is the radius of the spot and ω is the angular frequency. Ultimately, the spot radius a is shrunk to zero so that it becomes a point source and hence the details of the intensity distribution across the beam radius can be neglected. The real part of

$$\begin{aligned} -k\frac{\partial v}{\partial z} &= \exp[-i\omega t]\frac{Q}{\pi a^2}H(a-r) \\ &= \exp[-i\omega t]\frac{Q}{\pi a}\int_0^\infty J_1(\lambda a)\,J_0(\lambda r)\,d\lambda \end{aligned} \tag{5}$$

represents the flux and the discontinuous integral is Weber's well-known result. The boundary condition on the bottom surface, z = A, is

$$\frac{\partial u}{\partial z} = 0 \tag{6}$$

so the heat loss there is neglected.

Only the steady periodic behavior is of interest and it is easily verified that forms of the type $f(\lambda)\exp[\pm\eta z]\,J_0(\lambda r)\exp[-i\omega t]$ satisfy the heat flow equations given in Eqns. (3a, b) where f (λ) is an arbitrary function of λ and where

$$\eta = \sqrt{\lambda^2 + p^2} \qquad \text{with} \qquad p^2 = -\frac{i\omega}{\alpha} \tag{7}$$

The complex temperatures can then be represented by the integrals

$$v(r,zt) = \exp[-i\omega t]\int_0^\infty \left[E(\eta)\cosh\eta z + F(\eta)\exp[-\eta z]\right]J_0(\lambda r)\,\lambda\,d\lambda \tag{8a}$$

$$u(r,zt) \;=\; \exp[-i\omega t]\int_{0}^{\infty} D(\eta)\cosh\eta(A-z)\,J_0(\lambda r)\,\lambda\,d\lambda \tag{8b}$$

where the real parts are of interest here. The boundary condition in Eqn. (6) is satisfied by Eqn. (8b). The coefficients E (η), F (η) and D (η) (which depend only upon η), are found using Eqns. (4a), (4b) and (5); they are

$$\begin{aligned} F(\eta) &= \frac{Q}{k\pi n}\,\frac{J_1(\lambda a)}{\lambda a} \sim \frac{Q}{2k\pi\eta} \qquad \text{as } a \to 0 \\ D(\eta) &= \frac{Q}{2k\pi\eta}\left[\frac{1}{\sinh\eta A + 2A\,\rho\eta\,\sinh\eta B\,\sinh\eta C}\right] \\ E(\eta) &= \frac{Q}{2k\pi\eta}\left[\frac{e^{-\eta B}\left(\sinh\eta A + 2A\,\rho\eta\,\sinh\eta B\,\sinh\eta C\right) - \sinh\eta C}{\sinh\eta B\left(\sinh\eta A + 2A\,\rho\eta\,\sinh\eta B\,\sinh\eta C\right)}\right] \end{aligned} \tag{9}$$

where C = B – A. The term in Eqn. (8a) corresponding to the coefficient F (η) represents the temperature caused by a periodic point source at the origin in an infinite half space. The influence of the interface and the "images" generated by the top and bottom surfaces are given by the coefficient E (η). If the interface is perfectly conducing i.e. $\rho = 0$, the integral can be found in series form and is identical to the result obtained by using the method of images where point sources are symmetrically placed along the z axis. In general, for $\rho \neq 0$, it is necessary to resort to numerical integration of Eqns. (8a) and (b). In the experiments, the temperatures on the top and bottom surfaces are of special interest. These are given by

$$v(r,0,t) \;=\; \exp[-i\omega t]\left\{\frac{Q}{2\pi k}\,\frac{\exp[-pr]}{r} + \int_{0}^{\infty} E(\eta)\,J_0(\lambda r)\,\lambda\,d\lambda\right\} \tag{10a}$$

$$u(r,A,t) \;=\; \frac{Q}{2\pi k}\exp[-i\omega t]\left\{\int_0^\infty \frac{J_0(\lambda r)\,\lambda\,d\lambda}{\eta(\sinh\eta A + 2A\,\rho\eta\,\sinh\eta B\,\sinh\eta C)}\right\} \tag{10b}$$

Both of these expressions are in the form of complex numbers and the temperature is given by the real part. For example the complex temperature on the bottom can be written as

$$u(r,A,t) \;=\; |u(r,A,t)|\exp[-i(\omega t-\phi)]$$

and the phase lag is the argument ϕ of the complex portion given by the {...} brackets.

2.3 Determination of Thermal Diffusivity ($\rho = 0$)

In the absence of an interface (ρ=0), the phase lag is determined by the thermal diffusivity, α. For the purpose of determining α, it is convenient to measure the temperature on the top surface (e.g. P_1 in Fig. 2). In this case, the integral in Eqn. 10 can be evaluated as an infinite series, yielding the result

$$v_0(r,0,t) = \frac{Qe^{-i\omega t}}{2\pi k}\sum_{n=0,\pm2,\pm4,\ldots}\frac{\exp[-\beta(1-i)\,R_n]}{R_n} \tag{11}$$

where $R_n = \sqrt{r^2 + n^2\,A^2}$. This result is equivalent to that obtained from the method of images, using a line of image sources placed along the z-axis with the sources located symmetrically at intervals of 2A so as to satisfy the adiabatic conditions at $z = 0$ and $z = A$. The quantity given by the summation is denoted S and can be written as

$$S \;=\; |S|\,e^{i\phi} \;=\; \sum_{n=0,\pm2,\pm4\ldots}\exp\left[\frac{-\beta(1-i)\,R_n}{R_n}\right] \tag{12}$$

where ϕ is the phase lag with respect to the input source.

Figure 3(a) shows the variation in ϕ with βr for various values of r/A. When $r/A << 1$, the term corresponding to $n = 0$ in Eqn. (12) dominates. This situation is identical to that of a point source in an infinite body, wherein the phase lag is simply $\phi = \beta r$. For larger values of r/A, the image sources contribute progressively more to the sum. When $r/A >> 1$, the behavior resembles that of a *line* source along $z = 0$. The summation can then be approximated by

$$S \rightarrow \frac{1}{A}\int_0^\infty \frac{e^{-\beta(1-i)r\sqrt{1+\varsigma^2}}}{\sqrt{1+\varsigma^2}}\, d\varsigma = \frac{K_o(\beta(1-i)\,r)}{A} \qquad (13)$$

where K_o is a modified Bessel function of the second kind of order zero. This solution is also shown on Fig. 3(a). It provides a good approximation to the point source solution for $r/A \geq 1$ and low values of βr. Furthermore, using the asymptotic properties of the Bessel function, the phase lag tends to

$$\phi \;=\; \beta r + \pi/8 \qquad (14)$$

for high values of βr, as shown in Fig. 3(a).

Solutions for the phase lag at other locations on the specimen can be derived in a similar manner. For example, the temperature along the bottom surface can be written as

$$u_o(r,A,t) \;=\; \frac{Qe^{-i\omega t}}{2\pi k} \sum_{n=\pm1,\pm3,\pm5\ldots} \frac{\exp[-\beta(1-i)R_n]}{R_n} \qquad (15)$$

and the phase lag then obtained from the argument of the summed series. Some numerical results for the phase lag along the bottom surface are presented in Fig. 3(b).

2.4 Effect of Interface Resistance on the Phase Lag

In the presence of an interface with a finite conductance ($\rho \neq 0$), the phase lag is larger than it is in the pristine material. This lag can be measured and interpreted most conveniently on the bottom surface directly beneath the heat source (point P_0 in Fig. 2). Here the case where the interface is at the mid-plane, i.e. $B = C = A/2$, is considered. The expression for u (0, A, t), from Eqn. (10b), is

$$u(0,A,t) = \frac{Q}{2\pi k}\exp[-i\omega t]\left\{\int_0^\infty \frac{\lambda\, d\lambda}{\eta\left(\sinh\eta A + A\rho\eta\{\cosh\eta A - 1\}\right)}\right\} \quad (16)$$

This integral was solved using Simpson's parabolic formula. For the limiting case where $\rho = 0$ the results of this numerical integration were identical to those obtained using the series in Eqn. (15). Fig. 4 shows the variation in phase lag ϕ with βA ($= \sqrt{\pi f/\alpha}\ A$) for values of ρ ranging from 0 to 10^3.

Approximate solutions for the phase lag ϕ at high and low frequencies have been obtained as described below and here an alternate form for the integral in Eqn. (16) is given. By defining the two quantities

$$\begin{aligned} \sigma &= pA = \beta A(1-i) \\ X &= \eta A \end{aligned} \quad (17)$$

the integral can be rewritten as

$$u(0,A,t) \;=\; \frac{Q}{2\pi k A}\exp[-i\omega t]\left\{\int_{\sigma}^{\infty} \frac{dX}{\sinh X + \rho X(\cosh X - 1)}\right\} \tag{18}$$

which has been obtained by the change in variable.

2.4.1 High Frequency Behavior ($\beta A > 2$)

At sufficiently high frequencies, the magnitude of pA becomes large so that the hyperbolic terms can be replaced by exponentials. This is a reasonable approximation for $\beta A > 2$. The integral in (16) can be rewritten as

$$u(0,A,t) \sim \frac{Q\,e^{-i\omega t}}{\pi k A}\int_{\sigma}^{\infty} \frac{\exp(-X)\,dX}{1+\rho X} = \frac{Q\,e^{-i\omega t}}{\pi k A}\,\frac{\exp(1/\rho)}{\rho}\,\mathrm{Ei}(Y) \tag{19}$$

where

$$Y = \sigma + 1/\rho \tag{20}$$

and

$$\mathrm{Ei}(Y) = \int_{Y}^{\infty} \frac{\exp(-X)}{X}\,dX \tag{21}$$

Ei (Y) is the exponential integral whose properties are well known. For example, Ei (Y) ~ e^{-Y}/Y when $|Y| >> 1$, and Ei (Y) ~ -ln (Y) when $|Y| << 1$. For intermediate values of Y, the integral must be evaluated using known algorithms: the Taylor series for small values of Y and the method of continued fractions for large values of Y. In this limit, the phase lag is given by

$$\phi = \arg\{\mathrm{Ei}(Y)\} \tag{22}$$

Eqn. (22) is reasonably accurate in the domain $\beta A > 2$, as shown by the dotted lines in Fig. 4.

A further approximation can be made when $Y = \sigma + 1/\rho$ becomes large, either at very high frequencies ($\beta A >> 1$) or when the interface resistance is low ($\rho \to 0$). From an experimental viewpoint, the measurement of temperature is difficult at very high frequencies because the penetration depth is small and hence the signal decays rapidly with distance; consequently, the case of practical interest is the one in which $\rho \to 0$. The exponential integral then becomes

$$\mathrm{Ei}(Y) \sim \frac{\rho}{(1+\rho\sigma)} \exp\left[-\left(\sigma + \frac{1}{\rho}\right)\right] \tag{23}$$

and the corresponding phase lag is

$$\phi \sim \beta A + \arctan\left(\frac{\rho\beta A}{1+\rho\beta A}\right) \approx \beta A(1+\rho) \tag{24}$$

This is a useful formula because it reveals the first order effect of the interface upon the phase lag. It becomes increasingly more accurate as ρ becomes small compared with unity.

2.4.2 *Low Frequency Behavior* ($\beta A \leq 0.1$)

There is a singularity in the phase lag near $\beta A = 0$ as $\rho \to \infty$; the phase lag jumps from 0 to $\pi/2$ over the approximate range $0 < \beta A < 1\sqrt{\rho}$, as shown below.

The origin of this jump can be explained in the following way. Differentiating u in Eqn. (18) with respect to σ yields the expression

$$\frac{\partial u(0,A,t)}{\partial \sigma} = -\left(\frac{Qe^{-i\omega t}}{2\pi kA}\right)\left(\frac{1}{\sinh\sigma+\rho\sigma(\cosh\sigma-1)}\right) \tag{25}$$

The quantity in the denominator of the last term near $\sigma = 0$ becomes

$$\sinh\sigma + \rho\sigma[\cosh\sigma-1] \sim \frac{\sigma}{2}\left(1+\sigma^2(1+3\rho)/6\right) \tag{26}$$

For a prescribed value of ρ, it is possible to let $\sigma \to 0$ so that the first term $(\sigma/2)$ becomes dominant and consequently the integral exhibits a logarithmic singularity. However, for sufficiently large values of ρ, the second term soon dominates, such that the dominant term after integration is σ^{-2}; the argument of this term is $\pi/2$. This occurs when the magnitude of $\sigma^2 \rho$ becomes large compared with unity, or equivalently, when $\beta A >> \sqrt{\rho}$. Indeed, this is the phase lag obtained for large values of ρ near $\beta A = 0$.

Inserting Eqn. (26) into the denominator of Eqn. (25) and integrating gives

$$u(0,A,t) \sim \frac{Qe^{-i\omega t}}{2\pi kA}\ \ln\left(1+\frac{6}{(1+3\rho)\,\sigma^2}\right) \tag{27}$$

The resulting phase lag is

$$\phi \sim \arctan\left\{\frac{2\arctan\mu}{\ell n(1+\mu^2)}\right\} \tag{28a}$$

where

$$\mu = \frac{3}{(\beta A)^2 (1+3\rho)} \tag{28b}$$

The low frequency approximation (Eqn. 28) is shown on Fig. 4 by the dotted lines. It is accurate in the domain $\beta A \leq 0.1$.

3. EXPERIMENTS

3.1 Thermal Diffusivity

The utility of the phase lag technique in determining thermal diffusivity was evaluated using a stainless steel alloy with known thermal properties # (Table I). The experiments were performed using the apparatus shown schematically in Fig. 5. The apparatus consists of a 0.5 W diode laser, mounted on a precision x-y-z translation stage with a precision of ~10 µm, and modulated with a lock-in amplifier. The measurements were made on a steel disk with a 34 mm diameter and 2.5 mm thickness. A type T thermocouple was affixed to the surface at the center of the disk using epoxy. The same surface was coated subsequently with a thin layer of carbon in order to reduce its reflectivity. The phase lag at the thermocouple location was obtained by comparing the laser input signal with the thermocouple signal using the lock-in amplifier. Phase lag measurements were made at frequencies ranging from ~0.05 – 2.6 Hz, and at three distances from the thermocouple location: 1.5, 2.0 and 2.5 mm.

To increase the absorption of the incident laser beam, the samples were coated with a sputtered carbon layer that was less than 0.1 µm in thickness. Assuming that the carbon layer is amorphous, a conservative lower-limit estimate for the thermal

---

# Obtained from the NIST Standard Reference Materials Program.

diffusivity is on the order of 10^{-6} m^2/s. Hence, the upper limit for the phase difference due to the bulk of the carbon layer is about 0.2 mrad at a frequency of 1 Hz. This is negligible compared to the phase difference measured for the bulk samples. The interface between the carbon layer and the underlying sample could also pose a thermal resistance. However, since the interface is chemically bonded, it is expected that this resistance would be much lower than that of the bulk sample studied in this paper.

The experimental results are plotted in Fig. 6. They are presented in the form of phase lag *differences*, $\Delta\phi$, obtained at two locations, separated by a distance Δr. (The use of the phase lag at only one location leads to a small systematic error because of the thermal resistance of the thermocouple/steel contact. This effect is eliminated when calculating the difference between two phase lag measurements at the same frequency.) Also shown on the figure are the computed curves, using the analysis presented in Section 2.3 and the reported thermal diffusivity of the alloy ($\alpha = 3.8 \times 10^{-6}$ m^2/s). Excellent correlations are obtained between the calculated curves and the experimental measurements.

3.2 Thermal Conductance of Interfaces

The effects of interfaces were studied using a series of model systems comprising two circular stainless steel disks, each ground and polished to a final thickness of 1.25 mm. The disks were polished to produce a unidirectional lay and the surface roughness measured orthogonal to the polishing direction using a Sloan Dektak II profilometer. The RMS value of the surface roughness was determined to be 0.42 μm.

Various types of "interfaces" were produced between the two disks. The first was obtained by simply clamping together the disks with two binder clips, with the polishing directions of the two surfaces oriented perpendicular to one another. The force associated with the clips was measured to be ≈ 50N and the calculated average pressure was 0.015 MPa. The top surface was coated with a thin layer of carbon and a thermocouple subsequently attached to the bottom surface. The laser was focused on the top surface, directly above the thermocouple. Phase lag measurements were made over the frequency range 0.05 to 1 Hz. For comparison, a parallel series of measurements at the same frequencies was made on the pristine sample with the same total thickness (2.5 mm). The differences in phase lags in the two specimens at each frequency were used to determine the interface conductance. In order to change the interface conductance, thin sheets of a commercial linear low density polyethylene (LLDPE), ~13 μm thick, were placed between the steel disks, the disks clamped together and the phase lag measurements repeated. Specimens containing 1, 2 and 4 polyethylene sheets were characterized.

Figure 7(a) shows the variation in the phase lag, $\Delta\phi_i$, associated solely with the interface, along with the calculated curves that give the best fit to the data*. The trends in the calculated phase lag with frequency for a fixed interface conductance closely follow the ones obtained experimentally. This self-consistency provides confidence in both the theoretical results and the measurement technique. The variation in the effective interface resistance, 1/h, with the number of polyethylene sheets is plotted in Fig. 7(b). The trend is linear (with the exception of the point at n = 0, corresponding to the contact between the two steel disks), and can be rationalized in the following way.

The effective thermal resistance of the interfacial region in the presence of the polyethylene sheets can be partitioned into three components:

---

* The assumed interface condition in Eqn. 4 neglects the thermal mass of the interfacial region. Strictly, this condition is not satisfied for the cases in which the polyethylene sheets are inserted between the stainless steel disks, because of their finite thermal mass. An analysis that incorporates this effect is presented in the Appendix. It demonstrates that, for the present system, the phase lag is altered by < 3% when the finite thermal mass is taken into account.

$$\frac{1}{h} = \frac{2}{h_{p/s}} + \frac{n-1}{h_{p/p}} + \frac{n t_p}{k_p} \qquad (29)$$

where n is the number of sheets. The first term represents the resistance associated with the two interfaces between the polyethylene and the stainless steel, each with a conductance $h_{p/s}$; the second is the resistance of the polyethylene/polyethylene interfaces, with each interface having a conductance $h_{p/p}$; and the third is the resistance of the polyethylene itself, with t_p being the thickness of one sheet and k_p the thermal conductivity of the polyethylene. For the purpose of comparing this model with the data in Fig. 7(b), Eqn. 29 is re-written as

$$\frac{1}{h} = \left[\frac{2}{h_{p/s}} - \frac{1}{h_{p/p}}\right] + n\left[\frac{t_p}{k_p} + \frac{1}{h_{p/p}}\right] \qquad (30)$$

The resistance is predicted to increase linearly with n, which agrees well with the measured trend. Upon performing a linear regression analysis of the data and using the reported value for k_p (Table I) along with Eqn. 30, the relevant conductances were determined to be $h_{p/p} = 3.0\text{x}10^4$ W/m^2 K and $h_{p/s} = 2.1\text{x}10^4$ W/m^2 K. By comparison, the measured conductance of the steel/steel interface is $h_{s/s} = 1.1\text{x}10^4$ W/m^2 K.

The ranking of the three conductance values can be rationalized on the basis of surface roughnesses and the elastic/plastic properties of the constituent phases. Notably, because of the roughness of the stainless steel disks and the high modulus and strength of the steel, the interface conductance $h_{s/s}$ is expected to be the lowest of the three. The polyethylene has extremely low modulus and yield stress and will readily deform locally upon contact with the steel, yielding a more conductive interface ($h_{p/s} > h_{s/s}$). Indeed, the measured values yield a ratio $h_{p/s}/h_{s/s} \approx 2$.

Moreover, because of the smooth surfaces of the polyethylene sheets, the thermal contact between the polyethylene sheets is expected to be better yet. This, too, is in agreement with the experiments ($h_{p/p}/h_{p/s} \approx 1.5$).

At the most rudimentary level, the absolute value of the conductance of the steel/steel contact can be rationalized on the basis of the surface roughness, assuming that heat flow occurs by conduction through the air gap between the two surfaces. (The latter assumption can be justified on the basis of the very low pressures used in clamping the two disks together and thus the low area fraction of contacting asperities.) Thus the interface conductance is predicted to be

$$h \approx k_a / \delta \tag{31}$$

where k_a is the thermal conductivity of air at ambient temperature (0.024 W/mK) and δ is the RMS separation between the two surfaces. Taking this separation to be approximately twice the RMS roughness of one of the two surfaces, the resulting predicted conductance is $h_{s/s} \approx 2.9 \times 10^4$ W/m^2 K, which is of the same order as the measured value of 1.1×10^4 W/m^2 K.

4. CONCLUDING REMARKS

The present technique of periodic heating and phase lag measurement provides a relatively simple and quick determination of both the thermal diffusivity of solids and the thermal conductance of cracks and interfaces. The phase lag measurements used for thermal diffusivity determination are most readily interpreted when both the penetration depth of the thermal wave (the inverse of the wave number, β) and the distance between the thermocouple and the heating source are small compared to the dimensions of the specimen (e.g. thickness). In this limit, the phase lag is related to the thermal diffusivity through a simple quadratic equation. For other cases, solutions can be obtained for the phase lag in terms of the specimen geometry, the modulation frequency and the thermal diffusivity of the material, by solving the heat flow equations subject to the appropriate boundary conditions. Analogous solutions can be obtained for test specimens or structures containing interfaces or cracks, thus providing quantitative information about the thermal conductance of the defects. It is expected that the analysis could be extended to evaluate the thermal diffusivity of the constituent phases in multilayered systems.

ACKNOWLEDGMENTS

Funding for this work was provided by an ARPA AASERT Award (Contract No. DAAH04-94-G-0374) along with ONR Contract No. N00014-97-1-0394.

REFERENCES

1. A. Hirschman, J. Dennis, W. Derksen, and T. Monohan, "An Optical Method for Measuring the Thermal Diffusivity of Solids", *International Developments in Heat Transfer,* Part IV, ASME, New York, 1961, pp. 863-869.

2. A. Rosencwaig and A. Gersho, "Theory of the Photoacoustic Effect with Solids", *Journal of Applied Physics,* **47** [1] 64-69 (1976).

3. A. Rosencwaig, "Theoretical Aspects of Photoacoustic Spectroscopy", *Journal of Applied Physics,* **49** [5] 2905-2910 (1978).

4. K.D. Maglic, A. Cezairliyan, V.E. Peletsky, Compendium of Thermophysical Property Measurement Methods, Volume 1 Survey of Measurement Techniques, Plenum Press, New York, 1984, pp. 299-456.

5. O. Pessoa, Jr., C.L. Cesar, N.A. Patel, H. Vargas, C.C. Ghizoni, and L.C.M. Miranda, "Two-beam Photoacoustic Phase Measurement of the Thermal Diffusivity of Solids", *Journal of Applied Physics,* **59** [4] 1316-1318 (1986).

6. M. Reichling and H. Gronbeck, "Harmonic heat flow in isotropic layered systems and it's use for thin film thermal conductivity measurements", *Journal of Applied Physics,* **75** [4] 1914-1922 (1994).

7. T. Kemp, T.A. Srinivas, R. Fettig, and W. Ruppel, "Measurement of Thermal Diffusivity of Thin Films and Foils Using a Laser Scanning Microscope", *Review of Scientific Instruments,* **66** [1] 176-181 (1995).

8. L. Fabbri and P. Fenici, "Three-dimensional Photothermal Radiometry for the Determination of Thermal Diffusivity of Solids", *Review of Scientific Instruments,* **66** [6] 3593-3600 (1995).

9. D. DeVecchio, D. Russel, and P. Taborek, "Measurement of Thermal Diffusivity of Small, High Conductivity Samples Using a Phase Sensitive Technique", *Review of Scientific Instruments,* **66** [6] 3601-3605 (1995).

10. S. D. Preston, "A review of techniques for measuring the thermal diffusivity of thin films and coatings", *High Temperatures - High Pressures,* **27/28** 111-134 (1995/1996).

11. X.Y. Yu, L. Zhang, and G. Chen, "Thermal-wave Measurement of Thin-film Thermal Diffusivity with Different Laser Beam Configurations", *Review of Scientific Instruments,* **67** [6] 2312-2316 (1996).

12. D.P. Almond and P. M. Patel, Photothermal Science and Techniques, Chapman & Hall, London, 1996.

13. J. Opsal and A. Rosencwaig, "Thermal-Wave Depth Profiling: Theory", *Journal of Applied Physics,* **53** [6] 4240-4241 (1982).

14. J.P. Monchalin, J.L. Parpal, L. Bertrand, and J.M. Gagne, "Thermal Contact Probing by the Photoacoustic Effect", *Applied Physics Letters,* **39** [1] 391-393 (1981).

15. P.K. Kuo, L.D. Favro, L.J. Inglehart, R. L. Thomas and M. Srinivasan, "Photoacoustic phase signatures of closed cracks", *Journal of Applied Physics.* **53** [2] 1258-1260 (1982)

16. K.R. Grice, L.J. Inglehart, L.D. Favro, P.K. Kuo and R.L. Thomas, "Thermal wave imaging of closed cracks in opaque solids", *Journal of Applied Physics.,* **54** [11] 6245-6255 (1987)

17. T.M. Yonushonis, R.J. Sanford, T. Ahmed, L.D. Favro, P.K. Kuo and R.L. Thomas, "Infrared thermal wave imaging of thermal barrier coatings for diesel applications", *American Ceramic Society Bulletin,* **71** [8] 1191-1202 (1992)

18. L.D. Favro, P.K. Kuo, R.L. Thomas and S.M. Shepard, "Thermal wave imaging for aging aircraft inspection", *Materials Evaluation,* **51** [12] 1386-1389 (1993).

19. M. G. Cooper, B. B. Mikic, and M. M. Yanovich, "Thermal Contact Conductance" *International Journal of Heat and Mass Transfer,* **12** 279-300 (1969).

20. L. S. Fletcher, "Recent Developments on Contact Conductance Heat Transfer", *ASME Journal of Heat Transfer,* **110** 1059-1070 (1988).

21. C. V. Madhusudana and L. S. Fletcher, "Solid Spot Thermal Conductance of Zircaloy-2/Uranium Dioxide Interfaces", *Nuclear Science and Engineering,* **83** 327-332 (1983).

22. M. Williamson and A. Majumdar, "Effect of Surface Deformations on Contact Conductance", *ASME Journal of Heat Transfer,* **114** 802-810 (1992).

23. H. S. Carslaw and J. C. Jaeger , Conduction of Heat in Solids, Second edition, Clarendon Press, Oxford, UK, 1986.

24. K. R. McDonald, F. W. Zok, J. R. Dryden and A. Majumdar, "The Thermal Conductance of Delamination Cracks in a Fiber-reinforced Ceramic Matrix Composite", in preparation (1997).

25. I.N. Sneddon, The Use of Integral Transforms, McGraw-Hill, New York, 1972.

26. J. G. Hust and A. B. Lankford, "Standard Reference Materials 1460, 1461 and 1462: Austenitic Stainless Steel Thermal Conductivity and Electrical Resistivity as a Function of Temperature from 2 to 1200 K", National Bureau of Standards Certificate, May 1984.

27. R. J. Crawford, Plastics Engineering, Second edition, Pergamon Press, Oxford, UK, 1987, p. 33.

28. R. Campbell, personal communication, Holometrix, Inc., Beford, MA.

APPENDIX

Effect of the Thermal Mass of the Interphase on the Phase Lag

The analysis presented in Section 2 is based on the assumption that the interfacial region (or *interphase*) has no thermal mass. This leads to the two interface conditions given by Eqn. (4); notably, the heat flux just above the interface is equivalent to that just below it, and that the temperature drop across the interface is (k/h) du/dz. In the model experiments involving the polyethylene sheets, the interphase has a finite thermal mass and the interface conditions of Eqn. (4) are not strictly valid. However, as demonstrated below, the magnitude of the error that is introduced in neglecting the thermal mass of the interphase is small for the range of frequencies used in making the present measurements.

The effects of the thermal mass of the interphase on the phase lag across the specimen have been addressed by performing a one-dimensional heat flow analysis of the sandwich specimens, treating the interphase as a finite layer that is in intimate contact with the surrounding matrix slabs. The geometry is shown in Fig. A1. The thickness of the interphase is L and each of the matrix slabs is of thickness, B. Heat flow is in the z-direction. The relevant thermal properties of the two phases are the volumetric specific heat, c, the thermal conductivity, k, and the thermal diffusivity, α. (Naturally, only two of these three are independent.) The properties of the interphase are denoted with a subscript i and those of the matrix with a subscript m.

Following a straightforward procedure, the Laplace-transformed temperatures on the bottom and top surfaces, u_B and u_T, and their derivatives, $f_B = du_B/dz$ and $f_T = du_T/dz$, are found to be related through a matrix equation of the form

$$\begin{bmatrix} u_B \\ f_B \end{bmatrix} = \begin{bmatrix} M_{11} & M_{12} \\ M_{21} & M_{22} \end{bmatrix} \begin{bmatrix} u_T \\ f_T \end{bmatrix} \qquad \text{(A1)}$$

The determinant of the matrix M is unity and the only element required for determining the phase lag is

$$M_{22} = \cosh(qA)\,\cosh(2\rho\kappa qA) + \left(\frac{\kappa^2+1}{2\kappa}\right)\sinh(qA)\sinh(2\rho\kappa qA) \qquad \text{(A2)}$$

where $A = 2B$, $q = \sqrt{-i\omega/\alpha}$, $\rho = k_m L/2A\,k_i$ and $\kappa = \sqrt{c_i\,k_i/c_m\,k_m}$. The parameter κ represents the normalized thermal mass of the interphase. If the bottom surface is insulated, then

$$f_B = M_{21}\,u_T + M_{22}\,f_T = 0 \qquad \text{(A3)}$$

Substituting this result into Eqn. A1 and using the fact that the determinant of M is unity yields a simple relationship between the two temperatures:

$$u_B/u_T = 1/M_{22} \qquad \text{(A4)}$$

The phase lag of the thermal wave at the bottom with respect to the heat input at the top is then the argument of the complex quantity $1/M_{22}$.

If the thermal mass of the interphase is negligibly small ($\kappa \to 0$), Eqn. (A2) reduces to

$$M_{22} = \cosh(qA) + \rho qA\sinh(qA) \qquad \text{(A5)}$$

This result corresponds exactly with the interface condition in Eqn. (4).

The phase lag associated with the polyethylene sheets sandwiched between the stainless steel plates has been calculated using the material properties in Table I and the results plotted on Fig. A2. Comparisons are made between the computed phase lag taking into account the thermal mass (through Eqn. (A2)) and that which is obtained when the thermal mass is neglected (Eqn. (A5)). The results are plotted only over the frequency ranges that were used in the experiments. Over these ranges, the effects of thermal mass are small, resulting in no more than an ~ 3% increase in the phase lag. The effects would be more pronounced if either the layer thickness or frequency was greater.

Table I Thermal Properties of the Stainless Steel and the LLDPE

Material	Volumetric Heat Capacity, c (J/m^3 K)	Thermal Conductivity, k (W/mK)	Thermal Diffusivity, α (m^2/s)
Stainless Steel	3.8×10^6 [26, 28]	14.3 [26]	3.8×10^{-6}*
LLDPE	2.1×10^6 [27]	0.33 [27]	1.6×10^{-7}*

* Calculated from the other data, using $\alpha = k/c$.

FIGURE CAPTIONS

Figure 1	Optical micrograph showing a delamination crack in a unidirectional Nicalon-reinforced magnesium aluminosilicate (MAS) matrix. The crack was produced by loading an edge-notched beam in 4-point flexure.
Figure 2	A schematic of the specimen geometry.
Figure 3	Phase lag measured on (a) the top surface and (b) the bottom surface of a plate, heated at a point on the top surface. Also shown in (a) are the solutions for a line source, situated along the z-axis, as well as the asymptotic limit of the line source for large values of βr.
Figure 4	Influence of the interface conductance, characterized by the parameter ρ, on the phase lag measured across the plate at $r = 0$. The dashed lines at low values of βA are given by the approximate solutions in Eqn. (28). The dotted lines at high values of βA are the approximation of Eqn. (22). The solid lines are the exact numerical results.
Figure 5	Schematic of the experimental technique.
Figure 6	Determination of the thermal diffusivity of the stainless steel, using measurements of phase lag difference obtained from 2 locations (either 1 and 2 or 1 and 3), along with the analysis presented in Section 2.3
Figure 7	Experimental data and calculated curves for the phase lags obtained on the stainless steel sandwich specimens, showing the effects of the polyethylene sheets on (a) the phase lag, $\Delta\phi_i$, associated with the interface itself, and (b) the interface conductance. The solid line in (b) is a least squares fit of the data for $n = 1, 2$ and 4.
Figure A1	Schematic of the geometry used to assess the effects of the thermal mass of the interphase on the phase lag.
Figure A2	Variation in the predicted phase lag associated with the polyethylene sheets sandwiched between the stainless steel disks. The dashed lines are

the predictions that take into account the finite thermal mass (through Eqn. (A2)) whereas the solid ones are based on the model that neglects this effect (Eqn. (A5)).

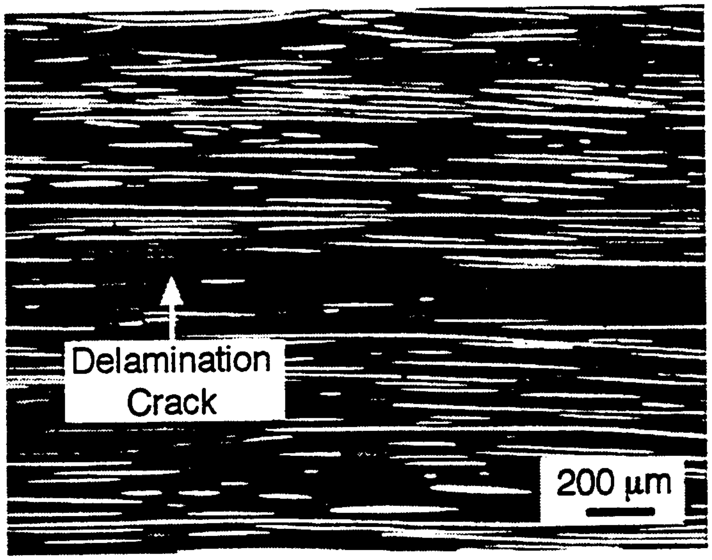
Delamination
Crack
200 µm

Figure 1

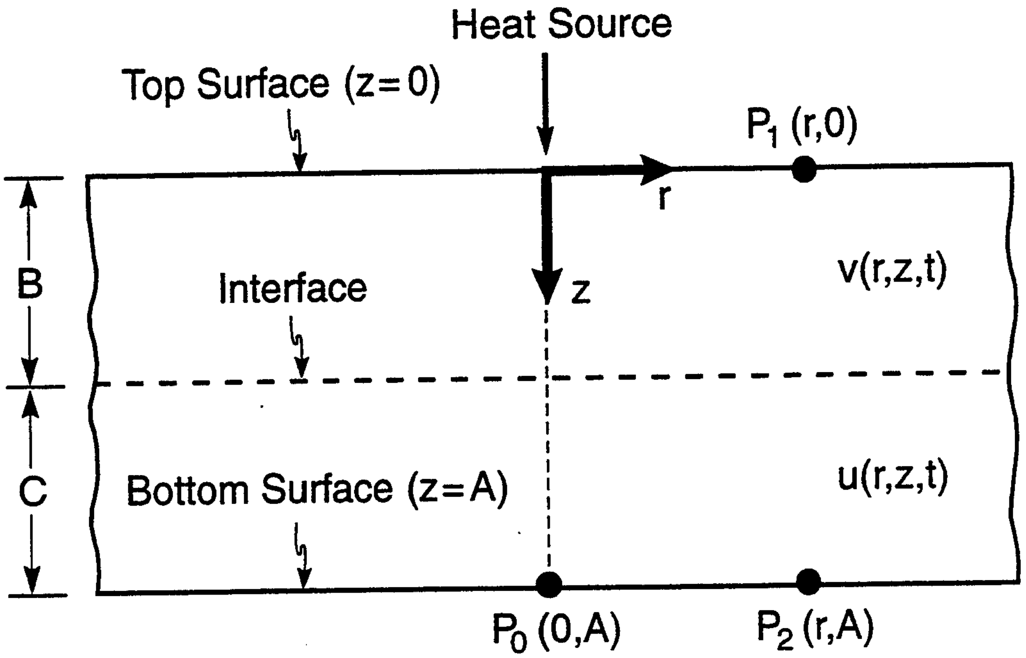
Heat Source
Top Surface (z=0)
P1 (r,0)
r
B
Interface
z
v(r,z,t)
C
Bottom Surface (z=A)
u(r,z,t)
P0 (0,A)
P2 (r,A)

Figure 2

Zok.URI•3/97•amk•D15#1896-1

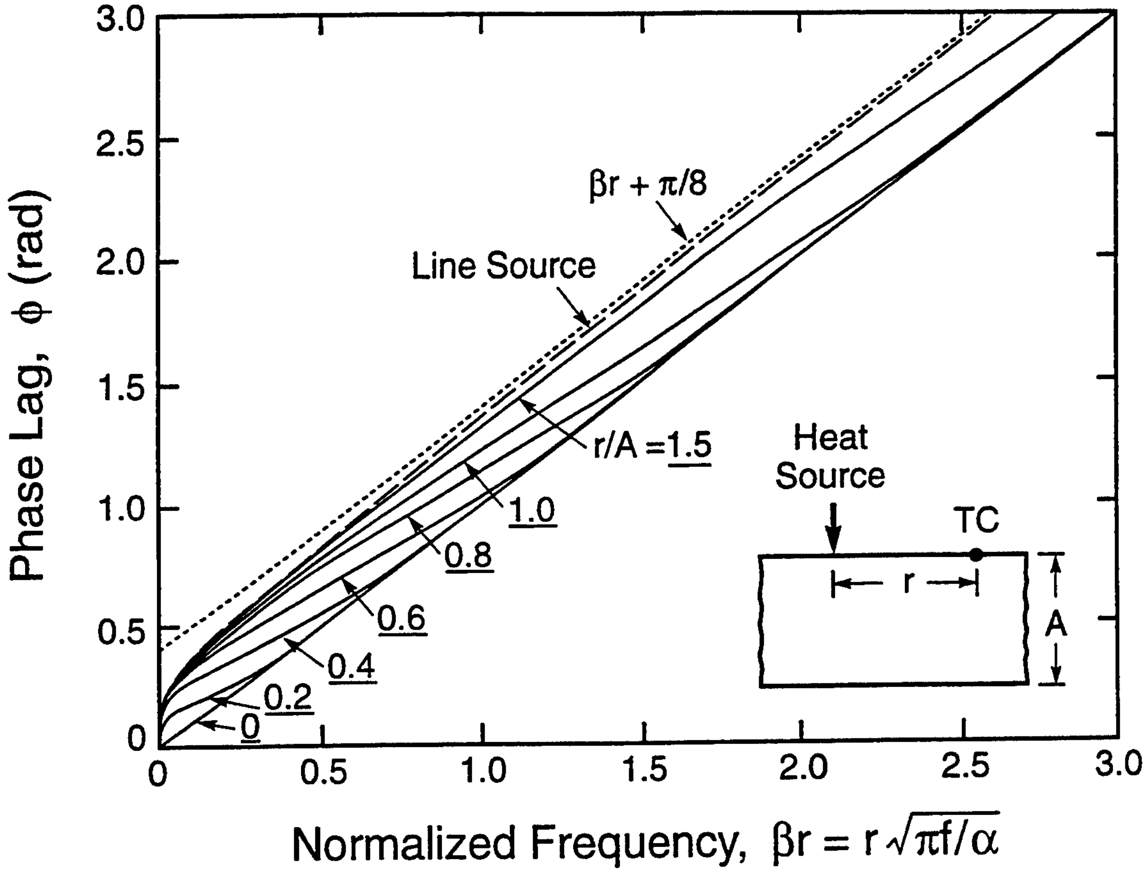

Figure 3(a)

Zok.A.URI•5/97•amk•D16#1911-1

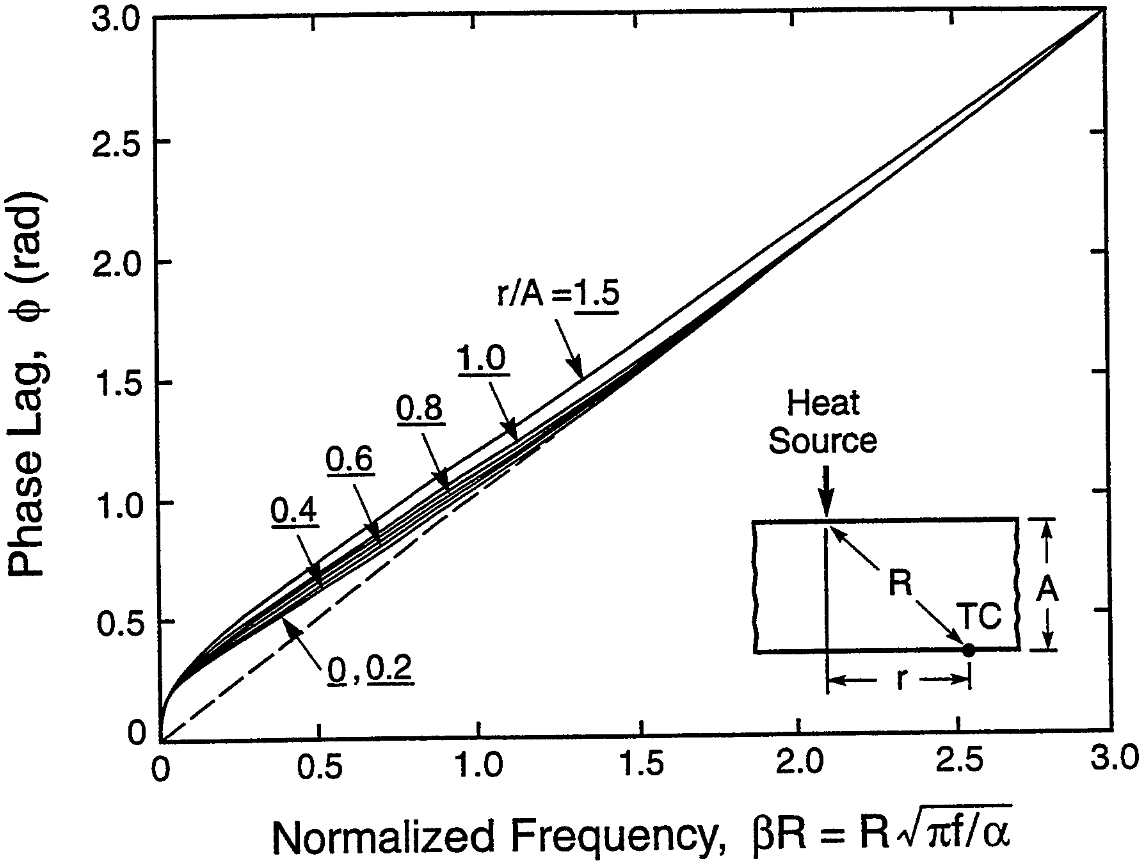

3.0
2.5
2.0
1.5
1.0
0.5
0
Phase Lag, ϕ (rad)
0
0.5
1.0
1.5
2.0
2.5
3.0
Normalized Frequency, $\beta R = R\sqrt{\pi f/\alpha}$
r/A = 1.5
1.0
0.8
0.6
0.4
0, 0.2
Heat Source
R
TC
A
r

Figure 3(b)

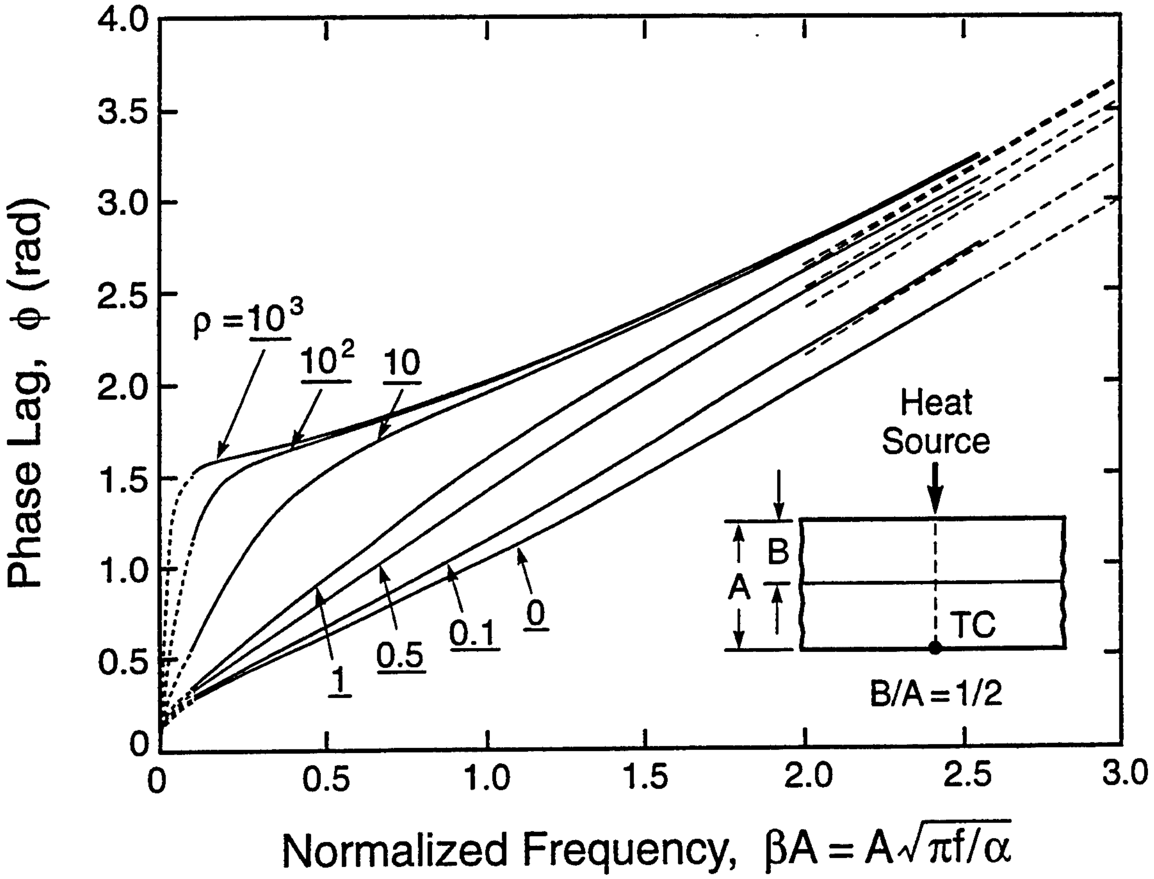

Figure 4

Zok.A.URI•5/97•amk•D16#1911-3

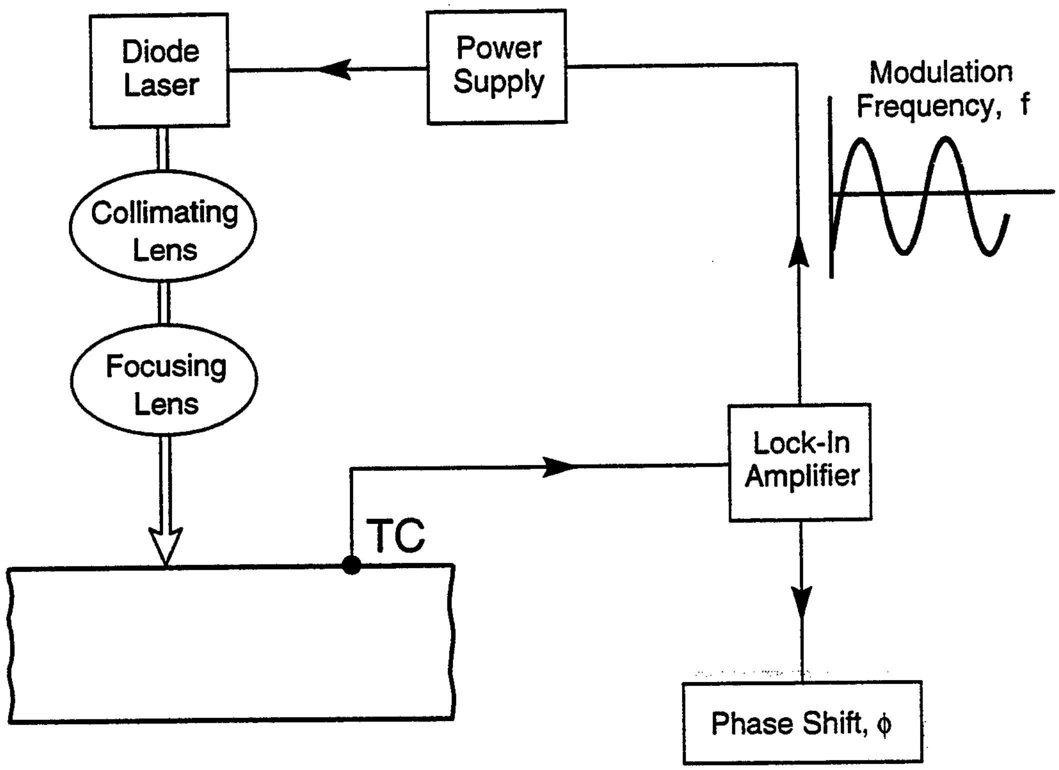
Diode Laser
Power Supply
Modulation Frequency, f
Collimating Lens
Focusing Lens
Lock-In Amplifier
TC
Phase Shift, ϕ

Figure 5

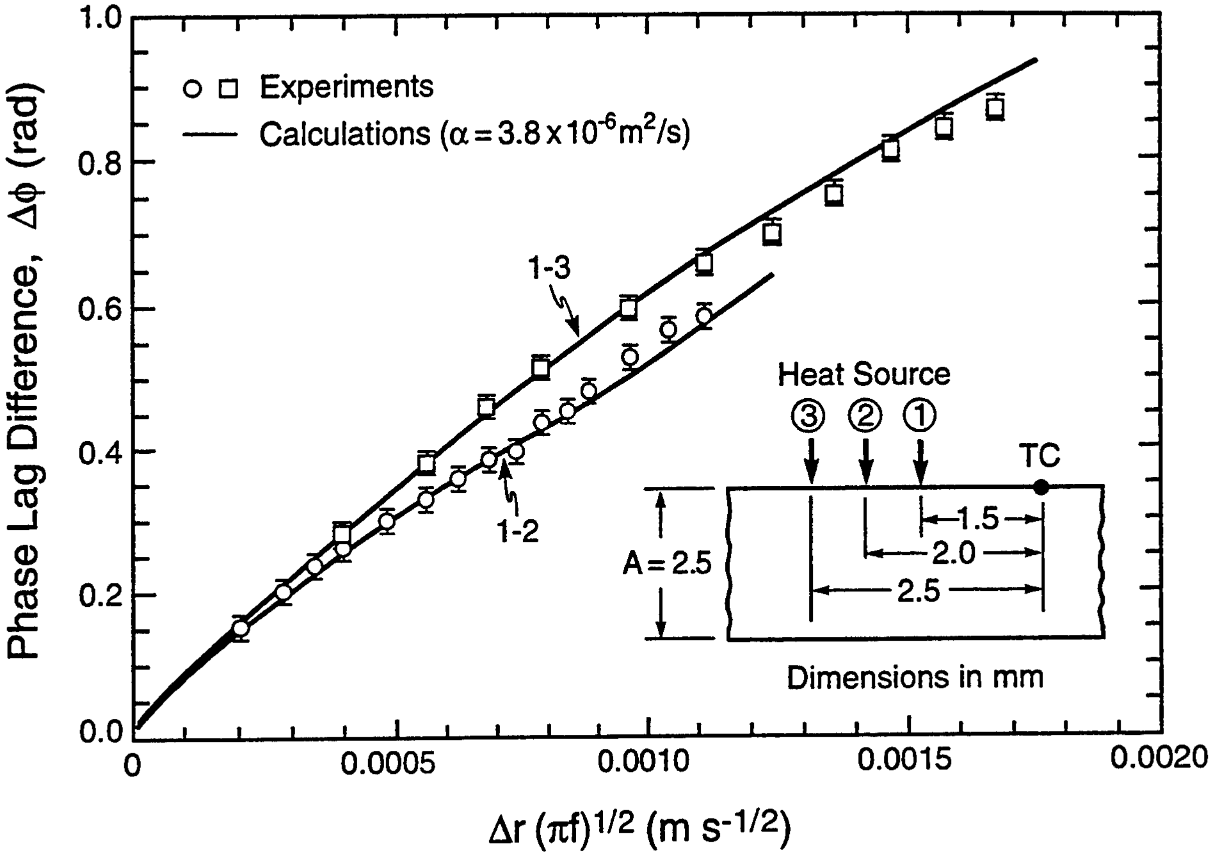

Figure 6

Zok.A.URI•5/97•amk•D16#1911-4

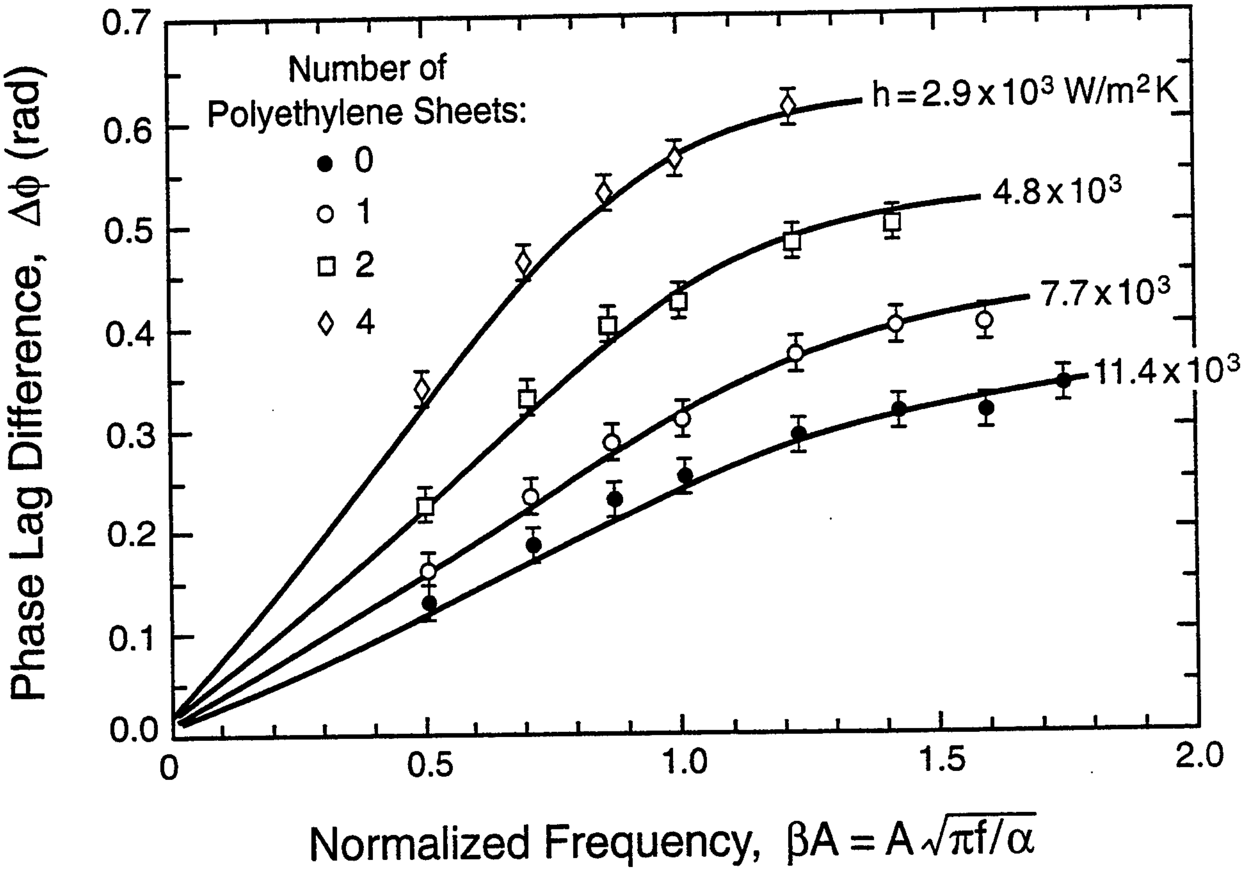

Figure 7(a)

Zok.A.URI•5/97•amk•D16#1911-5

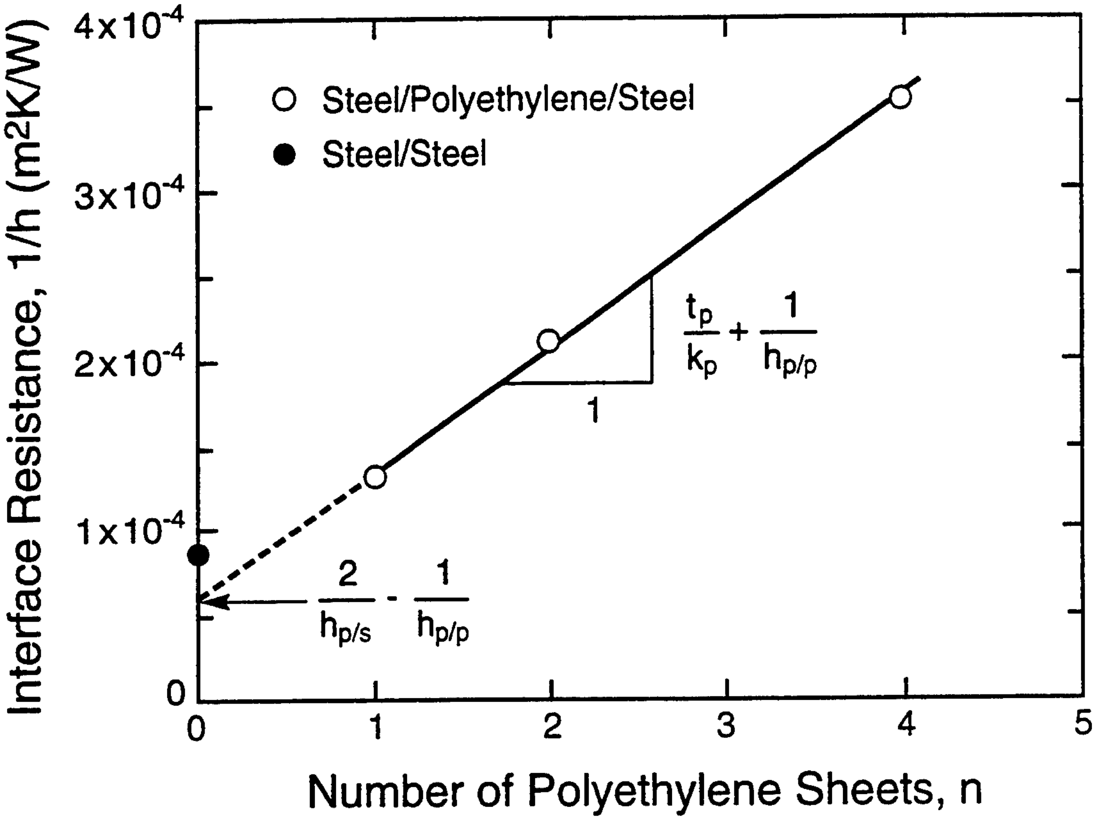

Figure 7(b)

Zok.A.URI_D16#1911-7.ps

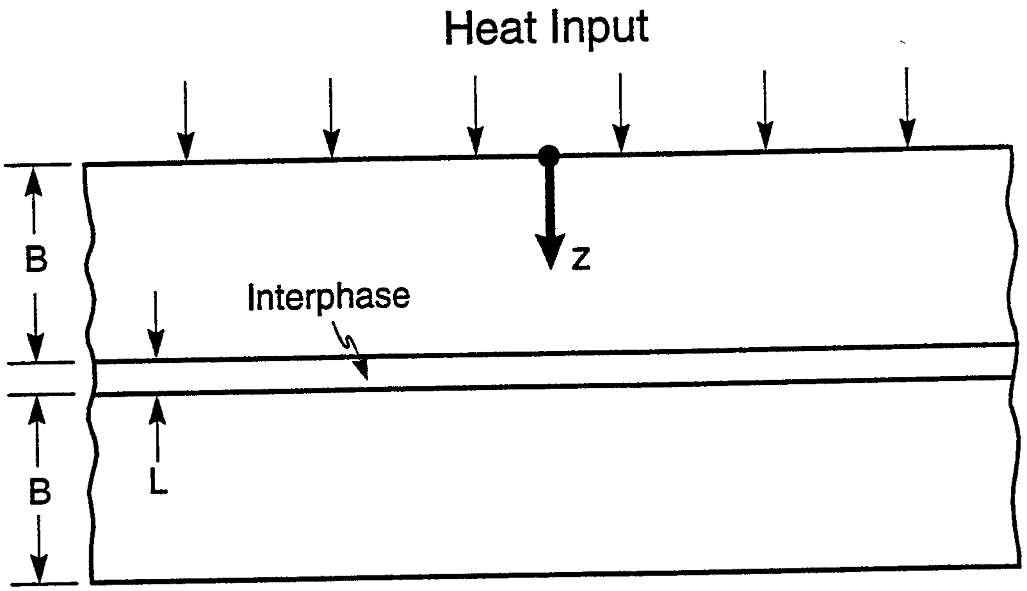
Heat Input
z
B
Interphase
L
B

Figure A1

Zok.AASERT•6/97•amk•D16#1914-1

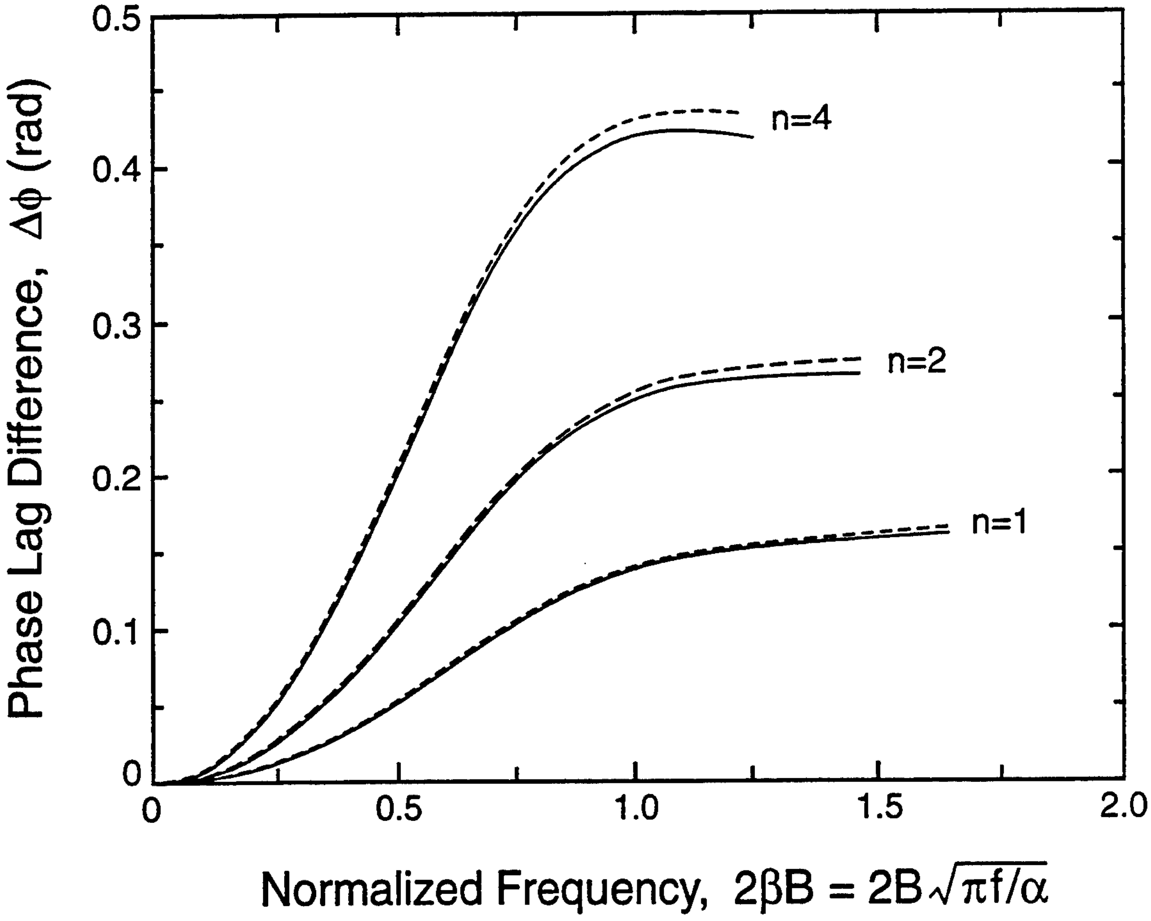

Figure A2

Zok.ASSERT.6/97•D16#1914-2

Determination of fibre strength distributions from bundle tests using optical luminescence spectroscopy

By J. He and D. R. Clarke

Materials Department, College of Engineering, University of California,
Santa Barbara, CA 93106-5050, USA

The tensile strength distribution of fibres is a key constitutive property of fibre reinforced composites and is often described using Weibull statistics. However, the standard experimental methods used for obtaining the Weibull parameters are tedious and prone to error. In this paper, Weibull parameters of polycrystalline α-Al_2O_3 fibres (Nextel 610) are determined from piezospectroscopic measurements using photostimulated Cr^{3+} luminescence (fluorescence) during fibre bundle tests. The fibre bundle stress, the stress on the surviving fibres and the survival probability can all be obtained by deconvolution of the luminescence spectra. Furthermore, a qualitative method is developed to assess whether the fibres in a bundle are aligned by monitoring the broadening of luminescence linewidth as a function of the applied load. The tensile strength distributions of Nextel 610 fibres are evaluated in the as-received condition and following heat treatments at 1000, 1200 and 1300 °C in air. The strength of fibres extracted from an Al-0.8% Mg alloy matrix composite are also characterized. The results show a significant strength degradation after heat treatment above 1000 °C with a broadening of the fibre strength distribution. The test of the extracted fibres also indicates no degradation in fibre strength during processing of a metal matrix composite (MMC) at 780 °C.

1. Introduction

Most of the thermomechanical properties, such as strength, creep and fatigue, of fibre reinforced metal and ceramic matrix composites are profoundly affected by the strength distribution of the constituent fibres (Kelly & Macmillan 1986; Curtin 1991; He *et al.* 1993). The strength properties of fibres are generally statistical in nature and are usually obtained by either of two experimental procedures. The first, the single fibre test in which, ideally, hundreds of individual fibres are tested, is tedious, requires considerable care and is prone to error due to damage when handling the individual fibres for testing especially small diameter fibres. The second method is the fibre bundle test (Chi *et al.* 1984; Phani 1988), which minimizes the amount of handling and damage.

The testing of fibre bundles has increased in popularity in recent years, since the process is much more convenient and the results are believed to be more pertinent to the actual strengths exhibited by fibres in a finished fibre-reinforced composite. However, good alignment of the fibres in the bundle is essential in order to accurately

Proc. R. Soc. Lond. A (1997) **453**, 1881–1901
Printed in Great Britain
© 1997 The Royal Society
TEX Paper

Table 1. *Reported properties of Nextel 610 alumina fibres*

property	value
composition	$> 99\%$ Al_2O_3
elastic modulus (GPa)	380–400
average thermal expansion coefficient (20–500 °C) ($°C^{-1}$)	7×10^{-6}
density ($g\ cm^{-3}$)	3.90–3.96
filaments per tow	360–420
diameter (µm)	10–12
grain size (nm)	60

determine the fibre strength distribution from bundle tests. In fact, a technique to evaluate whether the fibres are aligned within a bundle has yet to be developed. There is also almost always some variation in the actual number of fibres in a fibre tow, but generally more importantly is the fact that some fibres are damaged and fractured during shipping and handling. As a result, the actual number of load-carrying fibres in a bundle test is generally unknown and usually overestimated, which usually leads to an underestimate of the fibre bundle strength.

In this contribution we use a piezospectroscopic technique, based on the photostimulated luminescence (fluorescence) from trace Cr^{3+} impurities in α-Al_2O_3 (Grabner 1978; Ma & Clarke 1993), to determine the strength distribution of alumina fibres during the fibre bundle test. The piezospectroscopic technique has been developed in the last few years as a non-intrusive measurement of stresses and strains in alumina-containing materials and structures (Ma & Clarke 1993; Sergo *et al.* 1995; Lipkin & Clarke 1996). We show that piezospectroscopic measurements performed during fibre bundle tests provides a convenient and reliable method for the rapid acquisition of statistical data of fibre strength distributions. Although the work described utilizes Cr^{3+} luminescence piezospectroscopy and is applied to alumina fibres, the same methodology is applicable to other fibres using other spectroscopic techniques, such as Raman spectroscopy and x-ray diffraction.

Using the piezospectroscopic methodology described in the first part of this paper, a systematic study of the room temperature tensile strength distribution of Nextel 610 polycrystalline α-Al2O3 fibres (3M Corporation, St. Paul, MN) is described in the second part. Nextel 610 fibres have several unique properties (shown in table 1) which make them useful for reinforcement of metal and ceramic matrix composites, including high strength, high elastic modulus and excellent chemical and oxidative stability (Deve & McCullough 1995; McCullough *et al.* 1994). The fibres are tested in the form of a size-coated continuous tow in its as-received condition and after exposure to air at 1000, 1200 and 1300 °C for various times. The strength of fibres extracted from an Al alloy matrix composite are also characterized to establish the extent of fibre degradation during composite consolidation.

2. Theoretical background

(*a*) *Weibull statistics of a fibre bundle*

The strength distribution of brittle ceramic fibres is generally described using weakest-link statistics. In the present work it is assumed that the distribution of single fibre strength under tension follows the two-parameter Weibull function (Weibull 1951)

$$P_{\mathrm{S}}(\sigma) = \exp\left[-\frac{V}{V_0}\left(\frac{\sigma}{\sigma_0}\right)^m \right], \tag{2.1}$$

where P_{S} is the probability of survival of single fibres of volume V up to a stress σ, V_0 is a reference volume, σ_0 is the reference strength and m is the Weibull modulus. If the diameter, D, of all fibres is assumed to be the same, then equation (2.1) can be written as

$$P_{\mathrm{S}}(\sigma) = \exp\left[-\frac{L}{L_0}\left(\frac{\sigma}{\sigma_0}\right)^m \right]. \tag{2.2}$$

Here, L is the fibre gauge length and L_0 is the reference length. Note that equation (2.2) can also be related to the applied strain ε via Hooke's law, $\sigma = E\varepsilon$.

For a perfectly aligned elastic fibre bundle, initially consisting of N_0 fibres, the number of surviving fibres after an uniformly applied strain ε is

$$N_{\mathrm{S}}(\varepsilon) = N_0 \exp\left[-\frac{L}{L_0}\left(\frac{\varepsilon}{\varepsilon_0}\right)^m \right]. \tag{2.3}$$

This expression can be related to the applied tensile load on the fibre bundle as a whole by

$$F(\varepsilon) = AN_0E\varepsilon \exp\left[-\frac{L}{L_0}\left(\frac{\varepsilon}{\varepsilon_0}\right)^m \right]. \tag{2.4}$$

This expression represents the load–strain relationship for a bundle of fibres under tension, where A is the average cross-sectional area of a single fibre and E is the Young's modulus of the fibre. If the applied stress on the bundle, the bundle stress, σ_{B}, is defined as

$$\sigma_{\mathrm{B}} = \frac{F(\varepsilon)}{AN_0}, \tag{2.5}$$

then equation (2.4) can be rewritten as a relation between the bundle stress, σ_{B}, and the stress on the surviving fibres,

$$\sigma_{\mathrm{B}} = \sigma \exp\left[-\frac{L}{L_0}\left(\frac{\sigma}{\sigma_0}\right)^m \right]. \tag{2.6}$$

This equation forms the basis for the work described in this paper since the piezospectroscopic technique provides a direct measurement of the stress in the bundle and, by fitting the data obtained, equation (2.6) can be solved to determine the Weibull parameters σ_0 and m.

(*b*) *The piezospectroscopic effect and its application to fibre tests*

Alumina fibres, in common with many other alumina ceramics, contain trace levels of Cr^{3+} ions. These ions are known to substitute for Al^{3+} ions in the corundum structure of alpha-alumina. When photostimulated, the d^3 electrons are excited to a higher energy and, in relaxing back to their ground state, emit characteristic photons. The two strongest emission lines, the R1 and R2 lines, are at frequencies of 14 403 and 14 433 cm^{-1}, respectively (figure 1*a*). (This photoluminescence is the basis for the three-level ruby laser.) When the alumina crystal lattice is deformed elastically, the frequencies of the R1 and R2 lines shift, a phenomenon known as the piezospectroscopic effect. The change in frequency, $\Delta\nu$, of the fluorescence spectra can be

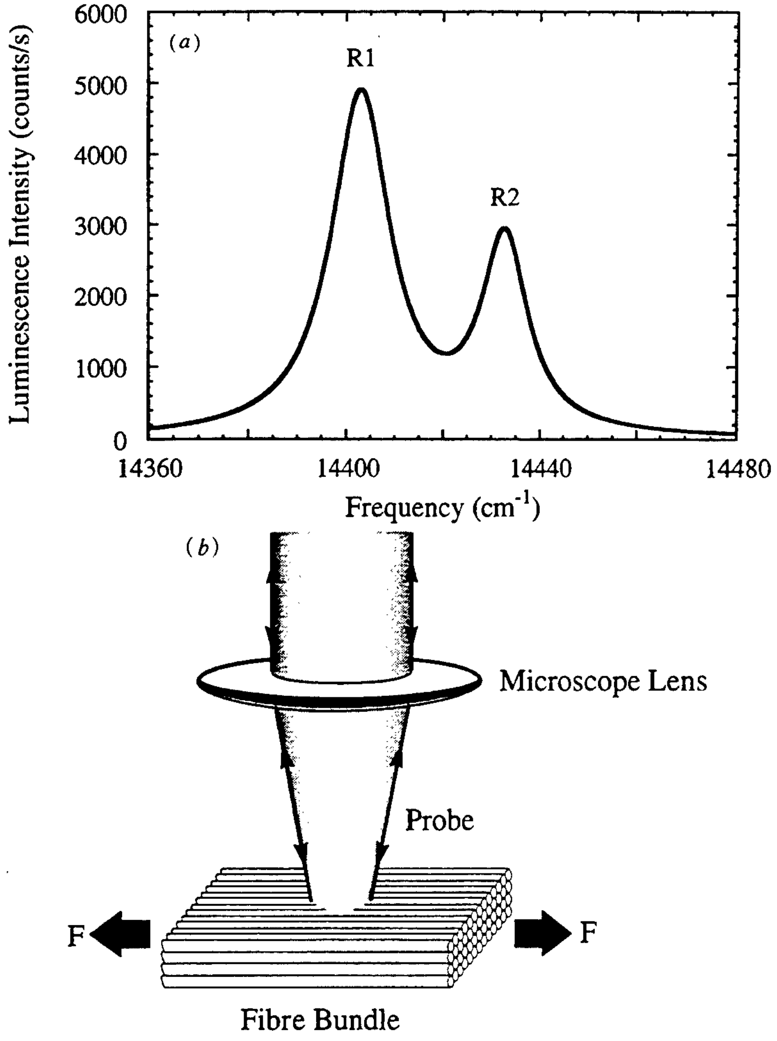

Figure 1. (*a*) R line luminescence from polycrystalline alumina fibres (Nextel 610). (*b*) Schematic arrangement for the piezospectroscopic measurement of the stresses in fibres. The size of the illuminated region, and hence the number of fibres included, depends on the size of the optical probe which can be varied by the choice of the objectve lens and the collection optics.

related to the strain state, but for many applications, including that discussed in this work, it is more convenient to relate it to stress. In the stress state formulism, the frequency shift is given by the tensorial equation (Grabner 1978; He & Clarke 1995)

$$\Delta\nu = \Pi_{ij}\sigma^*_{ij} + \Lambda_{ijkl}\sigma^*_{ij}\sigma^*_{kl} + \dots \tag{2.7}$$

where Π_{ij} and Λ_{ijkl} are the first- and second-order piezospectroscopic coefficients and σ^*_{ij} is the stress state defined in the crystallographic basis of the host alumina lattice. The full piezospectroscopic tensor, Π_{ij}, has been accurately determined for the R line fluorescence (He & Clarke 1995). Although the results verify the existence of second-order piezospectroscopic coefficients, Λ_{ijkl}, the piezospectroscopic relation for R2 line is essentially linear and the off-diagonal terms of tensor Π_{ij} for R1 and R2 lines are negligible compared with the principal terms.

For polycrystalline alumina, such as the Nextel 610 fibres, a knowledge of the crystallographic orientations of each individual grain is required for the full evaluation

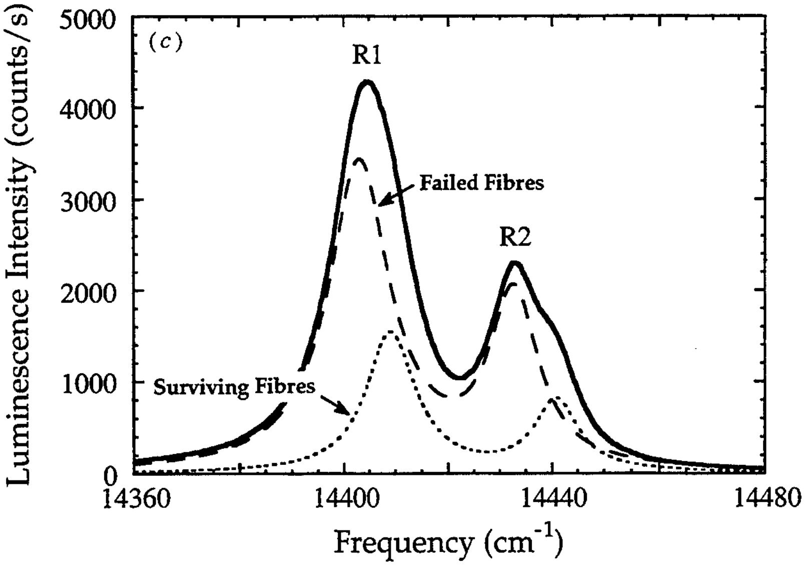

Figure 1. (*c*) R line luminescence collected during a fibre bundle test. The spectrum (shown by the solid line) consists of the luminescence signal from failed fibres, which are not under stress, as well as from the surviving fibres. Deconvolution of the two signals gives both the failure and survival probabilties.

of equation (2.7). However, although it has been demonstrated that the optical axis of an α-Al_2O_3 crystal can be determined from the intensity ratio of R1 to R2 lines (He & Clarke 1997), the optical probes used in the work described here are much larger than the grain size (*ca.* 60 nm) of the fibres investigated. Under such conditions, and in the absence of any crystallographic texture, the mean frequency shift of a fluorescence spectra can be determined by averaging equation (2.7) over all possible crystallographic orientations. The resulting frequency shift is found to only depend on the trace of the applied stress tensor averaged over the volume probed (Ma & Clarke 1993) and is given by the relation†

$$\overline{\Delta\nu} = \tfrac{1}{3}\Pi_{ii}\sigma_{jj}, \qquad (2.8)$$

where the value of the trace of the piezospectroscopic tensor Π_{ii} for the R2 line is 7.61 cm^{-1} GPa^{-1} (He & Clarke 1995). (This result is correct even for crystal structures having non-zero off-diagonal terms in their piezospectroscopic coefficient tensor (He 1996).) As a result, the frequency shift of the R2 line is proportional to the trace of the stress tensor and is used in this work.

This piezospectroscopic relationship forms the basis of the fibre bundle test shown schematically in figure 1*b* in which a bundle of fibres is strained by the application of a tensile load and the photostimulated R line luminescence recorded as a function of applied load. Since the luminescence from every Cr^{3+} ion in the fibres is indepedent, the luminescence spectra contains information, through the piezospectroscopic shift, about the stress in each individual fibre. So, provided the luminescence is simultaneously collected from a statistically significant number of fibres, analysis of the spectrum can yield information about the fibre strength distribution as described in the following.

---

† The relation was derived by Q. Ma without considering the polarization effects of the fluorescence spectra. Our recent study (He & Clarke 1997) on the R lines polarization indicates that its effect on equation (2.7) can be neglected in the case of Cr^{3+} fluorescence from polycrystalline Al_2O_3.

In addition to the relation between the mean frequency shift and the average stress, another general relationship can be established, namely that between the shape of the luminescence line and the variations in stress within the volume of material from which the luminescence is collected. (This volume is henceforth denoted the probe volume for brevity.) The material under different stresses within the probe will luminesce at different frequencies and cause an apparent peak broadening of the overall spectrum. As a result, the peak broadening is generally proportional to the variation in stress within the probe volume. The general treatment relating spectral shapes to the spatial property distribution has recently been presented by Lipkin & Clarke (1995). The effect of an arbitary stress distribution can be related to the measured peak shape by assuming that the probability of causing a frequency shift, $\Delta\nu$, can be expressed as a weighting function $W(\Delta\nu)$. Then the average peak shift is

$$\overline{\Delta\nu} = \int \Delta\nu W(\Delta\nu)\,\mathrm{d}\Delta\nu. \tag{2.9}$$

The broadening, defined as the difference between the widths of the peak from the stressed regions and from the stress free regions, is then

$$\sqrt{\langle\Delta\nu^2\rangle} = \sqrt{\int (\Delta\nu)^2 W(\Delta\nu)\,\mathrm{d}(\Delta\nu) - (\overline{\Delta\nu})^2}. \tag{2.10}$$

These relationships assume a continuous distribution in the stress variations. However, there are important instances, pertinent to the fibre bundle test in which the stress contributions from one or two regions are disproportionately large. One such example considered in the following occurs when a fibre bundle is under stress but contains a number of broken fibres.

The broadening expressed by equation (2.10) is that caused by spatial variations in stress, an extrinsic effect. This is additional to the relatively small intrinsic broadening, in fact a decrease in broadening, of about 0.4 $\mathrm{cm}^{-1}\,\mathrm{GPa}^{-1}$, that occurs on loading under constant stress. (A similiar decrease in broadening is observed with single crystal ruby in high-pressure diamond anvil cells.)

(c) *Peak shifts and broadening for a perfectly aligned fibre bundle*

In the case of a perfectly aligned fibre bundle under load, the fibres can be either intact, in which case they sustain a fixed strain, or they are broken, in which case they are stress free. As a result there are only two values of the weighting function $W(\Delta\nu)$. If expressed in terms of the fibre stress, $\sigma = E\varepsilon$, and assuming a Weibull distribution, the weighting functions are then

$$W(\sigma) = P_{\mathrm{S}}(\sigma) = \exp\left[-\frac{L}{L_0}\left(\frac{\sigma}{\sigma_0}\right)^m\right] \quad \text{and} \quad W(0) = 1 - P_{\mathrm{S}}(\sigma). \tag{2.11}$$

From equations (2.9) and (2.11), the average shift from a fibre bundle is then

$$\overline{\Delta\nu} = \tfrac{1}{3}\Pi_{ii}\sigma \exp\left[-\frac{L}{L_0}\left(\frac{\sigma}{\sigma_0}\right)^m\right] = \tfrac{1}{3}\Pi_{ii}\sigma_{\mathrm{B}}. \tag{2.12}$$

This equation provides the theoretical basis for determining the fibre bundle stress from the luminescence measurements.

Furthermore, from equations (2.10)–(2.12), the peak broadening can be expressed as a function of the stress on the surviving fibres

$$\sqrt{\langle\Delta\nu^2\rangle} = \tfrac{1}{3}\Pi_{ii}\sigma\sqrt{P_{\mathrm{S}}(\sigma)P_{\mathrm{f}}(\sigma)}, \tag{2.13}$$

where $P_S(\sigma)$ is the survival probability defined in equation (2.1) and $P_f(\sigma) = 1 - P_S(\sigma)$ is the failure probability. It should be pointed out that the broadening behaviour is analysed by assuming the increase in linewidth is solely due to the stress variations within the probed volume. In consequence, the small peak narrowing of the luminescence from polycrystalline Al_2O_3 under uniform tensile stress has been neglected.

(*d*) *Determination of the survival probability*

As discussed in the previous section, for a well aligned fibre bundle there are only two distinct stress values in the bundle after the failure of weakest fibres. Therefore, the broadening is not symmetric and the spectrum consists of two superimposed spectra, shown schematically in figure 1*c*, one from the stressed fibres and one from the failed fibres. Because the failed fibres do not bear any of the applied load, the peak frequency and linewidth are the same as for a stress-free fibre. Additionally, as mentioned above, the linewidth of the spectra from the surviving fibres is a function of tensile stress on the fibres ($-0.4\,\text{cm}^{-1}\,\text{GPa}^{-1}$). The only unknown variables in analysing the spectrum are the frequency shift from the surviving fibres and the relative intensity of the two spectra. As a result, the frequency shifts of the spectra from the surviving fibres and hence their tensile stress can be deconvoluted by fitting the collected fluorescence spectra to a combination of two sets of R line spectra, one from failed fibres and the other from surviving fibres. The survival probability, $P_S(\sigma)$, can then be directly determined from the ratio of the area under the surviving fibre spectrum to that of the overall spectrum.

(*e*) *Assessing fibre alignment*

If the fibres in the bundle are not all aligned, then in a constant load or displacement test, the strain in each fibre will not be identical. As a result, the luminescence broadening will not decrease with applied stress at $0.4\,\text{cm}^{-1}\,\text{GPa}^{-1}$ as is the case for a single fibre under tension, but rather increase as indicated by equation (2.10). In general, the degree of misalignment will not be known *a priori*. However, from a practical point of view, it is probably important only to know whether the fibres in a selected bundle are aligned or not. In a bundle of misaligned fibres, as individual fibres begin to fail, the broadening is expected to increase with applied load more than that predicted by equation (2.13). Thus, the luminescence broadening as a function of applied stress provides a direct means of assessing whether the fibres in a bundle are aligned.

(*f*) *Fibre diameter variation*

In the fibre bundle experiments described in this work, a variation in diameter of the fibres within a bundle does not cause any luminescence broadening since the mechanical testing is performed under constant displacement conditions. Variations in fibre diameter do, however, lead to a variation in the tested volume, V, of individual fibres within a constant gauge length (equation (2.1)). This, in turn, alters the survival probability from that expected for a bundle of fibres having the same diameter. The quantitative effect of variations in fibre diameter on the survival probability can be determined as follows.

For cylindrical fibres having diameters D, equation (2.1) can be rewritten as

$$P_S(\varepsilon) = \exp\left[-\frac{L}{L_0}\frac{D^2}{D_0^2}\left(\frac{\varepsilon}{\varepsilon_0}\right)^m\right], \qquad (2.14)$$

Assuming a Gaussian distribution in fibre diameter,

$$p_N(D) = \frac{1}{\sqrt{2\pi}\delta} \exp\left[-\frac{(D-D_0)^2}{2\delta^2} \right], \tag{2.15}$$

then the overall survival probability of a fibre bundle up to a strain, ε, is

$$P_{\mathrm{S}}(\varepsilon) = \int_0^{+\infty} \frac{1}{\sqrt{2\pi}\delta} \exp\left[-\frac{(D-D_0)^2}{2\delta^2} \right] \exp\left[-\frac{L}{L_0}\frac{D^2}{D_0^2}\left(\frac{\varepsilon}{\varepsilon_0}\right)^m \right] \mathrm{d}D, \tag{2.16}$$

where D_0 is the average fibre diameter and standard deviation of δ.

The survival probability $P_{\mathrm{S}}(\varepsilon)$ can then be expressed analytically in terms of the coefficient of variation, κ, of the fibre diameter and the Weibull parameters

$$P_{\mathrm{S}}(\varepsilon) = \tfrac{1}{2}\left(1 + \operatorname{erf}\left[\frac{\left(\frac{1}{\kappa}\right)^2}{\sqrt{2}\sqrt{\left(\frac{1}{\kappa}\right)^2 + 2\frac{L}{L_0}\left(\frac{\varepsilon}{\varepsilon_0}\right)^m}} \right]\right) \times \frac{\left(\frac{1}{\kappa}\right)}{\sqrt{\left(\frac{1}{\kappa}\right)^2 + 2\frac{L}{L_0}\left(\frac{\varepsilon}{\varepsilon_0}\right)^m}} \exp\left[\frac{-\frac{L}{L_0}\left(\frac{1}{\kappa}\right)^2\left(\frac{\varepsilon}{\varepsilon_0}\right)^m}{\left(\frac{1}{\kappa}\right)^2 + 2\frac{L}{L_0}\left(\frac{\varepsilon}{\varepsilon_0}\right)^m} \right], \tag{2.17}$$

where $\operatorname{erf}[z]$ is the error function and

$$\kappa = \delta / D_0. \tag{2.18}$$

Based on equation (2.17), the effect of diameter variation on the fibre bundle behaviour is proportional to the magnitude of κ. Such effect is negligible for fibres with κ value being smaller than 20%. In the case of Nextel 610 fibres, the value of κ is around 5–6%. Therefore, the diameter of fibres in the bundle can be considered to be uniform, as is done in the following analysis.

3. Experimental procedure and analysis

(*a*) *Sample preparation and heat treatments*

A Nextel 610 fibre tow treated with a polyvinylalcohol (PVA) sizing was supplied by 3M Corporation (lot number A0078-0113). The mean fibre diameter and the number, N_{tow}, of fibres in the tow were found from electron micrographs of sliced end views of aluminum-embedded samples. The mean fibre diameter was $12.1 \pm 0.7\,\mu\mathrm{m}$ (average of 186 fibres). The number of fibres in the tow was found to be 377 ± 6 by averaging over several cross sections at 2 m intervals along the tow. Piezospectroscopic measurements under unixial stress, described in the following section, were made on different portions of the tow. Some were performed on portions of the tow in its as-received condition whereas other portions were first heat treated in air. Four different heat treatments were conducted: 1000 °C for 1 h, 1200 °C for 1 h, 1200 °C for 4 h and 1300 °C for 1 h, with heating and cooling rates being 5 and 10 °C min^{-1}, respectively. Following each heat treatment, a couple of drops of 3-wt% polyvinylacetate-methanol solution were applied to each loose bundle for ease

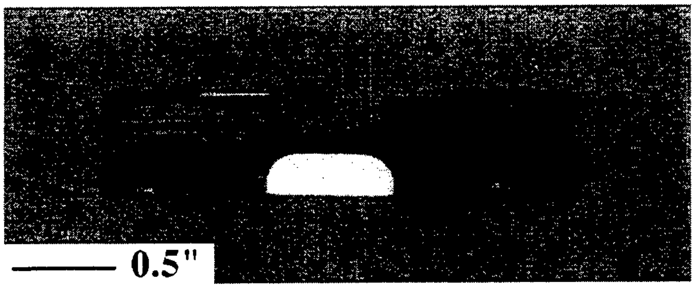

Figure 2. Optical micrograph of a number of fibre tows extracted from a Al-0.8%Mg MMC. The test specimen was prepared by preferentially etching the centre section of the matrix away from a MMC sample using 49% HF. The black appearance is given by the carbon coating on the fibres. The white feature is a piece of polycrystalline Al_2O_3 providing the structural support during handling and was removed before the bundle test. The typical thickness of the bundles was 0.4 mm and, with the neck section of 2 mm in width, they usually consist of 15–20 fibre tows.

of handling. As the alcohol solution evaporated and the epoxy hardened, the fibres in the bundle were pulled together by the increasing capillary force thereby self-aligned the fibres. Another advantage of the epoxy was that it also protected the Al_2O_3 fibres from any possible stress corrosion during the bundle tests, a phenomenon known to occur in moist air.

The strength of the fibres inside the MMC was characterized by testing fibre bundles after they were extracted from an Al-0.8% Mg alloy matrix composite by etching. The particular MMC from which the fibres were extracted was made at UCSB by squeeze casting with a peak processing temperature of 780 °C for 1 h (Cao *et al.* 1992). The matrix at the centre portion of the standard tensile test samples (dog bone geometry) were preferentially etched away by 49% HF solution with the ends of samples protected by candle wax and Teflon tapes (shown in figure 2). The gauge length of the extracted fibre bundle at the centre was 0.5 inch. A typical bundle of extracted fibres had a cross-section of $0.4 \times 2\ \mathrm{mm}^2$ and contained 15–20 fibre tows.

(*b*) *Piezospectroscopic measurements during fibre bundle tests*

The piezospectroscopic measurements were made using an optical microprobe consisting of an attached argon ion laser, operating at a wavelength of 514.5 nm, as an excitation source, and an attached spectrometer (Model T64000, Instruments SA, Edison, NJ). The laser beam was focused onto the fibres using the objective lens of the microscope and the same lens used to collect the luminescence. One of the advantages of this configuration is that the probe volume can be changed conveniently by selecting the objective lens with different magnifying power and the size of the apertures. Although the system is capable of high spatial resolution mapping down to less than 1 μm, a large probe volume is desired in the case of fibre bundle tests so as to excite fluorescence from a large number of fibres simultaneously, a sufficient large number that the results of piezospectroscopic measurements will accurately reflect the statistical nature of the fibre strength distribution.

As shown schematically by the configuration in figure 1*b*, the optical path of the system is perpendicular to the fibre axes. A 4X/0.10 Nikon objective lens was used to collect the luminescence spectra. The probed volume was determined as follows. The transverse probe profile was determined by sweeping the probe across a fibre bundle from the edge to the interior and monitoring the increase in the R line luminescence intensity. The probe response function, $B(x)$, was then deconvoluted by

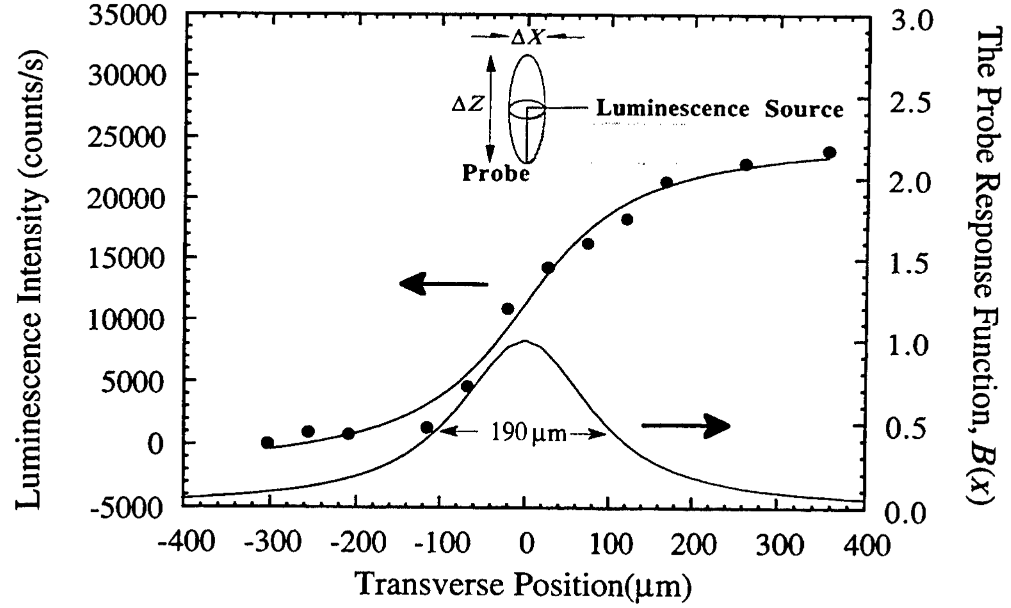

Figure 3. The experimental data for the transverse probe profile using a 4X/0.10 Nikon lens used to both illuminate the fibre bundle and collect the stimulated luminescence. The R line luminescence intensity increases as the probe sweeps across the fibre bundle from the edge to the interior as shown. The probe response function $B(x)$ is deconvoluted by differentiating the intensity profile with respect to the transverse position.

differentiating the intensity profile with respect to centre position of the probe, as shown in figure 3. Here, for convenience, the probe diameter is defined as the FWHM (full width at half maximum) of the response function. In the case of the 3M fibre bundle, the probe diameter for 4X/0.10 lens was 190 µm at 5 mW of laser power at the laser. The longitudinal probe profile or the depth of field is difficult to determine accurately, primarily because of grain boundary scattering within the polycrystalline fibres. However, an estimate can be made by comparing the R line intensity from a fibre bundle with that collected from a polished metal matrix composite (MMC) reinforced with the same fibres. The polished surface of the MMC was arranged to be parallel with the fibre axes, so the luminescence signal only came from the layer of fibres exposed to the free surface. By using the same objective lens, the luminescence intensity from the fibre bundle was more than ten times as intense as that collected from the MMC sample. Therefore, we concluded that the probe penetrates, and the signal is collected from, at least ten layers of fibres below the surface. Combining these results of the transverse and longitudinal probe size, the probe formed by the 4X/0.10 lens effectively collected luminescence from about 150 fibres, a number large enough to provide statistically significant data on the fibre strength distribution.

(*c*) *Mechanical tests of fibre bundles*

Tensile tests were conducted on a thread driven stainless steel test frame (shown in figure 4) that fits under the optical microprobe. The load was monitored using a 250 pound load cell. The ends of fibre bundles were attached to cardboard tabs, similar to those used in single filament tests, using an epoxy adhesive. To ensure good alignment, the bundle ends were placed into straight, shallow grooves that had been stamped along the centre line of the tabs. All fibre bundles were tested under 1 inch gauge length and five tests were performed in each condition. The samples of extracted fibre bundles (0.5 inch gauge length) were tested by directly mounting

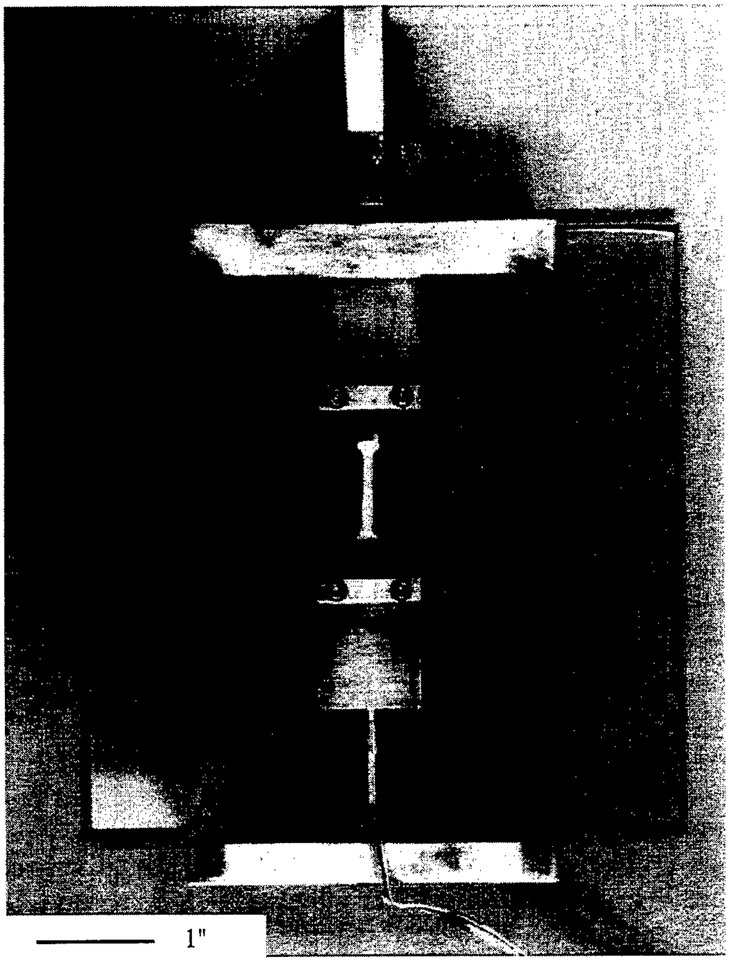

Figure 4. Optical micrograph of the stainless steel tensile test frame. The sample shown here is an extracted bundle of fibre tows as in figure 2.

the sample ends on the crossheads of the tensile frame using super glue. Tensile testing under displacement controlled conditions was chosen since this method has the advantage that as fibres break, their load is not transferred to the remaining fibres causing them, in turn, to break. As a result, the system is more stable mechanically and single fibre fracture could be investigated over a larger strain range compared with tests using a constant crosshead speed.

During the tests, a luminescence spectrum was collected with the fibres under constant tensile load with an integration time of typically 10 s. The displacement was increased incrementally and a luminescence spectrum was collected at each load. In order to explore the whole distribution of the fibre strength, extreme care was taken to ensure that the displacement, and hence load, increments were sufficiently small around the peak load so that the fibre bundle would remain stable after the load began to drop. In most of the cases, the bundle did not break until the load decreased to less than half of the maximum attainable value.

(*d*) *Determination of the fibre bundle stress*

According to equation (2.12), the average frequency shift of the luminescence R line corresponds to the bundle stress defined in equation (2.5), provided the probe includes a sufficient number of fibres. As a result, there should be a linear relation

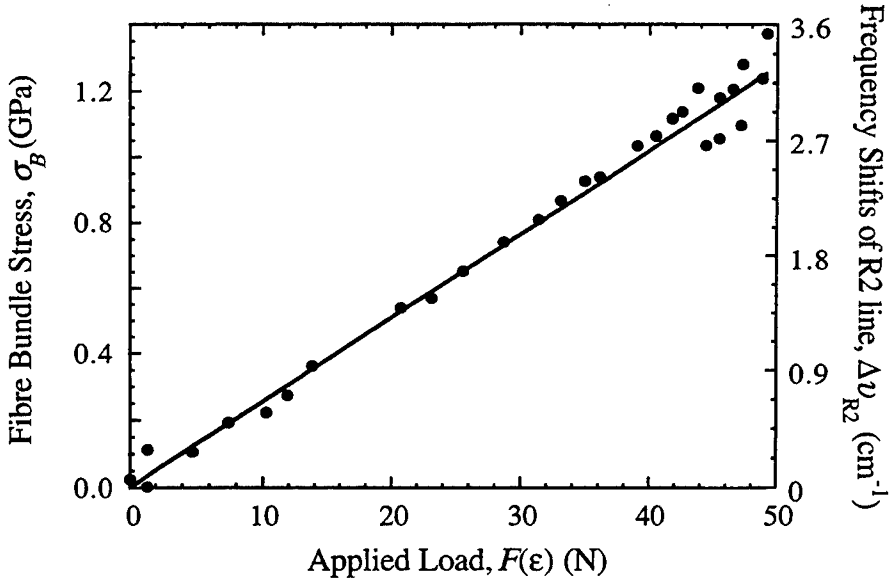

Figure 5. A typical load–stress curve for Nextel 610 fibre bundle. Here the bundle stress is deconvoluted from the average frequency shift using equation (2.8). The slope of the line corresponds to the overall cross-section of the initial load carrying fibres. Based on the average fibre diameter (12.06 μm), the number of initial load carrying fibre is 339 in this particular case, about 90% of the 377 fibres in the tow.

between mechanical load on the bundle and the value of stress deconvoluted from the piezospectroscopic measurements. This was indeed found and is shown by the linear slope of the load–stress curve plotted in figure 5. The slope is equal to the cross-section area of the bundle, AN_0, thereby enabling the initial number of load carrying fibres, as well as the extent of damage due to shipping and handling, to be evaluated by comparison with the actual number of fibres, N_{tow}, in the tow.

(e) *Peak broadening and fibre alignment*

To establish how the peak broadening changes with applied stress, the FWHM broadening of the R2 luminescence line was measured for both the as-received fibre tow as well as for a number of extracted fibre bundles from the dog-bone shaped sample. The data are shown in figures 6*a*,*b*.

As indicated, there is no peak broadening at the initial stage of loading of the as-received fibre tow and the linewidth becomes somewhat narrower with increasing load. At higher loads, substantial peak broadening occurs and the FWHM reaches a maximum after passing the peak load on the fibre bundle. As the load drops further, the linewidth decreases again and approaches the stress-free state. This set of observations is considered to be consistent with the expected behaviour of a well aligned fibre bundle under the tensile load. At first, there are no fibre failures under load, so the load is uniformly distributed through the whole bundle and consequentially the broadening should be the same as that of a single polycrystalline fibre under the same tensile stress. The decrease in the linewidth during the initial stage of bundle tests is similar to that observed from individual fibres under uniaxial tension where the value of FWHM of R lines decrease linearly as the tensile stress increases with the slope of $-0.4\ \mathrm{cm}^{-1}\ \mathrm{GPa}^{-1}$ (He 1996). With increasing load, some of the weaker fibres presumably fail. The broadening is then due to a superposition of the lines from the stressed, surviving fibres and the decreasing number of surviving fibres. As a result, the FWHM of the R lines will reach a maximum and then decrease to the stress-free

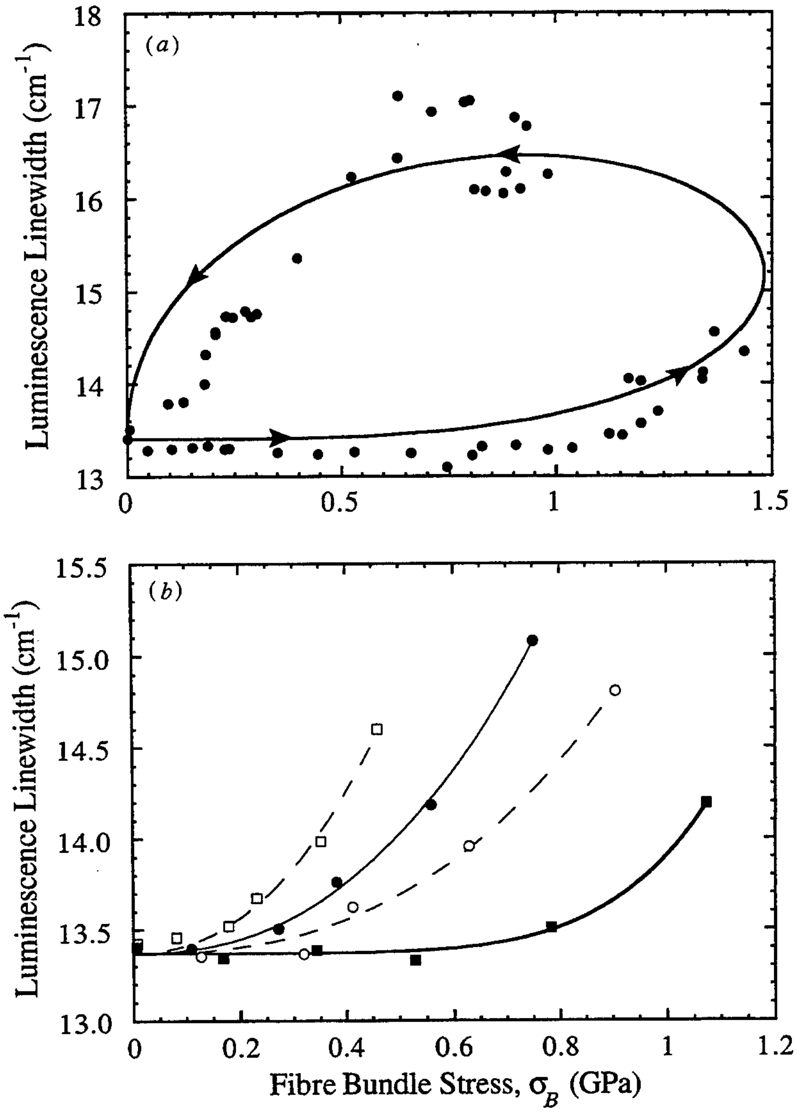

Figure 6. The broadening of the R2 line as a function of the fibre bundle stress for the as-received fibre tow (*a*) and fibre bundles extracted from the composite (*b*). In (*a*) the loading sequence is indicated by the arrows along the loop. The superimposed loop represents the broadening behaviour predicted by equation (2.12). The different symbols in (*b*) correspond to the behaviour of spectra collected from different fibre bundles.

value as the proportion of surviving fibres continues to diminish. Superimposed on the data of figure 6*a* is the broadening predicted using equation (2.13). Except for the discrepancy towards the end of the test, where notably far fewer fibres are under load, the prediction agrees reasonably well with the experimental observation.

The data from the different extracted fibre tows exhibit similiar behaviour to that of the as-recieved tow except that the onset of extensive broadening varies substantially from one tow to another. This variation is attributed to the fact that the fibres in the extracted tows are not as well aligned as in the as-received condition due to the distortions produced during the squeeze casting of the composite. During casting, the pressure infiltration of the molten matrix into the fibre bundles can disrupt the arrangement of fibres and cause both substantial weaving and bending

Table 2. *Weibull parameters of Nextel 610 fibres determined from piezospectroscopic measurements*

		heat treated				
parameter	as-received	1000 °C for 1 h	1200 °C for 1 h	1200 °C for 4 h	1300 °C for 1 h	extracted
σ_0 (GPa)	2.58 ± 0.14	2.55 ± 0.09	2.40 ± 0.03	1.75 ± 0.09	1.60 ± 0.10	
m	5.30 ± 0.50	4.20 ± 0.40	2.90 ± 0.70	6.50 ± 0.40	6.10 ± 0.90	
σ_B (GPa)	1.59 ± 0.06	1.40 ± 0.08	1.25 ± 0.09	1.10 ± 0.06	0.97 ± 0.10	1.56 ± 0.12[a]
N_0/N_{tot}	$90 \pm 5\%$					

[a] All values here are based on 1 inch gauge length. The strength for fibre bundles extracted from the MMC is calculated from results of 0.5 inch gauge length, assuming $m = 5.3$.

within each fibre bundle. As a result, when a load is initially imposed on the bundle of extracted fibres, some of the fibres are not stretched and hence do not carry any load. Therefore, in most cases, there is a stress variation within the optical probe as soon as a load is applied, causing a peak broadening as shown in figure 6*b*. However, there are some bundles in which the fibres are well aligned locally and the luminescence spectra collected from these behave similarly to the as-received fibre tow. The data obtained from one such bundle are indicated by the solid squares in figure 6*b*. The results of the extracted fibre bundle tests presented later are based on the luminescence spectra collected from these well aligned bundles.

4. Results and discussion

The strength distribution of the 3M Nextel 610 fibres obtained from the piezospectroscopic measurements of fibre tows after various heat treatments are presented in figures 7 and 8, along with that of as-received tows. Figures 7*a–e* show the data of bundle stress versus stress on the surviving fibres for the as-received tows, fibres heat treated at 1000 °C for 1 h, 1200 °C for 1 and 4 h and 1300 °C for 1 h, respectively. Figures 8*a–e* show the corresponding survival probability, $P_S(\sigma)$, determined from the luminescence intensity ratio. An interesting feature of the data is that the initial value of survival probability $P_S(0)$ is not 100%, but rather is usually between 85 and 93%. This is due to the presence of a proportion of fibres that end within the gauge length of the bundle, presumably due to fibre damage introduced during manufacture, shipping and handling. This is consistent with the observation (figure 5) that the number of initial load carrying fibres, N_0, is always smaller than 377, the total number of fibres, N_{tot}, counted in the tow. Because of this lower number of load carrying fibres, equation (2.1) has to be normalized by the proportion of initial load-carrying fibres

$$P_S(\sigma) = \frac{N_0}{N_{tot}} \exp\left[-\frac{L}{L_0}\left(\frac{\sigma}{\sigma_0}\right)^m \right]. \tag{4.1}$$

The Weibull parameters are determined by fitting the data in figures 7 and 8 using two parameter Weibull statistics shown in equations (2.6) and (4.1). The results are summarized in table 2.

In figure 9, the data of bundle stress versus stress on the surviving fibres from

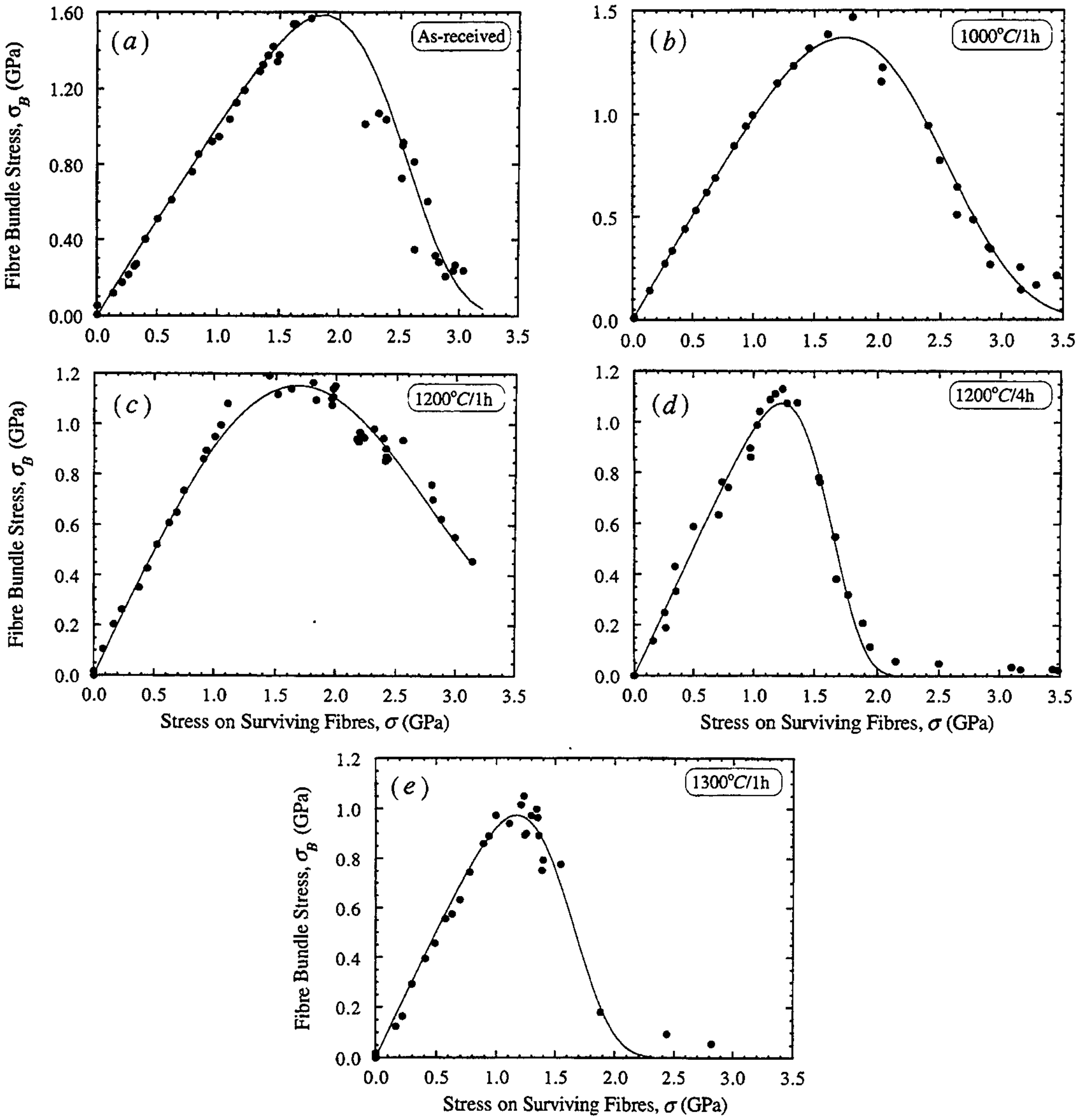

Figure 7. Bundle stress versus fibre stress data for 3M Nextel 610 fibre tows. (*a*) As received and after heat treatments at: (*b*) 1000 °C for 1 h; (*c*) 1200 °C for 1 h; (*d*) 1200 °C for 4 h; (*e*) 1300 °C for 1 h. The fitted curves are based on the two parameter Weibull function in equation (2.5) with $L = L_0 = 1$ inch.

the extracted fibre bundles are shown. As discussed in the previous section, the test results are based on the luminescence spectra collected from those well-aligned portions. In contrast to the data from the as-received and heat-treated bundles, the data do not extend much beyound the peak stress. This was due to the relatively large number of the bundles of extracted fibres used and hence the high mechanical load on the jig during testing. (We did not wish to damage the extracted fibres by trying to separate them after etching away the alloy matrix and hence it was necessary to test several bundles simultaneously.) At the highest loads, the stainless steel loading frame was somewhat compliant with the result that as fibres broke, their load was transferred to the remaining fibres leading to catastrophic failure of the fibre bundle. As a result, we are unable to determine the Weibull modulus for the extracted fibres although the bundle strength itself is well characterized, as

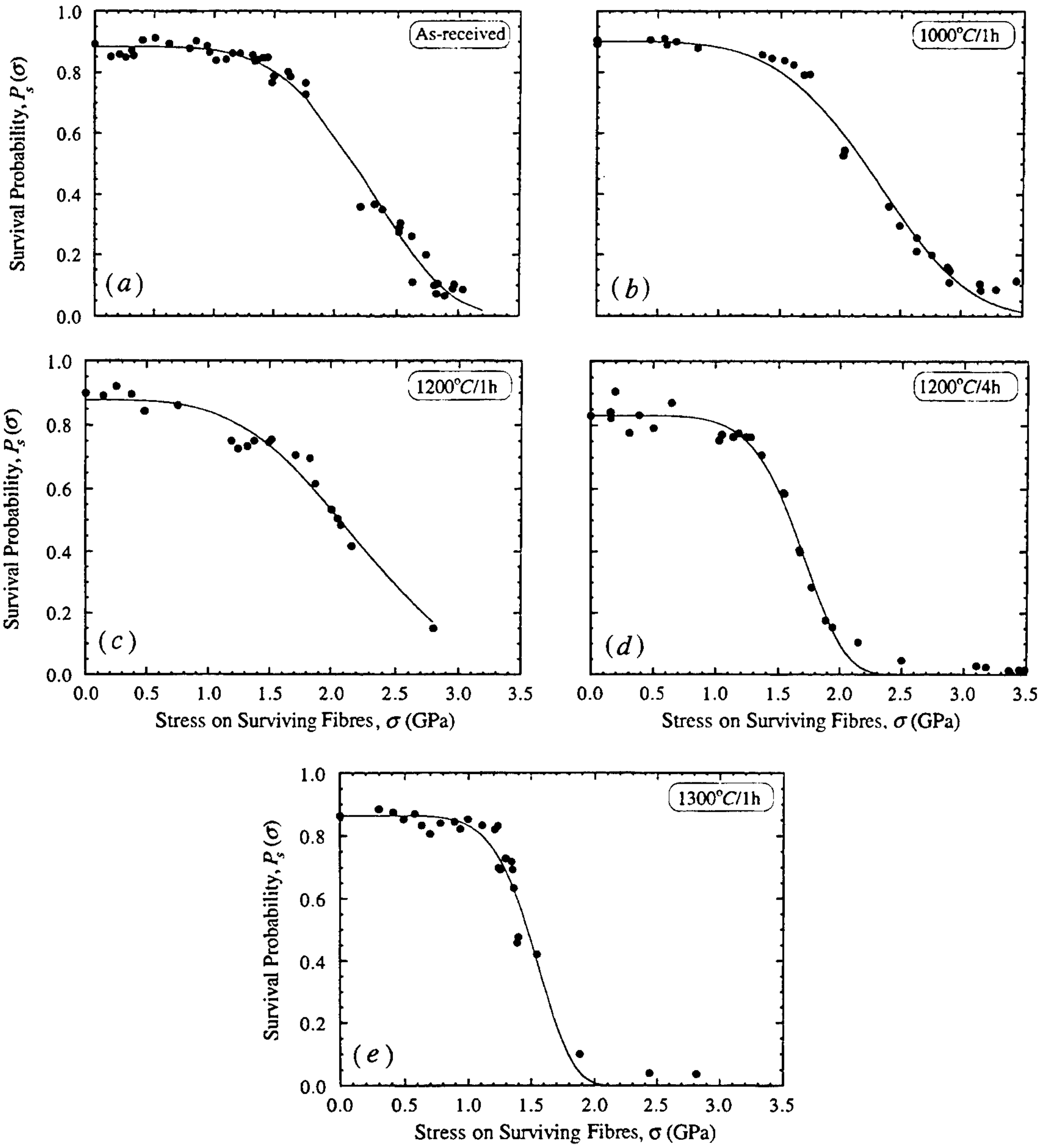

Figure 8. The fibre survival probability obtained from the luminescence intensity ratio as a function of stress on the bundle.

can be seen from the data in figure 10. Its value was 1.79 GPa at a 0.5 inch gauge length, which is similiar to the bundle strength of 1.59 GPa for as-received fibres at 1 inch gauge length (σ_B ($L = 0.5$ inch) $= 1.14\sigma_B$ ($L = 1$ inch) for $m = 5.3$). Thus, we conclude that the processing of MMC by squeeze casting at 780 °C does not cause significant degradation of the strength of Nextel 610 fibres.

The room temperature bundle strength of Nextel 610 fibres after various heat treatments in air for 1 h are summarized in figure 10. The solid line through the data is a guide to the eye but its shape suggests that greater strength degradation occurs at higher temperatures. The results clearly show that there is no loss in strength after exposure to high temperature in air up to 900 °C. This agrees with the measurements on Nextel 610 fibres made by Das (1995) indicating no strength degradation for thermal exposure at 982 °C in air for 2000 h. Strength degradation, however, becomes

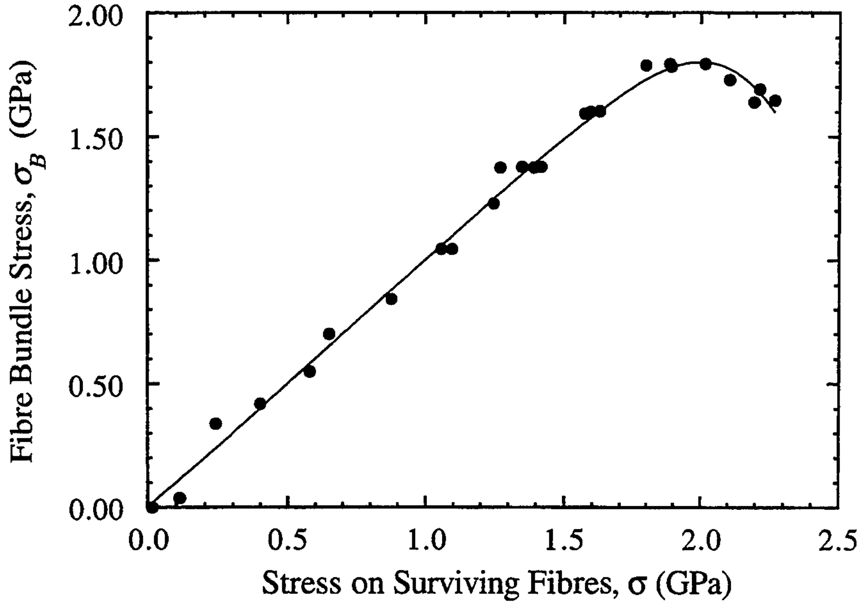

Figure 9. Bundle stress versus fibre stress data for a bundle of fibres extracted from the composite.

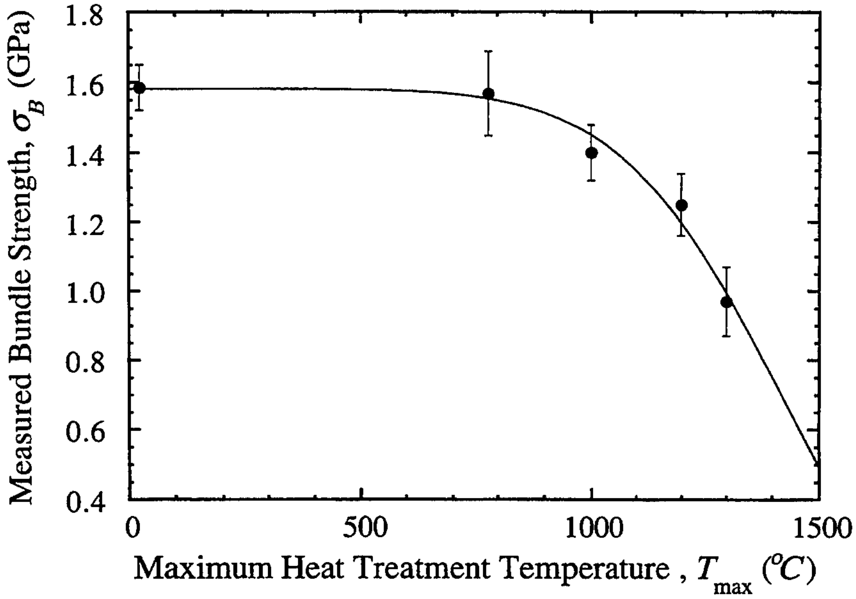

Figure 10. Fibre bundle strength at 1 inch gauge length as a function of the maximum heat treatment temperature for 1 h. The data at 780 °C are converted from the results of the extracted bundles with a guage length of 0.5 inch.

significant for heat treatment temperatures exceeding *ca.* 900 °C and increases with temperature. Nevertheless, the bundle strength at room temperature after heating to 1300 °C is still more than 50% of that of the as-received fibres.

It is interesting to compare our results on room temperature tensile strength with previous high temperature tensile strength study (Wilson *et al.* 1993) made on Nextel 610 fibres. Due to their relatively poor creep properties (Wilson *et al.* 1992), the high temperature tensile strength of 610 fibres falls precipitiously at 1300 °C. How-

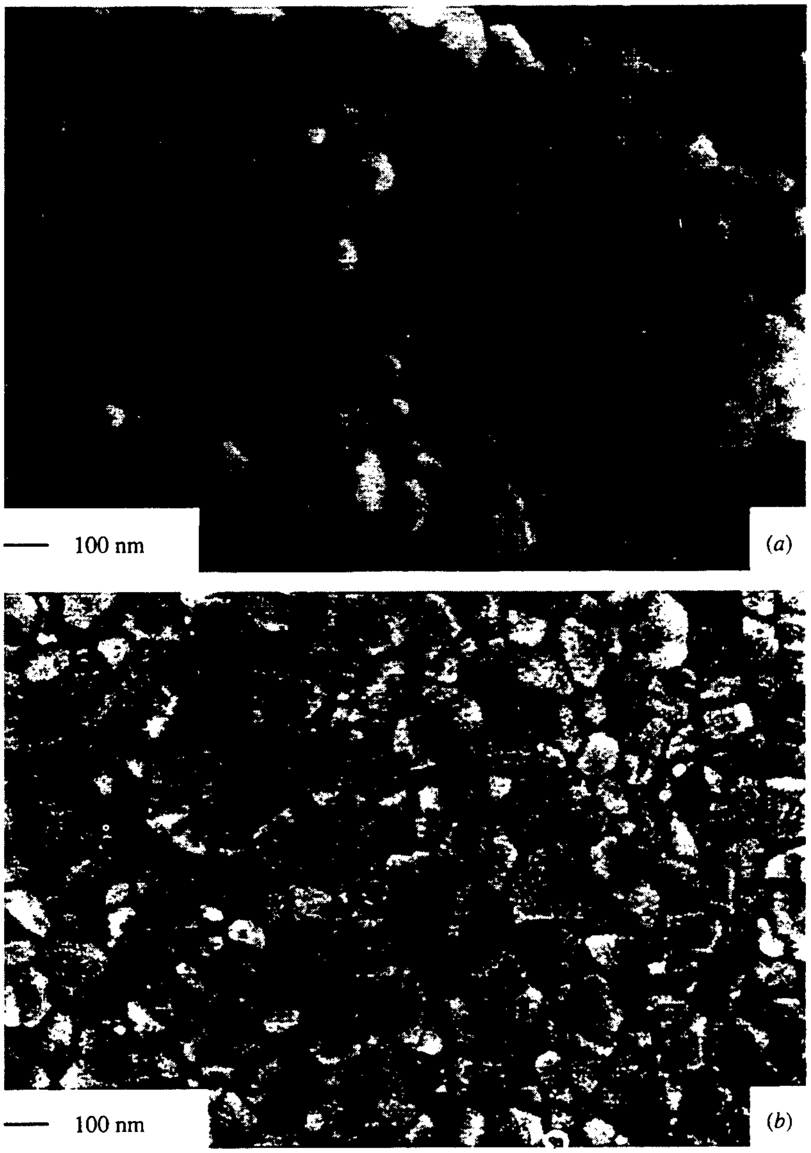

Figure 11. SEM micrographs of (*a*) fracture surface of Nextel 610 fibres in MMC and (*b*) outer surface of fibres heat treated in air at 1200 °C for 4 h.

ever, the thermal degradation on their room temperature tensile strength is mainly governed by the change in microstructure rather than the creep rate.

Examination of the data (table 2) indicates that in addition to the strength degradation, the Weibull modulus decreases from 5.3 for the as-received fibres to 2.9 for fibres treated at 1200 °C for 1 h. This indicates that the strength distribution becomes broader after the exposure to high temperature. However, the trend is reversed after annealing at high temperature (1300 °C) or for a longer period (1200 °C for 4 h). As described below, these latter changes in the Weibull modulus are probably due to the bonding between touching fibres rather than the degradation of individual fibres.

Degradation of a number of fibres as a result of high temperature annealing has been noted previously and it has been suggested that strength degradation can be due to microstructural changes such as grain coarsening and grain boundary grooving

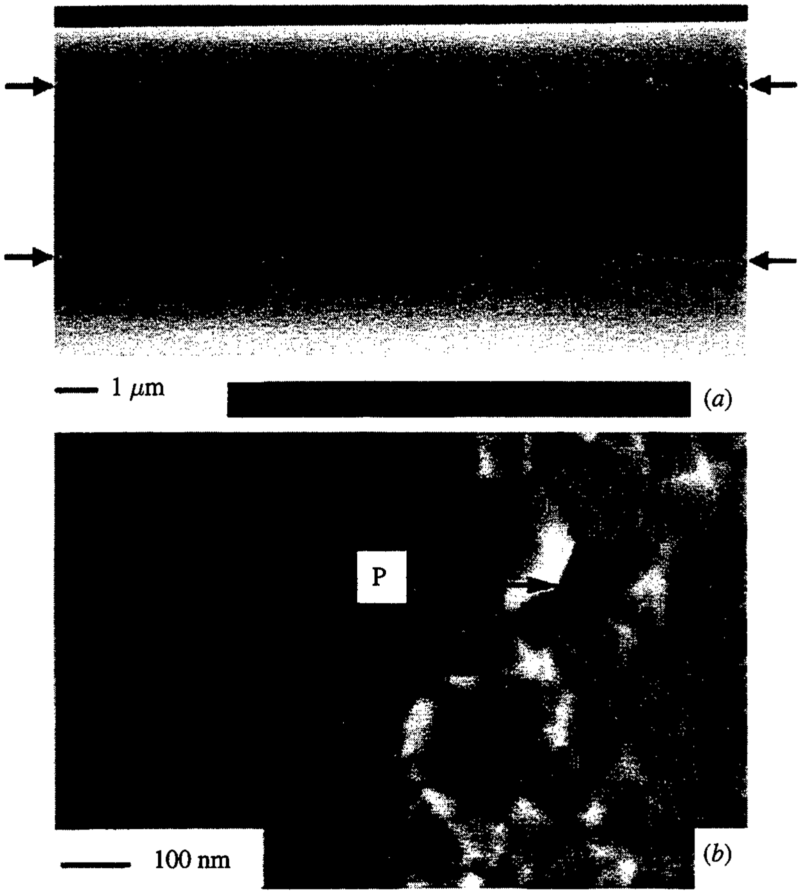

Figure 12. Low magnification (*a*) and high magnification (*b*) SEM micrographs of surface defects on Nextel 610 fibres after heating in air at 1200 °C for 4 h.

at the fibre surface. To determine whether the strength degradation we observe is due to microstructural changes we compared the microstructure of the surfaces of all the fibres. The surface of the as-received fibres was very smooth and we were unable to image individual grains or grain boundaries. In comparison, the surface of the fibres heat treated at 1200 °C for 4 h exhibited substantial grain boundary grooving. However, in comparing the grain size of the extracted fibres, which had been heated at 780 °C for 1 h (figure 11*a*), with that of the fibres that had been heated at 1200 °C for 4 h (figure 11*b*), little grain growth is evident. These comparisons would suggest that grain boundary grooving was responsible for the strength degradation but would not account for the increase in Weibull modulus after 4 h at 1200 °C and 1 h at 1300 °C.

The only difference in appearance between the fibres heated at 1200 °C for 4 h and at 1300 °C for 1 h, and those fibres heated at lower temperature and shorter times, were lines of defects running parallel to the fibre axes (figure 12*a*). Closer examination (figure 12*b*) reveals a much rougher surface morphology at these defects than elsewhere on the fibre surface. There is evidently some grain coarsening at these line defects and pores of comparable size with the pores and grains distributed irregularly along the lines of defects. Additionally, these line defects lie about 60° apart around the circumference of the fibres. Based on these observations, we believe that the line defects are the result of sintering between touching fibres at high temperature leading to the formation of necks along the line of fibre contact. When the fibres are separated, the fracture of these necks cause some grains to be pulled out leaving behind large pores. Since these line defects are formed at the same temperature as the Weibull modulus increases, it suggests that the bonding between the fibres affects the bundle strength distribution. This would be consistent with a previous study by Hill & Okoroafor (1995) which showed that interfibre friction could substantially increase the Weibull modulus determined from bundle tests. Although the interfibre friction was expected to be greatly reduced in the current study by applying drops of sizing to the fibre bundle, the necks formed during high temperature treatment could nevertheless provide moderate friction between touching fibres, leading to the observed increase in Weibull modulus of fibres treated at 1200 °C for 4 h and 1300 °C for 1 h.

5. Summary

A methodology for determining the strength distribution of polycrystalline alumina fibres from their luminescence spectra during mechanical stressing has been described. The measurements, based on the piezospectroscopic properties of alumina, sample a large number of fibres simultaneously and provides a convenient means of characterizing fibre strength. Both the bundle stress and the stress on the surviving fibres, as well as the survival probability, can be deconvoluted from optical luminescence spectra collected during fibre bundle tests. Furthermore, from the luminescence broadening during loading it is possible to assess whether the fibres are aligned with the loading direction, an essential prerequisite for an accurate bundle test.

Using the piezospectroscopic methodology, the room temperature tensile strength of Nextel 610 fibres has been studied in their as-received condition as well as after various high temperature treatments in air. It is found that the strength is retained after heat treatment in air up to 900 °C. Then, the thermal degradation of fibre strength becomes more and more severe as the heat treatment temperature is increased. The strength distribution also becomes broader. Significant grain boundary grooving is observed after fibres are heated at high temperature and it is also believed that necks start to form between touching fibres after prolonged treatment at 1200 °C and exposure to 1300 °C. In contrast, the processing of MMC at low temperature (780 °C) does not appear to cause significant strength degradation of the fibres.

The authors thank Dr H. E. Deve and Dr D. M. Wilson at 3M Corporation for helpful discussions and supplying the fibres. This work was supported by the Advanced Research Projects Agency University Research Initiative at UCSB under contract N00014-92-J-1808.

References

Cao, H. C., Yang, J. & Evans, A. G. 1992 The mode I fracture resistance of unidirectional fiber-reinforced aluminum matrix composites. *Acta Metall. Mater.* **40**, 2307–2313.

Chi, Z., Chou, T.-W. & Shen, G. 1984 Determination of single fiber strength distribution from fiber bundle tests. *J. Mater. Sci.* **19** 3319–3324.

Curtin, W. A. 1991 Theory of mechanical properties of ceramic-matrix composites. *J. Am. Ceram. Soc.* **74**, 2837–2845.

Das, G. 1995 Thermal stability of single crystal and polycrystalline alumina fibers and 85% Al_2O_3-15% SiO_2 fibers. *Cer. Eng. Sci. Proc.* **17**, 977–986.

Deve, H. E. & McCullough, C. 1995 Continuous-fiber reinforced Al composites: a new generation. *J. Metals* **47**, 33–37.

Grabner, L. 1978 Spectroscopic technique for the measurement of residual stress in sintered Al_2O_3. *J. Appl. Phys.* **49**, 580–83.

He, J. 1996 Ph.D. thesis, University of California, Santa Barbara.

He, J. & Clarke, D. R. 1995 Determination of the piezospectroscopic coefficients for chromium-doped sapphire. *J. Am. Ceram. Soc.* **78**, 1347–1353.

He, J. & Clarke, D. R. 1997 The polarization dependence of the Cr^{3+} R line fluorescence from sapphire and its application to crystal orientation and piezospectroscopic measurement. *J. Am. Ceram. Soc.* **80**, 69–78.

He, M. Y., Evans, A. G. & Curtin, W. A. 1993 The ultimate tensile strength of metal and ceramic-matrix composites. *Acta Metall. Mater.* **41**, 871–878.

Hill, R. & Okoroafor, E. U. 1995 Weibull statistics of fiber bundle failure using mechanical and acoustic emission tests: the influence of interfibre friction. *Compos.* **26**, 699–705.

Kelly, A. & Macmillan, N. H. 1986 *Strong solids*, 3rd edn. Oxford: Clarendon.

Lipkin, D. M. & Clarke, D. R. 1995 Sample-probe interactions in spectroscopy: sampling microscopic property gradients. *J. Appl. Phys.* **77**, 1855–1863.

Lipkin, D. M. & Clarke, D. R. 1996 Measurement of the stress in oxide scales formed by oxidation of alumina-formed alloy. *Oxid. Met.* **45**, 267–280.

Ma, Q. & Clarke, D. R. 1993 Stress measurement in single-crystal and polycrystalline ceramics using their optical fluorescence. *J. Am. Ceram. Soc.* **76**, 1433–1440.

McCullough, C., Deve, H. E. & Channel, T. E. 1994 Mechanical response of continuous fiber-reinforced Al_2O_3-Al composites produced by pressure infiltration casting. *Mater. Sci. Engng* A **189**, 147–154.

Phani, K. K. 1988 Evaluation of single-fiber strength distribution from fiber bundle strength. *J. Mater. Sci.* **23**, 941–945.

Sergo, V., Clarke, D. R. & Pompe, W. 1995 Deformation bands in ceria-stabilized tetragonal zirconia/alumina. I. Measurement of the internal stresses. *J. Am. Ceram. Soc.* **78**, 641–644.

Weibull W. 1951 A statistical distribution function of wide applicability. *J. Appl. Mech.* **18**, 293.

Wilson, D. M., Lueneburg, D. C. & Lieder, S. L. 1992 High temperature properties of Nextel 610 and alumina-based nanocomposite fibers. *Cer. Eng. Sci. Proc.* **14**, 609–627.

Wilson, D. M., Lueneburg, D. C. & Lieder, S. L. 1993 Microstructure and high temperature properties of Nextel 720 fibers. *Cer. Eng. Sci. Proc.* **15**, 1005–1014.

Received 12 December 1996; accepted 27 March 1997

journal

J. Am. Ceram. Soc., 80 [1] 69-78 (1997)

Polarization Dependence of the Cr^{3+} R-Line Fluorescence from Sapphire and Its Application to Crystal Orientation and Piezospectroscopic Measurement

Jun He* and David R. Clarke*

Materials Department, College of Engineering, University of California, Santa Barbara, California 93106-5050

The room-temperature polarization characteristics of the ruby R lines have been studied by monitoring the fluorescence intensity as a function of excitation direction relative to the crystallographic axes of the ruby crystal. The R lines are strongly polarized in the basal plane but have no preferred vibration direction within the basal plane. However, the degree of polarization, *P*, of the R1 and R2 lines is not the same, being P_{R1} = 87% and P_{R2} = 62%. The phenomenon is explained in terms of the absorption anisotropy and the probability of spontaneous emission. The findings provide the basis for a high-spatial-resolution spectrophotometric method to determine the optical *c*-axis of chromium-doped Al_2O_3 crystals using the angular dependence of the intensity ratio of the R2 line to the R1 line. The application to the orientation determination of sapphire fibers embedded in composites and the corresponding residual stress components are discussed together with the possibility of measuring the texture in the Al_2O_3 polycrystalline thin films such as oxidation scales. Furthermore, the consequences of polarization orientation on piezospectroscopic measurements are discussed.

I. Introduction

The optical spectra of ruby (Cr^{3+}-doped sapphire) have been studied extensively since the late 1950s and are generally considered to be well interpreted in terms of ligand field theory.[1-5] As a result, the polarization of ruby absorption is well understood. However, the polarization characteristics of its spontaneous emission have not been detailed, apart from reports that the total emission is strongly polarized.[6,7]

During the last five years, a high-spatial-resolution (~1 μm) strain-mapping technique has been developed using the piezospectroscopic properties of ruby.[8,9] By monitoring the frequency change of the Raman-line (R-line) fluorescence, a variety of residual stress problems, as well as the response to applied stresses, has been studied in Al_2O_3-containing monolithic and multiphase materials.[10-12] As shown in Fig. 1, the two closely spaced R lines result from nonphonon radiative transitions from its first excited state ($2\bar{A}$ and $\bar{E}$ doublet) to its ground state of the Cr^{3+} ion ($^4A_2$). In addition to the precision in stress measurements, the technique facilitates a more complete determination of the stress tensor with a knowledge of the crystallographic orientation.[13] Therefore, a technique to determine the crystallographic orientations of Al_2O_3 materials with comparable spatial resolution is required. The X-ray resolution is limited by the beam size, usually on the order of 1 mm unless microfocus facilities are available. One motivation of the present study is to develop a technique to determine the crystallographic orientation of small regions of Al_2O_3 by studying the polarization characteristics of their R-line fluorescence. Additionally, precise knowledge of the fluorescence polarization is important in stress measurements in polycrystalline materials, in which the stress-induced line shifts are averaged over all possible crystallographic orientations and a weighting function resulting from the polarization dependence may need to be included.

The anisotropic absorption properties have been commonly used to align optically uniaxial crystals with their optical axes, at least qualitatively. Although the emission process is more complex than that of the absorption, the ruby fluorescence should inherit the optically uniaxial properties from the corundum structure. In this work, a series of experiments were performed to study the polarization characteristics of R-line fluorescence. As a result, the intensity ratio (R2/R1) is determined as a function of the angle between the optical *c*-axis of the crystal and the direction of the ***E*** vector of the incident light so that it can be used to measure the ***c***-axis orientation in Al_2O_3 quantitatively. After a brief description of the experimental procedures, the results obtained are presented in Section III. The theoretical interpretation described in Section IV, along with a comparison with previous literature data, is then followed by examples of application of this phenomenon.

II. Experimental Details

(1) Fluorescence Measurement

We have used optical microscopy to stimulate and collect the excited fluorescence in the backscattering mode. The optics have been described in detail previously.[13] An objective lens of 10× magnifying power, with a numerical aperture of 0.3, was used in most of our work. Because of the nature of the holographic gratings in the spectrometer, the collection efficiency is highly polarized, with the efficiency reaching a maximum when the ***E*** vector of the fluorescence is parallel to the opening direction of the entrance slit, and it reduces to zero when ***E*** is perpendicular to the slit opening. Therefore, the overall effect is equivalent to inserting a polarizer in front of the spectrometer. For descriptive purposes, the direction normal to the slit is referred to here as the collection direction, ***S***, of the spectrometer. An argon-ion laser served as the excitation source, operating at 488.0 and 514.5 nm. Three thin plates of ruby were cut from a large, single crystal (0.05 wt% Cr^{3+}) and machined to 5 mm × 5 mm, with a thickness of ~1 mm. Both extended surfaces were polished to an optical finish. Using X-ray Laue back-reflection, the normals of the extended surface are aligned within ±0.5° with the crystallographic ***c***-, ***a***-, and ***m***-axes, respectively. The collected R1 and R2 fluorescence lines were fitted to a double pseudo-Voigtian function, and the intensity of the individual line was quantified by the area under each peak. Through the course of the experiments, lenses with higher magnifying power (50× and 100×) and various laser powers

---

R. H. French—contributing editor

Manuscript No. 192113. Received December 28, 1995; approved June 25, 1996.

Supported by the Advanced Research Projects Agency University Initiative at UCSB, under Contract No. N00014-92-J-1808.

*Member, American Ceramic Society.

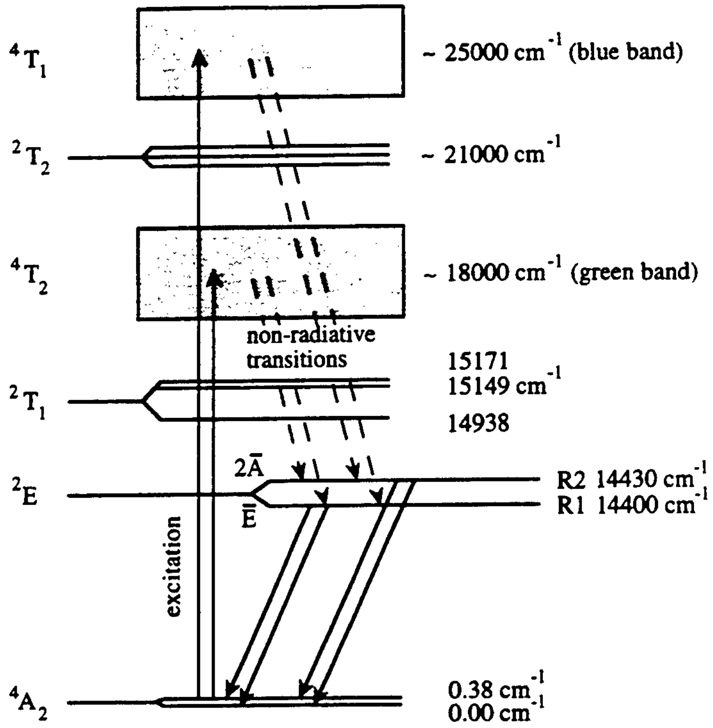

Fig. 1. Low-lying electronic levels of Cr^{3+} in sapphire, designated by their representations in the cubic-field terms (O_h group) on the left. Fine structures, labeled on the right-hand side, result from the trigonal-field distortion of the corundum lattice and spin-orbit interactions. Splitting of the ground state, $^4A_2$, is too small to be resolved in the R-line optical spectra at room temperature.

also were used. The R-line polarization was independent of all of them. Furthermore, no line shifts or changes of splitting between R lines were observed. This convinced us that thermal equilibrium was preserved during excitation. Still, for all data presented later, the laser output power used was ~1 mW.

Two sets of experiments were performed to investigate the emission polarization, as well as the effect of absorption anisotropy. In the first series, the normal to the ruby-plate extended surface was aligned with the optical axis of the system, as shown in Fig. 2. Meanwhile, the *E* vector of the linear-polarized laser output was kept normal to the entrance slit. Then, each ruby plate was rotated about its extended surface normal and the R-line intensity change was recorded as a function of θ, the angle between the optical *c*-axis of the crystal and the direction *S* of the spectrometer. The laser output power was constant during each experiment, and the same experiments were performed under excitation of the 488.0 and 514.5 nm laser lines.

Results from the first series of experiments reflected the combined effects of absorption and emission anisotropy of ruby. Then, a second series of experiments were conducted to separate these two effects. Although the extended surface of each sample was still perpendicular to the optical axis of the system, in this set of experiments, one of the two in-plane crystallographic axes was aligned parallel to the direction *S* ($\theta = 0°$ or 90°). During the experiment, the *E* vector of the laser was rotated about the optical axis using a 1/4 waveplate. The fluorescence was recorded as a function of the angle ϕ, which is the angle between the laser *E* vector and the ruby optical axis (shown in Fig. 2). Since there was no change of the crystallographic direction relative to the direction of maximum sensitivity of the spectrometer, the variation in the R-line fluorescence intensity was then solely due to the anisotropic absorption introduced by the rotation of the laser *E* vector relative to the ruby crystal.

Because all the experiments performed involved the rotation of either the laser *E* vector or the ruby crystal relative to the optical system, the polarization characteristics of the system transmissibility must be included in the analysis. A white light source in the transmission mode of the microscope was used for this evaluation. A polarizer was inserted between the white light source and the optical system, then the intensity of transmitted light was recorded at the R lines and the laser frequencies when the polarizer was rotated about the optical axis of the system. The transmissibility was slightly different for two incident illuminations with their *E* vector being perpendicular to each other. All data presented have been corrected from this angular variation of the system.

(2) *Absorption Measurements*

The absorption spectra of ruby have previously been studied under a variety of experimental conditions.[1,14–16] The absorption-peak positions and intensities are dependent on Cr^{3+} concentration, temperature, and pressure. An increase in any of these parameters causes broadening and intensification of the spectra; however, pressure induces a blue shift (move to high energies), whereas increases in temperature and chromium concentration tend to shift the absorption bands to lower energies. Also, a shift in the absorption spectra of the extraordinary (π-polarized) and ordinary (σ-polarized) rays occurs. All these effects have been well quantified. For dilute ruby at ambient conditions, the peak wavelengths for the blue and green bands are 398 and 543 nm for extraordinary rays and 412 and 558 nm for ordinary rays, respectively.[16] Unfortunately, there are no reported values of ruby absorption coefficients at the wavelengths used in our fluorescence experiments (488.0 and 514.5 nm).

Therefore, we measured the absorption coefficients for the same ruby crystals used in our fluorescence experiments. The absorption measurements were performed using a variable angle spectroscopic ellipsometer (J. A. Woollam Co., Lincoln, NE). The linear polarized monochromatic light was produced by a 75 W xenon lamp (with functional bandwidth of 200–1100 nm) in combination with a monochromator and a calcite Glan–Taylor prism. The sample was analyzed on a motorized goniometer, and the transmitted and reflected light were collected by a silicon photodiode detector. The transmission scans were conducted at normal incidence, whereas the reflection scans were performed at an incidence angle of 12° to the surface

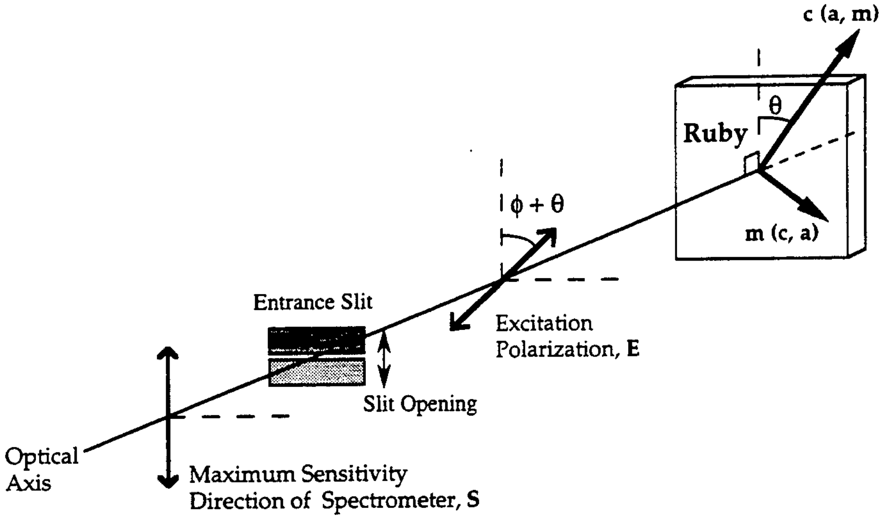

Fig. 2. Schematic diagram of the optical backscattering arrangement used in the fluorescence measurements. Direction of maximum sensitivity of the spectrometer, S, the slit configuration and opening direction, and the optic axis are indicated, as well as the polarization direction of the light used to excite the fluorescence. Notation $c(a,m)$ denotes the orientation of the ruby crystallographic axes in successive experiments.

normal. The measurements for the absorption of σ-polarized light ($E \perp c$) and π-polarized light ($E \parallel c$) were made over the range of 300–800 nm with steps of 1 nm.

III. Results

The R1 and R2 emission lines are strongly polarized and consist of two polarization components. The E field of the weak component is parallel to the c-axis, and that of the dominant component lies within the basal plane but has no preferred vibration direction in the plane. Figure 3 shows the π- and σ-polarized emission components of the R lines, where π and σ polarization refer to the radiation polarized with the E field parallel to and perpendicular to the c-axis of the ruby crystal, respectively. A large difference in the intensity ratio between two components, I^e_σ/I^e_π, exists, with values of 14.2 and 4.2 for the R1 and R2 lines, respectively. (The superscript e refers to emission, and the intensity I is the total area under the fluorescence line.) Defining the degree of polarization, P, by the ratio

$$P = \frac{I^e_\sigma - I^e_\pi}{I^e_\sigma + I^e_\pi} \qquad (1)$$

then the values for the R1 and R2 lines are $P_{R1} = 87\%$ and $P_{R2} = 62\%$, respectively. Because of the polarization characteristics of the spectrometer, the fluorescence signal collected will be a function of θ, the angle between the c-axis and the spectrometer direction, S (Fig. 2):

$$I^e(\theta) = I^e_\pi \cos^2\theta + I^e_\sigma \sin^2\theta \qquad (2)$$

Thus, the intensity ratio of the R2 line to the R1 line gradually changes from a maximum value of 1.64 at $\theta = 0°$ to a minimum of 0.48 at $\theta = 90°$ in the first series of experiments. The angular dependence of the intensity ratio is plotted in Fig. 4 as a function of θ, with excitation at 514.5 and 4.88.0 nm. The identity (within the experimental scatter) of the two profiles, despite the difference in absorption cross section, Ω, at these two frequencies, indicates that the R-line intensity ratio is independent of the absorption process. However, plotting the I(R1) or I(R2) individually (Fig. 5) revealed the anisotropy of the ruby absorption, as will be discussed in a following section. Both profiles have the same functional form:

$$I^e(\theta) = B(\cos^2\theta + C\sin^2\theta)\left(\cos^2\theta + \left(\frac{I^e_\sigma}{I^e_\pi}\right)\sin^2\theta\right) \qquad (3)$$

Here, B is a constant that depends on the incident laser intensity and C is numerically equal to 1.4 and 2.0 for the 488.0 and 514.5 nm excitations, respectively.

The second series of the experiments verified that terms in the first set of parentheses in Eq. (3) were, indeed, the anisotropy of the ruby absorption. Figure 6 shows the intensity variation of both fluorescence polarization components with the angle ϕ, using 514.5 nm excitation. All four profiles exhibit the same angular dependence, with the only difference being in the numerical value of the constant D:

$$I^e(\phi) = D(\cos^2\phi + C\sin^2\phi) \qquad (4)$$

The constant C has the same value as determined previously in Eq. (3).

The absorption spectra of our ruby sample for polarized light are plotted in Fig. 7 in terms of the absorption coefficient α ($\alpha = \Omega c$). The data were derived from transmittance data, and the chromium concentration, c, was 1.22×10^{19} cm^{-3}. The dichroic ratios (Ω_σ/Ω_π) at 488.0 and 514.5 nm were 1.6 and 2.1, respectively.

IV. Discussion and Applications

The luminescence intensity depends on the number of the Cr-3d electrons raised to excited states and on the probability that an excited electron will then return to its ground state by emission of a photon. The number of electrons raised to excited states depends on the strength of the absorption transitions. The transitions from the $^4A_2$ ground state to the $^4T_2$ and $^4T_1$ broad bands are spin allowed and relatively strong, whereas those to the sharp levels—$2\bar{A}$, $\bar{E}$, $^2T_1$, and $^2T_2$—are spin forbidden. However, no matter which excited state is attained by optical excitation, almost all the excited electrons ultimately end up in the $2\bar{A}$ and $\bar{E}$ states by nonradiative transitions from high-energy states. Therefore, if N electrons are excited per second, an equal number of electrons will decay back to the ground state under thermal equilibrium conditions. Three different decay paths are possible: radiative transitions through nonphonon R lines and nearby phonon vibronic sidebands, and nonradiative transitions. The vibronic sidebands of the R lines result from the creation or destruction of one or more quanta of lattice vibrational energy (phonons or local modes) occurring simultaneously with the electronic transitions. They are relatively weak bands in emission and absorption, extending over ~1000 cm^{-1} from the R lines (not shown in Fig. 1). Under continuous excitation, the absorption process is in equilibrium with the emission process and can be related by

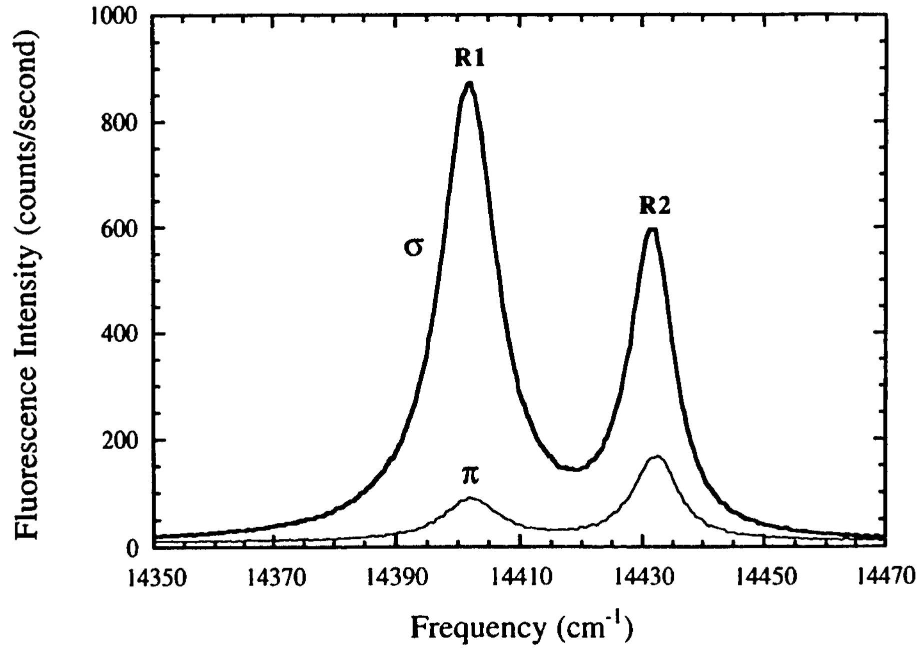

Fig. 3. Polarized emission of the ruby R lines at room temperature. Laser E vector was parallel to the collection direction S. Symbols π and σ refer to the polarizations of the extraordinary and ordinary rays, respectively.

$$N = N(R) + N_{\mathrm{vib}} + N_{\mathrm{nr}} \qquad (5)$$

where $N(R)$, N_{vib}, and N_{nr} are the number of electrons that decay through R-line emission, vibronic sidebands, and nonradiative transition, respectively. Under equilibrium, the distribution among the three decay paths is determined by the pertinent transition probabilities, which, in turn, are proportional to the absorption cross section through a Boltzmann distribution.

Noting that $N(R) = N(2\bar{A}) + N(\bar{E})$, then

$$\frac{N(2\bar{A})}{N(\bar{E})} = \exp\left(\frac{\Delta E}{kT}\right) = K \qquad (6a)$$

$$I(\mathrm{R1}) \propto \int_{\mathrm{R1}} \Omega \, d\nu N(\bar{E}) \propto \int_{\mathrm{R1}} \Omega \, d\nu \left(\frac{1}{1+K}\right) N \qquad (6b)$$

$$I(\mathrm{R2}) \propto \int_{\mathrm{R2}} \Omega \, d\nu N(2\bar{A}) \propto \int_{\mathrm{R2}} \Omega \, d\nu \left(\frac{K}{1+K}\right) N \qquad (6c)$$

where $\int_{\mathrm{R1}} \Omega \, d\nu$ and $\int_{\mathrm{R2}} \Omega \, d\nu$ are the integrated absorption cross sections for R lines. At ambient and stress-free conditions, the splitting between R1 and R2 lines, ΔE, is 30 cm^{-1}; thus, the Boltzmann factor, K, is 0.87. N is directly proportional to the intensity loss or absorbed, ΔI, as light is transmitted through a unit thickness of ruby. Using the Beer–Lamber law that $I_0/I = \exp(\Omega^{\mathrm{ex}} cd)$, where Ω^{ex} is the absorption cross section at the excitation frequency, c the chromium concentration, and d the thickness of the crystal, the intensity change can be written as

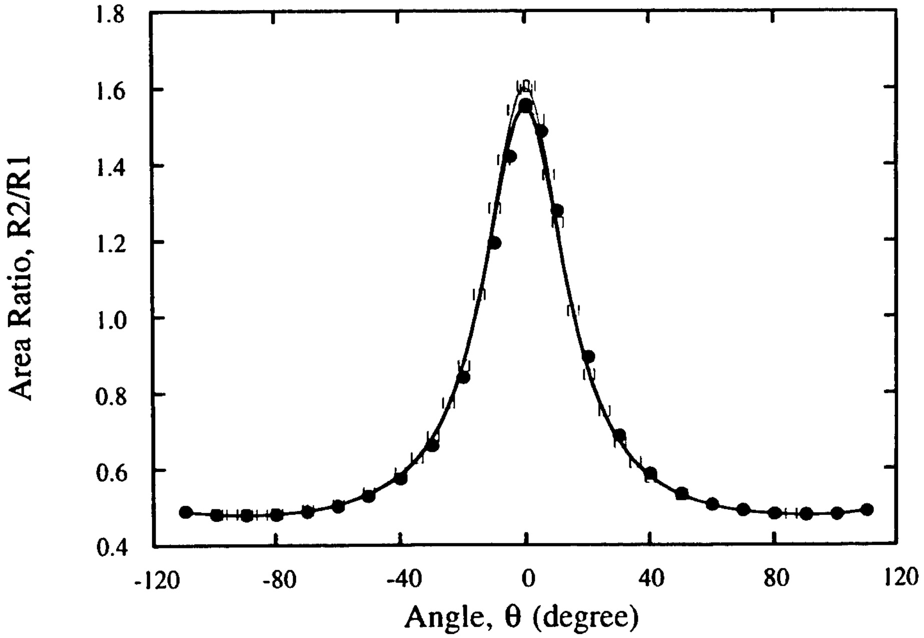

Fig. 4. Angular dependence of the R2/R1 intensity ratio, using two different excitation frequencies ((●) 488.0 nm and (☐) 514.5 nm).

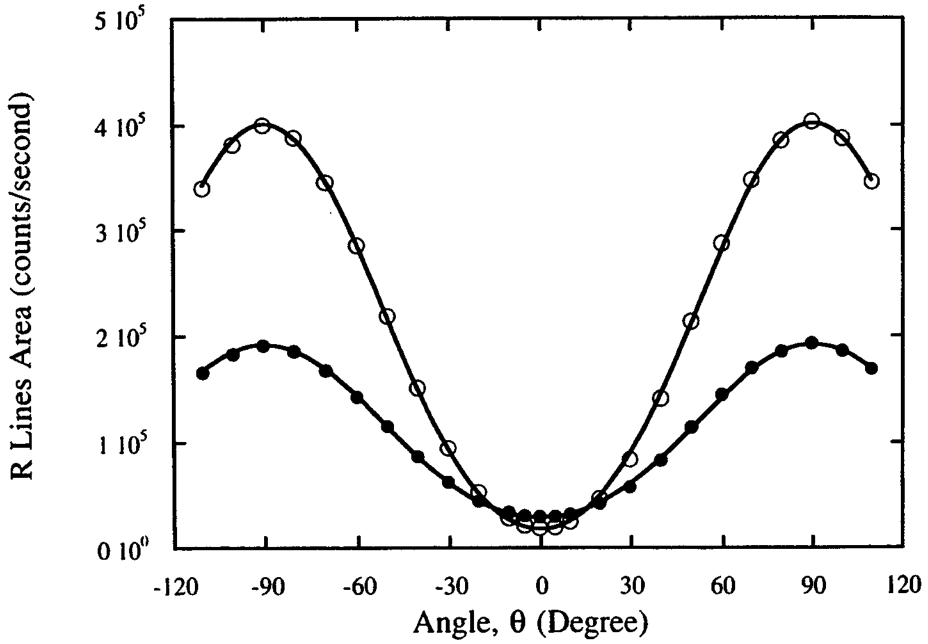

Fig. 5. Angular dependence of two R-line intensities ((○) R1 and (●) R2), using 488.0 nm excitation.

$$\Delta I = \frac{(I_0 - I)}{d} = \frac{I_0}{d}[1 - \exp(-\Omega^{ex}cd)] \tag{7}$$

In our case, the probe has a maximum depth resolution of <200 μm; thus, $\Delta I \approx (\Omega^{ex}c)I_0$. (This approximation tends to break down when an ultralong working distance lens is used, because they usually have low magnifying power (<5×).) Combining Eqs. (6) and (7), we obtain

$$I(\mathrm{R1}) \propto \int_{\mathrm{R1}} \Omega\, d\nu \left(\frac{1}{1 + K}\right)(\Omega_\pi^{ex} \cos^2 \phi + \Omega_\sigma^{ex} \sin^2 \phi) \tag{8a}$$

$$I(\mathrm{R2}) \propto \int_{\mathrm{R2}} \Omega\, d\nu \left(\frac{K}{1 + K}\right)(\Omega_\pi^{ex} \cos^2 \phi + \Omega_\sigma^{ex} \sin^2 \phi) \tag{8b}$$

By comparison with the phenomenological Eqs. (3) and (4), C is equal to the dichroic ratios, $\Omega_\sigma^{ex}/\Omega_\pi^{ex}$, at the excitation frequency. Furthermore, the value of C from the fluorescence measurements (fitting value) and absorption spectra agree with each other to within 15%.

The fluorescence and absorption measurements confirm that the emission and absorption are essentially independent processes with characteristic angular dependence. Therefore, the fluorescence intensity ratio between two polarization components, I_σ^c/I_π^c, is simply the integrated dichroic ratios at the R1 and R2 frequencies. The literature usually only gives the peak values of the R-line absorption cross section, Ω^R. Realizing that

$$\int_{\mathrm{R}} \Omega\, d\nu \propto \Omega^R w_R \tag{9}$$

where w_R is the full width at half maximum of the emission/absorption line,* the integrated dichroic ratios for the R lines is equal to the dichroic ratio at peak frequency, $\Omega_\sigma^R/\Omega_\pi^R$. Based on the literature value,[14] we estimate the integrated dichroic ratios to be 13.7 and 4.21 for R1 and R2, respectively. This agrees well with our measurements of 14.2 and 4.2 for I_σ^c/I_π^c of the R1 and R2 lines. Because the collected fluorescence signal depends on θ, as shown in Eq. (2), the intensity ratio of R2 to R1 should have the following angular dependence:

$$\frac{I(\mathrm{R2})}{I(\mathrm{R1})} = \left(\frac{\int_{\mathrm{R2}} \Omega_\pi\, d\nu \cos^2 \theta + \int_{\mathrm{R2}} \Omega_\sigma\, d\nu \sin^2 \theta}{\int_{\mathrm{R1}} \Omega_\pi\, d\nu \cos^2 \theta + \int_{\mathrm{R1}} \Omega_\sigma\, d\nu \sin^2 \theta}\right) K \tag{10}$$

Indeed, the observed angular dependence plotted in Fig. 4 can be fitted to Eq. (11):

$$\frac{I(\mathrm{R2})}{I(\mathrm{R1})} = E\left(\frac{\cos^2 \theta + F \sin^2 \theta}{\cos^2 \theta + G \sin^2 \theta}\right) \tag{11}$$

with E, F, and G having the values 1.64, 4.2, and 14.2, respectively. In comparison with Eq. (10),

$$E = \left(\frac{\int_{\mathrm{R2}} \Omega_\pi\, d\nu}{\int_{\mathrm{R1}} \Omega_\pi\, d\nu}\right) K = \left(\frac{\Omega_\pi^{R2} w_{R2}}{\Omega_\pi^{R1} w_{R1}}\right) K \tag{12a}$$

$$F = \frac{\int_{\mathrm{R2}} \Omega_\sigma\, d\nu}{\int_{\mathrm{R2}} \Omega_\pi\, d\nu} \tag{12b}$$

and

$$G = \frac{\int_{\mathrm{R1}} \Omega_\sigma\, d\nu}{\int_{\mathrm{R1}} \Omega_\pi\, d\nu} \tag{12c}$$

and, again, the fitted values agree with those predicted.

Equation (11) provides the basis for an experimental determination of the orientation of a sapphire crystal (containing a trace amount of Cr^{3+}) from the R-line intensity ratio. When implemented in optical microscopy, this orientation technique is capable of high spatial resolution. Although a single measurement of the intensity ratio only gives the angle θ, the direction cosines of the *c*-axis can be evaluated by three consecutive fluorescence measurements, in which the laser ***E*** vectors are successively set perpendicular to each other. This can be easily achieved by using a 1/4 waveplate or simply by rotating the sample. In many cases, however, a knowledge of only the angle between the *c*-axis and one particular direction, such as the fiber axis, is required.

To illustrate the utility of the orientation technique, we consider the following application: the determination of the orientation of sapphire-fiber reinforcements in composites and the

---

*At room temperature, w_{R1} = 11.0 cm^{-1} and w_{R2} = 8.7 cm^{-1} for 0.05 wt% ruby. The two widths are independent of crystal orientation.

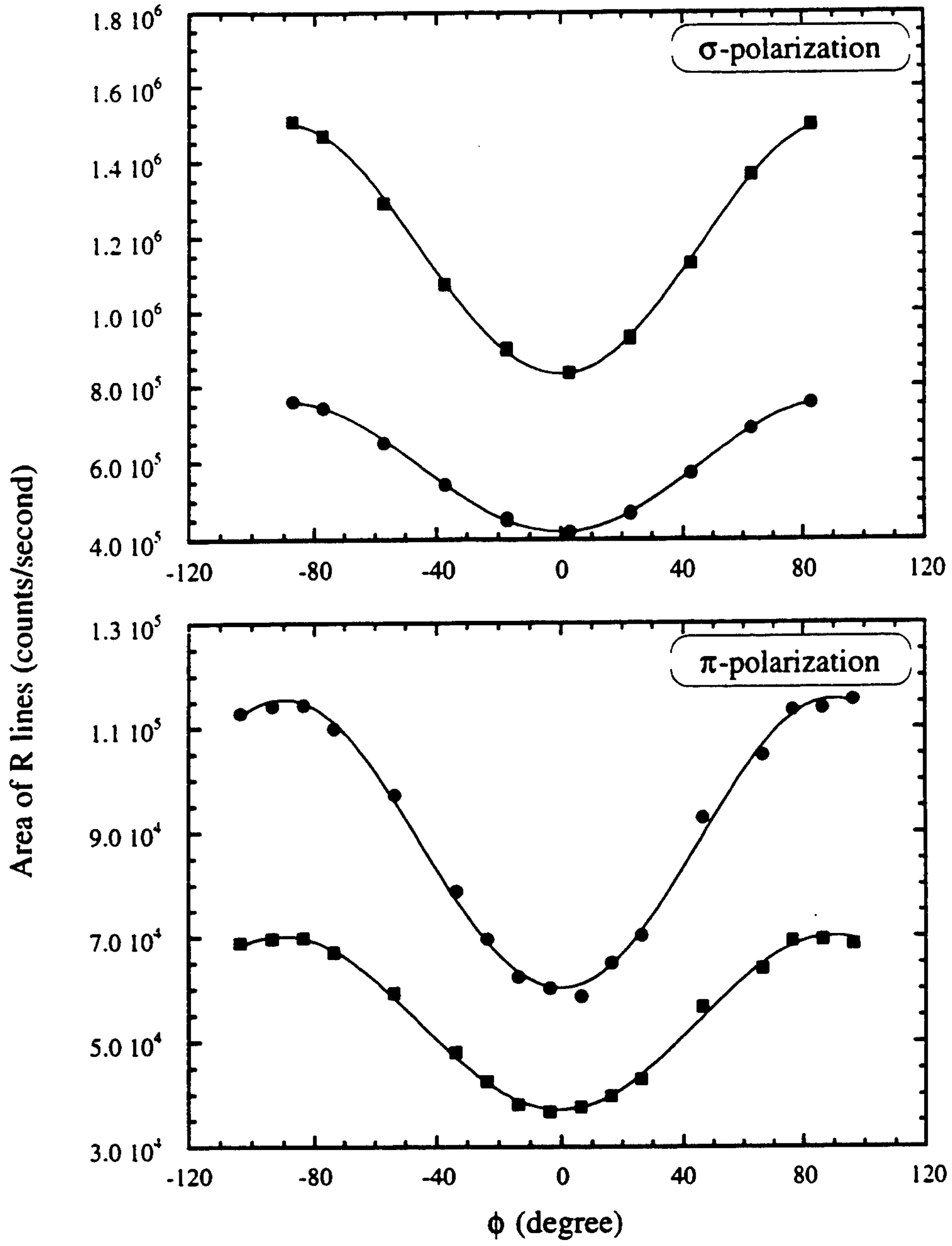

Fig. 6. Variation of the two R-line intensities ((■) R1 and (●) R2), as a function of the angle between the laser *E* vector and the ruby *c*-axis for the two polarization components σ and π (514.5 nm excitation).

subsequent piezospectroscopic analysis of the residual stress in the fiber. (The fibers are under a residual, internal stress because, on cooling from the fabrication temperature, strains develop because of the difference in thermal expansion between the fibers and the matrix.) Because of the crystallographic anisotropy of the elastic modulus and the thermal expansion coefficient of sapphire, substantial variations in the internal stress distribution in one fiber to the next can occur, because of variations in the angle between the crystal *c*-axis and the fiber axis. Therefore, the precise knowledge of the *c*-axis direction is essential to determine the stress distribution. The small cross section of the fibers useful for reinforcement (typically $d \approx 100$ μm or smaller) precludes standard X-ray analysis, and, in addition, analysis of individual fibers identified in a microscope is generally desirable. As a specific example, in Fig. 8, we compare the R-line spectrum from a sapphire fiber embedded in a γ-TiAl intermetallic matrix composite to that from a free-standing *c*-axis sapphire fiber. (The fiber end was exposed by sectioning the composite.) The change in the R-line intensity ratio is a result of the existence of a finite angle θ between the fiber axis of the embedded fiber and its crystallographic *c*-axis (Fig. 9). Using the experimental measurement of the R2/R1 ratio and Eq. (11), the angle was determined to be 71° by analyzing a set of spectra recorded at three perpendicular polarization directions. This angle was subsequently verified by X-ray measurements after extracting the fiber by etching away the matrix. In addition to the intensity variation, the comparison of the two spectra in Fig. 8 also indicates a frequency shift induced by residual stresses in the embedded fiber. Using R-line fluorescence, evaluation of the axial and radial stress components in *c*-axis sapphire fibers in various matrix materials has been demonstrated elsewhere to be possible in conjunction with elasticity calculation[10,17] or by the use of the full piezospectroscopic tensor.[18] Having used the R2/R1 ratio to determine the crystallographic orientation of the fiber, we can extend the piezospectroscopic analysis to sapphire fibers with random orientations, as described in Appendix A. If the angle between the

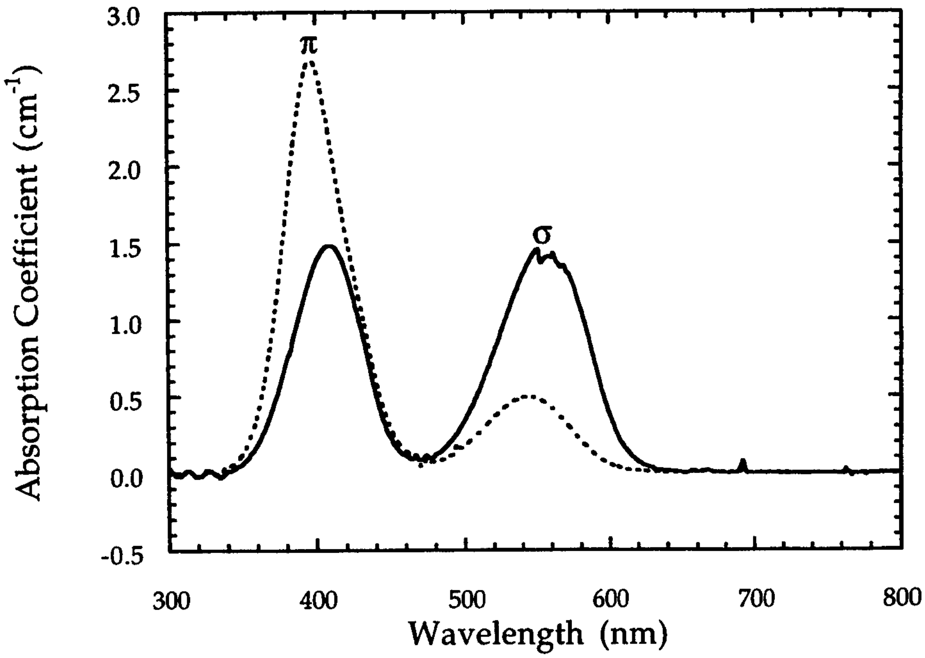

Fig. 7. Absorption coefficient α (cm^{-1}) at 300 K as a function of wavelength for (—) $E \perp c$ (σ) and (- - -) $E \parallel c$ (π).

fiber axis and the sapphire *c*-axis is θ, then the fluorescence peak shift can be related to the stress components defined in the fiber coordinate system shown in Fig. 9, using Eqs. (A-1), (A-2), and (A-5) from Appendix A:

$$\Delta\nu_{R1} = 3.26(\sigma_{11} + \sigma_{22}\cos^2\theta + \sigma_{33}\sin^2\theta) + 1.53(\sigma_{22}\sin^2\theta + \sigma_{33}\cos^2\theta) \qquad (13a)$$

$$\Delta\nu_{R2} = 2.73(\sigma_{11} + \sigma_{22}\cos^2\theta + \sigma_{33}\sin^2\theta) + 2.16(\sigma_{22}\sin^2\theta + \sigma_{33}\cos^2\theta) \qquad (13b)$$

Because only two equations based on fluorescence peak shifts alone have been shown, an additional relationship between the three stress components is evidently required. This can be obtained by relating the residual stresses in an off-axis fiber embedded in a matrix to the thermal mismatch strain based on an Eshelby type of calculation. Additionally, for small angular misalignments, σ_{rr} and $\sigma_{\theta\theta}$ are sufficiently similar that they can be assumed to be the same, and, thus, the axial and radial stresses can be obtained directly from Eqs. (13) to a good approximation.

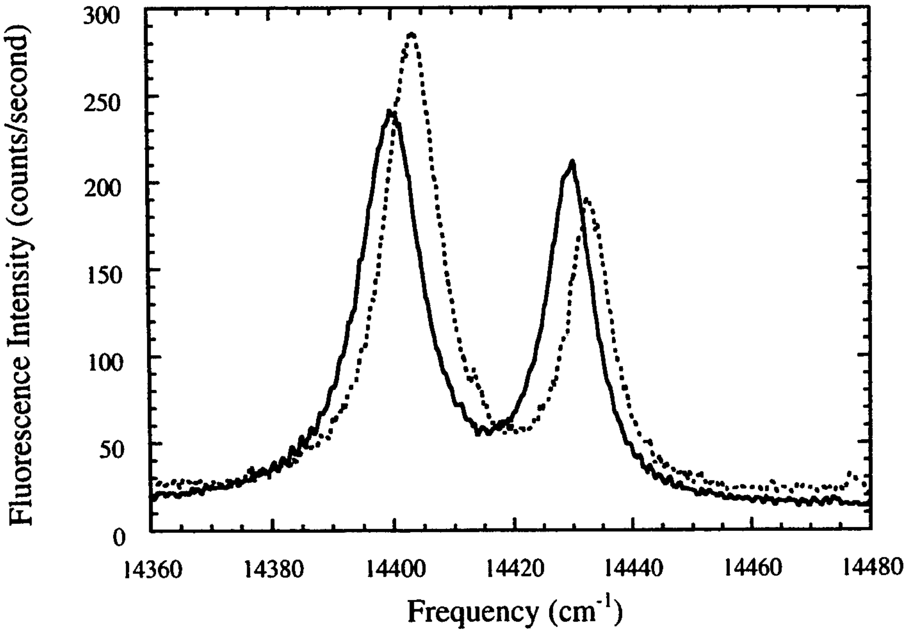

Fig. 8. Fluorescence spectra from (- - -) a free-standing *c*-axis sapphire fiber and (—) a sapphire fiber embedded in a γ-TiAl intermetallic matrix. Angle between the fiber axis and the crystallographic *c*-axis of the embedded fiber can be determined from the R2/R1 intensity ratio, as described in the text. Relative frequency shift is due to the residual stress in the embedded fiber.

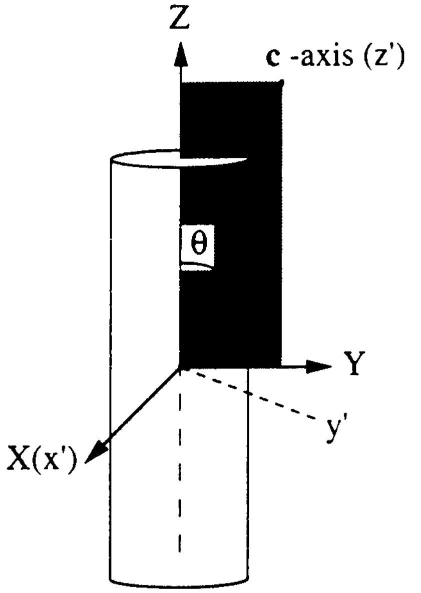

Fig. 9. Schematic diagram illustrating the crystallographic coordinates and the reference fiber frame for an off-axis sapphire fiber.

In addition to the orientation determination of single crystals, the R-line fluorescence from polycrystalline Al_2O_3 also provides information about any preferential distribution, or texture, of the *c*-axes. The R-line intensity ratio for a perfectly random polycrystalline alumina has been calculated in Appendix B. The result is plotted in Fig. 10 for excitation wavelengths of 350–600 nm. With a knowledge of the intensity ratio for perfectly random grain orientations, obtaining information about the texture in polycrystalline alumina is possible by examining the intensity ratio of its R-line fluorescence. This may well be of importance in the cases of thin-film or oxide scale in which a continuous change in grain-orientation distribution during growth is present. For instance, in a recent study[12] on oxide scales formed by oxidation of aluminum-containing alloys, a large local variation of the R-line intensity ratio was observed, as well as a variation with oxide thickness.

Finally, calculation of the possible impact of the R-line polarization on the values of stress determined by piezospectroscopic measurements is worthwhile. One direct consequence is that the collected fluorescence intensity will depend on the crystallographic orientation relative to the laser **E** vector, as well as the collection direction **S**. Therefore, all grains in a random polycrystalline alumina do not contribute evenly to the overall fluorescence intensity, and the angular distribution, $I(\theta)$, is given by Eqs. (B-1) in Appendix B under a fixed optical setting ($\mathbf{E} \parallel \mathbf{S}$). The previous analysis[9] of the piezospectroscopic measurements in polycrystalline ceramics was based on the assumption of a uniform intensity distribution. For a grain with arbitrary orientation, the frequency shift due to an applied stress field is given by the following relation:

$$\Delta\nu = \Pi_{ij} a_{ik} a_{jl} \sigma_{kl} \tag{14}$$

where the transformation matrix a_{ij} is defined in Eq. (A-4). Π_{ij} is the piezospectroscopic coefficient defined in Appendix A. The angular distribution of the fluorescence intensity serves as a weighting function in calculating the average frequency shift, and the direction of the laser **E** vector is selected as the **Z**-axis of the laboratory coordinate. The average frequency shift due to an applied stress field is then given as

$$\overline{\Delta\nu} = \frac{\iiint p(\theta,\phi,\psi) I(\theta) \Delta\nu \, d\theta \, d\phi \, d\psi}{\iiint p(\theta,\phi,\psi) I(\theta) \, d\theta \, d\phi \, d\psi} \tag{15}$$

The probability, $p(\theta,\phi,\psi)$, of a grain oriented at (θ,ϕ,ψ) is shown in Eq. (B-2) in Appendix B. Equation (15) then reduces to

$$\begin{aligned} \overline{\Delta\nu} &= \tfrac{1}{3}(\Pi_{11} + \Pi_{22} + \Pi_{33})(\sigma_{11} + \sigma_{22} + \sigma_{33}) \\ &\quad + H(\Pi_{11} + \Pi_{22} - 2\Pi_{33})(\sigma_{11} + \sigma_{22} - 2\sigma_{33}) \end{aligned} \tag{16a}$$

where

$$H = \frac{6 + s + t - 8st}{21(3 + 2s + 2t + 8st)} \tag{16b}$$

Here, s is the integrated dichroic ratio for the R1 or R2 line and t is dichroic ratio at the excitation frequency. The first part of the Eq. (16*a*) is identical to the earlier result by Ma and Clarke,[9] where the polarization-induced intensity variation was not

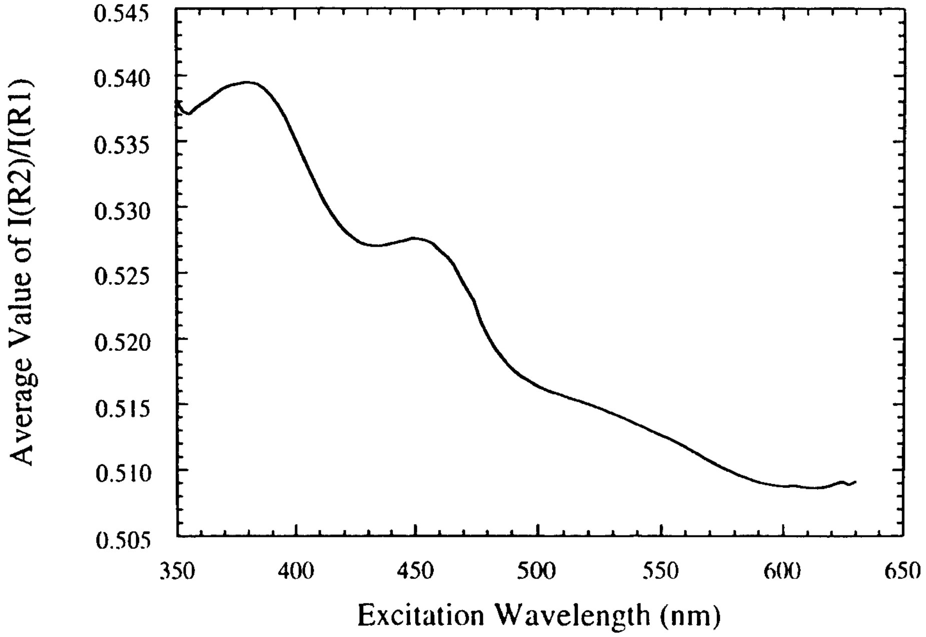

Fig. 10. Average intensity ratio of the R2 line to the R1 line from a randomly distributed polycrystalline Al_2O_3, as a function of excitation wavelength. Data below 350 nm and above 630 nm are not included because of the large scatter in measured absorption dichroic ratio.

included. The polarization characteristics of the R lines introduces the second term in Eq. (16*a*), which distinguishes the stress along the laser **E** vector, σ_{33}, from the other two stress components. The constant H is plotted in Fig. 11 as a function of the excitation wavelength. From this, the correction factor H does not exceed 5% for the excitation range of 300–650 nm. Therefore, the polarization-dependent term in Eq. (16*a*) can generally be ignored in all but the highest-precision stress measurements made using piezospectroscopic techniques. (In cubic materials, this second term is zero.)

V. Summary

The polarization characteristics of the ruby R lines have been studied, and the value of degrees of polarization are reported for R1 and R2 lines. The measured emission polarization characteristics of the R lines can be successfully interpreted in terms of the absorption dichroic ratio at the excitation and R-line frequencies. Consequently, a spectrophotometric determination of the sapphire *c*-axis is introduced, using the angular dependence of the R-line intensity ratio. This technique can be used to obtain highly localized orientation information on single crystals as well as polycrystalline Al_2O_3. The effects of the polarization dependence on piezospectroscopic measurements also have been discussed. Resolving stress components in a randomly oriented single crystal by the full piezospectroscopic tensor becomes feasible. Also, the effect of the angular dependence of fluorescence intensity can generally be neglected during stress measurement in polycrystalline Al_2O_3. With further calibration, the present framework can be adapted by other optically active crystalline materials, such as Cr:MgO, Ti:Al_2O_3, and Ti:YAG, and various color centers.

APPENDIX A

Stress Measurement in Sapphire Fibers

Our recent calibration[13] of the ruby piezospectroscopic coefficients revealed small differences in Π_{11} and Π_{22}. However, for the sake of simplicity, we have ignored this refinement for compressive loading. Average values defined by linearly fitting the observed R-line shifts under uniaxial compression along the ***a***- and ***m***-axes are used here, which are then 3.26 and 2.73 cm^{-1}/GPa for the R1 and R2 lines, respectively. The piezospectroscopic relationship (Eq. (6) in our previous work[13]) may then be written as

$$\Delta\nu_{R1} = 3.26(\sigma^*_{11} + \sigma^*_{22}) + 1.53\sigma^*_{33} \qquad \text{(A-1}a\text{)}$$

$$\Delta\nu_{R2} = 2.73(\sigma^*_{11} + \sigma^*_{22}) + 2.16\sigma^*_{33} \qquad \text{(A-1}b\text{)}$$

where σ^*_{ij} is the stress state defined in the crystallographic basis of ruby lattice. The stress on crystal structure, σ^*_{ij}, can be related to the applied/residual stress components by

$$\sigma^*_{ij} = a_{ik}a_{jl}\sigma_{kl} \qquad \text{(A-2)}$$

where a_{ij} is the matrix transforming crystallographic axes, $\mathbf{x}'_j$, to reference coordinate, X_i, in which the applied/residual stresses are defined:

$$X_i = a_{ij}\mathbf{x}'_j \qquad \text{(A-3)}$$

In terms of the usual Euler angles (θ,ϕ,ψ), the transformation matrix is

$$a_{ij} = \begin{pmatrix} \cos\phi\cos\psi - \sin\phi\cos\theta\sin\psi & -\cos\phi\sin\psi - \sin\phi\cos\theta\cos\psi & \sin\theta\sin\phi \\ \sin\phi\cos\psi + \cos\phi\cos\theta\sin\psi & -\sin\phi\sin\psi + \cos\phi\cos\theta\cos\psi & -\sin\theta\cos\phi \\ \sin\theta\sin\psi & \sin\theta\cos\psi & \cos\theta \end{pmatrix} \qquad \text{(A-4)}$$

where $0 \le \theta \le \pi$, $0 \le \phi \le 2\pi$, and $0 \le \psi \le 2\pi$.

The assumption of isotropic piezospectroscopic properties in the basal plane enables the stress state in off-axis sapphire fiber to be expressed analytically. If the fiber axis of a sapphire fiber embedded in a composite lies at an angle θ to its *c*-axis, then the number of independent residual stress components increases to three, as a result of the crystallographic anisotropy in the thermal expansion of sapphire. Using the coordinate system indicated in Fig. 9, the fiber axis is the ***Z***-axis, and the ***Y***-axis is a projection of the crystallographic *c*-axis onto the ***Z***-plane. Because of the assumed basal-plane isotropy in the piezospectroscopic properties, we can simply set the z'-axis of crystallographic basis along its *c*-axis and let the $\mathbf{x}'$-axis coincide with the fiber X-axis. As a result, $\phi = \psi = 0$ in this case, then the transformation matrix is

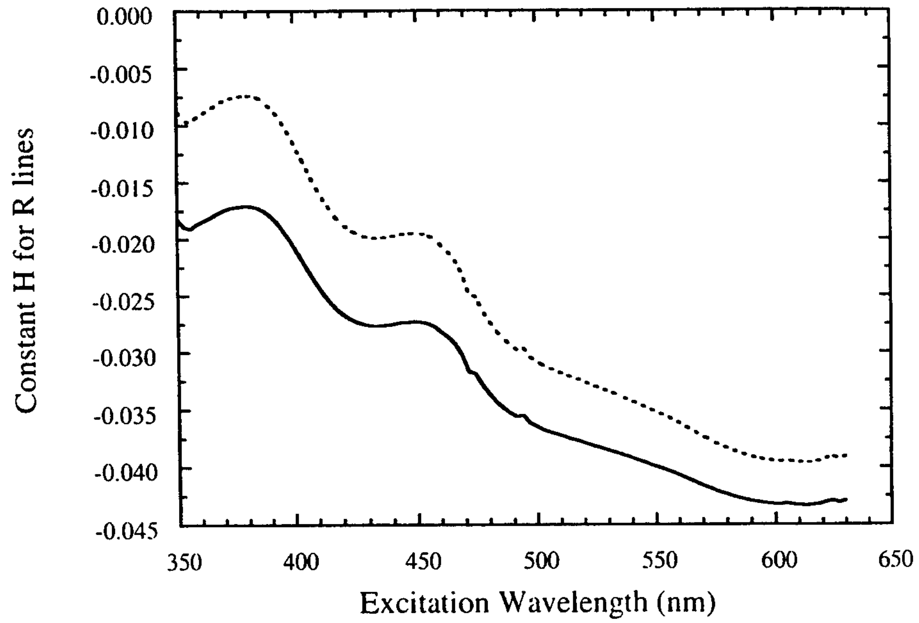

Fig. 11. Variation of constant H (Eq. (16*b*)) for the R lines with the excitation wavelength ((—) R1 and (---) R2). Values of the integrated dichroic ratio used in the calculation are 14.2 and 4.2 for the R1 and R2 lines, respectively. Dichroic ratio of excitation was obtained from the absorption spectra in Fig. 7.

$$a_{ij} = \begin{pmatrix} 1 & 0 & 0 \\ 0 & \cos\theta & -\sin\theta \\ 0 & \sin\theta & \cos\theta \end{pmatrix} \tag{A-5}$$

which can be used in the evaluation of the stress components.

APPENDIX B

Average R-Line Intensity Ratio in Polycrystalline Al_2O_3

If we ignore the fluorescence excited by the scattered light from grain boundaries,[†] the emission from every grain in a polycrystalline Al_2O_3 can be treated independent of each other, and the overall emission polarization effects can be treated as a simple summation of the spectra from individual grains. As a result, the average intensity ratio of the R2 line to the R1 line is the ratio of the overall intensity of the R2 lines to that of the R1 lines. In the case of the laser $\boldsymbol{E}$ vector parallel to the collection direction $\boldsymbol{S}$, the R-line intensity is just a function of θ, as indicated in Eq. (3). In terms of ruby optical constants, then Eq. (3) can be written as

$$I(\mathrm{R2}) \propto \left(\int_{\mathrm{R2}} \Omega_\pi \, \mathrm{d}\nu \cos^2\theta + \int_{\mathrm{R2}} \Omega_\sigma \, \mathrm{d}\nu \sin^2\theta\right) \times (\Omega_\pi^{\mathrm{ex}} \cos^2\theta + \Omega_\sigma^{\mathrm{ex}} \sin^2\theta)\frac{K}{1+K} \tag{B-1a}$$

$$I(\mathrm{R1}) \propto \left(\int_{\mathrm{R1}} \Omega_\pi \, \mathrm{d}\nu \cos^2\theta + \int_{\mathrm{R1}} \Omega_\sigma \, \mathrm{d}\nu \sin^2\theta\right) \times (\Omega_\pi^{\mathrm{ex}} \cos^2\phi + \Omega_\sigma^{\mathrm{ex}} \sin^2\phi)\frac{1}{1+K} \tag{B-1b}$$

If the orientations of the grains are random, then the probability of a grain oriented at (θ,ϕ,ψ) is given by

$$p(\theta,\phi,\psi) = \left(\frac{1}{8\pi^2}\right) \sin\theta \, \mathrm{d}\theta \, \mathrm{d}\phi \, \mathrm{d}\psi \tag{B-2}$$

By averaging over all possible angles, the average R-line intensity ratio is obtained:

$$\overline{I(\mathrm{R2})/I(\mathrm{R1})} = \frac{\iiint p(\theta,\phi,\psi) I(\mathrm{R2}) \, \mathrm{d}\theta \, \mathrm{d}\phi \, \mathrm{d}\psi}{\iiint p(\theta,\phi,\psi) I(\mathrm{R1}) \, \mathrm{d}\theta \, \mathrm{d}\phi \, \mathrm{d}\psi} = \frac{\left(3 + \frac{2\Omega_\sigma^{\mathrm{ex}}}{\Omega_\pi^{\mathrm{ex}}}\right)\int_{\mathrm{R2}} \Omega_\pi \, \mathrm{d}\nu + \left(2 + \frac{8\Omega_\sigma^{\mathrm{ex}}}{\Omega_\pi^{\mathrm{ex}}}\right)\int_{\mathrm{R2}} \Omega_\sigma \, \mathrm{d}\nu}{\left(3 + \frac{2\Omega_\sigma^{\mathrm{ex}}}{\Omega_\pi^{\mathrm{ex}}}\right)\int_{\mathrm{R1}} \Omega_\pi \, \mathrm{d}\nu + \left(2 + \frac{8\Omega_\sigma^{\mathrm{ex}}}{\Omega_\pi^{\mathrm{ex}}}\right)\int_{\mathrm{R1}} \Omega_\sigma \, \mathrm{d}\nu} K \tag{B-3}$$

Rewriting Eq. (B-3) in terms of constants E, F, and G, defined in Eq. (12), and using the fitting values presented previously,

$$\overline{I(\mathrm{R2})/I(\mathrm{R1})} = 1.64\left(\frac{11.4 + \frac{35.6\Omega_\sigma^{\mathrm{ex}}}{\Omega_\pi^{\mathrm{ex}}}}{31.4 + \frac{115.6\Omega_\sigma^{\mathrm{ex}}}{\Omega_\pi^{\mathrm{ex}}}}\right) \tag{B-4}$$

The result is plotted in Fig. 10 for excitation wavelengths of 350–600 nm, based on the frequency dependence of absorption dichroic ratio, $\Omega_\sigma^{\mathrm{ex}}/\Omega_\pi^{\mathrm{ex}}$, measured in this work. It shows that the overall intensity ratio varies very slowly with the change of the excitation wavelength.

Acknowledgments: The authors are grateful to V. Srikant for making the absorption measurements and to John Bowers for helpful discussions.

References

[1]S. Sugano and Y. Tanabe, "Absorption Spectra of Cr^{3+} in Al_2O_3, Part A. Theoretical Studies of the Absorption Bands and Lines," *J. Phys. Soc. Jpn.*, **13**, 880–99 (1958).

[2]S. Sugano and I. Tsujikawa, "Absorption Spectra of Cr^{3+} in Al_2O_3, Part B. Experimental Studies of the Zeeman Effect and Other Properties of the Line Spectra," *J. Phys. Soc. Jpn.*, **13**, 899–910 (1958).

[3]D. S. McClure, "Optical Spectra of Transition-Metal Ions in Corundum," *J. Chem. Phys.*, **36**, 2757–79 (1962).

[4]R. M. Macfarlane, "Analysis of the Spectrum of d^3 Ions in Trigonal Crystal Fields," *J. Chem. Phys.*, **39**, 3118–26 (1963).

[5]D. S. McClure, "Electronic Spectra of Molecules and Ions in Crystals Part II. Spectra of Ions in Crystals"; pp. 399–524 in *Solid State Physics*, Vol. 9. Edited by F. Seitz and D. Turnbull. Academic Press, New York and London, U.K., 1959.

[6]B. V. Thosar, "The Polarization of Luminescence of Ruby," *Phys. Rev.*, **60**, 616 (1941).

[7]B. V. Thosar, "Polarization of Luminescence in Crystals," *J. Chem. Phys.*, **10**, 246 (1942).

[8]S. E. Molis and D. R. Clarke, "Measurement of Stress Using Fluorescence in an Optical Microprobe: Stresses around Indentations in a Chromium-Doped Sapphire," *J. Am. Ceram. Soc.*, **73**, 3189–94 (1990).

[9]Q. Ma and D. R. Clarke, "Stress Measurement in Single-Crystal and Polycrystalline Ceramics Using Their Optical Fluorescence," *J. Am. Ceram. Soc.*, **76**, 1433–40 (1993).

[10]Q. Ma, L. C. Liang, D. R. Clarke, and J. W. Hutchinson, "Mechanics of the Push-Out Process from *In Situ* Measurement of the Stress Distribution along Embedded Sapphire Fibers," *Acta Metall. Mater.*, **42**, 3299–308 (1994).

[11]V. Sergo, D. R. Clarke, and W. Pompe, "Deformation Bands in Ceria-Stabilized Tetragonal Zirconia/Alumina: I. Measurement of the Internal Stresses," *J. Am. Ceram. Soc.*, **78** [3] 633–40 (1995).

[12]D. M. Lipkin and D. R. Clarke, "Measurement of Stress in Oxide Scales Formed by Oxidation of Aluminum-Containing Alloys," *Oxid. Met.*, **45** [3/4] 267–80 (1996).

[13]J. He and D. R. Clarke, "Determination of the Piezospectroscopic Coefficients for Chromium-Doped Sapphire," *J. Am. Ceram. Soc.*, **78** [5] 1347–53 (1995).

[14]D. M. Dodd, D. L. Wood, and R. L. Barns, "Spectrophotometric Determination of Chromium Concentration in Ruby," *J. Appl. Phys.*, **35**, 1183–86 (1964).

[15]C. P. Poole Jr., "The Optical Spectra and Color of Chromium Containing Solids," *J. Phys. Chem. Solids*, **25**, 1169–82 (1964).

[16]D. C. Cronemeyer, "Optical Absorption Characteristics of Pink Ruby," *J. Opt. Soc. Am.*, **56**, 1703–706 (1966).

[17]Q. Ma and D. R. Clarke, "Measurement of Residual Stresses in Sapphire Fiber Composites Using Optical Fluorescence," *Acta Metall. Mater.*, **41**, 1817–23 (1993).

[18]Q. Ma and D. R. Clarke, Stress Measurement Using Optical Fluorescence, AMD, Vol. 181, *Experiments in Smart Materials and Structures*. Edited by K.-S. Kim. American Society of Mechanical Engineers, New York, 1993. □

[†] This assumption may not be valid if probes with large depths of field relative to grain size are used. In this case, grains far below the surface can be excited by the light penetrating through grain boundaries above, and scattering could change the polarization of the incident light substantially. The ideal case is thin films with columnar grains.

Pergamon

0956-7151(95)00341-X

Acta mater. Vol. 44, No. 6, pp. 2353–2359, 1996
Elsevier Science Ltd
Copyright © 1996 Acta Metallurgica Inc.
Printed in Great Britain. All rights reserved
1359-6454/96 $15.00 + 0.00

RESIDUAL STRESSES IN DIELECTRICS CAUSED BY METALLIZATION LINES AND PADS

M. Y. HE[1], J. LIPKIN[1], D. R. CLARKE[1], A. G. EVANS[2] and M. TENHOVER[3]
[1]Materials Department, University of California, Santa Barbara, CA 93106-5050,
[2]Division of Applied Sciences, Harvard University, Pierce Hall, Cambridge, MA 02138 and
[3]Wendell Research Center, Carborundum Company, Niagara Falls, NY, U.S.A.

(Received 12 May 1995; in revised form 25 August 1995)

Abstract—Residual stresses in dielectrics and semiconductors induced by metal lines, pads and vias can have detrimental effects on the performance of devices and electronic packages. Analytical and numerical calculations of these stresses have been performed for two purposes. (1) To illustrate how these stresses relate to the residual stress in the metallization and its geometry; (2) to calibrate a piezo-spectroscopic method for measuring these stresses with high spatial resolution. The results of the calculations have been presented using non-dimensional parameters that both facilitate scaling and provide connections to the stresses in the metal, with or without yielding. Preliminary experimental results obtained for Au/Ge eutectic pads illustrate the potential of the method and the role of the stress analysis.

1. INTRODUCTION

Residual stresses have an important (and sometimes, crucial) influence on the fabrication and reliability of many devices [1–3]. Both intrinsic and thermal expansion mismatch stresses are involved [4]. A knowledge base has been established that provides some understanding about the origin of these stresses [4], as well as their effect on decohesion at interfaces and on cracking [5, 6]. However, a continuing problem is the quantitative prediction of the magnitude of these stresses and of the incidence of decohesion and cracking.

The principal problem concerns the stresses induced by the metallization. These are caused either by interconnects or vias or by the brazes used to attach the Si to the dielectric [1, 2]. Residual stresses associated with metallization have previously been measured by one of two methods: beam bending and X-rays [7, 8]. These methods have been used with continuous metal films on either dielectric or semiconductor substrates. Beam curvature and X-ray line shift measurements give the average stress in the metal. In special cases, X-ray methods can measure the stress gradient as a function of depth normal to the interface [9].

The greater challenge is to address the spatial distribution of stress in the substrate when the metallization is patterned to form interconnects, vias or pads. These stresses dominate interface decohesion and cracking [5, 6]. So far, measurements have been sparse and calculations limited. Laser-based piezo-spectroscopic methods have the requisite resolution [10–12]. These methods include fluorescence [10, 11] and Raman spectroscopy [12]. Either method is capable of obtaining stress information in the substrate around the metallization.

One purpose of the present study is to demonstrate the fluorescence spectroscopy method for obtaining stresses in a dielectric substrate with high spatial resolution. The other is to inter-relate these stresses to those in the metal. Numerical calculations and preliminary experiments performed on eutectic metal pads are used for these purposes.

2. STRESS MEASUREMENT METHOD

2.1. *Approach*

A gold–germanium eutectic on Cr-doped sapphire (ruby) was chosen as the model metal/dielectric system, such that stress measurements could be made using a piezo-spectroscopic technique, based on the systematic shift of fluorescence lines with stress [10]. Electrons excited from the chromium ions in the ruby by a laser decay back to the ground state, emitting photons in the process. In stress-free ruby, these photons occur at two characteristic frequencies. Application of stress perturbs the local environment of the chromium ion, shifting the fluorescence lines to higher or lower frequencies, depending on the stress state [11, 13]. This frequency shift $\Delta\nu$ can be related to the stresses in the sapphire lattice σ_{ij}, by the following constitutive relation [13]:

$$\Delta\nu = \Pi_{ii}\sigma_{ii} \qquad (1)$$

where Π_{ii} is the first-order piezo-spectroscopic coefficient. Second-order effects are small for the configurations used in the present study and are neglected. However, $\Delta\nu$ is affected by the temperature [13], such that laser-induced temperature changes can be problematical, unless independently measured.

2.2. Experimental procedures

Stress measurements have been made in the substrate surface by employing a chromium "in-diffusion" technique [14], wherein only the top (micron-thick) layer of the substrate fluoresces. For this purpose, a basal plane oriented sapphire substrate was prepared by evaporating 200 Å of chromium onto one surface, followed by heating in a vacuum furnace for 2 h at 1500°C to diffuse the chromium into the sapphire. The metal features were created by DC Magnetron sputtering. The first two layers comprised an adhesion layer of W/Ti and a diffusion barrier of Pt/Rh, each ~100 nm thick. The final 40 μm thick Au/Ge layer had the eutectic composition. The features comprised square pads, 2.1 mm on edge, having rounded corners (Fig. 1). A typical surface profile is shown in Fig. 1(a). A magnification of the edge is shown in Fig. 1(b). However, there was significant variability in the edge profile from pad to pad.

Stress measurements were made using an Optical Microprobe in which a laser beam could be focused to a spot ~1 μm diameter. Samples were probed across the center of each feature by translating in 1 μm steps using a linear actuator. Argon reference spectra were used to correct for mechanical drift in the optics. The temperature was monitored to account for peak shifts due to temperature changes. The spectra were analyzed using a commercial software package, wherein each peak was fit to a mixed Gaussian–Lorentzian function. The central position of each peak was used to determine the stress by taking a point far from the feature as a stress-free reference.

2.3. Spatial convolution

When the stresses exhibit large spatial variability over short distances, the finite size of the optical probe convolutes the stress function, $\sigma(x)$ with the probe response function, $p(x)$. In order to deconvolute the measured fluorescence profile, $p(x)$ must be experimentally calibrated. This was done by using a step-source. The function $C(x)$ measured at such a source is simply related to $p(x)$, by,

$$p(x) \propto \mathrm{d}C/\mathrm{d}x. \tag{2}$$

Experimentally, a step function has been created by placing a 200 Å thick line of Au onto a Cr^{3+} doped sapphire substrate. Scanning in 1 μm steps across the edge has given the convolution of the probe function with a step function shown in Fig. 2(a). Upon fitting the derivatives to a Lorentzian, [Fig. 2(b)], the probe

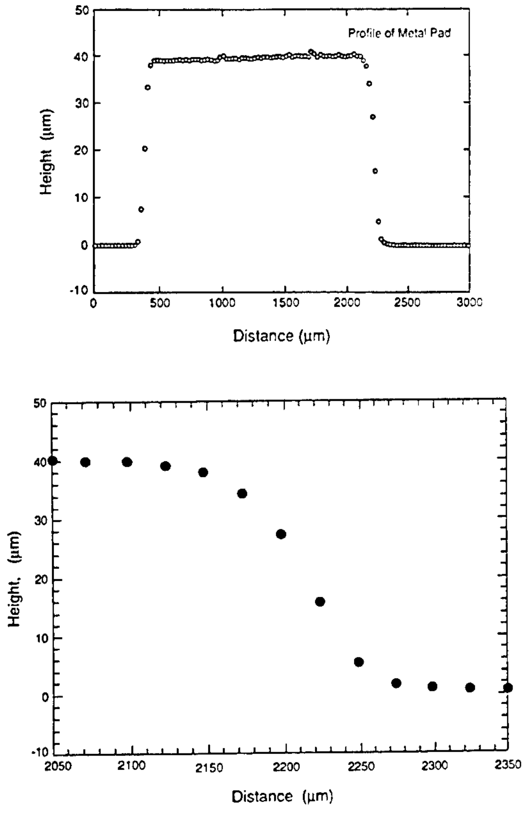

Fig. 1. (a) Atomic force microscopy scan of Au/Ge eutectic pad on sapphire substrate; (b) magnification of the edge profile.

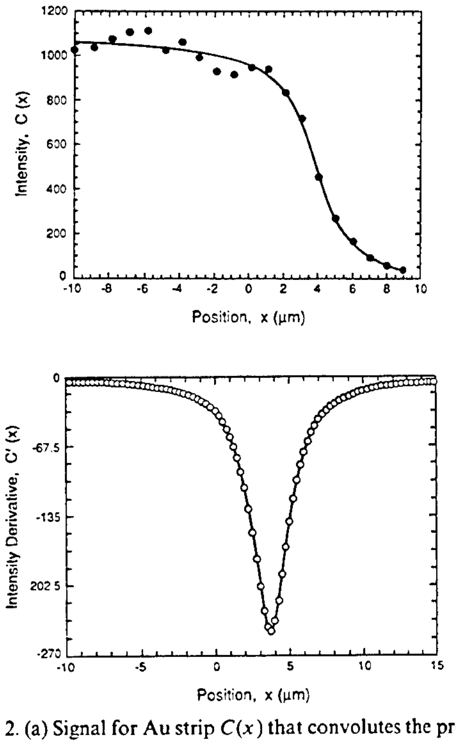

Fig. 2. (a) Signal for Au strip $C(x)$ that convolutes the probe function $p(x)$ with the step function. (b) The derivative of $C(x)$ that gives the probe width.

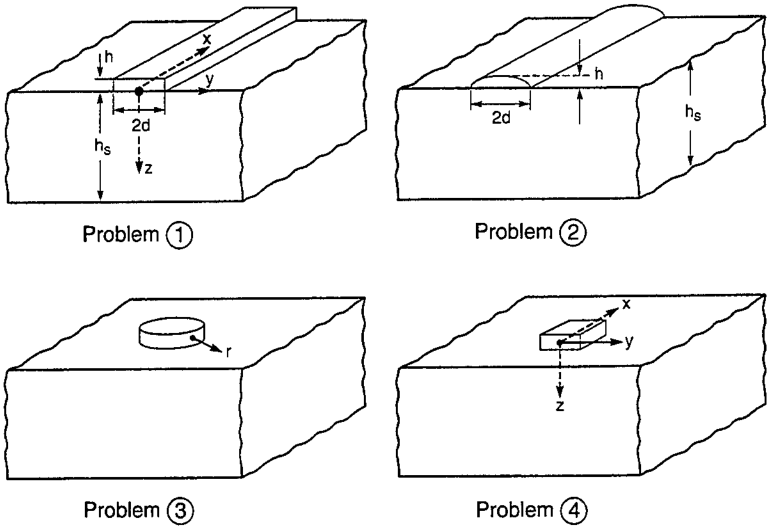
h
x
y
2d
h_s
z
Problem ①
h
2d
h_s
Problem ②
r
Problem ③
x
y
z
Problem ④

Fig. 3. The metallization geometries used for the numerical calculations.

width at half maximum was found to be 3 μm. The high spatial resolution of the fluorescence probing is thus affirmed.

3. STRESS ANALYSIS

3.1. *Procedure*

A finite element method has been used to calculate the stresses in the dielectric. Four representative metallization geometries have been used: a line having uniform thickness [Fig. 3(a)], a line having constant curvature [Fig. 3(b)], a circular pad [Fig. 3(c)] and a square pad [Fig. 3(d)] both with constant thickness. The dielectric is considered to be elastic and the metal elastic–perfectly plastic, with yield strength, σ_0. Residual strain in the system has been motivated by a mismatch in thermal expansion coefficient between the metal, α_m, and the dielectric, α_d ($\Delta\alpha = \alpha_m - \alpha_d$), and a cooling temperature, ΔT (Fig. 4).

3.2. *Analytical approximations*

Useful principles are established by means of approximate analytical calculations (Fig. 5). A pair of line forces in the x-axis, P per unit thickness,

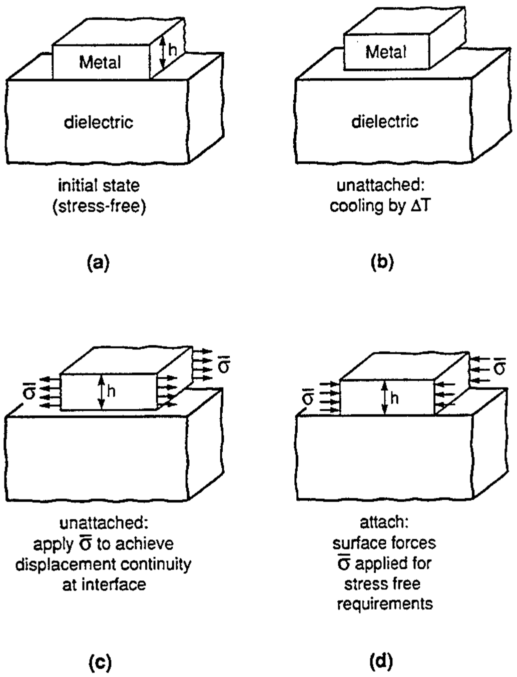
Metal
h
dielectric
Metal
dielectric
$\bar{\sigma}$
h
$\bar{\sigma}$
$\bar{\sigma}$
h
$\bar{\sigma}$

initial state (stress-free)

(a)

unattached: cooling by ΔT

(b)

unattached: apply $\bar{\sigma}$ to achieve displacement continuity at interface

(c)

attach: surface forces $\bar{\sigma}$ applied for stress free requirements

(d)

Fig. 4. The differential strain that causes the stresses in the substrate.

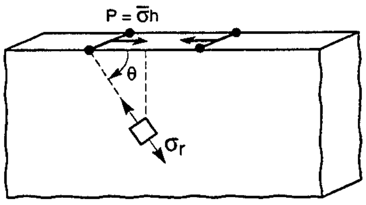
$P = \bar{\sigma}h$
θ
σ_r

(a) Stresses Induced by Surface Forces, P

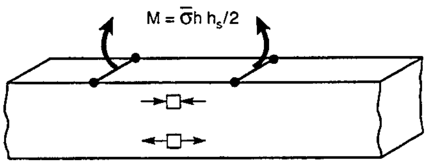
$M = \bar{\sigma}h\, h_s/2$

(b) Bending Induced Stresses

Fig. 5. The forces and moments imposed by the metallization used to obtain analytical estimates for the stress in the dielectric.

is applied to the dielectric surface where the film terminates ($y = +\mathrm{d}$), such that,

$$P = -\bar{\sigma}h \tag{3}$$

where $\bar{\sigma}$ is the average misfit (residual) stress in the film and h is the film thickness. The stresses σ_{yy} in the dielectric around thin metal strips, width $2d$, are then obtained from the following formulae [Fig. 5(a)]. The stresses along the dielectric surface ($z = 0$), are [15]

$$\frac{\sigma_{yy}d}{\bar{\sigma}h} = \frac{4/\pi}{[(y/d)^2 - 1]} \tag{4a}$$

and along the symmetry plane ($y = 0$),

$$\frac{\sigma_{yy}d}{\bar{\sigma}h} = \frac{4/\pi}{[(z/d)^2 + 1]}. \tag{4b}$$

The large tensile stress concentrations near the edge are a particular concern for fracture in the dielectric and for interface debonding.

For finite substrates thickness h_s, bending occurs and redistributes the stress. The stresses induced by bending are given by beam theory [Fig. 5(b)]. The stresses near the surface ($z \approx 0$) are [15]

$$\frac{\sigma_{yy}d}{\bar{\sigma}h} = \frac{3d}{h_s} \tag{5a}$$

and along the symmetry plane ($y = 0$),

$$\frac{\sigma_{yy}d}{\bar{\sigma}h} = -\frac{3d}{h_s}\left[\left(1 - \frac{2z}{h_s}\right)\right]. \tag{5b}$$

The total stresses in the dielectric substrate are the sum of equations (4) and (5).

For plane strain ($\varepsilon_{xx} = 0$), the σ_{xx} stresses can be readily obtained from σ_{yy} because $\sigma_{zz} \approx 0$, giving,

$$\sigma_{xx} = \nu\sigma_{yy} \tag{6a}$$

such that

$$\sigma_{xx} + \sigma_{yy} = \sigma_{yy}(1 + \nu). \tag{6b}$$

3.3. Numerical results

The finite element method was used to obtain detailed results for the substrate stresses induced by metal lines or pads (Fig. 3). Problems 1 and 2 (metal lines) were treated as plane strain and problem 3 (metal pad) as axisymmetric. For comparison, a 3-D finite element analysis has been performed for a square pad, problem 4. A general purpose finite element code, ABAQUS, with eight-node biquadratic elements is used for the plane strain and axisymmetric calculations and 20-node quadratic brick elements for the 3-D calculations.

3.3.1. Uniform thickness metallizations. The analytical approximations have established that the normalized stresses in the dielectric, $\sigma_{ij}d/\sigma_0 h$, are only dependent on the system geometry. They are independent of the material properties. This was first affirmed by finite element results calculated for narrow lines with a range of properties: $E_d/E_m = 1$–6 and $\bar{\sigma}_0/E_m = 0.0005$–$0.007$ (subscript d for dielectric and m for metallization).

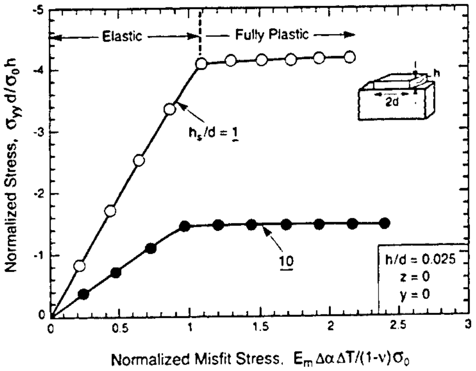

Fig. 6. Effect of misfit strain on the stress induced in the dielectric beneath a thin metal line ($z = y = 0$).

All subsequent results are for, $E_d/E_m = 6$ and $\sigma_0/E_m = 0.001$. The system geometries were varied within the ranges $0.04 \leq h/d \leq 0.1$ and $1 \leq h_s/d \leq 10$. A typical finite element mesh includes 760 elements and 2409 nodes. A convergence study revealed that these meshes provided accurate results.

(i) Narrow Lines

The normalized σ_{yy} stresses in the dielectric at the symmetry plane, near the interface ($y = 0$, $z = 0$), are plotted in Fig. 6 as functions of the normalized misfit stress, $\Omega = E_m\Delta\alpha\Delta T/(1 - \nu)\sigma_0$. The σ_{yy} stress increases linearly with increase in Ω until the metal line has fully yielded, at $\Omega \approx 1$. Thereafter, the σ_{yy} remains constant. The stress distributions along the symmetry plane ($y = 0$) after the metal line has fully yielded are summarized in Figs 7 and 8 (for $h/d = 0.025$, 0.04, 0.1 and $h_s/d = 1$, 10). Note that the same normalized stresses would obtain before yielding, if the yield strength σ_0 were replaced by the misfit stress in the metal. For a relatively thin substrate ($h_s/d = 1$), the stresses vary linearly with the distance from the surface, because the stresses are dominated by bending (Fig. 7). For thicker substrates, the

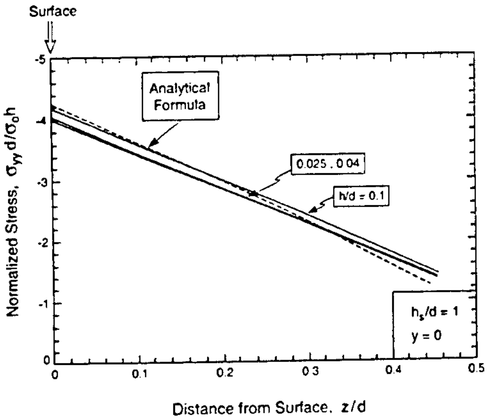

Fig. 7. Stresses in the dielectric beneath the metal ($y = 0$) for a fully yielded narrow metal line, $h_s/d = 1$. The analytical results are also shown.

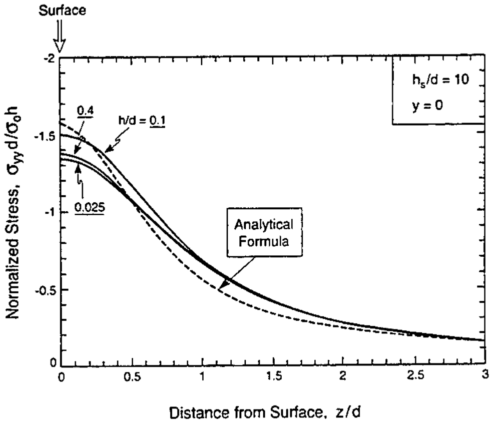

Fig. 8. Stresses in the dielectric beneath the metal ($y = 0$) for a fully yielded narrow, thin metal line, $h_s/d = 10$.

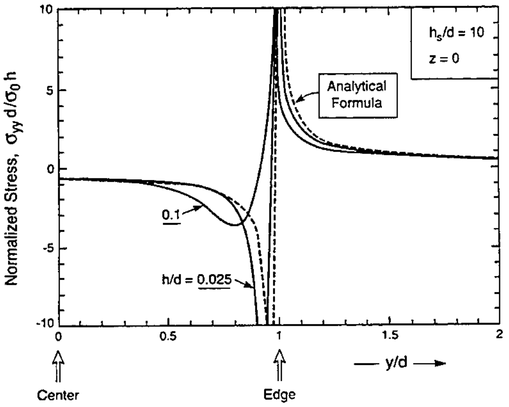

Fig. 9. Stresses in the dielectric, near the surface ($z = 0$) for a fully yielded narrow, thin metal line ($h_s/d = 10$). The analytical result is also shown.

stresses vary rapidly near the metal strip (Fig. 8) and are given with good accuracy by the analytical formula [equation (4)]. The large stress concentrations near the edge ($z = 0$, $y = d$) are confirmed (Fig. 9). Moreover, the numerical results approach the analytical results at smaller h/d (Fig. 9).

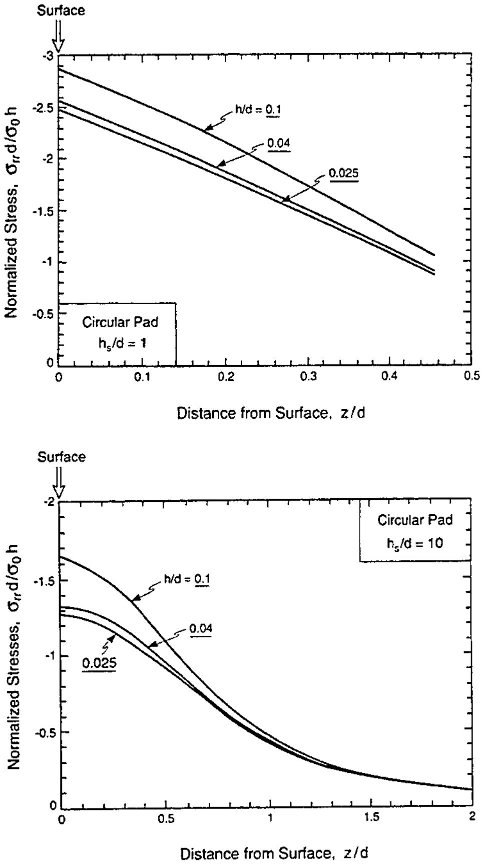

Fig. 10. Stresses in the substrate beneath a circular pad, at the symmetry location ($y = 0$): (a) thin substrate, $h_s/d = 1$; (b) thick substrate, ($h_s/d = 10$).

(ii) Circular Pad

The equivalent results for the circular pad are summarized in Figs 10 and 11. As for the line, the

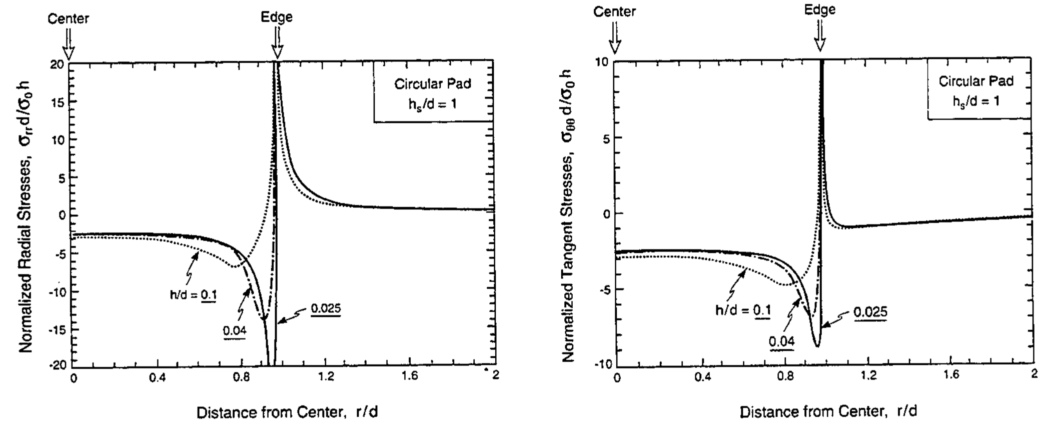

Fig. 11. Stresses near the surface of the dielectric ($z = 0$) beneath a circular pad, ($h_s/d = 10$): (a) radial stresses; (b) tangential stress.

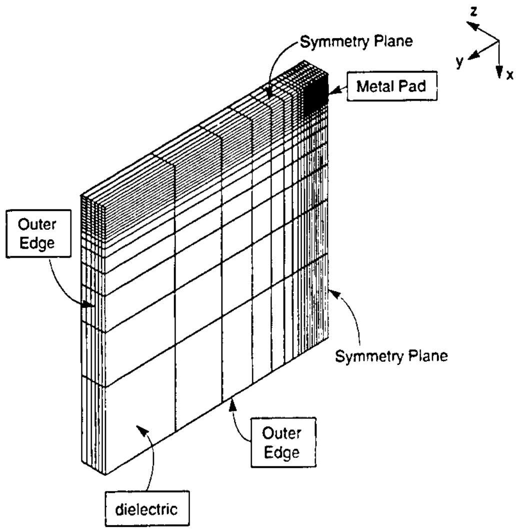

Fig. 12. The finite element mesh used for analysis of the square pad. For symmetry reasons, only 1/4 of the pad/substructure need be analyzed. The metal pad is at the top right outlined by ABCD. It is located on the face projected onto the plane of the figure.

film becomes fully plastic when $\Omega \geq 1$. The stress distributions along the symmetry plane ($y = 0$) after the metal pad has fully yielded are summarized in Fig. 10 (for $h/d = 0.025$, 0.05, 0.1 and $h_s/d = 1$, 10). For a relatively thin substrate ($h_s/d = 1$), the stresses again vary linearly with the distance from the surface [Fig. 10(a)]: whereas, for thicker substrates, the stresses vary rapidly near the metal strip [Fig. 10(b)]. The numerical results for the radial σ_{rr} and tangential $\sigma_{\theta\theta}$ stresses near the edge and the interface (Fig. 11) indicate higher stresses at smaller h/d.

(iii) Square Pad

The 3-D finite element analysis performed for a square pad, with $h/d = 0.025$, $h_s/d = 10$, includes 2900 20-node quadratic brick element and 13923 nodes (Fig. 12). The computation required about 17 h of CPU time to complete 10 increments, to ensure that the metal pad had fully yielded. The σ_{yy} stresses along the symmetry plane ($x = 0$, $z = 0$) near the interface, after the metal pad has fully yielded (Fig. 13), coincide closely with the axisymmetric values, except in the region near the edge. This result suggests that the results for the circular pads can be used to a good approximation for square pads.

3.3.2. Curved lines. For a line with constant curvature, the σ_{yy} stress distributions along the interface ($z = 0$) after the metal line has fully yielded are summarized in Fig. 14 (for $h/d = 0.1$, 0.2, 1.0 and $h_s/d = 10$). These stresses are compressive at the center of the line, but become tensile near the edge and reach a maximum at the edge. A comparison with the solution for a line of uniform thickness [Fig. 14(b)] illustrates one similarity and two differences. The stresses along the symmetry plane ($y = 0$) are similar. However, when the line has a curved surface, the compressive edge stress concentration is absent and the tensile concentration has substantially reduced magnitude. A rounded edge having the measured profile indicated in Fig. 1(b) causes similar effects [Fig. 14(b)] but the stress reductions are much smaller.

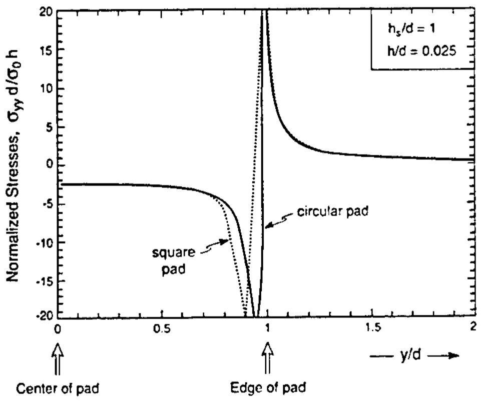

Fig. 13. The σ_{yy} stresses near the surface ($z = 0$) for the square pad, compared with those for the circular pad ($h_s/d = 10$).

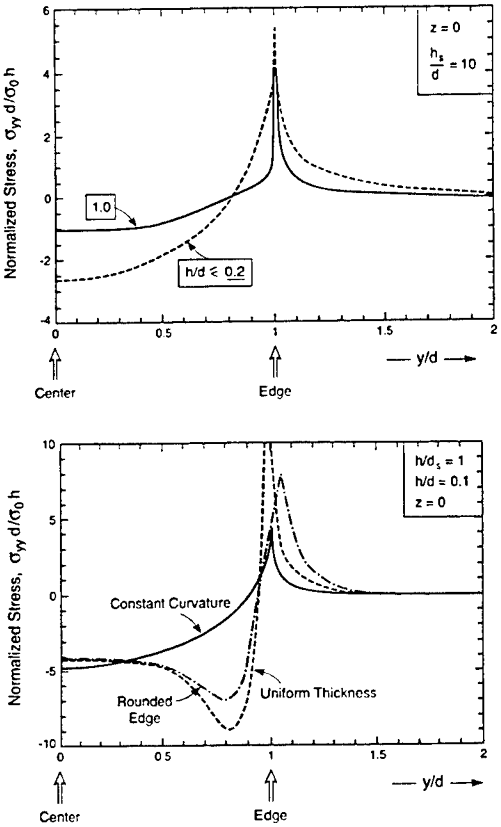

Fig. 14. (a) The σ_{yy} stresses near the surface ($z = 0$) of a line having constant curvature ($h_s/d = 10$); (b) a comparison of the σ_{yy} stresses for lines having different profiles.

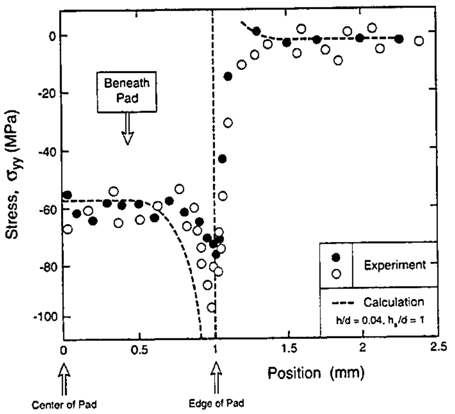

Fig. 15. Two experimental results for the σ_{yy} stresses beneath a Au/Ge square pad on sapphire. Also plotted is the stress calculated for a pad having the measured profiled indicated in Fig. 1(c).

4. PRELIMINARY EXPERIMENTAL RESULTS

Fluorescence scans made across the center of the flat, square Au/Ge pads are indicated in Fig. 15. The line shifts exhibit the same four features evident in the stresses: (i) sharp maxima at the edges of the pads; (ii) a minimum at the pad center; (iii) a rapid approach to zero beyond the pads; and (iv) a sign change from regions beneath the pad to those outside. The line shifts beneath the pads were quite reproducible, but there was appreciable pad-to-pad variability in the magnitude of the pads at the pad termination.

A convenient means for comparing the measured peak shifts with the calculated values is to *first* use the results near the pad center, where the stresses are relatively uniform and essentially unaffected by the probe width. *Subsequently*, the full spatial distribution can be correlated. For circular, flat pads ($h_s/d \approx 10$, the stresses near the center) are (Figs 10 and 11),

$$\sigma_{rr} \approx \sigma_{\theta\theta} = -2.6\sigma_o h/d \qquad (7)$$

$$\sigma_{zz} \approx \sigma_{zx} \approx \sigma_{zy} \approx 0.$$

The line shift [equation (1)] is thus

$$\Delta\nu \approx 5.2\Pi_{ii}(\sigma_o h/d) \qquad (8a)$$

enabling the stress in the metallization to be expressed as

$$\sigma_o \approx \frac{\Delta\nu\,(d/h)}{5.2\Pi_{ii}}. \qquad (8b)$$

Inserting the measured line shift gives a stress $\sigma_o \approx 600$ MPa. This stress is comparable with the tensile yield strength for this eutectic, estimated by hardness indentation as 550 MPa. The implication is that the thermal expansion mismatch, upon cooling after deposition, has been sufficient to cause yielding of the eutectic. However, there is an elevation in the temperature induced by the laser, which has not been accounted for in the analysis. Further study would be needed to address this effect.

The probe used in these studies has sufficiently narrow width (3μm) that the convolution of the calculated stresses with the probe function $p(x)$, is essentially the same as the stress itself. Hence, it should be possible to superpose the measured stresses directly onto the values calculated for the pad with the rounded edges (Fig. 15). The measured values, though having extensive variability at the edges, appear to reproduce the calculations.

5. CONCLUDING REMARKS

Stresses induced in a dielectric substrate by surface metallizations have been calculated for a range of geometric configurations. The stresses attain maximum values dictated by the yield strength of the metal. These arise whenever the misfit strains caused by thermal expansion, etc. are large enough to exceed the yield strain. There are large stress concentrations near the edges of the lines. These stress peaks can be diminished by altering the profile of the metallization, toward a more rounded configuration.

Piezo-spectroscopic measurements of the stress in sapphire induced by metal pads have been made. The principal finding is that the stresses measured beneath the pad (in the sapphire), where edge effects have a minimal influence, coincide closely with the calculated values.

REFERENCES

1. A. T. English and C. M. Melliar-Smith, *Ann. Rev. Mater. Sci.* **8,** 459 (1978).
2. R. R. Tummala, *J. Am. Ceram. Soc.* **74,** 894 (1991).
3. R. R. Tummala and E. J. Rymaszewski, *Microelectronic Packaging Handbook.* Van Nostrand-Reinhold, New York (1989).
4. W. D. Nix, *Mater. Trans.* **20A,** 2217 (1989).
5. J. W. Hutchinson and Z. Suo, *Adv. appl. Mech.* **29,** 63 (1992).
6. A. G. Evans and J. W. Hutchinson, *Acta metall. mater.* **43,** 2507 (1985).
7. M. E. Thomas, M. P. Harnett and J. E. McKay, *J. Vac. Sci. Technol.* **A6,** 2570 (1988).
8. I. C. Noyan and J. B. Cohen, *Residual Stress-Measurement by Diffraction and Interpretation.* Springer-Verlag, NY (1987).
9. B. Eigenmann, B. Scholtes and E. Macherauch, *Surf. Engng* **7,** 221 (1993).
10. Q. Ma and D. R. Clarke, *AMD,* **181,** American Society of Mechanical Engineers, 27 (1993).
11. D. M. Lipkin and D. R. Clarke, *Fract. Mech.* **25,** 250 (1995).
12. Q. Ma, S. Chiras, D. R. Clarke and Z. Suo, *J. appl. Phys.* **78,** 1614 (1995).
13. J. He and D. R. Clarke, *J. Am. Ceram. Soc.* **78,** 1347 (1995).
14. Q. Wen, D. R. Clarke, N. Yu and M. Nastasi, *Appl. Phys. Lett.* **66,** 293 (1995).
15. S. Timoshenko and J. N. Goodier, *Theory of Elasticity.* McGraw-Hill, NY (1950).

Pergamon

Acta mater. Vol. 45, No. 8, pp. 3481–3489, 1997
© 1997 Acta Metallurgica Inc.
Published by Elsevier Science Ltd. All rights reserved
Printed in Great Britain
1359-6454/97 $17.00 + 0.00

PII: S1359-6454(96)00395-3

CONVERGENT DEBONDING OF FILMS AND FIBERS

M. Y. HE[1], A. G. EVANS[2] and J. W. HUTCHINSON[2]

[1]Materials Engineering Department, University of California, Santa Barbara, California and [2]Division of Engineering and Applied Sciences, Harvard University, Pierce Hall, Cambridge, MA 02138, U.S.A.

(Received 16 August 1996)

Abstract—Debonding of films attached to substrates as well as fibers embedded in matrices typically involves initiation, steady-state propagation and a final transient as the debond converges on an edge or another debond. The emphasis in this paper is on the mechanics of the transient. Under most circumstances, a converging debond crack is characterized by an energy release rate that approaches zero, causing the crack to arrest without attaining full debonding. The relevance of this phenomenon will be discussed with reference to the measurement of toughness for thin film interfaces and the overall stress–strain behavior of ceramic matrix composites. © *1997 Acta Metallurgica Inc.*

1. INTRODUCTION

Residually stressed thin films debond from attached substrates when the stress and/or the film thickness becomes sufficiently large. The qualitative relation between the energy release rate G motivating growth of a plane strain interface crack is sketched in Fig. 1(a) for a film with a uniform residual stress σ and thickness t. When the crack tip is remote from the edges of the film, steady-state propagation conditions prevail with energy release rate

$$G_{ss} = \frac{1 - \nu_1^2}{2}\frac{\sigma^2 t}{E_1} \qquad (1)$$

where E_1 and ν_1 are the Young's modulus and Poisson's ratio of the film. When the crack is either short or long such that its tip is within several thicknesses of the edge, it "senses" the edge, and G decreases below the steady-state value of equation (1), approaching zero as the distance between the tip and the edge becomes small. Because equation (1) is the maximum energy release rate, the fail-safe criterion against debonding is: $G_{ss} < \Gamma_i$, where Γ_i is the interface toughness at the relevant mode mixity.

Tests to measure the interface toughness of thin film–substrate systems often employ steady-state conditions [1, 2] because the mechanics is simple and because accurate measurement of the crack length is not required. For such tests to be effective, a sharp pre-crack must be introduced. Otherwise, an initiation barrier exists. Often, there is a barrier [Fig. 1(a)] such that the combination of stress and thickness needed to initiate interface crack propagation exceeds that required for steady-state growth, causing $G_{ss} > \Gamma_i$. The debond event is then dynamic, with the crack arresting when the tip approaches the far edge. Such a test would be designated unsuccessful in the sense that G_{ss} [equation (1)] cannot be identified with Γ_i. However, when the relation between G and the crack length as the tip approaches the far edge is known, quantitative conclusions about Γ_i can be made from measurements of the distance between the edge and the arrested crack tip. One purpose of the present paper is to supply the necessary solutions.

The crack arrest phenomenon is depicted in Fig. 2 [3]. It comprises a Ni–polymer bilayer on a polymer monolayer well bonded to a stiff substrate. The interface of interest is that joining the two polymers. The residual tension in the top polymer film is not sufficient to debond the interface. Therefore, a superlayer of Ni with strong adherence to the polymer and a large residual tension has been deposited. It is this stress which supplies the energy needed to debond the polymer–polymer interface. This occurs when the Ni film becomes sufficiently thick that super critical conditions are attained. Further details are given in Section 3.3. Here, it is noted that removal of an initiation barrier requires a complex additional step in specimen preparation [2]. Consequently, determination of the interface toughness from the arrest location of the debond cracks facilitated the testing and also gave more robust data.

Related transient interface debonding is displayed by fibers embedded in brittle matrices. The behavior illustrated in Fig. 1(b) applies to a composite layer with uni-directional fibers carrying an overall stress $\bar{\sigma}$ parallel to the fibers. When matrix cracks develop, a debond propagates up the fiber. The combined effects of applied stress, friction and residual stresses must be superimposed for complete analysis of debond evolution [4, 5]. Here, only the contribution due to the applied stress $\bar{\sigma}$ will be addressed to highlight the convergence effect. There is again an initiation barrier because the energy release rate for very short debonds emerging from the tip of the matrix crack is below its

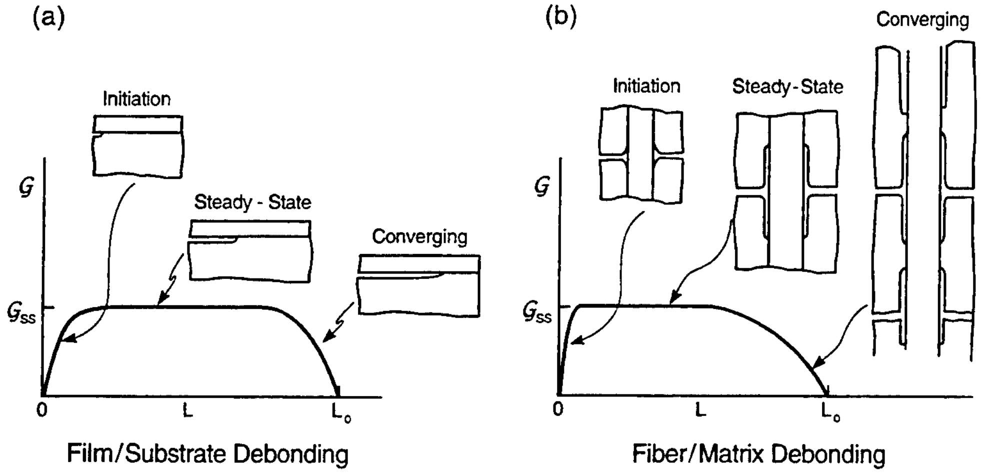
(a)
Initiation
Steady - State
Converging
$\mathcal{G}$
$\mathcal{G}_{ss}$
0
L
L_o
Film/Substrate Debonding
(b)
Converging
Initiation
Steady-State
$\mathcal{G}$
$\mathcal{G}_{ss}$
0
L
L_o
Fiber/Matrix Debonding

Fig. 1. Three stages of debonding for films and fibers.

steady-state magnitude [5]. In steady-state, the energy release is given by [4]:

$$G_{ss} = \frac{(1-f)}{4f^2}\frac{(1-\nu^2)\bar{\sigma}^2 R}{E}, \tag{2}$$

where f is the volume fraction of the fibers and R is their radius. This particular expression is restricted to fibers and matrix having the same isotropic elastic constants, E and ν. The effects of elastic mismatch are addressed later. As a debond spreads along the fiber and converges on another debond extending in the opposite direction from the neighboring matrix crack, the energy release rate approaches zero, as indicated in Fig. 1(b). The converging debonds arrest leaving a portion of the fiber still attached to the matrix. This behavior has implications for the overall stress–strain behavior of the composite discussed in Section 4.

2. THE ASYMPTOTIC LIMIT FOR A CONVERGING DEBOND

Consider two converging crack tips sufficiently close that the only relevant length is the distance ΔL separating them, as depicted by the plane strain problem in Fig. 3. This limit also provides a reasonable approximation for a debond tip approaching a free edge, discussed in connection with

Fig. 2. Thin polymer lines on a Si substrate with a SAM interface, plus a Ni superlayer. The intact ligament length gives the interface toughness.

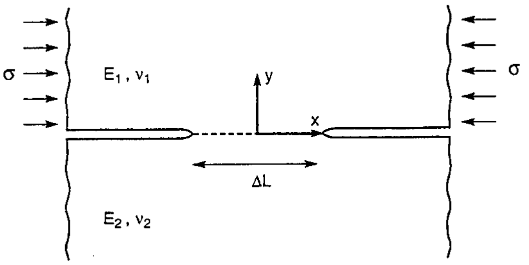

Fig. 3. Geometry and loading for asymptotic debonding problem.

Fig. 1(a). Moreover, it applies to debonds converging along a fiber, because plane strain is attained when the debond tips are close. Subsequent numerical results for the energy release rate will be seen to approach this asymptotic limit in the transition between steady-state and full debonding.

The solution to the problem of isotropic elastic half-planes joined along the interface on $y = 0$, $|x| < \Delta L/2$ and loaded by a remote stress $\sigma_{11} = -\sigma$ in the upper half-plane can be obtained using the complex variable method of elasticity. Similar solutions have been presented by Rice and Sih [6] and Erdogan [7]. The two Dundurs parameters, α and β, measuring the elastic mismatch between the two half-planes enter the solution, as does the so-called oscillation index ϵ defined in terms of β by

$$\epsilon = \frac{1}{2\pi} \ln \left(\frac{1-\beta}{1+\beta} \right). \tag{3}$$

In plane strain, the Dundurs parameters are given by

$$\alpha = \frac{\bar{E}_1 - \bar{E}_2}{\bar{E}_1 + \bar{E}_2}$$

$$\text{and} \quad \beta = \frac{1}{2} \frac{\mu_1(1-2\nu_2) - \mu_2(1-2\nu_1)}{\mu_1(1-\nu_2) + \mu_2(1-\nu_1)}, \tag{4}$$

where $\bar{E} = E/(1-\nu^2)$ and $\mu = E/(2(1+\nu))$ is the shear modulus.

The tractions acting on the bonded portion of the interface are given by

$$\sigma_{22} + i\sigma_{12} = -\frac{i(1-\alpha)\sigma}{2\sqrt{1-\beta^2}} \frac{x e^{-i\epsilon \ln\left(\frac{\Delta L - 2x}{\Delta L + 2x}\right)}}{\sqrt{\Delta L^2 - 4x^2}}. \tag{5}$$

For the crack with tip at $x = -\Delta L/2$, stress intensity factors K_1 and K_2 are defined such that on the interface a short distance r ahead of the tip [8]

$$\sigma_{22} + i\sigma_{12} = \frac{(K_1 + iK_2) r^{i\epsilon}}{\sqrt{2\pi r}}. \tag{6}$$

For the converging debond crack advancing from the left in Fig. 3, the stress intensity factors are

$$K_1 + iK_2 = \frac{i(1-\alpha)\sigma\sqrt{\pi \Delta L}\,(\Delta L)^{-i\epsilon}}{4\sqrt{2(1-\beta^2)}}. \tag{7}$$

The associated energy release rate is given by

$$G = \frac{1-\beta^2}{E_*}\left(K_1^2 + K_2^2\right) = \frac{(1-\alpha)^2\sigma^2\pi\Delta L}{32E_*}. \tag{8}$$

where $E_*^{-1} = (1/2)(\bar{E}_1^{-1} + \bar{E}_2^{-1})$. This result for G normalized by G_{ss} in equation (1) gives

$$\frac{G}{G_{ss}} = \frac{\pi}{16}(1-\alpha)\frac{\Delta L}{t}. \tag{9}$$

Note that G vanishes as the debond tips converge. The energy release rate is a strong function of the elastic mismatch α, but it is independent of β. The mode measure ψ, defined as $\tan\psi = \sigma_{12}/\sigma_{22}$ a distance r ahead of the tip, is obtained from equation (7) as

$$\psi = \frac{\pi}{2} + \epsilon \ln\left(\frac{r}{\Delta L}\right). \tag{10}$$

When $\beta = 0$, the crack tip loading is mode II, with $K_2 = (1-\alpha)\sigma\sqrt{\pi\Delta L}/(4\sqrt{2})$. Otherwise, the tip experiences mixed-mode conditions.

3. THIN FILM DEBONDING

3.1. *Homogeneous films under uniform residual stress*

Various thin film debonding scenarios can be imagined. Figures 4(a)–(c) illustrate the three considered here. The simplest to represent is that depicted in Fig. 4(a) where the elastic energy release in a film with a uniform tensile pre-stress σ drives two interface cracks converging upon each other from opposite directions. The interface stress intensity

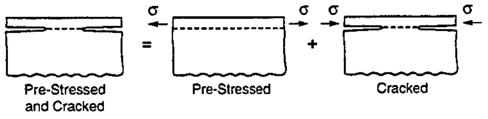

(a) Symmetric Debonds

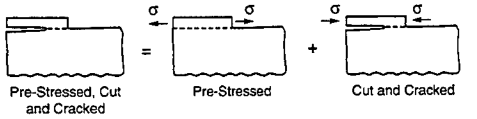

(b) Debond Approaching Film Edge

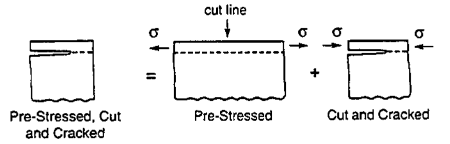

(c) Debond Approaching Film/Substrate Edge

Fig. 4. The scenarios for convergent debonding of thin films.

factors and the energy release rates are determined from the solution to the second of the two elasticity problems indicated on the right in Fig. 4(a). This problem is symmetric with respect to the y-axis. Primary attention, however, is directed towards the second scenario, Fig. 4(b), whereby a uniformly pre-stressed film is terminated at $x = 0$, exposing a free edge. An interface crack propagates from the left towards the free edge. Again, the second elasticity problem on the right in Fig. 4(b) needs to be solved as the crack converges upon the free edge. In this case, the compressive stress σ acting on the right hand free edge of the film is an essential feature of the solution. Since only elastic behavior is considered, the sequence of cutting followed by interface cracking need not be treated as separate events. In the third scenario, Fig. 4(c), both the pre-stressed film and the substrate is terminated along $x = 0$, with the debond crack approaching the free edge. Results for this scenario have not been computed. They are expected to be similar to Fig. 4(b), especially when the substrate is stiff compared with the film.

Results have been computed using a finite element model of the problems depicted in Fig. 4. The width of the model is taken to be 300 t, while the depth of the substrate is taken as 20 t. The bottom of the substrate is constrained against vertical displacement but free to displace horizontally. A highly refined mesh is used in the vicinity of the crack tip. The J-integral is used to evaluate G, and ψ is computed by fitting theoretical crack tip opening and shear displacement amplitudes to the numerical values. An excellent check on the accuracy of the model is provided by the analytical results for the steady-state limit [equation (1)] which is approached at sufficiently large $\Delta L/t$. The corresponding limit for the measure of mode mixity is $\psi = \omega(\alpha)$, where ω is tabulated by Suo and Hutchinson [9]; in the absence of elastic mismatch, $\omega(0) = 52.1^\circ$. Trends in G for four mismatch parameters α are presented in Fig. 5(a) for the second scenario described above. Apart from the curve for $\alpha = -1$ corresponding to the limit of a rigid substrate, the results have been computed with $\beta = 0$. The companion results for the mode-mixity measure, ψ, for the non-rigid substrates are displayed in Fig. 5(b).

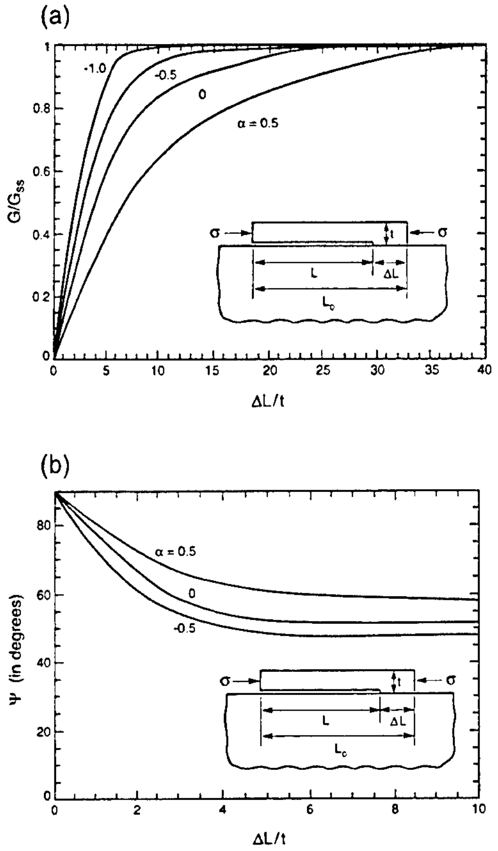

Fig. 5. Energy release rate (a) and measure of mode mixity (b) for convergent debonds.

The debond begins to sense the edge of the film when the tip is within 5–20 times the film thickness, depending on the elastic mismatch. This distance is surprisingly large. It is this feature of the converging debond which allows graceful arrest and makes measurement of interface toughness feasible. Figure 6(a) illustrates the approach to the asymptotic limit [equation (9)] for both symmetrically converging debonds and a debond converging on an edge for a mismatch where the film is compliant relative to the substrate, $\alpha = -1/2$. For this mismatch, the asymptotic result becomes accurate for the symmetrically convergent debonds when $\Delta L/t$ is about 1/2, but it somewhat overestimates the energy release rate for a debond converging on a free edge. A comparison with the asymptotic result over the full mismatch range is given in Fig. 6(b) at $\Delta L/t = 2$, for which there is essentially no difference between the numerical results for the two cases. Another important implication of Fig. 6 is that, when the remaining ligament is greater than about $t/2$, the energy release rate of a symmetrically converging debond is essentially indistinguishable from that for a debond converging on a free edge the same distance away. In other words, the debond is unable to distinguish another debond from a free edge until it has approached to within a film thickness.

Converging debond phenomena have been observed for films delaminating under nominally axisymmetric conditions with an external interface crack propagating inward debonding the remaining circular ligament [10]. As in the plane strain cases analysed here, the energy release rate approaches zero as the remaining ligament is debonded [11]. Gao's [12] result for the asymptotic limit when the ligament radius a becomes small compared to the film thickness is $G = (1 - \nu)\sigma^2 a/[\pi(1 + \nu)E]$ for the case in which the film and substrate have no elastic mismatch and σ is the equi-biaxial pre-stress.

3.2. Homogeneous films under non-uniform residual stress

For completeness, results are derived which enable the determination of G and ψ for the case [Fig. 4(b)] in which a crack converges upon a cut edge when the film has a residual stress that varies through its thickness, $\sigma(y)$. Let $\bar{\sigma} = 1/t \int_0^t \sigma(y)\,dy$ be the average residual stress and M be the moment of distribution about the film midplane, i.e. $M = \int_0^t \sigma(y)(y - t/2)\,dy$. The results presented in the previous sub-section apply for the contribution due to $\bar{\sigma}$. Results for G and ψ for M with $\bar{\sigma} = 0$ are given in Fig. 7 for several α with $\beta = 0$. Note that a two-part composition of the solution [such as that in Fig. 4(b)] applies here also, but with M acting in the opposite sense (Fig. 7). The results apply when $M > 0$, such that the residual stress in the film is tensile at its top surface and compressive at the substrate interface. The debond crack is open; it would be closed when $M < 0$. In steady-state,

$$\bar{G}_{ss} = \frac{1-\nu_1^2}{E_1}\frac{6M^2}{t^3} \tag{11}$$

while $\psi_{ss} = -\pi/2 + \omega(\alpha)$ when $M > 0$, but $\psi_{ss} = -\pi/2$ (mode II) when $M < 0$. The most notable feature brought out by Fig. 7, relative to the results for $\bar{\sigma}$ in Fig. 5, is the considerably smaller domain in which the interface crack departs from steady state.

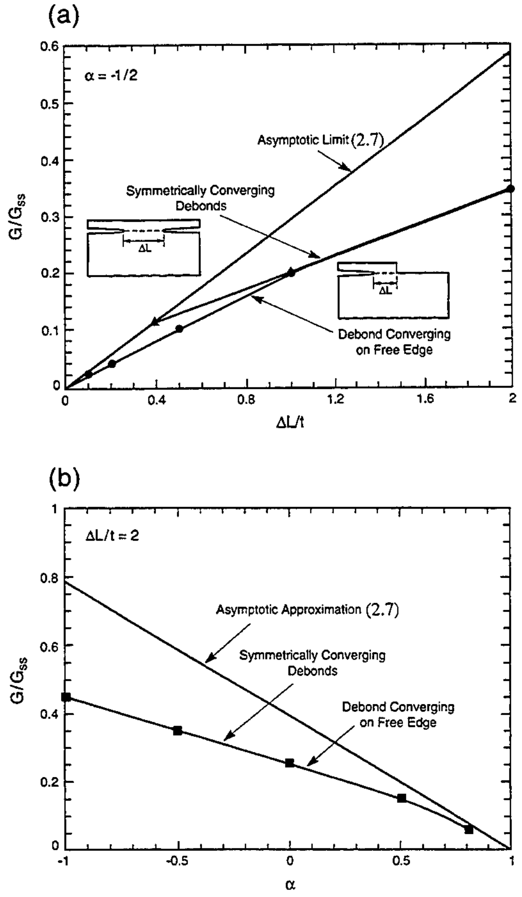

Fig. 6. Comparison of numerical results and asymptotic formula (9) for two cases of convergent debonds: (a) $\alpha = -1/2$; (b) $\Delta L/t = 2$.

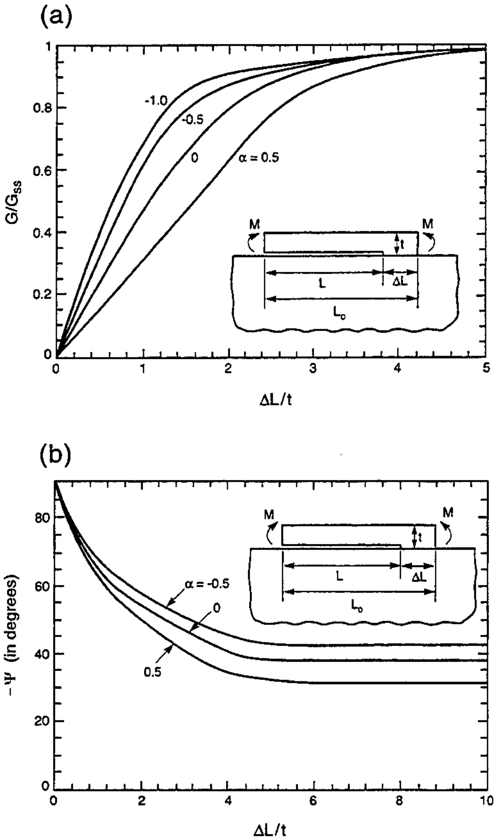

Fig. 7. Energy release rate (a) and measure of mode mixity (b) for converging debond for residual stress equivalent to a moment per unit length M.

Under combined $\bar{\sigma}$ and M, G_{ss} and ψ_{ss} are given by

$$GMa_{ss} = \frac{1-\nu_1^2}{E_1}\left[\frac{\bar{\sigma}^2 t}{2} + \frac{6M^2}{t^3}\right] \tag{12}$$

and

$$\tan\psi_{ss} = \frac{\sqrt{12}M\cos\omega + \bar{\sigma}h^2\sin\omega}{-\sqrt{12}M\sin\omega + \bar{\sigma}h^2\cos\omega}. \tag{13}$$

When the crack is not in steady state, G cannot be obtained by an addition of the respective energy release rates (due to $\bar{\sigma}$ and M). Then, G and ψ must be obtained from a linear superposition of the stress intensity factors. When $\beta = 0$, the respective contributions are obtained from Figs 5 or 7 using $K_1 = \sqrt{E \cdot G}\cos\psi$ and $K_2 = \sqrt{E \cdot G}\sin\psi$. Then, the desired results are generated using $G = (K_1^2 + K_2^2)/E\cdot$ and $\tan\psi = K_2/K_1$.

3.3. Two-layer films: A stressed metal layer on top of a compliant polymer layer

It becomes increasingly difficult to present comprehensive results for multi-layer delamination. Closed form results under steady-state conditions can be obtained for G, but not for ψ. General results for converging debonds where the film is multi-layered are even harder to obtain, but a surprisingly accurate and simple formula for the energy release rate can be derived for a two-layer film comprised of a stiff pre-stressed layer attached to a compliant underlayer. We begin by presenting a limited set of finite element results for a two-layer film having individual layers representative of the epoxy–Ni system discussed in the Introduction, illustrated in Fig. 2 [3]. The purpose of these experiments was to study debonding of polymer–polymer interfaces with systematically varying interface chemistry. For this purpose, a self assembled monolayer (SAM) with either a CH_3 or a COOH end member, has been placed on a Si substrate. An epoxy layer of thickness $t_1 = 1\ \mu m$ has been superposed. The top Ni layer, deposited by vapor deposition, is subject to an intrinsic residual tension of the order of 1 GPa. It is the elastic energy stored in this layer that drives the debond crack, when the layer thickness exceeds a critical value. The mechanics model analyzed numerically for this case is shown in the insert in Fig. 8. For the purpose of calculating G, the SAM is ignored because it is very thin. The interface lies between the epoxy layer (E_1, ν_1, t_1) and the infinitely thick Si substrate (E_2, ν_2). The Ni layer (E_3, ν_3, t_3) on top has a residual tension, σ. The epoxy layer also supports a small residual tension, but the elastic energy stored in this layer is less than 1% of that in the Ni layer and can be ignored.

The numerical results in Fig. 8 display the energy release rate G as a function of $\Delta L/t_1 \equiv (L_0 - L)/t_1$ for two values of E_1/E_3 representative of the expected moduli ratio of an epoxy to Ni. The ratio E_3/E_2 Ni to silicon is about unity, the Poisson ratios have been chosen as $\nu_1 \cong 0.5$, $\nu_2 = 0.25$ and $\nu_3 = 0.33$, and the ratio of the two-layer thicknesses is taken to be $t_3/t_1 = 0.4$, corresponding to the films in Fig. 2. In Fig. 8, G has been normalized by $(1 - \nu_3^2)\sigma^2 t_3/(2E_3)$ which is slightly greater than the steady-state energy release rate G_{ss} as can be seen in Fig. 9. Because the epoxy layer is so compliant compared with the Ni layer, almost all of the residual elastic energy stored in the Ni layer is released by the debonded two-layer film (subject to plane strain constraint in the out-of-plane direction). As the stiffness of layer #1 increases compared to that of layer #3, more elastic energy remains in the debonded two-layer film. Nevertheless, even when $E_3 = E_1$, Fig. 9 shows that G_{ss} is only reduced by 25% below that estimated upon assuming that all the elastic energy in the top layer is released.

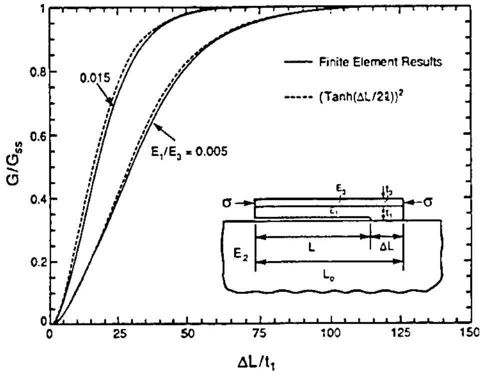

Fig. 8. Energy release rate for convergent debonding for a bi-layer film where the top layer is subject to a residual stress σ, with $t_3/t_1 = 0.4$ and the other parameters are specified in the text.

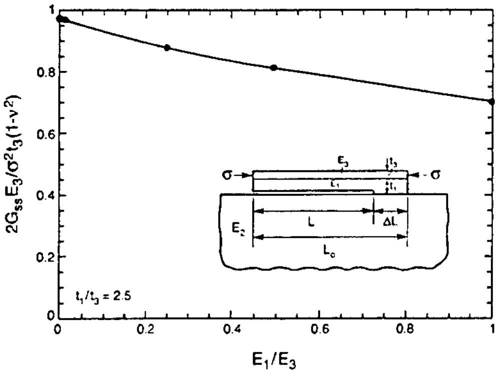

Fig. 9. Effect of modulus ratio E_1/E_3 on steady-state energy release rate of a bi-layer film with $t_3/t_1 = 0.4$ and only the top layer subject to residual tension.

The result derived in the Appendix for the two-layer system shown in the insert in Fig. 8 is

$$\frac{G}{G_{ss}} = \tanh^2\left(\frac{\Delta L}{2l}\right) \quad \text{where} \quad l = \sqrt{\frac{\bar{E}_3 t_1 t_3}{\mu_1}} \tag{14}$$

with $\bar{E}_3 = E_3/(1 - \nu_3^2)$ and $\mu_1 = E_1/[2(1 + \nu_1)]$. Equation (14) is expected to be accurate if the shear stiffness of layer 1 is small compared to the extensional stiffness of layer 3 such that l is large compared to the total thickness of the film. Predictions obtained from equation (14) for the two cases considered in Fig. 8 are included there as dashed line curves. The simple formula clearly provides a reasonably accurate description of the energy release rate of the converging debond.

The curves in Fig. 8 for the debond converging on the free edge of the film show that G departs from the steady-state limit at large $\Delta L/t_1$, especially when the lower of the two layers is relatively compliant. For example, for $E_1/E_3 = 0.005$, the interface crack first senses the free edge of the film when its tip is about 75 t_1 from the edge. The experiments on the epoxy–Ni films, such as those in Fig. 2, show that such distances are characteristic of the ligament size. It is evident from the limited set of results presented here that widely disparate moduli of the layers has a major effect on the behavior as the debond converges on the free edge. Another issue yet to be addressed is the role of plastic deformation in the polymer generated by the debond crack tip. The relevance of elastic analysis must be closely examined if the plastic zone becomes comparable in size to the layer thickness.

4. FIBER DEBONDING

The trend of energy release rate of a mode II debond spreading along a fiber and approaching a debond progressing in the opposite direction is shown in Fig. 1(b). The focus is on the contribution due to the applied stress $\bar{\sigma}$. A transverse section axisymmetric cell model (Fig. 10) has a fiber radius R, and cell outer radius R_0, such that the volume fraction of the fibers is $f = (R/R_0)^2$. The axial load carried by the composite is $\pi R_0^2\bar{\sigma}$. Matrix cracks have formed and are spaced $2L_0$. Axisymmetric debond cracks spread along the fiber from the matrix cracks with current length L. The debonds are considered to be closed mode II cracks, consistent with the residual stresses present in the composite systems of interest. The elastic properties are taken to be isotropic with E_f, ν_f, E_m and ν_m as the elastic constants for the fiber and matrix, respectively. The boundary conditions on the lateral sides of the cell mimic the interaction between cellular units in a composite. The shear traction is zero and the radial displacement is constrained to be independent of the axial coordinate such that the average radial component of traction is zero. This boundary condition has been labeled Type II [4].

When the debond length L is larger than about one fiber radius and when $\Delta L \equiv L_0 - L$ is sufficiently large compared to R, the interface crack propagates in steady-state (G independent of L). (In this section the distance between the debond crack tips is taken to be $2\Delta L$ rather than ΔL, as in Sections 2 and 3.) When there is no elastic mismatch between the fiber and matrix, G_{ss} is given by equation (2). With elastic mismatch,

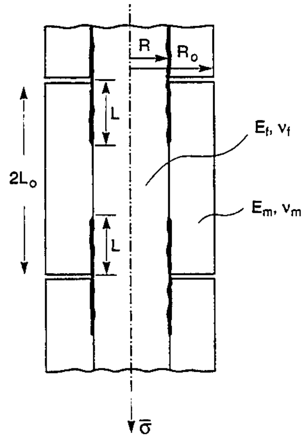

Fig. 10. Cylindrical cell model of a uni-directional ceramic matrix composite with fiber–matrix debonds emerging from neighboring matrix cracks and converging towards each other.

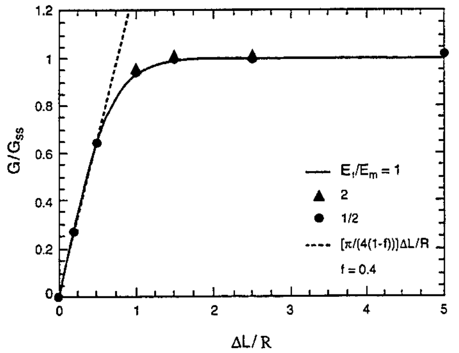

Fig. 11. Energy release rate for debond crack tips approaching each other along a fiber and comparison with the asymptotic result (18).

$$G_{ss} = c_1^2\frac{\bar{\sigma}^2 R}{E_m}, \tag{15}$$

where the algorithm for computing the coefficient $c_1(f, E_f/E_m, \nu_f, \nu_m)$ is given by Hutchinson and Jensen [4]. On any debonded segment, the average stress in the fiber is $\bar{\sigma}_f = \bar{\sigma}/f$. The asymptotic limit in Section 2 is expected to apply when ΔL becomes sufficiently small compared to R. With $\bar{\sigma}_f$ identified with $-\sigma$, as well as E_1 and ν_1 with the properties of the fiber, and E_2 and ν_2 with those of the matrix, from equation (8)

$$G = \frac{(1-\alpha)\bar{\sigma}^2\pi\Delta L}{16f^2\bar{E}_f}, \tag{16}$$

where $\bar{E}_f = E_f/(1-\nu_f^2)$. Thus, as the debonds converge, with $\Delta L/R$ approaching zero,

$$\frac{G}{G_{ss}} = \frac{(1-\alpha)\pi E_m}{16f^2c_1^2\bar{E}_f}\frac{\Delta L}{R}. \tag{17}$$

When there is no elastic mismatch this reduces to

$$\frac{G}{G_{ss}} = \frac{\pi}{4(1-f)}\frac{\Delta L}{R}. \tag{18}$$

A numerical evaluation of the coefficient multiplying $\Delta L/R$ in equation (17) shows that it depends weakly on the elastic mismatch, and thus equation (18) is a reasonably good approximation except for large mismatch. Specifically, for $f = 0.4$, the coefficient in equation (17) is about 7% above that in equation (18) when the fiber is twice as stiff as the matrix and 7% below when the matrix is twice as stiff as the fiber. Even when the corresponding stiffness ratios differ by a factor of five, the error in using equation (18) is only about 15%.

Numerical results for G normalized by G_{ss} in equation (15), computed by a finite element analysis, are presented in Fig. 11 as a function of the normalized half-spacing between the converging debond crack tips, $\Delta L/R$. The calculations have been

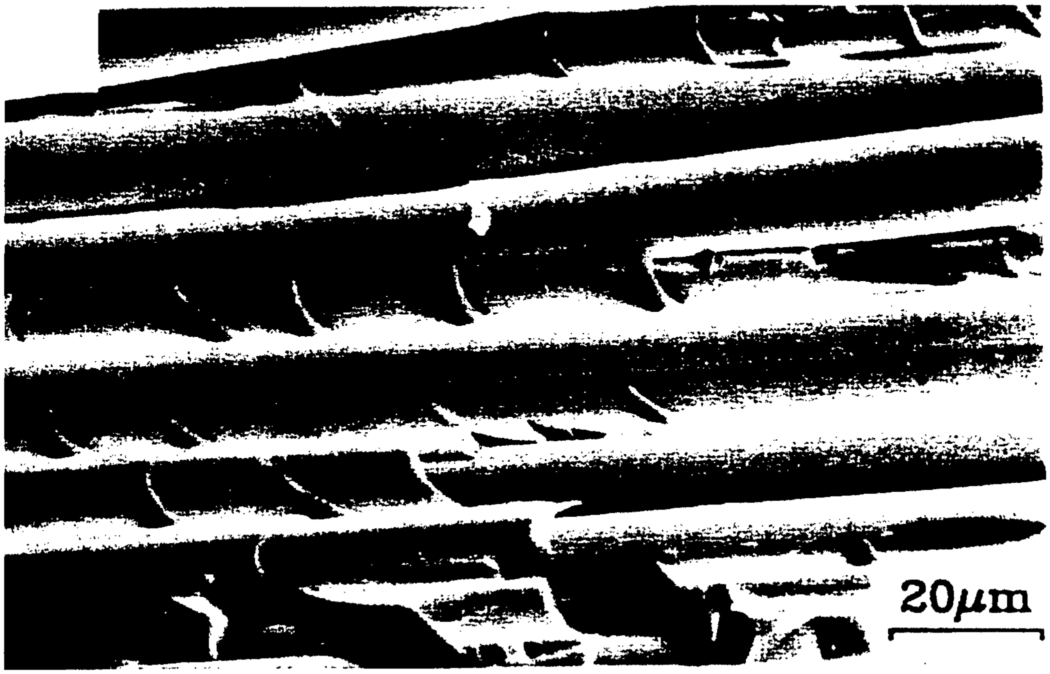

Fig. 12. A CMC transversely separated after tensile loading in the 0/90 orientation up to 90% of the ultimate tensile strength. The protruberences represent the regions of intact interface as debond convergence that were ruptured upon transverse separation [13].

carried out with $f = 0.4$, $\nu_f = \nu_m = 0.2$, and $E_f/E_m = 1/2$, 1 and 2. The numerical results validate the observation that G/G_{ss} has little dependence on elastic mismatch. The variation of the coefficient of $\Delta L/R$ in equation (17) over the three values of E_f/E_m is negligible and not even observable for the asymptotic limit shown as the dashed line in Fig. 11. The numerical results show that the asymptotic limit (18) is an excellent approximation when $\Delta L/R \leqslant 1/2$, and that steady state persists until the debond tips are within about $2R$. Thus, the converging debonds on a fiber do not begin to sense each other until they are much closer than those for thin films.

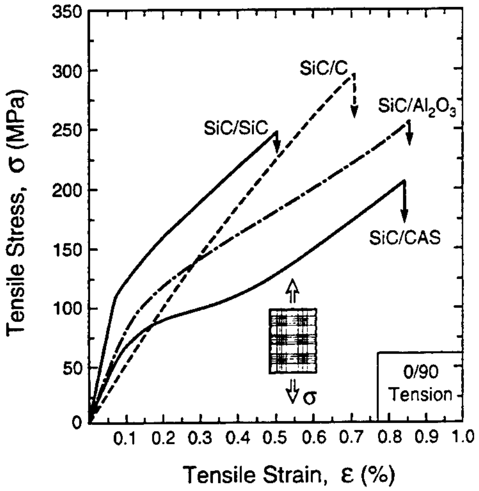

Fig. 13. Tensile stress–strain curves showing various levels of strain hardening that reflects the role of debond convergence [14].

There are two practical consequences of debond convergence. The first is that the debonds never intersect. Intact segments always exist midway between matrix cracks. This intact material becomes evident when a CMC is dissected parallel to the fibers, subsequent to tensile tests (Fig. 12). A periodic array of ridges is apparent on the dissected surface [13]. These ridges have previously been used to highlight matrix cracks and to measure crack densities. The second effect of convergence is on the effective strain hardening. As the debonds approach, the rate of inelastic straining decreases, resulting in an increase in the strain hardening coefficient. This behaviour is manifest in CMCs with low friction stress (SiC–CAS) as an upturn in the stress (Fig. 13) at larger strain levels. In CMCs with high friction (SiC–SiC), it results in a high strain-hardening rate throughout the inelastic deformation process (Fig. 13), concomitant with a larger matrix crack density [14]. It also rationalizes discrepancies found between measurements of constituent properties from hysteresis strains and simulations that neglect the convergence effect.

Acknowledgements—This work has been supported in part by the DARPA University Research Initiative through grant N00014-92-J-1808, by the NSF through grant DMR-94-00396 and by the Division of Engineering and Applied Sciences at Harvard University.

REFERENCES

1. Evans, A. G. and Dalgleish, B. J., *Acta metall. mater.*, 1992, **40,** Suppl. S295.
2. Bagchi, A., Lucas, G. E., Suo, Z. and Evans, A. G., *J. Mater. Res.*, 1994, **9,** 1734.
3. Zhuk, A., Evans, A. G., Whitesides, G. and Hutchinson, J. W., to be published.
4. Hutchinson, J. W. and Jensen, H. M., *Mech. Mater.*, 1990, **9,** 139.
5. He, M. Y., Wu, B.-X., Evans, A. G. and Hutchinson, J. W., *Mech. Mater.*, 1994, **18,** 213.
6. Rice, J. R. and Sih, G. C., *J. appl. Mech.*, 1965, **32,** 418.
7. Erdogan, F., *J. appl. Mech.*, 1965, **32,** 403.
8. Rice, J. R., *J. appl. Mech.*, 1988, **55,** 98.
9. Suo, Z. and Hutchinson, J. W., *Int. J. Fracture*, 1990, **43,** 1.
10. Drory, M. D., Thouless, M. D. and Evans, A. G., *Acta metall.*, 1988, **36,** 2019.
11. Thouless, M. D., *Acta metall.*, 1988, **36,** 3131.
12. Gao, H., *Int. J. Fracture*, 1990, **45,** 131.
13. Cao, H. C., Bischoff, E., Sbaizero, O., Rühle, M. and Evans, A. G., *J. Amer. Ceram. Soc.*, 1990, **73,** 1691.
14. Domergue, J.-M., Heredia, F. E. and Evans, A. G., *J. Amer. Ceram. Soc.*, 1996, **79,** 161.

APPENDIX: APPROXIMATE ANALYSIS OF THE TWO-LAYER SYSTEM

The two-layer system with the numbering and notation for the thicknesses and moduli shown in the insert of Fig. 8 is adopted. We begin by considering the symmetric geometry shown farthest to the right in Fig. 4(a). Denote the total width of the remaining ligament by $2b$ and the length of each crack by a. The pre-stress in layer 3 is σ. Analysis of the problem on the right in Fig. 4(a) will provide the energy release rate, as previously discussed, with σ acting in the sense shown ($\sigma > 0$). Layer 1 has no pre-stress. Let $\bar{E}_3 = E_3/(1 - \nu_3^2)$ be the plane strain tensile modulus of layer 3, while $\mu_1 = E_1/(2(1 + \nu_1))$ is the shear modulus of layer 1. If the shear stiffness of layer 1 is small compared to the tensile stiffness of layer 3, the length of the shear lag zone through which the film stress is transferred to the substrate will be large compared to the total film thickness. We capitalize on this feature and employ a one-dimensional analysis as follows.

Let $\bar{\sigma}(x)$ be the average stress acting parallel to the film in layer 3, with the origin of x taken as the center of the remaining ligament. Direct attention to the remaining ligament, $-b < x < b$. Let $\tau(x)$ be the shear stress at the interface between layers 1 and 3, and let $u(x)$ be the displacement of this interface in the x-direction. With $()' \equiv \mathrm{d}()/\mathrm{d}x$, $\gamma = u/t_1$ is the average shear strain in layer 1 and $\epsilon = u'$ is the extensional strain at the bottom of layer 3. Equilibrium of layer 3 requires $\bar{\sigma} = \tau/t_3$. Using $\tau = \mu_1\gamma$ and $\bar{\sigma} = \bar{E}_3\epsilon$ in this equilibrium equation, one obtains $u'' - l^2 u = 0$ where l is defined in equation (14). The solution to this equation, subject to symmetry about $x = 0$ and $\bar{\sigma} = -\sigma$ at $x = -b$ (or $x = +b$), is

$$u = -\frac{\sigma l}{\bar{E}_3}\frac{\sin\mathrm{h}(x/l)}{\cos\mathrm{h}\,(b/l)}. \tag{A.1}$$

Let U be the displacement in the x-direction at the left end of the film at $x = -(a + b)$, and denote the potential energy of the left half of the system by PE. (Because the two halves are equal, attention is directed only to the left half.) For prescribed σ, one can readily show that $PE = -\frac{1}{2}\sigma U t_3$. Approximate U as the sum of $u(-b)$ from equation (A.1) and $\sigma a/\bar{E}_3$, representing contraction of the unattached segment lying to the left of $x = -b$:

$$U = \frac{\sigma}{\bar{E}_3}\left[a + l\tan\mathrm{h}\left(\frac{b}{l}\right)\right]. \tag{A.2}$$

The effect of layer 1 on the contraction of the unattached segment is neglected, consistent with the assumption that layer 3 is much stiffer than layer 1. Then, from

$$G = -\frac{\mathrm{d}PE}{\mathrm{d}a} = \frac{1}{2}\sigma t_3\frac{\mathrm{d}U}{\mathrm{d}a}, \tag{A.3}$$

one obtains

$$\frac{G}{G_{ss}} = \tan\mathrm{h}^2\left(\frac{b}{l}\right) \tag{A.4}$$

where $G_{ss} = \sigma^2 t_3/(2\bar{E}_3)$. The final step in arriving at equation (14) is to identify ΔL (defined in the insert in Fig. 8) with $2b$, in accordance with the discussion in the body of the paper to the effect that the tip can hardly distinguish a free edge from another debond crack.

Pergamon

Int. J. Solids Structures Vol. 34, No. 30, pp. 3941–3951, 1997
© 1997 Elsevier Science Ltd
All rights reserved. Printed in Great Britain
0020–7683/97 $17.00 + .00

PII: S0020–7683(97)00018–8

A MODEL OF EVOLVING DAMAGE BANDS IN MATERIALS

Y. HUANG
Department of Mechanical Engineering—Engineering Mechanics,
Michigan Technological University, Houghton, MI 49931, U.S.A.

X. Y. GONG and Z. SUO
Department of Mechanical and Environmental Engineering, University of California,
Santa Barbara, CA 93106, U.S.A.

and

Z. Q. JIANG
Department of Mechanical Engineering—Engineering Mechanics,
Michigan Technological University, Houghton, MI 49931, U.S.A.

(*Received* 31 *March* 1996; *in revised form* 9 *December* 1996)

Abstract—This paper develops a model that incorporates damage band evolution at three levels: (i) at the mechanism level, the damage mechanisms, such as diffusive void growth and fatigue cracks, determine the damage growth rate; (ii) at an intermediate level, the damage band is modeled as springs connecting undamaged materials, and the spring constants change as damage develops; (iii) at the continuum level, the damage band is modeled as an array of dislocations to satisfy equilibrium. We demonstrate this model with an example of a band of microcracks subject to remote tensile cyclic stress. It is observed that damage rapidly grows at the weakest regions in the band, and a macroscopic crack nucleates while the overall damage level is still very low. The model shows that there exists a critical number of cycles for macroscopic crack nucleation, $N_{\text{nucleation}}$, which depends on materials as well as the amplitude of applied cyclic stress. This critical number of cycles is insensitive to the size of damage cluster, but decreases rapidly as the local excess of damage increases. © 1997 Elsevier Science Ltd.

1. INTRODUCTION

Engineering materials exhibit time-dependent degradation and failure under creep, stress-corrosive cracking, or cyclic loading conditions. Although failure mechanisms vary in different materials, they all display one common characteristic: damage originates from localized regions and evolves to a macroscopic crack. The present paper investigates the evolution of localized damage bands over time/cycles, and the relation between micro-damage and macroscopic nucleation of defects. Following an earlier attempt (Ye, 1992), the model includes three levels—the mechanism level, the intermediate level, and the continuum level. (i) At a sufficiently fine resolution, damage processes such as power law creep voids, diffusive voids, shear fatigue cracks are incorporated to determine the damage growth rate. (ii) At an intermediate level, localized damage bands are modeled as springs connecting undamaged materials. The spring compliances are nonuniform, increasing as the damage evolves. (iii) At the continuum level, the localized damage band, growing in an otherwise undamaged material, is modeled as an array of dislocations. The equilibrium provides the governing equation for the local stress. The model estimates the critical time or cycle number at which a macroscopic defect nucleates. For simplicity, the model is limited to two dimensional analysis.

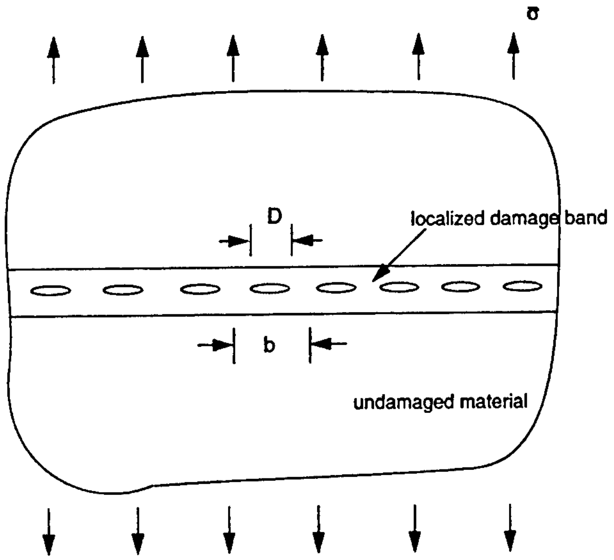

Fig. 1. A localized damage band, where b is the average spacing between microscale damage, and D is the average size of microscale damage.

2. GENERAL DESCRIPTION OF THE MODEL

Figure 1 shows an example of damage band. It is a weak region in an otherwise elastic material, and is the potential band for deformation localization. The thickness of the band is much smaller than the characteristic length of the sample. The material is assumed to be subject to remote uniform tensile stress $\bar{\sigma}$. Other types of loading can be analyzed similarly, such as shear fatigue (Ye, 1992) and thermal cycling (Huang *et al.*, 1997). Three levels discussed in the previous section are prescribed in the following.

2.1. *Mechanism level*

Let ω be the nondimensional damage parameter, such as the normalized microcrack size or void size. The limit $\omega = 0$ corresponds to the undamaged state in the material. Its growth rate, in general, is governed by the current damage state and the local stress σ, i.e.,

$$\frac{\partial \omega}{\partial t} = \frac{1}{t_0} \bar{F}\left(\frac{\sigma}{\sigma_0}, \omega\right) \tag{1}$$

where t is the time or cycle number, t_0 is a reference time or cycle number, σ_0 is a reference stress, and function $\bar{F}$ depends on the specific damage mechanism in the material. For many damage mechanisms, the damage evolution rate can be related to the local stress σ through a power law

$$\frac{\partial \omega}{\partial t} = \frac{1}{t_0} F(\omega)\left(\frac{\sigma}{\sigma_0}\right)^n \tag{2}$$

where the power n is a material property, and the nondimensional function $F(\omega)$ represents the damage growth rate when the local stress reaches the reference stress. In general, $F(\omega)$ is a monotonically increasing function of ω since the damage growth rate increases with the damage level.

2.2. *Intermediate level*

Beyond the elastic stretch in the undamaged material, there is an additional stretch across the band, δ, due to localized damage. The additional stretch δ is related to the local stress σ through a bridging law,

$$\frac{\delta}{\delta_0} = \overline{C}\left(\frac{\sigma}{\sigma_0}, \omega\right) \tag{3}$$

where δ_0 is a material length, and the function $\overline{C}$ can be obtained from a micromechanics model for the specific damage mechanism in the material. In cases such as in stress corrosion cracking (Cao *et al.*, 1987) or shear fatigue (Ye, 1992), the stretch is linear in the stress so that eqn (3) can be written as

$$\frac{\delta}{\delta_0} = C(\omega)\frac{\sigma}{\sigma_0} \tag{4}$$

where $C(\omega)$ is the linear spring compliance, which is also a monotonically increasing function of ω since the spring is more compliant as the damage level increases.

2.3. *Continuum level*

The localization band can be regarded as an array of dislocations. The local stress in the band, σ, is caused by the remote uniform stress, $\bar{\sigma}$, and by the dislocations (Rice, 1968):

$$\sigma(x) = \bar{\sigma} - \frac{E'}{4\pi}\int_{-\infty}^{\infty} \frac{\partial\delta(\xi)}{\partial\xi}\frac{\mathrm{d}\xi}{x-\xi} \tag{5}$$

where E' is Young's modulus E for plane stress or $E/(1-\nu^2)$ for plane strain, ν is Poisson's ratio, and x is the coordinate in the direction of the band.

The distribution of the damage state ω, the additional stretch δ, and the local stress σ are governed by the differential and integral equations in eqns (2), (4) and (5). For a given initial damage distribution, these governing equations can be solved numerically to evolve the damage distribution as time or cycle increases.

3. MICROCRACK DAMAGE IN FATIGUE AND THE NUCLEATION OF A MACROSCOPIC CRACK

The model outlined in the previous section is demonstrated here through an example of microcracks in a localized band subjected to remote tensile cyclic stress, $\Delta\bar{\sigma}$. As shown in Fig. 1, the average spacing between microcracks is b, and the average size of microcracks is D. The damage parameter ω is defined by

$$\omega = \frac{D}{b}. \tag{6}$$

The limit $\omega = 0$ corresponds to an undamaged material, while $\omega = 1$ represents the critical state when microcracks coalesce and a macroscopic crack nucleates.

3.1. *Mechanism level*: *damage evolution rate*

The damage mechanism in this example is the fatigue growth of microcracks. There have been extensive studies on small fatigue cracks (e.g., Suresh and Ritchie, 1984, also Suresh, 1991, for detailed discussion and documentation). The fatigue growth rate of microcracks is influenced by many factors, such as microstructures (e.g., Pearson, 1975, Lankford, 1982, Tanaka *et al.*, 1983), T-stress level, plastic zone size, crack closure effect around tips of microcracks (e.g., Allen and Sinclair, 1982, Suresh and Ritchie, 1984, Fleck and Newmann, 1988), and environmental effect (e.g., Gangloff, 1981). Dowling (1977) suggested that the cyclic J-integral ΔJ provides a measure of the driving force for fatigue growth of small cracks, and the growth rate is approximately proportional to ΔJ^m (m is a material property). Though the following analysis can be applied to any laws governing fatigue growth of microcracks, Paris law is used here for simplicity,

$$\frac{\mathrm{d}D}{\mathrm{d}N} = \beta(\Delta K)^n \tag{7}$$

where N is the number of cycles, β and n are material properties, and ΔK is the cyclic stress intensity factor at a microcrack tip. For the configuration in Fig. 1, ΔK is related to the cyclic local stress $\Delta\sigma$ by (see Appendix A for details)

$$\Delta K = \Delta\sigma\sqrt{b\tan\frac{\pi}{2}\omega} \tag{8}$$

where b is the average spacing between microcracks in the band. The damage growth rate can then be found as

$$\frac{\mathrm{d}\omega}{\mathrm{d}N} = \beta b^{n/2-1}\,\sigma_0^n\,F(\omega)\left(\frac{\Delta\sigma}{\sigma_0}\right)^n \tag{9}$$

where

$$F(\omega) = \left(\tan\frac{\pi}{2}\omega\right)^{n/2}. \tag{10}$$

3.2. *Intermediate level*: *bridging law*

Due to the presence of microcracks, there is an additional cyclic stretch across the band, $\Delta\delta$, beyond the uniform stretch associated with undamaged materials. This additional cyclic stretch comes from the cyclic opening of microcracks in the band. A micromechanics model is described in Appendix A, and $\Delta\delta$ is related to the cyclic local stress $\Delta\sigma$ by the bridging law

$$\Delta\delta = \frac{4}{\pi}\frac{b}{E'}\ln\frac{1}{\cos\left(\frac{\pi}{2}\omega\right)}.\Delta\sigma. \tag{11}$$

It can be rewritten as

$$\frac{\Delta\delta}{b\frac{\sigma_0}{E'}} = C(\omega)\frac{\Delta\sigma}{\sigma_0} \tag{12}$$

where

$$C(\omega) = \frac{4}{\pi}\ln\frac{1}{\cos\left(\frac{\pi}{2}\omega\right)}. \tag{13}$$

For an undamaged material ($\omega = 0$), $C(\omega)$ is zero such that there is no additional cyclic stretch. In the other limit when microcracks start to coalesce ($\omega = 1$), $C(\omega)$ approaches to infinity so that the local stress is zero and the spring is completely broken. Therefore, there is no bridging at this moment ($\omega = 1$) and a macroscopic crack is nucleated.

3.3. *Continuum level: stress equilibrium*

For a uniform remote cyclic stress $\Delta\bar{\sigma}$, the stress equilibrium eqn (5) takes the form

$$\Delta\sigma(x) = \Delta\bar{\sigma} - \frac{E'}{4\pi}\int_{-\infty}^{\infty} \frac{\partial \Delta\delta(\xi)}{\partial \xi} \cdot \frac{\mathrm{d}\xi}{x-\xi}. \tag{14}$$

For a given damage distribution $\omega(x)$, eqns (12) and (14) give a linear integral equation for $\Delta\sigma$ (or $\Delta\delta$).

3.4. *Normalization*

An important equivalence between the amplitude of applied cyclic stress $\Delta\bar{\sigma}$ and number of cycles N can be established by the following normalization:

$$N' = \frac{N}{\beta^{-1} b^{1-(n/2)} (\Delta\bar{\sigma})^{-n}}, \sigma' = \frac{\Delta\sigma}{\Delta\bar{\sigma}}, \delta' = \frac{\Delta\delta}{b\dfrac{\Delta\bar{\sigma}}{E'}}, x' = \frac{x}{b}. \tag{15}$$

The governing eqns (9), (12) and (14) then become

$$\frac{\partial \omega}{\partial N'} = F(\omega)(\sigma')^{n} \tag{16a}$$

$$\delta' = C(\omega)\sigma' \tag*{(16b))}$$

$$\sigma' = 1 - \frac{1}{4\pi}\int_{-\infty}^{\infty} \frac{\partial \delta'}{\partial \xi'} \cdot \frac{\mathrm{d}\xi'}{x'-\xi'}. \tag{16c}$$

It is evident that the number of cycles N appears together with the amplitude of remote cyclic stress $(\Delta\bar{\sigma})^n$ through the normalized cycle number N'. Therefore, a small amplitude of applied cyclic stress $\Delta\bar{\sigma}$ is equivalent to a large number of cycles, and vice versa. This is similar to the *S-N* curve in the empirical fatigue design. (This conclusion results from the Paris law, and may not hold for non-power law damage growth rate.)

At a given cycle N', the damage distribution $\omega(x')$ is known. The combination of eqns (16b) and (16c) solve the stress distribution $\sigma'(x')$, and then eqn (16a) updates the damage distribution $\omega(x')$ for an increment of cycle $\Delta N'$. The procedure then repeats for the next cycle number, $N' + \Delta N'$.

3.5. *Initial distribution of damage in the band*

The damage parameter ω is considered as a continuum variable in the continuum analysis. This is rather similar to the Gurson's (1975) model for a voided, dilating material, which was derived from a cell analysis, but has been successfully applied in the continuum theory. Following Ohno and Hutchinson (1984) and Huang and Hutchinson (1989), the following initial damage distribution is taken to represent a cluster of damage in the band

$$\omega(x) = \omega_{\text{average}} + (\omega_{\max} - \omega_{\text{average}}) \exp\left[-\frac{1}{2}\left(\frac{x}{\lambda b}\right)^2\right] \tag{17}$$

where ω_{average} and $\omega_{\max}$ are the average and maximum damage level in the band, and $2\lambda b$ represents the size of the damage cluster. The nondimensional parameter $\omega_{\max} - \omega_{\text{average}}$ and 2λ characterize the excess of damage in the band and ratio of the size of damage cluster to average microcrack spacing, respectively.

3.6. *Results and discussions*

Details of the numerical method to solve governing eqn (16) are given in Appendix B. A value of power $n = 2$ is fixed in the present study. Results in Figs 2–4 are for initial damage parameters $\omega_{\text{average}} = 0.01$, $\omega_{\max} = 0.10$, and $2\lambda = 1$. This represents a highly localized cluster of damage that has the size of approximately b, and the excess of damage in the band is much larger than the average damage level. The initial damage profile is shown in Fig. 2, vs the normalized distance in the band, x/b. As the cycle number increases, the damage distribution evolves very nonuniformly in the band. Damage at the center ($x = 0$) increases significantly faster than the average level (Fig. 2). For example, ω increases from 0.1 to 1 at the center while the average ω is changed by approximately 0.1. Therefore, damage evolution is rather concentrated at the weakest regions in the material. This is similar to the deformation localization in voided ductile materials (Ohno and Hutchinson, 1984, Huang and Hutchinson, 1989).

The distributions of additional stretch δ and local stress σ are shown in Figs 3 and 4, respectively. It is observed that the evolutions of δ and σ are also very concentrated. As the damage parameter ω at the center approaches one, the corresponding additional stretch is much larger than the average level, and the local stress approaches zero such that bridging effect starts to disappear at the center. The number of cycles at this moment is critical because microcracks start to coalesce and a macroscopic crack is to be nucleated. This critical number of cycles for crack nucleation, denoted by $N_{\text{nucleation}}$, characterizes the maximum number of cycles the material can sustain before a macroscopic crack appears. It depends on the material, the amplitude of applied cyclic stress $\Delta\bar{\sigma}$, as well as the initial distribution of damage in the band. For initial damage parameters given above, this critical number is $N_{\text{nucleation}} = 1.503\beta^{-1}b^{1-(n/2)}(\Delta\bar{\sigma})^{-n}$ (Fig. 2).

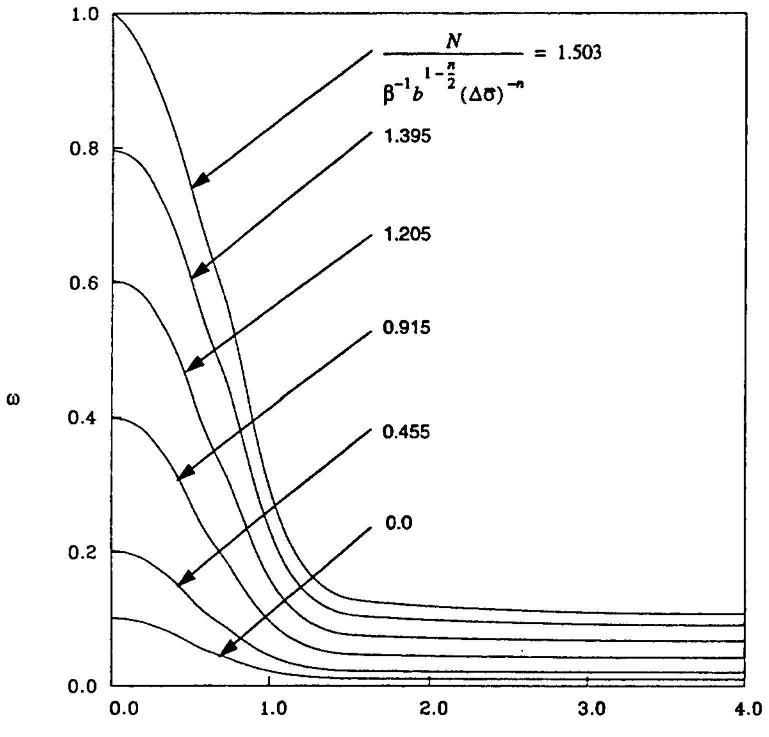

Fig. 2. Damage distribution, ω, in the band for several normalized number of cycles, $\beta b^{(n/2)-1}(\Delta\bar{\sigma})^n N$, where the average initial damage level $\omega_{\text{average}} = 0.01$, excess of damage in the band $\omega_{\max} - \omega_{\text{average}} = 0.09$, normalized size of the damage cluster $2\lambda = 1$, power $n = 2$, and b is the average spacing between microcracks. The number of cycles when ω reaches one is the critical number cycle for crack nucleation, $N_{\text{nucleation}}$.

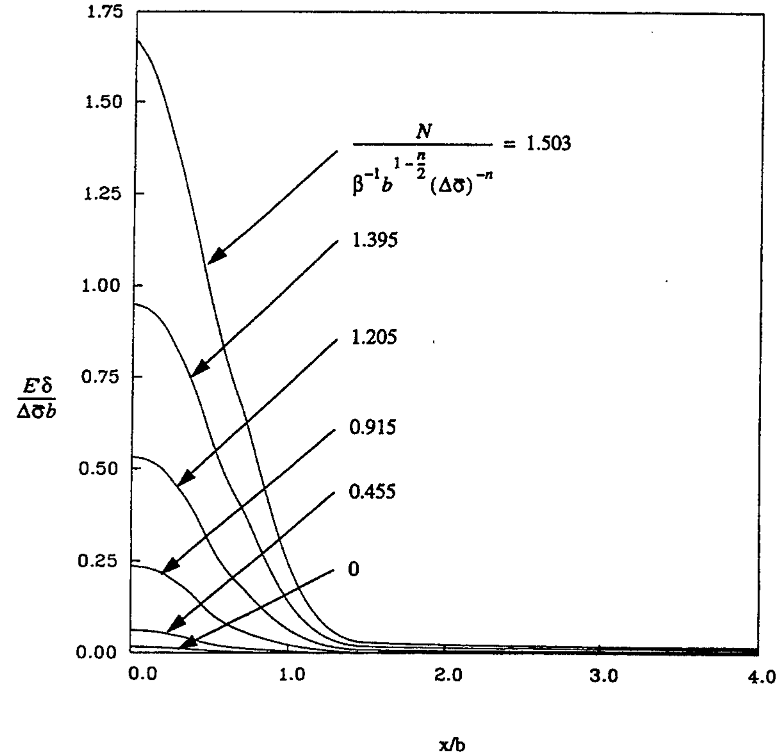

Fig. 3. The distribution of normalized additional stretch across the band for several number of cycles, $\beta b^{(n/2)-1}(\Delta\bar{\sigma})^n N$, where the average initial damage level $\omega_{\text{average}} = 0.01$, excess of damage in the band $\omega_{\max} - \omega_{\text{average}} = 0.09$, normalized size of the damage cluster $2\lambda = 1$, power $n = 2$, and b is the average spacing between microcracks.

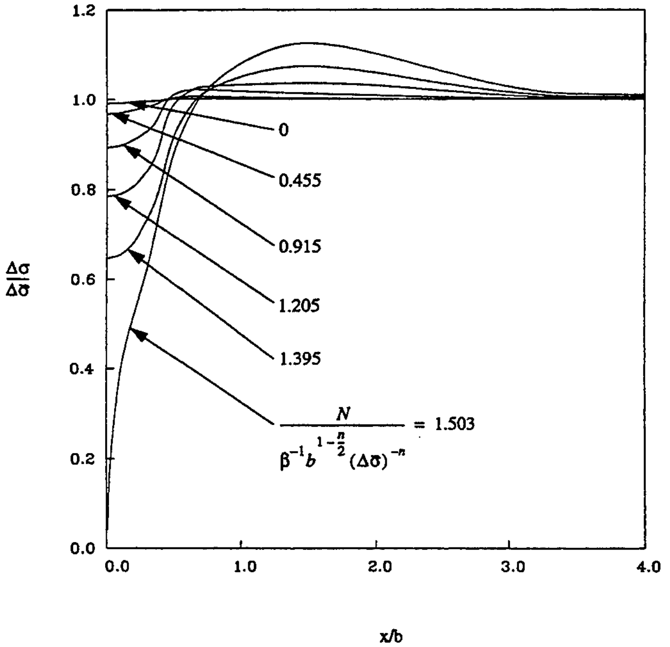

Fig. 4. The distribution of normalized stress in the band for several number of cycles, $\beta b^{(n/2)-1}(\Delta\bar{\sigma})^n N$, where the average initial damage level $\omega_{\text{average}} = 0.01$, excess of damage in the band $\omega_{\max} - \omega_{\text{average}} = 0.09$, normalized size of the damage cluster $2\lambda = 1$, power $n = 2$, and b is the average spacing between microcracks.

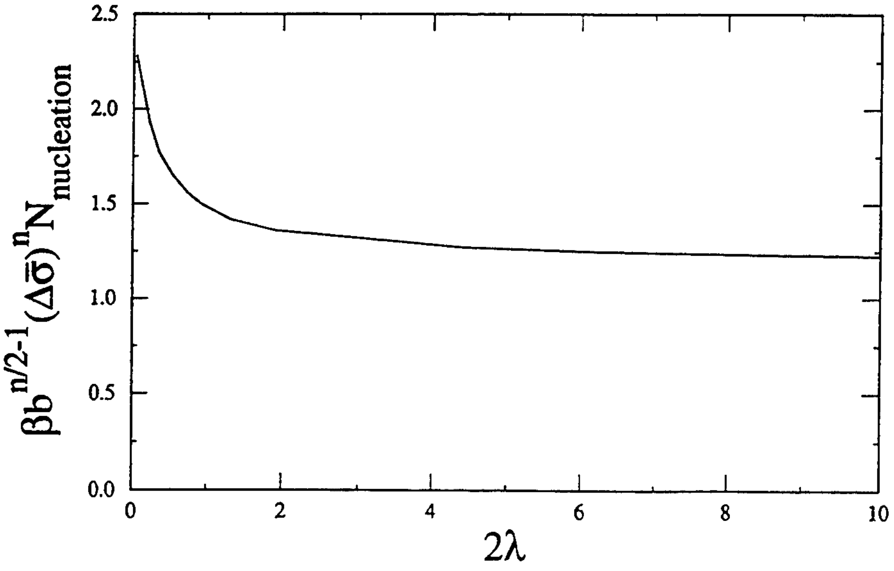

Fig. 5. The normalized critical number of cycles for crack nucleation, $\beta b^{(n/2)-1}(\Delta\bar{\sigma})^n N_{\text{nucleation}}$, vs the normalized size of damage cluster, 2λ, for the average initial damage level $\omega_{\text{average}} = 0.01$, excess of damage in the band $\omega_{\max}-\omega_{\text{average}} = 0.09$, and power $n = 2$.

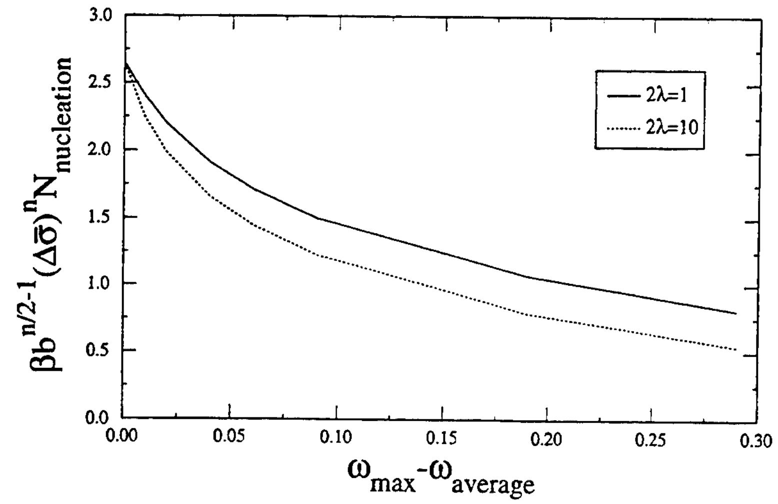

Fig. 6. The normalized critical number of cycles for crack nucleation, $\beta b^{(n/2)-1}(\Delta\bar{\sigma})^n N_{\text{nucleation}}$, vs the excess of damage in the band, $\omega_{\max}-\omega_{\text{average}}$, for a small damage cluster ($2\lambda = 1$) as well as a large one ($2\lambda = 10$), where the average initial damage level $\omega_{\text{average}} = 0.01$, and power $n = 2$.

The normalized critical number of cycles for crack nucleation, $\beta b^{(n/2)-1}(\Delta\bar{\sigma})^n N_{\text{nucleation}}$, is shown in Fig. 5 vs the normalized cluster size 2λ for $\omega_{\max} = 0.10$, $\omega_{\text{average}} = 0.01$ and power $n = 2$. As the cluster size increases, the critical number of cycles rapidly approaches to an asymptote, approximately $1.2\beta^{-1}\ b^{1-n/2}(\Delta\bar{\sigma})^{-n}$. Therefore, only small damage clusters whose sizes are less than twice the microcrack spacing can achieve a significant increase in the critical numbers of cycles (Fig. 5), hence to improve the fatigue life of the material.

The normalized critical number of cycles for crack nucleation, $\beta b^{(n/2)-1}(\Delta\bar{\sigma})^n N_{\text{nucleation}}$, is shown in Fig. 6,, vs the excess damage in the band, $\omega_{\max}-\omega_{\text{average}}$, for a small cluster ($2\lambda = 1$) as well as a large one ($2\lambda = 10$). It is clearly observed that the critical number of cycles for crack nucleation is rather insensitive to the size of the damage cluster since two curves in Fig. 6 are very close. However, the critical number of cycles is reduced significantly as the excess of damage in the band increases. One can conclude that the nucleation of a macroscopic crack is very sensitive to the local excess of damage, but not the size of a damage cluster.

4. CONCLUDING REMARKS

A model is presented to investigate damage evolution in a localized weak zone in materials. It includes modeling at three different levels: (i) on the mechanism level, damage mechanisms, such as diffusive void growth, fatigue cracks, are incorporated to determine the damage growth rate; (ii) on an intermediate level, localized damage bands are modeled as springs connecting undamaged materials, and spring constants are obtained from micromechanics models; (iii) on the continuum level, a localized damage band is modeled as an array of dislocations governed by the stress equilibrium.

The model is demonstrated through an example of microcracks in a localized band subjected to remote tensile cyclic stress. It is observed that damage evolution is rather concentrated at the weakest regions in the material, where damage rapidly accumulates and a macroscopic crack nucleates while the overall damage level is still very low. The model shows that there exists a critical number of cycles for crack nucleation, $N_{\text{nucleation}}$, which depends on the material, the amplitude of applied cyclic stress, as well as the initial distribution of damage in the band. This critical number of cycles for crack nucleation is found to be relatively insensitive to the size of a damage cluster, but decreases rapidly as the local excess of damage increases.

The assumptions made in the above demonstrational example significantly simplify the analysis without changing the time-dependent degradation characteristics in materials. They can be improved by incorporating realistic material features in the model. For example, the cluster of defects in eqn (17) can be replaced by realistic nonuniform defect distributions in materials (Boucier *et al.*, 1986, Spitzig *et al.*, 1988, Huang, 1993). The material and component geometries under complex loading conditions can be studied by the finite element method on the continuum level instead of the integral equation approach in eqn (5). The evolution of some damage (such as fatigue growth of microcracks, see Suresh, 1991) follows eqn (1) rather than the power law in eqn (2). The nonlinear bridging law in eqn (3) may be more appropriate than the linear one in eqn (4) for certain materials and loadings. By incorporating all these features in the analysis, the present model has the potential to connect the damage evolution process on the mechanism level to the material and component design on the continuum level.

Acknowledgements—YH gratefully acknowledges the financial support from NSF Grant No. INT-94-23964 and from the ALCOA Foundation. The work done at UCSB was supported by ARPA through a URI contract N-0014-92-J-1808.

REFERENCES

Allen, R. J. and Sinclair, J. C. (1982) The behavior of short cracks. *Fatigue Engineering Materials Structures* **5**, 343–347.

Boucier, R. J., Koss, D. A., Smelser, R. E. and Richmond, O. (1986) The influence of porosity on the deformation and fracture of alloys. *Acta Metallica Materiala* **34**, 2443.

Cao, H. C., Dalgleish, B. J., Hsueh, C. H. and Evans, A. G. (1987) High-temperature stress corrosion cracking in ceramics. *Journal of the American Ceramic Society* **70**, 257–264.

Dowling, N. E. (1977) Crack growth during low-cycle fatigue of smooth axial specimens. In *Cyclic Stress-Strain and Plastic Deformation Aspects of Fatigue Crack Growth*, STP 637, pp. 97–121. American Society of Testing and Materials, Philadelphia.

Fleck, N. A. and Newmann, J. C. (1988) Analysis of crack closure under plane strain conditions. In *Mechanics of Fatigue Crack Closure*, STP 982, pp. 319–341. American Society of Testing and Materials, Philadelphia.

Gangloff, R. P. (1981) The criticality of crack size aqueous corrosion fatigue. *Research Mechanica Letters* **1**, 299–306.

Gurson, A. L. (1975) Plastic flow and fracture behavior of ductile materials incorporating void nucleation, growth and interaction. Ph.D. thesis, Brown University.

Huang, Y. (1993) The role of nonuniform particle distribution in plastic flow localization. *Mechanics of Materials* **16**, 265.

Huang, Y. and Hutchinson, J. W. (1989) A model study of the role of nonuniform defect distribution on plastic shear localization. In *Role of Modeling in Materials Design*, ed. Embury, J. D., AIME, p. 129.

Huang, Y., Jiang, Z. Q., Chandra, A., Hu, K. X. and Yeh, C.-P. (1997) A model study of thermal fatigue in layered electronic assemblies. *ASME Transactions.—Journal of Electronic Packaging* (submitted).

Lankford, J. (1982) The growth of small fatigue cracks in 7075-T6 aluminium. *Fatigue Engineering Materials Structures* **5**, 233–248.

Ohno, N. and Hutchinson, J. W. (1984) Plastic flow localization due to non-uniform void distribution. *Journal of the Mechanics and Physics of Solids* **32**, 63–85.

Pearson, S. (1975) Initiation of fatigue cracks in commercial aluminum alloys and the subsequent propagation of very short cracks. *Engineering Fracture Mechanics* **7**, 235–247.

Rice, J. R. (1968) Mathematical analysis in the mechanics of fracture. In *Fracture: An Advanced Treatise*, ed. Liebowitz, H. vol. 2. Academic Press, New York, pp. 191–311.

Spitzig, W. A., Smelser, R. E. and Richmond, O. (1988) The evolution of damage and fracture in iron compacts with various initial porosities. *Acta Metallica Materiala* **36**, 1201.

Suresh, S. (1991) *Fatigue of Materials*. Cambridge University Press, Cambridge, England.

Suresh, S. and Ritchie, R. O. (1984) Propagation of short fatigue cracks. *International Metals Reviews* **29**, 445–476.

Tada, H., Paris, P. C. and Irwin, G. R. (1985) *The Stress Analysis of Cracks Handbook*. Del. Research, St. Louis, MO.

Tanaka, K., Hojo, M. and Nakai, Y. (1983) Crack initiation and early propagation in 3% silicon iron. In *Fatigue Mechanisms: Advances in Quantitative Measurement of Fatigue Damage*, STP 811, pp. 207–232. American Society of Testing and Materials, Philadelphia.

Ye, T. (1992) The Micromechanics of Shear Fatigue. MS thesis, Dept. Mech. Engr., Univ. California, Santa Barbara.

APPENDIX A

The additional stretch across the band, δ, comes from the opening of microcracks. By averaging the crack opening displacement in the band (Fig. 1), one has

$$\delta = \frac{1}{b}\int_{-D/2}^{D/2} \delta_{\text{open}}\,\mathrm{d}x \tag{A1}$$

where δ_{open} is the crack opening displacement, and can be estimated using a configuration of periodically distributed cracks as (Tada *et al.*, 1985)

$$\delta_{\text{open}} = \frac{4\sigma b}{\pi E'}\cos h^{-1}\frac{\cos\dfrac{\pi x}{b}}{\cos\dfrac{\pi D}{2b}} \quad \text{for } |x| \leqslant \frac{D}{2}. \tag{A2}$$

The substitution of eqn (A2) into eqn (A1) leads to eqn (11).

For periodically distributed microcracks in Fig. 1, the stress intensity factor is (Tada *et al.*, 1985)

$$K = \sigma\sqrt{b\tan\frac{\pi D}{2b}} \tag{A3}$$

which becomes the same as eqn (8) by changing K and σ to ΔK and $\Delta\sigma$, respectively.

APPENDIX B

From symmetry $\sigma(-x) = \sigma(x)$ and $\delta(-x) = \delta(x)$, eqns (16b) and (16c) can be rearranged to

$$\frac{\delta(x)}{C(\omega)} = 1 - \frac{1}{2\pi}\int_0^{\infty} \frac{\xi}{x^2-\xi^2}\frac{\partial\delta}{\partial\xi}\,\mathrm{d}\xi \quad \text{for } x > 0. \tag{B1}$$

By the following change of variables, the interval $(0, +\infty)$ for x and ξ is transformed to $(-1, 1)$ for u and t

$$x = \frac{1+u}{1-u}, \xi = \frac{1+t}{1-t}. \tag{B2}$$

For each given damage profile $\omega(x)$, the additional stretch δ is expanded in terms of Chebyshev polynomial

$$\delta(u) = \sum_{j=1}^{M} a_j T_{j-1}(u) \tag{B3}$$

where T_j is the Chebyshev polynomial of degree j, and a_j is the coefficient to be determined. By the standard collocation method, eqn (B1) becomes M linear algebraic equations and can be solved numerically.

Equation (16a) is an ordinary differential equation for the damage parameter ω. It can be solved by the Runge-Kutta method if the local stress distribution $\sigma(x)$ is known. Therefore, the numerical procedures to obtain the damage state ω, local stress σ, and additional stretch δ are

I. For the initial damage distribution $\omega(x)$ in eqn (17), solve the integral eqn (B1) by the expansion [eqn (B3)] and collocation method in order to obtain the distribution of the additional stretch $\delta(x)$ and local stress $\sigma(x)$ in the band;

III. For the known local stress distribution $\sigma(x)$, solve eqn (16a) by the Runge-Kutta method and get the new damage distribution $\omega(x)$ at the next cycle;

III. For the new damage distribution $\omega(x)$, solve eqn (B1) in order to get the corresponding additional stretch $\delta(x)$ and local stress $\sigma(x)$ for this cycle;

IV. Repeat steps II and III until the maximum value of ω in the band reaches 1. The corresponding number of cycles is the critical cycle number for crack nucleation.

Effect of Interfacial Carbon on Adhesion and Toughness of Gold-Sapphire Interfaces

Don M. Lipkin
General Electric Corporate Research & Development
One Research Circle, Niskayuna, NY 12309

David R. Clarke
Materials Department, University of California
Santa Barbara, CA 93106-5050

Anthony G. Evans
Division of Engineering and Applied Sciences, Harvard University
Cambridge, MA 02138

Abstract

The effect of carbon on the interfacial fracture of gold-sapphire bonds is quantified by partitioning the measured fracture energy into the works of adhesion and plastic dissipation. The variation in each quantity with interfacial carbon is independently measured. The strong correlation between interfacial adhesion and plastic dissipation suggests synergistic coupling between crack-tip bond rupture and the surrounding plastic deformation in the metal. Possible origins of the observed sensitivity of adhesion to carbon heat treatment are discussed.

I. Introduction

With an increasing number of applications requiring metal-ceramic bonds, there is a compelling need to understand the strong link between bond reliability and interfacial properties [1-4]. However, the thermodynamics and micromechanics of metal-ceramic interfacial fracture are still, for the most part, underdeveloped. One notable gap is the lack of a quantitative correlation between atomic-scale adhesion and macroscopic bond integrity.

Adhesion is a thermodynamic parameter characterizing the state of the interface and respective free surfaces, whereas macroscopic performance metrics such as strength and toughness include phenomena occurring in the bulk materials, particularly plastic dissipation in the metal. Because plasticity and adhesion are dependent quantities, it is impossible to fundamentally understand the macroscopic, plasticity-dominated response of a metal-ceramic bond without consideration of interfacial adhesion. Yet despite substantial experimental strength and toughness data for metal-ceramic systems (e.g., [5]), predictive models of macroscopic properties as a function of the intrinsic interfacial parameters are lacking. The present work addresses this need by establishing definitive experimental evidence that an interfacial impurity (i.e., carbon) can affect the metal-ceramic fracture energy through a modification of the interfacial adhesion.

Experimental evidence supports an adhesion-toughness correlation for grain-boundary segregation in homogeneous metals [2]. Analogous results for metal-ceramic interfaces are sparse. Elssner *et al.* [6] evaluated the influence of silver, sulfur, and titanium impurities on the fracture energy of niobium-sapphire bicrystals and Gangopadhyay and Wynblatt [7] studied the effects of interfacial nickel segregant on the interfacial and surface energies of lead and gold sessile drops on graphite. Otherwise, there are only qualitative correlations between bond strength and work of adhesion [1,8-15],[1] as well as between macroscopic interfacial strength and fracture resistance [16]. In general, systems that form strong bonds, such as aluminum-alumina, exhibit fracture behavior dictated by the bulk properties of the adjoining materials, namely ductile fracture in the metal or cleavage fracture in the ceramic. More weakly bonded systems, such as gold-alumina, generally fracture by an interfacial debonding mechanism accompanied by plasticity in the metal.

Ideally brittle interfacial fracture entails the rupture of atomic bonds, whence the fracture energy, Γ, is simply the work of creating two new surfaces from an interface [18]. In this idealized regime (Griffith fracture), $\Gamma = W_{ad}$, where W_{ad} is the thermodynamic work of adhesion of the interface $[W_{ad} = (\gamma_m + \gamma_c) - \gamma_{mc}]$. However, even apparently brittle fracture is accompanied by a finite amount of plastic dissipation (Fig. 1), W_p, where W_p is the irreversible (or plastic) work [19]. The fracture resistance is therefore:

$$\Gamma = W_{ad} + W_p \tag{1}$$

Eqn. 1 does not emphasize the intricate interdependence of the plastic work on the work of adhesion. In fact, W_p is not an independent material parameter but rather a function of W_{ad} [20]. The crack-tip separation process (characterized by W_{ad}) is highly non-linearly coupled to the applied loading via the plastic zone surrounding the crack tip [21]. Accordingly, small variations in the work of adhesion -- as might result from interfacial segregation -- profoundly affect the work of fracture. It is precisely this phenomenon that we presently seek to establish and quantify, using the gold-sapphire system as a model and measuring the effects of interfacial carbon on the works of adhesion and fracture, respectively.

---

[1] In reference 14, the correlation was made between strength and the melting temperature of the metal, which scales with the metal surface energy [10,17] and hence the work of adhesion. In references 12 and 13, the correlation was made between strength and free energy of oxide formation of the metal, which in turn scales with the work of adhesion [15].

II. The Gold-Sapphire:Carbon System

To isolate the fundamental characteristics of interfacial fracture from such secondary contributions as interface roughness or variations in bulk component properties, the metal-ceramic system should form no reaction interphases and, at least nominally, fracture by an interfacial debonding mechanism. Gold and sapphire have been shown to form no mutual reaction products upon solid-state bonding, resulting in an atomically sharp, highly planar interface between the metal and ceramic phases [22]. Furthermore, previous studies using the gold-sapphire system [22,23] have confirmed that fracture nominally proceeds by interfacial debonding (see Fig. 1).

To modify adhesion in the gold-sapphire system without affecting changes in the constitutive properties of the metal, the interfacial species must be virtually insoluble in the gold at room temperature. Further, the dopant must be interfacially active, in the sense that solute atoms reside at the interface in preference to the respective bulk components (whether the solute acts as a thermodynamic segregant or a second-phase precipitate). Carbon is ideally suited to be the interfacial modifier in the gold-sapphire system. Apart from its ubiquity as a common impurity in a broad range of materials systems and processing conditions, carbon exhibits moderate solubility in gold very near the melting temperature of the metal, while its solubility drops dramatically with decreasing temperature (Fig. 2 [24]). Because low-solubility solutes tend to segregate more strongly than those with high solubility [25,26], carbon is a likely candidate for altering interfacial adhesion. At the same time, the negligible room-temperature solubility of carbon in gold minimizes any impact on the bulk constitutive properties of the metal. Due to the refractory nature of sapphire and on the basis of available kinetic and thermodynamic data [27,28], dissolution of carbon or formation of reaction products in the sapphire-carbon system is not expected at the temperatures required for gold-sapphire diffusion bonding.

Table I lists the surface free energies of gold, sapphire, and carbon. For convenience, all solid surface energies are calculated at 1000°C using the available surface entropy terms, $d\gamma_{sv}/dT$. Some of the relevant room-temperature bulk properties of gold and sapphire are compiled in Table II.

III. Preparation of Sapphire-Gold-Sapphire Sandwiches

Specimen preparation consisted of three steps: 1) cleaning and annealing of the respective bulk materials, 2) creating sapphire-gold-sapphire sandwiches, and 3) heat treating the sandwiches to provide the desired interfacial properties. Details of each procedure are outlined below.

Single-crystal sapphire substrates[2] were subjected to a series of chemical cleaning and annealing steps to degrease the surface, oxidize and remove superficial metallic contaminants, and anneal out structural defects [29]. The substrates were degreased in trichloroethylene (TCE), followed by acetone (ACE), isopropyl alcohol (IPA) and a deionized water (DI) rinse. Degreased samples were washed in NaOH, piranha-etched ($1H_2O_2$:$1H_2SO_4$) and rinsed in DI.[3] The substrates were subsequently oxygen-plasma etched, washed in hydrofluoric acid (HF), rinsed in DI, and nitrogen-gas dried. The clean sapphires were covered with high-purity alumina furniture to prevent dust contamination and air-annealed 2-4 hr. at 1300°C.

---

[2] HEMLITE (0001) sapphire bar stock, 80-50 finish, Crystal Systems, Salem, MA.

For the preliminary tests described in Section IV, gold foil constituted the majority of the metal volume. In subsequent investigations, including all of the fracture toughness evaluations described in Section V, the entire gold layer was deposited by electron-beam evaporation. In the foil technique, the clean substrates were coated with a thin layer of evaporated gold (Fig. 3a). The gold, typically 0.5 μm thick, was intended to provide a nominally pure metal-sapphire interface. The gold-sapphire bond was created by cold-pressing (at 11 MPa) a degreased and annealed 25 μm thick gold foil[4] sandwiched between the two sapphire substrates, as shown in Fig. 3b. Annealing of the heavily worked foils (3 hours at 1000°C in air) was intended to oxidize superficial organic contaminants and reduce the yield strength to aid the initial stages of the bonding process [30].

The foil-sandwiching procedure resulted in bonds having reasonably good mechanical integrity; however, the nominal purity of the foil was inferior to that of typical evaporation sources and use of the foil introduced additional handling procedures susceptible to further contamination. In response to these concerns, the foil was eliminated in the fracture studies (Section V) and the entire gold thickness (10-15 μm) was electron-beam evaporated onto the sapphire substrates (half of the total gold thickness on each substrate). The bond was then created by mating the freshly evaporated gold surfaces immediately after removing from the evaporation chamber. Aside from using higher purity gold,[5] the procedure also reduced (from four to two) the number of gold surfaces exposed to the ambient prior to consolidation.

After mechanical sandwiching, all bonds were heat treated in ambient air at approximately 98% of the homologous temperature of gold (1030-1050°C). A distributed pressure of approximately 10 kPa aided bonding. The duration of the bonding treatment ranged from 24 to 72 hours, with no noticeable changes in the microstructure or interfacial mechanical properties observed beyond the first 24 hours.

After bonding, the sandwiches were cut into bars for mechanical testing and machined to the specifications of the test geometries. These specimens were either tested as-bonded (subsequently designated heat treatment "A") or subjected to various auxiliary heat treatments prior to testing. Oxidizing- and reducing-atmosphere post-bonding heat treatments were intended to modify the interfacial chemistry and corresponding mechanical properties. Oxygen heat treatments ("O") were carried out in an alumina tube furnace with the specimens located directly on a clean alumina substrate. An oxygen flow rate of ~10 cc/min was used, and the gas was passed through a desiccating column prior to introduction into the furnace.

---

[3] These and subsequent cleaning steps were performed using Teflon beakers to avoid recontamination with silica.

[4] 99.95% purity, Johnson Matthey, Ward Hill, MA.

[5] 99.999% purity slugs, Williams Advanced Materials, Buffalo, NY.

The reducing treatments involved either heating in a graphite-fixtured vacuum furnace (heat treatment "V") or encapsulation in carbon-loaded ampoules (heat treatment "C"). In the former, the as-bonded sandwiches were heat treated 48 hours at 1020°C between the graphite rams of a vacuum hot-press. In the latter, the bonded sandwiches were encapsulated (in ambient atmosphere) inside a quartz ampoule filled with fine graphite powder (Fig. 3c). The ampoule was heated to temperatures slightly below those used for diffusion bonding (2-8 hours at 1000-1020°C), allowing carbon to oxidize and be transported to and along the gold-sapphire interface.

Examination of fracture surfaces by SEM (Fig. 4a) and AES (Fig. 4b) reveals the presence of carbon at the gold-sapphire interfaces of carbon-treated bonds. As the series of micrographs in Fig. 5 shows, prolonged heat treatment in a carbon-rich environment led to formation of cusp-shaped morphological instabilities along the gold grain boundaries, especially along the sample edges. Ultimately, these instabilities resulted in complete solid-state de-wetting of the gold from the sapphire. For all of the studies described below, the duration of the carbon heat treatment was deliberately adjusted to preclude such macroscopic de-wetting of the gold.

IV. Adhesion Measurements

Extensive interfacial porosity was generally observed subsequent to bonding. The pores are believed to originate from air trapped in the gold during the initial consolidation of the sandwich, that migrate to the gold-sapphire interface during subsequent heat treatment. (Coalescence of vacancies generated during evaporation was discounted due to the existence of extensive porosity along gold grain boundaries.)

Fortuitously, carbon heat treatment was found to be accompanied by a drastic change in the interfacial pore morphology, providing not only a convenient indicator of carbon, but also a means of measuring the interfacial work of adhesion (Fig. 6). The transition from highly faceted pores in the as-bonded samples to nearly isotropic pores after introduction of carbon is attributed to changes in the gold-sapphire interfacial surface energies (as indicated by the Wulff plot). In some of the more extreme cases, carbon precipitates were apparent on the pore surfaces and along the interface. The work of adhesion, W_{ad}, was calculated from the equilibrium contact angle between the metal and ceramic phases, θ, and surface energy of the metal, γ_{mv}, via the Young-Dupré relation:

$$W_{ad} = \gamma_{mv}(1+\cos\theta) \qquad (2)$$

allowing the effect of carbon heat treatment on adhesion to be quantified through the corresponding change in interfacial contact angle.[6] To measure θ, one of the sapphire substrates was carefully removed by stress-corroding the interface in water, thus revealing the gold surface. Contact angles were measured on these fracture surfaces using atomic force microscopy (AFM) by taking profile scans across several pores (Fig. 7). The contact angle histograms of Figure 8 reveal a definitive increase in contact angle – approximately 20° – resulting from carbon heat treatment.

Combining Eqn. 2 with the contact angle data of Fig. 8 and the gold surface energy from Table I, the gold-sapphire work of adhesion is seen to decrease by a factor of two, from 0.6 to 0.3 J/m^2, upon heat treatment in carbon. In calculating the adhesion, the surface energy of gold is assumed to be unaffected by the presence of carbon [7].

V. Fracture Measurements

The double-cleavage drilled compression (DCDC) specimen geometry, Fig. 9, was used to determine gold-sapphire interfacial fracture energies [33,34]. The DCDC test provides a stable, mode-I crack over a large range of crack extension, while allowing *in situ* observation of the fracture process through the sapphire substrates. Having the remote phase angle of loading near zero also simplifies correlation between existing numerical and analytical models, avoiding complications associated with shear tractions in the crack wake.

For the present studies, W = 2 mm, H = 4 mm, L = 40 mm, and R = 1 mm. On the basis of dimensional analysis, the energy release rate, $\mathcal{G}$, scales as:

$$\mathcal{G} = \frac{\pi\sigma^2 R}{E'} f\left(\tfrac{a}{R}, \tfrac{W}{R}\right), \qquad (3)$$

where σ is the applied compressive stress and E' is the plane strain Young's modulus [$E' = E/(1-\nu^2)$, ν is Poisson's ratio]. The function f was numerically determined for the present geometry using finite elements analysis [33]. In the range $\frac{W}{2R} \le \frac{a}{R} \le 15$, f can be approximated as:

$$f\left(\tfrac{a}{R}, \tfrac{W}{R}\right) = \left[\tfrac{W}{R} + \left(0.235\tfrac{W}{R} - 0.259\right)\tfrac{a}{R}\right]^{-2} \qquad (4)$$

Compressive load was applied through a servo-hydraulic test frame.[7] During the course of the test, the extension of the crack was monitored, and Eqns. 3-4 used to correlate the applied load to the critical energy release rate. Platen alignment was maintained using a hemisphere-in-socket tungsten carbide fixture, while Teflon tape was used to facilitate sliding at the specimen-platen interface. The interfacial fracture process was monitored using a tele-microscope[8] connected to a video recorder and monitor. The microscope was mounted on a motorized xyz stage, with the z-axis (parallel to the loading and crack extension direction) connected to a linear variable differential transformer (LVDT) for position tracking. The load, crosshead displacement, and LVDT position were simultaneously fed to a computer, with a corresponding real-time video record of the fracture process. From these data, the full details of the crack extension process were reconstructed after the test.

---

[6] Strictly speaking, Eqn. 2 is invalid if crystallographic facetting occurs. An alternate technique based on aspect ratio measurements uses the shape of equilibrated crystals to uniquely define the work of adhesion [31,32]. However, because preliminary results showed general agreement between works of adhesion determined using contact angle and aspect ratio measurements, the former measure is retained for its relative simplicity.

[7] MTS 810, Material Test System, Minneapolis, MN.

Representative micrographs of the fracture process captured from the video recording (Fig. 10a) reveal that the carbon-treated (A+C) samples fractured by interfacial cleavage at a steady-state fracture energy near 1 J/m^2. In contrast, the carbon-free (A+O) sample fractured at a significantly larger energy, approaching 250 J/m^2 at steady state. Although fracture still proceeded by interfacial separation (as verified by studying *post mortem* fracture surfaces), substantial plastic deformation occurred in the gold, as evidenced by the large fracture energy and microscopic blunting behind the crack tip (Fig. 10b).

The two-order-of-magnitude difference in steady-state fracture energy between samples that have and have not undergone a carbon heat treatment is evident in the resistance curves obtained from the DCDC fracture tests (Fig. 11). Further, while the fracture energy of the carbon-treated (A+C) samples is just a few times in excess of the corresponding work of adhesion, that of the as-bonded (A) and post-oxidized (A+O) samples exceeds the work of adhesion by more than two orders of magnitude.

Table III summarizes the salient features of the DCDC test results. The fracture resistance of the gold-sapphire interfaces is seen to fall into one of two broad categories. One applies to samples heat treated in an oxidizing environment (A, A+O), including those that were heat treated in carbon and subsequently re-oxidized (A+C+O). These samples have steady-state fracture energies approaching 250 J/m^2. The second category applies to samples whose final heat treatment was in a carbon environment (A+C). The steady-state fracture energy of these samples ranges from 1 to 2 J/m^2.

The one notable exception to the above categorization of post-bonding treatments is the sample heated in a graphite-laden vacuum furnace after the bonding treatment (A+V). Contrary to expectations, this sample exhibited a fracture energy only slightly below that of the oxidized samples, although the heat treating atmosphere was reducing and presented a substantial source of carbon.[9] As suggested by post-mortem examination of the fracture surfaces, this behavior relates to the limited kinetics of carbon transport to (and perhaps along) the interface in the absence of oxygen. Coincidentally, the fracture surface was marked by patchy regions of ductile void growth interspersed with regions of interfacial cleavage fracture (Fig. 12).

---

[8] Questar QM100, Questar Dakin Barlow, USA.

[9] The specimen was packed in graphite foil during heat treatment; the furnace furniture was also graphite.

VI. Discussion

a) Carbon Diffusion

In samples heat treated in carbon-laden ampoules, the spatial uniformity of the pore-shape change (Section IV) was used as *prima facie* evidence that the carbon had sufficient time to diffuse across the entire interface. There are no kinetic data for carbon diffusion in bulk gold and sapphire, let alone along gold-sapphire interfaces. However, indirect experimental evidence suggests that, at the heat treating temperatures used, carbon diffusion is negligibly slow through bulk sapphire [27] and gold [35], and is therefore likely to be governed by the rate of transport along the gold-sapphire interface. In the presence of oxygen, carbon transport ***to*** the interface is unlikely to be the rate-limiting step due to the high mobilities of CO in the gaseous phase, while carbon diffusion along the interface is severely hindered in the absence of oxygen. In a reducing, high-vacuum atmosphere, atomic surface diffusion is the only viable mechanism for carbon transport; with this as the rate-limiting step in the carbon heat treating process, it is reasonable to expect the vacuum-treated sample (A+V) to suffer little carbon embrittlement compared with the carbon-treated samples (A+C).

In addition to carbon mobility, there is evidence that gold mobility itself is affected by the heat treatments. As confirmed by the contact angle measurements, gold wets sapphire very poorly, both before and after heat treating in carbon. It is therefore not surprising that there is a tendency toward de-wetting of the gold foil from the sapphire. However, this instability occurs after relatively short times (and well below the melting temperature of gold) in the carbon-treated samples (Fig. 5), whereas no such instability is observed at the same temperature even after 100 hours in air. These observations suggest that carbon may be a self-diffusion enhancer for gold, a phenomenon documented in a number of systems in the microelectronics industry, including gold in silicon [36,37] and beryllium in GaAs [38].

b) Effect of Adhesion on Fracture Energy

To clarify the relationship between plastic dissipation and adhesion, the measured fracture energy is plotted against the measured work of adhesion in Figure 13. The datum at the origin of the plot corresponds to the degenerate case of an unbonded interface. Furthermore, the experimental results of Reimanis *et al.* [22,23] on gold foils sandwiched between sapphire substrates (see Appendix) have been superimposed. The differences in fracture energy and adhesion measured by Reimanis relative to the present results are attributed to interface contamination in the former. Contamination is likely to have originated from the relatively low-grade foil and noncleanroom processing conditions in the Reimanis experiments. Although carbon was not intentionally introduced to the interface, contaminants residing at the free surfaces prior to bonding were likely to have remained in the reducing atmosphere of the graphite-laden diffusion-bonding vacuum furnace. In fact, the fracture energy reported by Reimanis is only slightly below that of the present A+V sample, which is believed to be somewhat cleaner due to higher-purity starting materials and the use of an oxidizing environment in the primary bonding heat treatment.

There is an indisputable correlation between interfacial adhesion and plastic dissipation within the metal (Fig. 13). The correlation is highly non-linear, suggesting that the coupling between the dissipative terms of Eqn. 1 is strongly synergistic. When W_{ad} is sufficiently low, crack-tip bond rupture occurs across the interface with no plastic dissipation (i.e., background dislocation motion is not activated). This is the regime of ideal, or Griffith, cleavage fracture. As adhesion increases, dislocation plasticity initiates under the influence of the crack-tip field, such that interfacial decohesion is accompanied by plastic deformation of the metal. Essentially, W_{ad} functions as a non-linear valve, regulating the irreversible energy dissipated prior to crack-tip bond rupture [20]. When W_{ad} becomes sufficiently large, a transition from interfacial debonding to bulk-dominated fracture of the metal or ceramic is anticipated [16]. If the ceramic does not fail first, this transition would manifest itself in persistent crack-tip blunting via dislocation emission [39] and ductile void growth at the metal-ceramic interface [16]. Upon transition from interfacial debonding to bulk-dominated fracture, the macroscopic fracture energy may become altogether independent of the interfacial strength, governed solely by the constitutive properties of the bulk phases. In fact, evidence of an incipient transition in fracture mechanism was observed in sample A+V, where regions of both brittle debonding and ductile void growth were evident (Fig. 12). In this particular instance, the occurrence of ductile void growth is believed to have been promoted by regions of higher-than-typical interfacial pore density rather than higher interfacial adhesion.

c) Effect of Carbon on Gold-Sapphire Adhesion

An unmistakable correlation between the post-bonding heat treatment, the work of adhesion, and the interfacial fracture energy has been demonstrated. After a short carbon heat treatment, the work of adhesion decreases from approximately 0.6 to 0.3 J/m^2 with a corresponding -- and precipitous -- drop in the interfacial fracture resistance, from ~250 to ~1 J/m^2. The nominal, or air-bonded value of W_{ad} is fully consistent with recent calculations of the gold-sapphire van der Waals adhesion energy, estimated between 0.6 and 0.9 J/m^2 [40]. Although a quantitative measure for the amount of carbon in the respective samples would have been preferred, attempts to quantify the interfacial carbon by secondary ion mass spectrometry (SIMS) were unsuccessful due to interference from carbon impurities in the bulk sapphire. A subsequent attempt to use an isotopic carbon tracer (^{13}C) also failed, this time due to interference from $H^{12}C$. However, SIMS did reveal that the concentration of carbon in bulk gold was negligible in both as-bonded and carbon-treated samples, consistent with the assumptions made in Section II.

While the effects of carbon heat treatment on the adhesion and fracture resistance of the gold-sapphire interface have been clearly demonstrated, the physical origin for the drop in W_{ad} associated with carbon treating remains unclear. Three possible causes attributable to the heat treatment have been considered: carbon precipitation at the interface, carbon segregation to the interface, and carbon-induced reduction of the oxygen activity at the interface.[10]

The solid-solubility line for the gold-carbon system (Fig. 2) indicates that dissolved carbon is expected to precipitate at the gold-sapphire interface upon cooling from the heat treatment temperature. In fact, examination of fracture surfaces by SEM (Fig. 4a) and AES (Fig. 4b) provides ample evidence of carbon precipitation. However, as these precipitates occupy only a small area fraction of the interface, they should induce only local variations in the interfacial properties. The precipitate can reduce the local interfacial work of adhesion to the lesser of the cohesive energy of carbon, carbon-gold adhesion, or carbon-sapphire adhesion, as would be evident from the actual fracture path. However, away from the precipitate -- and therefore over the majority of the interfacial area -- the work of adhesion remains unaffected. In this sense, the precipitate can be thought of as a generalized interfacial pore having a finite value of W_{ad} (and conversely, an interfacial pore is just a degenerate precipitate in the limit $W_{ad} \rightarrow 0$). Noting the relatively weak dependence of fracture toughness on interfacial porosity and on the basis of available cleavage-plasticity coupling models [21], the possibility that carbon precipitates are entirely responsible for the observed two-order-of-magnitude embrittlement is discounted. Instead, we turn to interfacial segregation as a possible explanation.

There is a general correlation between the segregation enrichment ratio (defined as the equilibrium ratio of interfacial to bulk concentration of the segregating species) and the solid solubility of the solute. Making an estimate based on the relations proposed by Seah and Hondros [41], the enrichment ratio is approximately 10^4 for the gold-carbon system at the heat treatment temperature and 2×10^5 at 600^oC,[11] corresponding to a several-monolayer coverage of carbon at the saturation limit. It is widely accepted that interfacial segregation alters the interfacial work of adhesion [42];

---

[10] All other effects that may be associated with the carbon heat treatment, such as secondary contamination or microstructural changes, are considered to have at most a second-order influence on the interfacial properties and have been eliminated from consideration based on chemical analysis and careful experimental control.

[11] It is difficult to estimate the enrichment ratio of carbon in sapphire and gold-sapphire couples due to the sluggish diffusion kinetics at the temperatures considered. For that very reason, however, it is expected that estimates based on carbon-gold alone should suffice for a first-order estimate.

however, the adsorption isotherms of carbon on gold (let alone carbon on the gold-sapphire interface) are virtually unobtainable quantities, precluding a quantitative prediction of adhesion reduction based on thermodynamic relations. *Ab initio* calculations of metal-ceramic interfaces are few in number, and even fewer consider the effect of impurity species on adhesion. However, Hong *et al.* have shown that a single carbon monolayer at the Ag-MgO interface reduces the work of adhesion from 0.95 to 0.67 J/m^2 [43] and from 3.50 to 3.16 J/m^2 in the Mo-$MoSi_2$ system [44].[12] Carbon could behave in a similar manner at the gold-sapphire interface. Hong *et al.* attribute the decrease in adhesion to the increase in strain energy accompanying impurity insertion at the interface (i.e., the bonds across the interface are stretched in proportion to the covalent radius of the impurity and weakened as the crystals on either side of the interface are forced apart), mediated somewhat by the chemical interaction.

Before ascribing the observed adhesion reduction to carbon segregation, a third possibility should be considered, namely that carbon reduces the gold-sapphire adhesion not by direct segregation but by reducing the interfacial oxygen activity. That this should be the case for metals that readily dissolve oxygen (e.g., Ag, Cu) or that form reaction oxides (e.g., Fe, Al, Ni, Si) is comprehensible, and numerous studies appear to confirm this effect [e.g., 45-55]. However, gold neither forms stable oxides nor has any appreciable oxygen solubility [56]. In fact, Chatain and coworkers have found no variation in the contact angle of molten gold on sapphire over a 20-order-of-magnitude range of oxygen partial pressures ($<10^{-15}$ to 5×10^4 Pa) [57]. Noting that the surface tension of neither gold nor sapphire changes with oxygen pressures in the range 10^{-9} to 1 Pa [57], we conclude that gold-sapphire adhesion is essentially insensitive to oxygen activity. Yet several investigators report enhanced gold-oxide adhesion in the presence of oxygen. For instance, Moore and Thornton found that gold pellets melted on sapphire and fused silica substrates formed such strong adhesive bonds in an oxygen atmosphere that fracture occurred in the substrate when the pellet was pried loose in shear, while pellets melted in vacuum were so weak that they spontaneously fell off upon cooling [58]. Bailey and Black observed that gold-alumina solid-state reaction bonds formed in air and oxygen exhibited ~100% higher shear strengths than bonds formed in low-oxygen atmospheres (N_2, H_2, Ar, vacuum) [59]. A similar conclusion was reached by Allen and Borbidge for gold-alumina bonds formed in oxidizing and reducing (H_2) atmospheres [60]. Pask and Fulrath reported a decrease in the contact angle of molten sodium disilicate glass on gold, from ~65° in vacuum, Ar, He, N_2, CO, CO_2, H_2, and H_2O atmospheres to 35° in the presence of oxygen;

---

[12] This trend is not, however, unequivocal: carbon *increases* W_{ad} in the Al-MgO system from 0.55 to 0.66 J/m^2 [43]. This apparent anomaly is ascribed to the large strain imposed upon the aluminum in the calculation in order to force epitaxy with the MgO. The decrease in strain energy needed to interstitially accommodate the C atoms, along with the contribution from chemical bonding energy, are believed to outweigh the strain energy cost of stretching the lattice in this system.

furthermore, the wetting improvement was accompanied by an increased adhesion strength [46]. Pedraza and coworkers found that the peel strength of the gold-alumina bond could be increased from 0.1 to 50 MPa by laser-irradiating the alumina in an oxygen-rich (O_2 or air) atmosphere prior to gold deposition [61]. Studying gold films deposited on glass and silicon, Martin and coworkers noted a 3-4 order-of-magnitude adhesion enhancement (as measured by the scratch test) in oxygen-ion-assisted deposition, while argon- and hydrogen-ion-assisted deposition resulted in poor adhesion [62].

Auger spectroscopy [61] and X-ray photoelectron spectroscopy [62] on oxygen-treated gold-sapphire interfaces detect no structural or chemical changes in the bulk constituents. However, Auger spectroscopy of the interface [61] and radioactive gold tracer experiments [58] suggest that a stable gold oxide may be forming at the interface *despite* the fact that in bulk states, all known oxides of gold are spontaneously reduced above 250°C. The broad reproducibility of oxygen-induced adhesion enhancement suggests that this phenomenon is more than a spurious side-effect. Nevertheless, most of the above observations can be ascribed to the interaction of oxygen with inadvertent carbon contamination. In fact, poor surface preparation prior to bonding has been shown to result in carbon contamination on sapphire [49] and metal [63,64] surfaces. Upon bonding, these adsorbed contaminants are likely to be trapped at the interface, lowering the interfacial energy. In addition to pre-existing surface impurities, one can also imagine impurity adsorption during deposition or wetting experiments, caused by dirty atmospheric chambers, especially when low-purity gases or dirty mechanical pumps are used. Indeed, such contamination effects are consistent with Holmquist and Pask's observations of a reversible wetting-dewetting transition of glass on platinum as they alternately increased and decreased the ambient air pressure in their sessile drop vacuum chamber [65]. This behavior was only observed when the vacuum cold trap was bypassed, and the transition was attributed to carbon adsorption onto the platinum surface. They estimated that the observed increase in wetting angle could be explained if the carbon depressed the surface energy of platinum by a mere 0.05 J/m^2. If surface contamination were the source of the adhesion modification in the above studies, it would not be surprising that exposure to an oxygen-rich atmosphere either immediately prior to or during the bond formation would enhance the resulting adhesion by gettering strongly reducing contaminants. Such a hypothesis is consistent with Chatain's sessile drop experiments, where the substrate was meticulously cleaned and high-purity (99.9999%) gold was used, and an oxygen-independent contact angle was reported [57]. It is also consistent with our observation that carbon-embrittled interfaces recover the majority of their nominal fracture resistance and adhesion subsequent to re-oxidation.

VII. Summary

Using gold-sapphire as a model metal-ceramic system, we found that adhesion can be increased by heat treatment in an oxygen-rich atmosphere and reduced by heat treatment in a carbon-rich environment. Fracture-mechanical tests revealed that the interfacial fracture energy is strongly coupled to these adhesion modifications: a two-order-of-magnitude reduction in fracture energy was measured for samples in which the adhesion itself was reduced only two-fold. The suggested mechanism responsible for this dramatic embrittlement is carbon segregation to the interface, wherein the carbon diffuses along the interface (maintaining local equilibrium with the bulk gold) and subsequently forms a monolayer-thick interfacial segregant layer. The reversibility of the detrimental effects of carbon heat treatment upon re-oxidation suggest that the interfacial carbon can be gettered by oxygen.

Although the precise mechanism of carbon-induced adhesion reduction in the gold-sapphire system remains equivocal, we can generalize that the thermochemical history of components containing load-bearing metal-ceramic bonds must be carefully controlled if superior mechanical properties are to be achieved. Contamination introduced during bonding can lead to catastrophic weakening of the bonds. On the other hand, there is evidence that adhesion reduction can in some instances be reversed by post-fabrication treatment in a suitable environment.

Table I Surface Energies of Gold, Sapphire, and Carbon

Material	γ_{sv} [a] [J /m^2]	$d\gamma_{sv}/dT$ [J /m$^2\cdot$°C]	γ_{lv} [b] [J /m^2]	$d\gamma_{lv}/dT$ [mJ /m$^2\cdot$°C]	T_m [°C]	Refs.
Gold	1.40	-0.43	1.14	-0.18	1064	17,66,67
c-Sapphire	0.77	-0.12	0.57	-0.12	2054	68-70
Graphite					~3550 [c]	69
a-plane	1.13	-0.17	--	--		
c-plane	1.01	-0.13	--	--		

[a] at 1000°C
[b] at $T=T_m$
[c] sublimes at ~3370°C

Table II Selected Physical Properties of Gold and Sapphire

Material	E [a] [GPa]	ν [a]	σ_o [MPa]	n	α [a,b] [10^6 °C^{-1}]	Refs.
Gold	78±2	0.42	<10	0.5	16.9	71
Sapphire	380±20	0.26	--	--	8.5	72-73

[a] polycrystalline values;
[b] averaged over 20-1020°C

Table III Steady-State Fracture Energies for Gold-Sapphire DCDC Specimens

heat treatment[a]	A+C	A+O	A	A+C+O	A+V
Γ_{ss} [J/m^2]	1-2	250	250	230+	150

[a] A = as-bonded (in air), 48 hr. @1040°C
C = carbon-treated, 8 hr. @1000°C
O = oxygen-treateded, 48 (A+O) or 100 (A+C+O) hr. @1025°C
V = vacuum-treated, 48 hr. @1020°C

VIII. References

1. M.Nicholas, "The Strength of Metal-Alumina Interfaces," *J.Mater.Sci.*, **3** 571-6 (1968).
2. D.P.Pope and M.A.Smith, "Debonding of Metal/Ceramic Interfaces: the Role of Segregation," in Metal-Ceramic Interfaces, pp.326-34, ed. by M.Rühle, A.G.Evans, M.F.Ashby, and J.P.Hirth, eds., Pergamon Press, New York, (1990).
3. S.Suresh and A.Needleman (eds.), Interfacial Phenomena in Composites: Processing, Characterization, and Mechanical Properties, Elsevier Applied Science, London (1989).
4. K.K.Chawla, Composite Materials: Science and Engineering, pp.79-86, Springer Verlag, NY (1987).
5. J.M.Howe, "Bonding, Structure, and Properties of Metal/Ceramic Interfaces: Part 1, Chemical Bonding, Chemical Reaction, and Interfacial Structure," *Int.Materials Rev.*, **38**[5] 233-56 (1993).
6. D.Korn, G.Elssner, H.F.Fischmeister, and M.Rühle, "Influence of Interface Impurities on the Fracture Energy of UHV Bonded Niobium-Sapphire Bicrystals," *Acta metall.*, **40**[Suppl] s355-60 (1992); G.Elssner, D.Korn, and M.Rühle, "The Influence of Interface Impurities on Fracture Energy of UHV Diffusion Bonded Metal-Ceramic Bicrystals," *Scripta met.*, **31**[8] 1037-42 (1994).
7. U.Gangopadhyay and P.Wynblatt, "Influence of Segregation Effects on the Energies of Lead/Graphite and Gold/Graphite Interfaces," *Mat.Res.Soc.Symp.Proc.*, **318** 393-8 (1994); U.Gangopadhyay and P.Wynblatt, "Modification of the Gold/Graphite Interfacial Energy by Interfacial Adsorption of Nickel," *J.Mat.Sci.*, **30**[1] 94-100 (1995).
8. J.T.Klomp, "Ceramic-Metal Interactions," *Mat.Res.Soc.Symp.Proc.*, **40** 381-91 (1985).
9. W.J.O'Brien and G.Ryge, "Relation between Molecular Force Calculations and Observed Strengths of Enamel-Metal Interfaces," *J.Am.Ceram.Soc.*, **47**[1] 5-8 (1964).
10. M.G.Nicholas, "Interactions at Oxide-Metal Interfaces," *Mat.Sci.Forum*, **29** 127-50 (1988).
11. J.T.Klomp, "Ceramic-Metal Reactions and their Effect on the Interface Microstructure," in Ceramic Microstructures '86: Role of Interfaces, pp. 307-17, ed. by J.A.Pask and A.G.Evans, Materials Science Research, V.21, Plenum Press, New York (1987).
12. S.V.Pepper, "Shear Strength of Metal-Sapphire Contacts," *J.Appl.Phys.*, **47**[3] 801- 8 (1976).
13. R.M.Crispin and M.G.Nicholas, "The Wetting and Bonding Behaviour of Some Nickel Alloy-Alumina Systems," *J.Mater.Sci.*, **11**[1] 17-21 (1976).
14. J.T.Klomp, "Bonding Metals to Ceramics and Glasses," *Am.Ceram.Soc.Bull.*, **51**[9] 683-8 (1972).
15. A.P.Tomsia, E.Saiz, B.J.Dalgleish, and R.M.Cannon, "Wetting and Strength Issues in Ceramic/Metal Bonding," Proceedings of the 4th Japan International SAMPE Symposium, pp.347-56 (1995).
16. A.G.Evans and B.J.Dalgleish, "The Fracture Resistance of Metal-Ceramic Interfaces," *Acta metall.*, **40**[Suppl] s295-306 (1992); A.G.Evans and B.J.Dalgleish, "The Fracture Resistance of Metal/Ceramic Interfaces," *Mater.Sci.Eng.*, **A162**[1-2] 1-13 (1993).
17. L.E.Murr, Interfacial Phenomena in Metals and Alloys, pp.102,110,124,155, Addison-Wesley, Reading, MA (1975).
18. A.A.Griffith, "The Phenomena of Rupture and Flow in Solids," *Phil.Trans.Roy.Soc. Lond.*, **A221** 163-98 (1920).
19. E.Orowan, *Trans.Instn.Engrs.Shipbuilders Scot.*, **89** 165 (1945).
20. J.R.Rice, "An Examination of the Fracture Mechanics Energy Balance from the Point of View of Continuum Mechanics," in Proceedings of the 1st International Conference on Fracture, pp.309-40, ed. by T.Yokobori, T.Kawasaki, and

J.L.Swedlow, Sendai, Japan (1966).
21. D.M.Lipkin, D.R.Clarke, and G.E.Beltz, "A Strain-Gradient Model of Cleavage Fracture in Plastically Deforming Materials," *Acta mater.*, **44**, 4051 (1996); D.M.Lipkin, G.E.Beltz, and D.R.Clarke, "A Model of Cleavage along Metal/Ceramic Interfaces," *Mat.Res.Soc.Symp.Proc.*, 91-6 (1997).
22. I.E.Reimanis, B.J.Dalgleish, M.Brahy, M.Rühle, and A.G.Evans, "Effects of Plasticity on the Crack Propagation Resistance of a Metal/Ceramic Interface," *Acta metall.*, **38**[12] 2645-52 (1990).
23. I.E.Reimanis, B.J.Dalgleish, and A.G.Evans, "The Fracture Resistance of a Model Metal/Ceramic Interface," *Acta metall.*, **39**[12] 3133-41 (1991).
24. H.Okamoto and T.B.Massalski, "Au-C (Gold-Carbon)," Binary Alloys Phase Diagrams, T.B.Massalski, ed. 2nd ed. ASM International, 1990.
25. M.P.Seah and E.D.Hondros, "Grain Boundary Segregation," *Proc.Roy.Soc.Lond.*, **A335**[1601], 191-212 (1973).
26. E.D.Hondros and M.P.Seah, "Segregation to Interfaces," *Intl.Metals Rev.*, **22**, 262-301 (1977).
27. L.M.Foster, G.Long, and M.S.Hunter, "Reactions Between Aluminum Oxide and Carbon: The Al_2O_3-Al_4C_3 Phase Diagram," *J.Am.Ceram. Soc.*, **39**[1] 1-11 (1956).
28. V.A.Borodin, A.M.Ionov, and T.N.Yalovets, "Void Formation upon Annealing of Shaped Sapphire Crystals," *J.Crystal Growth*, **104**, 157-64 (1990).
29. E.D.Richmond, "XPS Analysis of the Sapphire Surface as a Function of High Temperature Vacuum Annealing," *Mat.Res.Soc.Symp.Proc.*, **159** 253-6 (1990).
30. A.Hill and E.R.Wallach, "Modelling Solid-State Diffusion Bonding," *Acta metall.*, **37**[9] 2425-37 (1989).
31. R.M.Pilliar and J.Nutting, "Solid-Solid Interfacial Energy Determinations in Metal-Ceramic Systems," *Phil.Mag.*, **16** 181-8 (1967).
32. W.L.Winterbottom, "Equilibrium Shape of a Small Particle in Contact with a Foreign Substrate," *Acta metall.*, **15**[2] 303-10 (1967).
33. M.Y.He, M.R.Turner, and A.G.Evans, "Analysis of the Double Cleavage Drilled Compression Specimen for Interface Fracture Energy Measurements over a Range of Mode Mixities," *Acta metall.*, **43**[9] 3453-8 (1995).
34. M.R.Turner, B.J.Dalgleish, M.Y.He, and A.G.Evans, "A Fracture Resistance Measurement Method for Bimaterial Interfaces Having Large Debond Energy," *Acta metall.*, **43**[9] 3459-65 (1995).
35. R.B.McLellan, "The Solubility of Carbon in Solid Gold, Copper, and Silver," *Scripta Metall.*, **3**, 389-92 (1969).
36. M.J.Hill and P.M.Van Iseghem, "Influence of Carbon Concentration on Gold Diffusion in Silicon," pp.715-25, in Semiconductor Silicon 1977, ed. by H.R. Huff and E.Sirtl, The Electrochemical Society, Princeton, NJ (1977).
37. Y.Itoh, Y.Sugita, and T.Nozaki, "Effect of Carbon and Oxygen Precipitation on Gold Diffusion in Silicon," *Jpn.J.Appl.Phys.*, **28**[10] 1746-9 (1989).
38. E.Tokumitsu, J.Shirakashi, S.Nozaki, M.Konagai, and others, "Anomalous Enhancement of Beryllium Diffusion in Heavily Carbon-Doped GaAs," pp.681-6, in Gallium Arsenide and Related Compounds 1992 (Proceedings of the Nineteenth International Symposium), Karuizawa, Japan, ed. by T.Ikegami, F.Hasegawa, Y.Takeda, Bristol, UK (1993).
39. J.R.Rice and R.Thomson, "Ductile Versus Brittle Behaviour of Crystals," *Phil. Mag.*, **29**[1] 73-97 (1974); J.R.Rice, "Dislocation Nucleation from a Crack Tip: an Analysis Based on the Peierls Concept," *J.Mech.Phys.Solids*, **40**[2] 239-71 (1992).
40. D.M.Lipkin, J.N.Israelachvili, and D.R.Clarke, "Estimating the Metal-Cermic van der Waals Adhesion Energy," pending publication in *Phil.Mag.A* (1997).
41. M.P.Seah and E.D.Hondros, "Grain Boundary Segregation," *Proc.Roy. Soc.Lond.*, **A335**[1601], 191-212 (1973).
42. J.P.Hirth, and J.R.Rice, *Met.Trans.*, **11A**, 1501 (1980).

43. T.Hong, J.R.Smith, and D.J.Srolovitz, "Theory of Metal-Ceramic Adhesion," *Acta metall.*, **43**[7] 2721-30 (1995); J.R.Smith, T.Hong, and D.J.Srolovitz, "Metal-Ceramic Adhesion and the Harris Functional," *Phys.Rev.Lett.*, **72**[25] 4021-4 (1994).
44. T.Hong, J.R.Smith, and D.J.Srolovitz, "Impurity Effects on Adhesion: Nb, C, O, B, and S at a Mo/MoSi$_2$ Interface," *Phys.Rev.B*, **47**[20] 13615-25 (1993); T.Hong, J.R.Smith, and D.J.Srolovitz, "Impurity Effects on Adhesion," *Phys.Rev.Lett.*, **70**[5] 615-8 (1993).
45. M.Humenik and W.D.Kingery, "Metal-Ceramic Interactions: III, Surface Tension and Wettability of Metal-Ceramic Systems," *J.Am.Ceram.Soc.*, **37**[1] 18- 23 (1954).
46. J.A.Pask and R.M.Fulrath, "Fundamentals of Glass-to-Metal Bonding: VIII, Nature of Wetting and Adherence," *J.Am.Ceram.Soc.*, **45**[12] 592-6 (1962).
47. D.Chatain, F.Chabert, V.Ghetta, and J.Fouletier, "New Experimental Setup for Wettability Characterization under Monitored Oxygen Activity: II, Wettability of Sapphire by Silver-Oxygen Melts," *J.Am.Ceram.Soc.*, **77**[1] 197-201 (1994).
48. J.E.Lazaroff, P.D.Ownby, and D.A.Weirauch, "Wetting in an Electronic Packaging System: I, Wetting of Tungsten by Glass in Controlled Oxygen Partial Pressure Atmospheres," *J.Am.Ceram.Soc.*, **78**[3] 539-44 (1995).
49. S.V.Pepper, "Shear strength of Metal-Sapphire Contacts," *J.Appl.Phys.*, **47**[3] 801-8 (1976).
50. D.Chatain, L.Coudurier, and N.Eustathopoulos, "Wetting and Interfacial Bonding in Ionocovalent Oxide-Liquid Metal Systems," *Revue Phys.Appl.*, **23** 1055-64 (1988); N.Eustathopoulos, D.Chatain, and L.Coudurier, "Wetting and Interfacial Chemistry in Liquid Metal-Ceramic Systems," *Mater.Sci.Eng.*, **A135** 83-8 (1991).
51. B.Drevet, D.Chatain, and N.Eustathopoulos, "Wettability and Three-Phase Equilibria in the (Au-Si)/Al$_2$O$_3$ System," *J.Chim.Phys.*, **87** 117-26 (1990).
52. N.Eustathopoulos and B.Drevet, "Interfacial Bonding, Wettability and Reactivity in Metal/Oxide Systems," *J.Phys.III France*, **4** 1865-81 (1994).
53. R.Terry, K.Baker, and N.M.Rodriguez, "*In Situ* Electron Microscopy Studied of the Behavior of Metal Particles on Ceramic Substrates," *Mat.Res.Soc.Symp.Proc.*, **357** 11-6 (1995).
54. A.C.D.Chaklader, W.W.Gill, and S.P.Mehrotra, "Predictive Model for Interfacial Phenomena Between Molten Metals and Sapphire in Varying Oxygen Partial Pressures," pp. 421-32, in Materials Science Research, V.14, "Surfaces & Interfaces in Ceramic and Ceramic-Metal Systems," ed. by J.Pask and A.G.Evans, Plenum Press, New York, NY (1981).
55. R.Sangiorgi, A.Passerone, and R.Minisini, "Influence of Oxygen Partial Pressure on Wettability of Vitreous Silica by Molten Silver," pp. 445-55, in Materials Science Research, V.14, "Surfaces & Interfaces in Ceramic and Ceramic-Metal Systems," ed. by J.Pask and A.G.Evans, Plenum Press, New York, NY (1981).
56. K.C.Hsieh, J.P.Neumann, and Y.A.Chang, "Au-O (Gold-Oxygen)," Binary Alloys Phase Diagrams, T.B.Massalski, ed. 2nd ed. ASM International, 1990.
57. D.Chatain, F.Chabert, V.Ghetta, and J.Fouletier, "New Experimental Setup for Wettability Characterization under Monitored Oxygen Activity: I, Role of Oxidation State and Defect Concentration on Oxide Wettability of Gold," *J.Am. Ceram.Soc.*, **76**[6] 1568-76 (1993).
58. D.G.Moore and H.R.Thornton, "Effect of Oxygen on the Bonding of Gold to Fused Silica," *J.Res.Natl.Bur.Stand.*, **62**[3] 127-35 (1959).
59. F.P.Bailey and K.J.T.Black, "The Effect of Ambient Atmosphere on the Gold-to-Alumina Solid State Reaction Bond," *J.Mater.Sci.Lett.*, **13** 1606-8 (1978).
60. R.V.Allen and W.E.Borbidge, "Solid State Bonding of Noble Metals to Alumina, the Effect of Ambient Atmosphere," in Science of Ceramics, Vol.12, Ed. By P.Vincenzini, Grafiche Galeati, Imola, Italy (1984).
61. A.J.Pedraza, R.A.Kumar, and D.H.Lowndes, "Improved Adhesion of Gold Films Sputter-Deposited on Laser-Treated Thermally Annealed Alumina," *Appl.Phys.Lett.*,

66[9] 1065-7 (1995); J.Park, A.J.Pedraza, and W.R.Allen, "Auger Electron Spectroscopy of Metallic Film/Laser-Irradiated Alumina Couples," *Mat.Res.Soc. Symp.Proc.*, **357** 59-65 (1995); A.J.Pedraza, M.J.DeSilva, R.A.Kumar, and D.H.Lowndes, "The Adhesion of Metallic Films to Laser-irradiated Alumina," *J.Appl.Phys.*, **77**[10] 5176-9 (1995).

62. P.J.Martin, W.G.Sainty, R.P.Netterfield, and A.N.Buckley, "Oxygen-Ion-Assisted Deposition of Thin Gold Films," *Vacuum*, **35**[12] 621-4 (1985).
63. E.D.Richmond, "XPS Analysis of the Sapphire Surface as a Function of High Temperature Vacuum Annealing," *Mat.Res.Soc.Symp.Proc.*, **159** 253-6 (1990).
64. B.Gibbesch and G.Elssner, "Ultra High Vacuum Diffusion Bonded Nb-Al_2O_3 and Cu-Al_2O_3 Joints – the Role of Welding Temperature and Sputter Cleaning," *Acta metall.mater.*, **40s** s59-s66 (1992).
65. G.Holmquist and J.A.Pask, "Effect of Carbon and Water on Wetting and Reactions of B_2O_3-Containing Glasses on Platinum," *J.Am.Ceram.Soc.*, **59**[9-10] 384-6 (1976).
66. V.K.Kumikov and Kh.B.Khokonov, "On the Measurement of Surface Free Energy and Surface Tension of Solid Metals," *J.Appl.Phys.*, **54**[3] 1346-50 (1983).
67. B.J.Keene, "Review of Data for the Surface Tension of Pure Metals," *Intl. Materials Rev.*, **38**[4] 157-92 (1993).
68. W.D.Kingery, "Metal-Ceramic Interactions: IV, Absolute Measurement of Metal-Ceramic Interfacial Energy and the Interfacial Adsorption of Silicon from Iron-Silicon Alloys," *J.Am.Ceram.Soc.*, **37**[1] 42-5 (1954).
69. S.K.Rhee, "Critical Surface Energies of Al_2O_3 and Graphite," *J.Am.Ceram.Soc.*, **55**[6] 300-3 (1972).
70. W.D.Kingery, H.K.Bowen, and D.R.Uhlman, Introduction to Ceramics, 2nd ed., p.183, John Wiley & Sons, New York, NY (1976).
71. Metals Handbook, Vol.2, Properties and Selection: Nonferrous Alloys and Special-Purpose Materials, 10th Ed., pp.704 & 1116, ASM International, Materials Park, OH (1990).
72. J.B.Wachtman and D.G.Lam, "Young's Modulus of Various Refractory Materials as a Function of Temperature," *J.Am.Ceram.Soc.*, **42**[5] 254-60 (1959); J.B.Wachtman, W.E.Tefft, D.G.Lam, and C.S.Apstein, "Exponential Temperature Dependence of Young's Modulus for Several Oxides," *Phys.Rev.*, **122**[6] 1754-9 (1961).
73. Y.S.Touloukian, Thermophysical Properties of Matter, Vol.13: "Thermal Expansion – Nonmetallic Solids," IFI/Plenum, New York, NY (1977).
74. H.M.Jensen, J.W.Hutchinson, and K.-S.Kim, "Decohesion of a Cut Prestressed Film on a Substrate," *Int.J.Solids Struct.*, **26**[9-10] 1099-114 (1990).

IX. Appendix

From Reimanis' [22,23] measurement of pore contact angles (and using the gold surface energy from Table I), we calculate the work of adhesion to be $W_{ad} \approx 0.41$ J/m^2. The corresponding interfacial toughness values cannot be compared directly to the ones presently measured due to differences in specimen and loading geometries. However, Reimanis did not observe a noticeable effect of foil thickness on the steady-state fracture energies [23], which approached approximately 150 J/m^2 in foils ranging in thickness from 10 to 100 μm. There is, however, a substantial correction that needs to be made to account for the difference in mode mixity between the four-point flexure geometry used by Reimanis ($\psi \approx 45^\circ$) and the DCDC geometry used in the present study ($\psi = 0^\circ$). An empirical correction has been proposed by Jensen *et al.* [74]:

$$\Gamma^{\Psi=0} = \Gamma(\Psi)\left[1-(1-\lambda)\sin^2(\Psi)\right], \qquad \text{(A1)}$$

where λ is a parameter that ranges from 0 to 1 and indicates the sensitivity of the fracture energy to mixity angle. Using data for gold-sapphire, Reimanis found $\lambda \approx 0.2$ to give a best fit, from which we calculate the correction factor between the four-point flexure and DCDC geometries to be approximately 0.6. Therefore, the mode-I equivalent steady-state fracture energy from the work of Reimanis is 90 J/m^2, as indicated in Fig. 13.

X. Figure Captions

Fig. 1 Classification of the observed modes of interfacial fracture in metal-ceramic systems, in the absence of an interfacial reaction product. Strong interfaces fracture by one of two mechanisms dominated by the bulk components: (a) ductile fracture in the metal or (b) cleavage fracture in the ceramic. (c) Weaker interfaces have been found to exhibit brittle debonding, accompanied by plasticity in the metal layer. In this mechanism, the amount of plastic dissipation in the metal is strongly dependent on the work of adhesion.

Fig. 2 Gold-carbon phase diagram [24]. Shaded box indicates temperature range used for bonding and heat treating. Note the rapid drop in solid-solubility of carbon with decreasing temperature.

Fig. 3 Illustration of procedure used to prepare gold-sapphire-gold composite sandwiches: (a) electron-beam deposition of gold on sapphire substrates, (b) consolidation and diffusion bonding (gold foil insert optional), and (c) introduction of interfacial carbon via an encapsulated post-bonding heat treatment.

Fig. 4 (a) Secondary electron image of a gold fracture surface created after mechanically testing a sapphire-gold-sapphire sandwich that was carbon heat treated (A+C), indicating location of interfacial pores. (b) Carbon-Auger electron (272 eV) image of region shown in (a), indicating the non-uniformity of the interfacial carbon distribution (inset: Auger electron spectrum). As expected (e.g., [7]), carbon adsorption to the pore surfaces is minimal.

Fig. 5 Evolution of morphological instability with increasing duration (and temperature) of carbon heat treatment for (a) 8 hr. at 1020°C, (b) 16 hr. at 1020°C, (c) 144 hr. at 1030°C, and (d) 16 hr. at 1030°C. All foils were 25 μm thick except (c), which was 100 μm thick.

Fig. 6 Optical (top) and scanning electron (bottom) micrographs showing characteristic change in interfacial pore morphology as carbon is introduced into nominally pure systems. (a) As-bonded and (b) heat treated in carbon for 4 hours at 1020°C.

Fig. 7 SEM micrographs of as-bonded (left) and carbon-treated (right) interfaces. (b) Corresponding AFM traces across representative interfacial pores. Arrows indicate region from which contact angles are measured.

Fig. 8 Histograms representing the distribution of interfacial contact angles of gold on sapphire (a) in the air-bonded samples and (b) after carbon heat treatment. Note the 20°

increase in contact angle associated with the carbon heat treatment.

Fig. 9 Schematic of the double-cleavage drilled compression (DCDC) fracture geometry used in the present study.

Fig. 10 Images of interfacial fracture taken *in situ* during DCDC fracture experiments. (a) Crack-tip cleavage of carbon-treated sample (A+C) at a steady-state fracture energy of 1.25 J/m^2. Note that the crack tip remains sharp and straight as it progresses from top to bottom in the sequence i-iv. Note also the interference fringes in the crack wake, indicating the low crack-opening displacement profile. (b) Fracture of an as-bonded sample with an oxygen heat treatment (A+O). The sequence i-iv tracks the crack front at fracture resistance values of 20, 75, 150, and 245 J/m^2 (steady state), respectively. Note the progression from crack-tip cleavage to constrained debonding between ii and iii.

Fig. 11 Resistance curves for fracture along the gold-sapphire interface in the DCDC configuration: (a) as-bonded [A] and oxygen heat treated [A+O] samples and (b) carbon heat treated [A+C] samples. The shaded regions along the left axis correspond to the measured works of adhesion, while those along the right axis show the range of steady-state fracture energies representative of the respective heat treatments.

Fig. 12 Portion of the fracture surface of sample A+V, showing a transition from interfacial debonding to ductile void growth. Intermediate region corresponds to void growth that was interrupted by interfacial debonding prior to complete necking of the gold.

Fig. 13 Experimentally derived dependence of gold-sapphire fracture energy on the interfacial work of adhesion. Solid circles represent data obtained in the present study, while open circle corresponds to the adjusted datum taken from Reimanis *et al.* [22,23]. The difference between work of fracture and work of adhesion is taken to represent the work of plastic deformation according to Eqn. 1.

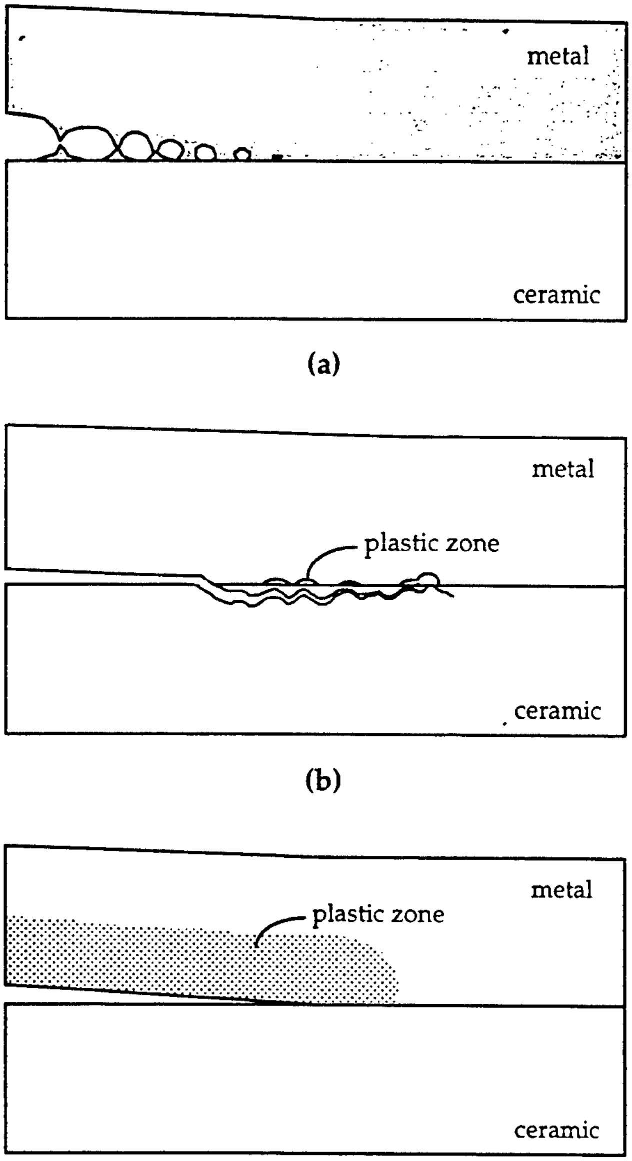
metal
ceramic
metal
plastic zone
ceramic
metal
plastic zone
ceramic

(a)

(b)

(c)

Fig. 1

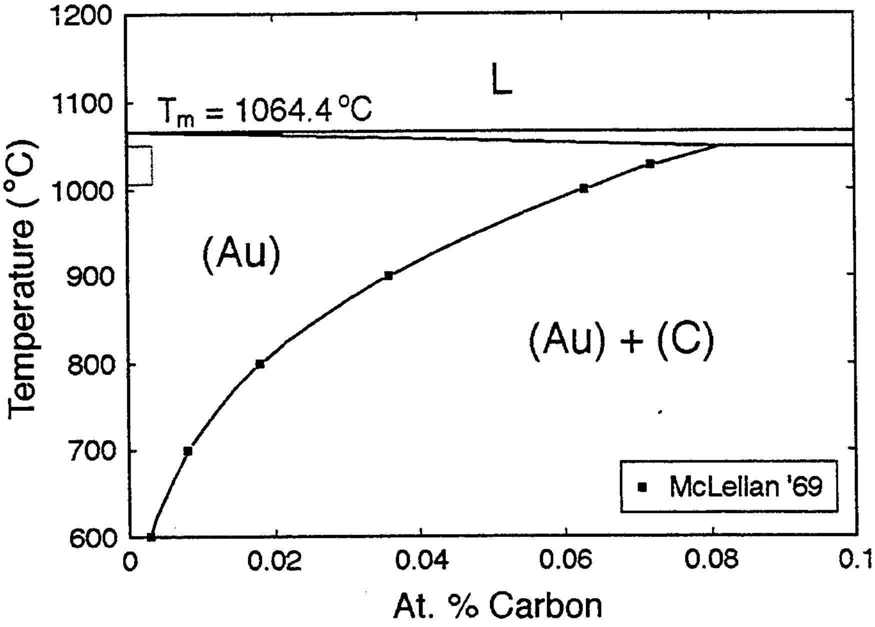
1200
1100
1000
900
800
700
600
0
0.02
0.04
0.06
0.08
0.1
Temperature (°C)
At. % Carbon
L
T_m = 1064.4 °C
(Au)
(Au) + (C)
■ McLellan '69

Fig. 2

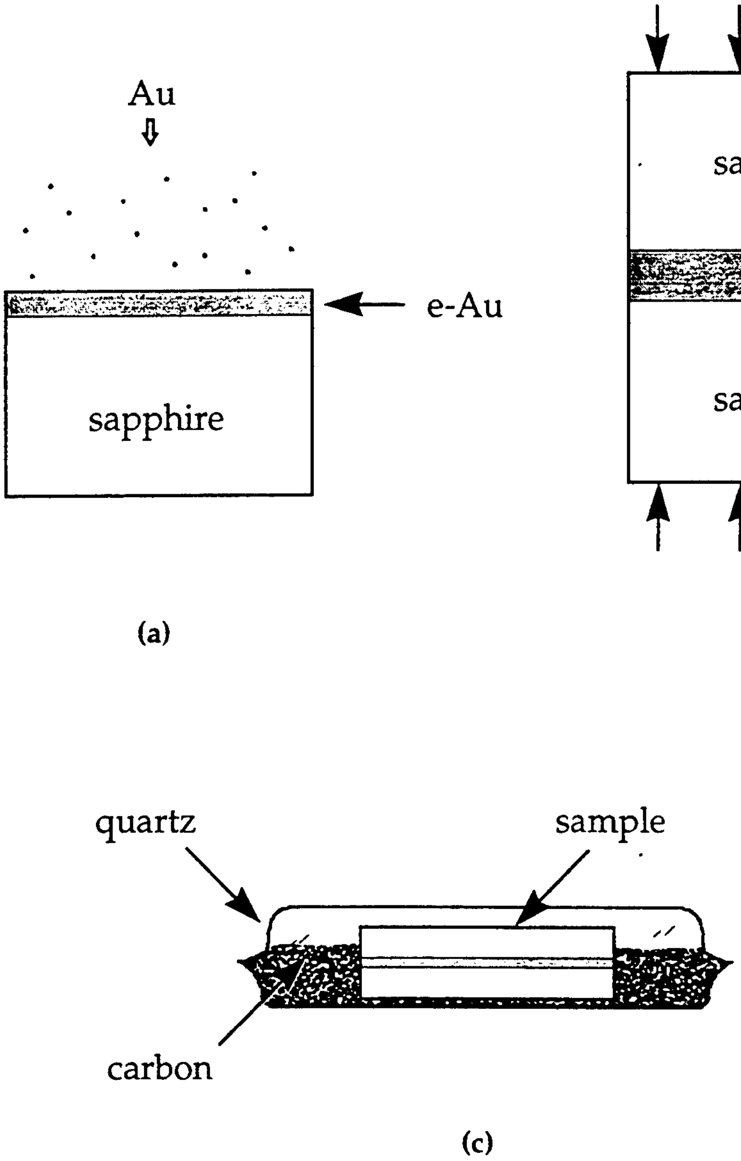
Au
e-Au
sapphire
(a)
sapphire
gold
sapphire
(b)
quartz
sample
carbon
(c)

Fig. 3

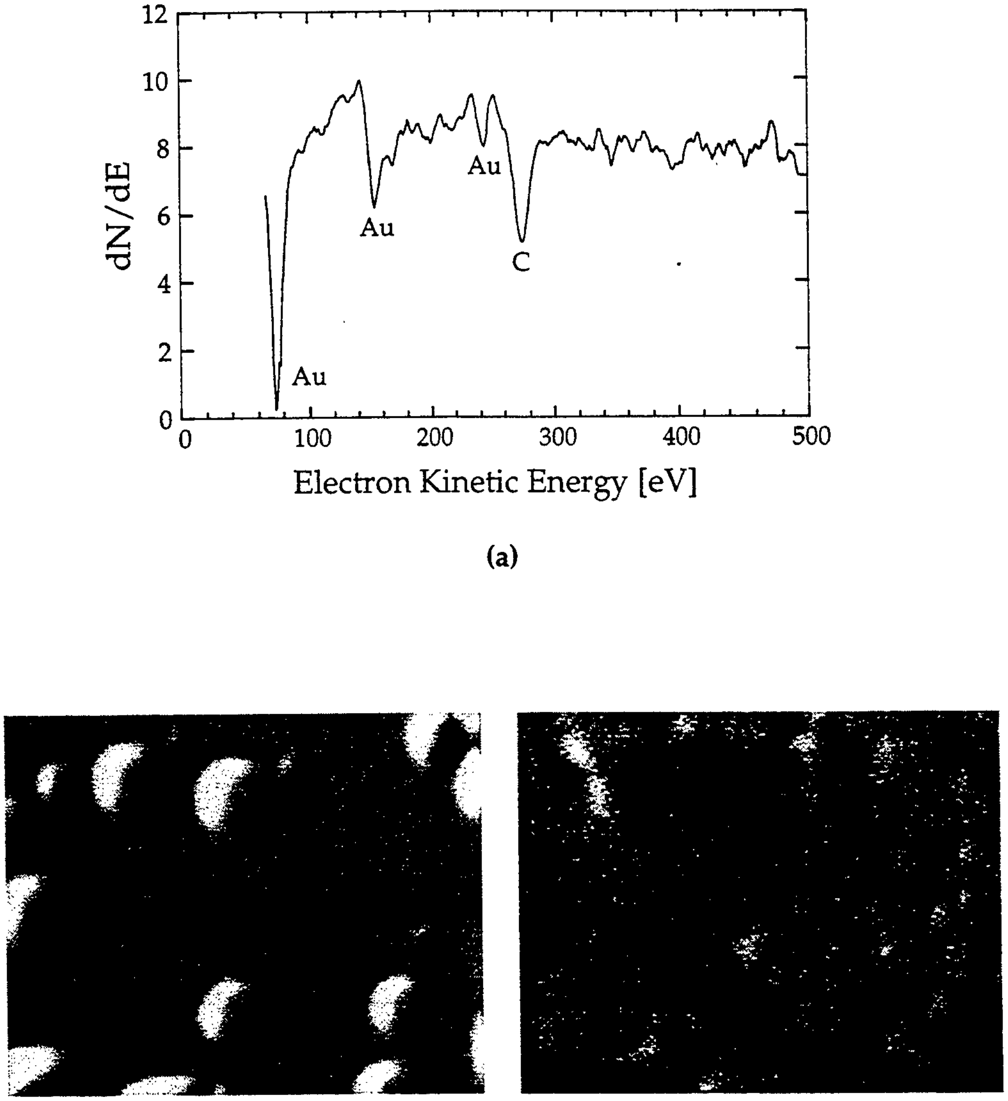
12
10
8
6
4
2
0
dN/dE
0
100
200
300
400
500
Electron Kinetic Energy [eV]
Au
Au
Au
C

(a)

(b)

(c)

Fig. 4

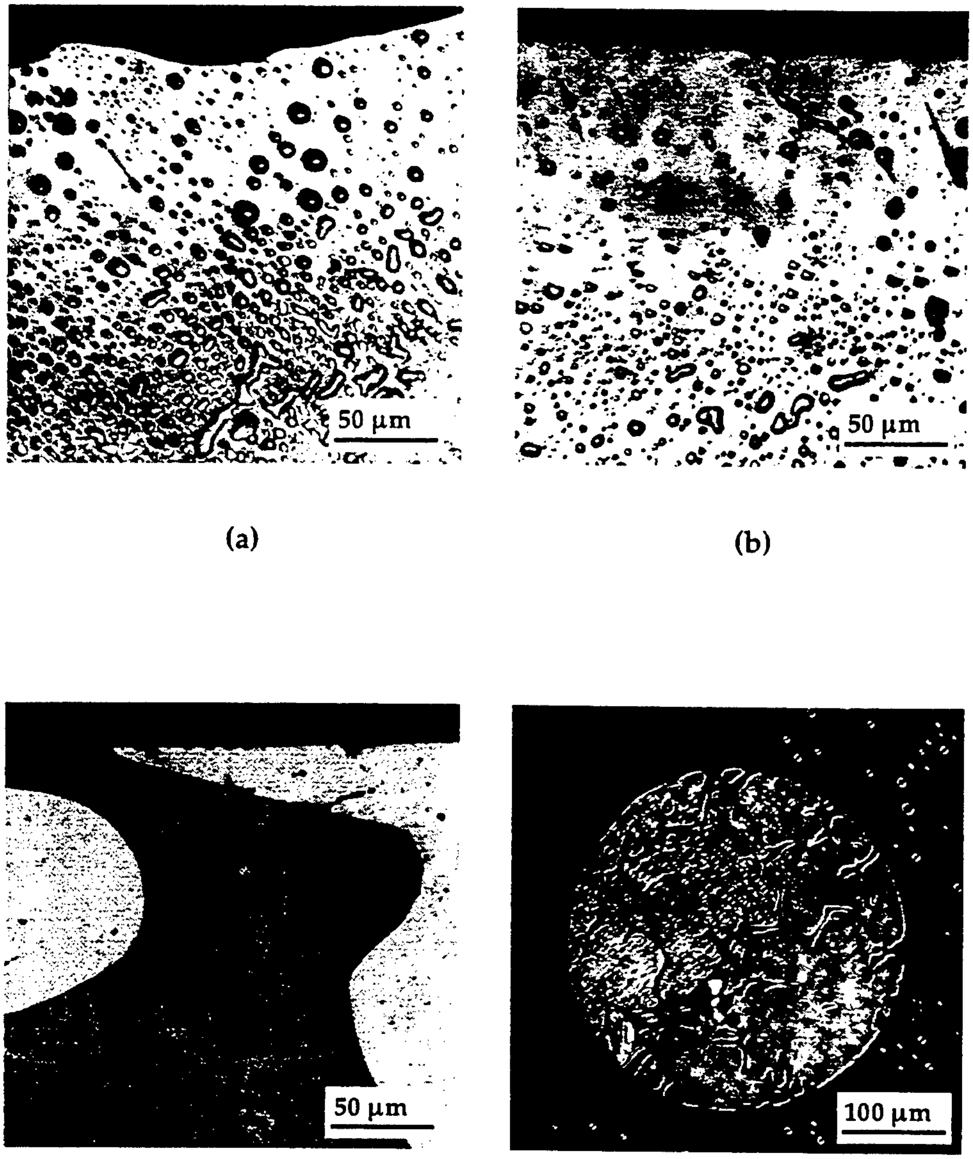
50 µm
50 µm
50 µm
100 µm

(a)

(b)

(c)

(d)

Fig. 5

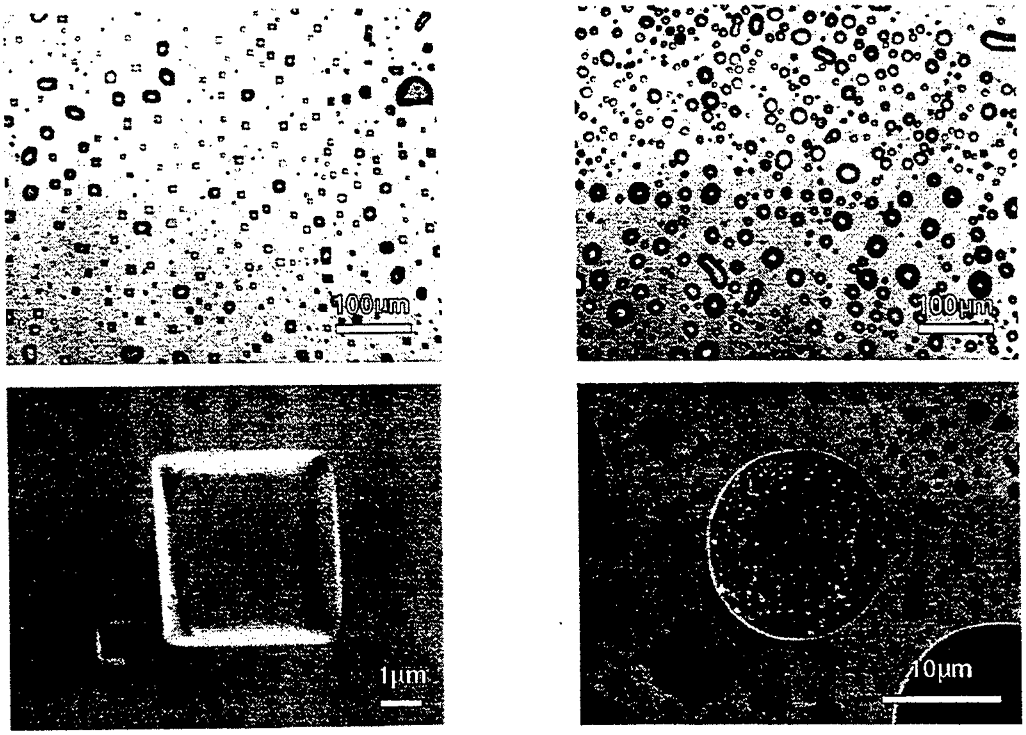
100μm
1μm
100μm
10μm

(a) (b)

Fig. 6

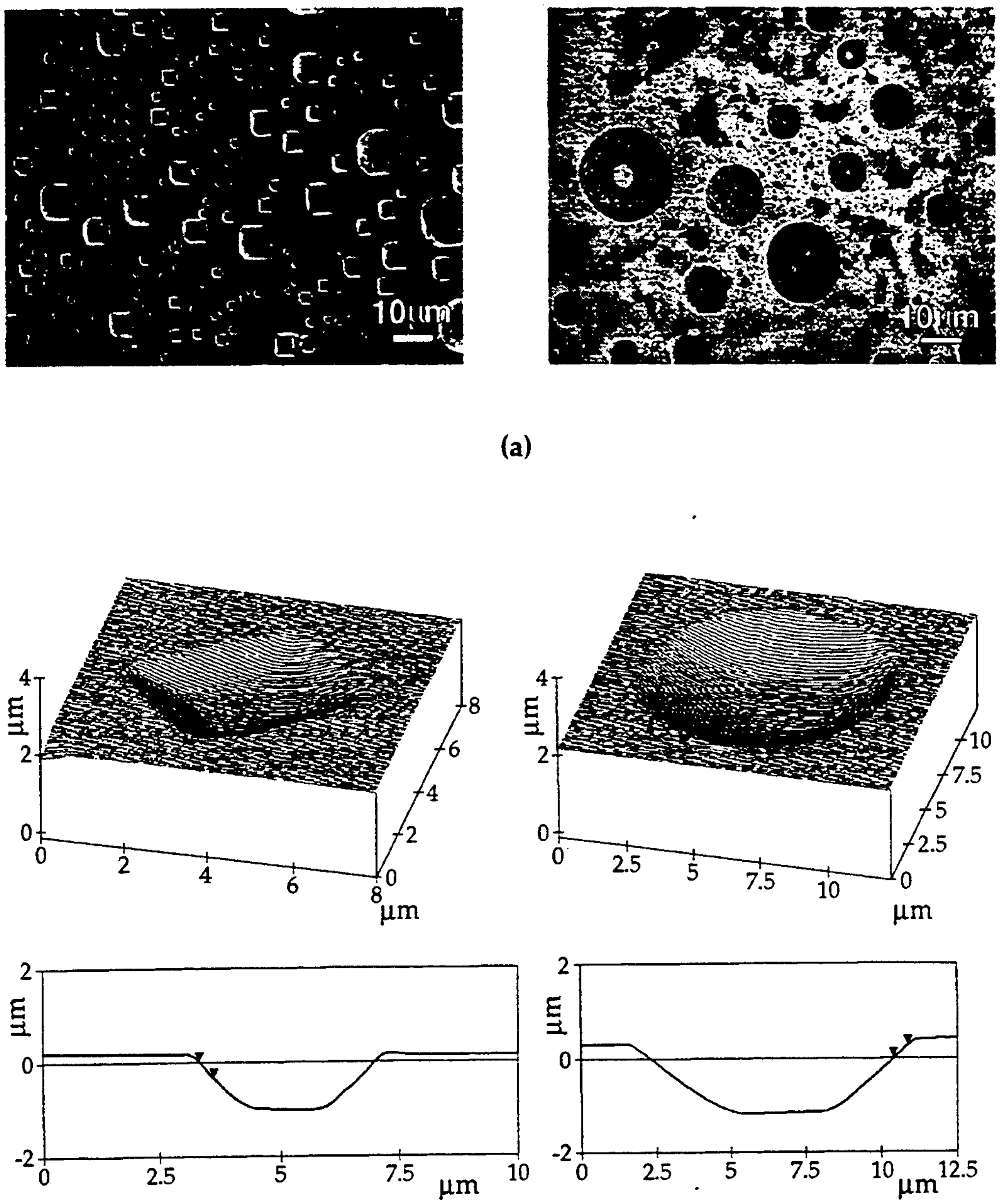
10µm
10µm
4
µm
2
0
0
2
4
6
8
0
2
4
6
8
µm
4
µm
2
0
0
2.5
5
7.5
10
0
2.5
5
7.5
10
µm
2
µm
0
-2
0
2.5
5
7.5
µm
10
2
µm
0
-2
0
2.5
5
7.5
10
µm
12.5

(a)

(b)

Fig. 7

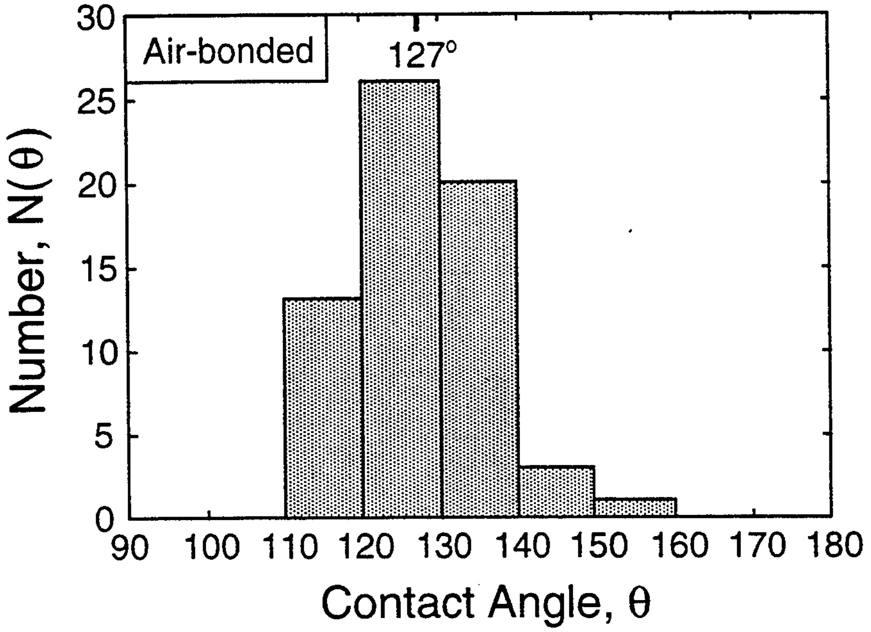
Air-bonded
127°
Number, N(θ)
30
25
20
15
10
5
0
90 100 110 120 130 140 150 160 170 180
Contact Angle, θ

(a)

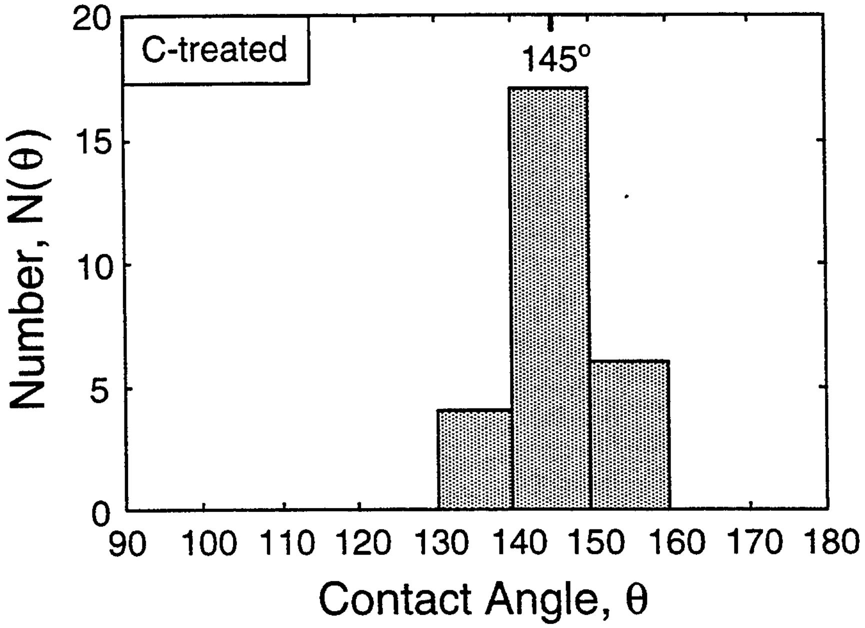
C-treated
145°
Number, N(θ)
20
15
10
5
0
90 100 110 120 130 140 150 160 170 180
Contact Angle, θ

(b)

Fig. 8

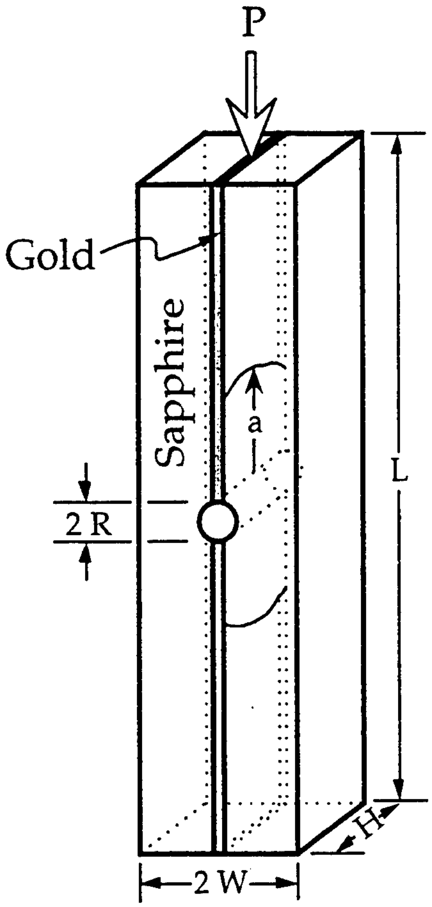
P
Gold
Sapphire
a
2 R
L
H
2 W

Fig. 9

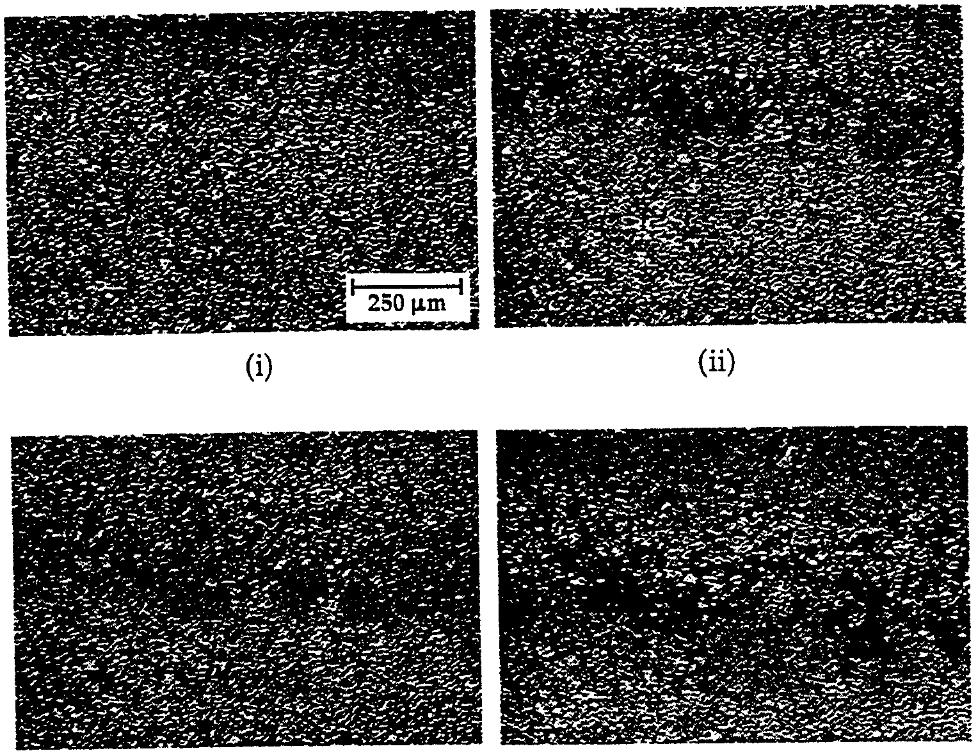

(i) (ii)

(iii) (iv)

(a)

Fig. 10

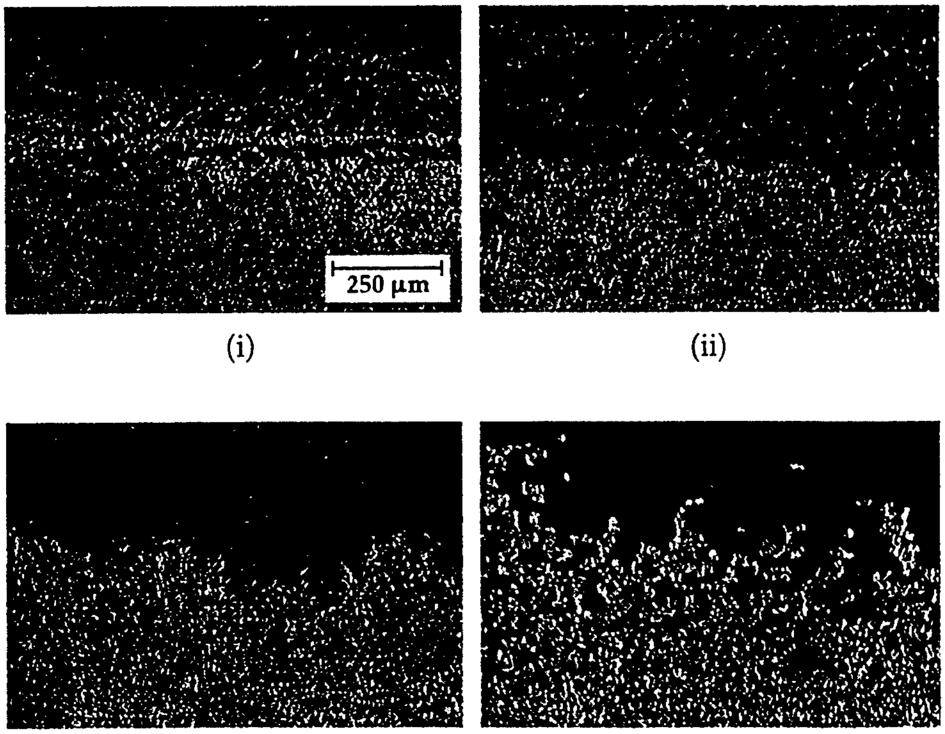

(i) (ii)

(iii) (iv)

(b)

Fig. 10

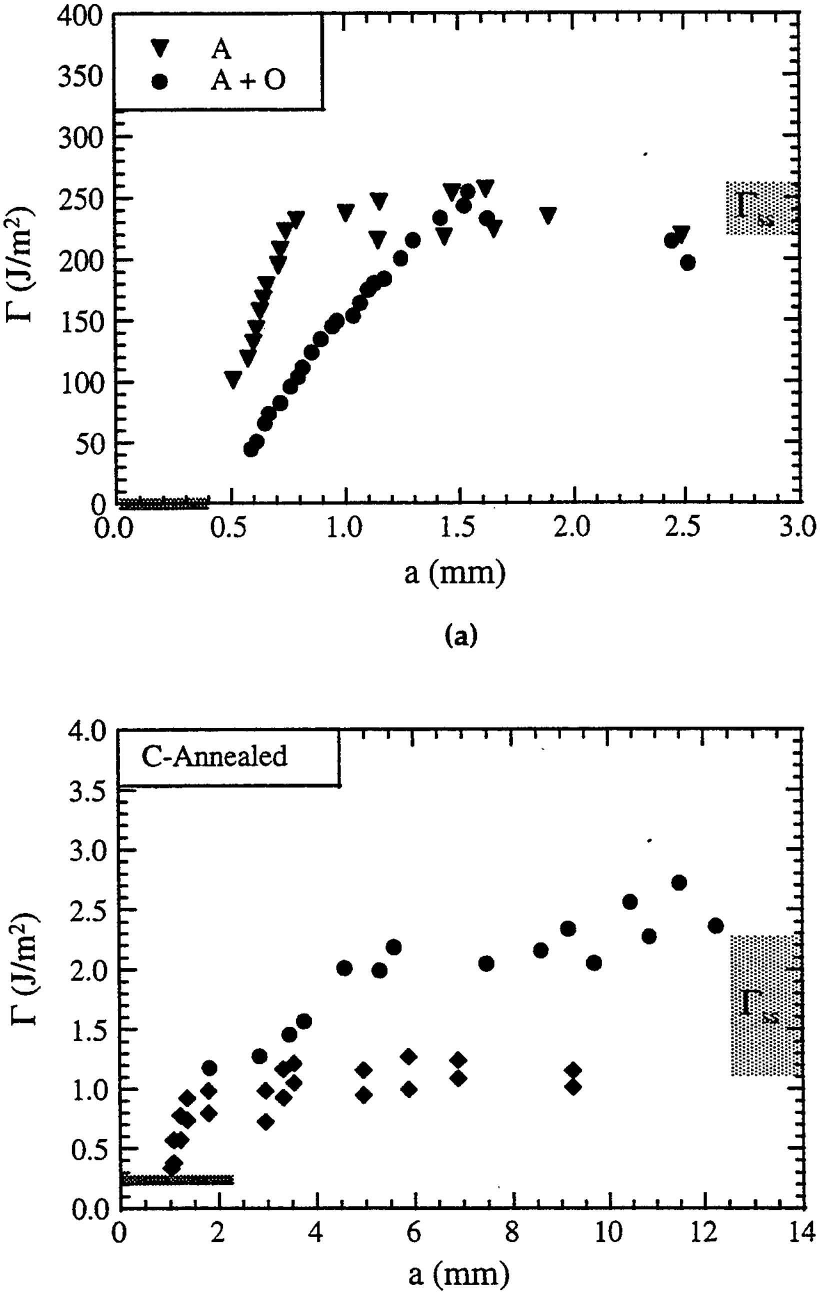
400
350
300
250
200
150
100
50
0
Γ (J/m²)
A
A + O
Γ_{ss}
0.0
0.5
1.0
1.5
2.0
2.5
3.0
a (mm)
4.0
3.5
3.0
2.5
2.0
1.5
1.0
0.5
0.0
Γ (J/m²)
C-Annealed
Γ_{ss}
0
2
4
6
8
10
12
14
a (mm)

(a)

(b)

Fig. 11

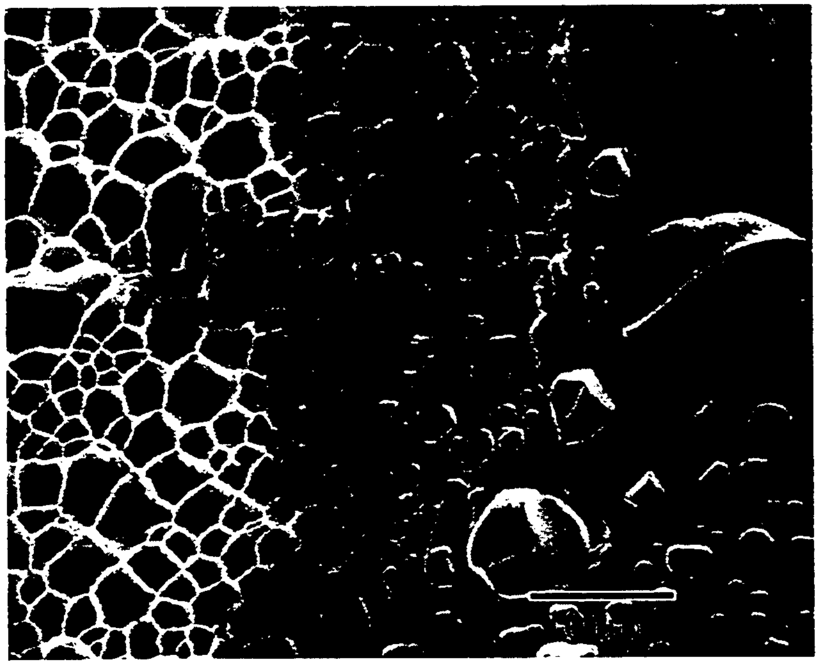

Fig. 12

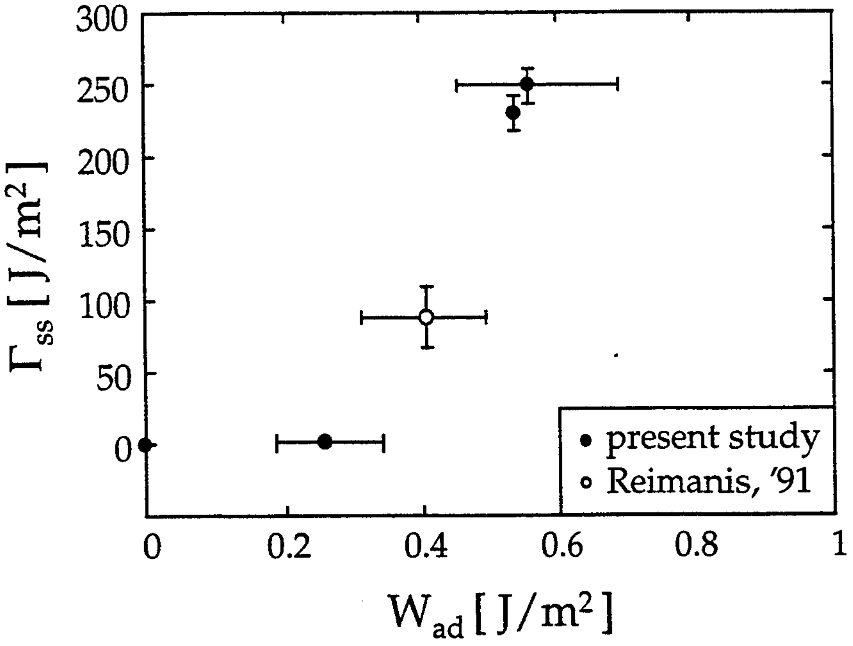

300
250
200
150
100
50
0
Γ_{ss} [J/m^2]
0
0.2
0.4
0.6
0.8
1
W_{ad} [J/m^2]
● present study
○ Reimanis, '91

Fig. 13

Philosophical Magazine A, 1997, Vol. 76, No. 4, 715–728

Estimating the metal–ceramic van der Waals adhesion energy

By Don M. Lipkin†, Jacob N. Israelachvili and David R. Clarke

Materials Department, University of California, Santa Barbara, CA 93106-5050,
USA

[*Received 24 August 1996 and accepted in revised form 14 January 1997*]

Abstract

We invoke the Lifshitz theory of van der Waals forces to derive a simple, analytical expression for the adhesion across a planar metal–ceramic interface. The van der Waals energy is conveniently expressed as a function of readily accessible bulk properties of the respective materials. Application to several non-reactive metal–sapphire systems shows the predicted van der Waals energy to provide a good lower-bound estimate of the measured adhesion energy. Apart from platinum and palladium, where strong metal–aluminium interactions have been predicted, adhesion energies in noble-metal systems are well accounted for by van der Waals interactions alone. Not surprisingly, adhesion in the more chemically active metals exceeds the van der Waals energy.

§ 1. Introduction

Previous investigations have shown that the adhesion between metals and ceramics is sensitive to subtle variations in interfacial chemistry (Hirth and Rice 1980, Seah 1980, Anderson, Wang and Rice 1987b, Rice and Wang 1989, Rice, Suo and Wang 1990, Hong, Smith and Srolovitz 1993a, b, 1995, Gangopadhyay and Wynblatt 1994, 1995, Smith, Hong and Srolovitz 1994, Lipkin 1996, Lipkin, Evans and Clarke 1997b). Furthermore, even the slightest variations in adhesion are associated with dramatic changes in the microscopic mechanical properties (Pepper 1976, Gibbesch and Elssner 1992, Korn, Elssner, Fischmeiter and Rühle 1992, Elssner, Korn and Rühle 1994, Koski, Hölsa, Ernoult and Rouzand 1996, Lipkin 1996, Lipkin, Beltz and Clarke 1997a, Lipkin, Clarke and Beltz 1996). In spite of its critical importance, however, the adhesive bond between metals and ceramics has proved difficult to quantify by either simulation or experimental measurement.

Modern electron bonding theories of metal–ceramic adhesion provide a far more rigorous description of the adhesive bond than was previously available, allowing improved estimates of the energetics of interface formation in an ever-growing range of systems. Among atomistic simulation methods that have recently been applied to metal–ceramic interfaces, a number employ *ab initio* calculations based on self-consistent density functional theory (Ohuchi, French and Kasowski 1987, Kasowski, Ohuchi and French 1988, Blöchl, Das, Fischmeister and Schönberger 1990, Freeman, Li and Fu 1990, Schönberger, Andersen and Methfessel 1992, Li, Wu,

---

†Present address: General Electric Company, Corporate Research & Development, One Research Circle, Niskayuna, NY 12309, USA.

0141–8610/97 $12·00 © 1997 Taylor & Francis Ltd.

Freeman and Fu 1993, Hong, Smith and Srolovitz 1994, 1995, Rao, Wu and Freeman 1995) and Hartree–Fock theory (Heifets, Orlando, Dovesi, Pisani and Kotomin 1994). In addition, various semi-empirical methods have been employed, including the Harris functional approximation (Smith *et al.* 1994, Hong *et al.* 1995), the tight-binding method (Yamamoto, Kohyama, Ebata and Kinoshita 1989), molecular orbital theory (Johnson and Pepper 1982, Anderson *et al.* 1987a), and models incorporating image charge interactions (Duffy, Harding and Stoneham 1992, Stoneham and Tasker 1985, 1987a, b, 1988, Finnis, Stoneham and Tasker 1990, Finnis 1992). Unfortunately, these recent advances in the modelling of interfacial energetics have not resolved all of the issues, and fundamental disagreements over the merits and event the credibility of particular modelling approaches persist (see Finnis, Needs and Schönberger (1995), for instance). Meanwhile, all-electron calculations for complex materials systems, such as gold or platinium bonded to sapphire, remain prohibitively difficult.

The need to quantify interfacial adhesion, combined with the complexity of atomistic calculations, has led to some reliance in the materials community on simple analytical adhesion models. These have shown qualitative agreement with a number of observed trends, but claims of quantitative reliability have generally met with severe criticism. In the following sections, we review these models and offer an improved methodology for calculating the van der Waals contribution to metal–ceramic adhesion.

§ 2. REVIEW OF ANALYTICAL ADHESION MODELS

A single material parameter—the work of adhesion, W_{ad}—characterizes the degree to which a given metal–ceramic system bonds. The equilibrium work of adhesion of a metal–ceramic bond is formally defined as the reversible work associated with creating the respective free surfaces from a bonded interface:

$$W_{ad} = \gamma_{mv} + \gamma_{cv} - \gamma_{mc}, \tag{1}$$

where γ_{mv} and γ_{cv} are the surface energies of the metal and ceramic, respectively, and γ_{mc} is the energy of the bimaterial interface. This definition reveals that maximum adhesion obtains for systems where interfacial energy is minimized while the respective surface energies are maximized.

Semi-empirical descriptions of metal–ceramic bonding date back to the seminal work of Pask and Fulrath (1962) on glass–metal bonding. Based on sessile drop experiments with molten metals, they interpreted good wetting as an indication of strong chemical bonding. This dependence was justified on the basis of the Young–Dupré equation (which can be derived from simple virtual work arguments):

$$W_{ad} = \gamma_{mv}(1 + \cos\theta), \tag{2}$$

where θ is the equilibrium contact angle between the sessile drop and the ceramic substrate (fig. 1). From eqn. (2), we see that small contact angles (i.e., good wetting) correspond to high values of W_{ad} (i.e., good adhesion). Mechanistically, Pask argued, good adhesion must be an indication of the lowering of the interfacial energy between the glass and metal, such as occurs when an ionic or covalent chemical bond is formed across the interface by interchange or sharing of electrons, respectively. But what determines how strongly a given system will bond?

Fig. 1

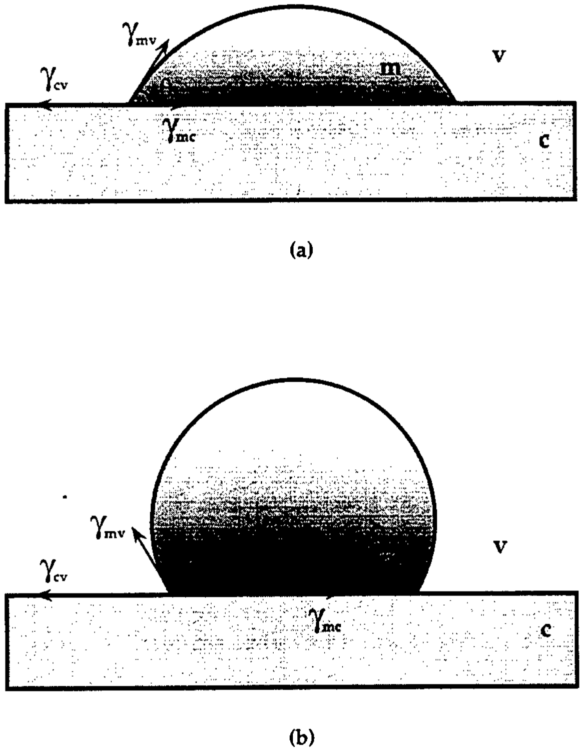

Liquid–metal sessile drop on a rigid ceramic substrate, showing (*a*) wetting and (*b*) non-wetting configurations.

There have been several attempts to develop a predictive model for the interfacial adhesion of metal–oxide systems. Humenik and Kingery (1954) noted the positive correlation between the observed wetting of oxides by molten metals (characterized by W_{ad}) and the corresponding oxygen affinity of the metals (characterized by the free energy of formation of the oxide of the liquid metal, ΔG_{mO}). To justify this observation, McDonald and Eberhart (1965) proposed a semi-empirical bonding model for the adhesion of metals to aluminium oxide. The model assumes that the metal atoms directly adjacent to the interface adsorb onto the terminating oxygen-ion plane of the alumina substrate. Identifying two unique adsorption sites for the metal atom on the oxygen-terminated basal plane of sapphire, they assumed that the adhesion energy can be fully partitioned. Thus, on one type of site, the metal atoms are bound entirely by van der Waals forces and on the other, the atoms are chemically bonded to the oxygen ions. The work of adhesion is then calculated by pairwise summation of the respective bond energies across the interface:

$$W_{\mathrm{ad}} = -(n_{\mathrm{chem}}\Delta G_{\mathrm{chem}} + n_{\mathrm{vdW}}/\Delta G_{\mathrm{vdW}}), \tag{3}$$

where n_i is the number of ith bond sites and ΔG_i the free energy of adsoprtion of the metal atom on the ith site ($i = \{\mathrm{chem, vdW}\}$). McDonald and Eberhart proposed that, to a good approximation, $\Delta G_{\mathrm{chem}} = \frac{1}{2}\Delta G_{\mathrm{mO}}$. Equation (3) therefore predicts a linear correlation between the work of adhesion and the free energy of oxide formation of the metal. For a small number of liquid metals on polycrystalline alumina, the dependence of W_{ad} on ΔG_{mO} was shown to qualitatively agree with the model (fig. 2 (*a*)).

In the ensuing years, refinements to the McDonald–Eberhart model have been suggested. To account for differences in adhesion between a given metal and different oxide substrates, Naidich (1981) suggested that the free energy of bulk metal oxide formation, ΔG_{mO}, should be weighted relative to the free energy of formation of the substrate oxide, ΔG_{MO}. Thus, the strongest adhesion obtains in systems with a high free energy of formation for the metal oxide and a low free energy of formation for the substrate oxide. Conversely, systems with very stable oxides are poorly wetted by metals with a low affinity for oxygen. In a compilation of contact angles of over 50 liquid metal–oxide systems, Naidich demonstrates an undeniable tendency for strongly oxidizing metals to wet the respective oxide substrates (fig. 2 (*b*)).

Chatain, Rivollet and Eustathopoulos (1986, 1987), Chatain, Coudurier and Eustathopolos (1988) and Eustathopoulos, Chatain and Coudurier (1991) noted the gross lack of correlation between the work of adhesion and free energy of oxide formation for a somewhat broader range of metals on alumina than that considered by McDonald and Eberhart (fig. 2 (*c*)). Believing the use of bulk energies of formation to be inadequate, Chatain proposed describing chemical interactions across the interface between both metal and oxygen (m–O) and metal and substrate-metal (m–M) using the enthalpies of mixing of the respective oxide elements in the metal. Neglecting van der Waals energies entirely, the work of adhesion was expressed as:

$$W_{ad} = -c(\mathcal{N} V_m^2)^{-1/3}(\Delta H^{\infty}_{O(m)} + \tfrac{1}{n}\Delta H^{\infty}_{M(m)}), \tag{4}$$

where c is a dimensionless fitting parameter (constant for a given oxide substrate), $\mathcal{N}$ is Avogadro's number, V_m is the molar volume of the metal, n is the stoichiometric ratio of oxygen to oxide metal ($M + \frac{n}{2}O_2 \rightarrow MO_n$), and $\Delta H^{\infty}_{i(m)}$ is the enthalpy of mixing at infinite dilution of atom i in the metal, where $i = \{O, M\}$. The high correlation between eqn. (4) and experimentally determined adhesion data for a number of metals on alumina (using $c = 0{\cdot}22$) is shown in fig. 2 (*d*).

One shortcoming of the above approaches to estimating adhesion is the failure to explain why the adhesion observed in some oxide–noble metal systems, notably Al_2O_3–Pt, is far in excess of the estimated van der Waals bond energy. In two distinct studies, both Klomp (1985, 1987) and Anderson *et al.* (1987a) have suggested that this discrepancy may be due to the neglect of metal–metal, or m–M, interactions. (It would be interesting to see Chatain's predictions for platinum–alumina adhesion, since some accounting for metal–metal interaction is inherent to the model. However, the calculation for platinum–sapphire is not performed in the cited papers.)

In fact, it is unlikely that W_{ad} is amenable to simple partitioning into the van der Waals and chemical contributions. Just as a given bond may at once have ionic and covalent character, it is erroneous to pre-assign exclusively chemical or van der Waals character to individual bonding sites. As a simple illustration, consider the prediction of the McDonald–Eberhart model in the limit of a non-oxidizing metal (for example, Pt, Au, Ag). Although the metal atom has little capacity to form chemical bonds with the oxyen, van der Waals forces should make a decisive contribution to the bonding energy. By assigning only two thirds of the sites to van der

Fig. 2

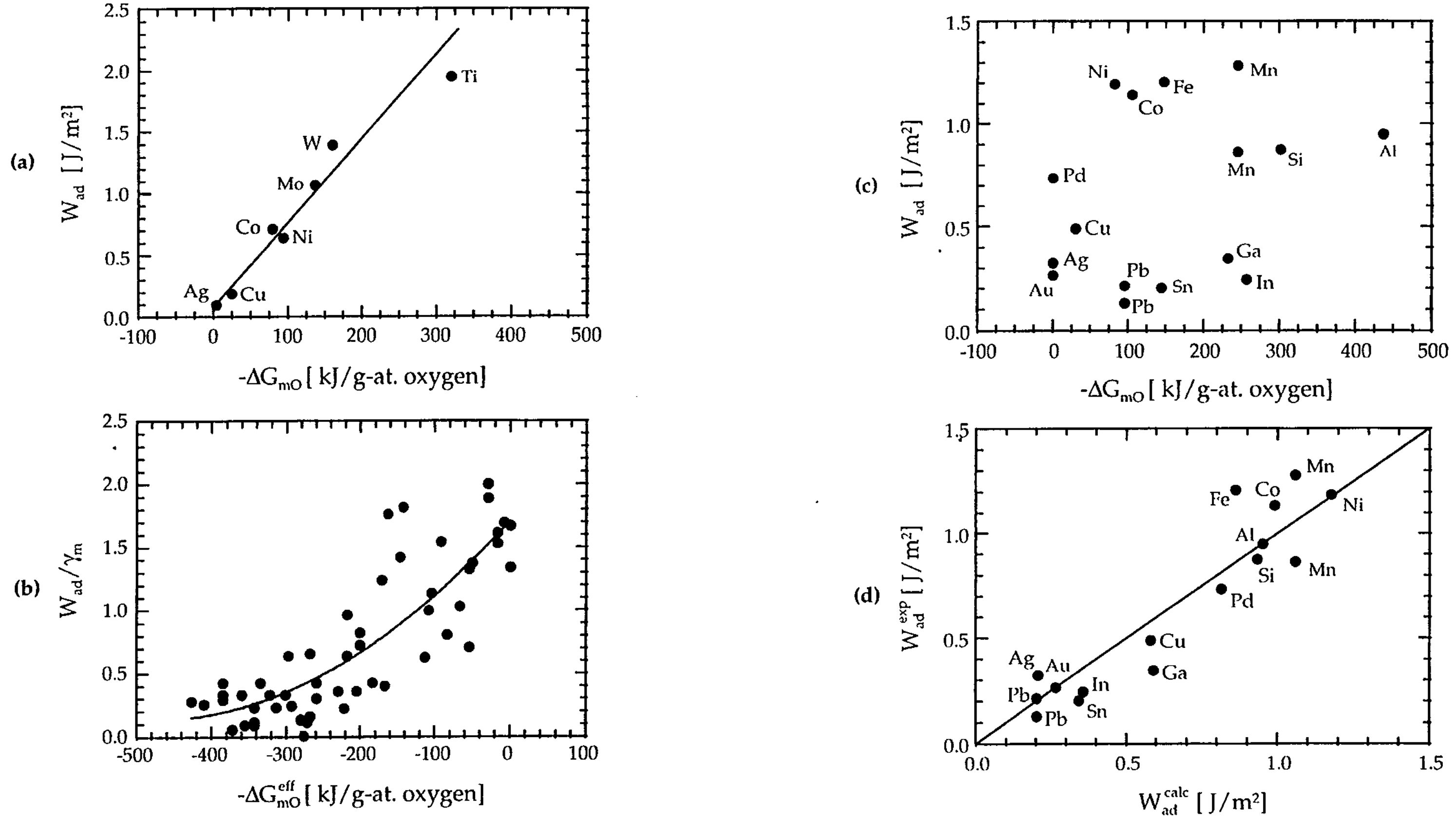

Correlation of various adhesion models to experimental data. (*a*) Work of adhesion of several metals on alumina plotted against the free energy of formation of the respective metal oxides, after McDonald and Eberhart (1965). (*b*) Relation between the normalized work of adhesion and the effective free energy of oxide formation, defined as $\Delta G^{eff}_{mO} \equiv \Delta G_{mO} - \Delta G_{MO}$, for more than 50 molten metals on various oxide substrates, after Naidich (1981). (*c*) Apparent discrepancy between work of adhesion and the free energy of oxide formation for a somewhat broader range of metals on alumina than presented in (*a*). (*d*) Comparison of experimentally determined works of adhesion to those calculated using a revised adhesion model based on mixing enthalpies (eqn. (4)) for the same set of metals on alumina as in (*c*). ((*c*) and (*d*) after Chatain *et al.* (1986, 1987, 1988) and Eustathopoulos *et al.* (1991).)

Waals bonding and allowing one third of the bonds to contribute nothing to adhesion, the McDonald–Eberhart model leads to an *a priori* underestimate of the net adhesion energy in excess of 30%!

The above discussion makes no claim of resolving the complex issues raised but is meant to emphasize the scope of uncertainty associated with estimating adhesion, especially the van der Waals contribution to this quantity. Of the two models described above, one neglcts the van der Waals contribution altogether while the other grossly underestimates the van der Waals contribution to adhesion. Our present aim is to propose an improved methodology for estimating the van der Waals energy and subsequently employ the model to assess the relative contribution of the van der Waals energy to the total work of adhesion for a number of metal–ceramic systems.

§ 3. CALCULATING METAL-CERAMIC W_{vdW}

Both the McDonald–Eberhart and Naidich adhesion models attempt to calcualte the contribution of van der Waals energy to the work of adhesion. However, these estimates are based on the pair potential (fig. 3 (*a*)) having the form:

$$w(r) = -C/r^6, \tag{5}$$

where $C = \frac{3}{2}\alpha_1\alpha_2 I_1 I_2/(I_1 + I_2)$ for London dispersion interactions (α_i and I_i are the electronic polarizability and ionization potential of the ith species, respectively). Although more accurate accounting methods have been proposed (for example, by Benjamin and Weaver (1959)), the total adhesive energy is most typically calcualted by summing the pairwise interactions across the metal–ceramic interace, assuming that the ceramic surface can be adequately represented as a terminating plane of oxide atoms. This approach entirely neglects all second- and higher-nearest-neighbour interactions, including those between the metal and oxide cations (m–M interactions). Compounding this error is the use of free-particle polarizability and ionization potentials (ionic for oxygen and atomic for metal) instead of values appropriate for the respective bulk phases. This simplification neglects such bulk phenomena as electron–hole excitations in the metal and charge transfer excitations in the oxide, to name a few. Yet another error arises from the estimates of the equilibrium interparticle separation r. As the radius is raised to the sixth power in the energy calculation, small errors in this quantity lead to gross errors in the estimated adhesion.

Barrera and Duke (1976) have formulated a more rigorous adhesion model based on continuum electrostatic theory, in which many of the above mentioned discrepancies are avoided. However, by virtue of its complexity, their model has proven difficult to implement (see, for example, Stoneham (1982–1983)). To provide a reasonable estimate of the van der Waals adhesion while maintaining some degree of simplicity, we turn to an alternate method for calculating the van der Waals energy. The analysis is based on the Lifshitz (1956) theory of van der Waals forces, employing the frequency-dependent dielectric function to calculate the Hamaker constant and hence the adhesion energy itself.

In the Lifshitz continuum approximation, if solids 1 and 2 interact through medium 3, then the Hamaker constant A can be expressed as (Israelachvili 1992)

Fig. 3

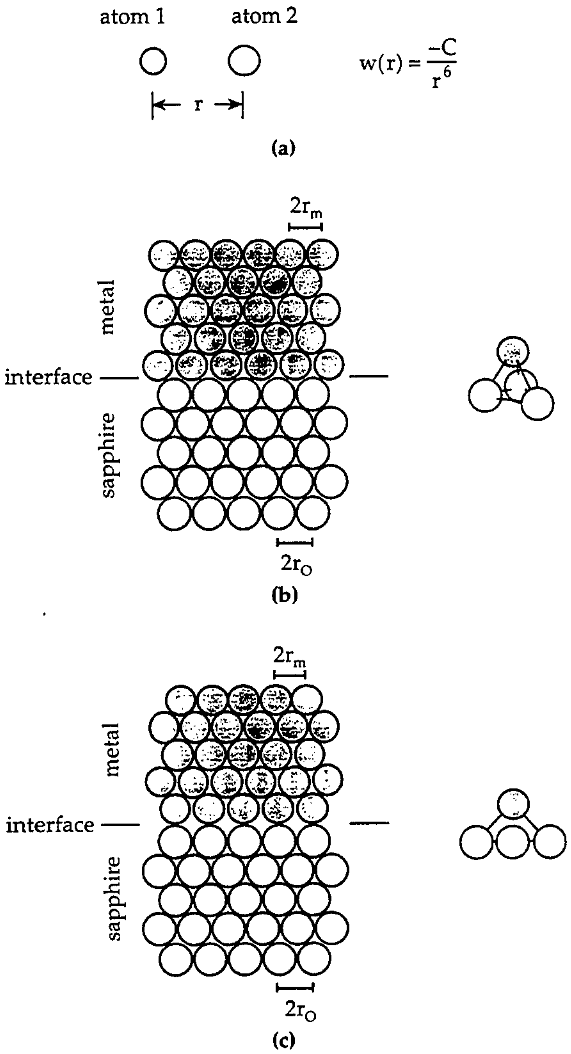

(*a*) Van der Waals pair potential, where r is the interatomic separation and C is related to the Hamaker constant through $A = \pi^2 C\rho_1\rho_2$. (*b*) Schematic of metal–ceramic interplanar interaction. The ceramic—in this case Al_2O_3—is assumed to terminate in a close-packed oxygen plane (the cation lattice is not shown). The close-packed metal plane is elastically strained at the interface to epitaxially match the oxygen lattice. The metal atoms are located on the oxygen interstitital sites, effectively extending the oxygen site lattice. This configuration is expected to give an upper bound to the van der Waals energy, W^+_{vdW}. (*c*) Interplanar interaction where the metal atoms are located directly above the oxygen ions. This configuration is expected to give a lower bound to the van der Waals energy, W^-_{vdW}.

$$A \approx \tfrac{3}{4}kT\left(\frac{\varepsilon_1 - \varepsilon_3}{\varepsilon_1 + \varepsilon_3}\right)\left(\frac{\varepsilon_2 - \varepsilon_3}{\varepsilon_2 + \varepsilon_3}\right) + \frac{3}{4}\frac{h}{\pi}\int_{\nu_1}^{\infty}\left(\frac{\varepsilon_1(i\nu) - \varepsilon_3(i\nu)}{\varepsilon_1(i\nu) + \varepsilon_3(i\nu)}\right)\left(\frac{\varepsilon_2(i\nu) - \varepsilon_3(i\nu)}{\varepsilon_2(i\nu) + \varepsilon_3(i\nu)}\right) \mathrm{d}\nu, \quad (6)$$

where $\nu_1 = 2\pi kT/h$, while ε_j and $\varepsilon_j(i\nu)$ are the static ($\nu = 0$) and frequency-dependent relative dielectric permittivities, respectively, for medium j. The first term in eqn. (6) gives the zero-frequency contribution to the van der Waals energy and consists of both the Debye (dipole–induced dipole) and Keesom (angle-averaged dipole–dipole) interactions. The second, frequency-dependent term accounts for London (induced dipole–induced dipole) interactions (Pauling 1970, Adamson 1982). For the case of metal–ceramic adhesion across vacuum (1≡m, 2≡c, 3≡v), and noting that $\varepsilon_{\mathrm{v}} = \varepsilon_{\mathrm{v}}(i\nu) \equiv 1$ and $\varepsilon_{\mathrm{m}} \to \infty$, eqn. (6) reduces to:

$$A \approx \tfrac{3}{4}kT\left(\frac{\varepsilon_{\mathrm{c}}-1}{\varepsilon_{\mathrm{c}}+1}\right) + \tfrac{3}{4}\frac{h}{\pi}\int_{\nu_1}^{\infty}\left(\frac{\varepsilon_{\mathrm{m}}(i\nu)-1}{\varepsilon_{\mathrm{m}}(i\nu)+1}\right)\left(\frac{\varepsilon_{\mathrm{c}}(i\nu)-1}{\varepsilon_{\mathrm{c}}(i\nu)+1}\right)\mathrm{d}\nu. \tag{7}$$

For the ceramic, the frequency dependence of the permittivity can be written as (Ninham and Parsegian 1970, Hough and White 1980, Israelachvili 1992, Bergström, Meurk, Arwin and Rowcliffe 1996):

$$\varepsilon_{\mathrm{c}}(i\nu) = 1 + \frac{\varepsilon_{\mathrm{c}} - n_{\mathrm{c}}^2}{1 + \nu/\nu_{\mathrm{rot.c}}} + \frac{n_{\mathrm{c}}^2 - 1}{1 + (\nu/\nu_{\mathrm{e.c}})^2}, \tag{8}$$

where $\nu_{\mathrm{rot.c}}$ is the molecular rotational relaxation frequency (infrared), $\nu_{\mathrm{e.c}}$ is the main electronic absorption frequency (ultraviolet or visible), and n_{c} is the refractive index of the medium in the visible range, well above $\nu_{\mathrm{e.c}}$. Because typically $\nu_{\mathrm{rot.c}} \ll \nu_1 \ll \nu_{\mathrm{e.c}}$, we may neglect the contribution of molecular rotation to the dispersion energy, thereby reducing eqn. (8) to a function of only one relaxation frequency:

$$\varepsilon_{\mathrm{c}}(i\nu) \approx 1 + \frac{n_{\mathrm{c}}^2 - 1}{1 + (\nu/\nu_{\mathrm{e.c}})^2}. \tag{9}$$

For metals, the static dielectric constant is infinite, and the frequency-dependent dielectric permittivity can be derived using the jellium approximation (Egerton 1986, Israelachvili 1992):

$$\varepsilon_{\mathrm{m}}(i\nu) = 1 + \frac{\nu_{\mathrm{e.m}}^2}{\nu^2 + \nu/\tau} \approx 1 + \left(\frac{\nu_{\mathrm{e.m}}}{\nu}\right)^2 \tag{10}$$

where $\nu_{\mathrm{e.m}}$ is the plasmon frequency of the free-electron gas and τ is the relaxation time characterizing the lattice damping of the plasma oscillations. To a first-order approximation, the lattice damping can be ignored, such that $\tau \to \infty$.

Substituting eqns. (9) and (10) into (7) and integrating over the frequency, we find that

$$\begin{aligned} A \approx \tfrac{3}{4}kT\left(\frac{\varepsilon_{\mathrm{c}}-1}{\varepsilon_{\mathrm{c}}+1}\right) &+ \tfrac{3}{4}\frac{h}{\pi}\frac{c_1\nu_{\mathrm{e.m}}/\nu_{\mathrm{e.c}}}{\sqrt{2}c_2[c_2^2 - (\nu_{\mathrm{e.m}}/\nu_{\mathrm{e.c}})^2]} \\ &\left\{\nu_{\mathrm{e.m}}\left[\tan^{-1}\left(\frac{\sqrt{2}}{c_2}\frac{\nu_1}{\nu_{\mathrm{e.c}}}\right) - \frac{\pi}{2}\right] - c_2\nu_{\mathrm{e.c}}\left[\tan^{-1}\left(\sqrt{2}\frac{\nu_1}{\nu_{\mathrm{e.m}}}\right) - \frac{\pi}{2}\right]\right\} \end{aligned} \tag{11}$$

where, for convenience, we have defined $c_1 \equiv n_{\mathrm{c}}^2 - 1$ and $\mathrm{c}_2 \equiv (n_{\mathrm{c}}^2 + 1)^{1/2}$.

We can simplify eqn. (11) by noting that the entropic zero-frequency term can never exceed $\frac{3}{4}kT$ (for example, $\sim 3 \times 10^{-21}$ J at 300 K). As we shall see shortly, for metal–ceramic adhesion, this term is approximately two orders of magnitude smaller than the finite-frequency dispersion energy term and can therefore be neglected. Furthermore, because $\nu_1 \ll \nu_{e,c}$ and $\nu_1 \ll \nu_{e,m}$, the arctangent terms are negligibly small compared to $\pi/2$. Simplifying and rearranging, we arrive at a simple new expression for the Hamaker constant of a metal–ceramic interface:

$$A \approx \frac{3h}{8} \frac{c_1 \nu_{e,m} \nu_{e,c}}{\sqrt{2} c_2 (c_2 \nu_{e,c} + \nu_{e,m})}, \tag{12}$$

where c_1 and c_2 are functions of the refractive index of the ceramic, as defined above.

Having derived an expression for the Hamaker constant of a planar metal–ceramic bond, we are now in a position to estimate the non-chemical contribution to the total work of adhesion. We restrict our analysis to the specific case of a (111) fcc metal on oxygen-terminated (0001) sapphire. We elastically strain the close-packed metal lattice to bring it into site coincidence with the close-packed oxygen lattice of basal-plane sapphire. (For the present estimate, we ignore the elastic strain energy introduced by this operation.) For the initial calculation, we assume that the metal atoms sit in the interstitial sites of the anion lattice (i.e., two cation sites and one vacancy site). As illustrated in fig. 3 (*b*), for each metal atom in contact with the ceramic surface, three bonds are created, resulting in a net binding energy of $3w = 3C/(r_O + r_m)^6$, where r_O and r_m are the hard-sphere radii of the oxygen and metal in their respective bulk structures. Each surface oxide atom occupies an area equal to $2\sqrt{3} r_O^2$. Recalling that, by definition, $A = \pi^2 C \rho_O \rho_m$, and noting that $\rho_i = \sqrt{2}/8 r_i^3$ is the bulk atomic density of component *i*, the work of adhesion can be estimated as

$$W_{vdW}^{+} \approx \frac{3C/(r_O + r_m)^6}{2\sqrt{3} r_O^2} \approx \frac{16\sqrt{3} A}{\pi^2 r_O^2} \left[\left(\frac{r_O}{r_m} \right)^{\frac{1}{2}} + \left(\frac{r_m}{r_O} \right)^{\frac{1}{2}} \right]^{-6}. \tag{13}$$

Note that for $0{\cdot}69 < r_O/r_m < 1{\cdot}46$, the term within the square brackets in eqn. (13) does not deviate from 2^{-6} by more than 10%. Because lattice mismatch beyond these bounds would surely render the epitaxial assumption invalid, we can safely simplify eqn. (13) to

$$W_{vdW}^{+} \approx \frac{\sqrt{3} A}{4\pi^2 r_O^2}. \tag{14}$$

Clearly, eqn. (14) represents an upper bound to W_{vdW} due to our idealization of the packing structure at the interface. In fact, lattice mismatch and crystallographic misorientation will reduce the coordination of the interface atoms from the maximum value of 12. By assuming the worst-case scenario of atom-on-atom packing across the interface (fig. 3 (*c*)), wherein the nearest-neighbour coordination is reduced to 10, we can make a lower-bound estimate of W_{vdW}. In this configuration, one nearest-neighbour bond and six second-nearest-neighbour bonds are formed. (The interaction energy due to third- and higher-nearest-neighbour bonds is negligible.) Noting that the second-nearest-neighbour distance is $(5r_{\mathrm{O}}^2 + 2r_{\mathrm{O}}r_{\mathrm{m}} + r_{\mathrm{m}}^2)^{1/2}$, we can write

$$\begin{aligned} W_{\mathrm{vdW}}^{-} &\approx \frac{C/(r_{\mathrm{O}}+r_{\mathrm{m}})^6 + 6C/(5r_{\mathrm{O}}^2 + 2r_{\mathrm{O}}r_{\mathrm{m}} + r_{\mathrm{m}}^2)^3}{2\sqrt{3}r_{\mathrm{O}}^2}, \\ &\approx \frac{16A}{\sqrt{3}\pi^2 r_{\mathrm{O}}^2}\left\{\left[\left(\frac{r_{\mathrm{O}}}{r_{\mathrm{m}}}\right)^{\frac{1}{2}} + \left(\frac{r_{\mathrm{m}}}{r_{\mathrm{O}}}\right)^{\frac{1}{2}}\right]^{-6} + 6\left[5\left(\frac{r_{\mathrm{O}}}{r_{\mathrm{m}}}\right) + \left(\frac{r_{\mathrm{m}}}{r_{\mathrm{O}}}\right) + 2\right]^{-3}\right\}. \end{aligned} \tag{15}$$

As above, we find that the second term can be approximated as $2^{-6} + 6(8)^{-3} = 7/256$, so that eqn. (15) reduces to

$$W_{\mathrm{vdW}}^{-} \approx \frac{7A}{16\sqrt{3}\pi^2 r_{\mathrm{O}}^2}. \tag{16}$$

Note that the magnitude of the lower bound is nearly half that of the upper-bound value, eqn. (14).

Three features of the metal–ceramic adhesion estimate represented by eqns. (14) and (16) should be noted. First, the $1/r^6$ potential of eqn. (5) has been replaced by a weaker, $1/r^2$ dependence, significantly mediating the error associated with approximation of interatomic distances. Second, although the metal radius does not explicitly appear in eqns. (14) and (16), the metal-specific contribution to the work of adhesion enters implicitly through our calculated Hamaker constant. Finally, the present method uses the interplanar spacing across the interface as an *a priori* input. Thus, while van der Waals forces contribute strongly to the adhesion energy, forces such as Pauli repulsion define the hard-sphere radii used to calculate the interaction energy across the interface.

Values of the relevant constants for a number of fcc metals and sapphire are compiled in table 1. For sapphire, $n_{\mathrm{c}} = 1{\cdot}77$ at a wavelength of 500 nm (Malitson 1962). The Hamaker constant is calculated using the exact solution, eqn. (11), but

Table 1. Parameters for sapphire and several fcc metals used for W_{vdW} calculations.

	r (Å)[a]	ν_{e} ($\times 10^{15}$ s^{-1})[b]	A ($\times 10^{-19}$ J)	W_{vdW}^{-} (J m^{-2})	W_{vdW}^{+} (J m^{-2})
Al_2O_3	1·19	3·2	—	—	—
Ag	1·44	6·0	2·84	0·57	0·86
Al	1·43	3·7	2·13	0·43	0·64
Au	1·44	6·2	2·88	0·58	0·87
Cu	1·28	4·6	2·44	0·46	0·75
Ni	1·25	4·7	2·47	0·46	0·76
Pb	1·75	3·4	2·00	0·43	0·55
Pd	1·38	6·2	2·87	0·56	0·87
Pt	1·39	5·9	2·80	0·55	0·85

[a] Hard-sphere radii, calculated directly from room-temperature lattice parameters (Joint Committee on Powder Diffraction Spectra 1992): $r_{\mathrm{O}} = a_{\mathrm{Al_2O_3}}/4$ and $r_{\mathrm{m}} = a_{\mathrm{m}}/2\sqrt{2}$.

[b] Taken from Isaacson (1975) and Glicksman (1971) for metals and from Bergström *et al.* (1996), Hough and White (1980) and Gervais (1991) for sapphire.

never differs by more than 0·5% from the simplified solution, eqn. (12). In all cases, A is within the range $2\text{–}3\times10^{-19}$ J. Using the calculated Hamaker constant and the tabulated hard-sphere radii, the upper- and lower-bound van der Waals contributions to metal-sapphire adhesion are estimated using eqns. (13) and (15), respectively. Again, we find that the exact solutions are generally within 10% of the significantly simpler, metal-radius-independent relations of eqns. (14) and (16).

§ 4. SUMMARY

It is interesting to compare the calculated van der Waals energies for a number of fcc metal–saphire systems to experimentally measured works of adhesion. Because the present calculations were made using room-temperature data, while experimental adhesion determinations are typically made at elevated temperatures, a temperature correction to the respective surface energies was first necessary. The temperature-corrected thermodynamic parameters, taken from the available literature, are compiled in table 2. From table 1, the calculated adhesion energies are seen to fall entirely between 0·4 and 0·9 J m^{-2}. This is also the range of measured adhesion energies for the noble metal–sapphire systems, excepting platinum and palladium.

In fig. 4, we plot the calculated van der Waals and measured adhesion energies against the normalized oxygen reactivity of the respective metals. (This measure is chosen for the present comparison in spite of our earlier reticence, primarily because of its convenience in ranking the chemical reactivity of a wide range of metals, provided the substrate remains the same in all cases.) As expected, the van der Waals energy accounts for the majority of the observed adhesion in gold, silver

Table 2. Room-temperature (25°C) thermodynamic parameters.

	γ_{sv} (J m^{-2})[a]	dγ_{sv}/dT (mJ m^{-2} °C^{-1})[b]	γ_{mc} (J m^{-2})[c]	dγ_{mc}/dT (mJ m^{-2} °C^{-1})[d]	W_{ad} (J m^{-2})
Al_2O_3	0·89	−0·12	—	—	—
Ag	1·60	−0·47	1·75	−0·30	0·74
Al	1·20	−0·40	(0·89)	−0·26	(1·20)
Au	1·82	−0·43	1·86	−0·28	0·85
Cu	2·00	−0·50	2·10	−0·31	0·79
Ni	2·76	−0·60	2·52	−0·36	1·13
Pb	0·63	(−0·25)	(1·12)	−0·18	(0·40)
Pd	(2·69)	(−0·60)	(2·00)	−0·36	(1·58)
Pt	2·94	−0·60	1·59	−0·36	2·24

[a] Value for Al_2O_3 taken from Rhee (1972). Values for Ag, Al, Au, Cu, Ni, Pb and Pt taken from Kumikov and Khokonov (1983). Value for Pd estimated from Keene (1993), using $\gamma_{sv} \approx 1{\cdot}2\gamma_{lv}$.

[b] Value for Al_2O_3 taken from Rhee (1972). Values for Ag, Al, Au, Cu, Ni and Pt taken from Murr (1972, 1975). Values for Pb and Pd estimated from Keene (1993), using $d\gamma_{sv}/dT \approx 2(d\gamma_{lv}/dT)$.

[c] Values for Ag, Au, Cu, and Ni calculated from raw data of Pilliar and Nutting (1967). Value for Pt taken from McLean and Hondros (1971). Values for Al, Pb and Pd are estimated from molten-metal sessile drop values (Chatain *et al.* 1986).

[d] Calculated using the empirical estimate suggested by Klomp (1985, 1989): $d\gamma_{mc}/dT \approx \frac{1}{2}(d\gamma_{mv}/dT + d\gamma_{cv}/dT)$.

Fig. 4

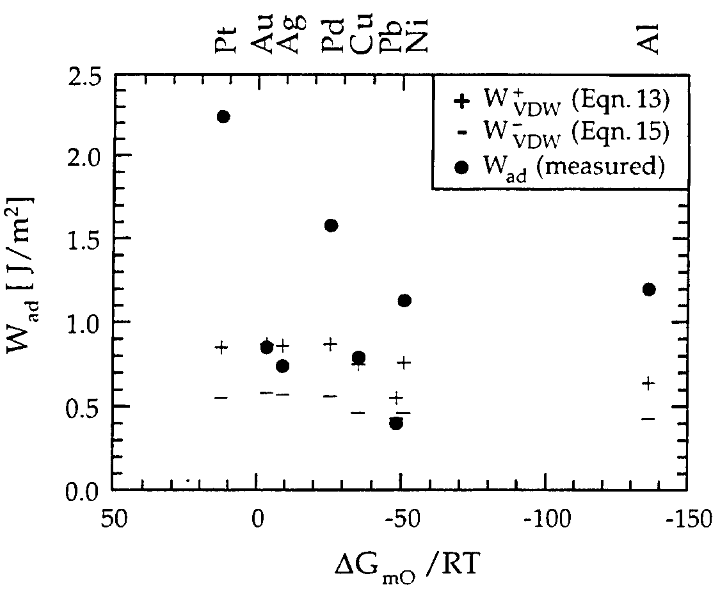

Comparison of calculated van der Waals energies and measured works of adhesion for eight fcc metals bonded to Al_2O_3. The upper- and lower-bound estimates of W_{vdW} are indicated by + and −, respectively, whereas the experimentally measured adhesion energies (normalized to their room temperature values) are indicated by solid circles. The abscissa, representing a measure of the chemical reactivity of the metal, is the non-dimensionalized free energy of oxide formation of the metal (g-atomic basis), taken from Kubaschewski, Alcock and Spencer (1993).

and copper, all of which are expected to exhibit little chemical interaction across the interface. Good agreement is also obtained with lead. On the other hand, the van der Waals energy underestimates the adhesion in the more reactive metals (the latter include those having a substantially negative free energy of oxide formation, such as nickel and aluminium, as well as those exhibiting strong metal–aluminium interactions, such as platinum and palladium). The anomalous behaviour of platinum and palladium, as ranked by the free energy of oxide formation, underscores the disadvantage to using the latter as a sole metric of the propensity toward strong chemical adhesion.

To summarize, we have proposed a methodology for estimating the van der Waals contribution to adhesion across a metal–ceramic interface. Based on the Lifshitz continuum theory of van der Waals forces, the estimate offers an improvement over the often-criticized technique of pairwise summation of London dispersion forces. These results, although avoiding many of the subtleties inherent to such calculations, provide an elegant—and arguably reasonable—analytical estimate of an otherwise unwieldly quantity. In an application of the present model to a series of metal–sapphire systems, we find that the van der Waals energy provides an accurate lower bound to the measured work of adhesion. This lower bound is approached by the least reactive metals, whereas the chemical contribution to adhesion plays a substantial role in the more reactive metals.

ACKNOWLEDGMENTS

The authors are grateful to Dr Diane J. Isaacson, who kindly provided the plasmon energy data used in the present calculations.

REFERENCES

ADAMSON, A. W., 1982, *Physical Chemistry of Surfaces*, 4th Edn (New York: Wiley).

ANDERSON, A. B., RAVIMOHAN, CH., and MEHANDRU, S. P., 1987a, *Surf. Sci.*, **183**, 438.

ANDERSON, P. M., WANG, J.-S., and RICE, J. R., 1987b, *Proceedings of the 34th Sagamore Army Materials Research Conference on Innovations in Ultrahigh-Strength Steel Technology*, edited by G. B. Olson, M. Azrin and E. S. Wright (Watertown, MA: US Army Laboratory Command).

BARRERA, R. G., and DUKE, C. B., 1976, *Phys. Rev.* B, **13**, 4477.

BENJAMIN, P., and WEAVER, C. 1959, *Proc. Roy. Soc.* A, **252**, 418.

BERGSTRÖM, L., MEURK, A., ARWIN, H., and ROWCLIFFE, D. J., 1996, *J. Am. Ceram. Soc.*, **79**, 339.

BLÖCHL, P., DAS, G. P., FISCHMEISTER, H. F., and SCHÖNBERGER, U., 1990, *Metal–Ceramic Interfaces*, edited by M. Rühle, A. G. Evans, M. F. Ashby and J. P. Hirth (New York: Pergamon Press), pp. 9–14.

CHATAIN, D., COUDURIER, L., and EUSTATHOPOULOS, N., 1988, *Rev. Phys. Appl.*, **23**, 1055.

CHATAIN, D., RIVOLLET, I., and EUSTATHOPOULOS, N., 1986, *J. Chim. Phys.*, **83**, 561; 1987, *ibid.*, **84**, 201.

DUFFY, D. M., HARDING, J. H., and STONEHAM, A. M., 1992, *Acta. metall.*, **40**, s11.

EGERTON, R. F., 1986, *Electron Energy-Loss Spectroscopy* (New York: Plenum Press), pp. 151–159.

ELSSNER, G., KORN, D., and RÜHLE, M., 1994, *Scripta metall. mater.*, **31**, 1037.

EUSTATHOPOULOS, N., CHATAIN, D., and COUDURIER, L., 1991, *Mater. Sci. Engng* A, **135**, 83.

FINNIS, M. W., 1992, *Acta metall.*, **40**, s25.

FINNIS, M. W., NEEDS, R. J., and SCHÖNBERGER, U., 1995, *Phys. Rev. Lett.*, **74**, 3083.

FINNIS, M. W., STONEHAM, A. M., and TASKER, P. W., 1990, *Metal–Ceramic Interfaces*, edited by M. Rühle, A. G. Evans, M. F. Ashby and J. P. Hirth (New York: Pergamon Press), pp. 35–44.

FREEMAN, A. J., LI, C., and FU, C. L., 1990, *Metal–Ceramic Interfaces*, edited by M. Rühle, A. G. Evans, M. F. Ashby and J. P. Hirth (New York: Pergamon Press), pp. 2–8.

GANGOPADHYAY, U., and WYNBLATT, P., 1994, *Mater. Res. Soc. Symp. Proc.*, **318**, 393; 1995, *J. Mater Sci.*, **30**, 94.

GERVAIS, F., 1991, *Handbook of Optical Constants of Solids II*, edited by E. D. Palik (New York: Academic Press), pp. 761–75.

GIBBESCH, B., and ELSSNER, G., 1992, *Acta metall.*, **40**, s59.

GLICKSMAN, M., 1971, *Solid State Physics*, **26**, 275.

HEIFETS, E., ORLANDO, R., DOVESI, R., PISANI, C., and KOTOMIN, E. A., 1994, *Second International Conference on Computer Simulation of Radiation Effects in Solids*, Santa Barbara, CA.

HIRTH, J. P., and RICE, J. R., 1980, *Metal. Trans.*, **11A**, 1501.

HONG, T., SMITH, J. R., and SROLOVITZ, D. J., 1993a, *Phys. Rev.* B, **47**, 13 615; 1993b, *Phys. Rev.Lett.*, **70**, 615; 1994, *J. Adhesion Sci. Technol.*, **8**, 837; 1995, *Acta metall.*, **43**, 2721.

HOUGH, D. B., and WHITE, L. R., 1980, *Adv. Colloid Interface Sci.*, **14**, 3.

HUMENIK, M., and KINGERY, W. D., 1954, *J. Am. Ceram. Soc.*, **37**, 18.

ISAACSON, D., 1975, *Compilation of r_s Values*, New York University Internal Report.

ISRAELACHVILI, J. N., 1992, *Intermolecular and Surface Forces*, 2nd Edn (New York: Academic Press).

JOHNSON, K. H., and PEPPER, S. V., 1982, *J. Appl. Phys.*, **53**, 6634.

Joint Committee on Powder Diffraction Spectra, 1992, Card nos. 4-784, 42-1468.

KASOWSKI, R. V., OHUCHI, F. S., and FRENCH, R. H., 1988, *Physica* B, **150**, 44.

KEENE, B. J., 1993, *Int. Mater. Rev.*, **38**, 157.

KLOMP, J. T., 1985, *Mater. Res. Soc. Symp. Proc.*, **40**, 381; 1987, *Fundamentals of Diffusion Bonding*, edited by Y. Ishida (New York: Elsevier), p. 3; 1989, *Surfaces and Interfaces* *of Ceramic Materials*, edited by L.-C. Dufour, C. Monty and G. Petot-Ervas (Boston, MA: Kluwer Academic), pp. 375–92.

Korn, D., Elssner, G., Fischmeister, H. F., and Rühle, M., 1992, *Acta metall.*, **40**, s355.

Koski, K., Hölsa, J., Ernoult, J., and Rouzaud, A., 1996, *Surf. Coat. Technol.*, **80**, 195.

Kubaschewski, O., Alcock, C. B., and Spencer, P. J., 1993, *Materials Thermochemistry*, 6th Edn (New York: Pergamon).

Kumikov, V. K., and Khokonov, Kh.B., 1983, *J. appl. Phys.*, **54**, 1346.

Li, C., Wu, R., Freeman, A. J., and Fu, C. L., 1993, *Phys. Rev.* B, **48**, 8317.

Lifshitz, E. M., 1956, *Sov. Phys.-JETP*, **2**, 73.

Lipkin, D. M., 1996, *Metal–Ceramic Fracture: Effects of Interfacial Adhesion*, Ph.D. Dissertation, University of California, Santa Barbara.

Lipkin, D. M., Beltz, G. E., and Clarke, D. R. 1997a, *Mater. Res. Soc. Symp. Proc.*, Vol 436 (Pittsburgh, Pennsylvania: Materials Research Society), pp. 91–96.

Lipkin, D. M., Clarke, D. R., and Beltz, G. E., 1996, *Acta mater.*, **44**, 4051.

Lipkin, D. M., Evans, A. G., and Clarke, D. R., 1997b (in preparation).

Malitson, I. H., 1962, *J. Opt. Soc. Am.*, **52**, 1377.

McDonald, J. E., and Eberhart, J. G., 1965, *Trans. Met. Soc. AIME*, **233**, 512.

McLean, M., and Hondros, E. D., 1971, *J. Mater. Sci.*, **6**, 19.

Murr, L. E., 1972, *Scripta Metall.*, **6**, 203; 1975, *Interfacial Phenomena in Metals and Alloys* (London: Addison-Wesley), pp. 122–7 & 153–7.

Naidich, Yu. V., 1981, *Prog. Surf. Membrane Sci.*, **14**, 353.

Ninham, B. W., and Parsegian, V. A., 1970, *Biophysical J.*, **10**, 646.

Ohuchi, F. S., French, R. H., and Kasowski, R. V., 1987, *J. appl. Phys.*, **62**, 2286.

Pask, J. A., and Fulrath, R. M., 1962, *J. Am. Ceram. Soc.*, **45**, 592.

Pauling, L., 1970, *General Chemistry*, 3rd Edn. (San Francisco, CA: Freeman).

Pepper, S. V., 1976, *J. appl. Phys.*, **47**, 801.

Pilliar, R. M., and Nutting, J., 1967, *Phil. Mag.*, **16**, 181.

Rao, F., Wu R., and Freeman, A. J., 1995, *Phys. Rev.*, B, **51**, 10052.

Rhee, S. K., 1972, *J. Am. Ceram. Soc.*, **55**, 300.

Rice, J. R., Suo, Z., and Wang, J.-S., 1990, *Metal–Ceramic Interfaces*, edited by M. Rühle, A. G. Evans, M. F. Ashby and J. P. Hirth (New York: Pergamon Press), pp. 269–94.

Rice, J. R., and Wang, J.-S., 1989, *Mater. Sci. Engng*, A, **107**, 23.

Schönberger, U., Andersen, O. K., and Methfessel, M., 1992, *Acta metall.*, **40**, s1.

Seah, M. P., 1980, *Acta metall.*, **28**, 955.

Smith, J. R., Hong, T., and Srolovitz, D. J., 1994, *Phys. Rev. Lett.*, **72**, 4021.

Stoneham, A. M., 1982–1983, *Appl. Surf. Sci.*, **14**, 249.

Stoneham, A. M., and Tasker, P. W., 1985, *J. Phys.* C., **18**, L543; 1987a, *Ceramic Microstructures '86: Role of Interfaces*, Materials Science Research Vol. 21, edited by J. A. Pask and A. G. Evans (New York: Plenum Press), pp. 155–65; 1987b, *Phil. Mag.* B, **55**, 237; 1988, *Surface and Near-Surface Properties of Oxide Materials*, edited by L. C. Dufour and J. Nowotny (Amsterdam: Elsevier Press).

Yamamoto, R., Kohyama, M., Ebata, Y., and Kinoshita, M., 1989, *Proceedings of the Materials Reseaerch Society International Meeting on Advanced Materials* Vol. 8, *Metal–Ceramic Joints*, edited by M. Doyama *et al.* (Pittsburgh, Pennsylvania: Materials Research Society), p. 183.

LASER-ULTRASONIC EVALUATION OF DAMAGE IN UNIDIRECTIONAL CERAMIC MATRIX COMPOSITES

Y.-M. Liu, T. E. Mitchell, Center for Materials Science, Mail Stop K765
Los Alamos National Laboratory, Los Alamos, NM 87545, U. S. A.
and H. N. G. Wadley, Department of Materials Science and Engineering, School of Engineering and Applied Science, University of Virginia, Charlottesville, VA 22903, U. S. A.

INTRODUCTION

Ceramic matrix composites (CMCs) have attracted great attention because of their potential for high temperature structural applications. Among the CMCs, calcium aluminosilicate (CAS) glass ceramic composite reinforced by Nicalon™ SiC fiber with a carbon-rich interface has been extensively investigated because of their "notch-insensitivity": stresses near holes and notches can be redistributed by inelastic deformation in the form of multiple matrix cracking [1-3]. Thus, stress concentrations can be alleviated near these sites and the risk of catastrophic failure is consequently reduced.

Understanding damage evolution during the deformation of CMCs is very important for constitutive model development of as well as materials design. To contribute to these goals, techniques for *in-situ* monitoring of damage initiation and accumulation are needed. In previous work, damage was characterized mostly by the change of Young's modulus along the loading direction (measured by loading/unloading) in conjunction with metallography [1,4,5]. However, this approach does not provide detailed insight into the anisotropic nature of damage, or about the cumulative effects of fiber-matrix debonding/sliding, radial cracking and shear deformation. In this study, we have pursued an *in-situ* laser-ultrasonic technique to nondestructively measure the anisotropic stiffness degradation under loading.

When a laser pulse is directed at a sample surface, high frequency acoustic waves can be generated by thermal or ablation mechanisms depending on the incident power intensity [6,7]. The resulting propagation of elastic waves through an anisotropic media can then be characterized by the well-known Christoffel equation [8]:

$$\Omega(V, \boldsymbol{n}) = \det\left|C_{ijkl}\, n_j n_l - \rho V^2 \delta_{ik}\right| = 0, \tag{1}$$

where C_{ijkl} are the second-order elastic stiffness constants of the material, $\boldsymbol{n}$ is a unit vector along the bulk wave propagation direction, ρ is the density of the medium, V is the phase velocity and δ_{ik} is the Kroneker delta. Based on a set of wave velocities measured along various propagation directions, the elastic constants can be deduced by fitting the experimental data to the solutions of the Christoffel equation through nonlinear optimization procedures. Unidirectional composites can be regarded as transversely isotropic materials. Using abbreviated stiffness subscripts, the five independent elastic constants are C_{11}, C_{33}, C_{12}, C_{13} and C_{44}, while $C_{22} = C_{11}$, $C_{23} = C_{13}$, $C_{55} = C_{44}$ and $C_{66} = (C_{11} - C_{12})/2$. As damage accumulates in such composites, the elastic moduli are reduced, resulting in a decrease of the wave propagation velocities [9].

When damage in the form of cracking occurs, elastic waves are generated, i.e., acoustic emission occurs. These dynamic elastic signals propagate through the composites and cause surface displacements which can be ultrasonically detected by a piezoelectric transducer attached to the sample surface [10,11]. This nondestructive technique also provides additional insight into the evolution of damage. In the present study, acoustic emission (AE) events were continuously recorded during loading/unloading of CAS/SiC composite. This was combined with data obtained from laser-ultrasonic and mechanical testing to shed new light on the damage evolution process in unidirectional fiber-reinforced ceramic composite materials.

EXPERIMENTAL

Tensile specimens of dimensions 150 mm × 10 mm × 3 mm with continuous fibers parallel to the loading direction (the length direction of the specimen) were cut from the unidirectional CAS/SiC composite plate (provided by Corning Inc.). The specimen ends were bonded with aluminum tabs using modified epoxy (3M Company) to ensure even load transfer. Tensile testing was performed on an Instron 4200 machine at room temperature. Axial strain was measured by a 2.54 cm gauge length extensometer.

Laser pulse was generated by a Q-switch 1.064 µm wavelength Nd:YAG laser. Pulses with an energy of about 5 mJ were delivered to the loaded sample through an optical fiber [12,13]. A laser scan along the two principal directions of the sample was controlled by an X-Y-Z positioner. Ultrasonic wave arrivals were detected by two broadband piezoelectric transducers in contact with the sample. The detected signal was transferred to digital oscilloscopes. The chosen coordinates and the experimental setup are shown schematically in Fig. 1.

During the experiments, a laser scan was performed at a pre-set stress level, and then repeated after unloading to 10 MPa. Before each scan, the laser source was re-aligned to keep the laser scan along the same positions. Acoustic emission events were recorded continuously by the two sensors during the entire tensile test. The root-mean square average of the waveform amplitude was calculated automatically each time the waveform was recorded.

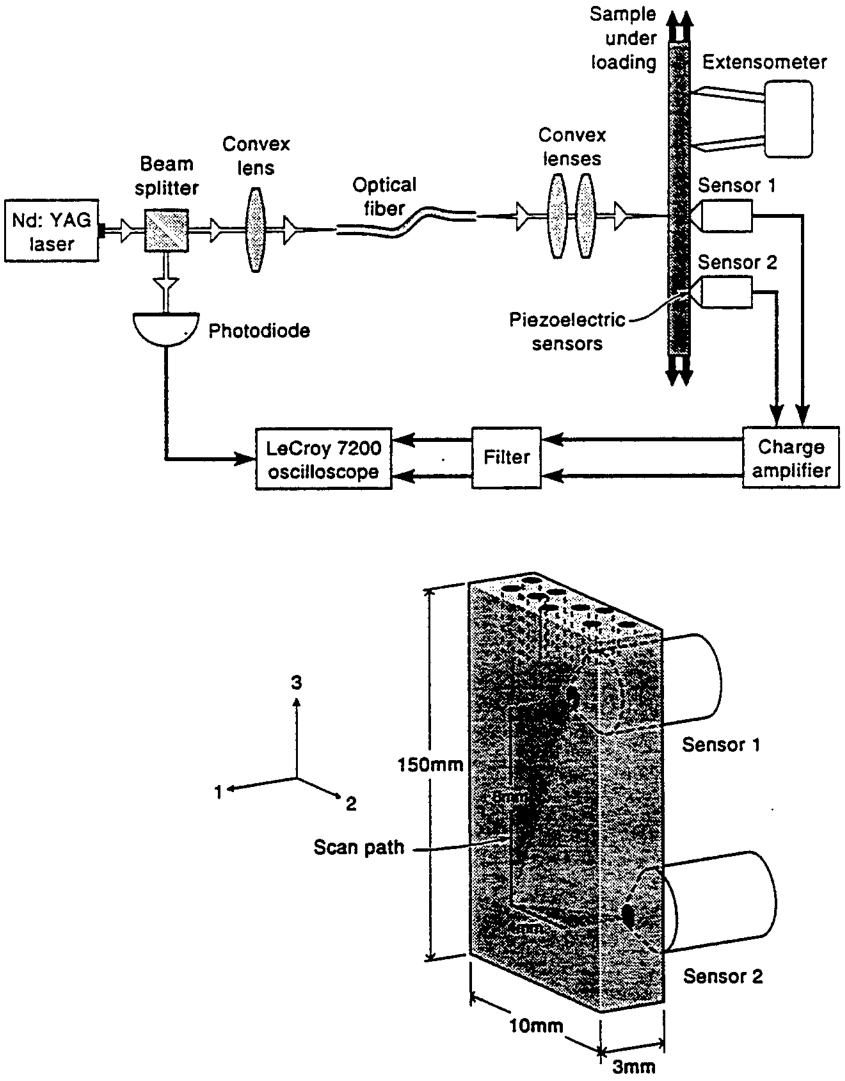
Sample under loading
Extensometer
Convex lenses
Convex lens
Beam splitter
Optical fiber
Nd: YAG laser
Sensor 1
Sensor 2
Photodiode
Piezoelectric sensors
LeCroy 7200 oscilloscope
Filter
Charge amplifier
3
1
2
150mm
Scan path
Sensor 1
Sensor 2
10mm
3mm

Fig.1. Experimental setup and scan-path for laser-ultrasonic experiments.

RESULTS AND DISCUSSION

Fig. 2 shows a tensile stress-strain curve for a unidirectional CAS/SiC sample during repeated loading/unloading up to 320 MPa. The acoustic emission events corresponding to loading the sample to 200 MPa are also shown in Fig. 2. Fig. 3 displays the accumulated AE counts during the entire loading/unloading

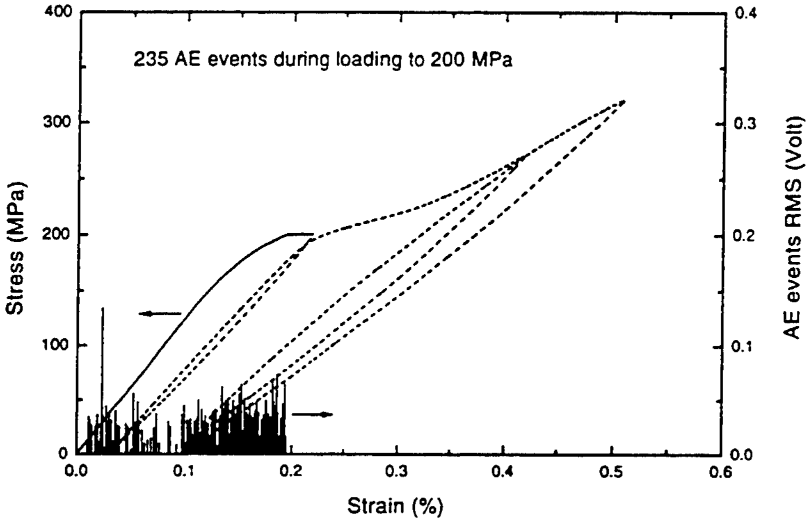

Fig. 2. Tensile stress-strain curve and corresponding AE events over stress range 0 ~ 200 MPa.

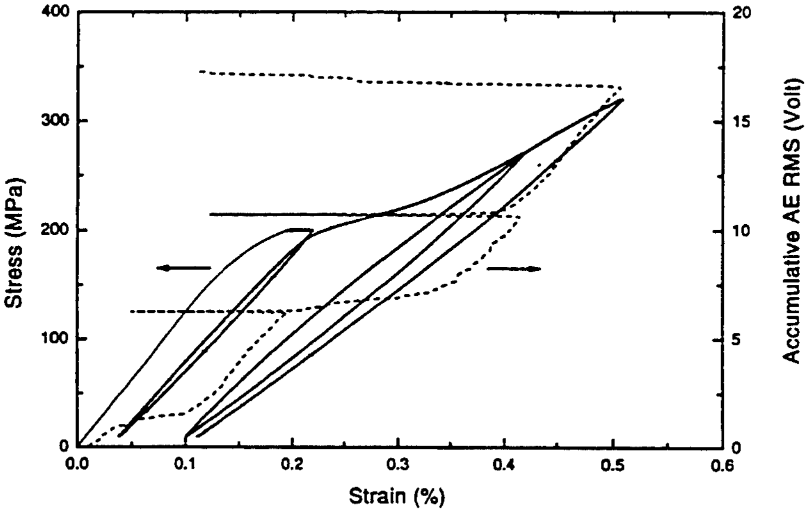

Fig. 3. Tensile stress-stain curve and accumulated AE during the entire loading/unloading cycles.

process. From these figures, it is clear that the σ-ε curve starts to deviate from linearity over the stress range of 130-150 MPa, which is the accepted matrix cracking stress threshold [1]. However, in the linear region, AE events are detected, associated with cracks extension from initial flaws formed during fabrication. They appear to have little effect on the macroscopic deformation behavior and they have only partially spread across the sample. With the development of matrix cracking, numerous AE events are detected and an appreciable amount of inelastic deformation occurs over the stress range of 130 MPa to 320 MPa. Fig. 4 (a)~(c) show matrix cracks at different loading stages.

During unloading from 320 MPa, a number of AE events were observed whereas only one or two AE signals were recorded when unloading from 200 MPa or 270 MPa. AE events during unloading might originate from interface sliding [14] and some crack closure effects; these results imply that limited damage are occurring on unloading and they are not sufficient to generate AE signals at low stress levels, although the hysteresis loops indicate that there was energy dissipation during unloading/reloading. The unloading curves from 270 MPa and 320 MPa (Fig. 2) indicate that the unloading elastic modulus does not change much, which implies that the density of matrix cracks seems to saturate near the end of the test (320 MPa) as shown in Fig. 4(b) and (c).

It is noticed that, for most paths of reloading, AE events do not occur during reloading until near the previous peak stress level. These observations indicate that unloading/reloading does not contribute to significant additional damage. Although the hysteresis loops were formed as a results of energy dissipation during loading/unloading through frictional sliding at the fiber/matrix interface, the results suggest that interface sliding at low damage levels is not sufficient to yield detectable AE signals.

With the development of damage, the elastic stiffnesses are degraded. This is manifest by a reduction of the ultrasonic wave velocity as well as a reduced unloading modulus on the stress-strain curve. The elastic stiffness constant C_{11} can be found directly from the longitudinal wave velocity at the epicenter position. In the transversely isotropic X_1X_2 plane, independent elastic constant measurements by the resonant ultrasound spectroscopy technique [15] indicated that $C_{44} \approx C_{66}$, thus, C_{44} (or C_{66}) can determined by averaging the shear velocity at different scan positions in the X_1X_2 plane, because the velocity of the pure shear wave is given by $V = \sqrt{C_{44} / \rho}$.

The other unknown elastic constants C_{33} and C_{13} are determined from the wave velocity measured within the principal X_1X_3 plane. Again, the two shear modes are not clearly distinguished, thus identifying C_{33} and C_{13} are based on the longitudinal wave speeds using Eq. (1) through a nonlinear curve fitting procedure.

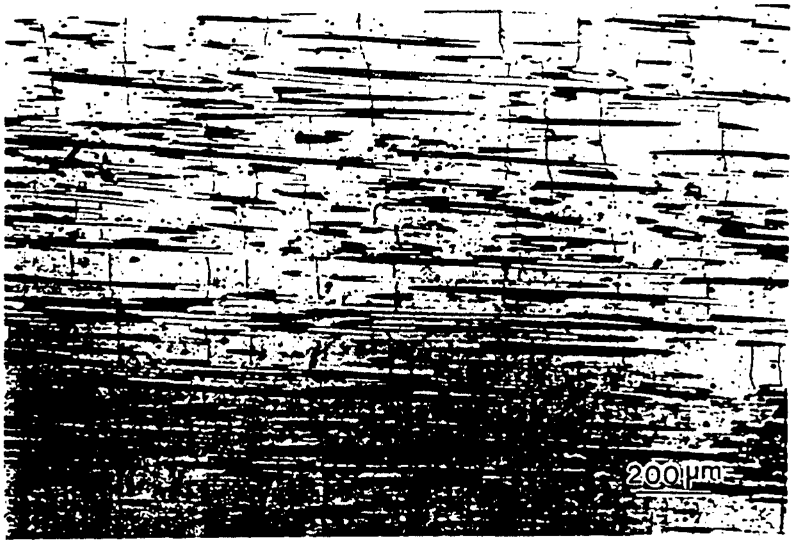

(a)

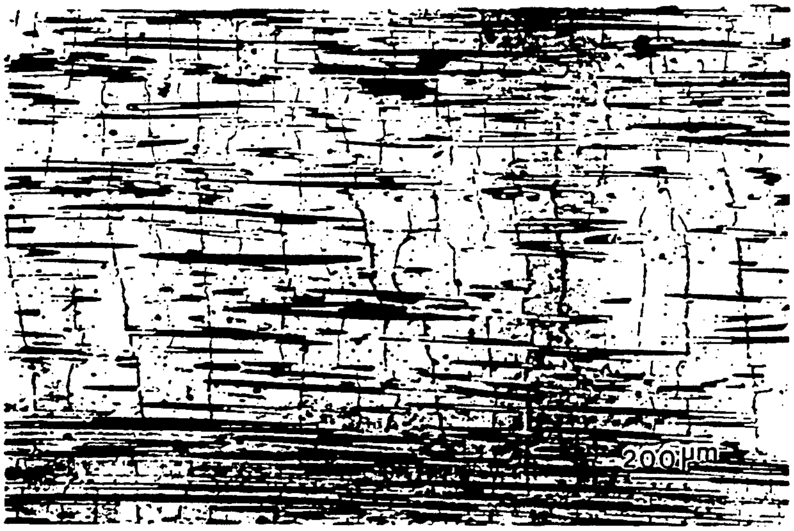

(b)

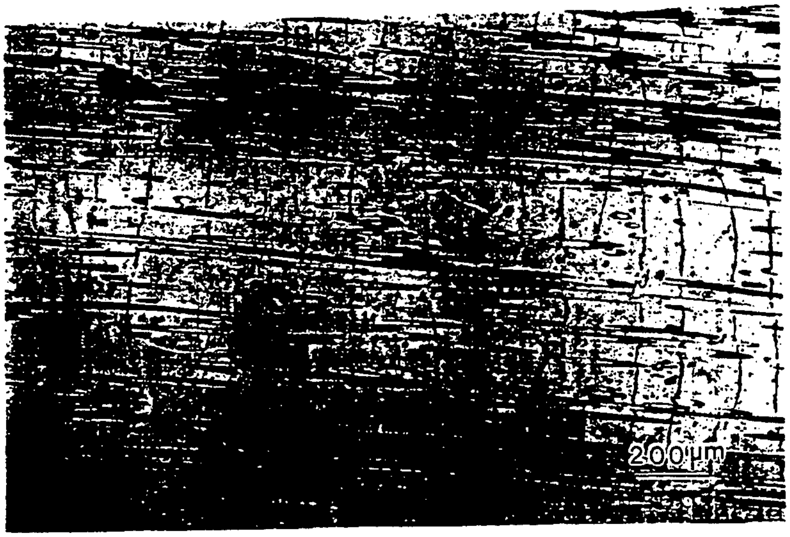

(c)

Fig. 4. Optical micrographs of replicas show surface matrix cracks at different stress levels: (a) 230 MPa; (b) 270 MPa; (c) 330 MPa.

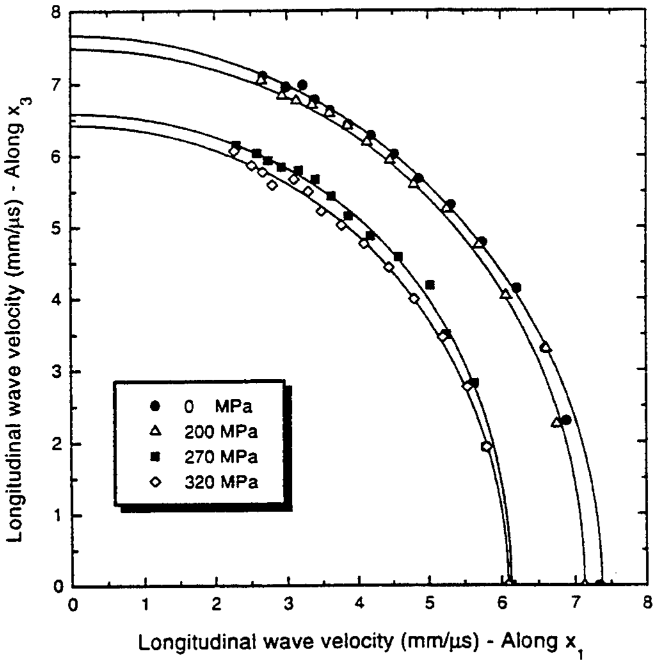

Fig. 5. Measured and curve fitted longitudinal wave velocity in X_1X_3 plane at four stress levels.

The measured wave velocities in the X_1X_3 plane together with the ones determined by curve fitting at four different stress levels (0, 200, 270 and 320 MPa) are plotted in Fig. 5. Significant delay in the wave arrival time is observed when the tensile stress is increased from 200 MPa to 270 MPa, and reflects the contribution of damage to the elastic properties. This is consistent with the plateau region shown on the σ-ε curve. Similar measurements and calculations were carried out for another sample at stress levels of 180 and 240 MPa.

The measurements performed at 10 MPa after unloading from each successively higher stress indicate that the wave arrival velocities increase slightly after unloading, although not significantly compared with the data before unloading. This result implies that there may be some crack closure but the damage certainly remained after unloading.

Elastic constants C_{11}, C_{33} and C_{44} together with the unloading elastic moduli E^* obtained from the partial unloading test are plotted in Fig. 6 (reloading modulus was used at the stress 180 MPa). C_{11}, C_{33} and E^* show the same reduction trend, although the degree of reduction near the end of matrix crack saturation for E^* seems to be less than that of C_{11} and C_{33}.

Laser-ultrasonic measurements showed that there is an overall degradation of the elastic stiffness constants. Micrographs of the fracture surface show "crack-

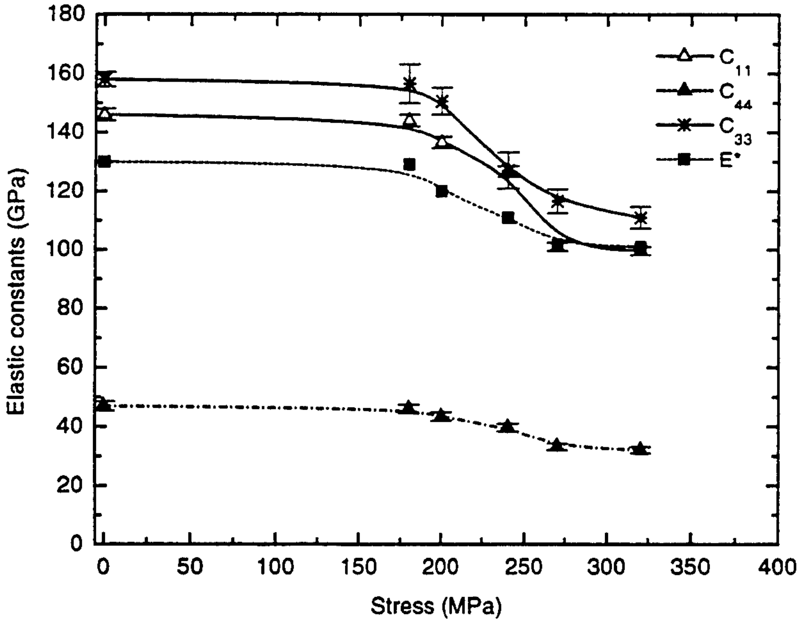

Fig. 6. Elastic constants determined by laser-ultrasonic method and unloading elastic modulus by tensile test.

like" discontinuities in the transverse plane normal to the loading direction [13]. The decrease of transverse elastic constants might be due to fiber/matrix interface debonding, residual matrix cracking and shear deformation involved in matrix crack propagation. This softening effect is still under investigation.

CONCLUSIONS

The laser-ultrasonic technique has been successfully applied to study damage evolution in a unidirectional fiber-reinforced CAS/SiC ceramic composite. Elastic constants were determined based on ultrasound wave velocity measurements along various propagation directions. The results show that wave propagation is sensitive to damage accumulation in the sample. In conjunction with AE recording, the nondestructive laser-ultrasonic method provides valuable knowledge of the overall anisotropic damage in fiber-reinforced ceramic composites. Damage accumulation under loading is manifest by a reduction of the elastic constants, AE signals, and the σ-ε hysteresis loops.

ACKNOWLEDGMENTS

This work was co-supported by DARPA through UCSB-URI and the US Department of Energy, Office of Basic Energy Sciences. Discussions with Y. Lu, D. Sypeck (University of Virginia), and A. G. Evans (Harvard University) are greatly appreciated.

REFERENCES

[1] D. S. Beyerle, S. M. Spearing, F. W. Zok, and A. G. Evans, "Damage and Failure in Unidirectional Ceramic-Matrix Composites", *J. Am.. Ceram. Soc.*, **75** [10] 2719-2725 (1992).

[2] C. Cady, T. J. Mackin, and A. G. Evans, "SiC/CAS: a Notch-Insensitive Ceramic-Matrix Composite", *J. Am. Ceram. Soc.*, **78** [1] 77-82 (1995).

[3] M. Y. He, B.-X. Wu, A. G. Evans, and J. W. Hutchinson, "Inelastic Strains due to Matrix Cracking in Unidirectional Fiber-Reinforced Composites", *Mech. Mater.*, **18** 213-229 (1994).

[4] M. Drissi-Habti, "Damage Development and Moduli Reduction in a Unidirectional SiC-MAS. L. Composite Tested Under Uniaxial Tensile Loading", *Script Metal. Mater.*, **33** 967-973 (1995).

[5] C. Cady, F. E. Heredia, and A. G. Evans, "In-Plane Mechanical Properties of Several Ceramic-Matrix Composites", *J. Am. Ceram. Soc.*, **78** [8] 2065-2078 (1995).

[6] S. J. Davies, C. Edwards, G. S. Taylor, and S. B. Palmer, "Laser-Generated Ultrasound: its Properties, Mechanisms and Multifarious Applications", *J. Phys. D.: Appl. Phys.*, **26** 329-348 (1993).

[7] C. B. Scruby, and L. E. Drain, *Laser Ultrasonics, Technique and Applications*, Adam Hilger, Bristol, 1990.

[8] B. A. Auld, *Acoustic Fields and Waves in Solids*, Krieger Publishing Company, Malabar, Florida, 1990.

[9] S. Baste, R. E. Guerjouma and B. Audoin, "Effect of Microcracking on the Macroscopic Behavior of Ceramic Matrix Composites: Ultrasonic Evaluation of Anisotropic Damage", *Mech. Mater.* **14** 15-31 (1992).

[10] C. B. Scruby, H. N. G. Wadley, and J. J. Hill, "Dynamic Elastic Displacements at the Surface of an Elastic Half-space due to Defect Sources", *J. Phys. D: Appl. Phys.*, **16** 1069-1083 (1983).

[11] D. G. Eitzen and H. N. G. Wadley, " Acoustic Emission: Establishing the Fundamentals", *Journal of Research of the National Bureau of Standards*, **89** 75-100 (1984).

[12] R. J. Dewhurst, A. G. Nurse, and S. B. Palmer, "High Power Optical Fibre Delivery System for the Laser Generation of Ultrasound", *Ultrasonics*, **26** 307-310 (1988).

[13] Y.-M. Liu, T. E. Mitchell, and H. N. G. Wadley, "Dynamic Elastic Observations of Damage in Fiber-Reinforced Ceramics", to be submitted to *Acta Mater.*, 1996.

[14] J.-J. Luo, S.-C. Wooh, and I. M. Daniel, "Acoustic Emission Study of Failure Mechanisms in Ceramic Matrix Composite under Longitudinal Tensile Loading", *Review of Progress in Quantitative Nondestructive Evaluation*, Vol. **13**, edited by D. O. Thompson and D. E. Chimenti, Plenum Press, New York, 1994.

[15] Y.- M. Liu, Y. He, F. Chu, T. E. Mitchell and H. N. G. Wadley, "Elastic Properties of Laminated CAS/SiC Composites Determined by Resonant Ultrasound Spectroscopy", submitted to *J. Am. Ceram. Soc.*, 1996.

Fiber Optic Measurement of Residual Stress in Ti-6Al-4V/SiC Fiber Composites Using Cr^{3+} Doped Sapphire Fibers

Gareth T. Munger and Haydn N. G. Wadley
Intelligent Processing of Materials Laboratory
School of Engineering and Applied Science
University of Virginia, Charlottesville, VA 22903.

Abstract

Sapphire fibers containing dilute concentrations of Cr^{3+} ions have been used to determine stress in a titanium matrix composite. The R1 and R2 luminescence peaks of the Cr^{3+} doped sapphire have been measured before and after the processing of a Ti-6Al-4V/SIGMA (SiC) fiber reinforced composite. The peak shifts have been related to the sapphire fiber's principal stresses using the well established piezospectroscopic relationships. A fiber located near the center of the sample had an axial stress value, $\sigma_{zz} = 876 \pm 147$ (MPa), while the sum of the inplane stress components, $(\sigma_{rr}+\sigma_{\theta\theta}) = -61 \pm 93$ (MPa). The thermal stresses that developed after processing have been modeled using the Generalized Method of Cells and used to develop a relationship between the stress of the sapphire witness fiber and that of the surrounding SIGMA fibers and the Ti-6Al-4V matrix.

1. Introduction

Silicon carbide fiber reinforced titanium composites have been proposed for use in high temperature applications such as gas turbine engines [1,2]. Three processing methods, molten spray deposition [3,4], vapor phase deposition [5-7] and powder slurry (tape) casting [8] are being developed for their synthesis. Each results in monotapes consisting of unidirectional fibers in a more or less uniformly distributed matrix. These monotapes are then consolidated to a near net shape component by a high temperature consolidation process such as hot isostatic pressing.

High temperature consolidation can activate many processes that contribute to a reduction in mechanical properties. Fiber-Matrix interactions at the interface [9-11], fiber microbending and fracture [12,13], porosity due to incomplete consolidation [14,15] and large residual stress accumulation during the cool down of the MMC from elevated temperatures [16,17] can all occur. The development of a successful process methodology requires a full understanding of these processes. Residual stresses are particularly important to understand. These originate from the difference between the coefficients of thermal expansion (CTE) of the metal-matrix (high CTE) and ceramic fiber (low CTE) and form as the composite cools from the elevated temperatures used for consolidation. This results in a compressive axial, radial and hoop stresses in the fiber that are balanced by tensile axial and hoop stresses in the matrix. The matrix hoop stress, if sufficiently large, can cause radial matrix cracking and a significant loss of strength in the transverse direction [18,19]. The residual matrix stresses in the axial direction can also effect longitudinal stress-strain response due to the premature initiation of plasticity or cracking [16,17].

Accurate, reliable non-destructive methods for measuring residual stress are needed to ensure the quality of these composites. Current methods of residual stress measurement such as x-ray or neutron diffraction are either insufficient in their depth of penetration (only ~50 micron for conventional x-ray diffraction) or are costly and require special synchrotron or neutron facilities. It has been shown that the luminescence from embedded sapphire fibers can be used to accurately measure residual stresses [16,20]. This idea is explored in the current study which investigates the use of a fiber-optic technique to measure the stress in a witness sapphire fiber and develops relationship between stresses in the silicon carbide fibers/titanium matrix and that in the embedded sapphire fiber.

2. Luminescence

Luminescence originates from the radiative transition of an electron from an excited state to one of lower energy. There are two types of luminescence; fluorescence and phosphorescence. Fluorescence involves a transition that is not forbidden by spin selection rules. These "spin allowed" transitions occur rapidly and quickly depopulate the excited state. Thus they have emission lifetimes of the order of nanoseconds. Phosphorescence transitions involve spin flips, and thus are "spin forbidden", and take much longer to occur. These forbidden transitions typically have emission lifetimes ranging from microseconds to seconds.

Most grades of aluminum oxide (including those used to synthesize sapphire fiber) contain trace amounts of chromium that exists as a Cr^{3+} ion in substitution sites for the aluminum in the corundum lattice. Blue or green light excites the ions to then excited ^2E_g and $^4A_{2g}$ sites. Due to spin-orbit, and the trigonal crystal field distortion, the ^2E_g state is split into the $\bar{E}$ and $^2\bar{A}$ states separated in wavenumber by approximately 30 cm^{-1}. The decay to the ground state from either is spin-forbidden, and results in a phosphorescence with a doublet spectrum. The doublet peaks are designated R1 and R2 and appear as two spectral lines at approximately 693nm and 694 nm [21].

R lines frequency shifting with applied stress was first report by Schawlow [22] in 1961. The phenomenon was further investigated by Foreman, et al. [23] at the National Bureau of Standards who explored it's use to calibrate and measure stress inside of diamond anvil cells. They calculated the wavelength shift-stress response to 20 GPa and reported it to be linear. Bell et al. [24-26] extended the scale to 550 GPa and reported that nonlinearites did not show in the line shift until the stress reached ~29 GPa. Recently, He and Clarke [27] have detected a slight nonlinearity in the *a*-crystallographic direction above a stress of ~500MPa.

Grabner [28] developed a relationship between the tensor components of stress and the line shift $\Delta\bar{v}$ (in cm^{-1}).

$$\Delta\bar{v} = \Pi_{ij}\sigma_{ij}^{c} \tag{1}$$

In eq(1), the Π_{ij} are piezospectroscopic constants (in GPa/cm^{-1}) and σ^c_{ij} are the applied stress components defined in the crystal coordinates (in GPa). He and Clarke [27] could detect no contributing shear components to Π_{ij}. In terms of the crystallographic coordinates,

$$\Delta\bar{v} = \Pi_{11}\sigma_a + \Pi_{22}\sigma_m + \Pi_{33}\sigma_c \tag{2}$$

where σ_a, σ_m, and σ_c denote stress in *a*, *m* and *c* crystallographic directions. Based on the fact that piezospectroscopic effect of the R lines is controlled by the point symmetry of Cr^{3+} ion in an undeformed trigonally symmetric crystal, it was assumed until recently that $\Pi_{11} = \Pi_{22}$. He and Clarke [27] found that Π_{11} for the *a* crystallographic direction is different than Π_{22} for the m direction for both the R1 and R2 lines. Numerical values for the Π_{ij} are summarized in Table 1.

Table 1: Piezospectroscopic constants report by He and Clarke [27]

Line	Π_{11}(GPa/cm^{-1})	Π_{22}(GPa/cm^{-1})	Π_{33}(GPa/cm^{-1})
R1 line	2.56	3.50	1.53
R2 line	2.65	2.80	2.16

For c-oriented fibers in metal matrix composites, the inplane residual stress components (σ_a and σ_m) are similar. For stress states where $\sigma_a \approx \sigma_m$ and $\sigma_c \gg \sigma_m$, σ_a one can approximate $\Pi_{11} \approx \Pi_{22}$ if one replaces Π_{11} and Π_{22} by $\Pi'_{11} = (\Pi_{11} + \Pi_{22})/2$. For this state of stress, both σ_c and the sum ($\sigma_a + \sigma_m$) can be calculated from measurements of $\Delta\bar{v}$ for both R lines. Values for Π'_{11} and Π_{33} deduced from He and Clarke's data are in quite close agreement with values measured by other researchers as shown in Table 2.

Table 2: Piezospectroscopic constants as reported by various researchers

	R1 line		R2 line	
Source	Π'_{11} (cm^{-1}/GPa)	Π_{33}(cm^{-1}/GPa)	Π'_{11} (cm^{-1}/GPa)	Π_{33}(cm^{-1}/GPa)
He and Clarke [27]	3.03	1.53	2.725	2.16
Schawlow *et al.* [29]	3.0	1.8	2.8	2.3
Kaplyanskii *et al.* [30]	3.2	1.4	2.8	1.9
Feher and Sturge[31]	2.7	1.8	2.4	2.2

Equation(1) can be rewritten in terms of the principle applied stresses using a standard transformation of tensors.

$$\sigma_{ij}^{c} = a_{im}\sigma_{mn}a_{jn} \tag{3}$$

In equation (3), a_{im} and a_{jn} are the coordinate transformation matrices and σ_{mn} is the stress tensor in the principle applied stress coordinate system. For a c-axis crystal aligned along the z-axis of stress, the equations can be written.

$$\Delta\bar{v} = \Pi'_{11}(\sigma_{rr} + \sigma_{\theta\theta}) + \Pi_{33}\sigma_{zz} \tag{4}$$

3. Experimental

3.1. Sample preparation

A cylindrical Ti-6Al-4V/SIGMA 1240 composite sample was constructed from sputter coated Ti-6Al-4V on SIGMA 1240 fibers. The SIGMA 1240 fiber is a tungsten cored ~100μm diameter silicon carbide fiber with a carbon-TiB_2 duplex coating. The near line of sight sputtering procedure resulted in an elliptical matrix coating with a small matrix grain size due to the low deposition temperature(~400C). A bundle of approximately 4000 matrix coated fibers, together with a centrally located sapphire fiber, was packed into a cylindrical canister. The sapphire fiber was supplied by Saphikon Inc. (New Hampshire) and was grown by an edge defined film fed growth (EFG) technique [32]. The canister consisted of a tube and two endcaps of commercially pure CP-2 titanium with a total length of 171mm, a diameter of 15.9 mm and a wall thickness of 1.6mm. The HIP canister was evacuated to the millitorr range and electron beam welded at Kin-Therm Inc.

The canister with coated fibers was then placed in an Asea Brown Boveri Autoclave Systems Inc. Minihipper and subjected to the consolidation cycle in Fig. 1. This cycle resulted in the complete densification of the composite and a SIGMA fiber fraction of 44.5%. The canister ends were subsequently removed to reveal the transverse plane of the fibers. The outer layer of can was left attached to the composite specimen (Fig. 2). One of the exposed sample ends was polished for the metallographic characterization and spectroscopic measurements. Micrographs of the embedded sapphire fiber and the surrounding SIGMA 1240 fiber and Ti-6Al-4V matrix material are shown in Figure 3.

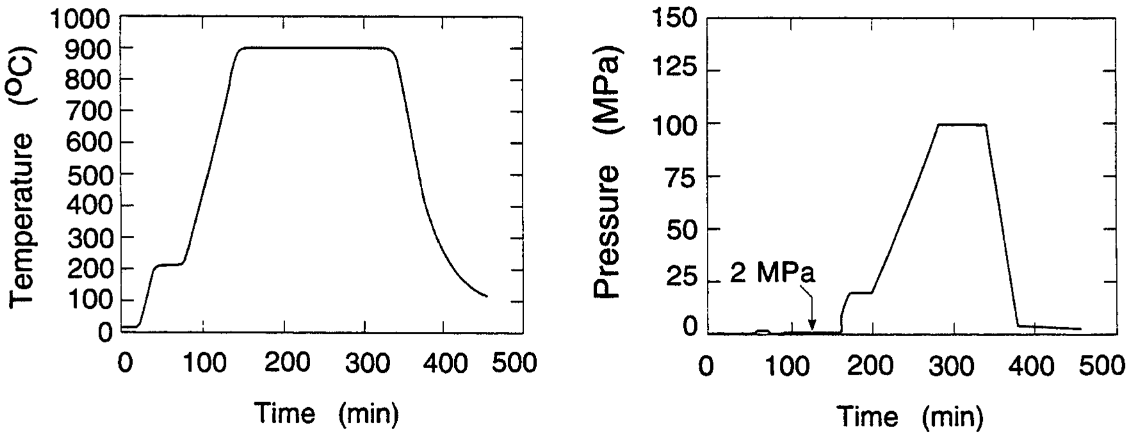

Figure 1. Temperature and Pressure cycle for the consolidation of the Ti-6Al-4V/Sigma 1240 Composite.

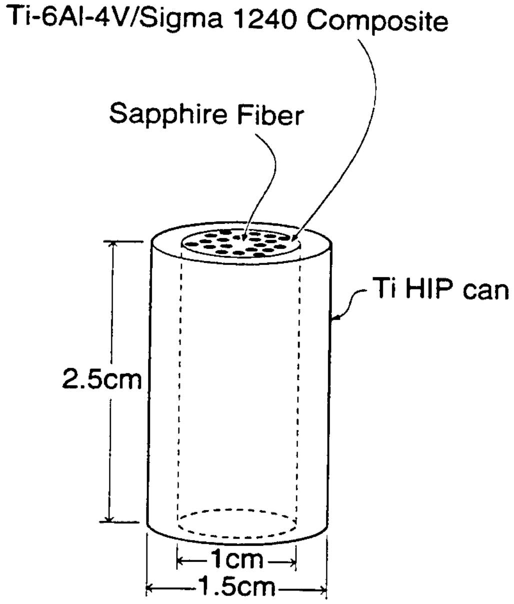
Ti-6Al-4V/Sigma 1240 Composite
Sapphire Fiber
Ti HIP can
2.5cm
1cm
1.5cm

Figure 2. Ti-6Al-4V/Sigma 1240 composite specimen with attached outer can and embedded sapphire fiber.

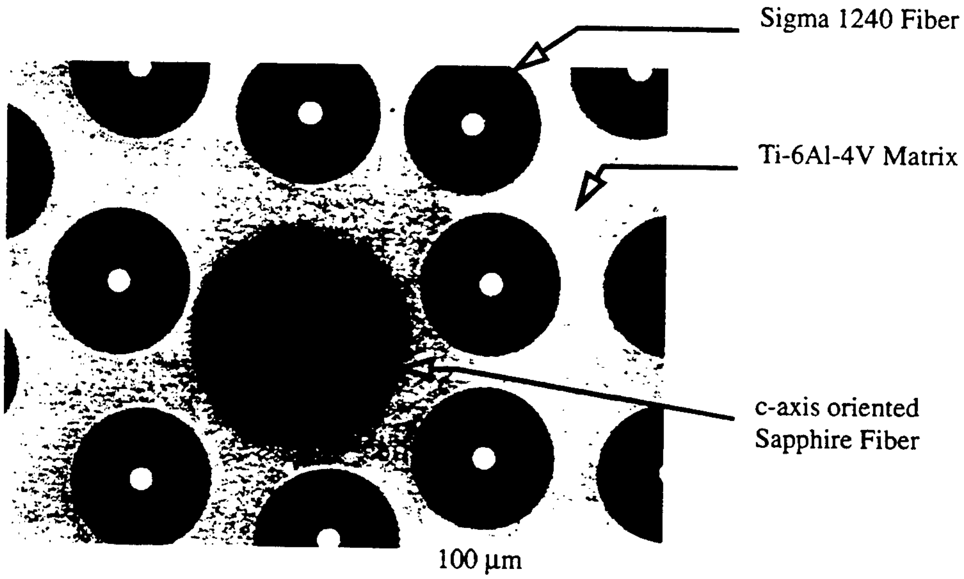
Sigma 1240 Fiber
Ti-6Al-4V Matrix
c-axis oriented
Sapphire Fiber
100 μm

Figure 3. SEM picture of the embedded sapphire fiber showing the local fiber and matrix layout

3.2. Spectroscopic measurements

Experimental data was collected using the fiber optic coupling system in Figure 4. An Ominchrome model 532-MAP air-cooled argon laser, set to lase at 514.5nm, was used to excite fluorescence in the chromium doped sapphire fiber. The laser beam was filtered through a $Cu(NO_3)_2$ filter to remove argon laser plasma lines, specifically the one at 696.543nm ($14358.94cm^{-1}$). The laser beam was then focused on to one end of a bifurcated optical fiber with a 5cm focal length convex lens. The common end of the bifurcated optical fiber was placed as close as possible to the end of fiber to be interrogated and aligned via a x-y-z stage to maximize the luminescence signal to the monochromator.

The second arm of the bifurcated fiber optic transmitted the luminescence signal to a 0.64m single grating monochromator(Instruments SA, model HR-640). Interfacing the fiber optic bundle to the monochromator slit was achieved using a 20mm and 60mm focal length convex lens. The slit used was 20mm in height and 11µm in width. The monochromator was equipped with a 110 x 110 mm flat grating with 1200groves/mm. The resolution at the R line luminescence wavelengths (~690nm) was approximately 0.017nm.

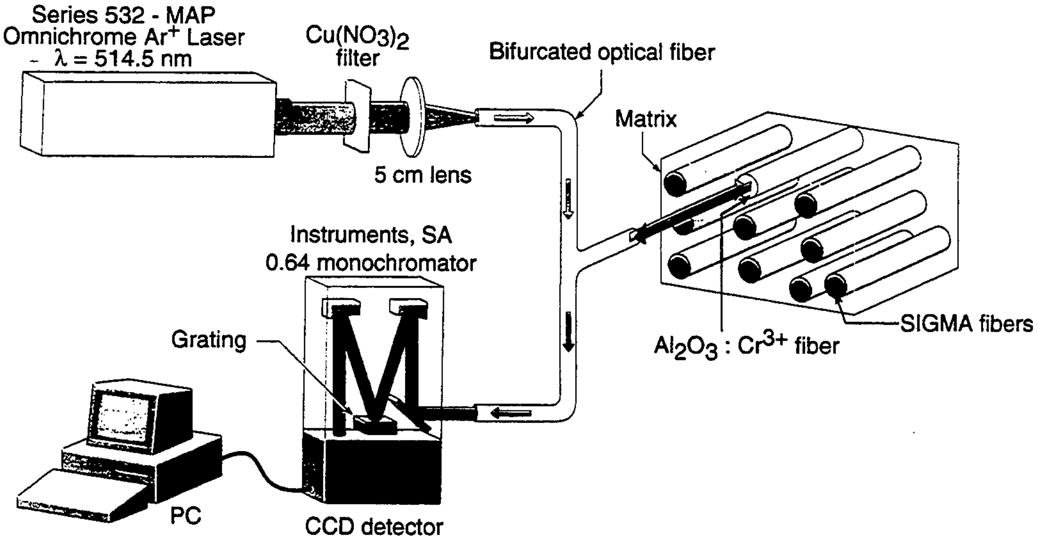
Series 532 - MAP
Omnichrome Ar+ Laser
- λ = 514.5 nm
Cu(NO3)2
filter
5 cm lens
Bifurcated optical fiber
Matrix
Instruments, SA
0.64 monochromator
Grating
Al2O3 : Cr3+ fiber
SIGMA fibers
PC
CCD detector

Figure 4. Schematic of experimental setup for luminescence measurements

A Spectraview-2D Charged-Coupled Device(CCD) was attached to the monochromator and used as a detector. The CCD array was a liquid nitrogen cooled array and has a spectral response from 400 to 1000nm. The signal from the CCD array was stored on a personal computer and the spectrum then fitted to a double lorentzian equation of the form

$$I(x) = \lambda_1 + \left[\frac{2}{\pi} \cdot \left(\frac{w_1 A_1}{w_1^2 + 4(x - p_1)^2} + \frac{w_2 A_2}{w_2^2 + 4(x - p_2)^2}\right)\right] \tag{5}$$

where I is the signal intensity, λ_1 is the background intensity level, A_1 and A_2 are the area of the peaks, w_1 and w_2 are the width of the peaks while p_1 and p_2 are the positions of the peaks are constants determined by the fitting routine. For the present problem a program was written using MATLAB^{TM} that fits the data to equation (5) using a nonlinear least square method. The algorithm used the Levenberg-Marquardt method to solve for the constants in equation (5).

3.3. Experiments

Spectra were obtained for the composite specimen as well as unstressed (unembedded) fibers to obtain a reliable unstressed peak position. Temperature was recorded for all samples by use of a Thinfilm RTD with an precision of ± 0.1°C (Omega Technologies Company). Continuous monitoring of the neon line at 692.7467nm insured that thermal fluctuations in the environment did not effect the measurements. Peak positions were then determined using of the method described and corrected for temperature variations using

$$\nu_i = \nu_i(T_o) + \alpha_i(T - T_{ref}) \tag{6}$$

where ν_i are the peak positions in cm^{-1}, α_i are the linear temperature correction coefficients for the R1 and R2 lines and T_{ref} is the reference temperature (23.0°C) to which all data was corrected. For the R1 peak, $\alpha_1 = -0.144 cm^{-1}/°C$, and for the R2 peak, $\alpha_2 = -0.134 cm^{-1}/°C$ [27]. The temperature corrected peak positions of the stressed fiber were then subtracted from the temperature correct peak positions of the unstressed fiber to get a peak shift, $\Delta\bar{\nu}$, due to the imposed stress state.

4. Results

A sample spectrum for the unembedded and embedded sapphire fibers is show in Figure 5. It is clearly seen that there is a shift to blue wavelengths (lower wavelength) for the embedded (stressed) sample which correlates with a large tensional (positive) stress component in the fiber. Temperature corrected peak positions for the unstressed and the embedded fibers are shown in Table 3. The errors for the measurements of peak positions for the individual fibers were calculated by finding the standard error of the mean for the fibers. From the data in Table 3, peak shifts due to imposed stresses can be calculated by subtracting the stressed peak positions from the unstressed peak positions. The peak shifts for the embedded fiber (Table 4) were then be used to calculate the stress components of the imposed stress state (Table 4) by inverting equation (4).

$$\sigma_{zz} = 1.275 \cdot \Delta\bar{v}_{R2} - 1.147 \cdot \Delta\bar{v}_{R1} \tag{7}$$

$$(\sigma_{rr} + \sigma_{\theta\theta}) = 0.909 \cdot \Delta\bar{v}_{R1} - 0.644 \cdot \Delta\bar{v}_{R2} \tag{8}$$

The stresses in Table 4 are positive tension for σ_{zz} component and small negative compressional values for the (σ_{rr} + $\sigma_{\theta\theta}$) component for the embedded fiber. The errors in stress were estimated by propagating the peak shift error through equations 7 and 8, and then computing the root mean error of the stress. The precisions is governed by the resolution of the spectrometer (0.017nm) and fluctuations in the temperature which creates thermal distortions in the grating and spectrometer.

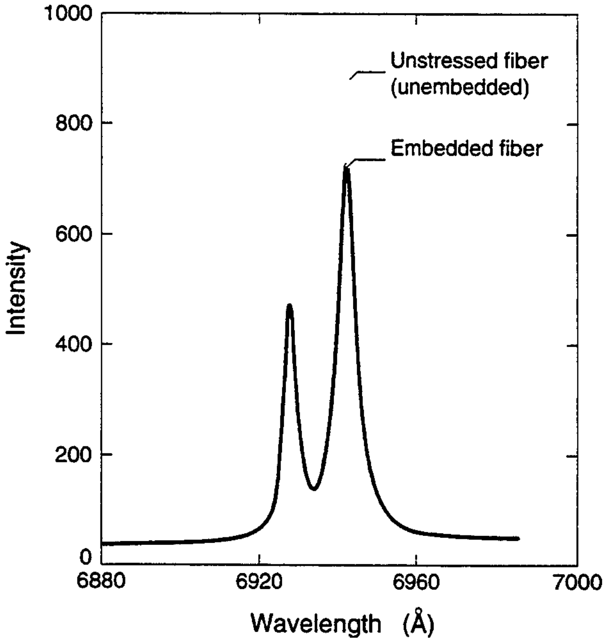

Figure 5. Luminescence spectra for the embedded fiber and an unembedded (unstressed) fiber showing a (blue) shift to shorter wavelength for the embedded fiber.

Table 3: R lines Peak Positions for an unstressed and an embedded fiber.

Fiber	ν_{R1}(cm^{-1})	ν_{R2}(cm^{-1})
Unstressed (unembedded) fiber	14403.24 ± 0.04	14433.08 ± 0.04
Embedded fiber	14404.41 ± 0.07	14434.81 ± 0.08

Table 4: R lines peak shifts and measured stress components for the embedded sapphire fiber in the Ti-6Al-4V/SIGMA 1240 composite

Fiber	$\Delta\bar{v}_{R1}(\mathrm{cm}^{-1})$	$\Delta\bar{v}_{R2}(\mathrm{cm}^{-1})$	σ_{zz} (MPa)	$\sigma_{rr} + \sigma_{\theta\theta}$ (MPa)
Embedded Fiber	1.16 ± 0.08	1.73 ± 0.09	876 ± 147	-61 ± 93

5. Modeling

The experimental system can be modeled using the generalized method cells (GMC) [33]. GMC accommodates materials that are either isotropic or transversely isotropic with either elastic or elastic-plastic constitutive behavior. The ability to model a material as transversely isotropic is necessary since the c-axis oriented sapphire fibers are not isotropic in nature. A GMC model analysis consists of four basic steps. The first is identification of a repeating volume element (RVE) which is the necessary amount composite material to be modeled for accurate result to be obtained. For the present problem the assumption that the sapphire fiber is effected by the material within three fiber diameters means the even though the RVE repeats its self in two dimensions the cell is large enough that adjacent sapphire fibers in repeated cells do not influence each other. This repeating volume element is then broken up into β x γ rectangular subcells and a material type is assigned to each subcell.

The macroscopic average stresses and strains in the RVE are then related to the microscopic stresses and strain of the individual subcells. Continuity of tractions and displacements in the average sense are the imposed on the interfaces between adjacent subcells. The continuity conditions along with microequilibrium establish a relation between microscopic total strains and plastic strains and the macroscopic strains by the use of the appropriate concentration tensors. The last step develops the overall macroscopic constitutive equations of the composite.

The Ti-6Al-4V, matrix metal, was modeled as an isotropic elastic-plastic material with a linear-hardening constitutive behavior. The sapphire fiber was modeled as a transversely isotropic elastic material while the SIGMA 1240 fibers were modeled as an isotropic elastic material. All of the material properties (CTE, Young's moduli, poisson's ratio, shear modulus, yield stress and hardening coefficient) were allowed to vary with temperature. The material property values used for the modeling are shown in the Appendix.

Using the micrograph of the embedded sapphire fiber shown if Figure 3, a 19x20 GMC grid was created for the region surrounding the embedded fiber. The temperature was decreased from 900°C to 25

°C and the stresses in each subcell computed. The average stresses in the sapphire fiber, the SIGMA fibers and the metal matrix were computed and are given in Table 5.

Table 5: Average modeled stresses using GMC in the constitutive material for the region near the embedded sapphire fiber.

Material	σ_{zz} (MPa)	$\sigma_{rr} + \sigma_{\theta\theta}$ (MPa)
Sapphire fiber	729	-1
Sigma 1240 fibers	-595	-76
Ti-6Al-4V matrix	376	58

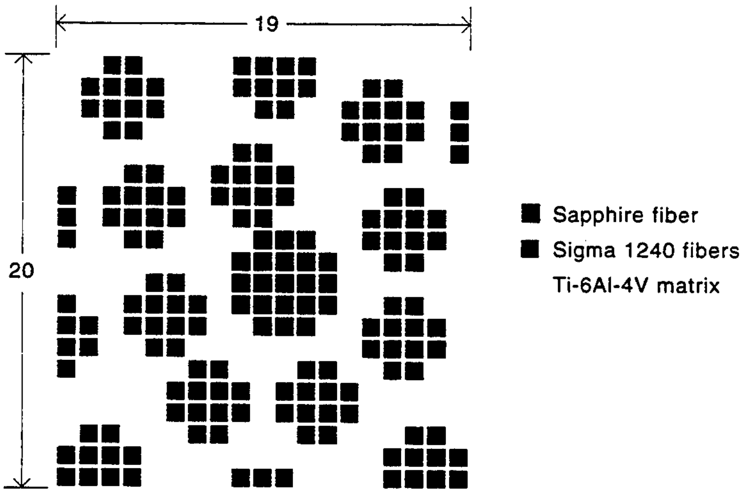

Figure 6. GMC grid for the embedded fiber showing the assigned subcells for the sapphire fiber, SIGMA 1240 fibers and Ti-6Al-4V matrix.

6. Discussion

Comparing the measured result for the embedded sapphire fiber in Table 4 to the GMC modeling results in Table 5, it is seen that the modeled results for the σ_{zz} and $\sigma_{rr} + \sigma_{\theta\theta}$ stresses are within the error of the measured values. The positive (tension) values in the sapphire fiber arises because its surroundings (composite) effective CTE is lower than that of the sapphire fiber even thought the Ti-6Al-4V matrix has a higher CTE than the sapphire fiber. A simple calculation for the effective CTE of the surrounding material can be made using a rule of mixtures. The axial CTE values at 25 °C for the SIGMA fiber, Ti-6Al-4V matrix, embedded sapphire fiber and the effective Ti-6Al-4V/SIGMA composite ($V_f = 44.5\%$) are given in Table 6.

Table 6: Axial CTE at 25 °C for the stated materials

Material	Axial CTE
SIGMA	$3.99 \times 10^{-6}/(°C)$
Ti-6Al-4V	$9.55 \times 10^{-6}/(°C)$
Sapphire	$7.67 \times 10^{-6}/(°C)$
Ti-6Al-4V/SIGMA ($V_f = 44.5\%$)	$6.90 \times 10^{-6}/(°C)$

Since the effective composite material outside of the sapphire fiber has a lower CTE in the axial direction than the sapphire fiber, the material as a whole can not shrink as much as the sapphire fiber in the axial direction, thus putting the sapphire into a state of tension axially. Thus by generating a modeled stress value that is equivalent to the measured stress value of the sapphire fiber, a mapping of the stress values to the stress in the SIGMA fibers and Ti-6Al-4V matrix surrounding the embedded sensing fiber can be accomplished

7. Summary

Luminescence sensing of an embedded sapphire fiber in a Ti-6Al-4V/Sigma 1240 composite has been accomplished. The measured result indicated that the sapphire fiber is in tension in the σ_{zz} component and a slight compression in the (σ_{rr}+$\sigma_{\theta\theta}$) component due to thermal cool down from consolidation temperature. The measured results were successfully predicted using the Generalized Method of Cell (Table 5). Further work needs to be done on the modeling of the sample to include the effect of tooling, pressure applied during cool down from consolidation temperature, creep of the matrix and can material and fiber alignment in the composite structure.

Acknowledgments

We would sincerely like to thank the help of Jacob Aboudi, Marek-Jerzy Pindera and Sarah Baxter in the implementation of the generalized method of cells. We would also like to thank D. Sypeck for help in obtaining SEM micrographs of the composite sample. This work was funded by the DARPA/ONR URI at Santa Barbara (S. Fishman, Program Manager).

References

1. D. L Anton and D. H. Shah, in *MRS Symposium Proceedings* (edited by C. T. Liu, A. I. Taub, N. S. Stoloff and C. C. Koch), Vol. 133, p. 361. MRS, Pittsburg (1989).
2. J. R. Stephens, in *Metal and Ceramic Matrix Composites: Processing, Modelling and Mechanical Behavior* (edited by R. B. Bhagat, A. H. Clauser, P. Kumar and A. M. Ritter), p. 3. TMS, Warrendale, PA (1990).
3. D. G. Bachman, *JOM* **42**, 17 (1990)
4. E. S. Russel, in *Thermal Structures and Materials for High Speed Flight* (edited by E. A. Thornton), *Progress in Astronautics and Aeronautics*, Vol. 140, p. 437. AIAA, Washingto D.C. (1992).
5. D. A. Hartwick and R. C. Cordi, in *Intermetallic Matrix Composites* (edited by D. L. Anton, P. L. Matrin, D. B. Miracle and R. McMeeking), Vol. 194, p. 65. MRS, Pittsburg (1990).
6. P. G. Partridge and C. M. Ward-Close, *Int. Mater. Rev.* **38**, 1 (1993).
7. H. E. Deve, D. M. Elzey, J. M. Warren and H. N. G. Wadley, in *Proc. 8th CIMTEC World Ceramic Congress and Forum on New Materials* (edited by P. Vincenzi), p. 313. Techna Srl, Faenze, Italy (1994).
8. P. K. Bradley, in *High Temperature Ordered Intermetallic Alloys II* (edited by N. S. Stoloff, C. C. Koch, C. T. Liu and O. Izumi), Vol. 81, p. 419. MRS, Pittsburg (1987).
9. I. W. Hall, J. L. Lim and J. Rizza, *J. Mater. Sci. Letter.* **10**, 263 (1991).
10. J. B. Davis, Y. Yang and A. G. Evans, *Acta metall. mater.* **43**, 259 (1995).
11. P. E. Cantonwine and H. N. G. Wadley, *Composite Eng.* **4**, 210 (1994).
12. J. M. Duva, W. A. Curtin and H. N. G. Wadley, *Acta metall. mater.* **43**, 1119 (1995).
13. J. F. Groves, D. M. Elzey and H. N. G. Wadley, *Acta metall. mater.* **40**, 2089 (1994).
14. R. Gampala, D. M. Elzey and H. N. G. Wadley, *Acta metall. mater.* **42** 3209 (1994).
15. R. Gampala, D. M. Elzey and H. N. G. Wadley, *Acta metall. mater.* **44** 1479 (1995).
16. H. Hough, J. Demas, T. O. Williams and H. N. G. Wadley, *Acta metall. mater.* **43**, 821 (1995).
17. T. Nakamura and S. Suresh, *Acta metall. mater.* **41**, 1665 (1993).
18. M. Taya and R. J. Arsenault, in *Metal Matrix Composites: Thermomechanical Behavior*, pp. 1-8. Pergamon Press, Oxford (1989)
19. J. M Larsen, W. C. Revelos and M. L. Gambone *Mater. Res. Soc. Proc.* **273**, 3 (1992).
20. Q. Ma and D. R. Clarke, *Acta metall. mater.* **41**, 1817 (1993).
21. J. H. Eggert, K. A. Goettel and I. F. Silvera, Phys. Rev B, 40, 5724 (1989).
22. A. L. Schawlow, in *Fine Structures and Properties of Chromium Fluorescence in Aluminum and Magnesium Oxide* (edited by J. R. Singer), pp.50-64. Columbia University Press, New York (1961)
23. R. A. Forman, G. F. Piermarini, J. D. Barnett and S. Block, *Science 176*, 284 (1972)
24. P. M. Bell, H. K. Mao and K. Goettel, *Science 226*, 542 (1984)
25. J. A. Xu, H. K. Mao and P. M. Bell, *Science 232*, 1404 (1986).
26. H. K. Mao, P. M. Bell., J. W. Shaner and D. J. Steinberg, *J. Appl. Phys.*, 49, 3276 (1978).
27. He and D. R. Clarke, *J. Am. Ceram. Soc.*, 78 [5], 1347 (1995).

28. L. Grabner, *J. Appl. Phys.*, 49 , 580 (1978).
29. A.L. Schawlow, A. K. Piksis and S. Sugano, *Phys. Rev.*, 122, 5, 1469 (1961)
30. A. A. Kaplyanskii and A. K. Przhevuskii, *Dokl. Akad. Nauk USSR* 142 313 (1962) [*Soviet Phys. Dokl.* 7, 37 (1962)]
31. E. Feher and M. D. Sturge, *Phys. Rev.* **172**, 244 (1968).
32. D. G. Backman, D. Wei, L. C. Filler, R. Irwin and J. Collins, in *Advanced Sensing, Modelling anc Control of Materials Processing* (edited by E. F. Matthys and B. Kushner), p. 3. The Minerals. Meatals and Materials Society, Warrendale, Pa (1992).
33. M. Paley and J. Aboudi, *Mech. of Mater.*, **14**, 127 (1992)
34. J. F. Durodola and B. Derby, *Acta. metall. mater.*, **42**, 5 , 1525 (1994).
35. U. Ramamurty, F.-C. Dary and F. W. Zok, *Acta. metall. mater.*, **44**, 8, 3397 (1996).
36. M.-J. Pindear, R. S. Salzar and T. O. Williams, *NASA Contractor Report 191142*, NASA Lewis Research Center, (1993).
37. J. Aboudi and M.-J. Pindera, *Int. J. Solids Structures*, **32**, 12, 1675 (1995).

Appendix

Table 7: Physical Properties used in modeling for a) sapphire fiber, b) SIGMA 1240 fiber and c) Ti-6Al-4V matrix

a) Sapphire [16]

Temp (°C)	α x (10^{-6} /C) c-axis	a-axis	E_{11} (GPa)	E_{33} (GPa)
24	7.64	6.76	423	460
100	7.76	6.86	420	457
300	7.84	7.12	413	451
500	8.27	7.36	405	445
700	8.45	7.58	398	439
900	8.58	7.77	391	433

Temp (°C)	ν_{12}	ν_{13}	G (GPa)
25	0.305	0.169	169.8
100	0.308	0.168	168.6
300	0.316	0.167	166.15
500	0.323	0.166	163.4
700	0.331	0.165	160.9
900	0.338	0.165	158.4

b) SIGMA 1240
[34,35,36]

Temp (°C)	E (GPa)	α x (10^{-6} /°C)	ν
25	360	3.99	.20
100	358	4.03	.20
300	354	4.16	.20
500	350	4.33	.20
700	346	4.47	.20
900	342	4.49	.20

c) Ti-6Al-4V [37]

Temp (°C)	E (GPa)	α x (10^{-6} /°C)	ν	σ_y (MPa)	SHP (GPa)
25	113.7	9.44	0.30	900	4.6
100	107.5	9.63	0.30	730	4.7
300	97.9	9.78	0.30	517	5.4
500	81.3	9.82	0.30	482	4.8
700	49.6	9.74	0.30	303	1.7
900	20.7	9.81	0.30	35	1.2

Motions of Microscopic Surfaces in Materials

Z. SUO

Mechanical and Environmental Engineering Department,
Materials Department
University of California,
Santa Barbara, CA

I. Introduction 194

II. Interface Migration: Formulation 196
  A. Nonequilibrium Thermodynamic Process 197
  B. Equation of Motion When Surface Tension Is Isotropic 201
  C. Weak Statement and Galerkin Method 202
  D. Geometric View 204
  E. Variational Principle 205
  F. Triple Junction; Equilibrium or Nonequilibrium 206

III. Interface Migration Driven by Surface Tension and Phase Difference . 209
  A. Spherical Particle in a Large Mass of Vapor 209
  B. Anisotropic Surface Tension: Rod- or Plate-Shaped Particles 211
  C. Self-Similar Profile: Thermal Grooving 212
  D. Steady-State Profile 215
  E. Grain-Boundary Migration in a Thin Film; Effect of Surface Evaporation 217
  F. Steady-Moving Interface Driven by Surface Tension and Phase Difference 221

IV. Interface Migration in the Presence of Stress and Electric Fields 222
  A. Free Energy 223
  B. Ellipsoidal Transformation Particle in Infinite Matrix under Remote Loading 227
  C. Growth of a Spherical Particle of Dilation 229
  D. Growth of a 180° Domain in Barium Titanate 230
  E. Explicit Formula for the Driving Pressure 234

V. Diffusion on Interface: Formulation 235
  A. General Considerations 235
  B. Differential Equations 238
  C. Weak Statements 241
  D. Multiple Kinetic Processes 244

VI. Shape Change due to Surface Diffusion under Surface Tension 245
  A. Rayleigh Instability 245
  B. A Row of Grains—A Model with Two Degrees of Freedom 250
  C. Grooving and Pitting 255
  D. Grain-Boundary Migration in Thin Film; Effect of Surface Diffusion 257
  E. Steady Surface Motion 259
VII. Diffusion on an Interface between Two Materials 261
  A. Rigid Inclusion Moving in a Matrix 262
  B. Diffusion-Controlled Interfacial Sliding 264
  C. Grain-Boundary Migration in Thin Film; Effect of Inclusion 266
VIII. Surface Diffusion Driven by Surface- and Elastic-Energy Variation ... 267
  A. Instability of a Flat Surface 268
  B. Pore-Shape Change 271
  C. Nosing, Cusping, and Subcritical Cracking 278
IX. Electromigration on Surface 279
  A. Surface Diffusion Driven by the Electron Wind 280
  B. Pore Drifting in the Electron Wind 283
  C. Pore Breaking Away from Trap 284
  D. Transgranular Slits 286
Acknowledgments 289
References 289

I. Introduction

Soap bubbles show up in kitchens, science museums, and popular books (e.g., Isenberg, 1978). There has long been a tradition of drawing analogies between soap films and microscopic surfaces in solids. The analogy, however, can be misleading. The air pressure in each bubble is uniform and relates to the bubble volume. The shapes of an assemblage of bubbles minimize the total film area for the given volume of every bubble. The shapes change when air is blown into the bubbles or diffuses across the films.

In solids, there exist phase boundaries, grain boundaries, domain walls, and bi-material interfaces. The stress in each solid grain is usually nonuniform, and the total surface area need not be minimal for given grain volumes. In addition to surface tension, the free energy results from stress, electric field, and composition gradient, etc. Kinetic processes include diffusion, creep, and reaction.

The motion of the microscopic surfaces affects material processing and performance. For a bulk material, an overall knowledge of the structure, such as the grain size distribution and pore volume fraction, is often adequate. For a film or a line, where the grain size is comparable to the film thickness and linewidth, an overall knowledge of structure is inadequate; for example, in submicron aluminum interconnects, the electromigration damage relates to structural details, e.g., crystalline texture, individual grain-boundary orientation (Thompson and Lloyd, 1993). In cases like this, the internal surfaces are better viewed as components of one single structure.

We can now analyze deformation in complex structures using general-purpose computer codes. It would help many technical innovations if we could do the same for the evolving structures in materials. With this in mind, this article reviews the recent development of an approach that treats surface motion in a way that resembles the finite element analysis of deformation. Attention is focused on two mass transport mechanisms: migration of, and diffusion on, an interface. Examples are also given for other mass transport mechanisms.

At the heart of the approach is a weak statement that combines the kinetic laws and the free energy variation associated with virtual surface motion. On one hand, this weak statement reproduces the differential equations of Herring (1951) and Mullins (1957). On the other hand, this weak statement forms the basis for various Galerkin-type methods. In the latter, a surface is described with a finite number of generalized coordinates, and the Galerkin procedure reduces the weak statement to a set of ordinary differential equations that evolve into the generalized coordinates.

Depending on one's purpose, one may describe a surface with either a few or many degrees of freedom. To study certain global aspects of the surface motion, one may describe the surface with a few degrees of freedom. Ideas in low-dimensional nonlinear dynamics apply. Even with a linear kinetic law, surface evolution is highly nonlinear because of large shape and topology changes. The surface may undergo instabilities and bifurcations.

Rigorously, a surface has infinitely many degrees of freedom. To resolve local details, one must describe the surface with many degrees of freedom. A systematic approach is to divide the surface into many small, but finite, elements and follow the motion of the nodes of the elements. The Galerkin procedure gives a viscosity matrix that connects the generalized forces and the generalized velocities. The procedure is analogous to the finite element analysis of deformation.

Most sections of this article may be read independently. The main exceptions are Sections II and V, which formulate, respectively, interface migration and interface diffusion. The subjects of all sections should be clear from the Table of Contents. Free energy is used throughout the article to study isothermal processes. (An entropy-based formulation is necessary if heat transfer plays a part.) The treatment is phenomenological with few references to the underlying atomic processes. Such continuum models are indispensable because a microstructural feature often contains a huge number of atoms. Technical processes are used to motivate the discussion, but the emphasis is on basic principles and simple demonstrations. Analytical solutions of several idealized models are included; they shed light on more complex phenomena, and may also serve as benchmark problems for general-purpose codes in the future. No attempt, however, has been made to review the literature exhaustively. By focusing on the principles and demonstrations, the reader should grasp what this line of thinking has to offer, and integrate it to his or her own way of thinking.

II. Interface Migration: Formulation

This section demonstrates the basic principles by examining a classical model with very few ingredients. An interface separates either two materials, or two phases of the same atomic composition, or two grains of the same crystalline structure. The free energy that drives the interface migration has contributions from many origins. This section includes only the interface tension, and the free-energy difference between the two phases in bulk.

Many kinetic processes may determine the velocity of the interface motion. If a phase transition generates a large amount of heat, such as during freezing, heat diffusion often limits the interface velocity. If the two phases have different compositions, such as in solution precipitation, mass diffusion in the phases often limits the interface velocity. In addition to diffusing over long range, atoms must leave one phase, cross the interface, and join the other phase. This last process will be referred to as interface migration. This section analyzes the situations in which long-range heat and mass diffusion are absent or rapid, so that the interface process limits its velocity.

This model arises from many phenomena; see Taylor *et al.* (1992) for a literature survey. The presentation here focuses on the free energy variation associated with the virtual motion of the interface, leading to a weak statement. The weak statement, much like its counterparts in continuum mechanics, is the basis for finite element methods. It has been used, for example, by Sun *et al.* (1994) to study void shape change in an elastic crystal via surface reaction, and by Cocks and Gill (1995) to study grain growth.

A. NONEQUILIBRIUM THERMODYNAMIC PROCESS

To be definite, here we will visualize the model in terms of one of its many applications: a solid particle in contact with its vapor. Atoms either condense from the vapor, or evaporate from the solid, both causing the interface to move. Imagine a situation in which atoms diffuse rapidly in the vapor, but react slowly on the interface, so that the vapor maintains a uniform composition and pressure. The vapor phase is in one equilibrium state, and the solid phase is in another equilibrium state. The two phases, however, are *not* in equilibrium with each other, so that one phase grows at the expense of the other. The ingredients of this nonequilibrium thermodynamic model follow.

1. *Free Energy*

Let γ be the surface tension (i.e., the free energy per area of the interface), which may depend on crystalline orientation. Let g be the difference in the free energy density of the two phases (i.e., the free energy increase associated with the condensation of unit volume of the solid). The introduction of the solid particle into the vapor changes the free energy of the entire system by

$$G = \int \gamma dA + gV. \tag{2.1}$$

The integral extends over the interface area A, and V is the volume of the solid particle. We will assume that the particle is immersed in a large mass of the vapor, so that g is constant as the reaction proceeds.

When the surface tension is isotropic (i.e., independent of crystalline orientation), $G = \gamma A + gV$. Thermodynamics requires that the reaction proceed to decrease the free energy. The surface tension is positive and therefore strives to decrease the surface area. When the solid surface is concave, such as a dent on a flat surface, γ favors condensation. When the solid surface is convex, such as a hillock on the surface, γ favors vaporization. The free energy density difference between the two phases, g, can be either positive or negative. When $g > 0$, it favors vaporization and reduces the particle volume. When $g < 0$, it favors condensation and increases the particle volume. In general, both γ and g affect interface motion.

2. *Virtual Migration and Driving Pressure*

Free energy by itself is insufficient to determine the particle shape change, because countless ways of shape change would reduce the free energy. To evolve the particle shape, the model needs more ingredients.

Figure 1 illustrates the motion of an interface by mass exchange between the solid and the vapor. A *virtual migration* of the interface is a small movement in the direction normal to the interface that need not

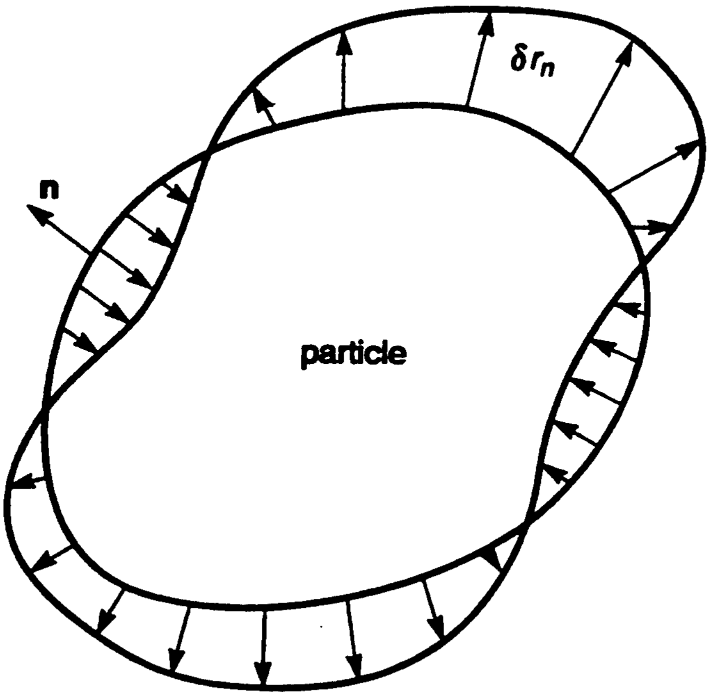

FIG. 1. An interface between a solid and a vapor undergoes a virtual motion. The magnitude of the virtual migration, δr_n, should be small, and may vary over the interface.

obey any kinetic law. The amount of the motion, δr_n, can differ from point to point over the interface. Associated with the virtual migration, the free energy varies by δG. Define a thermodynamic force, $\mathscr{P}$, as the free energy decrease associated with adding unit volume of atoms to the particle, namely,

$$\int \mathscr{P} \delta r_n \, dA = -\delta G. \tag{2.2}$$

The integral extends over the interface area. The virtual motion, δr_n, is an arbitrary function of the position on the interface, and (2.2) uniquely defines the quantity $\mathscr{P}$ at every point on the surface; an explicit formula is given later. The quantity has a unit of pressure (force/area or energy/volume), and has been variably called driving pressure, driving stress, or driving traction.

3. *Kinetic Law*

Let v_n be the *actual velocity* of the interface in the direction normal to the interface (i.e., the volume of atoms added to the particle per area per time). The actual velocity is taken to be a function of the driving pressure. Specifically, the velocity is taken to be linearly proportional to the driving pressure:

$$v_n = L\mathscr{P}. \tag{2.3}$$

Here L is the mobility of the interface. This quantity will be used as a phenomenological parameter of the model, to be determined by comparing model predictions with experimental observations. Thermodynamics requires that the interface move in the direction that reduces the free energy G, so that $L > 0$. Extension to nonlinear kinetic relations can be made (e.g., Loge and Suo, 1996).

The considerations above define the dynamics of surface motion. At a given time, the free energy variation determines the driving pressure, and the kinetic law updates the particle shape for a small time step. The process repeats for many time steps to evolve the surface.

The driving force is defined at every point on the surface, which is then used to specify the kinetic law. Such a kinetic law is local in that the rate at a point only depends on the force at this point. By no means is such a law universally correct. For example, crystal may grow at a step around a screw dislocation. The present approach is subject to the common restriction of a continuum theory: the theory applies when the length scale of interest is much larger than the length scale characteristic of defects.

4. *Atomic Origin of Interface Migration Mobility*

Before continuing with the phenomenological treatment, we make a digression and consider briefly the atomistic origin of L. One can obtain L from an atomistic picture of the reaction process. Formulas obtained this way may give approximately correct dependence on variables such as temperature, with parameters such as activation energy fitted to experimental data.

Consider, for example, an interface of two phases of the same composition, e.g., a grain boundary. The interface moves as atoms leave one phase, cross the interface, and attach to the other phase. Turnbull (1956) showed that the interface velocity is linear in the driving pressure if $\Omega\mathscr{P} \ll kT$, where Ω is the atomic volume, k Boltzmann's constant, and T the absolute temperature. The interface motion involves the same atomic process as self-diffusion on the interface. The interface mobility L relates to the self-diffusivity on the interface D by $L = \Omega^{2/3}D/kT$. The self-diffusivity is given approximately by $D = \nu b^2 \exp(-q/kT)$, where ν is the frequency of atomic vibration, b the atomic spacing, and q the activation energy for one atom to jump from one position to another.

This connection between L and D, however, is an oversimplification. For example, impurity atoms segregated to a grain boundary can affect L and D disproportionally. This empirical fact has long been used in ceramic sintering; impurities are added to inhibit grain growth without retarding densification.

As another example, consider a single-element crystal in contact with its vapor. Atoms in the two phases exchange at the interface by evaporation and condensation. Mullins (1957) showed for this case $L = p_0\Omega^2(2\pi m)^{-1/2}(kT)^{-3/2}$, where p_0 is the vapor pressure in equilibrium with the flat solid surface, and m the mass per atom. The process considered by Mullins involves the rate of the atoms of the vapor hitting the surface, and the atoms of the solid emitting to the vapor. The reaction on the surface is instantaneous, with no activation barrier. In general, however, a multielement crystal and a vapor of several molecular species react on the interface with activation barriers.

B. EQUATION OF MOTION WHEN SURFACE TENSION IS ISOTROPIC

When surface tension is isotropic, the solid-vapor interface at a given time is usually a smooth surface in three dimensions. The surface has the properties commonly studied in differential geometry: the area of a surface element dA; the unit vector normal to the surface $\mathbf{n}$, taken to direct the vapor phase; and the principal radii of curvature R_1 and R_2, taken to be positive for a convex particle. Of particular interest is the sum of the principal curvatures,

$$K = \frac{1}{R_1} + \frac{1}{R_2}.$$

Associated with the virtual migration δr_n, the interface area varies by

$$\delta A = \int K \delta r_n \, dA$$

and the particle volume varies by

$$\delta V = \int \delta r_n \, dA.$$

The integrals extend over the interface.

When the surface tension is isotropic, the free energy is $G = \gamma A + gV$. Consequently, associated with the virtual motion of the surface, the free energy varies by

$$\delta G = \int (\gamma K + g) \, \delta r_n \, dA. \qquad (2.4)$$

A comparison of (2.4) and (2.2) gives

$$\mathscr{P} = -\gamma K - g. \qquad (2.5)$$

This equation expresses the driving pressure in terms of the geometric parameter, K, and the energetic quantities, γ and g. As expected, γ tends to drive the surface in the direction toward the center of curvature, and g tends to cause the solid to shrink if $g > 0$.

A combination of (2.3) and (2.5) leads to

$$v_n = -L(\gamma K + g). \qquad (2.6)$$

This partial differential equation governs the interface motion.

Equation (2.5) contains the special case $\mathscr{P} = -\gamma K$, known as the Laplace-Young relation for liquid films (e.g., Isenberg, 1978), where $\mathscr{P}$ is the pressure difference between the two neighboring bubbles. This relation results from the equilibrium of a liquid film under the pressure difference and the surface tension. Such interpretations are misleading for a phase boundary in solid state.

C. WEAK STATEMENT AND GALERKIN METHOD

The partial differential equation (2.6) is not a good way to look at the general problem for several reasons. First, (2.6) is incorrect when surface tension is anisotropic. Second, because the problem in general has to be analyzed approximately, a partial differential equation need not be a good starting point. The following weak statement circumvents the difficulties of anisotropy, and leads to the Galerkin method in numerical analysis. Other merits of the weak statement will become evident as the subject develops.

Completely ignore Section B, and start from Section A again. Replace the driving pressure $\mathscr{P}$ in (2.2) with the interface velocity v_n by using the kinetic law (2.3), giving

$$\int \frac{v_n}{L} \delta r_n \, dA = -\delta G. \tag{2.7}$$

Make the following statement: the actual velocity, v_n, must satisfy (2.7) for virtual migration δr_n of *arbitrary* distribution on the interface. Following the terminology of variational calculus, we refer to this as the *weak statement* of the problem.

One may find an approximate interface velocity that satisfies (2.7) for a family of virtual motions (instead of *arbitrary* virtual motions). Obviously, the larger the family, the more accurate the approximation. This consideration leads to the Galerkin method, a formal presentation of which follows.

Model the surface with n degrees of freedom, writing $q_1, \ldots q_n$ for the generalized coordinates, and $\dot{q}_1, \ldots \dot{q}_n$ for the generalized velocities. For example, a sphere has one degree of freedom, its radius; a rod has two degrees of freedom, its radius and height; a general surface may be modeled by an assembly of triangles, with the positions of the vertexes being the generalized coordinates. Describe a surface by expressing the position vector on the surface, $\mathbf{x}$, as a function of two surface coordinates,

s_1 and s_2, and the time t. Using the generalized coordinates, we express the position vector as $\mathbf{x}(s_1, s_2; q_1, \ldots, q_n)$, with the time implicitly contained in the generalized coordinates.

The free energy is a function of the generalized coordinates, $G(q_1, q_2, q_3, \ldots)$. The generalized forces, $f_1, \ldots, f_n$, are the differential coefficients of the free energy, namely

$$\delta G = -f_1\,\delta q_1 - f_2\,\delta q_2 - \cdots - f_n\,\delta q_n\,. \tag{2.8}$$

Once the free energy function is known, the generalized forces are calculated from $f_i = -\partial G/\partial q_i$.

The virtual motion of the surface, δr_n, is linear in the variations of the generalized coordinates:

$$\delta r_n = \sum \left(\mathbf{n} \cdot \frac{\partial \mathbf{x}}{\partial q_i}\right) \delta q_i \equiv \sum N_i \delta q_i\,. \tag{2.9}$$

The shape functions N_i depend on the generalized coordinates. The interface velocity is linear in the generalized velocities:

$$v_n = \sum N_i \dot{q}_i\,. \tag{2.10}$$

Substituting the above into the weak statement, (2.7), we obtain

$$\sum_{i,j} H_{ij}\dot{q}_j\,\delta q_i = \sum_i f_i \delta q_i\,, \tag{2.11}$$

where

$$H_{ij} = \int \frac{N_i N_j}{L}\,dA. \tag{2.12}$$

Equation (2.11) holds for arbitrary virtual changes δq_i, so that the coefficient for each δq_i must equal. Thus,

$$\sum_j H_{ij}\dot{q}_j = f_i\,. \tag{2.13}$$

Equation (2.13) is a set of linear algebraic equations for the generalized velocities. Once solved, they update the generalized coordinates for a small time step. The process is repeated for many steps to evolve into the surface. Because the matrix H and the force column f depend on the generalized coordinate column q, (2.13) is a nonlinear dynamical system.

The physical interpretation of the matrix H is evident from (2.13): the element of the matrix, H_{ij}, is the resistant force in the q_i-direction when the state moves at unit velocity in q_j-direction. We will call H the viscosity matrix. From (2.12), H depends on the generalized coordinates but is independent of the generalized velocities or the positions on the interface. The viscosity matrix is symmetric and positive-definite.

D. GEOMETRIC VIEW

One can visualize the above formulation in geometric terms (Sun *et al.*, 1996, Yang and Suo, 1996). Imagine a hyperspace with the free energy as the vertical axis, and the generalized coordinates as the horizontal axes. The free-energy function, $G(q_1, q_2, q_3, \ldots)$, is a surface in this space, to be called the energy landscape. A point on the landscape represents in general a nonequilibrium state of the system, described with a set of values of the generalized coordinates and a value of the free energy. The bottoms of valleys on the landscape represent equilibrium states of the system.

A curve on the landscape represents an evolution path of the system. Thermodynamics requires that the system evolve to reduce the free energy, and therefore the evolution path be a descending curve on the landscape. Starting from any point other than a valley bottom on the landscape, infinite descending curves exist. Consequently, thermodynamics by itself does not set the evolution path. Nor does thermodynamics select one valley as a final equilibrium state among several valleys. The evolution path is set by thermodynamics and kinetics acting together.

At a point on the landscape, the slopes of the landscape represent the generalized forces. The Galerkin procedure assigns a viscosity matrix H at every point on the landscape. The generalized velocities are determined by $\dot{q} = H^{-1}f$, which gives the direction and magnitude of the incremental motion on the landscape. The evolution path is thus determined incrementally.

This global, geometric view does not add any new information to the problem, but does give an intuitive feel for a complex system. If the energy landscape contains several valleys, the one that will be reached by the system as the final equilibrium state will also depend on kinetics. A change in the kinetic parameters, without changing the energy landscape, may shift the system from moving to one valley to another. An example is given in Section VI.B. In the language of nonlinear dynamics, we say that the change of kinetic parameters changes the basins of attraction. Clearly, this is a universal theme of material processing.

E. VARIATIONAL PRINCIPLE

The following variational principle is equivalent to the weak statement in Section C. In numerical analysis, these two forms lead to an identical set of ordinary differential equations. In the remainder of the article, we will use the weak statement exclusively. The variational principle is included here for completeness.

Let $\overline{\omega}$ be a virtual interface velocity distribution, which need not satisfy any kinetic law. Associated with the virtual velocity, the free energy changes at rate $\dot{G}$. Introduce a functional

$$\Pi = \dot{G} + \int \frac{\overline{\omega}^2}{2L}\, dA, \tag{2.14}$$

which is a combination of the virtual free-energy rate and a term associated with the virtual rate. The functional is purely a mathematical construct, and has no clear physical meaning. Given an arbitrary virtual velocity distribution $\overline{\omega}$, one can compute a value of Π.

The variational principle is now stated: Of all the virtual velocity distribution $\overline{\omega}$, the actual distribution v_n minimizes Π.

The proof of the principle follows. According to (2.2), the virtual free energy rate is

$$\dot{G}(\overline{\omega}) = -\int \mathscr{P}\overline{\omega}\, dA,$$

which is linear in the virtual velocity. Consequently, the difference in Π is

$$\Pi(\overline{\omega} + v_n) - \Pi(v_n) = \dot{G}(\overline{\omega}) + \int \frac{v_n}{L}\overline{\omega}\, dA + \int \frac{\overline{\omega}^2}{2L}\, dA.$$

The actual velocity satisfies the kinetic relation $v_n/L = \mathscr{P}$. According to (2.2), the sum of the first two terms vanishes. Thus,

$$\Pi(\overline{\omega} + v_n) - \Pi(v_n) = \int \frac{\overline{\omega}^2}{2L}\, dA.$$

This is nonnegative for any virtual velocity distribution, hence the proof.

F. TRIPLE JUNCTION; EQUILIBRIUM OR NONEQUILIBRIUM

1. *Force on Triple Junction*

If the solid particle is polycrystalline, the free energy becomes

$$G = \gamma_S A_S + \gamma_b A_b + gV. \tag{2.15}$$

Here γ_S is the surface tension of the solid-vapor interface, γ_b the surface tension of the grain boundaries, A_S the area of the interface, and A_b the area of the grain boundaries. For simplicity, both surface tensions are taken to be isotropic.

As an example, Figure 2 shows that a grain boundary and two surfaces form a triple junction, i.e., a line in the third dimension. The length of the junction is l, and the two surfaces meet at angle Ψ (i.e., the dihedral angle). Move the junction by δy and the surfaces by δr_n, resulting in a virtual change in the free energy, δG. Define the driving force on the triple junction, f, and the driving force on the surface, $\mathscr{P}$, simultaneously by

$$fl\delta y + \int \mathscr{P}\delta r_n \, dA = -\delta G. \tag{2.16}$$

This is an extension of (2.2).

We may postulate separate kinetic laws for the junction and surface motion:

$$\dot{y} = L_t f, \; v_n = L\mathscr{P}, \tag{2.17}$$

where $\dot{y}$ is the velocity of the triple junction, L_t the junction mobility, and L the surface mobility. Equations (2.16) and (2.17) complete the modification.

One can find an explicit expression for the force on the triple junction. When the junction moves by distance δy, the area of the grain boundary

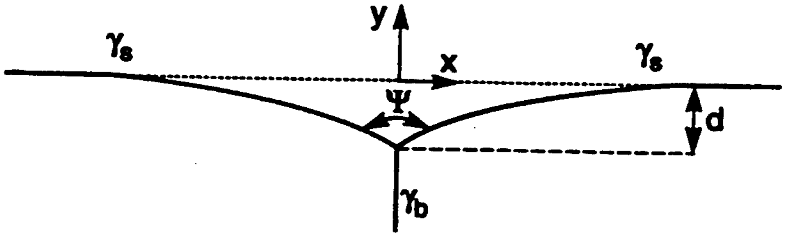

FIG. 2. A triple junction formed by a grain boundary and two free surfaces.

changes by $l\delta y$, and the area of the two surfaces changes by $-2\cos(\Psi/2)l\delta y$. Consequently, associated with the virtual motion of the junction and the surfaces, the free energy changes by

$$\delta G = \left(-2\gamma_S \cos\frac{\Psi}{2} + \gamma_b\right)l\delta y + \int(\gamma_S K + g)\,\delta r_n\,dA. \tag{2.18}$$

A comparison of (2.16) and (2.18) gives the expressions for the two driving forces:

$$f = 2\gamma_S \cos\frac{\Psi}{2} - \gamma_b,\ \mathscr{P} = -\gamma_S K - g. \tag{2.19}$$

The driving force on the junction, f, has a clear interpretation: it is the sum of the surface tensions projected along the y-axis. In this example, because of symmetry, we only need to consider the motion in the y direction. If the junction can move in both x and y directions, there are driving forces in both directions.

One can also include junction motion into the weak statement. Replace the forces in (2.16) with the velocities by using the kinetic laws (2.17), giving

$$\frac{\dot{y}}{L_t}l\delta y + \int\frac{v_n}{L}\,\delta r_n\,dA = -\delta G. \tag{2.20}$$

The actual velocities, $\dot{y}$ and v_n, satisfy (2.20) for arbitrary virtual motions, δy and δr_n. In this weak statement, the surface tension for both the grain boundary and the surfaces can be anisotropic, provided the free energy G is evaluated by a surface integral of the surface tension.

2. *Equilibrium Triple Junction*

The triple junction is commonly assumed to be in equilibrium at all times, even when the surfaces still move. That is, the driving forces on the triple junction vanish at all times. For the present example, setting $f = 0$ in (2.19) results in the well-known expression for the equilibrium dihedral angle Ψ_e:

$$\cos\frac{\Psi_e}{2} = \frac{\gamma_b}{2\gamma_S}. \tag{2.21}$$

This relation fixes the slope of the surfaces at the junction.

The assumption of equilibrium junction is justified by the relative rate of the junction motion and surface motion. It only takes a small number of atomic adjustments to reach the equilibrium angle, so that the time needed for the overall grain shape change is limited by the surface motion. The idea can be made definite as follows. Let d be a length scale that one likes to resolve from the model, e.g., the depth of the surface groove caused by the grain boundary underneath. The effect of the junction mobility is negligible if $L_t d/L \gg 1$.

Assume equilibrium junction is equivalent to prescribing an infinitely large junction mobility. Consequently, the first term in the weak statement (2.20) drops, which then becomes identical to (2.7). The weak statement (2.7) simultaneously determines the surface velocity and enforces the triple junction equilibrium. In applying the Galerkin procedure to the weak statement (2.7), one need not fix the dihedral angle to the equilibrium value. Rather, the equilibrium dihedral angle comes out as a part of the solution, approximately in a short time, consistent with the level of approximation of the entire surfaces.

In the terminology of variational calculus, the equilibrium dihedral angle is a *natural boundary condition*, which is enforced by the weak statement itself. The position of the end of the surface is an *essential boundary condition*, which must be enforced in addition to the weak statement.

3. *Nonequilibrium Triple Junction*

Situations exist where the junction mobility plays a role. For example, impurities segregated to the junctions may reduce the junction mobility, retarding the overall surface motion. The effect should be pronounced if the grain size is very small.

From (2.21), the junction may reach equilibrium only when $\gamma_b < 2\gamma_S$—that is, when the grain boundary is energetically more favored than two surfaces. If $\gamma_b > 2\gamma_S$, equilibrium will not be reached until the grain boundary is completely replaced by two parallel surfaces. In this case, a finite junction mobility prevents the junction from running at an infinite velocity.

Another example involves atomic decohesion along a grain boundary when the body is subject to a tensile stress normal to the grain boundary. The triple junction may be out of equilibrium, and the dihedral angle between the two free surfaces approaches 0°, instead of the equilibrium value of (2.21). The unbalanced force at the triple junction may drive a reaction that leads to the environmentally-assisted cleavage. Section VIII.C discusses a similar situation.

III. Interface Migration Driven by Surface Tension and Phase Difference

This section gives examples of interface migration under surface tension and free energy density differences between the two phases. Finite element schemes have been formulated on the basis of the weak statement (Cocks and Gill, 1995; Du *et al.*, 1996; Sun *et al.*, 1997). It is too early to judge them critically. Instead, this section gives an elementary demonstration of the Galerkin procedure, and describes several analytical solutions.

A. SPHERICAL PARTICLE IN A LARGE MASS OF VAPOR

When a small solid particle is introduced into a large mass of a vapor, the particle may change both shape and volume, as atoms evaporate to, or condense from, the vapor. We start with the simplest situation where the surface tension is isotropic and the solid particle is spherical. The system has only one degree of freedom, the radius of the sphere.

1. *Free Energy*

The introduction of a spherical particle of radius R into a large mass of vapor changes the free energy by

$$G = 4\pi R^2\gamma + \frac{4}{3}\pi R^3 g. \tag{3.1}$$

Here γ is the surface tension, and g the free-energy density difference between the two phases; γ is always positive, but g can be either positive or negative. If $g > 0$, the volume term reduces the free energy when the particle shrinks. If $g < 0$, the volume term reduces the free energy when the particle grows. We will concentrate on the case $g < 0$. Figure 3(a) sketches the free energy as a function of the particle radius. As R increases, G first increases when the surface term in (3.1) dominates, and then decreases when the volume term dominates.

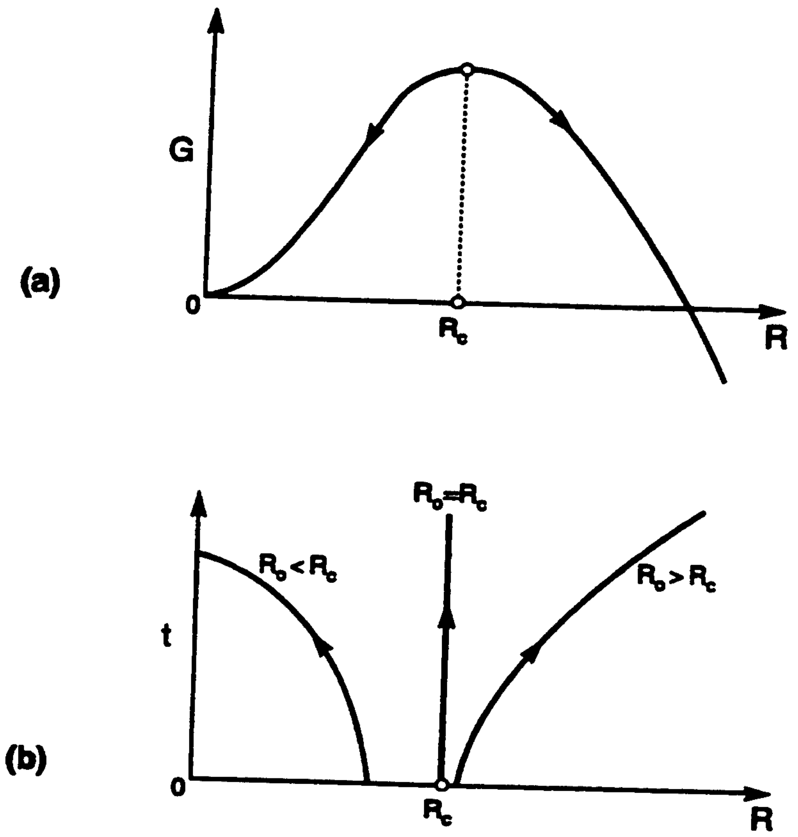

FIG. 3. A small solid particle in contact with a large mass of its vapor ($g < 0$). a) Free energy as a function of the particle radius. b) Particle of different initial radii evolve with the time.

The free energy maximizes at a finite particle radius, R_c. The significance of this maximum is readily understood. Imagine a particle of radius $R \neq R_c$. Thermodynamics requires that the particle change size to reduce G. If $R < R_c$, the particle shrinks to reduce G. If $R > R_c$, the particle grows to reduce G. The critical particle radius is determined by setting $dG/dR = 0$, giving

$$R_c = -2\frac{\gamma}{g}. \tag{3.2}$$

The two energetic parameters, γ and g, have different dimensions; their ratio defines this length.

2. *Kinetics*

Section II.B applies because the surface tension is isotropic. The driving pressure on the surface of the spherical particle of radius R is

$$\mathscr{P} = -\frac{2\gamma}{R} - g. \tag{3.3}$$

The kinetic law (2.3) relates the surface velocity to the driving pressure:

$$\frac{dR}{dt} = -L\left(\frac{2\gamma}{R} + g\right). \tag{3.4}$$

This ordinary differential equation governs the particle radius as a function of the time, $R(t)$. The energetic competition shows up again: the particle growth rate is positive if $R > -2\gamma/g$, and negative if $R < -2\gamma/g$.

Let R_0 be the particle radius at time $t = 0$. The solution to (3.4) is

$$(R - R_0) + R_c \ln\left|\frac{R - R_c}{R_0 - R_c}\right| = -Lgt. \tag{3.5}$$

Figure 3(b) sketches the radius as a function of the time. The behavior depends on the initial radius. A supercritical particle ($R_0 > R_c$) grows with the time without limit. A subcritical particle ($R_0 < R_c$) shrinks and disappears.

B. ANISOTROPIC SURFACE TENSION: ROD- OR PLATE-SHAPED PARTICLES

In the example above, the free energy alone decides whether the particle grows or shrinks, and the kinetics sets the time. This division in roles between energies and kinetics comes about because the system has only one degree of freedom. As discussed in Section II.D, when the system has more than one degree of freedom, the free energy alone does not determine the evolution path or the final equilibrium state. The following example has two degrees of freedom, and is used to illustrate the Galerkin procedure.

Imagine a crystal having anisotropic surface tension such that it grows to a prism with a square cross section. When a small particle of such a crystal is introduced into its vapor, it has two degrees of freedom: the base side B and the height C. The surface tensions on the prism bases and sides are γ_1 and γ_2, and the mobilities are L_1 and L_2. When the crystal grows by unit volume at the expense of the vapor, the phase change alone increases the free energy by g. The total free energy of the system, relative to the vapor without the particle, is

$$G(B,C) = 2\gamma_1 B^2 + 4\gamma_2 BC + gB^2C. \tag{3.6}$$

Associated with the virtual changes δB and δC, the free energy varies by

$$\delta G = (4\gamma_1 B + 4\gamma_2 C + 2gBC)\,\delta B + (4\gamma_2 B + gB^2)\,\delta C. \qquad (3.7)$$

The kinetic term on the left-hand side of (2.7) is

$$\int \frac{v_n}{L}\,\delta r_n\,dA = \frac{\dot{B}BC}{L_2}\,\delta B + \frac{\dot{C}B^2}{2L_1}\,\delta C. \qquad (3.8)$$

The weak statement requires that the sum of the two equations above vanish. Collect the coefficients of δB and δC, giving

$$\dot{B} = -L_2\left(\frac{4\gamma_1}{C} + \frac{4\gamma_2}{B} + 2g\right), \dot{C} = -L_1\left(\frac{8\gamma_2}{B} + 2g\right). \qquad (3.9)$$

These are coupled ordinary differential equations, to be integrated numerically once the initial particle dimensions are given. No numerical results will be presented here.

Brada *et al.* (1996) have used this approach to study coarsening of grains of a crystal with high surface-tension anisotropy. See Carter *et al.* (1995) for a demonstration of the effects of surface-tension anisotropy.

C. SELF-SIMILAR PROFILE: THERMAL GROOVING

In a polycrystalline particle, a grain boundary intersects with the particle surface, forming a triple junction, Figure 2. When heated, the surface *grooves* at the triple junction. The problem was solved by Mullins (1957). The surface motion reduces the grain-boundary area but increases the surface area, so that the total free energy decreases. Mass relocates by either evaporation or surface diffusion. This section summarizes Mullins' analysis for evaporation; Section VI.C will summarize his analysis for surface diffusion. When the groove depth d is so small that $gd/\gamma \to 0$, the effect of g on grooving is negligible. Mullins assumed that $g = 0$, namely, the vapor is in equilibrium with the flat solid surface. The groove depth is taken to be much smaller than the grain size, so that the two grains in Figure 2 are infinitely large. This is a two-dimensional problem in the plane normal to the triple junction.

In Figure 2, the x-axis coincides with the surface remote from the groove, and the y-axis with the grain boundary. Describe the surface shape at time t by function $y(x, t)$. The curvature of the surface is

$$K = -\frac{\partial^2 y/\partial x^2}{\left[1 + (\partial y/\partial x)^2\right]^{3/2}}.$$

The velocity normal to the surface is

$$v_n = \frac{\partial y/\partial t}{\left[1 + (\partial y/\partial x)^2\right]^{1/2}}.$$

The equation of motion (2.6) becomes

$$\frac{\partial y}{\partial t} = L\gamma_s \frac{\partial^2 y/\partial x^2}{1 + (\partial y/\partial x)^2}. \tag{3.10}$$

The initial and boundary conditions are as follows. The surface is initially flat, i.e.

$$y(x,0) = 0. \tag{3.11}$$

The surface remote from the groove is immobile at all times:

$$y(\pm\infty, t) = 0. \tag{3.12}$$

The triple junction is taken to be in equilibrium during grooving, so that the two surfaces meet at the equilibrium dihedral angle, Ψ_e, given by (2.21). This dihedral angle fixes the slope of the surface at the triple junction:

$$\frac{\partial}{\partial x} y(0,t) = m \equiv \frac{\cos(\Psi_e/2)}{\sin(\Psi_e/2)} = \frac{\gamma_b}{(4\gamma_s^2 - \gamma_b^2)^{1/2}}. \tag{3.13}$$

The partial differential equation (3.10), the initial condition (3.11), and the boundary conditions (3.12) and (3.13) determine the evolving surface profile, $y(x,t)$.

The initial geometry has no length scale, but the time and the mobility set a length scale, $\sqrt{L\gamma_s t}$. Consequently, the groove grows with a self-similar profile. Define the dimensionless coordinates:

$$X = \frac{x}{\sqrt{L\gamma_s t}}, Y = \frac{y}{\sqrt{L\gamma_s t}}. \tag{3.14}$$

Describe the groove profile by a function $Y(X)$. The partial differential equation (3.10) becomes an ordinary differential equation

$$2\frac{d^2Y}{dX^2} + \left[1 + \left(\frac{dY}{dX}\right)^2\right]\left(X\frac{dY}{dX} - Y\right) = 0. \tag{3.15}$$

The initial condition (3.11) and the boundary condition (3.12) both become

$$Y(\infty) = 0. \tag{3.16}$$

The boundary condition (3.13) becomes

$$\frac{d}{dX}Y(0) = m. \tag{3.17}$$

The boundary-value problem (3.15)–(3.17) is integrated numerically (Sun *et al.*, 1997). Figure 4 shows the groove profile for various dihedral angles. For a system with a larger ratio γ_b/γ_s, the dihedral angle Ψ_e is smaller, and the groove is deeper.

When the ratio γ_b/γ_s is small, the slope of the surface, dY/dX, is small. Dropping the high-order term $(dY/dX)^2$ in (3.15), the ordinary differential equation is linear, so that the groove depth must be linear in m. Mullins' (1957) calculation showed that, under the small-slope approximation, the groove depth is

$$d \approx 1.13m\sqrt{L\gamma_s t}\,. \tag{3.18}$$

Figure 5 plots the numerical solutions of the groove depth determined by both the exact and the linearized equations, indicating that Mullins' linear approximation is good for most purposes. The exact nonlinear solution has been used as a benchmark to check the accuracy of a finite element code (Sun *et al.*, 1997).

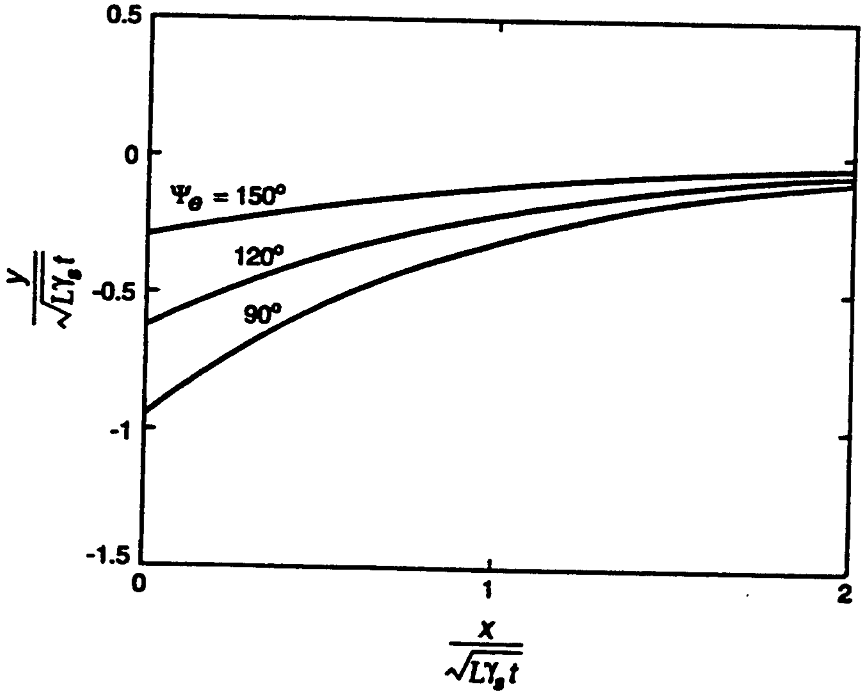

FIG. 4. The profile of the groove over a grain-boundary caused by evaporation.

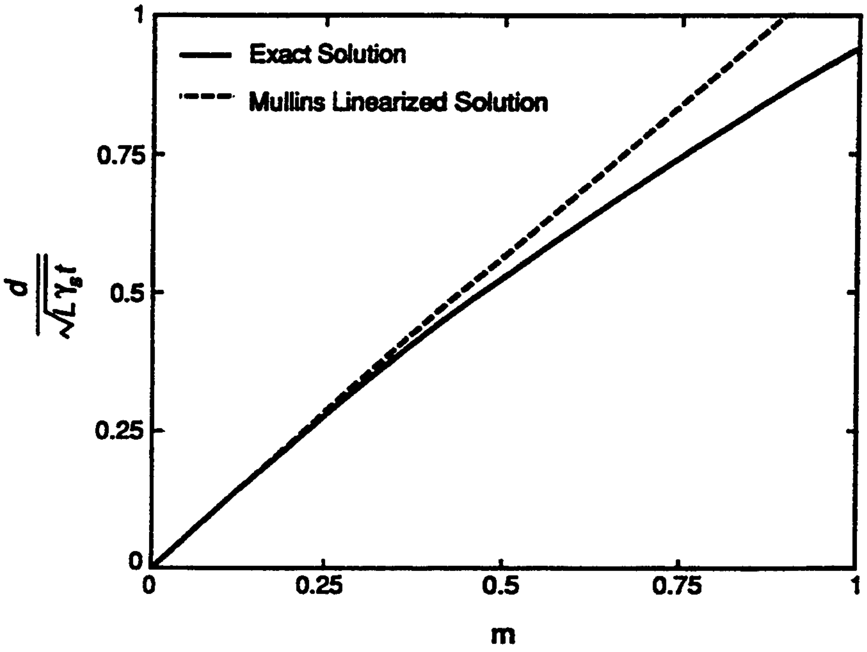

FIG. 5. The groove depth as a function of parameter m, which relates to the ratio γ_b/γ_s by (3.13).

D. STEADY-STATE PROFILE

1. *General Solution*

Mullins (1956) studied the steady-state surface motion, i.e., the entire surface moves in the same direction at the same velocity. The motion is motivated by surface tension, and the mass transport mechanism is evaporation-condensation. Both the surface tension and the mobility are taken to be isotropic. The governing equation is (2.6), setting $g = 0$. Figure 6 shows a surface moves in the y-direction at velocity v. The coordinates x and y move with the surface. A plane problem is considered where the surface shape is invariant along the axis normal to the x-y plane.

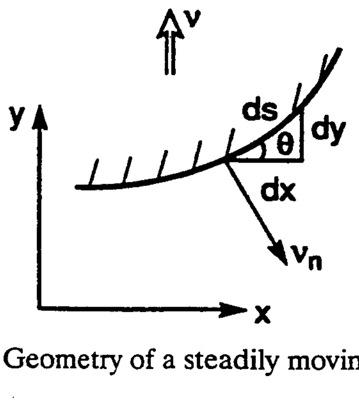

FIG. 6. Geometry of a steadily moving surface.

Let ds be the curve element, θ the angle of the element from the x-axis. Surface tension drives the surface to move toward the center of the curvature. Consequently, the surface must concave in the direction of the velocity, and the slope is restricted between $-\pi/2 \leq \theta \leq \pi/2$. According to our sign convention, the curvature, $K = d\theta/ds$, is positive on the entire curve, and the normal surface speed is $v_n = -v\cos\theta$. Equation (2.6) becomes

$$v \cos \theta = \frac{L\gamma d\theta}{ds}. \tag{3.19}$$

Observing that $\cos \theta \, ds = dx$, one readily integrates the above equation, giving

$$x = \frac{L\gamma}{v} \theta + x_0, \tag{3.20}$$

where x_0 is a constant to be determined by the boundary conditions. Similarly, with $\sin \theta \, ds = dy$, one integrates (3.19) and obtains

$$y = -\frac{L\gamma}{v} \ln(\cos \theta) + y_0, \tag{3.21}$$

where y_0 is another constant to be determined by the boundary conditions. Equations (3.20) and (3.21) together describe the shape of the steadily moving surface, with θ as a parameter. The following paragraphs illustrate simple applications.

2. *Steady-State Grooving*

When the groove size becomes appreciable relative to the grain size, the grooves of two adjacent grain boundaries interact, and the self-similar solution in Section III.C is no longer valid. The particle surface may recede with a profile and velocity independent of the time. Consider an idealized geometry with periodic grain boundaries of spacing D, Figure 7. The dihedral angle Ψ relates to the ratio γ_b/γ_s by (2.21). The surfaces move down to decrease the area of the grain boundaries, with no further

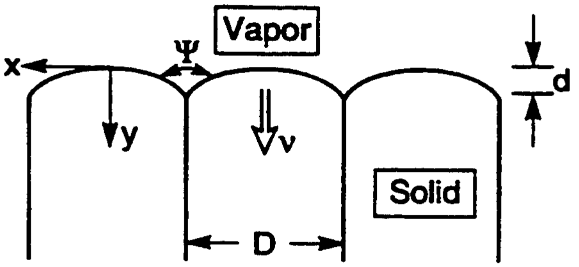

FIG. 7. Steady-state grooving over periodic grain boundaries caused by evaporation.

change in the surface area. The slopes are $\theta = \pm(\pi - \Psi)/2$ at the two adjacent triple junctions $x = \pm D/2$. With these as the boundary conditions, (3.20) determines the velocity:

$$v = (\pi - \Psi)\frac{L\gamma_s}{D}, \tag{3.22}$$

which is inversely proportional to the grain size. Equation (3.21) determines the groove depth:

$$\frac{d}{D} = -\frac{\ln\left(\sin\dfrac{\Psi}{2}\right)}{\pi - \Psi}. \tag{3.23}$$

3. *Velocity of an Abnormally Growing Grain*

Under certain conditions, in a polycrystal one grain grows much larger than the others, at the expense of the neighboring grains (Hillert, 1965). In Figure 7 replace the vapor phase with the large grain, and keep the small grains of size D. For one reason or another, the small grains do not grow, but the boundary between the large grain and the small grains moves with the mobility L_b. All the grain boundaries have the same surface tension γ_b, so that the dihedral angle is $\Psi = 2\pi/3$. Equation (3.22) becomes

$$v = \frac{\pi L_b \gamma_b}{3D}. \tag{3.24}$$

The large grain grows at a velocity inversely proportional to the size of the small grains.

E. GRAIN-BOUNDARY MIGRATION IN A THIN FILM; EFFECT OF SURFACE EVAPORATION

Consider a polycrystalline film on a single crystal substrate. The grains have a columnar structure. Due to crystalline anisotropy, some grains have lower film-surface tension and film-substrate interface tension than other grains. When the film is heated, the grains with low combined surface and interface tensions grow at the expense of other grains. The survival grains may have (in-plane) diameters much larger than the film thickness.

For example, Thompson *et al.* (1990) studied a thin Au film on a (100) surface of NaCl substrate. When the film is deposited at room temperature, the Au grains are very small and are of several orientations. After anneal at 325°C for three hours, the grains grow and the survival grains are predominantly of (111)Au ‖ (001)NaCl, with two in-plane orientations, $[1\bar{1}0]$Au ‖ [110]NaCl and $[1\bar{1}0]$Au ‖ $[1\bar{1}0]$NaCl. The two types of grains are crystallographically equivalent, and therefore have the same free energy. When the equivalent grains impinge, they stop growing. The NaCl substrate has a fourfold symmetry, and the (111) Au grains have a threefold symmetry. Minimization of the free energy in this case does not require lattice matching.

Yet another phenomenon may intervene: grooving at the intersections of the grain boundaries and the film surface may break the film. Assuming that the grain boundaries are immobile, Srolovitz and Safran (1986) and Miller *et al.* (1990) showed that the film breaks into islands if the ratio of the grain size to the film thickness exceeds a critical value. Miller *et al.* (1990) demonstrated that the prediction is consistent with the observation of a ZrO_2 film on a single crystal Al_2O_3 substrate.

Clearly the two processes—grain-boundary migration and surface grooving—compete to determine the fate of a polycrystalline film. Grain-boundary migration may lead to a large-grained, continuous film. Surface grooving may break the film into islands. Mullins (1958) analyzed the effect of grooving on grain-boundary motion, where the surface grooves via surface diffusion. He obtained a steady-state solution for a moving triple junction, but left the velocity of the motion undetermined because the grain-boundary motion was not analyzed. In simulating grain growth in thin films, Frost *et al.* (1992) modeled the effect of grooving by setting a threshold curvature in the kinetic law, below which grain boundaries remain stationary.

Brokman *et al.* (1995) analyzed a grain boundary moving in a thin sheet, including both surface diffusion and grain-boundary migration, which allow them to determine the steady-state velocity. In an independent study, Sun *et al.* (1997) analyzed a similar problem with either surface diffusion or surface evaporation. The following discussion draws on these studies, assuming surface evaporation. Surface diffusion will be discussed in Section VI.D.

1. *Grain-Boundary Motion When the Surface Remains Flat*

First imagine that the surface of the film is immobile and remains flat as the grain boundary migrates, Figure 8(a). The in-plane grain size is much larger than the film thickness, so that we focus on one grain boundary and

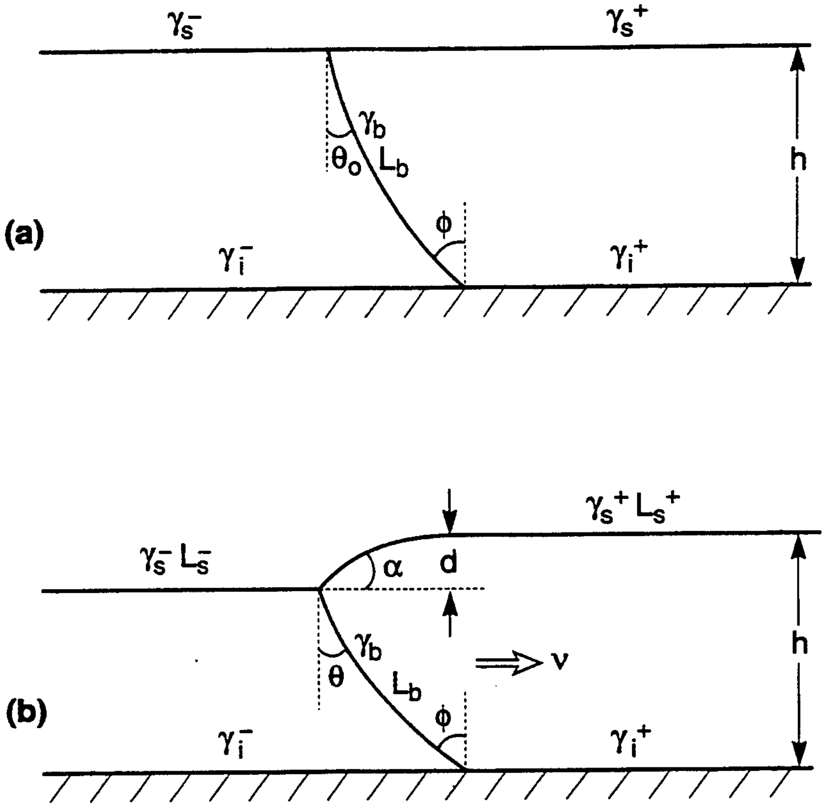

FIG. 8. A grain boundary migrates in a thin film. a) The free surface is immobile and remains flat. b) The free surface grooves due to evaporation.

ignore all the others. The two grains, labeled as + and −, have different surface tensions γ_s^+ and γ_s^-, and interface tensions γ_i^+ and γ_i^-. Denote the grain-boundary tension by γ_b, and the grain-boundary mobility by L_b. The grain boundary is taken to migrate to the right.

Because the film surface and the film-substrate interface are immobile, at the triple junctions the surface tensions do not balance in the vertical direction. Junction equilibrium in the horizontal direction determines the two angles in Figure 8(a):

$$\sin\phi = \frac{\gamma_i^+ - \gamma_i^-}{\gamma_b}, \sin\theta_0 = \frac{\gamma_s^- - \gamma_s^+}{\gamma_b}. \tag{3.25}$$

In the steady-state motion, the grain boundary is concave to the right, so that the two angles must satisfy $\phi > \theta_0$. Using (3.25), this condition becomes

$$\gamma_s^- + \gamma_i^- < \gamma_s^+ + \gamma_i^+ . \tag{3.26}$$

Thus, grain − must have smaller free energy than grain + for the grain boundary to migrate to the right.

The general solution (3.20) determines the grain-boundary velocity:

$$v = \frac{L_b \gamma_b (\phi - \theta_0)}{h}. \tag{3.27}$$

In the limiting case when both ϕ and θ_0 are small, (3.25) and (3.27) give

$$v = \frac{L_b[(\gamma_i^+ + \gamma_s^+) - (\gamma_i^- + \gamma_s^-)]}{h}$$

This limiting result reproduces that of Thompson *et al.* (1990).

2. *Simultaneous Grain-Boundary Migration and Surface Evaporation*

Now two kinetic processes occur simultaneously: the grain boundary migrates at mobility L_b, and the surface evaporates at mobility L_s, Figure 8(b). Assume that the vapor is in equilibrium with a flat-film surface, but atoms at the triple junction can evaporate. The entire configuration moves at a uniform speed v to the right. All the moving surfaces must concave in the direction of the velocity. The surface of the new grain must be straight, because a curved surface would concave to the wrong direction. Evaporation causes the new grain to be thinner than the parent grain by d.

Equilibrium at the top triple junctions in both horizontal and vertical directions requires that

$$\sin\theta = \frac{(\gamma_b)^2 + (\gamma_s^-)^2 - (\gamma_s^+)^2}{2\gamma_b\gamma_s^-}, \quad \gamma_s^+ \sin\alpha = \gamma_b \cos\theta. \tag{3.28}$$

The film-substrate interface is immobile, so that the angle ϕ is the same as in (3.25). The steadily moving grain boundary must concave in the direction of the velocity. Consequently, the two angles must satisfy $\phi > \theta$, namely

$$\gamma_i^+ - \gamma_i^- > \frac{(\gamma_b)^2 + (\gamma_s^-)^2 - (\gamma_s^+)^2}{2\gamma_s^-}. \tag{3.29}$$

An application of (3.20) to the grain boundary and to the surface of grain + gives

$$v(h - d) = L_b\gamma_b(\phi - \theta), \quad vd = L_s^+ \gamma_s^+ \alpha.$$

Solving the equations, we have the velocity

$$v = \frac{1}{h}[L_b \gamma_b (\phi - \theta)_+ L_s^+ \gamma_s^+ \alpha] \tag{3.30}$$

and the groove depth

$$\frac{d}{h} = \frac{1}{1 + \dfrac{L_b \gamma_b (\phi - \theta)}{L_s^+ \gamma_s^+ \alpha}}. \tag{3.31}$$

The thickness of the new grain depends, among other things, on the mobility ratio.

The effect of surface evaporation on the grain-boundary motion may be appreciated as follows. In the limiting case $L_S \ll L_b$, the groove depth is negligible compared to the film thickness (3.31). Even in this case, a tiny amount of evaporation significantly affects the grain-boundary motion by rotating the surfaces at the triple junction. Take, for example, $\gamma_s^+ = \gamma_s^- = \gamma_b$. Without evaporation (Figure 8(a)), $\theta_0 = 0°$; the grain boundary can move steadily to the right if $\phi > 0°$, i.e., if the two grains have infinitesimal differences in the film-substrate interface tensions. With evaporation (Figure 8(b)), $\theta = 30°$; the grain boundary can move steadily to the right if $\phi > 30°$, i.e., if the two grains have a finite difference in the film-substrate interface tensions.

On the basis of the weak statement (2.7), Sun *et al.* (1997) used finite elements to simulate the non-steady motion. When $\phi > \theta$, an initial configuration quite different from the steady-state quickly settles down to the steady-state. When $\phi < \theta$, the grain boundary drags the triple junction toward the substrate, and finally breaks the film.

F. STEADY-MOVING INTERFACE DRIVEN BY SURFACE TENSION AND PHASE DIFFERENCE

Under the small slope assumption, Brokman *et al.* (1995) gave an approximate steady-state solution for an interface driven by both surface tension and phase difference. The exact steady-state solution to the full nonlinear equation (2.6) follows. The problem has a length scale,

$$l = \gamma / g. \tag{3.32}$$

With the reference to Figure 6, $v_n = -v \cos \theta$ and $K = d\theta/ds$, (2.6) becomes

$$\frac{ds}{l} = \frac{d\theta}{c \cos \theta - 1}, \tag{3.33}$$

with the dimensionless constant being

$$c = \frac{v}{Lg}.$$

Noting that $dx = \cos ds$ and $dy = \sin \theta \, ds$, one can integrate (3.33) to give

$$\frac{x}{l} = \begin{cases} \dfrac{\theta}{c} + \dfrac{1}{c\sqrt{1-c^2}} \tan^{-1}\left(\dfrac{\sqrt{1-c^2}\sin\theta}{c - \cos\theta}\right) + \dfrac{x_0}{l}, & c^2 < 1 \\ \dfrac{\theta}{c} + \dfrac{1}{c\sqrt{c^2-1}} \tanh^{-1}\left(\dfrac{\sqrt{c^2-1}\sin\theta}{c - \cos\theta}\right) + \dfrac{x_0}{l}, & c^2 > 1 \end{cases} \tag{3.34}$$

$$\frac{y}{l} = -\frac{1}{c} \ln |c \cos \theta - 1| + \frac{y_0}{l}. \tag{3.35}$$

Here x_0 and y_0 are integration constants to be determined by boundary conditions.

IV. Interface Migration in the Presence of Stress and Electric Fields

In many material processes, elastic and electrostatic fields allow additional means of free-energy variation. For example, during a phase transition, the difference in the crystalline structures of the two phases induces a stress field (e.g., Eshelby, 1970; Abeyartne and Knowles, 1990; Lusk, 1994; Rosakis and Tsai, 1994). In a polycrystalline film, grains of different orientations have different elastic energy densities due to elastic or plastic anisotropy (e.g., Sanchez and Arzt, 1992; Floro *et al.*, 1994). In a ferroelectric crystal, domains of different polar directions have different elastic and electrostatic fields (e.g., Pompe *et al.*, 1993; Roytburd 1993; Jiang, 1994).

The main concepts in Section II.A still apply, with the modification that the free energy G includes the elastic energy and electrostatic energy. This, in turn, requires that the stress and electric fields be solved as boundary-value problems. After the fields are solved and the free energy

G computed, (2.2) defines the driving pressure on an interface, $\mathscr{P}$. The kinetic law (2.3) then updates the position of the interface.

The weak statement (2.7) still applies. A two-step finite element method would proceed as follows. At a given time, the first step solves the boundary-value problem of the stress and electric fields by using a conventional finite element code. The second step updates the interface position according to (2.13), where the driving forces on interface nodes can be calculated with a procedure described by Socrate and Parks (1993), and the viscosity matrix calculated according to (2.12). The whole procedure repeats for the next time increment. The approach would allow a relatively crude mesh to determine the elastic and electric field.

Often, the mismatch strain is too large to be accommodated elastically, and dislocations appear to partially relieve the stress. Similarly, electric charge carriers diffuse to partially accommodate the polarization mismatch. Finite element approach could also treat relaxation due to combined plastic deformation, electric conduction, and interface migration. These important effects are beyond the scope of this article and will be ignored. This section collects basic equations and gives elementary demonstrations.

A. FREE ENERGY

1. *Field Equations*

Subject a solid insulator to a field of displacement $\mathbf{u}$ and electric potential ϕ. The strain tensor $\mathbf{e}$ and the electric field vector $\mathbf{E}$ are the gradients:

$$e_{ij} = \frac{1}{2}(u_{i,j} + u_{j,i}), \quad E_i = -\phi_{,i}. \tag{4.1}$$

The conventional index notation is adopted. The insulator is separated into domains by interfaces (or domain walls). Consider an interface between two domains labeled as $+$ and $-$, with the unit vector normal to the interface, $\mathbf{n}$, pointing to domain $+$. Force $\mathbf{t}$ and charge ω are externally supplied on per unit area of the interface. The body force and the space charge inside the domains are taken to be negligible. In a domain both stress tensor σ and electric displacement vector $\mathbf{D}$ are divergence free:

$$\sigma_{ij,i} = 0, \quad D_{i,i} = 0. \tag{4.2}$$

Across the interface, they jump by

$$n_i[\sigma_{ij}^- - \sigma_{ij}^+] = t_j, \quad n_i[D_i^- - D_i^+] = -\omega. \tag{4.3}$$

Applying the divergence theorem, one obtains

$$\int t_i u_i \, dA = \int \sigma_{ij} e_{ij} \, dV, \quad \int \omega \phi \, dA = \int D_i E_i \, dV. \tag{4.4}$$

The integrals extend over the interface area A and the volume V. The equations above hold for any constitutive law.

2. *Free-Energy Density Function*

We will make the standard local equilibrium assumption: a free-energy function exists for every phase in the crystal, even though the crystal as a whole is not in equilibrium. At a fixed temperature, the Helmholtz free energy per unit volume of a phase, W, is a function of the strain and the electric displacement, $W(\mathbf{e}, \mathbf{D})$. When the state of the crystal varies, the energy density varies by

$$dW = \sigma_{ij} de_{ji} + E_i \, dD_i. \tag{4.5}$$

Once the energy density function is prescribed, the field equations and the boundary conditions define the boundary-value problem.

The crystal also stores energy in interfaces. Denote the surface energy per unit area of an interface by γ. An interface is assumed to be a sharp transition within a few atomic layers, so that electro-mechanical field is unaffected by the interface tension, and the interface tension unaffected by the electro-mechanical field.

3. *Free Energy of a Polydomain Crystal*

Prescribe a distribution of traction $\mathbf{t}$ and electric potential ϕ on the external surface of the crystal. On the part of the surface where the electric potential is not prescribed, e.g., the interface between the crystal and the air, we assume that negligible electric field lines escape from the crystal. This is a good approximation for a crystal having a large permittivity, where the prescribed electric potential does work on the crystal, not on the air.

The combination of the energy function and the field equations defines an electro-mechanical boundary-value problem. Once the field is solved, the Gibbs free energy of the entire crystal is calculated from

$$G = \int \gamma \, dA + \int W dV - \int \phi \omega \, dA - \int t_i u_i \, dA. \tag{4.6}$$

The first integral extends over the interfaces, the second over the volume of the body, the third over the potential-prescribed surface, and the fourth over the traction-prescribed surface.

4. *Deep-Well Approximation*

So far, the free-energy density W can be an arbitrary function of the electric displacements and strains. A useful approximation has often been adopted. Figure 9(a) illustrates the free-energy density for a one-dimensional model of a ferroelectric crystal at a fixed temperature. When the temperature is far below the Curie point, the free-energy density has two *deep wells* at D_s and $-D_s$, corresponding to the spontaneous polar states. Due to crystal symmetry, the spontaneous states have the same free energy, g. Figure 9(b) shows the *D*-*E* curve derived from the free energy function, $E = dW/dD$. The peak, E_c, is the field needed to switch polarization uniformly over the entire crystal, which is often much larger than the field needed to cause domain wall motion. Consequently, the state in each domain is near one of the spontaneous states, with approximately a linear *D*-*E* relation.

Consider in general a spontaneous state with the strain $\mathbf{e}^{(s)}$, the electric displacement $\mathbf{D}^{(s)}$, and the Helmholtz free energy per unit volume $g^{(s)}$. Expand the free energy density function by the Taylor series around this spontaneous state, retaining up to the quadratic terms:

$$\begin{aligned} W^{(s)} = g^{(s)} &+ \frac{1}{2} C_{ijkl}^{(s)} \left(e_{ij} - e_{ij}^{(s)} \right) \left(e_{kl} - e_{kl}^{(s)} \right) \\ &+ \frac{1}{2} \beta_{ik}^{(s)} (D_i - D_i^{(s)}) (D_k - D_k^{(s)}) \\ &+ h_{ikl}^{(s)} (D_i - D_i^{(s)}) (e_{kl} - e_{kl}^{(s)}) \end{aligned} \tag{4.7}$$

The first-order terms vanish because the stress and the electric field vanish at the spontaneous state. The coefficients C, β, and h characterize the elastic, dielectric, and piezoelectric responses near the spontaneous state.

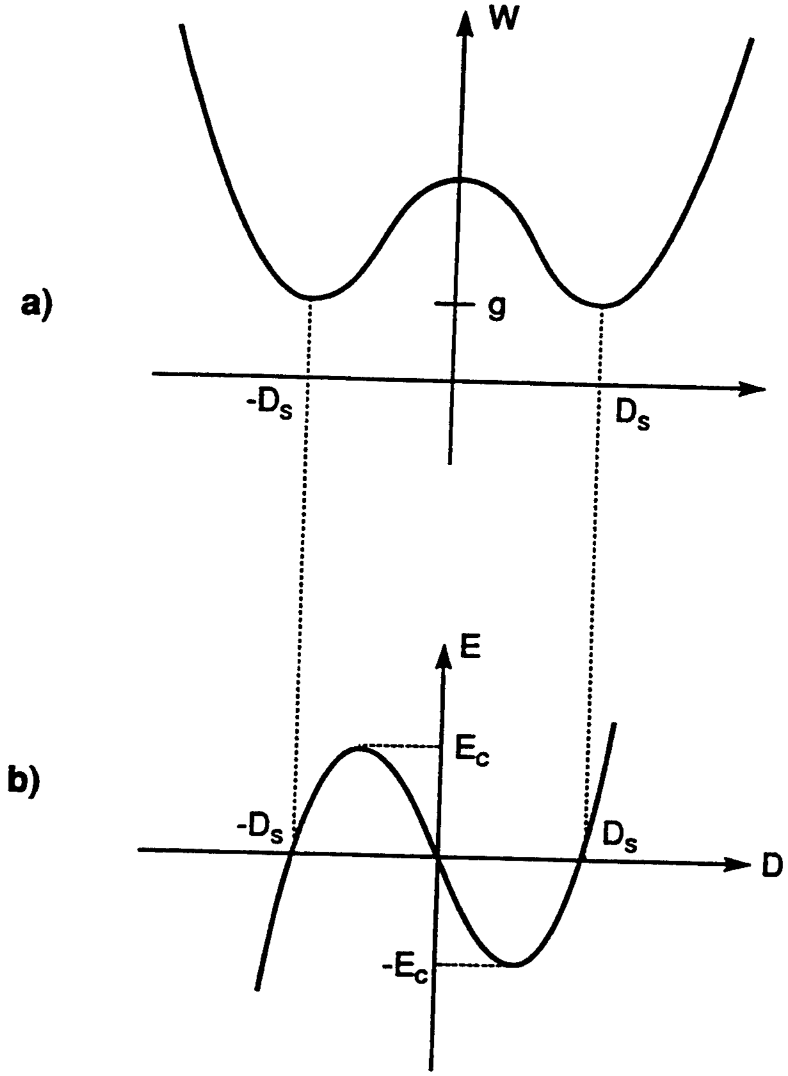

FIG. 9. a) The free-energy density as a function of the electric displacement. The free energy has deep wells when the crystal is in the ferroelastic state, far below the Curie temperature. b) The elastic field vs electric displacement curve. Only the linear parts of the curve near the spontaneous states are realized in a crystal.

The stress and the electric field are differential coefficients, (4.5), so that

$$\sigma_{ij} = C_{ijkl}^{(s)}(e_{kl} - e_{kl}^{(s)}) + h_{kij}^{(s)}(D_k - D_k^{(s)}), \tag{4.8}$$

$$E_i = \beta_{ik}^{(s)}(D_k - D_k^{(s)}) + h_{ikl}^{(s)}(e_{kl} - e_{kl}^{(s)}). \tag{4.9}$$

These linear relations are valid inside each domain. Together with the field equations, they define a linear, coupled, electro-mechanical boundary-value problem.

B. ELLIPSOIDAL TRANSFORMATION PARTICLE IN INFINITE MATRIX UNDER REMOTE LOADING

Numerical analysis is usually required to solve the boundary-value problem above. Fortunately, many analytic solutions exist for an ellipsoid inclusion in an infinite matrix subject to remote loads; see Osborn (1945) for dielectric, Eshelby (1957) for elastic, and Dunn and Wienecke (1996) for piezoelectric inclusions. The shape of ellipsoids is versatile enough to model many phenomena. A nice feature common to this class of problems is that all fields inside the ellipsoid are uniform. Here we will not list these solutions, but will discuss the calculation of the free energy. The discussion parallels that of Eshelby (1957) for an elastic inclusion.

Consider a transition from one solid phase to another. Without the constraint of the parent phase, the new phase would have a spontaneous strain $\mathbf{e}^s$, a spontaneous electric displacement $\mathbf{D}^s$, and a free energy change per volume g. All the three quantities are relative to the parent phase. When a small particle of the new phase grows inside the parent phase, both phases have stress and electric field. No dislocations, free charges, or other defects are present to relieve the field. Model the new phase particle by an ellipsoid, and denote its surface area by A and volume by V. Model the matrix as an infinite medium, and load it such that a uniform stress σ_{ij}^A and a uniform electric field E_i^A prevail far away from the particle. The free energy of the matrix in the absence of the particle, remotely loaded as described above, is the reference state. The free energy G defined by (4.6) is the sum of five contributions.

a) *Surface energy*

The phase boundary increases the free energy by

$$G_S = \int \gamma \, dA. \tag{4.10}$$

The integral extends over the ellipsoid surface. When the surface tension is isotropic, $G_S = \gamma A$. The surface energy resists particle growth.

b) *Energy due to phase difference*

When both phases are free from the stress and electric fields, the free-energy change due to the phase difference is

$$G_P = gV. \tag{4.11}$$

In our sign convention, the phase difference resists particle growth if $g > 0$.

The following three terms arise from various fields. Owing to the linearity of the problem, the free energy must be a bilinear form of the spontaneous quantities e_{ij}^s and D_i^s and the applied loads σ_{ij}^A and E_i^A. They may be grouped according to their physical significance.

c) *Work done by the applied load through spontaneous strain and electric displacement*

The work done by the applied load on the spontaneous strain and electric displacement changes the free energy by

$$G_W = -\left(\sigma_{ij}^A e_{ij}^s + E_i^A D_i^s\right)V. \tag{4.12}$$

A positive work reduces the free energy, and thereby motivates particle growth.

d) *Energy due to strain and polarization misfit*

In the absence of the applied loads, the spontaneous strain and electric displacement cause fields in the matrix and the inclusion. Let σ_{ij}^I and E_i^I be the fields in the inclusion; they are linear in e_{ij}^s and D_i^s, and various coefficients may be found in the above cited papers. The free-energy change due to the misfit is

$$G_M = -\frac{1}{2}\left(\sigma_{ij}^I e_{ij}^s + E_i^I D_i^s\right)V. \tag{4.13}$$

This contribution is a positive-definite quadratic form of e_{ij}^s and D_i^s, and resists particle growth.

e) *Energy due to heterogeneity (i.e., modulus difference)*

Imagine two infinite bodies, each subject to σ_{ij}^A and E_i^A at the infinity. One body is an infinite matrix without inclusion, and the other body is an infinite matrix containing an ellipsoidal inclusion. The constitutive laws are given by (4.8) and (4.9) with the spontaneous strain and electric displacement removed; C, β, and h are moduli for the matrix, and C^*, β^*, and h^* for the inclusion. The first body has uniform strain $\mathbf{e}$ and electric displacement $\mathbf{D}$ everywhere, and the second body has strain $\mathbf{e}^*$ and electric displacement **D*** in the inclusion. The free-energy difference between the two bodies is

$$G_H = -\frac{1}{2}\big[(C_{ijpq} - C^*_{ijpq})e_{ij}e^*_{pq} + (\beta_{ij} - \beta^*_{ij})D_iD^*_j$$
$$+ (h_{ikl} - h^*_{ikl})(e_{kl}D^*_i + e^*_{kl}D_i)\big]V. \tag{4.14}$$

This contribution is quadratic in σ^A_{ij} and E^A_i, and either motivates or resists particle growth, depending on the relative moduli of the two phases.

C. GROWTH OF A SPHERICAL PARTICLE OF DILATION

As an illustration, consider two phases of an identical chemical composition but with different crystalline structures. Without the constraint of the parent phase, the new phase would have a pure volume expansion with linear strain e_s, and a free-energy change per volume g, both being relative to the parent phase. The parent phase is loaded remotely by a hydrostatic stress σ. The electric effect is absent. We will assume that the new phase grows like a spherical particle in an infinite matrix. The system has one degree of freedom, the radius of the particle, R. Such an assumption excludes shape change, which may be important in some phenomena; for example, Johnson and Cahn (1984) showed that the spherical particle is unstable against shape change under certain conditions.

The elastic stress field for a spherical inclusion in an infinite matrix can be readily solved. For simplicity, we first assume that the two phases have similar elastic constants, with Y being Young's modulus, and ν Poisson's ratio. The free energy change due to the introduction of the particle into the matrix is

$$G(R) = 4\pi R^2\gamma + \frac{4}{3}\pi R^3\left(g - 3\sigma e_s + \frac{Ye_s^2}{1-\nu}\right). \tag{4.15}$$

The physical significance of each item is evident from the previous discussion.

The free energy has the same dependence on the radius as in the problem studied in Section III.A, so that the previous discussion applies. The driving pressure is given by

$$\mathscr{P} = -\frac{dG}{4\pi R^2\, dR} = -\frac{2\gamma}{R} - g + 3\sigma e_s - \frac{Ye_s^2}{1-\nu}. \tag{4.16}$$

The radius changes at rate

$$\frac{dR}{dt} = L\left(-\frac{2\gamma}{R} - g + 3\sigma e_s - \frac{Ye_s^2}{1-\nu}\right). \tag{4.17}$$

The solution to this ordinary differential equation is similar to (3.5).

Consider the case that the elastic constants for the two phases are different. Denote the bulk modulus and shear modulus of the parent phase by $B = Y/3(1-2\nu)$ and $\mu = Y/2(1+\nu)$, and B^* and μ^* for the corresponding quantities for the particle. The fourth term in (4.15) should be modified to

$$\frac{3e_s^2}{2}\left(\frac{1}{3B^*} + \frac{1}{4\mu}\right)^{-1}. \tag{4.18}$$

A fifth term should be added to (4.15),

$$\frac{\sigma^2}{2}\left(\frac{1}{B} - \frac{1}{B^*}\right)\left(\frac{1}{3B} + \frac{1}{4\mu}\right)\left(\frac{1}{3B^*} + \frac{1}{4\mu}\right)^{-1}. \tag{4.19}$$

This term motivates particle growth if the new phase has a lower bulk modulus than the parent phase.

D. GROWTH OF A 180° DOMAIN IN BARIUM TITANATE

Barium titanate ($BaTiO_3$) undergoes a phase transition at 130°C. Figure 10 shows the unit cells of the two phases. Above 130°C, the crystal is cubic, and the ions lie symmetrically in the unit cell. Between 0 and 130°C, the crystal is tetragonal, and the ions lie asymmetrically in the unit cell. We next concentrate on the changes at a fixed temperature between 0 and 130°C.

Depending on the position of the titanium ion relative to the center of the unit cell, the crystal may have polar direction of any one of the six *variants*. A load may shift the position of the titanium ion, and thereby rotate the polar axis from one direction to another. An electric field may rotate the polar direction by either 180° or 90°, but a stress may only rotate it by 90°. A 180° polar rotation does not result in any strain; a 90° polar rotation results in a strain.

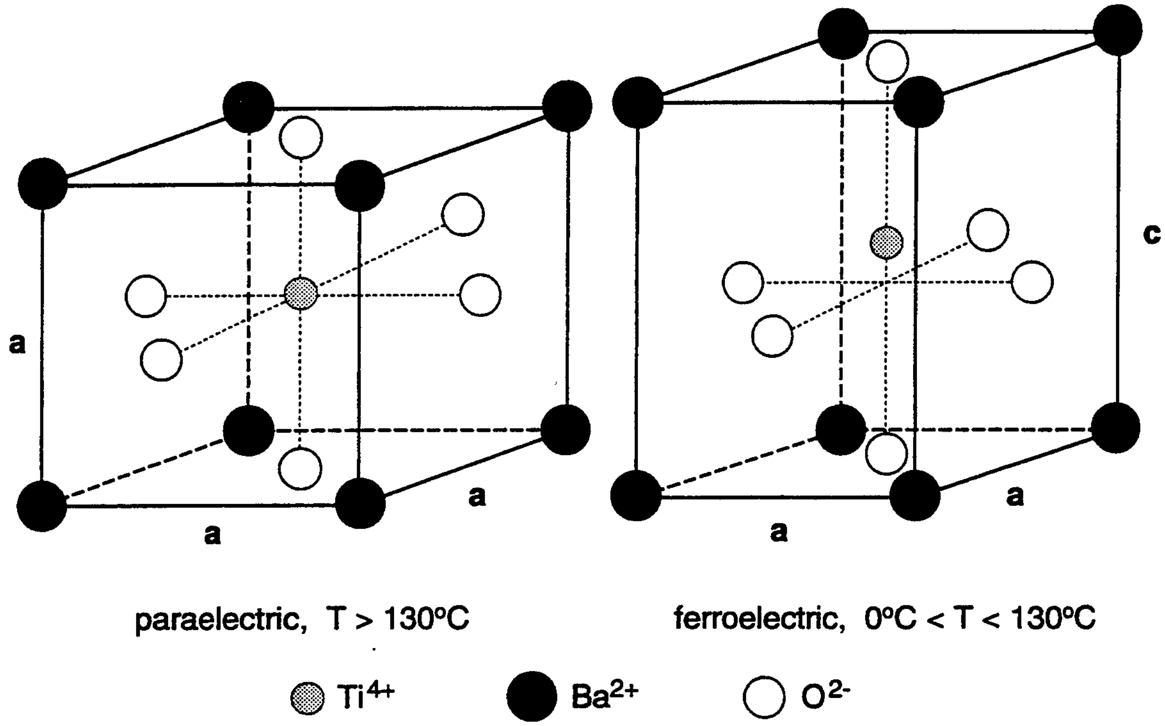

paraelectric, T > 130°C

ferroelectric, 0°C < T < 130°C

FIG. 10. The crystal structures of barium titanate ($BaTiO_3$). The high-temperature phase is nonpolar. The low-temperature phase is polar and the Ti ion is off the cell center.

The crystal changes its state by domain-wall migration. The loads needed to move the domain walls are much lower than the loads theoretically predicted to uniformly switch the crystal. In fact, the latter has never been observed. Miller and Savage (1959) observed that the domain walls in $BaTiO_3$ move at a wide range of velocities (10^{-9}–10^{-1} m/s). The new domains tend to start as spikes. In the following we review a model study of the growth of a small 180° domain, assuming that the growing domain is elliptic (Landauer, 1957; Loge and Suo, 1996). Rosakis and Jiang (1995) showed that sharp tips can emerge from the growing domain; their analysis will not be reviewed here.

Figure 11 illustrates the cross section of a cylindrical domain in a large parent domain having the opposite polarization. Because both domains have the identical spontaneous strain, the elastic and the piezoelectric effects may be ignored compared to the dielectric effects. The problem is further simplified by assuming isotropic domain wall energy, permittivity, and mobility. To avoid solving an electrostatic problem for complex-shaped inclusions, we approximate the cross section of the domain by a sequence of ellipses, evolving the domain with two generalized coordinates, the semi-axes α_1 and α_2.

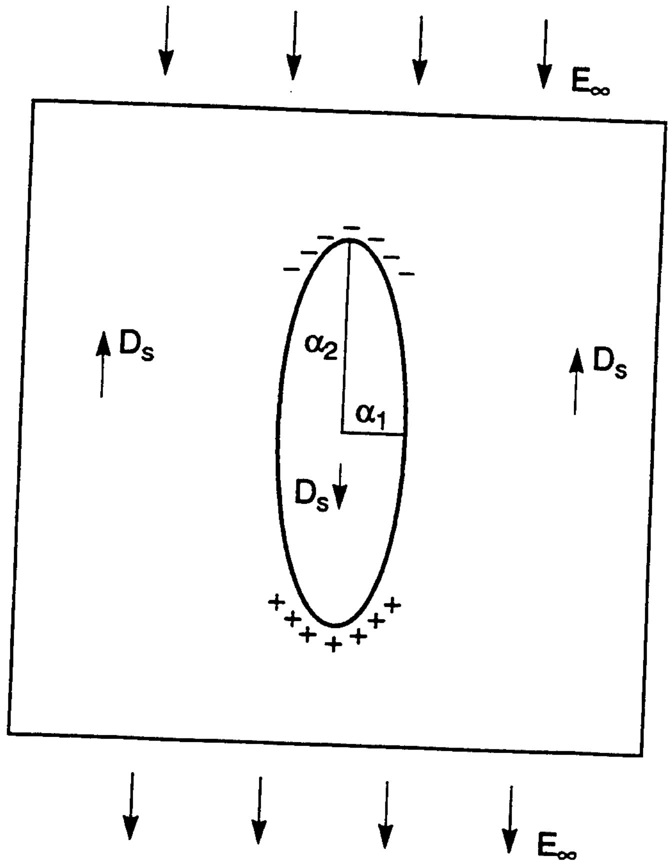

FIG. 11. A 180° domain grows in a parent phase driven by an electric field.

The free energy due to the introduction of the nucleus into the parent crystal is

$$G(\alpha_1, \alpha_2) = \gamma_S - 2D_s E_\infty \pi \alpha_1 \alpha_2 + \frac{2\pi \alpha_1^2 \alpha_2 D_s^2}{\varepsilon(\alpha_1 + \alpha_2)}. \tag{4.20}$$

Here, s is the perimeter of the ellipse, and ε is the permittivity. The first term is the domain wall energy, which resists the growth and tends to make the domain circular. The second term is the work term associated with polarization reversal, which drives the nucleus to grow and tends to make the nucleus circular. The third term is the depolarization energy induced by the discontinuity of the spontaneous polarization, which strongly resists the growth in the α_1 direction, but weakly resists the growth in the α_2 direction.

The problem has a characteristic length, $l_0 = \gamma\varepsilon/D_s^2$, which we will use to normalize the semi-axes of the ellipse. Figure 12 shows the contours of constant levels of free energy, normalized as $G/(2\pi l_0 \gamma)$. The loading level for the simulation is $\varepsilon E_\infty/D_s = 0.05$. The free-energy surface has a saddle point at $\alpha_1 = 13l_0$ and $\alpha_2 = 500l_0$, indicated by SP in Figure 12. The physical origin of this saddle point is evident. Along either the axis $\alpha_1 = 0$ or $\alpha_2 = 0$, when the needle-shaped domain elongates, both the work term and the depolarization energy vanish, and the domain-wall energy increases the total free energy. Along a path with a large aspect ratio α_2/α_1, the total free energy is low for both a very small and a very large nucleus, and reaches a peak for an intermediate one. The fate of a nucleus depends on its initial position on the thermodynamic surface. To decrease the free energy, a very small nucleus shrinks, and a very large nucleus grows. For a nucleus near the saddle point, its fate is determined by both the energetics and the kinetics. In all cases, the free-energy landscape alone does not determine the evolution path.

We next calculate the evolution path and rate. The differential equations (2.13) become

$$\begin{bmatrix} H_{11} & H_{12} \\ H_{21} & H_{22} \end{bmatrix} \begin{bmatrix} \dot{\alpha}_1 \\ \dot{\alpha}_2 \end{bmatrix} = \begin{bmatrix} f_1 \\ f_2 \end{bmatrix}. \tag{4.21}$$

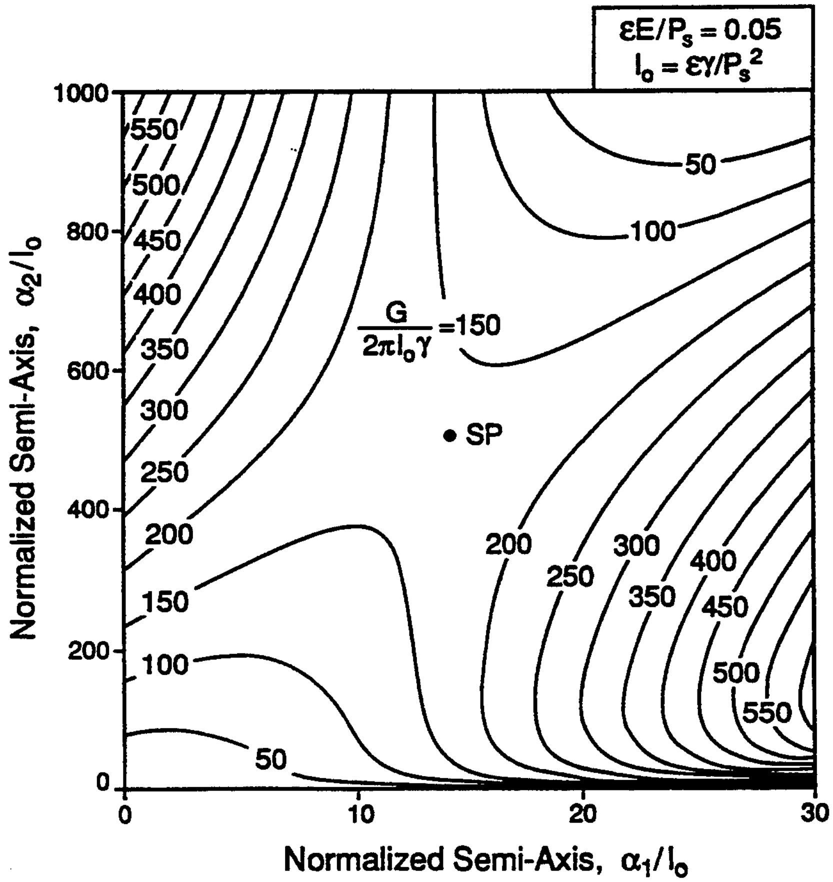

FIG. 12. Free energy contours for a 180° domain nucleus.

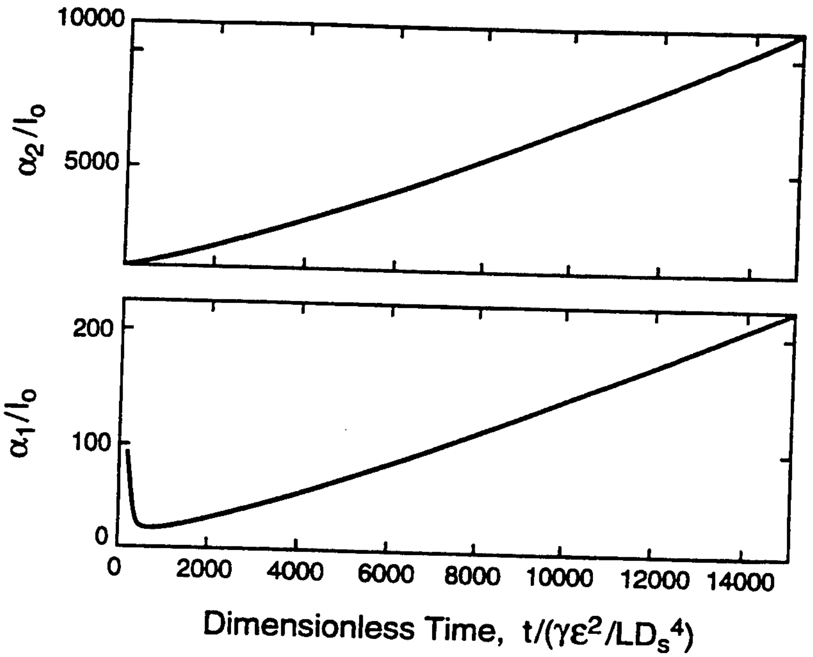

FIG. 13. The semi-axes of a 180° domain nucleus as functions of the time.

The expressions for the generalized forces and viscosities are given in Loge and Suo (1996). Given initial semi-axes of a nucleus, we trace its evolution by numerically integrating (4.31). The problem has a characteristic time, $t_0 = l_0^2/(L\gamma)$, which is used to normalize the time. Figure 13 shows the evolution of a nucleus of initial axes $\alpha_2 = 500l_0$ and $\alpha_1 = 200l_0$. The α_2-axis increases almost linearly with the time after some initial adjustment. The α_1-axis decreases first, and then increases slowly relative to the α_2-axes. The domain grows to a long needle in the direction of spontaneous polarization, because of the large effect of the depolarization energy.

E. EXPLICIT FORMULA FOR THE DRIVING PRESSURE

Eshelby (1956, 1970) called the following quantity the energy momentum tensor

$$P_{ij} = W\delta_{ij} - \sigma_{ik}e_{kj} - E_iD_j. \tag{4.22}$$

An interface separates domain + and domain −, with the unit normal vector **n** pointing toward domain +. Denote the sum of the principal curvatures of the interface by K. Assume that no external force or charge lie on the domain wall. Eshelby showed that, when the interface moves in the direction **n** by distance δr_n, the free energy of the crystal changes by

$$\delta G = \int \left[\gamma K - n_i (P_{ij}^{+} - P_{ij}^{-}) n_j \right] \delta r_n \, dA. \tag{4.23}$$

The interface tension γ is taken to be isotropic. A comparison of (4.23) with (2.2) gives the driving pressure on the interface

$$\mathscr{P} = -\gamma K + n_i (P_{ij}^{+} - P_{ij}^{-}) n_j. \tag{4.24}$$

If medium $-$ is taken to be a traction-free but strained solid, and medium $+$ the vacuum, (4.24) becomes

$$\mathscr{P} = -\gamma K - W. \tag{4.25}$$

Asaro and Tiller (1972) obtained this formula in analyzing surface motion. The equation of motion (2.3) becomes

$$v_n = -L(\gamma K + W). \tag{4.26}$$

V. Diffusion on Interface: Formulation

This section formulates mass diffusion on an interface. The interface may be either a free surface, or a grain boundary. The diffusion species are taken to be electrically neutral, so that only mass conservation need be enforced. The free energy has the same contributions as before, e.g., surface tension, external work, and elastic energy.

A. GENERAL CONSIDERATIONS

1. *Virtual Motion, Mass Conservation, and Interface Motion*

Figure 14 illustrates in three dimensions a surface that represents either a free surface or a grain boundary. Denote the unit vector normal to a surface element by **n**. An arbitrary contour lies on the surface, with the curve element *dl*, and the unit vector in the surface and normal to the curve element **m**. At a point on the contour, **m** and **n** are perpendicular to each other, and both are perpendicular to the tangent vector of the curve at the point.

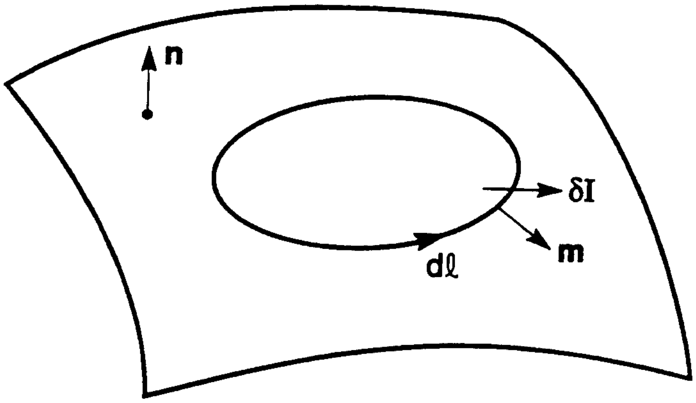

FIG. 14. An interface in the third dimension. Also drawn is an arbitrary contour lying on the interface.

Let $\delta \mathbf{I}$ be a vector field on the interface, such that $\delta \mathbf{I} \cdot \mathbf{m}$ is the number of atoms crossing unit length of the curve. As before, δ indicates a virtual motion, namely, the number of atoms is small and need not obey any kinetic law. Following Biot (1970), we refer to $\delta \mathbf{I}$ as the virtual mass displacement, to distinguish it from the atomic flux used below. Let $\delta \xi$ be the number of atoms added to the interface per unit area. Consider the interface area enclosed by the contour in Figure 14. Atoms move only on the interface, so that the number of atoms added to the area equals the number of atoms flowing in across the contour. Thus,

$$\int \delta \xi \, dA + \oint \delta \mathbf{I} \cdot \mathbf{m} dl = 0. \tag{5.1}$$

The first integral extends over the area of the interface enclosed by the contour, and the second over the contour. Equation (5.1) holds for any contour on the interface. Recall the surface divergence theroem, $\oint \delta \mathbf{I} \cdot \mathbf{m} dl = \int \nabla \cdot (\delta \mathbf{I}) \, dA$, where the operator ∇ is carried on the surface. (Some writers signify the surface operator with ∇_s.) Mass conservation requirements can also be expressed in terms of the surface divergence:

$$\delta \xi + \nabla \cdot (\delta \mathbf{I}) = 0. \tag{5.2}$$

The atomic flux, $\mathbf{J}$, is a vector field on the interface, such that $\mathbf{J} \cdot \mathbf{m}$ is the number of atoms across per length per time. Let $\dot{\xi}$ be the number of atoms added to unit area of the interface in unit time. Mass conservation requires an expression similar to (5.1),

$$\int \dot{\xi} \, dA + \oint \mathbf{J} \cdot \mathbf{m} dl = 0, \tag{5.3}$$

and an expression similar to (5.2),

$$\dot{\xi} + \nabla \cdot \mathbf{J} = 0. \tag{5.4}$$

We next connect $\dot{\xi}$ to the motion of the free surface and the grain boundary. The expressions are similar between $\delta\xi$ and the virtual motion of the interfaces. On a *free surface*, atoms of the solid diffuse from one part of the surface to another. Atoms added to a surface element cause the element to move in the direction toward the vacuum at the velocity $v_n = \Omega\dot{\xi}$. Here Ω is the volume per atom.

A *grain boundary* is taken to be in local equilibrium. The atoms inserted to the grain boundary instantaneously crystallize, rendering the atomic structure of the grain boundary invariant. Yet the inserted atoms may add to either one of the two grains. Evidently, $\dot{\xi}$ only determines the relative motion of one grain with respect to the other, but *not* the migration of the grain boundary itself. Denote the velocity of one grain relative to another by Δv_n, being positive when the two grains recede from each other. The atoms added to a grain-boundary element cause the two grains to drift apart at velocity $\Delta v_n = \Omega\dot{\xi}$.

The migration of the grain boundary is a degree of freedom independent of the relative motion of the two grains, and should be treated by the interface migration kinetics in the previous sections. Relative sliding of the two grains are often taken to be fast; see Section VII.B. Cocks (1992) considered a locally nonequilibrium grain boundary, which will not be reviewed here.

2. *Defining Diffusion Driving Force*

Associated with the virtual motion, $\delta\mathbf{I}$ and $\delta\xi$, the free energy of the system varies by δG. Define the driving force for diffusion, $\mathbf{F}$, as the reduction of the free energy associated with one atom moving unit distance on the interface. That is,

$$\int \mathbf{F} \cdot \delta\mathbf{I}\, dA = -\delta G. \tag{5.5}$$

The integral extends over the interface. Equation (5.5) holds for arbitrary virtual motion. The force $\mathbf{F}$ is a vector on the interface, and has a unit of force/atom.

3. *Kinetic Law*

Following Herring (1951), we adopt a linear kinetic law:

$$\mathbf{J} = M\mathbf{F}. \tag{5.6}$$

This equation defines the atomic mobility on the interface, M, which is a second-order tensor at any one point on the interface, and may also vary from point to point. In this article we will assume that the mobility is independent of the crystalline direction. The mobility is determined in practice either by observing a phenomenon such as surface grooving, or by an atomistic simulation.

The mobility relates to the self-diffusivity by the Einstein relation, $M = D\delta/\Omega kT$, where D is the self-diffusivity on the interface, δ the effective thickness of atoms that participate in mass transport, Ω the volume per atom, k Boltzmann's constant, and T the absolute temperature. The self-diffusivity is approximately $D = \nu b^2 \exp(-q/kT)$, where ν is the frequency of atomic vibration, b the atomic spacing, and q the activation energy.

Atomic mobility on an interface is sensitive to impurities. When the impurity atoms segregate to the interface, the interface has a much higher impurity concentration than the bulk crystal. For example, adding a few percents of copper to aluminum substantially slows down aluminum diffusion on grain boundaries (Ames *et al.*, 1970). This empirical fact has been used to make electromigration-resistant interconnects in integrated circuits.

B. DIFFERENTIAL EQUATIONS

The considerations above specify the surface diffusion problem. At a given time, the free-energy variation determines the driving force, the kinetic law relates the driving force to the flux, and the flux then updates the surface shape according to mass conservation. The procedure repeats for the next time increment.

These general considerations lead to two approaches for computation. One approach, due to Herring (1951), defines the chemical potential on the surface, leading to partial differential equations. This subsection lists these equations. The following subsection formulates an alternative approach on the basis of a weak statement. The two subsections can be read independently, in any order.

1. *Chemical Potential*

First consider an interface which is a closed surface in the third dimension. Herring (1951) defined the chemical potential of an interface element, μ, as the increase of the free energy associated with the addition of one atom to the element. Thus,

$$\delta G = \int \mu \, \delta\xi \, dA. \tag{5.7}$$

The integral extends over the surface. The chemical potential has a unit of energy/atom.

Using (5.6) and the divergence theorem, one obtains that

$$\begin{aligned} \delta G &= -\int \mu \nabla \cdot (\delta \mathbf{I}) \, dA \\ &= -\int [\nabla \cdot (\mu \, \delta \mathbf{I}) - (\nabla \mu) \cdot \delta \mathbf{I}] \, dA \\ &= -\oint \mu \, \delta \mathbf{I} \cdot \mathbf{m} \, dl + \int (\nabla \mu) \cdot \delta \mathbf{I} \, dA \end{aligned} \tag{5.8}$$

A closed interface does not have a boundary curve, so that the line integral vanishes.

A comparison of (5.5) and (5.8) equates the two area integrals for arbitrary distribution of $\delta \mathbf{I}$, so that the two integrands must be identical:

$$\mathbf{F} = -\nabla \mu. \tag{5.9}$$

The driving force is the negative gradient of the chemical potential. As expected, atoms diffuse from an interfacial element with high chemical potential to an interfacial element with low chemical potential.

Next consider the continuity conditions at a triple junction. As discussed in Section II.F, the local equilibrium assumption requires that the free-energy variation associated with the translation of the junction vanish. Consequently, the three interfaces meet at angles determined by the surface tensions. These considerations apply here. In addition, the local equilibrium assumption requires that the chemical potentials on the three interfaces be equal at the triple junction.

To see the last statement, consider three interfaces that meet at a straight line of length l. On the three interfaces I_1, I_2, and I_3 are the components of the $\mathbf{I}$ vector pointing to the junction. The junction is neither a mass sink nor a mass source, so that the net mass coming to the junction vanishes, $\delta I_1 + \delta I_2 + \delta I_3 = 0$. Recall that the chemical potential is the free-energy change associated with adding one atom. The free-energy change due to the atoms moving to the triple junction is $\delta G = -l(\mu_1 \delta I_1 + \mu_2 \delta I_2 + \mu_3 \delta I_3)$. A combination of the above two equations give $\delta G = -l(\mu_1 - \mu_3)\delta I_1 - l(\mu_2 - \mu_3)\delta I_2$. The local equilibrium assumption requires that $\delta G = 0$ for any virtual mass displacements δI_1 and δI_2. Consequently, the chemical potential is continuous across the triple point, $\mu_1 = \mu_2 = \mu_3$.

2. *Free Surface*

Mass conservation relates the velocity normal to the free surface to the flux divergence:

$$v_n + \Omega \nabla \cdot \mathbf{J} = 0. \tag{5.10}$$

As stated in Section IV.E, associated with adding atoms on the interface, the free energy varies by

$$\delta G = \int (\gamma K + W) \Omega \, \delta\xi \, dA. \tag{5.11}$$

The surface tension γ is isotropic, the sum of the two-principle curvature K is positive when the surface is convex, and W includes energy density due both to stress and electric field. A comparison between (5.7) and (5.11) gives the chemical potential on the surface,

$$\mu = \Omega(\gamma K + W). \tag{5.12}$$

The diffusion driving force is

$$\mathbf{F} = -\nabla(\Omega \gamma K + \Omega W). \tag{5.13}$$

A combination of (5.6), (5.10), and (5.13) gives

$$v_n = M \Omega^2 \nabla^2 (\gamma K + W). \tag{5.14}$$

This partial differential equation governs the motion of a free surface when the surface tension is isotropic.

3. *Grain Boundary*

Mass conservation relates the relative velocity of the two grains to the flux divergence:

$$\Delta v_n + \Omega \nabla \cdot \mathbf{J} = 0. \tag{5.15}$$

Let σ_n be the normal stress component on the grain boundary. To insert one atom to the grain boundary, the normal stress does work, varying the free energy by

$$\delta G = -\int \sigma_n \Omega \, \delta\xi \, dA. \tag{5.16}$$

Consequently, the chemical potential is

$$\mu = -\Omega \sigma_n. \tag{5.17}$$

The driving force for diffusion on the grain boundary is

$$\mathbf{F} = \Omega \nabla \sigma_n. \tag{5.18}$$

Atoms diffuse on the grain boundary from an element of low-normal stress to an element of high-normal stress. A combination of (5.6), (5.15), and (5.18) gives

$$\Delta v_n = -M\Omega^2 \nabla^2 \sigma_n. \tag{5.19}$$

This partial differential equation governs the normal-stress distribution in the grain boundary.

C. WEAK STATEMENTS

1. *Weak Statement When Interface Diffusion Is the Sole Rate Process*

Ignore Section V.B and start from Section V.A again. Consider a polycrystal particle with grain boundaries and free surfaces. We first assume that the grain boundaries do not migrate and grains are rigid, so that diffusion on interfaces is the only kinetic process. Replace the force in (5.5) with the flux using the kinetic law (5.6), giving

$$\int \frac{\mathbf{J} \cdot \delta \mathbf{I}}{M} \, dA = -\delta G. \tag{5.20}$$

The integral extends over all the interfaces in the system. Different interfaces, of course, may have different mobilities. The actual flux J satisfies (5.20) for all virtual motions that conserve mass, dictated by (5.1)–(5.4) on each interface and by flux continuity at every triple junction.

This formulation circumvents the differential equations in Section V.B, and the local quantities such as the chemical potential, the curvature of a free surface, and the normal stress in a grain boundary. The statement also enforces local equilibrium at the triple junctions, namely, (a) the interfaces meet at a junction with angles determined by the surface tensions, and (b) the chemical potentials of all the interfaces are equal at the junction. Should for any reason the two types of junction mobilities be finite, one could add them to the weak statement in the manner described in Section II.F.

2. *Variational Principle*

Needleman and Rice (1980) formulated a variational principle that includes grain-boundary diffusion, and devised a finite-element method on the basis of the variational principle. Extensions have been made to analyze several phenomena involving interface diffusion (e.g., Bower and Freund, 1993, 1995; Cocks, 1994; McMeeking and Kuhn, 1992; Sofronis and McMeeking, 1994; Suo and Wang, 1994; Svoboda and Riedel, 1995). Following the steps in Section II.E, one can prove the following variational principle. Of all virtual flux $\tilde{\mathbf{J}}$ that conserves mass, the actual flux minimizes the functional

$$\Pi = \dot{G} + \int \frac{\tilde{\mathbf{J}} \cdot \tilde{\mathbf{J}}}{2M}\, dA. \tag{5.21}$$

The weak statement and the variational principle lead to identical ordinary differential equations that evolve the generalized coordinates.

3. *Galerkin Procedure*

Interface diffusion differs from interface migration in one significant way. For interface diffusion, mass conservation is expressed by partial differential equations, (5.2) and (5.4). When the shape of the surface is axisymmetric or invariant in one direction, the surface divergence involves one-dimensional differentiation, which can be integrated readily. The Galerkin method proceeds as follows. Model the surface with n degrees of freedom, writing $q_1, \ldots, q_n$ for the generalized coordinates, and $\dot{q}_1, \ldots, \dot{q}_n$ for the generalized velocities. Following the same procedure as in Section II.C to compute the generalized forces f_i, the virtual displacement of the interfaces δr_n, and the velocity of the interfaces v_n. Integrate (5.2) and (5.4), and one obtains

$$\delta I = \sum Q_i\, \delta q_i, \quad J = \sum Q_i \dot{q}_i,$$

where Q_i plays the similar role as the shape functions. The weak statement (5.20) then leads to the same equation as (2.13), with the viscosity matrix being

$$H_{ij} = \int \frac{Q_i Q_j}{M} \, dA.$$

The shape of the surface is updated as before. We will demonstrate this method in later sections.

4. *Include Mass Conservation in Weak Statement*

The procedure above, however, fails for a general surface in three dimensions, because the surface divergence in (5.2) now consists of differentiation of two surface coordinates. Consequently, one cannot integrate (5.2) to relate $\delta \mathbf{I}$ to $\delta q_2, \ldots, \delta q_n$. What happens physically is clear. When the virtual motion of the surface is prescribed, mass conservation does not fully determine the virtual mass displacement. That is, a general surface requires degrees of freedom for $\delta \mathbf{I}$, in addition to the degrees of freedom for the surface shape. The following notes may be useful in this connection.

Mass conservation is a constraint, much like incompressibility in deformation analysis. One may use one of several methods in finite element methodology to include mass conservation in the weak statement. Here we use a penalty method as an illustration. Consider a closed surface for simplicity. Allow $\delta\xi$ and $\delta \mathbf{I}$ to vary independently, and associate a driving force λ with the new degree of freedom $\delta\xi + \nabla \cdot (\delta \mathbf{I})$, writing

$$\int \mathbf{F} \cdot \delta \mathbf{I} \, dA + \int \lambda [\delta\xi + \nabla \cdot (\delta \mathbf{I})] \, dA = -\delta G. \tag{5.22}$$

The integrals extend over the closed surface. Prescribe an independent kinetic law for this new degree of freedom:

$$\dot{\xi} + \nabla \cdot \mathbf{J} = M_0 \lambda. \tag{5.23}$$

The mobility M_0 is an adjustable parameter in the finite element analysis; when M_0 is very small, mass conservation (5.4) is recovered approximately. The weak statement becomes

$$\int \frac{\mathbf{J} \cdot \delta \mathbf{I}}{M} \, dA + \int \frac{1}{M_0} \left[\dot{\xi} + \nabla \cdot \mathbf{J} \right] [\delta\xi + \nabla \cdot (\delta \mathbf{I})] \, dA = -\delta G. \tag{5.24}$$

Incidentally, one can confirm that the parameter λ has a simple physical interpretation, $\lambda = -\mu$.

D. Multiple Kinetic Processes

Consider a grain boundary which both migrates and acts as a diffusion path. Let δr_n be the virtual migration of the grain boundary, $\delta \mathbf{I}$ be the virtual mass displacement on the grain boundary, and δG be the free-energy variation associated with the combined virtual motion. Define the migration driving pressure $\mathscr{P}$ and the diffusion driving force $\mathbf{F}$ simultaneously by

$$\int \mathscr{P} \delta r_n \, dA + \int \mathbf{F} \cdot \delta \mathbf{I} \, dA = -\delta G. \tag{5.25}$$

The integrals extend over the grain-boundary area. Equation (5.25) holds for any mass-conserving virtual motion. Replacing the driving forces by the kinetic laws of the two processes, (2.3) and (5.6), we have

$$\int \frac{v_n \, \delta r_n}{L} \, dA + \int \frac{\mathbf{J} \cdot \delta \mathbf{I}}{M} \, dA = -\delta G. \tag{5.26}$$

The actual migration velocity v_n and flux J satisfy this weak statement for arbitrary mass-conserving virtual motion.

Other kinetic processes can be similarly added to the weak statement. Take, for example, a system of interfaces that move by diffusion on the interfaces, and creep in the grains. The free energy consists of the external work and various interface tensions. The problem was first treated by Needleman and Rice (1980). Denote the virtual displacement field in the grains by δu_i, and the actual velocity field in the grains by v_i. We will assume that the solid is incompressible, i.e.,

$$v_{i,i} = 0. \tag{5.27}$$

Define the stress tensor, σ_{ij}, and the diffusion driving force F_i on the same basis, namely, as the energy-conjugates of their respective kinematic quantities. Thus,

$$\int \sigma_{ij} \, \delta u_{i,j} \, dA + \int F_i \, \delta I_i \, dA = -\delta G. \tag{5.28}$$

Interface diffusion obeys the kinetic law (5.6). For this demonstration, the grains deform according to a linear creep law:

$$\sigma_{ij} = \sigma_m \, \delta_{ij} + \eta(v_{i,j} + v_{j,i}). \tag{5.29}$$

Here, σ_m is the mean stress; η is the viscosity of the material; and $\delta_{ij} = 1$ when $i = j$, $\delta_{ij} = 0$ when $i \neq j$.

Replacing the diffusion driving force with the flux by (5.6), and the stress with the velocity gradient by (5.29), we obtain

$$\int 2\eta v_{i,j} \delta u_{i,j} \, dA + \int \frac{J_i \, \delta I_i}{M} \, dA = -\delta G. \tag{5.30}$$

The actual velocity and flux satisfy this weak statement for arbitrary virtual motion.

VI. Shape Change due to Surface Diffusion under Surface Tension

This section gives examples of shape changes motivated by surface tension. Most examples invoke surface diffusion as the only mass-transport mechanism. One example involves simultaneous grain-boundary migration and surface diffusion.

A. RAYLEIGH INSTABILITY

Over a century ago, John William Strutt Rayleigh noted that a jet of water is unstable and breaks to droplets under the action of surface tension. Similar phenomena occur in a solid state; see Rodel and Glaeser (1990) for an experimental demonstration and literature survey. For example, at a high temperature, a crack-like pore in a solid undergoes a sequence of morphological changes until the crack breaks into many small cavities. The crack first blunts its edge, from which finger-like channels emerge, and the channels then break into small cavities. The morphological changes shorten the distance over which mass transports, and therefore accelerate the crack healing.

Assume that the surface tension is isotropic, and the free energy of the system is the surface area times the surface tension. Of all figures of the same volume, the sphere has the lowest surface area, and therefore the lowest free energy. Why, then, does a cylinder evolve into many small spheres, rather than one, single large sphere?

Consider a long cylinder of radius R. Perturb the surface along the longitudinal direction of the cylinder. It can be shown that the perturbation reduces the surface area if its wavelength exceeds $2\pi R$. Further, Srolovitz and Safran (1986) compared a row of identical spheres with the long cylinder having the same total volume, and noted that the spheres have a smaller total surface area than the cylinder if the sphere radius exceeds $3R/2$. This sphere radius corresponds to an initial perturbation wavelength of $9R/2$. From these geometric (energetic) considerations, one expects that a sequence of configurations exists, from a cylinder to a row of spheres of large enough radii, with decreasing surface areas.

But these energetic considerations do not answer the question raised above. The answer has to do with kinetics. It takes a short time for a cylinder to evolve into a row of spheres. The spheres break the mass-transport path, preventing the system from reaching the minimal energy configuration, a single, large sphere. Here we have assumed a certain kind of mass-transport mechanism, such as fluid flow or solid diffusion. If, instead, the cylinder is sealed in a small bag, it will evolve to a single, large sphere via vapor transport.

Nichols and Mullins (1965a, b) carried out a linear stability analysis of a cylinder using several mass-transport mechanisms. For surface diffusion, they showed that a perturbation of wavelength, $\lambda_m = 2\sqrt{2}\,\pi R$, amplifies most rapidly. If the initial imperfections of all wavelengths have a similar amplitude, it is reasonable to expect that the finite sphere size corresponds to wavelength λ_m.

In what follows, the Rayleigh instability is used to illustrate the application of the weak statement. Surface-tension anisotropy is also included in the end of the analysis.

1. *Free Energy*

Figure 15 illustrates a long cylinder of initial radius R with isotropic surface tension γ. Perturb the cylinder to a wavy surface of revolution

$$r(z,t) = R\left[\rho(t) + \varepsilon(t)\cos\frac{2\pi z}{\lambda}\right], \qquad (6.1)$$

where r is the radius of the perturbed surface, z the axis of revolution, t the time, ρR the average radius, εR the amplitude, and λ the wavelength. If the family of the assumed virtual motion contains the exact solution, the Galerkin procedure leads to the exact solution; otherwise the

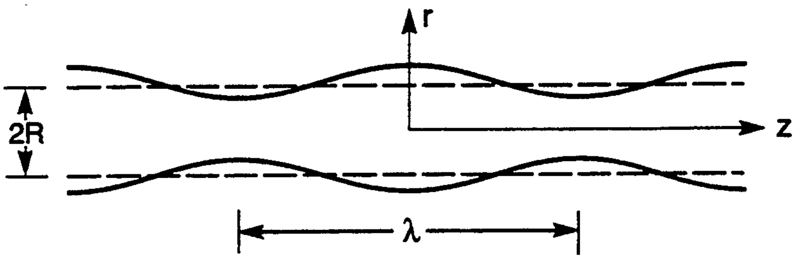

FIG. 15. Perturb a cylindrical surface to a surface of revolution with an undulation along the axial direction.

Galerkin procedure leads to an approximate solution. In this case, the family (6.1) happens to contain the exact solution of Nichols and Mullins (1965a, b).

Mass conservation requires that the volume be constant. Thus,

$$\int_0^\lambda \pi r^2\, dz = \pi R^2 \lambda, \tag{6.2}$$

which, to the leading term in ε, gives $\rho = 1 - \varepsilon^2/4$. Thus, the surface profile is

$$r = R\left[1 - \frac{\varepsilon^2}{4} + \varepsilon \cos\frac{2\pi z}{\lambda}\right]. \tag{6.3}$$

The wavelength λ is fixed in the linear stability analysis, so that this model has only one generalized coordinate: the perturbation amplitude ε.

The free energy of the column is the surface tension integrated over the column surface. In one wavelength the free energy is

$$G = \int_0^\lambda 2\pi r\gamma\left[1 + (\partial r/\partial z)^2\right]^{1/2} dz, \tag{6.4}$$

and to the leading term in ε,

$$G = 2\pi R\lambda\gamma + \frac{\pi}{2} R\lambda\gamma\left[\left(\frac{2\pi R}{\lambda}\right)^2 - 1\right]\varepsilon^2. \tag{6.5}$$

If the quantity in the bracket is negative, the free energy decreases as ε increases. Consequently, the amplitude of a perturbation grows if its wavelength exceeds a critical value

$$\lambda_c = 2\pi R. \tag{6.6}$$

This reproduces the condition established by Rayleigh.

2. *Kinetics*

Because of symmetry, $J = 0$ at $z = 0$. Mass conservation relates the flux $J(z)$ to the rate of the change of the volume between 0 and z. Thus,

$$2\pi r \Omega J = -\frac{\partial}{\partial t}\int_0^z \pi r^2\, dz. \tag{6.7}$$

To the first order in the perturbation, the above is

$$J = -\frac{R\lambda}{2\pi\Omega}\sin\left(\frac{2\pi z}{\lambda}\right)\dot{\varepsilon}. \tag{6.8}$$

The weak statement (5.20) becomes

$$\dot{\varepsilon} = \frac{\varepsilon}{\tau}, \tag{6.9}$$

with the characteristic time τ being

$$\tau = \frac{R^4}{\lambda\Omega^2 M}\left[1 - \left(\frac{2\pi R}{\lambda}\right)^2\right]^{-1}\left(\frac{2\pi R}{\lambda}\right)^{-2}. \tag{6.10}$$

For the initial condition $\varepsilon = \varepsilon(0)$ at $t = 0$, the solution to (6.9) is

$$\varepsilon(t) = \varepsilon(0)\exp\left(\frac{t}{\tau}\right). \tag{6.11}$$

Figure 16 shows the trend of the characteristic time (6.10). When $\lambda < 2\pi R$, the perturbation increases the free energy, $\tau < 0$, and the perturbation

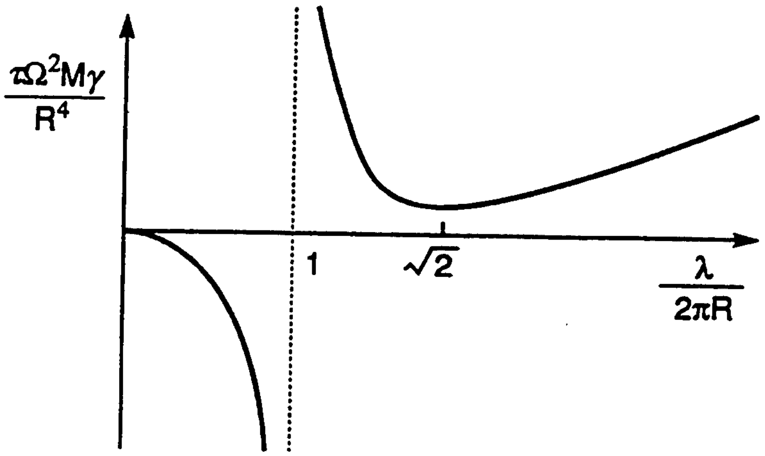

FIG. 16. The characteristic time as a function of the wavelength.

diminishes with the time. When $\lambda > 2\pi R$, the perturbation decreases the free energy, $\tau > 0$, and the perturbation amplifies with the time; τ minimizes at $\lambda_m = 2\sqrt{2}\,\pi R$, agreeing with the analysis of Nichols and Mullins (1965a, b).

The conclusion above is made on the basis of the linear stability analysis, where high-order terms of ε have been ignored. A complete simulation of the surface evolution is necessary to take into account the actual initial imperfection and large shape change (Nichols, 1976).

3. *Surface-Tension Anisotropy*

Imagine a crystal having transversely isotropic surface tension. The long cylinder of circular cross section has constant surface tension γ_0. When the cylinder becomes a surface of revolution, the surface tension is nonuniform along the longitudinal direction. Denote θ as the angle of the normal vector of an arbitary crystal plane, measured from the normal vector of the perfect cylinder. For small θ, the surface energy γ can be expanded in the powers of θ, assuming γ is a smooth function of θ. The crystal is assumed to have such a symmetry that the crystal plane at θ and the crystal plane at $-\theta$ have the identical surface energy. Consequently, the expansion only contains the even powers of θ. Take only the first two terms:

$$\gamma(\theta) = \gamma_0(1 - \alpha\theta^2). \tag{6.12}$$

Here the dimensionless number α indicates the anisotropy. When $\alpha > 0$, the crystal plane of the perfect cylinder has the largest surface tension of all the neighboring crystal planes.

Perturb the cylinder to a surface of revolution with profile (6.3). To the first order of ε,

$$\theta = -\frac{\partial r}{\partial z} = \frac{2\pi R}{\lambda}\varepsilon \sin\left(\frac{2\pi z}{\lambda}\right). \tag{6.13}$$

The free energy (6.4), to the leading order in ε, is

$$G = 2\pi R\lambda\gamma_0 + \frac{\pi}{2}R\lambda\gamma_0\left[(1 - 2\alpha)\left(\frac{2\pi R}{\lambda}\right)^2 - 1\right]\varepsilon^2. \tag{6.14}$$

The cylinder is unstable when the perturbation wavelength exceeds a critical value λ_c, given by

$$\left(\frac{\lambda_c}{2\pi R}\right)^2 = 1 - 2\alpha. \tag{6.15}$$

If the surface tension is very anisotropic, i.e., $\alpha > 1/2$, the cylinder is unstable for perturbations of any wavelength.

B. A ROW OF GRAINS—A MODEL WITH TWO DEGREES OF FREEDOM

An important distinction exists between a system of one degree of freedom and a system of multiple degrees of freedom. For a system of one degree of freedom (e.g., the spherical particle studied in Section III.A), the free energy is a function of the generalized coordinate (i.e., the particle radius), represented by a curve in a plane with the free energy as the vertical axis and the generalized coordinate as the horizontal axis. A point on the curve represents a nonequilibrium state; a minimum point on the curve represents an equilibrium state. Energetics requires that the state descend on the curve. Consequently, energetics alone determines the final state. Kinetics is restricted to the role of determining the time needed to approach the equilibrium state.

For a system of two degrees of freedom, the free energy is a function of two generalized coordinates. This function is a surface in a three-dimensional space, with the free energy as the vertical axis, and the two generalized coordinates as horizontal axes. A point on the surface represents a nonequilibrium state in general; the bottom of a valley represents an equilibrium state. Energetics requires that an evolution path be a descending curve on the surface. There are, however, countless descending curves on a surface from any point other than a bottom of a valley. Consequently, when a system has two or more degrees of freedom, energetics by itself does not determine the evolution path. Kinetics plays a more significant role than just timekeeping.

In the analysis above of the Rayleigh instability, the system is modeled with only one degree of freedom, the amplitude of the perturbation, ε. It gives the sensible predictions when the perturbation amplitude is small, but cannot predict the spacing of the final spheres. In fact, the system has infinitely many final equilibrium configurations, and simply cannot be modeled with one degree of freedom.

We next illustrate these general points in some detail with a row of grains (Sun *et al.*, 1996). Similar problems arise in an electrical interconnect (Srolovitz and Thompson, 1986), powder sintering (Cannon and Carter, 1989), and a fiber constrained on a substrate (Miller and Lange, 1989). Figure 17(a) illustrates a fiber of bamboo-like grain structure. The fiber consists of a row of identical grains, initially cylindrical in shape and connected at their ends, each grain being of length L_0 and diameter D_0. The grains change shape by mass diffusion on the surfaces and grain boundaries, under the action of surface and grain-boundary tensions, γ_s and γ_b. The fiber is unconstrained in the longitudinal direction. The grains are assumed to remain identical to one another (Figure 17(b)). They will evolve to either one of two equilibrium configurations: the isolated spheres (Figure 17(c)), or connected disks of truncated spheres (Figure 17(d)).

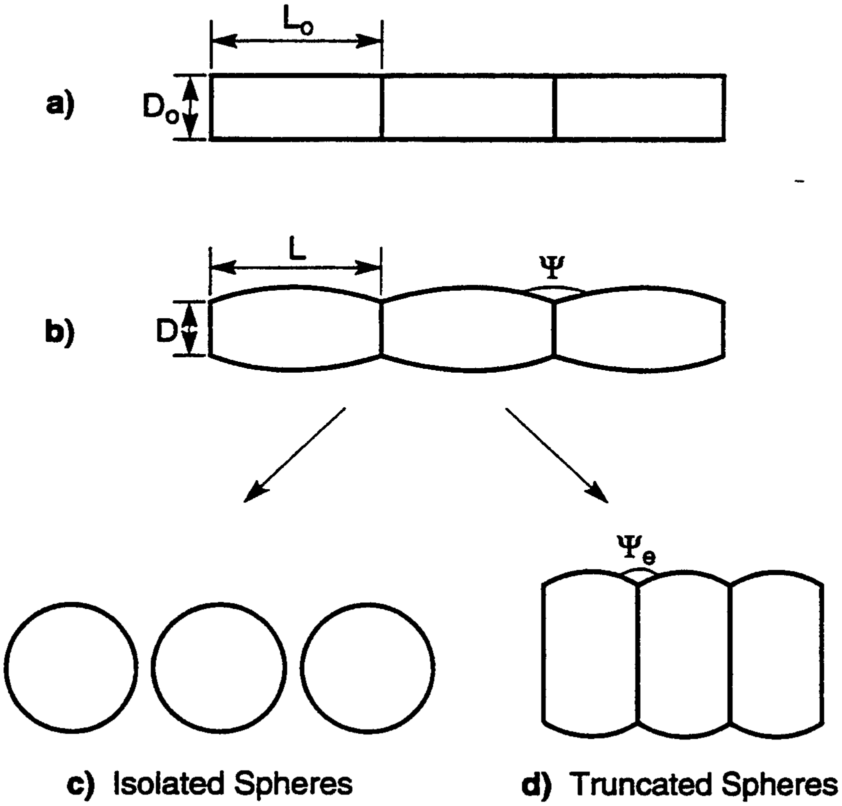

FIG. 17. (a) The initial cylinder-shaped grains. (b) Barrel-shaped grains approximate an intermediate, nonequilibrium state. (c) Grains pinch off and spheroidize, approaching an equilibrium state, a row of isolated spheres. (d) The array contracts as atoms diffuse out from the grain-boundaries and plate onto the free surfaces, approaching another equilibrium state, a touching array of truncated spheres.

The final equilibrium state is selected by an interplay between the free energy and the kinetic process. For most materials, $\gamma_b < 2\gamma_s$, and the isolated spheres in Figure 17(c) have higher free energy than the truncated spheres in Figure 17(d). For the fiber to groove along the triple junction, pinch off, and spheroidize, atoms need only diffuse on the surfaces of the grains. For the fiber to become truncated spheres, atoms must diffuse out of the grain boundaries to allow the grain length to shrink. If the atomic mobility on the grain boundary is much lower than that on the surface, $M_b \ll M_s$, which is true for many materials, the grains do not have the time to shorten significantly before they pinch off.

1. *Energy Landscape*

Approximate the shape of a nonequilibrium grain by a barrel formed by rotating a circular arc about a prescribed axis. The geometry is fully specified by three lengths: the arc radius R, the grain length L, and the grain-boundary diameter D. The volume of each grain is constant during evolution, which places a constraint. Consequently, within the approximation, the structure has only two degrees of freedom, which we chose to be the grain length L, and the dihedral angle, Ψ. Note that this approximation violates local equilibrium assumption at the triple junction.

Denote the area of the surface of a grain by A_s, and the area of a grain boundary by A_b. Consequently, the free energy per grain is

$$G = \gamma_s A_s + \gamma_b A_b . \tag{6.16}$$

When the triple junction reaches equilibrium, the dihedral angle, Ψ, reaches Ψ_e determined by (2.21). We will use Ψ_e to indicate the ratio γ_b/γ_s. The free-energy function, $G(L, \Psi)$, is computed in Miller and Lange (1989) and Sun *et al.* (1996).

Figure 18 shows the energy landscape for $L_0/D_0 = 2.5$ and $\Psi_e = 150°$. The upper-left corner terminates when the grains pinch off. Indicated on the landscape are the three special states: the initial cylinders, the isolated spheres, and the truncated spheres. From the initial state of the cylinders, the landscape descends steeply towards the minimum energy state of the truncated spheres. The landscape, however, does contain descending paths from the state of cylinders to the state of isolated spheres. Energy landscape, by itself, does not determine the evolution path.

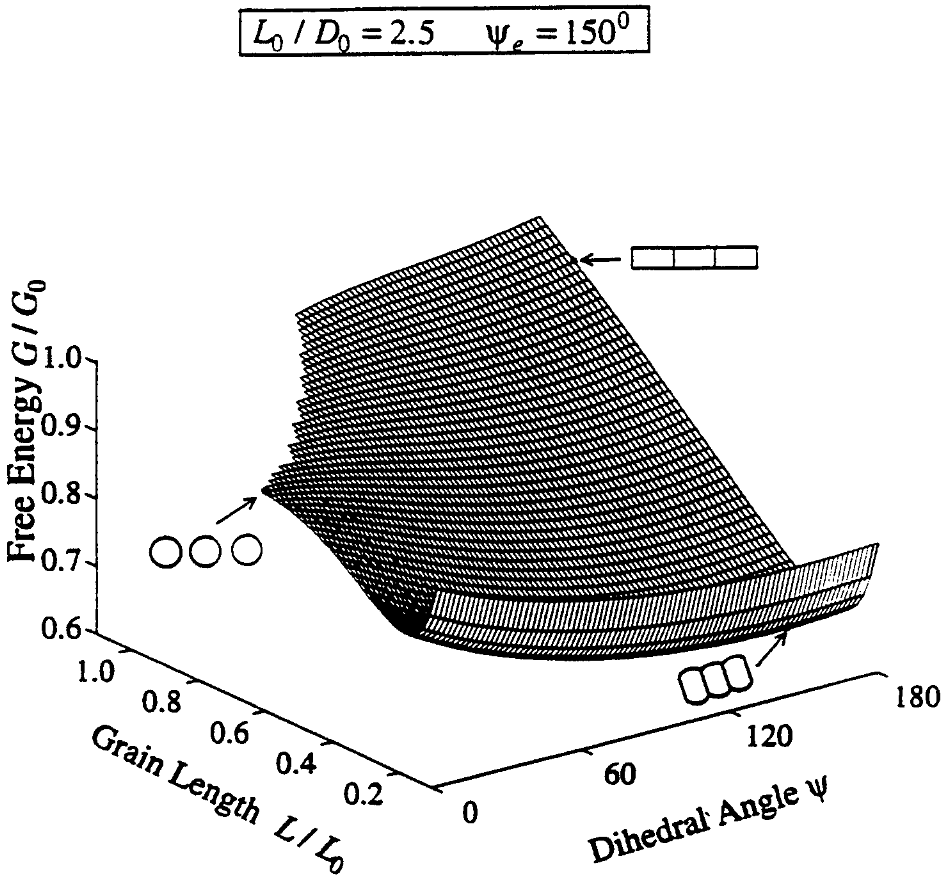

FIG. 18. Energy landscape: the free energy is a function of the generalized coordinates, the grain length and (nonequilibrium) dihedral angle. Three special states are indicated: the initial cylinders, the isolated spheres, and the truncated spheres.

2. *Evolution Path*

Denote the mobility on the grain boundary by M_b, and the mobility on the surface by M_s. The weak statement of the problem is

$$\int \frac{J_s}{M_s}\,\delta I_s dA_s + \int \frac{J_b}{M_b}\,\delta I_b dA_b = -\delta G. \tag{6.17}$$

The two integrals are over the surface and the grain boundary, respectively. Mass conservation relates the fluxes to the generalized velocities $\dot{L}$ and $\dot{\Psi}$. The Galerkin procedure leads to two ordinary differential equations that evolve the generalized coordinates, L and Ψ (Sun *et al.*, 1996).

The numerical solutions are plotted in Figure 19. The solid lines are the energy contours. After the grains pinch off, they spheroidize with only one degree of freedom, Ψ, as represented by the dashed line at the upper-left corner. The dotted lines are the evolution paths for various mobility ratios,

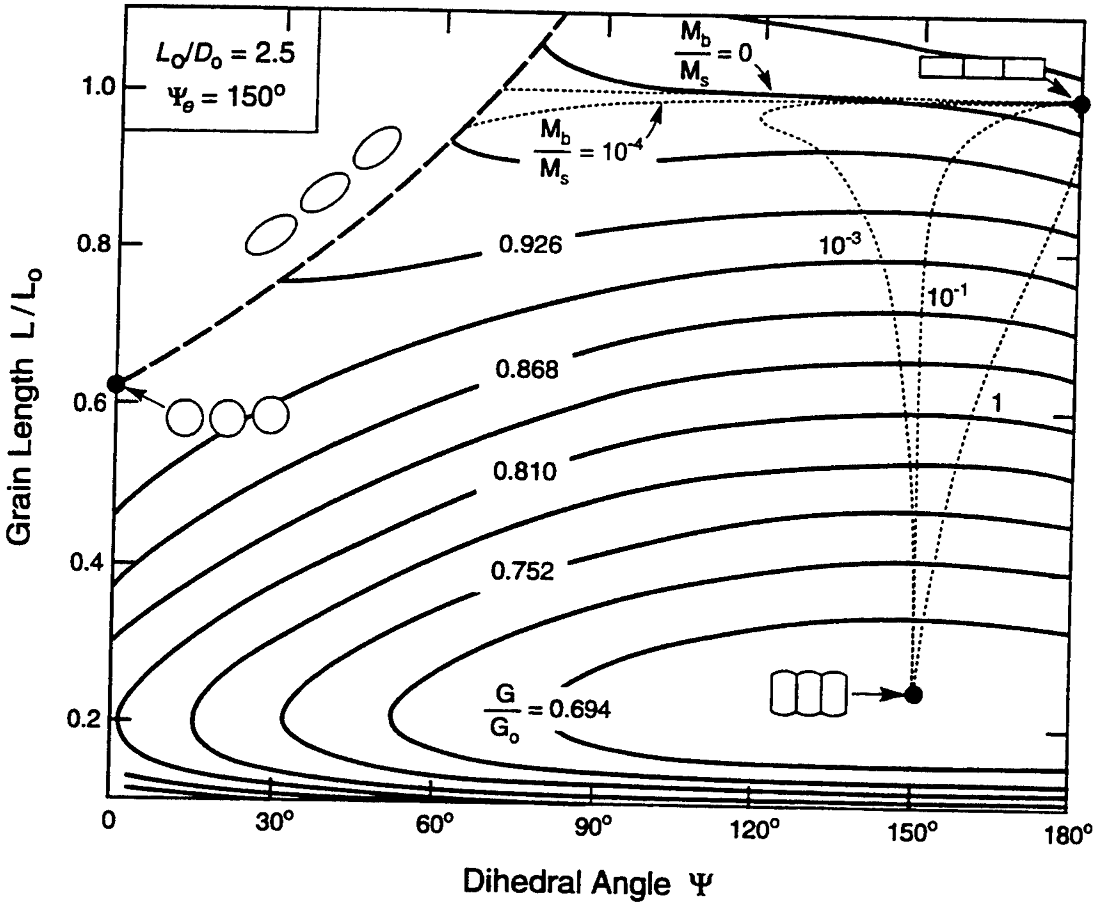

FIG. 19. The solid lines are the energy contours. The dotted lines are the evolution path when the grains are connected. The dashed line is the evolution path after the grains pinch off.

M_b/M_s. When the grain-boundary mobility is vanishingly small, $M_b/M_s = 0$, the grain length remains constant while the surface grooves; the grains pinch off and spheroidize, approaching a row of isolated spheres. Increasing the mobility ratio to $M_b/M_s = 10^{-3}$ allows the grains to contract to the state of truncated spheres. Consequently, everything else being fixed, a critical grain-boundary mobility exists, above which the grains contract to the lowest energy state, the truncated spheres. The evolution path depends on both energetics and kinetics.

Figure 20 draws a *morphological diversity map*. A point on the map represents a pair of parameters, L_0/D_0 and M_b/M_s. A boundary divides the plane into two regions. A parameter pair in one region makes the grains evolve to isolated spheres, and a parameter pair in the other region makes the grains evolve to truncated spheres.

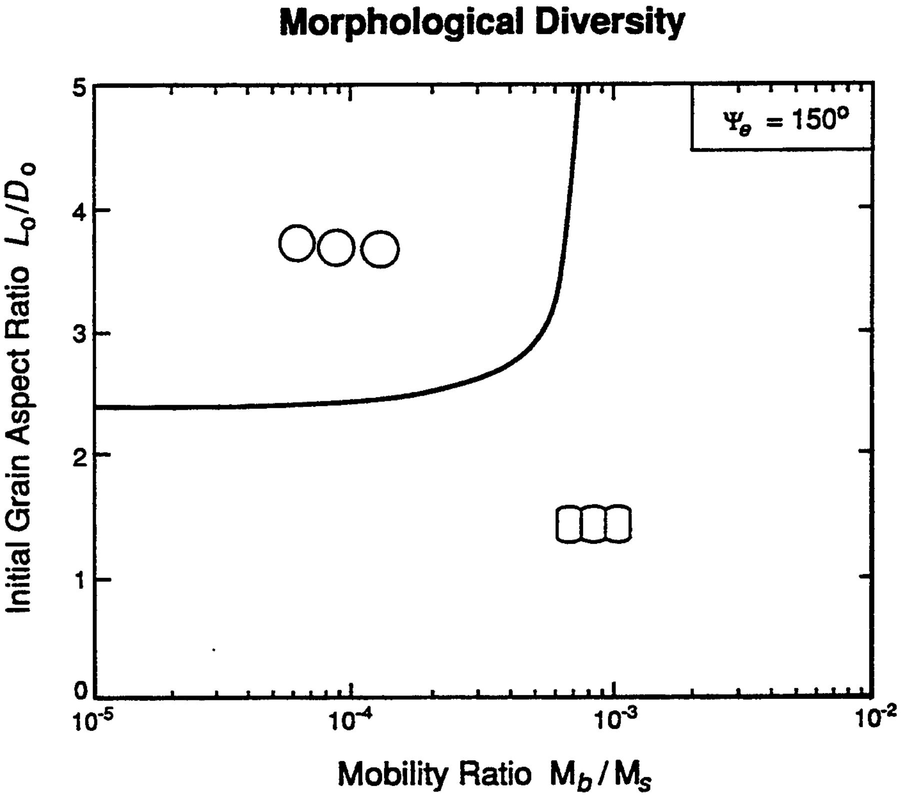

FIG. 20. A diversity map. The coordinates are the control parameters that do not change when the structure evolves. A boundary separates the plane into two regions. A fiber with the parameter group falling above the boundary evolves to isolated spheres. A fiber with the parameter group falling below the boundary evolves to truncated spheres.

C. GROOVING AND PITTING

Figure 21(a), page 256, illustrates a triple junction formed by a grain boundary and the free surface. The free surface is initially flat. When heated, atoms diffuse on the surface, leaving an indent along the triple junction, and two bumps over the grains. The size of the groove increases with the time. The forces that cause grooving are the surface and grain-boundary tensions. When the groove grows, the surface area increases somewhat, but the grain-boundary area decreases, so that the total free energy of the system reduces. Mullins (1957) analyzed this phenomenon, assuming that the surface and grain-boundary tensions, γ_s and γ_b, are isotropic, the grain boundary remains stationary, and no mass flows out from, or into, the grain boundary.

The equation for surface motion (5.14) becomes

$$v_n = B\nabla^2 K; \quad B \equiv M\Omega^2\gamma_s . \tag{6.18}$$

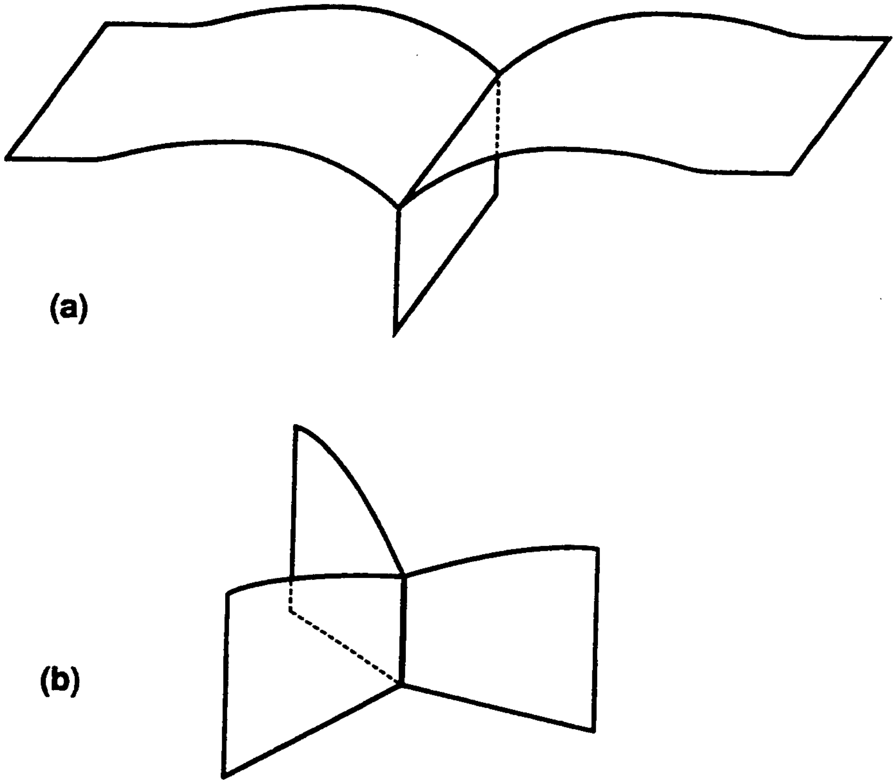

FIG. 21. (a) A surface groove over a grain boundary. (b) A surface pit over a three-grain junction.

Because the initial geometry has no length scale, the surface evolves with a self-similar profile: all lengths in the subsequent geometry scale with the time as $(Bt)^{1/4}$. For example, the groove depth (i.e., the distance from the groove root to the plane of the initial flat surface) scales as

$$d = k(Bt)^{1/4}. \tag{6.19}$$

The dimensionless coefficient k depends on the ratio γ_b/γ_s only. Mullins further simplified the problem by noting that the slope of the profile is typically small and the equation can be linearized. Under this simplification, k must be linear in the slope of the surface at the triple junction, m, defined by (3.13). Mullins' analysis gave $k = 0.78m$. The spacing between the peaks of the two bumps, w, has the same time scaling, but is independent of m under the small slope simplification. Mullins's analysis gave

$$w = 4.6(Bt)^{1/4}. \tag{6.20}$$

The groove width and depth may be measured experimentally. One can therefore deduce the surface tension and the surface diffusivity if γ_b has been determined by some other experiments. See Tsoga and Nikolopoulos (1994) for an experimental demonstration.

Figure 21(b) illustrates an intersection between the free surface and a three-grain junction. The surface grooves along the grain boundaries, and pits at the point of emergence of the three-grain junction. The surface profile is still self-similar, all lengths following the same time scaling as above. The pit depth obeys (6.19), the coefficient k depending on the ratios of various surface tensions involved. Genin *et al.* (1992) analyzed the problem, and found that k is greater than 0.78m, but within a factor of 3 for all the configurations considered by them.

Grain-boundary grooving and pitting may break a polycrysalline thin film on a substrate. If the grain size is much larger than the film thickness, (6.19) estimates the time needed for a three-grain junction to pit through the film thickness. However, if the grain size is comparable to the film thickness, mass transported from the grooves piles up on the grains, stopping the grooving process. Srolovitz and Safran (1986) and Miller *et al.* (1990) demonstrated that a critical ratio of grain size and film thickness exists, below which the grains reach an equilibrium configuration without breaking the film. Such an equilibrium state, however, may be unstable against grain growth. The coupled process of grain growth and surface grooving-pitting has not been analyzed.

D. GRAIN-BOUNDARY MIGRATION IN THIN FILM; EFFECT OF SURFACE DIFFUSION

Mullins (1958) investigated the effect of surface diffusion on the migration of a grain boundary. Figure 22 illustrates a triple junction of a grain boundary and two free surfaces. Two rate processes are involved: migration of the grain boundary and diffusion on the free surfaces. Dragged by the grain boundary, the groove moves to the right. Mullins solved the problem of the groove moving in a steady state, with constant velocity v

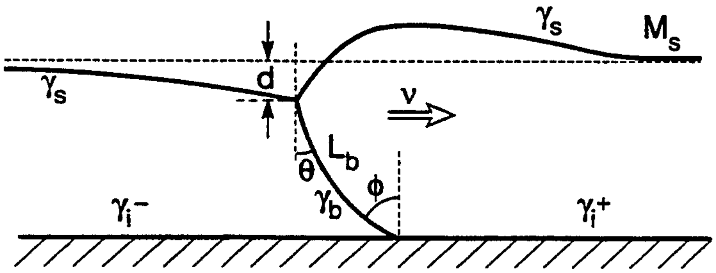

FIG. 22. A grain boundary moving in a thin film. Surface diffusion causes grooving at the triple junction.

and depth d. The significant features of his solution may be summarized as follows.

The steady velocity v and the material constant B in (6.18) define a length:

$$l = (B/v)^{1/3}. \tag{6.21}$$

This length sets the *scale* of the steady-state profile of the free surfaces. In particular, the groove depth, d, is linear in l. The *shape* of the translating groove depends on the ratio of the mobilities of the two surfaces, and the ratios of various surface tensions. Mullins assumed that the two surfaces have the identical mobility and surface tension. Consequently, only the ratio of the grain boundary and surface, γ_b/γ_s, enters the problem. Under the assumption that the surface slope is small, Mullins found that the steady-state groove depth is

$$d = \frac{\gamma_b}{3\gamma_s}\left(\frac{B}{v}\right)^{1/3}. \tag{6.22}$$

Everything else being equal, the larger the velocity, the smaller the groove depth.

Like surface evaporation, surface diffusion rotates the surfaces at the triple junction. The rotation angle θ in Figure 22 only depends on γ_b/γ_s. Mullins' solution gives

$$\theta = \frac{\gamma_b}{6\gamma_s}. \tag{6.23}$$

The rotation angle is independent of the steady velocity.

In his original analysis, Mullins (1958) did not specify the force that drives the grain-boundary migration, leaving the steady velocity undetermined. Following the works cited in Section III.E, we consider a grain boundary migrating in a thin film, driven by the difference in the interface tensions, γ_i^+ and γ_i^- (Figure 22). The slope ϕ is determined by the equilibrium of the triple junction in the horizontal direction (3.25). For the grain boundary to move to the right, it must concave toward the right, $\phi > \theta$, namely,

$$\frac{\gamma_i^+ - \gamma_i^-}{\gamma_b} > \frac{\gamma_b}{6\gamma_s}. \tag{6.24}$$

The effect of surface diffusion on grain-boundary migration is similar to surface evaporation discussed in Section III.E.

When $\phi > \theta$, from (3.20), the velocity of the grain boundary is given by

$$v = L_b \gamma_b \frac{(\phi - \theta)}{(h - d)}. \tag{6.25}$$

Simultaneously solving (6.22) and (6.25) gives v and d. The nonlinear equations have a unique real-valued solution. The solution depends on ϕ, θ, and the dimensionless ratio

$$\frac{\Omega^2 M_s}{h^2 L_b}, \tag{6.26}$$

involving the surface diffusion mobility M_s, the grain-boundary migration mobility L_b, the film thickness h, and the atomic volume Ω. Everything else being fixed, d/h increases with the parameter (6.26). Consequently, a thin film is more likely to break than a thick film.

E. STEADY SURFACE MOTION

1. *Surface Invariant in One Direction*

The profile of such a surface is described by the curve in a cross section. Assume, as a boundary condition or a symmetry condition, that the flux at a point on the surface vanishes. Let the origin of the coordinate (x, y) coincide with this point, Figure 23. Focus on a segment of the curve

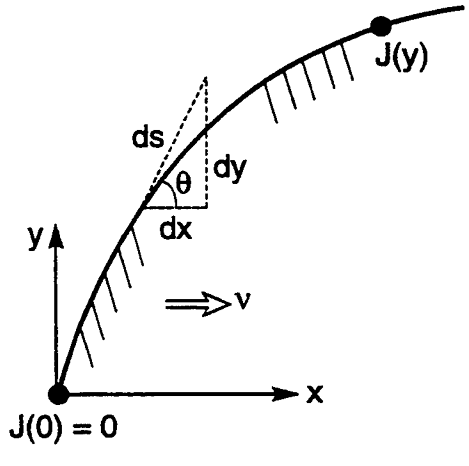

FIG. 23. Geometry of a steady-state surface profile.

between the origin and the point at y. Mass conservation relates the flux out of the segment, $J(y)$, to the steady velocity v:

$$J = \frac{vy}{\Omega}. \tag{6.27}$$

Assume isotropic surface tension γ and diffusion mobility M. The curvature K is positive for a convex surface. The flux relates to the curvature gradient along the surface:

$$J = -\frac{M\gamma\Omega\, dK}{ds}. \tag{6.28}$$

A combination of the two equations above gives that

$$\frac{dK}{ds} = -\frac{y}{l^3}. \tag{6.29}$$

The length l is defined by (6.21). Recall geometric relations,

$$\frac{d\theta}{ds} = -K, \frac{dy}{ds} = \sin\theta, \frac{dx}{ds} = \cos\theta. \tag{6.30}$$

Equations (6.29) and (6.30) give the complete set of ordinary differential equations. Note that only the last two equations are nonlinear, which may be linearized when the slope is small, as Mullins (1958) did. The equation set can be integrated with suitable boundary conditions. For a closed curve, the size of the problem is set by giving the area enclosed by the curve.

Chuang and Rice (1973) showed that a slit-like cavity may extend on a grain boundary if mass diffuses rapidly into the boundary ahead of the tip. Thouless (1993) and Klinger *et al.* (1995) studied slit formation on parallel grain boundaries. The co-evolution of pores and grains during sintering sets the microstructure of a final product. Spears and Evans (1982) examined the steady motion of a pore on a three-grain junction, and its relation with coarsening of pores and grains. The stability of the steady-state solutions has not been studied in general, but the available transient solutions show the validity of some steady-state solutions. Pharr and Nix (1979) and Thouless (1993) demonstrated that, under certain conditions, a rounded void on a grain boundary stressed in tension evolves to the steady-state slit solution of Chuang and Rice (1973).

2. *Surface of Revolution*

Now Figure 23 represents a surface of revolution around the x-axis. Assume that the flux at the apex vanishes, $J = 0$ at $y = 0$. Mass conservation relates the flux $J(y)$ to the steady velocity v:

$$J = \frac{vy}{2\Omega}. \tag{6.31}$$

The flux relates to the curvature gradient still by (6.28). For the surface of revolution, the sum of the principal curvatures is

$$K = -\frac{d\theta}{ds} + \frac{\cos\theta}{y}. \tag{6.32}$$

The set of ordinary equations are

$$\frac{dK}{ds} = -\frac{y}{2l^3}, \quad \frac{d\theta}{ds} = -K + \frac{\cos\theta}{y}, \quad \frac{dy}{ds} = \sin\theta, \quad \frac{dx}{ds} = \cos\theta. \tag{6.33}$$

They may be solved under analogous conditions as above.

Hsueh *et al.* (1982) examined the steady motion of a pore attached on a grain boundary, and the conditions under which the pore detaches from the grain boundary.

VII. Diffusion on an Interface between Two Materials

An interface between two materials is a rapid diffusion path for impurity atoms and atoms of the two materials. This section concerns with the latter. Both materials are taken to be rigid. (Sofronis and McMeeking, 1994 considered the combined interface diffusion and matrix creep in composite materials, which will not be considered here.) On an Al-Al_2O_3 interface, for example, one expects that aluminum diffuses much faster than oxygen, the latter being tied by the stronger atomic bonds. The situation is unclear on an Al-Al_2Cu interface: either aluminum or copper may be the dominant diffusion species on the interface. If aluminum diffusion dominates, the situation is similar to the aluminum-alumina interface. If copper diffusion dominates, in order for one copper atom to leave an interface element, one Al_2Cu unit dissolves and donates two aluminum atoms to the aluminum crystal. Similarly, for one copper atom to add to an interface element, one Al_2Cu unit forms and accepts two aluminum atoms from the aluminum crystal. See Ma and Suo (1993) for a discussion on such an interface. This section focuses on the situation exemplified by the aluminum-alumina interface, where no mass exchanges across the interface.

A. RIGID INCLUSION MOVING IN A MATRIX

Refer to the material that diffuses on the interface as *matrix*, and the material that does not diffuse as *inclusion*. Subject to a force, atoms of the matrix diffuse from one part of the interface to another. To accommodate the space, the inclusion moves like a rigid body—translating and rotating—relative to the matrix. The shape of the interface remains invariant. The mobility of the atoms on the interface determines both the translation and rotation velocities, which may change with time. This situation arises in several important phenomena in materials. For example, when an inclusion attaches to a grain boundary, the speed of the combined entity depends on the mobilities of both the inclusion and the grain boundary. Consequently, the inclusion may retard the grain-boundary migration.

As a demonstration, we will only consider inclusion translation. Let $\mathbf{v}$ be the translation velocity of the inclusion relative to the matrix, $\mathbf{J}$ the flux of the matrix atoms, Ω the volume per matrix atom, and $\mathbf{n}$ the unit vector normal to the interface pointing to the matrix. Assume that neither the inclusion nor the matrix deforms, so that the volume added to an interface element must be accommodated by the inclusion motion:

$$\mathbf{n} \cdot \mathbf{v} = \Omega \nabla \cdot \mathbf{J}. \tag{7.1}$$

Similarly, let $\delta \mathbf{r}$ be the virtual translation of the inclusion, and $\delta \mathbf{I}$ the virtual mass displacement. Mass conservation requires that

$$\mathbf{n} \cdot \delta \mathbf{r} = \Omega \nabla \cdot (\delta \mathbf{I}). \tag{7.2}$$

The driving force for the inclusion translation, $\mathbf{f}$, is the free-energy reduction associated with the inclusion translating unit distance, namely,

$$\delta G = -\mathbf{f} \cdot \delta \mathbf{r}. \tag{7.3}$$

This force can be calculated once the free energy is known as a function of the inclusion position. Equation (5.5) defines the diffusion driving force, and (5.6) prescribes the kinetic law. The weak statement (5.20) still applies.

Analytical solution can be readily found for an inclusion having a shape invariant in one direction subject to a force perpendicular to that direction, or for an axisymmetric inclusion subject to a force in the direction of the symmetry axis.

1. *Axisymmetric Inclusion*

With reference to Figure 23, the interface is a surface of revolution. The force f, defined by (7.3), is in the direction of the axis of revolution, the x-axis; y is the radius of the surface of revolution. The inclusion translates at velocity v in the x-direction. Mass conservation relates the flux J to the velocity v, and the virtual mass displacement δI to the virtual translation δr:

$$J = \frac{y}{2\Omega} v, \quad \delta I = \frac{y}{2\Omega} \delta r. \tag{7.4}$$

The weak statement (5.20) becomes

$$\int \left(\frac{y}{2\Omega} \right)^2 \frac{v\, \delta r}{M} \, dA = f \delta r,$$

giving

$$v = \frac{4M\Omega^2 f}{\int y^2 \, dA}. \tag{7.5}$$

The integral extends over the area of the interface. For a spherical inclusion of radius R, $\int y^2 \, dA = 8\pi R^4/3$, so that

$$v = \frac{3M\Omega^2 f}{2\pi R^4}. \tag{7.6}$$

The approximate solution given by Shewmon (1964) has the same form as (7.6), but a different coefficient.

2. *Two-Dimensional Problem*

Figure 23 now represents an inclusion having a shape invariant along the axis normal to the plane of the paper, subject to a force in the x-axis. Energy is on a per thickness basis, so that f is the force on a per unit thickness of the inclusion. We will assume that the particle translates in the x-axis; the method, however, is general. Let J_0 be the flux on the interface at $y = 0$, and J the flux at a general point y on the interface. Mass conservation requires that

$$J = J_0 + \frac{y}{\Omega} v, \quad \delta I = \delta I_0 + \frac{y}{\Omega} \delta r. \tag{7.7}$$

The weak statement (5.20) becomes

$$\int \frac{1}{M}\left(J_0 + \frac{y}{\Omega} v\right)\left(\delta I_0 + \frac{y}{\Omega} \delta r\right) ds = f\delta r.$$

The integral extends over the cross-section curve of the interface. Because the two virtual variations, δr and δI_0, are independent, the equation splits above to two equations

$$\Omega J_0 \int ds + v \int y ds = 0. \tag{7.8}$$

$$\Omega J_0 \int y ds + v \int y^2 ds = \Omega^2 M f. \tag{7.9}$$

They solve J_0 and v.

When a problem has a symmetry, and the origin of the y-axis is so placed that $\int y ds = 0$, the solution is $J_0 = 0$ and

$$v = \frac{M\Omega^2 f}{\int y^2 ds}. \tag{7.10}$$

For example, a cylindrical inclusion of radius R translates at velocity

$$v = \frac{M\Omega^2 f}{\pi R^3}. \tag{7.11}$$

B. DIFFUSION-CONTROLLED INTERFACIAL SLIDING

Two-bonded materials under a shear stress may slide relative to each other. If the interface is flat, they slide by a viscous shear process on the interface. If the interface deviates from a perfect plane, the shear process alone does not accommodate the sliding. The asperity on the interface may be accommodated by plastic flow or fracture. Raj and Ashby (1971) proposed an alternative process, which operates at low stresses and high temperatures, when the bulk of the materials is rigid. Figure 24 illustrates two materials bonded by an interface with steps. Under the applied shear stress, τ, the interface is under tension at locations like A, and compression at locations like B. The gradient of the normal stress causes atoms of at least one material to diffuse on the interface, and thereby accommodates sliding. In this picture, sliding consists of two rate processes: viscous shear and interfacial diffusion. The two processes are in series; the slower one limits the sliding rate. Raj and Ashby gave experimental evidence indicating that it is often mass diffusion, rather than viscous shear, that limits the sliding rate. Similar considerations suggest that inclusion particles on a grain boundary may retard grain-boundary sliding (Raj and Ashby, 1972).

Following Raj and Ashby (1971), we consider an interface with periodic steps (Figure 24). The ratio of the step height to the period, h/λ, is typically small and is exaggerated in the figure. Due to symmetry, the flux vanishes at the middle of the step height, where the origin of the y-axis is placed. We next apply (7.10) to one period of the bi-material. The force on one period is

$$f = \tau\lambda.$$

The integral over the interface within one period is

$$\int y^2 ds = \frac{1}{4}\lambda h^2 + \frac{1}{6}h^3. \tag{7.12}$$

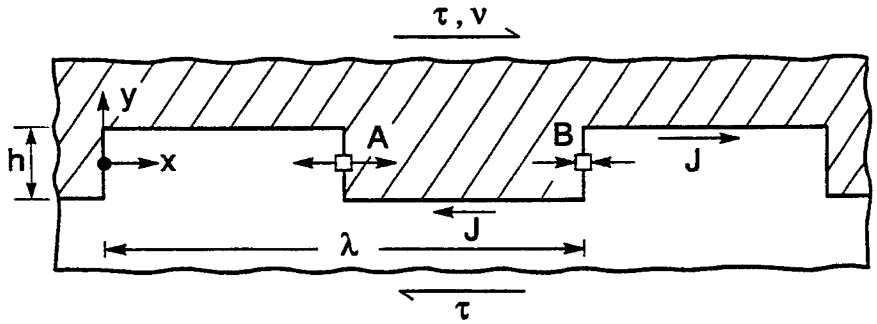

FIG. 24. A bi-material interface with periodic steps. The rate of sliding is limited by diffusion on the interface to accommodate the asperity.

Consequently, the two materials slide at a relative velocity

$$v = \frac{4M\Omega^2\tau}{h^2\left(1 + \dfrac{2h}{3\lambda}\right)}. \tag{7.13}$$

This reproduces the approximate result of Raj and Ashby (1971) in the limit $h/\lambda \to 0$.

C. GRAIN-BOUNDARY MIGRATION IN THIN FILM; EFFECT OF INCLUSION

Figure 25 illustrates a grain boundary migrating in a thin film of thickness h, motivated by the difference in the film-substrate interface tensions of the two grains, γ_i^+ and γ_i^-. The grain boundary also drags a semi-circular inclusion of radius R on the film surface. The surface tensions of the two grains at the free surfaces, γ_s, are taken to be the same. The inclusion retards the grain-boundary motion if the inclusion itself has low mobility. We will only consider a two-dimensional problem where the inclusion is a cylinder. The film-substrate interface is taken to be immobile, so that the angle at the triple junction, ϕ, is given by (3.25).

The grain-boundary migration can be modeled by the steady-state solution in Section III.D. The grain boundary moves at a velocity

$$v = \frac{L\gamma_b(\phi - \theta)}{h - R}. \tag{7.14}$$

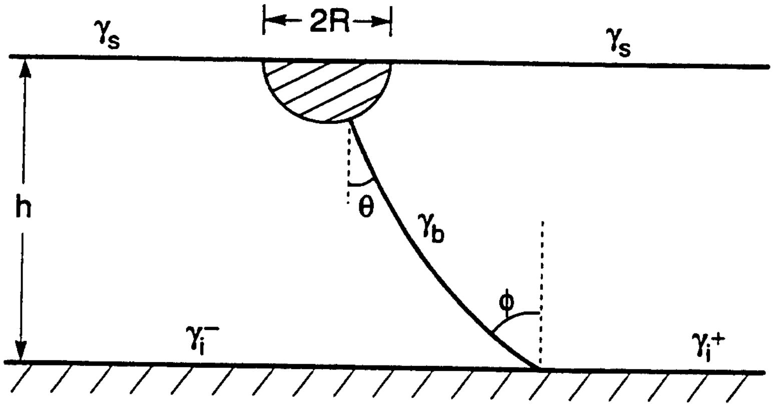

FIG. 25. A grain boundary in a thin film, pinned by an inclusion.

The grain-boundary tension exerts a force on the inclusion, $f = \gamma_b \sin\theta$. Equation (7.11) gives the velocity of the inclusion

$$v = \frac{2M\Omega^2 \gamma_b \sin\theta}{\pi R^3}. \tag{7.15}$$

The angle θ falls between 0 and ϕ, and is determined by equating the velocities above. Consequently, the angle θ is solved from

$$\frac{\sin\theta}{\phi - \theta}\left(1 - \frac{R}{h}\cos\theta\right) = \frac{\pi L R^3}{2M\Omega^2 h}. \tag{7.16}$$

The inclusion retards the grain-boundary migration substantially if $\theta \to \phi$, or

$$\frac{LR^3}{M\Omega^2 h} \gg 1. \tag{7.17}$$

This condition involves the film thickness and particle radius, the migration mobility of the grain-boundary L, and the diffusion mobility of the inclusion-film interface M.

VIII. Surface Diffusion Driven by Surface- and Elastic-Energy Variation

A small crystal can sustain a high stress without fracture or plastic deformation. At an elevated temperature, the elastic energy can motivate mass diffusion. For example, when a film is deposited on a substrate with similar crystal structure having a few percent difference in lattice constant, the film strains to match the substrate lattice constant. The stress in the film would exceed 1 GPa were all relaxation processes suppressed. When the film is thick, the stress is relieved by dislocations or cracks. When the film is thin and the temperature is high, the stress is relieved by mass diffusion, breaking the film into islands. See Leonard *et al.* (1994) for a demonstration with InAs on GaAs.

Surface diffusion driven by strain-energy variation is difficult to analyze. The stress field has to be solved as a boundary-value problem for every surface shape during evolution, which is analytically intractable for most technically interesting problems. The high-order differential equation (5.14) requires great care in the numerical analysis. In many situations, the stress is partially relieved by misfit dislocations; linear elasticity is inadequate. Due to these difficulties, only a few idealized problems have been solved.

This section discusses two such problems to give an impression of this class of phenomena. Each problem deals with an elastic body subject to a constant load. The free energy of the crystal, G, has three contributions: the surface energy U_S, the elastic energy U_E, and the applied load times the displacement, i.e., $G = U_S + U_E -$ load × displacement. Linear elasticity dictates that $2U_E =$ load × displacement. Consequently, the free energy of an elastic solid under constant load is

$$G = U_S - U_E. \tag{8.1}$$

A. INSTABILITY OF A FLAT SURFACE

First consider a large piece of crystal under no external stress. A surface of the crystal is flat and has isotropic surface tension. If scratched, the surface heals as the surface tension motivates mass to flow to restore the minimum energy configuration, the flat surface. Mullins (1959) analyzed the flattening process via several mass-transport mechanisms, including surface diffusion.

Next, subject the crystal to a uniaxial stress parallel to the flat surface. The crystal is taken to deform elastically. The flat surface is unstable: a small-amplitude perturbation amplifies if its wavelength exceeds a critical value. The phenomenon was independently analyzed by Asaro and Tiller (1972), Grinfeld (1986), Srolovitz (1989), and Gao (1991). The perturbation grows to a surface crack running into the bulk of the crystal, transverse to the applied stress direction (Chiu and Gao, 1993; Yang and Srolovitz, 1993; Yakobson, 1993). Suo and Yu (1997) extended the analysis to an elastic polycrystal surface. Gao (1994) and Freund (1995) surveyed the related problems.

Spencer *et al.* (1991) and Freund and Jonsdottir (1993) analyzed the similar instability in a film strained by a substrate. The undulation may break the film into islands, if atoms of the substrate do not diffuse at the temperature. Wong and Thouless (1995) studied the ratio of the island height and radius as a function of the misfit strain and various surface tensions. Seifert *et al.* (1996) demonstrated that the surface energy anisotropy is important in island formation.

1. *Energetics*

What follows describes the essential findings of the initial surface instability. To focus on main ideas, we treat the plane stress problem of a semi-infinite elastic crystal subject to a uniform stress, σ, parallel to the free surface of the crystal. The surface tension of the crystal, γ, is isotropic.

Consider the energy variation when the flat surface is perturbed. The perturbed surface has a larger area than the flat surface, so that U_S increases with the perturbation. Under a constant load, a body with a perturbed surface has a larger displacement at the loading point than a body with the flat surface (i.e., the undulation makes a body more compliant), so that U_E also increases with the perturbation. According to (8.1), the surface tension favors the flat surface, but the stress favors the perturbed surface: the two forces compete to determine whether the perturbation diminishes or amplifies.

To be specific, perturb the flat surface by a wave of amplitude q and period λ:

$$y(x,t) = q(t)\cos\frac{2\pi x}{\lambda}. \tag{8.2}$$

Here, y is the height of the perturbed free surface from the initial flat surface, the x-axis coincides with the flat surface, and t is the time. The amplitude q is the generalized coordinate in this problem. Following the previous authors, we will carry out a linear stability analysis, with $q/\lambda \ll 1$. The energies will be calculated to the leading order in q/λ, per period per unit thickness, relative to the energies of the stressed crystal with the flat surface.

The undulation increases the surface energy by

$$U_S = \frac{\pi^2\gamma}{\lambda}q^2. \tag{8.3}$$

This is readily obtained by calculating the length of the curve (8.2). Because a change in the sign of q leaves the curve length unchanged, U_S is proportional to q^2 to the leading order in q.

For a similar reason, the elastic energy variation U_E is proportional to q^2 to the leading order in q. In addition, linear elasticity dictates that U_E

be proportional to σ^2/Y, where Y is Young's modulus. A dimensional analysis shows that

$$U_E = \beta \frac{\sigma^2}{Y} q^2, \tag{8.4}$$

where β is a dimensionless number of order unity. An elasticity problem of the wavy surface can be solved analytically to the leading order in q/λ, giving $\beta = \pi$; see the papers cited previously.

A combination of (8.3) and (8.4) gives the free-energy difference between the solid with a wavy surface and the solid with a flat surface:

$$G = \left(\frac{\pi^2 \gamma}{\lambda} - \frac{\pi \sigma^2}{Y} \right) q^2. \tag{8.5}$$

The free energy decreases when the quantity in the bracket is negative. Consequently, the perturbation amplifies when the wavelength λ exceeds a critical value, given by

$$\lambda_c = \pi Y \gamma / \sigma^2. \tag{8.6}$$

Because the elastic energy is quadratic in the applied stress σ, the flat surface undulates under both tension and compression.

2. *Kinetics*

The profile (8.2) with $q/\lambda \ll 1$ has velocity normal to the surface $v_n = \dot{q} \cos(2\pi x/\lambda)$. Mass conservation relates the atomic flux to the normal velocity by $\partial J/\partial s = -v_n/\Omega$. For a small-amplitude perturbation, the curve length s can be replaced by x. An integration gives

$$J = -\left[\frac{\lambda}{2\pi\Omega} \sin \frac{2\pi x}{\lambda} \right] \dot{q}. \tag{8.7}$$

A similar relation connects the virtual mass displacement δI and virtual amplitude δq. The weak statement (5.20) leads to

$$\dot{q} = \frac{q}{\tau}, \tag{8.8}$$

distortion changes the pore volume and shape by a small amount; large changes require creep or mass transport. If the crystal creeps rapidly and surface diffusion is slow, the pore increases volume and becomes needle-shaped in the pulling direction (e.g., Budiansky *et al.*, 1982; Needleman and Rice, 1980).

This subsection is concerned with the situation where surface diffusion is so rapid that the crystal creeps negligibly during the time of interest. On the basis of several theoretical studies (Stevens and Dutton, 1971; McCartney, 1976; Gao, 1992, 1995; Suo and Wang, 1994; Sun *et al.*, 1994; Wang and Suo, 1997), we suggest the following sequence of events in the Newcomb and Tressler experiments. When the fiber is under no stress, the pore has a rounded shape maintained by the surface tension. When the fiber is under a tensile stress, the pore changes shape via surface diffusion. Two outcomes are expected. If the applied stress is small, the pore reaches an equilibrium shape close to an ellipsoid, as a compromise between the stress and the surface tension (Figure 26(a)). If the applied stress is large, the pore keeps changing shape and develops a sharp crack tip which grows in the direction transverse to the applied tensile stress (Figure 26(b)).

On forming the sharp tip, further crack elongation is no longer limited by self-diffusing on the pore surface. Atomic bonds break at the crack tip by the intense stress, possibly assisted by the environmental species inside

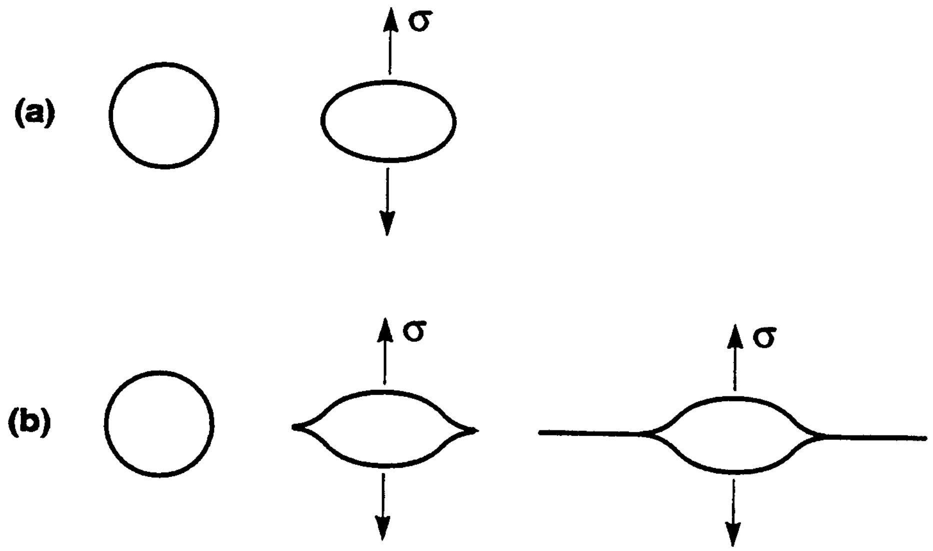

FIG. 26. a) A pore under a small stress reaches an equilibrium configuration, which is approximately an ellipse. b) A pore under a large stress develops sharp noses, followed by subcritical cracking.

the pore. The rate of crack growth may be limited by transport of the environmental species to, or reaction at, the crack tip (Lawn, 1993). Once the crack grows large enough, fast fracture breaks the entire crystal. The fiber spends its lifetime mainly in two stages: self-diffusion to grow the sharp tip, and the subcritical cracking after the sharp tip has formed. Which stage takes the longer time depends on the material, chemical environment, and temperature.

2. *Energetics of Crack Emergence*

Compare two crystals, one with a spherical pore, and the other a nonspherical pore. Both crystals are subject to the same tensile load remote from the pores. The pores have the same volume. Because the sphere has the minimal surface area among pores of the same volume, the nonspherical pore increases the surface energy U_S. Because a body with a flattening pore transverse to the loading axis is more compliant than a body with a spherical pore, the nonspherical pore increases the elastic energy U_E. Consequently, according to (8.1), the two forces compete to determine the pore shape: the surface tension favors a spherical pore, and the applied stress favors a crack.

Let a_0 be the initial pore radius, σ the stress, γ the surface tension, and Y Young's modulus. Express the relative importance of the elastic energy and the surface-energy variations with a dimensionless number

$$\Lambda = \frac{\sigma^2 a_0}{Y_\gamma}. \tag{8.11}$$

When Λ is small, the surface energy variation dominates, and the pore reaches an equilibrium state of approximately ellipsoidal shape. When Λ is large, the elastic-energy variation dominates, and a crack emerges from the pore.

The following reviews the calculation of Suo and Wang (1994). The surface tension is taken to be isotropic. Consider a plane-stress problem of a cylindrical pore in an infinite crystal, subject to stresses σ_1 and σ_2 in the x- and y-directions. Initially, the pore is a circle of radius a_0. Under the action of the surface tension and stresses, atoms diffuse on the pore surface, causing the pore to evolve to a sequence of noncircular shapes.

We will first approximate the evolving shapes by a family of ellipses. Mass conservation requires that the area of the ellipses be the same as the area of the initial circle, πa_0^2. Consequently, the system has only one degree of freedom, the ratio of the two semi-axes of the ellipses, written as

$$\frac{(1+m)}{(1-m)}. \tag{8.12}$$

The circle corresponds to $m = 0$, the slit in the x-direction to $m \to 1$, and the slit in the y-direction is $m \to -1$.

Energies are calculated on the unit thickness basis, and the initial state is taken to be the ground state. The surface energy equals the surface tension times the perimeter of the ellipse. Relative to the circular pore, an elliptic pore has surface energy

$$U_S = \frac{a_0\gamma}{\sqrt{1-m^2}} \int_0^{2\pi} (1 + m^2 - 2m\cos 2\theta)^{1/2}\, d\theta - 2\pi a_0 \gamma. \tag{8.13}$$

The integral is evaluated numerically.

The stress field can be found in elasticity textbooks. The elastic-energy difference between a body with an elliptic pore and a body with a circular pore is computed from (4.14), giving

$$U_E = \frac{2\pi a_0^2}{Y}\left(\frac{m}{1-m}\sigma_2^2 - \frac{m}{1+m}\sigma_1^2\right). \tag{8.14}$$

The total free energy G is given by (8.1).

Figure 27(a) displays the free energy at several constant levels of Λ for a pore in a body under $\sigma_1 = \sigma_2$. Here, G is the free energy of the crystal with an elliptic pore, and the G_0 is the free energy of the crystal with a circular pore. Each minimum and maximum represents a stable and unstable equilibrium state, respectively. Three types of behaviors emerge depending on the value of Λ, i.e., the relative importance of elastic and surface energy, as follows.

(1) When $\Lambda = 0$, the surface tension dominates; G reaches a minimum at $m = 0$, and maxima at $m = \pm 1$. The circular void is stable and the two slits are unstable: any ellipse will relax to the circle.

(2) When $\lambda > \frac{3}{8}$, the stress dominates; G reaches the maximum at $m = 0$, and minima at $m = \pm 1$. The circle is unstable but the slits are stable: any elliptic void will collapse to the slits.

(3) For an intermediate level, $0 < \Lambda < \frac{3}{8}$, G reaches a local minimum at $m = 0$, two maxima at some $\pm m_c$, and two minima at $m = \pm 1$. The

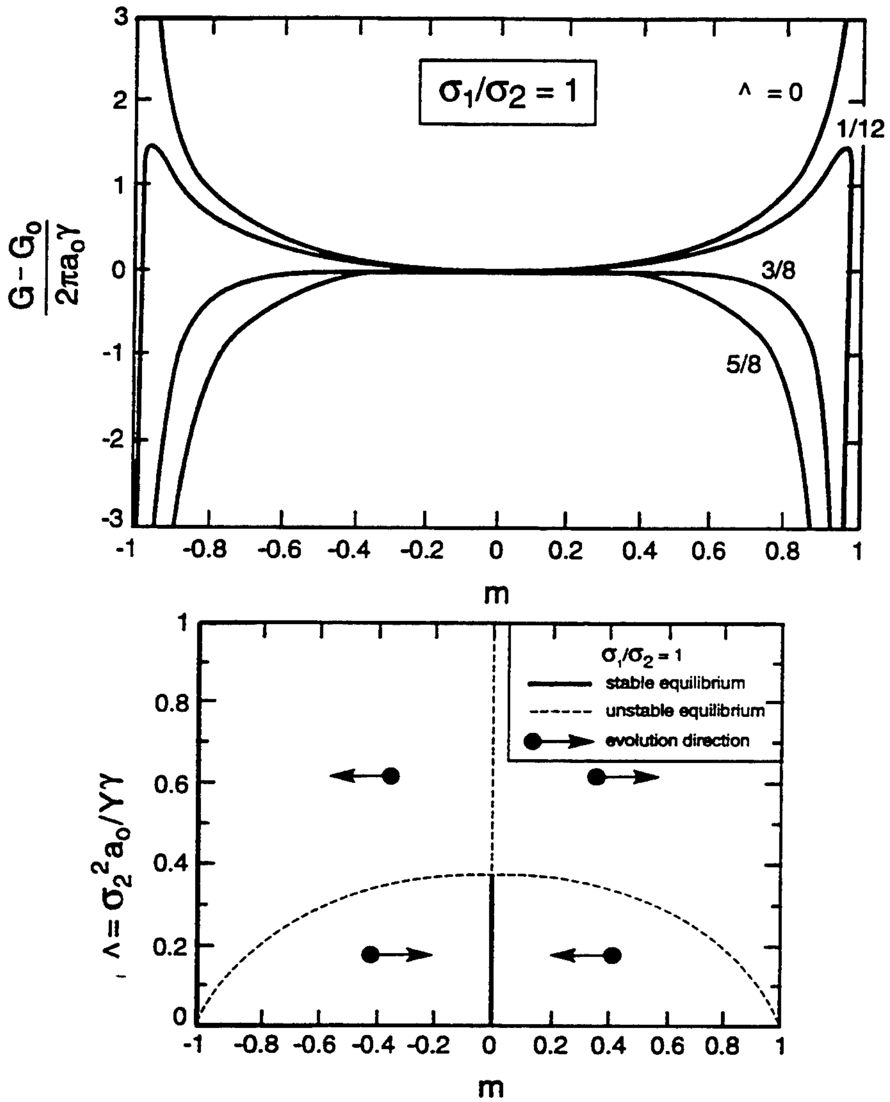

FIG. 27. Biaxial stress state $\sigma_1 = \sigma_2 = \sigma$. a) The free energy as a function of the void shape m at several levels of Λ. b) The bifurcation diagram is a combination of a subcritical pitchfork and two Griffith cracks.

maxima act as energy barriers: an ellipse of $|m| < m_c$ will relax to the circle, but an ellipse of $|m| > m_c$ will collapse to the slits.

The information above is projected onto the (Λ, m) plane, Figure 27(b). The heavy solid and dotted lines correspond to the stable and unstable equilibrium states, respectively. The two slits are stable for any $\Lambda > 0$, but unstable for $\Lambda = 0$. The circle $m = 0$ is metastable when $\Lambda < \frac{3}{8}$, but unstable when $\Lambda > \frac{3}{8}$. The dotted curve is the unstable equilibrium states, referred to as m_c in the preceding paragraph. These lines divide the (Λ, m) plane into four regions. A point in each region corresponds to an ellipse under a constant level of Λ, evolving toward a stable equilibrium state, either the circle or the slits. The evolution direction in each region is indicated by an arrow. An ellipse below the dotted curve relaxes to the circle, and an ellipse above the dotted curve collapses to a slit. An initially circular void will collapse if Λ exceeds the critical value $\Lambda_c = \frac{3}{8}$.

Figure 28(a) and 28(b) are for $\sigma_1/\sigma_2 = 0.8$, representative of any stress ratios in the interval $0 < \sigma_1/\sigma_2 < 1$. Several asymmetries are noted. For small Λ, the local minimum no longer occurs at $m = 0$, nor do the two maxima at the same value of $|m|$. At a critical value, still denoted as Λ_c, the minimum and the maximum on the right-hand side annihilate, but the maximum on the left-hand side persists. In Figure 28(b), the values of m minimizing G are the heavy-solid lines, and the values of m maximizing G

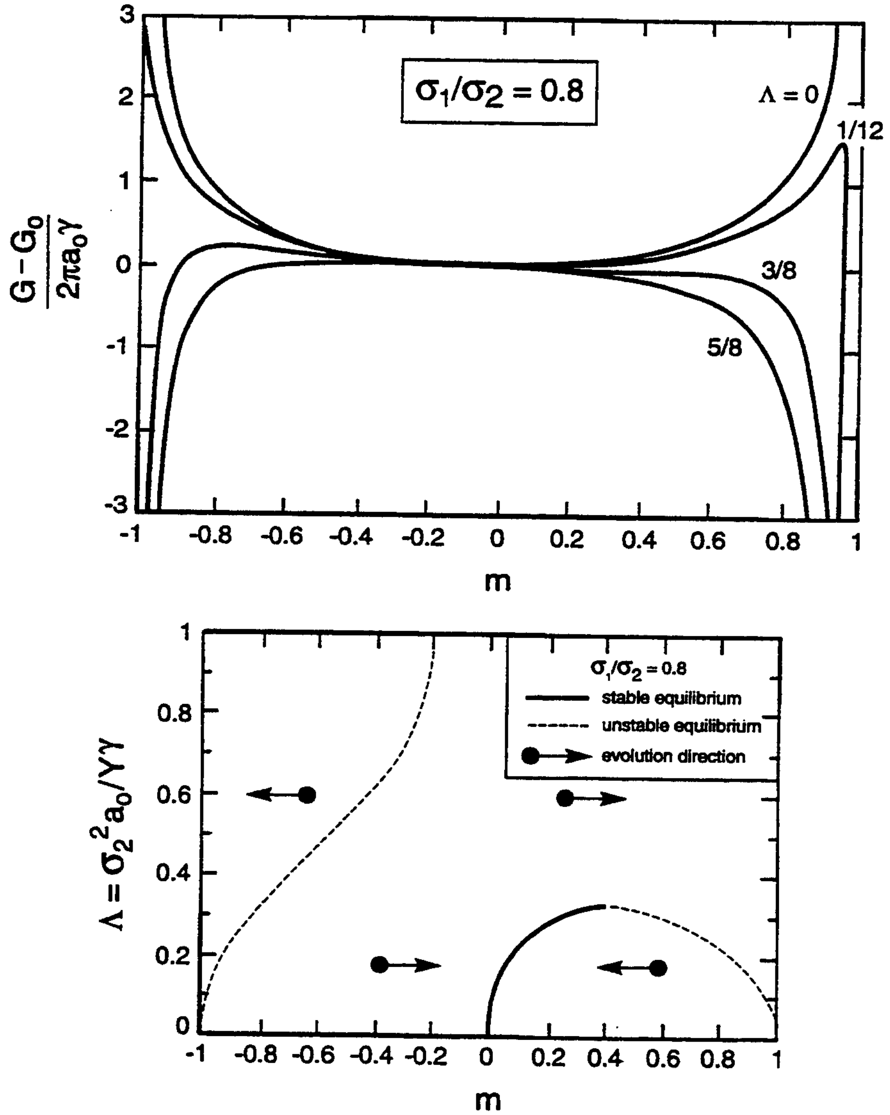

FIG. 28. Biased biaxial stress state $\sigma_1/\sigma_2 = 0.8$. a) The free energy as a function of the void shape m at several levels of Λ. b) Stability conditions projected on the (m, Λ) plane.

are the dotted lines. As expected, under the biased stress, the equilibrium shape is noncircular even for a small value of Λ. The heavy-solid curve ends at Λ_c, and is continued by the dotted curve.

Figure 29 gives the calculation Λ_c as a function of the stress ratio. The critical number does not vary significantly for the entire range of the stress ratio. Sun *et al.* (1994) gave the corresponding results for a three-dimensional pore.

3. *Kinetics*

Next, examine the kinetics of the pore-shape change using the weak statement. Normalize all the geometric lengths by the radius of the initial circular pore, a_0. From the weak statement we find that the problem has a characteristic time scale

$$t_0 = \frac{a_0^4}{M\Omega^2\gamma}, \tag{8.15}$$

which is used to normalize the time. Figure 30 plots the semi-axis of the ellipse, a, as a function of the time, for several levels of the loading parameter Λ. The body is remotely under stress state $\sigma_1 = \sigma_2$. The initial value is arbitrarily assigned to be $a/a_0 = 1.01$ at $t = 0$. The pore spends

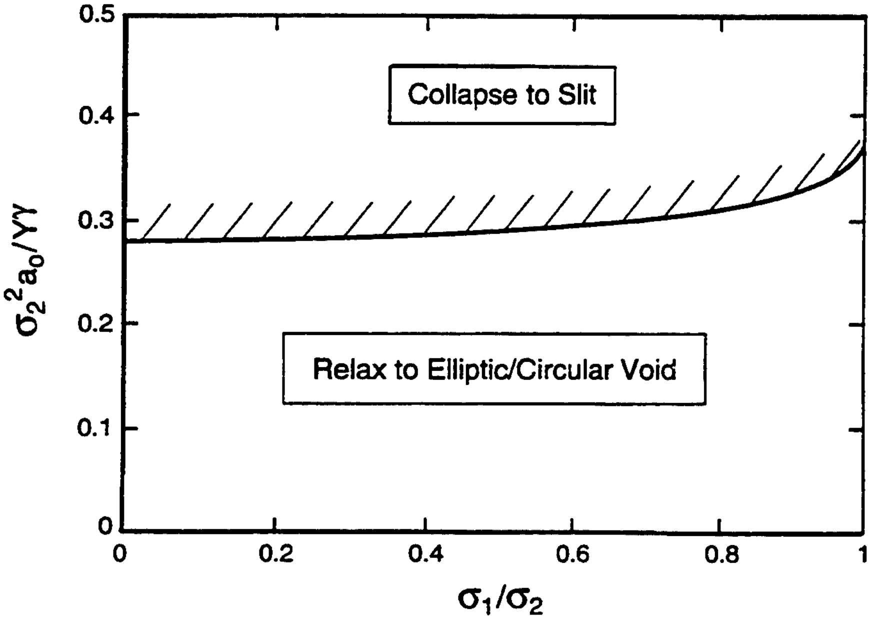

FIG. 29. The critical number Λ_c as a function of the stress ratio.

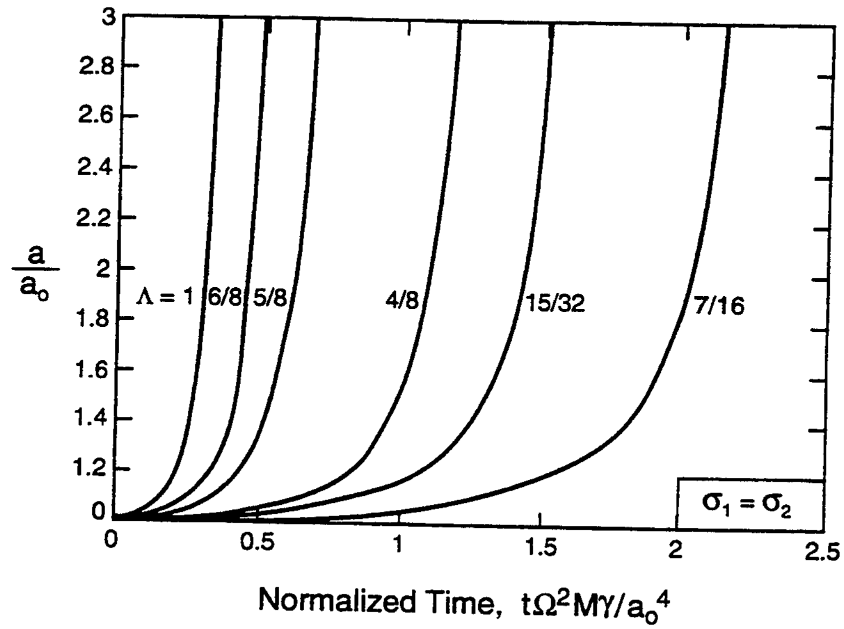

FIG. 30. The time for one ellipse to evolve to another.

most of its time deviating from the circle. After it became somewhat elliptic, the shape change is rapid.

C. NOSING, CUSPING, AND SUBCRITICAL CRACKING

Chiu and Gao (1993) and Yang and Srolovitz (1993) went beyond the linear stability analysis of Section VIII.A, and studied large deviation from the flat surface. They found that surface cracks emerge and grow into the bulk of the crystal. In Section VIII.B, we have approximated the evolving pore as ellipses. The pore shape, however, may significantly deviate from an ellipse during evolution. Wang and Suo (1997) allowed more degrees of freedom for the pore shape, determined the elastic field around the pore with a conformal mapping, and traced the evolution of the pore shape.

We next summarize the findings of these studies in the context of the shape change of a pore. The critical loading level, Λ_c, is still given approximately by the curve in Figure 29. When the loading level is below Λ_c, the circular pore evolves to a rounded shape, approximately elliptical if $\sigma_1 \neq \sigma_2$.

When the loading level exceeds Λ_c, the circular pore evolves with nearly elliptical shapes in the beginning, then develops noses, and sharpens to become cusps, as schematically illustrated in Figure 28(b). The noses shorten diffusion length and further concentrate stress: this is a selfamplifying process. The time needed from a circular shape to develop cusps takes the form

$$t_{\text{cusp}} = t_0 g(\Lambda). \tag{8.20}$$

When Λ just exceeds Λ_c, t_{cusp} is on the same order of the characteristic time t_0. When $\Lambda \gg \Lambda_c$, t_{cusp} is only a small fraction of the characteristic time t_0.

When the curvature at the nose tips increases and the noses become cusps, the stress becomes singular at the cusp tip. The stress field around a cusp tip has the same structure as that around a crack tip. The chemical potential at the cusp tip is ill-defined, because the cusp tip is no longer in local equilibrium. The situation is analogous to a triple junction with very low surface tension compared to the grain-boundary energy, Section II.E. Physically, another kinetic process takes over to limit the crack-extension velocity. If dislocations are unavailable or immobile, atomic bonds may cleave on the plane directly ahead of the cusp. The rate of crack extension may be limited by the transport of the environmental species or reaction at the crack tip (Lawn, 1993).

A common phenomenological description gives the crack velocity $\dot{a}$ depending on the driving force at the cusp, f, such as

$$\dot{a} = Cf^n, \tag{8.21}$$

where C is a rate coefficient, and typically $n > 1$; both parameters are used to fit the data of subcritical cracking experiments. The driving force here is defined as the free-energy reduction associated with the crack-advancing unit distance, namely

$$\delta G = -f\delta a. \tag{8.22}$$

The driving force is related to Irwin's elastic-energy rate, $\mathscr{G}$, and surface tension γ as

$$f = \mathscr{G} - 2\gamma. \tag{8.23}$$

IX. Electromigration on Surface

Interconnects in integrated circuits are made of aluminum alloys. They have small cross sections (less than 1 μm wide and about 0.5 μm thick), carry electric current up to 10^{10} A/m^2, and operate near half of aluminum's melting temperature (933° K). The flowing electrons exert a force on aluminum atoms (i.e., the electron wind force), motivating aluminum atoms to diffuse. The phenomenon—mass diffusion directed by electric current, known as electromigration—causes reliability problems in integrated circuits; see Thompson and Lloyd (1993) for a survey. This section reviews phenomena related to electromigration on surfaces.

A. SURFACE DIFFUSION DRIVEN BY THE ELECTRON WIND

1. *Electron Wind Force*

To outline essential behaviors, we examine a plane problem of a cylindrical pore in a conductor, Figure 31. Assume that atomic diffusion on the pore surface is the only mass-transport process. The electric field vector $\mathbf{E}_i$ is the gradient of the potential ϕ:

$$\mathbf{E}_i = -\phi_{,i}. \tag{9.1}$$

Electric charge conservation requires that the electric current density vector, $\mathbf{j}_i$, be divergence-free:

$$\mathbf{j}_{i,i} = 0. \tag{9.2}$$

The electric field relates to the current density by Ohm's law

$$\mathbf{E}_i = \rho \mathbf{j}_i, \tag{9.3}$$

where ρ is the resistivity. Aluminum crystal has a cubic symmetry, so that the resistivity is the same in all directions.

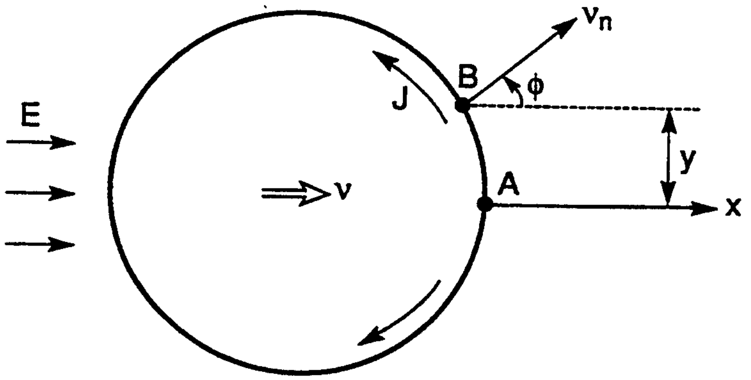

FIG. 31. A pore in an interconnect subjected to an electric field.

An aluminum interconnect is typically subject to an electric field below 1000 V/m. This electric field is amplified at the pore. For a pore without sharp edges, the amplification factor is about 2. Consequently, the electric field inside the pore is much lower than the electrical breakdown field of vacuum or dry air (around 1 MV/m). The pore can be modeled as an insulator, namely, $j_i n_i = 0$ at the pore surface.

The component of the electric field tangential to the pore surface is $E_t = -\partial\phi/\partial s$, where s is the curve length along the pore surface. The electron wind exerts a force on atoms on the pore surface. The force per atoms is proportional to the electric field E_t:

$$F_E = -Z^* e E_t, \tag{9.4}$$

where $Z^*(>0)$ is the effective valence, and $e(>0)$ the magnitude of the electron charge. The negative sign means that the force is in the direction of the electron flow. The effective valence may depend on crystal orientation.

2. *Weak Statements*

Let G be the free energy of the system, consisting of surface energy and electrostatic energy. They both vary when the pore changes shape. The relative magnitude of the two energies is described by a dimensionless number $\varepsilon E^2 R_0/\gamma$, where R_0 is the length representative of the pore size, γ the surface tension, and ε the permittivity of the medium inside the pore. For typical values, this number is much smaller than unity. Consequently, we will ignore the electrostatic energy, and take the free energy to be the surface energy:

$$G = \int \gamma ds. \tag{9.5}$$

The integral extends over the pore surface. The surface tension γ may depend on crystal orientation.

As before, we define the driving force for mass diffusion using virtual motion. Let δI be the mass displacement (i.e., the number of atoms across unit length on the surface). Associated with this virtual motion, the free energy changes by δG, and the electron wind force does work $\int F_E \, \delta I ds$. Define the diffusion driving force, F, by

$$\int F \delta I ds = -\delta G + \int F_E \delta I ds. \tag{9.6}$$

In other words, F is the reduction in the free energy plus the work done by the electron wind, associated with one atom moving unit distance on the surface. Evidently, (9.6) is an extension of (5.5).

Mass conservation takes the same form as in Section V, but a different sign convention is adopted here: the normal vector on the pore surface $\mathbf{n}$ now points to the solid. Mass conservation relates the virtual migration of the surface δr_n to the virtual mass displacement δI:

$$\delta r_n = \frac{\Omega \partial(\delta I)}{\partial s}. \tag{9.7}$$

Here Ω is the volume per atom. The surface velocity, v_n, relates to the atomic flux, J, by a similar relation:

$$v_n = \frac{\Omega \partial J}{\partial s}. \tag{9.8}$$

The linear kinetic law connects the flux with the total diffusion driving force:

$$J = MF. \tag{9.9}$$

Inserting (9.9) into (9.6), we obtain the weak statement of the problem:

$$\int \frac{J}{M} \delta I ds = -\delta G + \int F_E \delta I ds. \tag{9.10}$$

The actual flux J satisfies (9.10) for arbitrary virtual motion of the surface. Of all virtual flux $\tilde{J}$, the actual flux minimizes the functional

$$\Pi = \dot{G} - \int F_E \tilde{J} ds + \int \frac{\tilde{J}^2}{2M} ds. \tag{9.11}$$

3. *Equations for Isotropic Conductor*

Next, consider a conductor having isotropic surface tension and effective charge. The total driving force for atomic diffusion on the pore surface is

$$F = -Z^* eE_t + \frac{\Omega \gamma \partial K}{\partial s}. \tag{9.12}$$

The first term is the electron wind force, and the second the capillary force. The curvature K is positive for a rounded pore.

A combination of equations (9.8), (9.9), and (9.12) gives

$$\mathbf{n} \cdot \frac{\partial \mathbf{x}}{\partial t} = M \frac{\partial^2}{\partial s^2}(Z^* e\phi + \Omega \gamma K). \qquad (9.13)$$

The left-hand side is the velocity normal to the pore surface. This equation governs the motion of the pore surface.

B. PORE DRIFTING IN THE ELECTRON WIND

Small pores often appear in aluminum interconnects to relieve stresses caused by thermal-expansion mismatch or electromigration. The pores may move in the electron wind (Shingubara and Nakasaki, 1991; Besser *et al.*, 1992; Arzt *et al.*, 1994; Marieb *et al.*, 1995). Since electrons flow in the direction opposite to the electric field direction, atoms diffuse on the pore surface as indicated in Figure 31. Consequently, the pore migrates in the direction of the applied electric field.

Ho (1970) showed that, in an infinite isotropic conductor under a remote electric field, a circular pore can migrate without changing its shape. His solution is summarized as follows. Figure 31 illustrates a circular pore, radius R_0, in an infinite conductor subject to a remote electric field E. The electric field is nonuniform in the conductor, but is uniform inside the pore and equals $2E$. Because the electric potential is continuous across the pore surface, E_t is also continuous across the surface. Consequently, the electric field component tangential to the pore surface is

$$E_t = -\frac{2Ey}{R_0}. \qquad (9.14)$$

The electron wind force is

$$F_E = \frac{2eZ^*Ey}{R_0}. \qquad (9.15)$$

The isotropic surface tension does not cause diffusion on the surface of a circular pore, so that (9.15) is also the total diffusion-driving force.

On the pore surface in Figure 31, A is a symmetry point where the flux vanishes, and B is a point at height y. Let the circular pore translate at a uniform velocity v in the x-direction. In unit time, atoms of volume yv (per interconnect thickness) are removed from the segment AB, and flow out of the segment at point B. Mass conservation requires that the flux at point B be

$$J = \frac{yv}{\Omega}. \tag{9.16}$$

Connecting (9.15) and (9.16) with the kinetic law $J = MF$, one obtains the velocity of the pore

$$v = 2\frac{\Omega M Z^* e E}{R_0}. \tag{9.17}$$

The pore drifts in the direction of the applied electric field, at a velocity proportional to the applied electric field, and inversely proportional to the pore radius.

For a spherical pore in an infinite conductor subject to a remote electric field E, the electric field in the pore is uniform and equals $3E/2$. The velocity of the pore takes the same form as (9.17), with the coefficient 2 replaced with 3. Ho (1970) also studied drifting of a rigid inclusion. Ma and Suo (1993) showed how an Al_2Cu particle drifts in an aluminum matrix, as both copper and aluminum atoms diffuse on the particle-matrix interface. Suo (1994) studied the migration of edge-dislocation loops when atoms diffuse along the dislocation cores in the electron wind, and proposed the process as a mass transport mechanism in aluminum interconnects when other mechanisms are slow or absent.

The phenomena of defect migration provide means to determine atomic mobility experimentally. For example, by measuring the velocity and radius of a pore migrating in aluminum under a given electric field, one determines the parameter Z^*M from (9.17). An aluminum interconnect is usually covered by a thin film of aluminum oxide. The oxide film usually covers a pore near the surface, which should insulate the pore surface from contamination.

C. Pore Breaking Away from Trap

Grain boundaries and triple junctions may trap pores. Figure 32 shows a pore attached on a grain boundary. In the absence of the electric field, the pore eliminates part of the grain-boundary area, and therefore is in a low-energy state. Subject to an electric field, the pore moves by surface diffusion, and may break away from the grain boundary. Li *et al.* (1992)

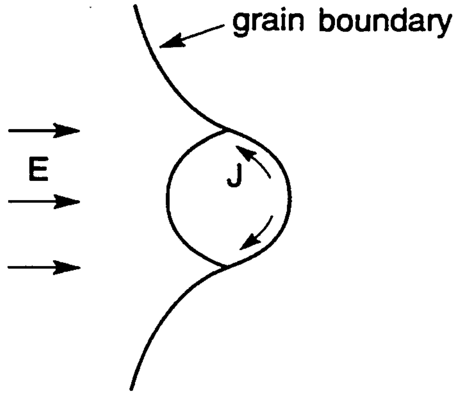

FIG. 32. A pore trapped by the grain boundary and driven by the electron wind.

and Wang *et al.* (1996) estimated the electric field needed for the pore to break away from a grain boundary.

Denote f_T as the force acting on the pore by the trap. For example, when the pore tries to break away from a grain boundary of tension γ_b, the grain boundary exerts a force (per interconnect thickness) on the pore, $f_T = 2\gamma_b$, in the direction opposing the breakaway. In equilibrium this force balances the electron wind force, and surface diffusion stops. Let the pore undergo a virtual translation in the x-direction by a displacement δa. Mass conservation requires that $\delta I = y\delta a/\Omega$. In equilibrium, the total virtual work vanishes:

$$\int F_E \delta I ds - f_T \delta a = 0. \tag{9.18}$$

Approximating the pore by a circle in integration, we obtain that

$$\frac{Z^* e E R_0^2}{\Omega f_T} = \frac{1}{2\pi}. \tag{9.19}$$

With material properties fixed, there exists a critical value of ER_0^2, above which the pore breaks away from the grain boundary. The numerical value on the right-hand side of (9.19) will change if the pore surface is allowed to change shape in the electron wind. The problem has not been solved exactly.

Pore attachment and breaking away are evident in many experimental studies (e.g., Besser *et al.*, 1992; Kraft *et al.*, 1993; Marieb *et al.*, 1995). Careful observations would lead to an estimate of the effective valence Z^*.

D. TRANSGRANULAR SLITS

Experimental evidence accumulated in the last few years has shown that an aluminum interconnect with a bamboo-like grain structure often fails by a transgranular slit. Micrographs of such slits were first published by Sanchez *et al.* (1992) and Rose (1992). The slits are about 100 nm thick, and nearly perpendicular to the current direction. The faces of a slit and its running direction favor special crystalline orientations. Joo and Thompson (1993) observed slits in single crystal aluminum interconnects.

It was, however, uncertain how the slits form by looking at the micrographs taken after the aluminum interconnects had failed. In a sequence of micrographs taken in interrupted electromigration tests, Kraft *et al.* (1993) and Arzt *et al.* (1994) discovered that pores not only drift, but also change shape. A rounded pore forms somewhere in the aluminum interconnect, travels for some distance, enlarges, and collapses to a slit. These authors also suggested a mechanism by which a pore changes shape. Figure 33 illustrates two asymmetric pore shapes. The shape in Figure 33(a) is critical because the electromigration flux from b to c is larger than that from a to b, so that mass depletes from b, and the pore elongates in the direction normal to the interconnect. By contrast, the shape in Figure 33(b) is uncritical because the electromigration flux from c to b is larger than that from b to a, so that mass accumulates at b, and the pore elongates in the direction along the interconnect.

Two forces compete to determine the pore shape: the electron wind favors a slit, but the surface tension favors a rounded pore. On examining the expression for the driving force (9.11), Suo *et al.* (1994) pointed-out

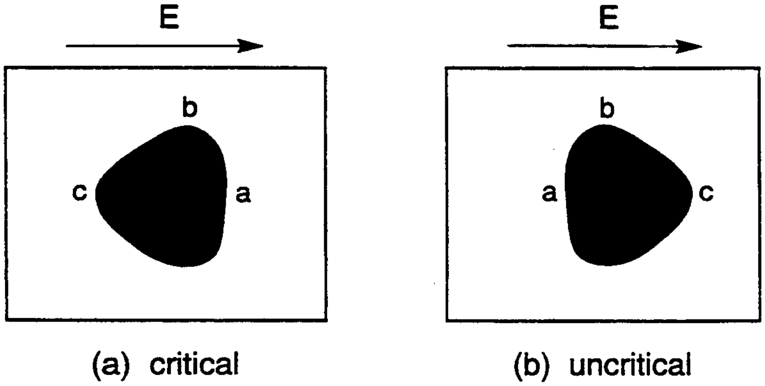

(a) critical (b) uncritical

FIG. 33. a) A pore with the critical asymmetric shape. b) A pore with the uncritical asymmetric shape.

that the relative importance of the electron-wind force and the capillary force is measured by a dimensionless number

$$\chi = \frac{Z^* e E R_0^2}{\Omega \gamma} \tag{9.20}$$

where R_0 is the radius of the rounded pore, and E the applied electric field. When χ is small, the surface energy dominates, and the pore remains rounded. When χ is large, the electron wind dominates, and the pore collapses to a slit. Note that the number has the same form as that for a pore to break away from a trap (9.19). Suo *et al.* (1994) also estimated the velocity and width of a well-formed slit.

Yang *et al.* (1994) and Maroudus (1995) attempted to estimate the critical number for the shape instability, χ_c. To circumvent the difficulty of solving the electric field around the pore, Yang *et al.* considered a model problem where the medium inside the pore is conducting and has the same resistivity as that of aluminum, and showed that such a pore becomes unstable above $\chi_c = 10.65$.

Marder (1994) carried out a rigorous linear-stability analysis. He confirmed the result above of the conducting pore. However, for the more realistic model, i.e., a circular insulating pore in an infinite conductor, he found that the pore is *stable* against infinitesimal shape perturbation for arbitrarily high χ. Mahadevan and Bradley (1996) independently carried out the same analysis.

Linear stability analysis has its limitation. A pore that is stable against infinitesimal perturbation need not be stable against finite perturbation. In practice, the initial pore is never a perfect circle; deviation may result from surface-tension anisotropy, finite-interconnect width, thermal stress, etc. To determine the pore stability under practical conditions, one must study finite initial imperfection and large shape change.

Kraft and Arzt (1995) and Bower and Freund (1995) studied numerically the stability of an insulating pore in an interconnect of a finite width. They determined the electric field in the conductor by using finite-element methods, and updated the pore shape according to the electron wind and capillary forces. A rounded pore is unstable above a critical level, χ_c, whose value depends on the initial pore radius to the linewidth ratio, R_0/w. Marder's linear-stability analysis shows that $\chi_c \to \infty$ as $R_0/w \to 0$. The complete $\chi_c(R_0/w)$ function is unavailable at this time.

Wang *et al.* (1996) considered an unsulating pore in an infinite conductor, and introduced finite imperfection to the initial pore shape. They used a conformal mapping to determine the electric field, and the weak statement to update the pore shape. They showed that the pore becomes unstable above χ_c, the magnitude of which depends on the type and magnitude of the initial imperfection. For example, the initial pore is taken to be an ellipse with the two semi-axis

$$\left(\sqrt{1+\varepsilon^2}-\varepsilon\right)R_0,\ \left(\sqrt{1+\varepsilon^2}+\varepsilon\right)R_0.$$

The form is chosen so that the area of the ellipse is πR_0^2. The imperfection ε takes finite values. As before, we use the characteristic time

$$t_0=\frac{R_0^4}{\Omega^2 M\gamma} \tag{9.21}$$

to normalize the time. Figure 34 shows the snapshots at time interval $0.06t_0$ of a pore with initial imperfection $\varepsilon = 0.1$. When χ is small, the pore migrates and changes its shape, but finally reaches a steady state. When χ is large, the pore collapses to a slit. Figure 35 plots χ_c as a function of the imperfection ε. The critical value drops sharply when moderate initial imperfection is introduced, and decreases somewhat thereafter.

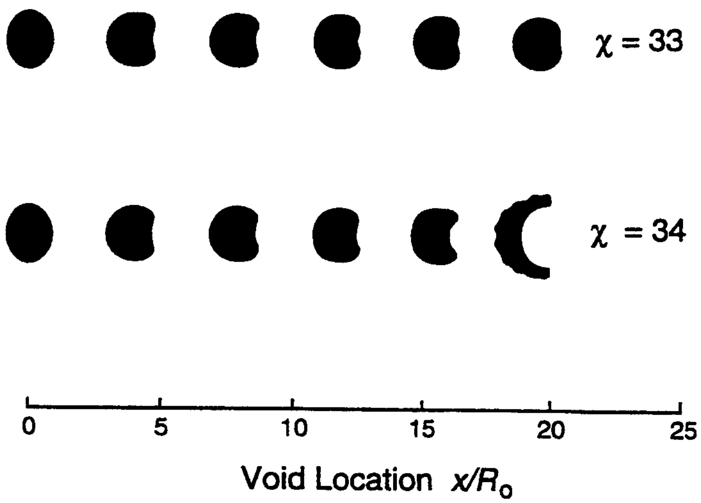

FIG. 34. Each row is a sequence of snapshots of a pore migrating in an interconnect, in the direction of the applied electric field, from the left to the right. The void is a perfect insulator. The initial perturbation is $\varepsilon = 0.1$.

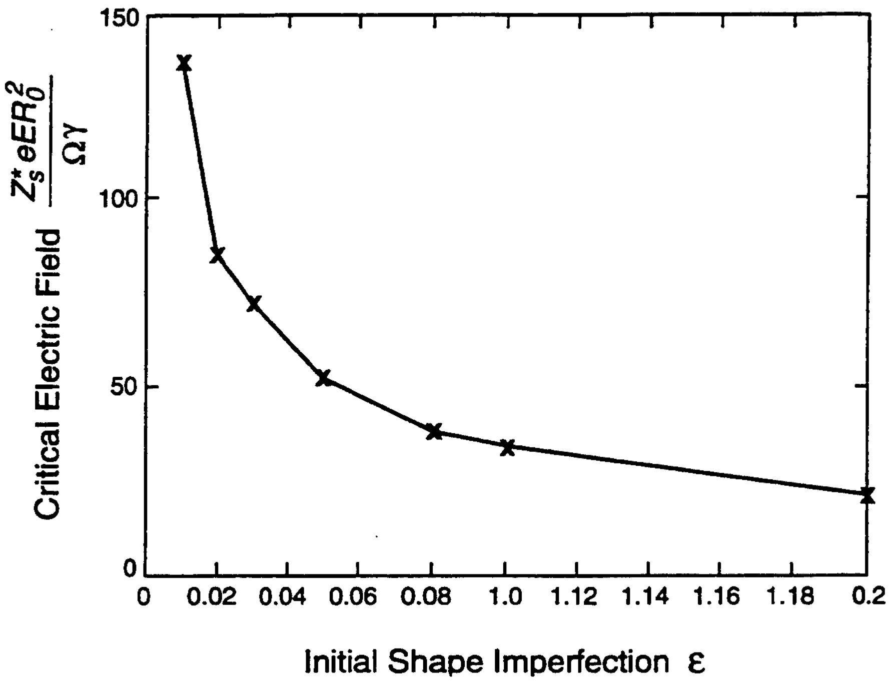

FIG. 35. The critical electric field as a function of the magnitude of the initial pore shape imperfection ε.

Acknowledgments

The writer is grateful to the National Science Foundation for a Young Investigator Award, to the Humboldt Foundation and the Max Planck Society for financing a sabbatical leave at the Max Planck Institute in Stuttgart hosted by Directors M. Ruhle and E. Arzt, and to Advanced Micro Devices for a grant under the supervision of Dr. J. E. Sanchez. Part of the work reviewed here was supported by ARPA through a URI contract N-0014-92-J-1808, by ONR through contract N00014-93-1-0110, and by NSF through grant MSS-9202165.

References

Abeyaratne, R., and Knowles, J. K. (1990). On the driving traction acting on a surface of strain discontinuity in a continuum, *J. Mech. Phys. Solids* **38**, 345–360.

Ames, I., d'Heurle, F. M., and Horstmann, R. (1970). Reduction of electromigration in aluminum films by copper doing. *IBM J. Res. Dev.* **14**, 461–463.

Arzt, E., Kraft, O., Nix, W. D., and Sanchez, J. E. Jr., (1994). Electromigration failure by shape change of voids in bamboo lines. *J. Appl. Phys.* **76**, 1563–1571.

Asaro, R. J., and Tiller, W. A. (1972). Interface morphology development during stress corrosion cracking: Part I. Via surface diffusion. *Metall. Trans.* **3**, 1789–1796.

Besser, P. R., Madden, M. C., and Flinn, P. A. (1992). *In situ* scanning electron microscopy observation of the dynamic behavior of electromigration voids in passivated aluminum lines. *J. Appl. Phys*. **72**, 3792–3797.

Biot, M. A. (1970). "Variational Principles in Heat Transfer." Oxford Univ. Press, Oxford.

Bower, A. F., and Freund, L. B. (1993). Analysis of stress-induced void growth mechanisms in passivated interconnect lines. *J. Appl. Phys*. **74**, 3855–3868.

Bower, A. F., and Freund, L. B. (1995). Finite element analysis of electromigration and stress induced diffusion in deformable solids. *Mater. Res. Soc. Symp Proc*. **391**, 177–188.

Brada, M., Clarke, D. M., and Suo, Z. (1996). Unpublished work.

Brokman, A., Kris, R., Mullins, W. W., and Vilenkin, A. J. (1995). Analysis of boundary motion in thin films. *Scr. Metall. Mater*. **32**, 1341–1346.

Budiansky, B., Hutchinson, J. W., and Slutsky, S. (1982). Void growth and collapse in viscous solids. "Mechanics of Solids, The Rodney Hill 60th Anniversaty Volume," (H. G. Hopkins and J. Sewell, eds.), pp. 13–45, Pergamon, Oxford.

Cannon, R. M., and Carter, W. C. (1989). Interplay of sintering microstructures, driving forces, and mass transport mechanisms. *J. Am. Ceram. Soc*. **72**, 1550–1555.

Carter, W. C., Roosen, A. R., Cahn, J. W., and Taylor, J. E. (1995). Shape evolution by surface diffusion and surface attachment limited kinetics on completely faceted surfaces. *Acta Metall. Mater*. **43**, 4309–4323.

Chiu, C. H., and Gao, H. (1993). Stress singularities along a cycloid rough surface. *Int. J. Solids Struct*. **30**, 2981–3012.

Chuang, T.-J., and Rice, J. R. (1973). The shape of intergranular creep cracks growing by surface diffusion. *Acta Metall*. **21**, 1625–1628.

Cocks, A. C. F. (1992). Interface reaction controlled creep. *Mech. Mater*. **13**, 165–174.

Cocks, A. C. F. (1994). The structure of constitutive laws for the sintering of fine grained materials. *Acta Metall. Mater*. **42**, 2197–2210.

Cocks, A. C. F., and Gill, S. P. A. (1995). A variational approach to two dimensional grain growth. Submitted in publication.

Du, Z.-Z., McMeeking, R. M., and Cocks, A. C. F. (1996). Manuscript in preparation.

Dunn, M. L., and Wienecke, H. A. (1996). Inclusions and inhomogeneities in transversely isotropic piezoelectric solids. *J. Mech. Phys. Solids*. Submitted for publication.

Eshelby, J. D. (1956). The continuum theory of lattice defects. *Solid State Phys*., **3**, 79–144.

Eshelby, J. D. (1957). The determination of the elastic field of an ellipsoidal inclusion, and related problems. *Proc. R. Soc. London* **A421**, 376–396.

Eshelby, J. D. (1970). Energy relations and the energy-momentum tensor in continuum mechanics. *In* "Inelastic Behavior of Solids" (M. F. Kanninen *et al*., eds.), pp. 77–115. McGraw-Hill, New York.

Floro, J. A., Thompson, C. V., Carel, R., and Bristowe, P. D. (1994). Competition between strain and interface energy during epitaxial grain growth in Ag films on Ni (001). *J. Mater. Res*. **9**, 2411–2424.

Freund, L. B. (1995). Evolution of waviness on the surface of a strained elastic solid due to stress-driven diffusion. *Int. J. Solids Struct*. **32**, 911–923.

Freund, L. B., and Jonsdottir, F. (1993). Instability of a biaxially stressed thin film on a substrate due to material diffusion over its free surface. *J. Mech. Phys. Solids* **41**, 1245–1264.

Frost, H. J., Thompson, C. V., and Walton, D. T. (1992). Simulation of thin film grain structures—II. Abnormal grain growth. *Acta Metall. Mater*. **40**, 779–793.

Gao, H. (1991). A boundary perturbation analysis for elastic inclusions and interfaces. *Int. J. Solids Struct*. **28**, 703–725.

Gao, H. (1992). Stress analysis of holes in anisotropic elastic solids: Conformal mapping and boundary perturbation. *Q. J. Mech. Appl. Math.* **45**, 149–168.

Gao, H. (1994). Some general properties of stress-driven surface evolution in a heteroepitaxial thin film structre. *J. Mech. Phys. Solids* **42**, 741–772.

Gao, H. (1995). The hypocycloid cavity: A path from a Griffith slit crack to a cusped cycloid surface. *Proc. R. Soc. London* **448**, 465–483.

Genin, F. Y., Mullins, W. W., and Wynblatt, P. (1992). Capillary instabilities in thin films: A model of thermal pitting at grain boundary vertices. *Acta. Metall.* **40**, 3239–3248.

Grinfeld, M. A. (1986). Instability of the separation boundary between non-hydrostatically stressed elastic body and a melt. *Sov. Phys. Dokl*, **31**, 831–834.

Herring, C. (1951). Surface tension as a motivation for sintering. "The Physics of Powder Metallurgy." (W. E. Kingston, ed.), pp. 143–179. McGraw-Hill, New York.

Hillert, M. (1965). On the theory of normal and abnormal grain growth. *Acta Metall.* **13**, 227–238.

Hsueh, C. H., Evans, A. G., and Coble, R. L. (1982). Microstructure development during final/intermediate stage sintering—I. Pore/grain boundary separation. *Acta Metall.* **30**, 1269–1279.

Ho, P. S. (1970). Motion of inclusion induced by a direct current and a temperature gradient. *J. Appl. Phys.* **41**, 64–68.

Isenberg, C. (1978). "The Science of Soap Films and Soap Bubbles." Reprinted in 1992 by Dover, New York.

Jiang, Q. (1994). On the driving traction acting on a surface of discontinuity within a continuum in the presence of electromagnetic fields. *Journal of Elasticity* **34**, 1–21.

Johnson, W. C., and Cahn, J. W. (1984). Elastically induced shape bifurcations of inclusions. *Acta Metall.* **32**, 1925–1933.

Joo, Y.-C., and Thompson, C. V. (1993). Evolution of electromigration-induced voids in single crystalline aluminum lines with different crystallographic orientations. *Mater. Res. Soc. Symp. Proc.* **309**, 351–357.

Klinger, L. M., Glickman, E. E., Fradkov, V. E., Mullins, W. W., and Bauer, C. L. (1995). Extensions of thermal grooving for arbitrary grain-boundary flux. *J. Appl. Phys.* **78**, 3833–3838.

Kraft, O., and Arzt, E. (1995). Numerical simulation of electromigration-induced shape changes of voids in bamboo lines. *Appl. Phys. Lett.* **66**, 2063–2065.

Kraft, O., Bader, S., Sanchez, J. E., and Arzt, E. (1993). Observation and modeling of electromigration-induced void growth in Al-based interconnects. *Mater. Res. Symp. Proc.* **309**, 199–204.

Landauer, R. (1957). Electrostatic considerations in $BaTiO_3$ domain formation during polarization reversal. *J. Appl. Phys.* **28**, 227–234.

Lawn, B. (1993). "Fracture of Brittle Solids." Cambridge Univ. Press, London.

Leonard, D., Pond, K., and Petroff, P. M. (1994). Critical layer thickness for self-assembled InAs islands on GaAs. *Phys. Rev. B* **50**, 11687–11692.

Li. C.-Y., Borgesen, P., and Korhonen, M. A. (1992). Electromigration-induced failure in passivated aluminum-based metallizations—the dependence on temperature and current density. *Appl. Phys. Lett.* **61**, 411–413.

Loge, R. E., and Suo, Z. (1996). Nonequilibrium thermodynamics of ferroelectric domain evolution. *Acta Metall. Mater.* **44**, 3429–3438.

Lusk, M. (1994). On martensitic phase nucleation with surface effects. *J. Mech. Phys. Solids* **42**, 241–282.

Ma, Q., and Suo, Z. (1993). Precipitate drifting and coarsening caused by electromigration. *J. Appl. Phys.* **74**, 5457–5462.

McCartney, L. N. (1977). Cavities under stress at high temperatures. *Acta Metall.* **25**, 221–230.

McMeeking, R. M., and Kuhn, L. T. (1992). A diffusional creep law for powder compacts. *Acta Metall. Mater.* **40**, 961–969.

Mahadevan, M., and Bradley, M. R. (1996). Stability of a circular void in a passivated, current-carrying metal film. *J. Appl. Phys.* in press.

Marder, M. (1994). Unpublished work.

Marieb, T., Flinn, P., Bravman, J. C., Gardner, D., and Madden, M. (1995). Observations of electromigration induced void nucleation and growth in polycrystalline and near-bamboo passivated Al lines. *J. Appl. Phys.* **78**, 1026–1032.

Maroudus, D. (1995). Dynamics of transgranular voids in metallic thin films under electromigration conditions. *Appl. Phys. Lett.* **67**, 798–800.

Miller, K. T., and Lange, F. F. (1989). The morphological stability of polycrystalline fibers. *Acta Metall.* **37**, 1343–1347.

Miller, K. T., Lange, F. F., and Marshall, D. B. (1990). The instability of polycrystalline thin films: Experiment and theory. *J. Mater. Res.* **5**, 151–160.

Miller, R. C., and Savage, A. (1959). Further experiments on the sidewise motion of 180° domain walls in $BaTiO_3$. *Phys. Rev.* **115**, 1176–1180.

Mullins, W. W. (1956). Two-dimensional motion of idealized grain boundaries, *J. Appl. Phys.*, **27**, 900–904.

Mullins, W. W. (1957). Theory of thermal grooving. *J. Appl. Phys.* **28**, 333–339.

Mullins, W. W. (1958). The effect of thermal grooving on grain boundary motion. *Acta Metall.* **6**, 414–427.

Mullins, W. W. (1959). Flattening of a nearly plane solid surface due to capillarity. *J. Appl. Phys.* **30**, 77–83.

Needleman, A., and Rice, J. R. (1980). Plastic creep flow effects in the diffusive cavitation of grain boundaries. *Acta Metall.* **28**, 1315–1332.

Newcomb, S. A., and Tressler, R. E. (1993). Slow crack growth in sapphire fibers at 800° to 1500°C. *J. Am. Ceram. Soc.* **76**, 2505–2512.

Nichols, F. A. (1976). On the spheroidization of rod-shaped particles of finite length. *J. Mater. Sci.* **11**, 1077–1082.

Nichols, F. A., and Mullins, W. W. (1965a). Morphological changes of a surface of revolution due to capillary-induced surface diffusion. *J. Appl. Phys.* **36**, 1826–1835.

Nichols, F. A., and Mullins, W. W. (1965b). Surface- (interface-) and volume-diffusion contribution to morphological changes driven by capillarity. *Trans. Metall. Soc.* **233**, 1840–1848.

Osborn, J. A. (1945). Demagnetizing factors of the general ellipsoid. *Phys. Rev.* **67**, 351–357.

Pharr, G. M., and Nix, W. D. (1979). A numerical study of cavity growth controlled by surface diffusion. *Acta Metall.* **27**, 1615–1631.

Pompe, W., Gong, X., Suo, Z., and Speck, J. S. (1993). Elastic energy release due to domain formation in the strained epitaxy of ferroelectric and ferroelastic films. *J. Appl. Phys.* **74**, 6012–6019.

Raj, R., and Ashby, M. F. (1971). On grain boundary sliding and diffusional creep. *Metall. Trans.* **2**, 1113–1127.

Raj, R., and Ashby, M. F. (1972). Grain boundary sliding, and the effects of particle on its rate. *Metall. Trans.* **3**, 1937–1942.

Rodel, J., and Glaeser, M. (1990). High-temperature healing of lithographically introduced cracks in sapphire. *J. Am. Ceram. Soc.* **73**, 592–601.

Rosakis, P., and Jiang, Q. (1995). On the morphology of ferroelectric domains. *Int. J. Eng. Sci.* **33**, 1–12.

Rosakis, P., and Tsai, H. (1994). On the role of shear instability in the modeling of crystal twinning. *Mech. Mater.* **17**, 245–259.

Rose, J. H. (1992). Fatal electromigration voids in narrow aluminum-copper interconnect. *Appl. Phys. Lett.* **61**, 2170–2172.

Roytburd, A. L. (1993). Elastic domains and polydomain phases in solids. *Phase Transitions* **45**, 1–33.

Sanchez, J. E., and Arzt, E. (1992). Effects of grain orientation on hillock formation and grain growth in aluminum films on silicon substrates. *Scr. Metall. Mater.* **27**, 285–290.

Sanchez, J. E., McKnelly, L. T., and Morris, J. W. (1992). Slit morphology of electromigration induced open circuit failures in finite line conductors. *J. Appl. Phys.* **72**, 3201–3203.

Seifert, A., Vojta, A., Speck, J. S., and Lange, F. F. (1996). Microstructural instability in single crystal thin films. Submitted for publication.

Shewmon, P. G. (1964). The movement of small inclusions in solids by a temperature gradient. *Trans. Am. Inst. Min. Eng.* **230**, 1134–1137.

Shingubara, S., and Nakasaki, Y. (1991). Electromigration in a single crystalline submicron width aluminum interconnection. *Appl. Phys. Lett.* **58**, 42–44.

Socrate, S., and Parks, D. M. (1993). Numerical determination of the elastic driving force for directional coarsening in Ni-superalloys. *Acta Metall. Mater.* **41**, 2185–2209.

Sofronis, P., and McMeeking, R. M. (1994). The effect of interface diffusion and slip on creep resistance of particulate composite materials. *Mech. Mater.* **18**, 55–68.

Spears, M. A., and Evans, A. G. (1982). Microstructure development during final/intermediate stage sintering—II. Grain and pore coarsening. *Acta Metall.* **30**, 1281–1289.

Spencer, B. J., Voorhees, P. W., and Davis, S. H. (1991). Morphological instability in epitaxially strained dislocation-free solid films. *Phys. Rev. Lett.* **67**, 3696–3699.

Srolovitz, D. J. (1989). On the stability of surfaces of stressed solids. *Acta Metall.* **37**, 621–625.

Srolovitz, D. J., and Safran, S. A. (1986). Capillary instabilities in thin films. *J. Appl. Phys.* **60**, 247–260.

Srolovitz, D. J., and Thompson, C. V. (1986). Beading instabilities in thin film lines with bamboo microstructures. *Thin Solid Films* **139**, 133–141.

Stevens, R. N., and Dutton, R. (1971). The propagation of Griffith cracks at high temperatures by mass transport processes. *Mater. Sci. Eng.* **8**, 220–234.

Sun, B., Suo, Z., and Evans, A. G. (1994). Emergence of crack by mass transport in elastic crystals stressed at high temperatures. *J. Mech. Phys. Solids* **42**, 1653–1677.

Sun, B., Suo, Z., and Cocks, A. C. F. (1996). A global analysis of structural evolution in a row of grains, *J. Mech. Phys. Solids* **44**, 559–581.

Sun, B., Suo, Z., and Yang. W. (1997). A finite element method for simulating interface motion, part 1: migration of phase and grain boundaries. *Acta Mater.* in press.

Suo, Z. (1994). Electromigration-induced dislocation climb and multiplication in conducting lines. *Acta Metall. Mater.* **42**, 3581–3588.

Suo, Z., and Wang, W. (1994). Diffusive void bifurcation in stressed solid. *J. Appl. Phys.* **76**, 3410–3421.

Suo, Z., Wang, W., and Yang, M. (1994). Electromigration instability: transgranular slits in interconnects. *Appl. Phys. Lett.* **64**, 1944–1946.

Suo, Z., Yu, H. (1997). Crack nucleation on elastic polycrystal surface in corrosive environment: low dimensional dynamic models. *Acta. Mater.* in press.

Svoboda, J., and Riedel, H. (1995). New solutions describing the formulation of interparticle necks in solid-state sintering. *Acta Metall. Mater.* **43**, 1–10.

Taylor, J. E., Cahn, J. W., and Handwerker, C. A. (1992). Geometric models of crystal growth. *Acta Metall. Mater.* **40**, 1443–1474.

Thompson, C. V., and Lloyd, J. R. (1993). Electromigration and IC interconnects. *MRS Bull.* **December 1993**, 19–25.

Thompson, C. V., Floro, J., and Smith, H. I. (1990). Epitaxial grain growth in thin metal films. *J. Appl. Phys.* **67**, 4099–4104.

Thouless, M. D. (1993). Effect of surface diffusion on the creep of thin films and sintered arrays of particles. *Acta Metall. Mater.* **41**, 1057–1064.

Tsoga, A., and Nikolopoulos, P. (1994). Groove angles and surface mass transport in polycrystalline alumina. *J. Am. Ceram. Soc.* 77, 954–960.

Turnbull, D. (1956). Phase changes, *Solid State Phys.* **3**, 225–306.

Wang, W. Q., and Suo, Z. (1997). Shape change of a pore in a stressed solid via surface diffusion motivated by surface and elastic energy variation. *J. Mech. Phys. Solids.* in press.

Wang. W. Q., Suo, Z., and Hao, T.-H. (1996). A simulation of electromigration-induced transgranular slits. *J. Appl. Phys.* **79**, 2394–2403.

Wong, D., and Thouless, M. D. (1995). Effect of elastic relaxation on aspect ratios during island growth of isotropic films. Submitted for publication.

Yakobson, B. I. (1993). Stress-promoted interface diffusion as a precursor of fracture. *J. Chem. Phys.* **99**, 6923–6934.

Yang, W. H., and Srolovitz, D. J. (1993). Cracklike surface instabilities in stressed solids. *Phys. Rev. Lett.* **71**, 1593–1596.

Yang, W., and Suo, Z. (1996). Global view of microstructural evolution: Energetics, kinetics and dynamical systems. *Acta Mech. Sin.* **12**, 144–157.

Yang, W., Wang, W.-Q., and Suo, Z. (1994). Cavity and dislocation instability under electric current. *J. Mech. Phys. Solids* **42**, 897–911.

DAMAGE EVOLUTION AND ACOUSTIC EMISSION MECHANISMS IN α_2+β / SCS-6 TITANIUM MATRIX COMPOSITES

D.J. Sypeck and H.N.G. Wadley
School of Engineering and Applied Science
University of Virginia
Charlottesville, VA 22903

Abstract - Damage evolution and acoustic emission mechanisms have been investigated during the tensile deformation of two $\alpha_2 + \beta$ titanium aluminide matrix composites reinforced with SCS-6 silicon carbide fiber. The alloys had distinctly different β phase morphologies and resulting ductilities. A Ti-14Al-21Nb matrix composite with a matrix failure strain significantly greater than the fiber exhibited annular microcracking of a brittle β-depleted matrix zone surrounding the fibers. Acoustic emission measurements indicated that this damage process increased rapidly near the composite yield point and continued at a constant rate thereafter. Acoustic emission detection of fiber fracture indicated that failure occurred after about four fiber fractures at a significantly lower stress than predicted by a global load sharing model. A Ti-13Al-15Nb-4Mo-2V-7Ta matrix composite with a matrix failure strain less than the fiber exhibited multiple matrix cracking. Acoustic emission measurements indicated that matrix cracking initiated well below the stress where primary matrix cracks were first visually observed. Failure occurred after numerous fiber fractures at a significantly lower fiber stress than predicted by a fiber bundle model. Damage evolution data obtained from the calibrated acoustic emission measurements were combined with a simple micro-mechanical model to predict the inelastic contribution of matrix cracking to the overall deformation behavior.

1. INTRODUCTION

Intermetallic matrix composites (IMC) consisting of titanium or nickel aluminides reinforced with continuous silicon carbide fiber have attracted interest because of their potentially high specific stiffness, strength and creep resistance over a wide range of operating temperatures [1-3]. Composites with matrices based on Ti_3Al+Nb ($\alpha_2 + \beta$) alloys and creep resistant SCS-6 SiC fibers are being explored for use above the temperature range of conventional titanium alloys (~600°C). The mechanical properties of these $\alpha_2 + \beta$ / SCS-6 composites are a function of their constituents properties [4-6], the interface debond and/or sliding stress [7] and the method or conditions used for their fabrication [8]. A variety of micromechanical models [6,8-12] have been proposed to predict the mechanical behavior of this class of composites. These analyze the consequences of fiber fragmentation and/or matrix yielding/cracking. Interface debond/sliding behavior are often included [8,11,12] while some also consider residual stresses arising from the fiber-matrix thermal expansion coefficient mismatch [13,14] or additional fiber microbending stresses and fiber breaks incurred during consolidation processing [8]. A key aspect of understanding and modeling the mechanical behavior of these composites involves a correct form for the evolution of damage during loading.

Since damage processes in IMC's are often brittle, they are likely to be accompanied by detectable acoustic emission (AE) [15-18]. Numerous investigations have reported AE from metal matrix composites (MMC's) [19-21]. In some, attempts have been made to locate sources [20,21]. In others, parameters of the recorded signals (e.g. amplitude, frequency spectra, etc.) have been proposed to "characterize" the AE events and to attempt the differentiation of one source "type" from another [19]. Many of these studies have relied upon ad hoc or empirical methods using data collected with instrumentation that is not capable of reproducing many important characteristics of the AE signal. Combined with an absence of models that establish fundamental relationships between damage mechanisms and signal parameters, such studies have been of limited value for characterizing damage evolution.

Here we pursue an alternative approach. The theoretical relationship between damage events and AE signals is briefly reviewed [22,23]. Because the dynamic elastic Green's tensor (this maps an AE source to the motion responsible for an AE signal) is uncalculated for conventional composite test pieces, a pulsed laser calibration method is used to determine an empirical relationship between the dipole magnitude (i.e. AE moment strength) of an AE event and a scalar parameter related to the energy of its corresponding AE signal. This allows recovery of the magnitude of the damage event (e.g. the crack opening volume) from the recorded AE. We do not attempt to seek its time dependence, its location nor its orientation within the sample, though this could be accomplished in principle. Two different $\alpha_2 + \beta$ / SCS-6 composites are studied. Correlations between the differing damage mechanisms, their acoustic emissions and the observed tensile behavior are then used to access the significance of damage evolution upon tensile performance.

2. ACOUSTIC EMISSION FUNDAMENTALS

2.1 Natural acoustic emission

Burridge and Knopoff [22] treated an abrupt failure process in an elastic body as an expanding dislocation loop and expressed spatial and material characteristics of the defect in terms of a distribution of "equivalent" body forces. Ignoring spatial variations of the source region (i.e. point sources), a single source centered at $\boldsymbol{x}'$ can be modeled by a source moment tensor [23]

$$M_{ij} = c_{ijkl}[u_k]\Sigma_l \tag{1}$$

where i and j indicate the direction and separation of body force dipoles. c_{ijkl} is the elastic constant tensor, $[u_k]$ is the displacement discontinuity across the defect in the k-th direction and Σ_l is the area of the source projected onto a plane having a normal in the l-th direction.

Consider the creation of a penny-shaped crack in an isotropic linear elastic medium under mode I loading. If the crack face displacement in the x_1' direction is Δ, and the crack face area, A, has a normal also in the x_1' direction, then three orthogonal dipoles model the source [16,22];

$$M_{ij} = \begin{bmatrix} (\lambda + 2\mu) & 0 & 0 \\ 0 & \lambda & 0 \\ 0 & 0 & \lambda \end{bmatrix} \cdot \Delta A \tag{2}$$

where λ and μ are the Lamé constants. The product, ΔA, is the cracks interior volume.

For a fiber fracture source in a unidirectional composite under tensile load in the fiber direction, mode I cracking of the fiber is usually accompanied by mode II shear at the fiber-matrix interface. Static equilibrium considerations necessitate that sliding must occur along a shear recovery length, $l = r_f T / 2\tau_s$, where r_f is the fiber radius, τ_s is the sliding stress at the interface and T is the fiber stress at the time of fracture and the remote stress thereafter. It is simple to show a crack opening;

$$\Delta = \frac{r_f T^2}{2E_f \tau_s} \tag{3}$$

where E_f is the Young's modulus of the fiber. Since far field contributions to the source moment tensor from shear at the fiber-matrix interface cancel due to symmetry, we find;

$$M_{ij} = \begin{bmatrix} (\lambda_f + 2\mu_f) & 0 & 0 \\ 0 & \lambda_f & 0 \\ 0 & 0 & \lambda_f \end{bmatrix} \cdot \frac{\pi r_f^3 T^2}{2E_f \tau_s} \tag{4}$$

where the f subscripts indicate parameters for the fiber.

The far field surface displacements (i.e. the AE signal) can also be modeled. Provided the source to receiver distance and the wavelengths of interest are much larger than the source dimensions [24], the time-dependent displacement in the i-th direction, $u_i(\boldsymbol{x}, t)$, at location, $\boldsymbol{x}$, and time, t, due to wave motion excited by body force dipoles at $(\boldsymbol{x}', t')$ is obtained by a convolution;

$$u_i(\boldsymbol{x}, t) = M_{jk} \int_0^t G_{ij,k}(\boldsymbol{x}; \boldsymbol{x}', t - t') S(t') dt' \tag{5}$$

where $S(t')$ is the source time-dependence (e.g. the crack volume history) and $G_{ij,k}(\boldsymbol{x}; \boldsymbol{x}', t - t')$ is the spatial derivative of the dynamic elastic Green's tensor [23]. It represents the displacement at $(\boldsymbol{x}, t)$ in the i-th direction due to a unit strength impulsive body force dipole concentrated at $(\boldsymbol{x}', t')$, acting in the j-th direction, with separation in the k-th direction. The dynamic elastic Green's tensor therefore represents the bodies elastic impulse response. Presently, this is uncalculated for conventional composite test pieces.

2.2 *Artificial acoustic emission*

The absorption of a laser pulse at the surface of a metal causes a transient thermal expansion that can be used for generating artificial AE [25,26]. For a uniform pulse of duration, t_0, the maximum increase in surface temperature is

$$\Delta T_s = 2I_0 \sqrt{\frac{t_0}{\pi \rho c_p k}} \tag{6}$$

where ρ is the mass density of the metal, c_p is the specific heat capacity, k is the thermal conductivity and I_0 is the absorbed laser flux density [26]. The thermoelastic source is well modeled by two orthogonal dipoles oriented in the plane of the irradiated area [26];

$$M_{11} = M_{22} = \left(\lambda + \frac{2}{3}\mu\right) \frac{3\alpha}{\rho c_p} (1 - R) E_0 \tag{7}$$

where α is the linear expansion coefficient of the metal, R is the reflectivity [26] and E_0 is the pulse energy. Thus, laser pulses can create dipoles of known magnitude which can be used to calibrate the acoustic response function of a test samples.

3. EXPERIMENTAL

3.1 Materials

Two $\alpha_2 + \beta$/ SCS-6 composite samples (4 ply) were supplied by General Electric Aircraft Engines (GEAE) (Cincinnati, OH). They were fabricated using plasma sprayed monotapes [27] by consolidation at 900-950°C [28]. The gauge sections of the dogbone samples were 25 mm long, 6 mm wide and 1 mm thick. One sample contained a 0.25 volume fraction, V_f, of SCS-6 fibers in a Ti-14Al-21Nb (wt.%) matrix while the other contained a 0.30 fiber volume fraction in a Ti-13Al-15Nb-4Mo-2V-7Ta (wt.%) matrix. The Ti-13Al-15Nb-4Mo-2V-7Ta matrix sample received a post fabrication heat treatment consisting of 1180°C / 6-10 minutes / He quench; 870°C / 1 hour / He quench; 705°C / 8 hours / vacuum cool. Similarly processed fiberless matrix samples were also supplied.

Elastic residual stresses were computed using the two phase composite cylinder methodology [29] (Table 1), with input properties found in Table 2. For the matrices, the linear expansion coefficient, α, and Poisson's ratio, ν, of titanium were used. The matrix radii of the concentric cylinders were 140 μm and 128 μm which corresponded to matrix volume fractions, $V_m = 1 - V_f$, of 0.75 and 0.70.

Table 1. Elastic residual stresses (at the fiber-matrix interface) in MPa.

	Ti-14Al-21Nb / SCS-6		Ti-13Al-15Nb-4Mo-2V-7Ta / SCS-6	
Stress component	Fiber	Matrix	Fiber	Matrix
Radial	-194	-194	-260	-260
Circumferential	-194	323	-260	484
Axial	-665	222	-812	348

Fiber push-out tests on 0.50 mm thick samples were used to estimate fiber-matrix interface debond/sliding stresses [34]. For the Ti-14Al-21Nb / SCS-6 system, the mean of five tests gave a complete debond stress of 116 MPa and an initial sliding stress, τ_s, of 113 MPa. The respective standard deviations were 14 MPa and 10 MPa. For the Ti-13Al-15Nb-4Mo-2V-7Ta / SCS-6 system, the complete debond stress was 154 MPa and the initial sliding stress was 123 MPa. The respective standard deviations were 18 MPa and 4 MPa. The debond surfaces of the Ti-14Al-21Nb / SCS-6 system were rough while that of the Ti-13Al-15Nb-4Mo-2V-7Ta / SCS-6 system were smooth [35].

A Weibull type analysis was used to characterize the tensile strength of the SCS-6 fiber in its pristine state [36,37]. For fibers having a length L, the expected value is of the form [38];

$$\bar{T} = \frac{\sigma_0}{L^{1/m}}\Gamma\left(1+\frac{1}{m}\right) \tag{8}$$

where $\Gamma(\eta) = \int_0^{\infty} z^{\eta-1}\exp(-z)dz$ is the Gamma function. Mean strengths [39] of tests with pristine 10-70 mm gauge length samples [40] gave $m = 17.3$ and $\sigma_0 = 5270$ MPa·mm$^{1/m}$ [35].

Table 2. Properties summary (25°C).

	Symbol	Units	Value [Reference]
SCS-6			
Radius	r_f	μm	70 [30]
Young's modulus	E_f	GPa	400 [30]
Poisson's ratio	ν_f	-	0.14 [31]
Linear expansion coefficient	α_f	1/K	$4.8 \cdot 10^{-6}$ [31]
Weibull modulus	m	-	17.3
Weibull normalizing constant	σ_0	MPa·mm$^{1/m}$	5270
Titanium			
Young's modulus	E	GPa	116 [32]
Poisson's ratio	ν	-	0.32 [32]
Linear expansion coefficient	α	1/K	$8.5 \cdot 10^{-6}$ [32]
Mass density	ρ	gm/cm^3	4.5 [33]
Specific heat capacity	c_p	J/(kg·K)	522 [33]
Electrical conductivity	s	1/(μΩ·m)	2.38 [32]
Relative permeability	μ_r	-	1 [32]
Thermal conductivity	k	W/(m·K)	21.9 [33]
Melting temperature	T_m	K	1953 [33]
Ti-14Al-21Nb			
Young's modulus	E_m	GPa	100
Yield stress	σ_y	MPa	580
Ti-13Al-15Nb-4Mo-2V-7Ta			
Young's modulus	E_m	GPa	114
Fracture stress	σ_u	MPa	601
Ti-14Al-21Nb / SCS-6			
Fiber volume fraction	V_f	-	0.25
Interface sliding stress	τ_s	MPa	113
Temperature change	ΔT	K	-900
Processing induced fiber breaks	$\hat{\rho}_0$	break/m	6
Ti-13Al-15Nb-4Mo-2V-7Ta / SCS-6			
Fiber volume fraction	V_f	-	0.30
Interface sliding stress	τ_s	MPa	123
Temperature change	ΔT	K	-1155
Processing induced fiber breaks	$\hat{\rho}_0$	break/m	10

3.2 Mechanical testing

An electromechanical testing machine equipped with a 50 kN loadcell, serrated face wedge action grips and a 10% capacity extensometer with a 12.7 mm gauge were used to measure stress and strain at ~25°C. Pressure clips and a thin layer of epoxy held the extensometer knife edges firmly in place, Fig. 1. Fiberless matrix samples were tested at a constant displacement crosshead rate of 0.025 mm/min while composite samples were tested at a slower rate of 0.005 mm/min to accommodate the large amount of on line AE data processing. Stress, strain and time were recorded on a personal computer at 2 second intervals.

3.3 Acoustic emission measurement

Two point contact piezoelectric sensors were symmetrically located near either end of the test samples (see Fig. 1). The sensors were our own version of a broad-band conical device [41] designed to measure out of plane displacement with no significant resonance in the 10 kHz to 2 MHz range [42,43]. They were connected via short coaxial leads to charge amplifiers having a rated 250 mV/pC sensitivity and 10 kHz to 10 MHz bandwidth. 20 kHz high-pass and 2 MHz low-pass filters were used after the amplifiers to attenuate environmental noise.

A LeCroy (Chestnut Ridge, NY) 7200 Precision Digital Oscilloscope recorded the AE. 20,000 data points were recorded per channel with 8 bit resolution over a 5 msec time interval (i.e. a 4 MHz sampling rate). The trigger point was offset to allow 4.5 msec of data beyond the trigger point and full capture of the exponential "ring-down" of most signals. A 0.1 V/division setting was used as the primary channel. When strong events overloaded the primary channel, a 1 V/division channel also captured the signal ensuring no loss of data. The time of the AE and their root mean square (RMS) voltages were written to the fixed disk drive of the oscilloscope.

3.4 Acoustic emission calibration

A 1.064 μm Nd:YAG Q-switched pulse laser with a 7 nsec (FWHH) pulse duration and 6 mm spot diameter was used to generate the thermoelastic AE source. Using $t_0 \sim 7$ nsec and properties of titanium, Table 2, Equation (6) indicated that melting begins at $E_0 \sim 108$ mJ for a sample at ~25°C. Ten RMS voltage and laser energy measurements were made every ~10 mJ up to ~100 mJ, Fig. 2. The AE moment strength of the thermoelastic source;

$$M = M_{11} + M_{22} \tag{9}$$

was obtained from Equation (7) as $M = 0.54E_0$. The relation between the AE signal RMS, V_{RMS} (in mV), and the AE moment strength, M (in N·mm), was well fitted by:

$$V_{RMS} = 270 \cdot \ln M - 233 \tag{10}$$

This procedure indicated a logarithmic dependence of signal upon source strength similar to that used for seismic magnitude scaling [44-46].

4. THE Ti-14Al-21Nb / SCS-6 SYSTEM

4.1 Microstructure characterization

The fibers were more or less uniformly spaced, Fig. 3, while the matrix consisted of an equiaxed α_2 (ordered hcp) Ti_3Al intermetallic phase with intergranular β (bcc). By-products of the consolidation process included a ~3 μm thick fiber-matrix reaction product, broken fibers ($\hat{\rho}_0 \sim 6$ breaks/m) and fiber microbending [27]. Radial (~1 per fiber, see Fig. 3) and annular cracks (~6-7 crack/mm) were also present. Both types of crack often extended into a surrounding (~10 μm thick) β-depleted matrix zone (see Fig. 3) and sometimes partially through the SCS layers. Apart from the β-depleted zones, the fiberless and composited matrices were quite similar.

4.2 Stress - strain - AE behavior

The fiberless Ti-14Al-21Nb matrix behaved in an elastic-nearly perfectly plastic fashion with a Young's modulus, E_m, of 100 GPa [35]. Yielding initiated at a stress, σ_y, of 580 MPa and a strain of 0.60%. Failure occurred at a stress of 612 MPa and a strain of 4.50%. 10 acoustic emissions were detected with a mean AE moment strength of 2.6 N·mm (0.2 N·mm standard deviation) during nominally elastic loading.

The Ti-14Al-21Nb / SCS-6 composite initially exhibited a slight non-linearity due to sample bending, Fig. 4. A linear (Stage I) behavior then occurred up to a stress, σ, of 475 MPa and a strain, ε, of 0.29%. A brief transition (indicative of matrix plasticity) and a second (Stage II) linear region of differing slope followed [38,47,48]. The measured modulus in Stage I was 178 GPa while in Stage II it was 88 GPa. Tensile failure occurred at a stress of 925 MPa and a strain of 0.79%. 1841 emissions (see Fig. 4) were detected throughout the loading. The mean AE moment strength was again 2.6 N·mm (1.3 N·mm standard deviation). The rate of AE activity for the composite increased rapidly as the applied stress exceeded about 400 MPa and approached steady state just beyond the point where the transition to Stage II occurred. The final integrated moment strength of all composite AE activity was 4710 N·mm. Four strong events having $M > 10$ N·mm were recorded toward the end of the test.

4.3 Damage observations after testing

Metallographic examinations of the longitudinally sectioned sample revealed annular β-depleted matrix zone cracks (these extended into the reaction products) which were more or less uniformly distributed along all fibers, Fig. 5. The cracks in the gauge section after testing were more severe (had a larger area and opening displacement) and were nearly twice as frequent (~11-

12 crack/mm) as those in the undeformed grip section. Occasionally these cracks extended all the way through the SCS layers and are similar to the observations of other researchers [49-51]. The ends of the annular cracks were not found to directly nucleate fracture of the underlying SiC.

The fracture surface exhibited significant crack deflection with typical fiber pull-out lengths of up to a fiber diameter or two [35]. Far from (several mm or more away) the fracture surface, there was no evidence of fiber fracture (other than processing damage). However, higher magnification uncovered the occasional occurrence of clusters of arrested annular fiber cracks, Fig. 6. These crack clusters were randomly distributed throughout the gauge section, but within a cluster, they exhibited a regular axial spacing with a ~50-60 μm separation. The cracks extended ~10-15 μm radially inward from near the midradius boundary (~39.5 μm from fiber center) and towards the carbon core forming an annular ring (see Fig. 6). Nearer to (within a few mm) the fracture surface, many closely spaced fiber fractures (less than one fiber diameter apart) and arrested annular fiber cracks were present. Just below (within a few fiber diameters) the fracture surface, several of the fibers had been extensively shattered, and some into very small wedge-shaped fragments running perpendicular to the direction of loading. Other researchers have related similar fragmentation to stress waves [52].

4.4 Acoustic emission mechanisms

A typical annular β-depleted matrix zone crack had a radial length of ~13 μm and thus a crack face area of, A, of ~6200 μm^2. The crack opening, Δ, was ~1.0 μm (see Fig. 5 and note that tensile loading opens the crack), and so the AE moment strength;

$$M = M_{11} + M_{22} + M_{33} \tag{11}$$

was ~1.8 N·mm where Equation (2) and Ti-14Al-21Nb moduli (Table 2) have been used. This damage process was therefore near the limit of detectability ($M \sim 2.5$ N·mm) and was probably responsible for the numerous "weak" signals observed during testing of the composite.

The four "strong" events having $M > 10$ N·mm were unlikely to be associated with β-depleted zone cracking. For example, the two emissions which occurred at stresses of 877 MPa and 884 MPa had moment strengths of 18.0 N·mm and 51.5 N·mm respectively. We believe that these signals were due to fiber fractures. Superposing elastic residual and applied stresses, the fiber stress, T, at the time of these fractures was ~2200 MPa. From Equation (3), using properties found in Table 2, the computed crack opening is ~3.8 μm. Equations (4) and (11) then give a moment strength of ~32.0 N·mm which is comparable to the range of values observed.

The short annular fiber cracks were probably not detected if occurring one at a time in these tests. They had a typical radial length of ~15 μm, an outer radius of ~39.5 μm and hence, an area of ~3000 μm^2. Their crack opening was ~0.3 μm (see Fig. 6 and note that tensile loading opens the crack) which corresponds to a moment strength of ~0.5 N·mm. This is below the baseline noise level ($M \sim 2.5$ N·mm) of the tests (their significance is discussed later).

4.5 Modeled stress - strain behavior

A global load sharing model modified to account for the effect of fiber breakage induced during consolidation processing [8] was used to predict the stress - strain behavior. Elastic residual stresses and matrix plasticity were additions to the model. The remote axial fiber and matrix stresses were found (elastic residual and applied stresses superimposed) using the composite cylinder methodology [29,53,54]. Composite strain (which was primarily controlled by elastic deformation of the unbroken fibers) entered the constitutive relation in this manner. Because the shear recovery length, $l = r_f T / 2\tau_s$, is a positive quantity, the absolute value of this was used as a model input during the early stages of loading (i.e. when the fiber is in residual axial compression) to ensure that consolidation fiber breaks were properly accounted for.

In Stage I, the modeled behavior was similar to that measured (see Fig. 4). The onset of matrix plasticity (i.e. Stage II behavior) was estimated using a von Mises criterion. Yielding was taken to initiate near the edge (~80 μm from fiber center) of the β-depleted zone (where the more deformable β phase begins) rather than at the fiber-matrix interface. The predicted axial strain at yielding was 0.28% which compared well with the measured value of 0.29%. In Stage II, axial constraint imparted by the fibers inhibited plastic flow of the matrix. Furthermore, since the maximum strains were small (0.79% axial strain at failure), remote fiber and matrix stresses were approximated by superimposing elastic yield point stresses with the additional incremental stresses developed after the matrix was deforming perfectly plastically [55]. The latter were computed using the elastic composite cylinder solution with an axial strain equal to the incremental strain beyond the yield point and tangent Stage II moduli. For the non-hardening matrix, the tangent Young's modulus and Poisson's ratio tended to zero and one half respectively, the plane strain bulk modulus was replaced by the elastic bulk modulus, $k_{pm} \rightarrow E_m / 3(1 - 2\nu_m)$, and the shear modulus remained unchanged [56]. The fiber retained its original elastic moduli. The measured Stage II modulus (see Fig. 4) was ~12% less than predicted. Since few fiber fractures occurred prior to sample failure, this reduced modulus is believed to be connected to the annular β-depleted zone cracking.

The computed fiber and matrix axial stresses at sample failure, $\sigma_f = 2464$ MPa and $\sigma_m = 535$ MPa, were reduced from their precomposited values. Thus, neither the fiber nor the matrix had achieved the full load bearing capacity exhibited prior to compositing. Although additional test data reported by GEAE using samples machined from the same panel had computed fiber stresses which were as much as ~34% higher [private communication] they were still significantly less than the model prediction based upon a retention of the pristine fiber strength. Strength measurements of fibers extracted from untested composites of similar composition to those tested here indicate that a ~20% loss of strength can accompany consolidation [57]. The underlying origin of this is at present unclear. It may be linked to chemical depletion of SCS layers or to their physical damage during processing. While processing damage (including fiber microbending) may lead to reductions in fiber strength when composited, fragmentation theory suggests that cumulative failure of the fibers should have occurred prior to sample failure. This was observed neither acoustically nor metallographically in our tests and indicates a noncumulative mechanism.

Lastly, we note that some fibers far from the fracture surface contained arrested annular cracks (see Fig. 6). Flaws of such a large size can usually exist in brittle silicon carbide fibers only when the tensile stress is less than a few MPa. They could have been caused by a combination of added static and dynamic stresses arising from damage including nearby fiber breaks [52,58]. Displacement constraint imparted by unbroken fibers in the same cross-sectional plane, the sometimes large compressive stresses found in regions of SCS-6 fibers [59] and microstructural changes at the mid-radius boundary [60] may have contributed to their arrest. Daniel [61] has used high speed photoelastic techniques to observe fiber damage of this type in model glass-Homalite composites. Were large fiber defects of this type to have occurred before the final catastrophic event, they would have significantly weakened the fibers and led to premature failure.

5. THE Ti-13Al-15Nb-4Mo-2V-7Ta / SCS-6 SYSTEM

5.1 Microstructure characterization

The fibers were more or less uniformly spaced, Fig. 7, while the matrix consisted of an equiaxed α_2 phase in a matrix of transformed β that contained a fine acicular $\alpha_2 + \beta$ microstructure. By-products of the consolidation process included a ~3 μm thick fiber-matrix reaction product zone, occasional broken fibers ($\hat{\rho}_0 \sim 10$ breaks/m) and fiber microbending. Short radial (see Fig. 7) and annular microcracks were observed in the reaction product. No β-depleted matrix zone existed near the fibers. However, islands of ~3-5 μm diameter not having typical α_2 or $\alpha_2 + \beta$ morphologies were observed near the fibers (see Fig. 7). These etched more slowly than the α_2 phase and were not found in the corresponding neat matrix. The fiberless and composited matrices were otherwise quite similar. Portions of the SCS-6 layers were observed to have decohered from the fibers and were trapped in the matrix (see Fig. 7). This coating damage has been linked to fiber thermal shock during the plasma spray deposition process [27] and may have contributed to the higher interface debond/sliding stresses measured for this system.

5.2 Stress - strain - AE behavior

The fiberless Ti-13Al-15Nb-4Mo-2V-7Ta matrix behaved in a brittle fashion with a Young's modulus, E_m, of 114 GPa [35]. Failure occurred at a stress, σ_u, of 601 MPa and a strain of 0.50%. 5 acoustic emissions were detected with a mean AE moment strength of 2.8 N·mm (0.3 N·mm standard deviation).

The Ti-13Al-15Nb-4Mo-2V-7Ta / SCS-6 composite exhibited a linear (Stage I) behavior up to a stress, σ, of 370 MPa and a strain, ε, of 0.19%, Fig. 8. Thereafter, unstable tensile behavior (including strain reversals and hysteresis) was observed. Other unpublished test data reported by GEAE have exhibited similar behavior for this system [private communication]. The strain reversals were consistent with the formation of cracks (and an accompanying increased compliance) outside the extensometer knife edge contact points. If the opening displacement of these cracks exceeded that needed to accommodate the imposed displacement rate, an elastic contraction of the gauge section can occur. Tensile failure occurred at a stress of 758 MPa and a strain of 0.88%. 1121 emissions (see Fig. 9) were detected but with a mean AE moment strength of 38.6 N·mm (248.4 N·mm standard deviation). The AE activity for the composite began at a stress of around 50 MPa and occurred at an approximately constant rate up to a stress of 370 MPa and a strain of 0.19%. At this point, dramatic increases in signal strength accompanied abrupt changes in stress - strain behavior until tensile failure. The integrated moment strength was found to be well fitted by a power-law relation;

$$\int_0^{\sigma} M(\eta)\,d\eta = \frac{10^{-6}\sigma^{3.7}}{1.05} \quad (\mathrm{N\cdot mm}) \qquad (12)$$

where the composite stress, σ, has units of MPa.

5.3 Damage observations after testing

Metallographic examinations of the longitudinally sectioned sample revealed extensive matrix cracking, Fig. 9, and many fractured fibers (some were associated with consolidation processing but the majority occurred during testing), Fig. 10. Annular reaction product and fiber cracks similar to those seen in the Ti-14Al-21Nb / SCS-6 system (see Figs. 5 and 6) were also found. The primary matrix cracks traversed the full cross-section and were spaced ~0.3-0.9 mm along the entire gauge length (see Fig. 9). The secondary matrix cracks (see Fig. 8) were arrested before traversing the full cross-section. Often, multiple fiber fractures with spacings of less than a fiber diameter (see Fig. 10) were observed far (several mm or more away) from the final fracture plane. The annular fiber cracks were again regularly spaced with a ~50-60 μm separation, however, they occurred much more frequently, and were more evenly distributed than in the Ti-14Al-21Nb / SCS-6 system. While matrix cracks and fiber fractures often penetrated at least one of the SCS layers, neither was observed to nucleate damage in the adjacent phase (with the possible exception of consolidation processing damage like that shown in Fig. 9. Large matrix crack opening displacements (see Fig. 10) were indicative of extensive sliding at the fiber-matrix interface. Even so, a relatively planar fracture surface with minimal fiber pull-out was observed [35]. Just below (within a few fiber diameters) the fracture surface, several of the fibers had been extensively shattered, and some into very small wedge-shaped fragments like that observed in the Ti-14Al-21Nb / SCS-6 system.

5.4 Acoustic emission mechanisms

Primary matrix cracks were the most likely origin of the many abrupt strain reversals seen in the stress - strain curves (see Fig. 8). The crack face areas, A, for these were ~4.2 mm^2. The first primary crack event appeared to occur at a stress, σ, of 370 MPa. A simple (one-dimensional) micro-mechanical model (see the Appendix) can be used to estimate the crack opening. Using Equation (A.8) and data from Table 2, the crack opening, Δ, is estimated to be ~3.0 μm. From Equation (2), the moment strength, $M = M_{11} + M_{22} + M_{33}$, was therefore ~4000 N·mm. This is a very strong event and appears to be the source of the significant number of observed signals in the ~1,000-10,000 N·mm range (see Fig. 8). The many events with smaller moments, $100 < M < 1,000$ N·mm, occurring after the first primary matrix crack are likely to have been caused by either (partial) matrix cracks that were arrested at fibers, or the intermittent extension of eventual primary cracks.

Fiber fractures were estimated to have moment strengths in the ~10-50 N·mm range (see section 4.5). Thus, many of the numerous events having similar strengths (see Fig. 8) were consistent with the extensive, metallographically observed, fracturing of fibers.

Annular reaction product cracks typically propagated through the entire ~3 μm thick fiber-matrix reaction product zone surrounding the fibers and thus had crack face areas of ~1350 μm^2. Crack openings were ~0.5 μm or less and so the corresponding moment strengths were in the neighborhood of ~0.2 N·mm. Similarly, arrested annular fiber cracks were expected to have moment strengths of ~0.5 N·mm (see section 4.5). Since the estimated strengths of both crack types is well below the detection threshold ($M \sim 2.5$ N·mm), we conclude that these were not acoustically detected in these experiments unless occurring many at a time.

5.5 Modeled stress - strain behavior

A simple matrix cracking (with no fiber fracture) micro-mechanical model (see the Appendix) was used to model the stress - strain behavior. The crack density evolution can be estimated from the AE data by noting that the moment strengths of matrix cracking events were much greater than those associated with other damage mechanisms. Let the number of completed matrix cracks at a given stress, σ, be proportional to the magnitude of the integrated moment data, Equation (12). Since there were about 45 cracks observed along the 25 mm gauge length at sample failure (i.e. when $\sigma = 758$ MPa), the crack half spacing dependence on stress is simply;

$$x' \sim \frac{10^{13}\sigma^{-3.7}}{0.8} \quad (\mu\text{m}) \tag{13}$$

where σ has units of MPa.

To compute the strain, ε, of the composite at a given stress, σ, Equation (13) was first solved for x'. This was then compared to the shear recovery length, l', obtained using Equation (A.1) with the remote matrix stress, σ_m, predicted using Equation (A.2) and parameters cited in Table 2. The residual fiber and matrix stresses were $\sigma_f^T = -812$ MPa and $\sigma_m^T = 348$ MPa (see Table 1). When $x' > l$, the situation was that depicted in Fig. 11(a), and Equation (A.9) gave the strain. When $x' \leq l$, the situation was that depicted in Fig. 11(b), and Equation (A.15) gave the strain.

Comparing results, the measured Stage I modulus of ~199 GPa slightly exceeded the model prediction (see Fig. 8). This occurs because the (continuous) power-law fit of the integrated moment curve, Fig. 8, slightly overestimated the amount of (discontinuous) cracking in this region. A rule of mixtures approximation gives a Stage I modulus of 200 GPa indicating that the effect of secondary cracking damage on Stage I stiffness is negligible. After the first primary crack event (at 370 MPa), the modeled stress - strain behavior compared favorably with the data up to a strain of about 0.5%. Beyond this, the modeled stiffness was slightly greater than measured (probably a consequence of neglecting fiber fractures in the model) and increased as the matrix cracking began to saturate.

The first primary matrix crack occurred at a strain of 0.19%. This corresponded to a strain which was 0.31% less than the measured failure strain (0.50%) of the fiberless matrix. By superimposing the elastic residual and the applied stresses, $\sigma_m = \sigma_m^* + \varepsilon E_m$, the computed axial matrix stress at the onset of matrix cracking, 565 MPa, is close to the value measured (601 MPa) for failure of the fiberless matrix sample. This may be somewhat coincidental since the flaw population that gives rise to a stochastic matrix strength is likely to be affected by compositing. Even so, the measured mean crack spacing (~0.56 mm) at failure agrees well with that predicted (~0.53 mm) using the Kimber-Keer model [62].

The mean fiber stress at failure for fibers bridging a primary matrix crack was 2527 MPa. Similar results were reported by GEAE using samples machined from the same panel [private communication]. As a lower bound prediction, a fiber bundle model [38] (with a 25 mm bundle length and SCS-6 parameters cited in Table 2) suggests bundle failure at a fiber stress of 3502 MPa and strain of 0.93%. Thus, the measured maximum fiber stress for our test was about 1000 MPa less than the typical tensile strength of a bundle of pristine, unprocessed fibers. Like the Ti-14Al-21Nb / SCS-6 system, the reinforcing fibers have performed in a weakened fashion when composited.

Since the amount of damage to the fibers (fractures and arrested annular cracks) was significant and often so closely spaced (see Fig. 10) that static equilibrium considerations could not explain the phenomena, dynamic stresses are thought to have contributed to their weakening. In fact, the acoustic emissions indicated that stress wave intensity was much greater in this composite system than in the Ti-14Al-21Nb / SCS-6 system. This, along with processing induced damage and microbending stresses is thought to be the origin of fiber weakening and premature failure of this composite.

6. SUMMARY

A laser calibrated acoustic emission approach was combined with relatively simple micromechanical models to deduce the evolution of damage processes during the tensile straining of two different intermetallic matrix composites.

A ductile matrix Ti-14Al-21Nb / SCS-6 composite emitted most of its detectable AE by annular microcracking of a brittle β-depleted matrix zone surrounding the fibers. This damage process increased rapidly near the composite yield point and continued at a constant rate thereafter. An estimate of the acoustic moment of a fiber fracture identified the occurrence of about four fiber fracture events prior to sample failure. Clusters of annular fiber cracks were observed metallographically. Their mechanism of origin remains unclear, but may have been linked to the dynamic unloading waves which accompanied final sample failure. A global load sharing model which included consolidation fiber breakage was modified to account for elastic residual stresses and matrix yielding. This model predicted a Stage II modulus that was ~12% greater than measured. The extra softening appears to be connected to the extensive β-depleted zone cracking. Cumulative fiber fragmentation was not observed, and a noncumulative mechanism was suspected, and may have contributed to a tensile failure at stresses significantly less than predicted.

A brittle matrix Ti-13Al-15Nb-4Mo-2V-7Ta / SCS-6 composite emitted strong AE from multiple matrix cracking. Matrix cracking initiated well below the stress where primary matrix cracks were first visually observed. Many of the smaller AE signals after the first primary crack event were consistent with mostly secondary cracks which had been arrested at fibers or intermittently extended to become primary cracks. Failure occurred after numerous fiber fractures at a fiber stress significantly lower than predicted by a fiber bundle model. The AE due to damage increased with stress in a power law fashion. Damage evolution data deduced from the acoustic emission measurements were combined with a relatively simple micro-mechanical model to predict the inelastic contributions of matrix cracks to the overall deformation behavior. Good agreement between the predicted and measured stress - strain behavior was found. Significant annular fiber cracks were observed and thought to be associated with the unloading waves associated with primary and secondary matrix cracking providing a mechanism for reducing the effective fiber strength.

Acknowledgments - We are grateful to A.G. Evans for discussions about the mechanisms of composite damage and to General Electric Aircraft Engines who supplied the samples. This work has been supported by the DARPA/ONR URI at UCSB (S. Fishman, Program Manager).

REFERENCES

1. R.A. MacKay, P.K. Brindley and F.H. Froes, *JOM* **42**, 23 (May 1991).
2. P.G. Partridge and C.M. Ward-Close, *Int. Mat. Rev.* **38** (1), 1 (1993).
3. C.M. Ward-Close and C. Loader, *Recent Advances in Titanium Matrix Composites*, (edited by F.H. Froes and J. Storer), p. 19. TMS, Warrendale (1995).
4. M.Y. He, A.G. Evans and W.A. Curtin, *Acta metall. mater.* **41** (3), 871 (1993).
5. D.P Walls, G. Bao and F.W. Zok, *Acta metall. mater.* **41** (7), 2061 (1993).
6. C.H. Weber, X. Chen, S.J. Connell and F.W. Zok, *Acta metall. mater.* **42** (10), 3443 (1994).
7. P.D. Warren, T.J. Mackin and A.G. Evans, *Acta metall. mater.* **40** (6), 1243 (1992).
8. J.M. Duva, W.A. Curtin and H.N.G. Wadley, *Acta metall. mater.* **43** (3), 1119 (1995).
9. B.W. Rosen, *AIAA Journal*, **2** (11), 1985 (1964).
10. C. Zweben, *AIAA Journal*, **6** (12), 2325 (1968).
11. W.A. Curtin, *J. Mat. Sci.* **26**, 5239 (1991).
12. M.Y. He, B.-X. Wu, A.G. Evans and J.W. Hutchinson, *Mech. Mat.* **18**, 213 (1994).
13. J. Aboudi, *Mechanics of Composite Materials*, Elsevier, Amstrerdam (1991).
14. M-J. Pindera, A.D. Freed and S.M. Arnold, *Int. J. Solids Structures* **30** (9), 1213 (1993).
15. C. Scruby, H. Wadley and J.E. Sinclair, *Phil. Mag. A*, **44** (2), 249 (1981).

16. H.N.G. Wadley and C.B. Scruby, *Int. J. Frac.*, p. 111 (1983).
17. R.B. Thompson and H.N.G. Wadley, in *Critical Reviews in Solid State and Materials Sciences* **16** (1), 37 (1989).
18. D.J. Sypeck and H.N.G. Wadley, *Review of Progress in Quantitative Nondestructive Evaluation* **15B**, (edited by D.O. Thompson and D.E. Chimenti), p. 1207, Plenum Press, New York (1996).
19. M.A. Hamstad, *Exp. Mech.*, p. 7 (March 1986).
20. M. Madhukar and J. Awerbuch, *Composite Materials: Testing and Design (Seventh Conference)*, ASTM STP 893, (edited by J.M. Whitney), p. 337, ASTM, Philadelphia (1986).
21. J.G. Bakuckas Jr., W.H. Prosser and W.S. Johnson, *NASA Technical Memorandum 107742*, Langley Research Center, Hampton, Virginia (1993).
22. R. Burridge and L. Knopoff, *Bull. Seis. Soc. Am.* **54** (6), 1875 (1964).
23. K. Aki and P.G. Richards, *Quantitative Seismology Theory and Methods*, Freeman, San Francisco (1980).
24. J.E. Michaels, *Ph.D. Thesis*, Cornell University, Ithaca (1984).
25. C.B. Scruby, H.N.G. Wadley, R.J. Dewhurst, D.H. Hutchins and S.B. Palmer, *Mat. Eval.* **39** (13), 1250 (1981).
26. C.B. Scruby and L.E. Drain, *Laser Ultrasonics Techniques and Applications*, Adam Hilger, Bristol (1990).
27. J.F. Groves, D.M. Elzey and H.N.G. Wadley, *Acta metall. mater.* **42** (6), 2089 (1994).
28. D. Pank, S. Veeck, K. Bain and J. Jackson, in *Titanium Metal Matrix Composites II*, WPAFB Workshop Proceedings WL-TR-93-4105, p. 158, WPAFB, Ohio (1993).
29. H. Poritsky, *Physics* **5**, 406 (1934). [Note: typographic error in Equation (15)]
30. Silicon Carbide (SCS) Filament Data, Textron Specialty Materials, Lowell, Massachusetts (1994).
31. C.T. Herakovich and J.S. Hidde, Ultramicroscopy **40**, 215 (1992).
32. *Handbook of Chemistry and Physics*, 63rd edition, CRC Press Inc., Boca Raton (1984).
33. F.P. Incropera and D.P. DeWitt, *Fundamentals of Heat and Mass Transfer*, John Wiley & Sons, New York (1990).
34. P.E. Cantonwine and H.N.G. Wadley, *Composites Eng.* **4** (1), 67 (1994).
35. D.J. Sypeck, *Ph.D. Dissertation*, University of Virginia, Charlottesville (1996).
36. W. Weibull, *J. Appl. Mech.* **18**, 293 (1951).
37. P. Kittl, *J. Appl. Mech.* **51**, 221 (1984).
38. A. Kelly and N.H. Macmillan, *Strong Solids*, Third Edition, Clarendon Press, Oxford (1986).
39. P. Martineau, M. Lahaye, R. Pailler, R. Naslain, M. Couzi and F. Cruege, *J. Mat. Sci.* **19**, 2731 (1984).
40. ASTM Designation D 3379, 1992 *Annual Book of ASTM Standards* **15.03**, 127 (1992).
41. T.M. Proctor Jr., *J. Acoust. Soc. Amer.* **71** (5), 1163 (1982).
42. D.J. Sypeck, *M.S. Thesis*, University of Virginia, Charlottesville (1990).
43. N.N. Hsu and F.R. Breckenridge, *Mat. Eval.* **39**, 60 (1981).
44. H. Kanamori, *J. Geophys. Res.* **82** (20), 2981 (1977).
45. K. Kasahara, *Earthquake Mechanics*, Cambridge University Press, Cambridge (1981).
46. K.E. Bullen and B.A. Bolt, *An Introduction to the Theory of Seismology*, Cambridge University Press, Cambridge (1985).
47. T.H. Courtney, *Mechanical Behavior of Materials*, McGraw-Hill, New York (1990).
48. A. Kelly and H. Lilholt, *Phil. Mag.* **20** (8), 311 (1969).
49. S.L. Draper, P.K. Brindley and M.V. Nathal, in *Developments in Ceramic and Metal-Matrix Composites*, (edited by Kamleshwar Upadhya), p. 189. TMS, Warrendale (1991).
50. A.G. Metcalfe, *J. Comp. Mat.* **1**, 356 (1967).
51. S. Ochiai and Y. Murakami, *J. Mat. Sci.* **14**, 831 (1979).

52. H.W. Herring, J.L. Lytton and J.H. Steele Jr., *Met. Trans.* **4**, 807 (1973).
53. A. Kelly, in *Chemical and Mechanical Behavior of Inorganic Materials*, (edited by A.W. Searcy, D.V. Ragone and U. Colombo), p. 523, Wiley-Interscience, New York (1968).
54. K.K. Chawla, *Composite Materials Science and Engineering*, Springer-Verlag, New York (1987).
55. L.J. Ebert, S.S. Hecker and C.H. Hamilton, *J. Comp. Mat.* **2** (4), 458 (1968).
56. R. Hill, *J. Mech. Phys. Solids* **12**, 213 (1964).
57. D.T. Russell, *M.S. Thesis*, University of Virginia, Charlottesville (1996).
58. B.A. Lerch and J.F. Saltsman, NASA Technical Memorandum 103620, Lewis Research Center, Cleveland, Ohio (1991).
59. F.E. Wawner, A.Y. Teng and S.R. Nutt, *Metal Matrix, Carbon, and SiC Composites*, NASA Conference Publication 2291, p. 29 (1983).
60. J.D. Casey and J. Geller, *Titanium Aluminide Composites*, WPAFB Workshop Proceedings WL-TR-91-4020, p. 59, WPAFB, Ohio (1991).
61. I.M. Daniel, *J. Comp. Mat.* **4**, 178 (1970).
62. A.C. Kimber and J.G. Keer, *J. Mat. Sci. Letters* **1**, 353 (1982).
63. J. Aveston, G.A Cooper and A. Kelly, in *The Properties of Fibrous Composites*, Conference Proceedings, National Physics Laboratory, Guildford, p. 15, IPC Science and Technology Press (1971).
64. B. Budiansky, J.W. Hutchinson and A.G. Evans, *J. Mech. Phys. Solids* **34** (2), 167 (1986).
65. W.A. Curtin, *Acta metall. mater.* **41** (5), 1369 (1993).
66. J.W. Hutchinson and H.M. Jensen, *Mech. Mat.* **9**, 139 (1990).

APPENDIX

Tensile Response of a Unidirectional Brittle Matrix Composite Loaded in The Fiber Direction

The prediction of inelastic deformation due to brittle matrix cracking in unidirectional fiber reinforced composites has been studied by Aveston *et al.* [63], Budiansky *et al.* [64] and more recently Curtin [65], who noted similarities between the matrix cracking process and the stochastic fiber fragmentation that often occurs in ductile matrix composites. He *et al.* [12] have conducted detailed finite element calculations of the inelastic strains associated with matrix cracking that compared favorably with analyses using shear lag models [66]. Here, a relatively simple (one-dimensional) elastic analysis is used.

If the faces of a matrix crack remain approximately straight, equilibrium considerations necessitate that fiber-matrix interface sliding must occur along a shear recovery length given by [63]:

$$l' = \frac{r_f \sigma_m V_m}{2 V_f \tau_s} \tag{A.1}$$

Along this length, matrix stress, σ_m', increases linearly from zero (at the crack plane) to the remote isostrain value, σ_m. Conversely, fiber stress, σ_f', decreases linearly from σ/V_f to the remote isostrain value, σ_f. Hence, the matrix supports less load than what would be expected for an uncracked (isostrained) composite while the fiber supports more. The difference in their changes of length gives rise to a matrix crack opening, Δ. Composite strain, ε, is simply the elongation of the (unbroken) fibers divided by their original length. Both are a function of the matrix crack spacing.

Since the site of cracking events is governed by the distribution and severity of defects [65], it is convenient to work with a mean crack spacing $2x'$ [12]. Two situations must be addressed. The first involves sliding along lengths less than one-half the mean crack spacing (i.e. when $x' > l'$), Fig. 11(a), while the second involves sliding along the entire length (i.e. when $x' \leq l'$), Fig. 11(b). The equilibrium relation, $\sigma = V_f\sigma_f + V_m\sigma_m$, is satisfied throughout. Subscripts f and m differentiate the fiber and matrix.

When $x' > l'$ (in the region $x \leq x' - l'$):

Stresses:

$$\sigma_f = \sigma_f^T + \hat{\varepsilon}E_f \qquad \sigma_m = \sigma_m^T + \hat{\varepsilon}E_m \tag{A.2}$$

Isostrain:

$$\hat{\varepsilon} = \frac{\sigma - V_f\sigma_f^T - V_m\sigma_m^T}{V_fE_f + V_mE_m} \tag{A.3}$$

Displacement (at $x = x' - l'$):

$$\hat{u} = \hat{\varepsilon}(x' - l') \tag{A.4}$$

When $x' > l'$ (in the region $x \geq x' - l'$):

Stresses:

$$\sigma_f' = \sigma_f + \frac{V_m\sigma_m}{V_f}\left(1 - \frac{x' - x}{l'}\right) \qquad \sigma_m' = \sigma_m\left(\frac{x' - x}{l'}\right) \tag{A.5}$$

Strains:

$$\varepsilon_f' = \frac{\sigma_f' - \sigma_f^T}{E_f} \qquad \varepsilon_m' = \frac{\sigma_m' - \sigma_m^T}{E_m} \tag{A.6}$$

Displacements (at $x = x'$):

$$u_f' = \frac{l'}{E_f}\left(\sigma_f - \sigma_f^T + \frac{V_m\sigma_m}{2V_f}\right) + \hat{u} \qquad u_m' = \frac{l'}{E_m}\left(\frac{\sigma_m}{2} - \sigma_m^T\right) + \hat{u} \tag{A.7}$$

When $x' > l'$:

Matrix crack opening:

$$\Delta = 2(u_f' - u_m') = \frac{r_fV_m[\sigma E_m + V_f(\sigma_m^TE_f - \sigma_f^TE_m)]^2}{2V_f^2E_fE_m(V_fE_f + V_mE_m)\tau_s} \tag{A.8}$$

Composite strain:

$$\varepsilon = \frac{u_f'}{x'} \tag{A.9}$$

When $x' \leq l'$:

Stresses (at $x = 0$):

$$\sigma_f = \frac{\sigma}{V_f} - \frac{2\tau_sx'}{r_f} \qquad \sigma_m = \frac{2\tau_sx'V_f}{r_fV_m} \tag{A.10}$$

Stresses:

$$\sigma_f' = \sigma_f + \frac{V_m\sigma_m}{V_f}\left(\frac{x}{x'}\right) \qquad \sigma_m' = \sigma_m\left(1 - \frac{x}{x'}\right) \tag{A.11}$$

Strains:

$$\varepsilon_f' = \frac{\sigma_f' - \sigma_f^T}{E_f} \qquad \varepsilon_m' = \frac{\sigma_m' - \sigma_m^T}{E_m} \tag{A.12}$$

Displacements (at $x = x'$:)

$$u_f' = \frac{x'}{E_f}\left[\sigma_f - \sigma_f^T + \frac{V_m\sigma_m}{2V_f}\right] \qquad u_m' = \frac{x'}{E_m}\left(\frac{\sigma_m}{2} - \sigma_m^T\right) \tag{A.13}$$

Matrix crack opening:

$$\Delta = 2(u_f' - u_m') = 2x'\left[\frac{1}{E_f}\left(\frac{\sigma}{V_f} - \sigma_f^T - \frac{\tau_sx'}{r_f}\right) + \frac{1}{E_m}\left(\sigma_m^T - \frac{\tau_sx'V_f}{r_fV_m}\right)\right] \tag{A.14}$$

Composite strain:

$$\varepsilon = \frac{u_f'}{x'} = \frac{1}{E_f}\left(\frac{\sigma}{V_f} - \sigma_f^T - \frac{\tau_sx'}{r_f}\right) \tag{A.15}$$

FIGURES

Fig. 1. Details of the strain and AE instrumentation. A knife edge extensometer and miniature piezoelectric sensors were used.

Fig. 2. Acoustic emission calibration curve. A laser generated thermoelastic source produced artificial AE of known moment strength for calibration.

Fig. 3. Ti-14Al-21Nb / SCS-6 composite (microstructure). A 0.25 volume fraction of SCS-6 fiber in a Ti-14Al-21Nb (wt.%) matrix. Consolidation processing damage included a cracked β-depleted matrix zone.

Fig. 4. Ti-14Al-21Nb / SCS-6 composite (stress - strain behavior and AE activity). A bi-linear behavior. The rate of AE activity increased rapidly near the composite yield point and continued at a constant rate thereafter. (a) Stress - strain behavior and AE moment strength. (b) AE event count and integrated moment.

Fig. 5. Ti-14Al-21Nb / SCS-6 composite (annular β-depleted matrix zone cracks). These were more severe and were nearly twice as frequent as those observed in the undeformed grip section. (a) Micrograph of a single crack. (b) Three-dimensional schematic of several cracks.

Fig. 6. Ti-14Al-21Nb / SCS-6 composite (annular fiber cracks). Clusters of these cracks extended radially inward from near the midradius boundary and towards the carbon core forming an annular ring. (a) Micrograph of a single crack. (b) Three-dimensional schematic of a crack cluster.

Fig. 7. Ti-13Al-15Nb-4Mo-2V-7Ta / SCS-6 composite (microstructure). A 0.30 volume fraction of SCS-6 fiber in a Ti-13Al-15Nb-4Mo-2V-7Ta (wt.%) matrix. Consolidation processing damage included cracked reaction products and SCS decohesion.

Fig. 8. Ti-13Al-15Nb-4Mo-2V-7Ta / SCS-6 composite (stress - strain behavior and AE activity). Unstable tensile behavior was observed. The strength of AE activity increased dramatically at the point where the first primary matrix crack was observed. (a) Stress - strain behavior and AE moment strength. (b) AE event count and integrated moment.

Fig. 9. Ti-13Al-15Nb-4Mo-2V-7Ta / SCS-6 composite (primary and secondary matrix cracks). Primary cracks traversed the whole cross-section and were present along the entire gauge length. Secondary cracks which arrested before traversing the whole cross section were also present. (a) Micrograph. (b) Three-dimensional schematic of primary and secondary matrix cracks.

Fig. 10. Ti-13Al-15Nb-4Mo-2V-7Ta / SCS-6 composite (closely spaced fiber fractures, annular fiber cracks and a primary matrix crack). Fiber fractures were numerous and often very closely spaced. Large matrix crack opening displacements were indicative of extensive sliding at the fiber-matrix interface.

Fig. 11. Ti-13Al-15Nb-4Mo-2V-7Ta / SCS-6 composite (micro-mechanical model of primary matrix cracking). A relatively simple (one-dimensional) elastic analysis was used to model the tensile strain response of the cracked composite. (a) $x' > l'$. (b) $x' \leq l'$.

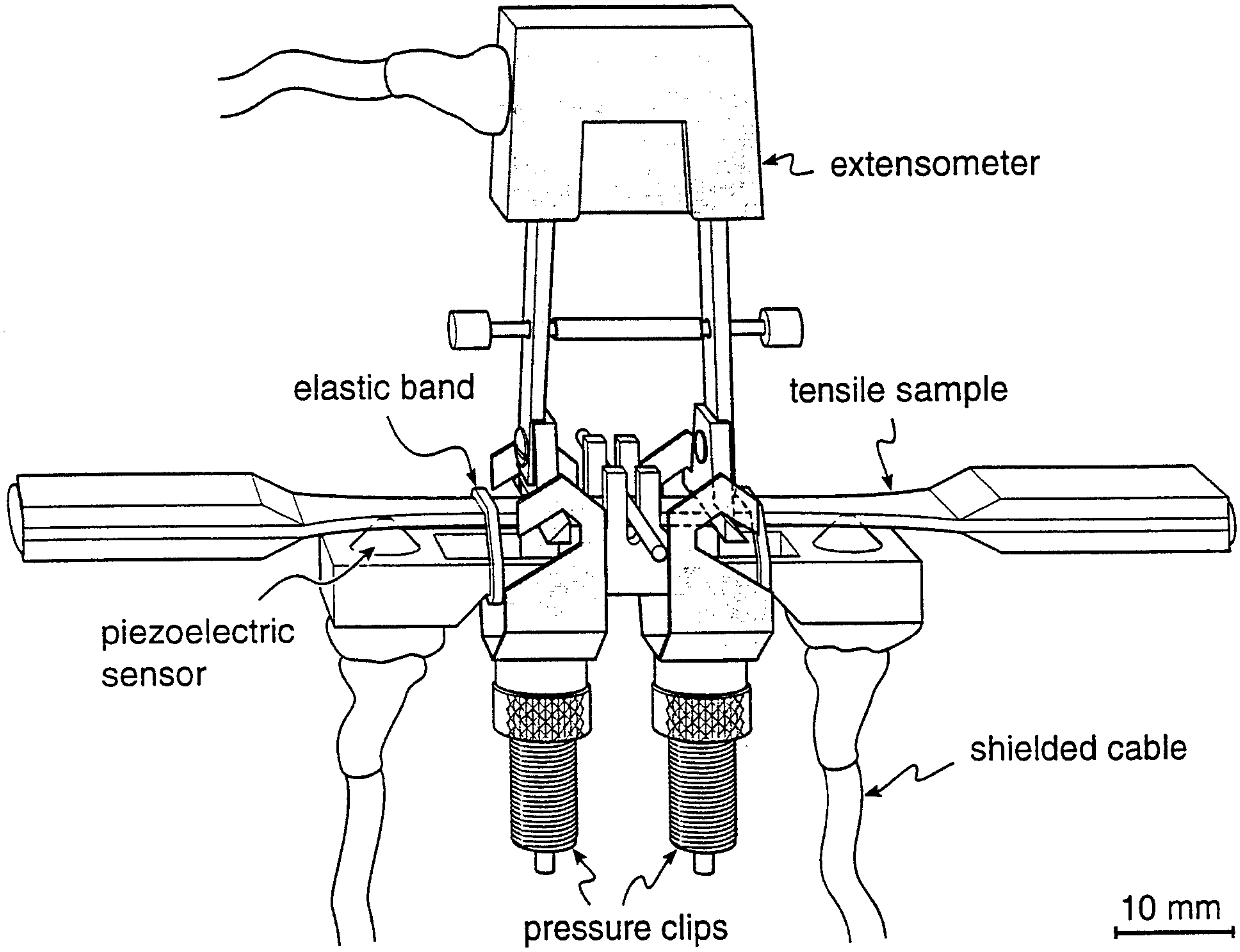
extensometer
elastic band
tensile sample
piezoelectric sensor
shielded cable
pressure clips
10 mm

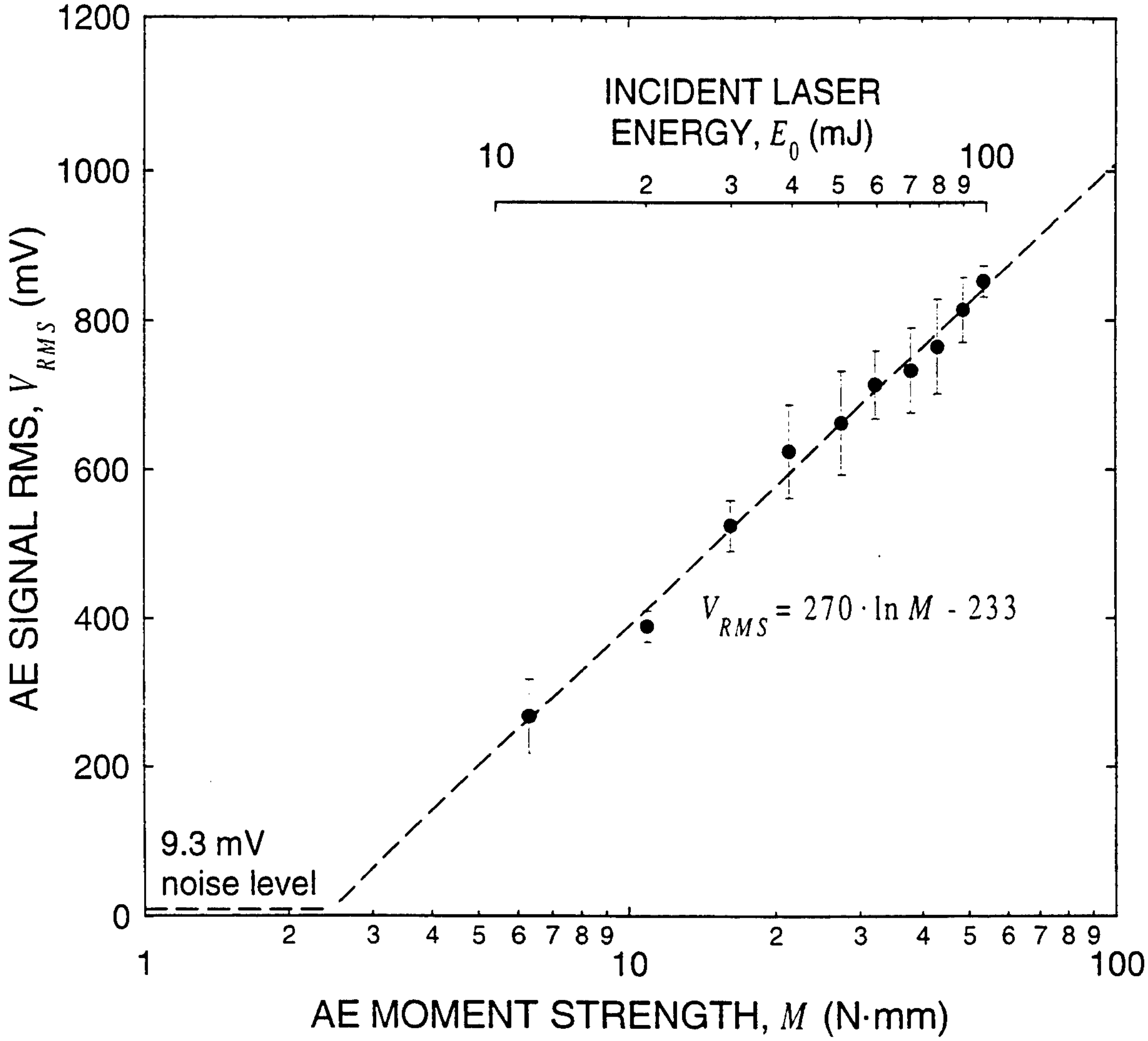
1200
1000
800
600
400
200
0
AE SIGNAL RMS, V_RMS (mV)
INCIDENT LASER
ENERGY, E_0 (mJ)
10
2
3
4
5
6
7
8
9
100
V_RMS = 270 · ln M - 233
9.3 mV
noise level
1
2
3
4
5
6
7
8
9
10
2
3
4
5
6
7
8
9
100
AE MOMENT STRENGTH, M (N·mm)

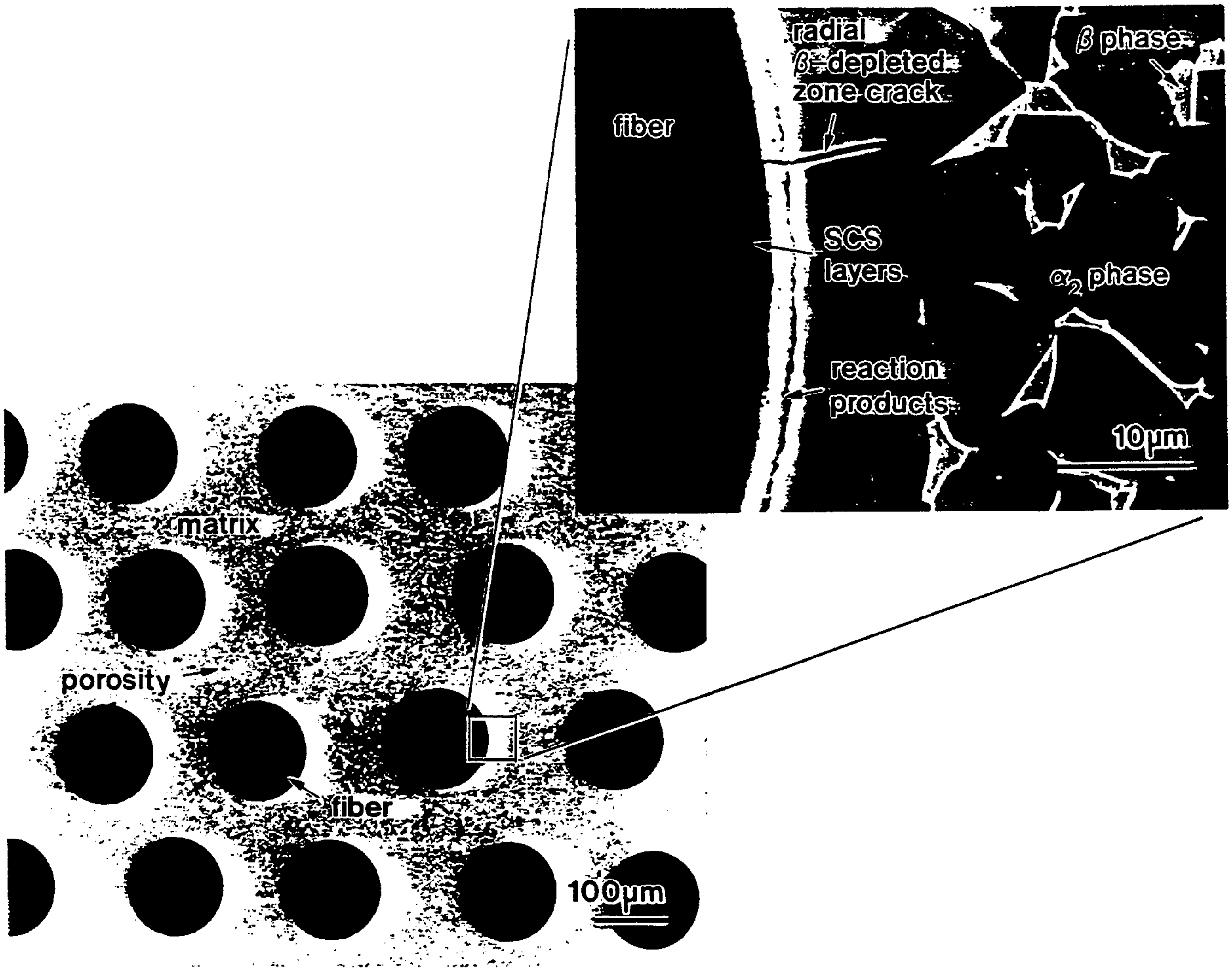
radial
β-depleted
zone crack
β phase
fiber
SCS
layers
α$_2$ phase
reaction
products
10μm
matrix
porosity
fiber
100μm

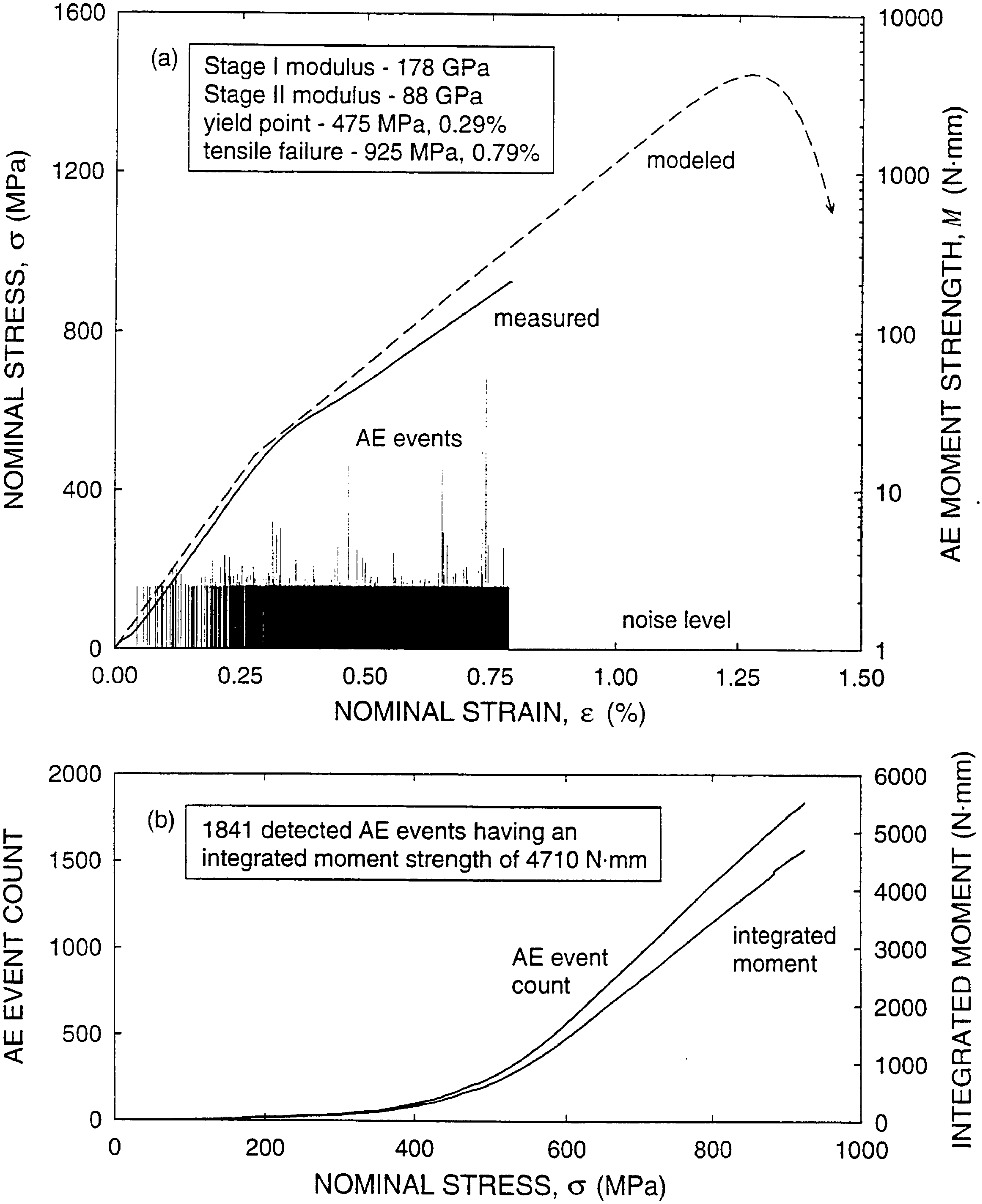
(a)
Stage I modulus - 178 GPa
Stage II modulus - 88 GPa
yield point - 475 MPa, 0.29%
tensile failure - 925 MPa, 0.79%
modeled
measured
AE events
noise level
NOMINAL STRESS, σ (MPa)
0
400
800
1200
1600
AE MOMENT STRENGTH, M (N·mm)
1
10
100
1000
10000
NOMINAL STRAIN, ε (%)
0.00
0.25
0.50
0.75
1.00
1.25
1.50
(b)
1841 detected AE events having an integrated moment strength of 4710 N·mm
AE event count
integrated moment
AE EVENT COUNT
0
500
1000
1500
2000
INTEGRATED MOMENT (N·mm)
0
1000
2000
3000
4000
5000
6000
NOMINAL STRESS, σ (MPa)
0
200
400
600
800
1000

(a)

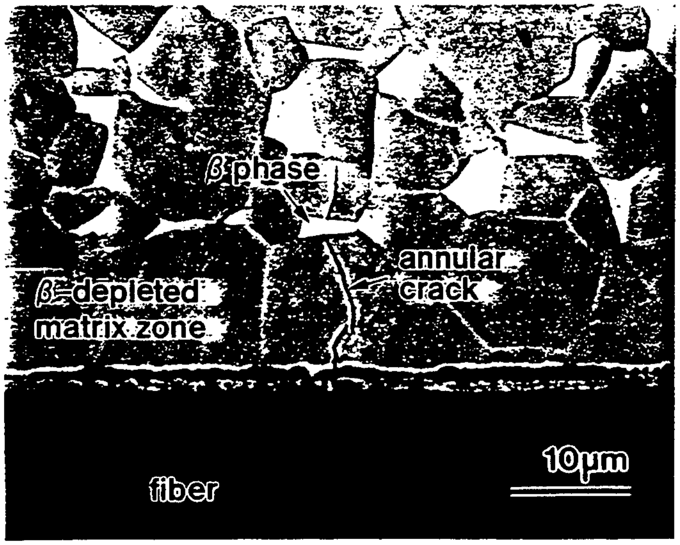
β phase
annular crack
β-depleted matrix zone
fiber
10μm

(b)

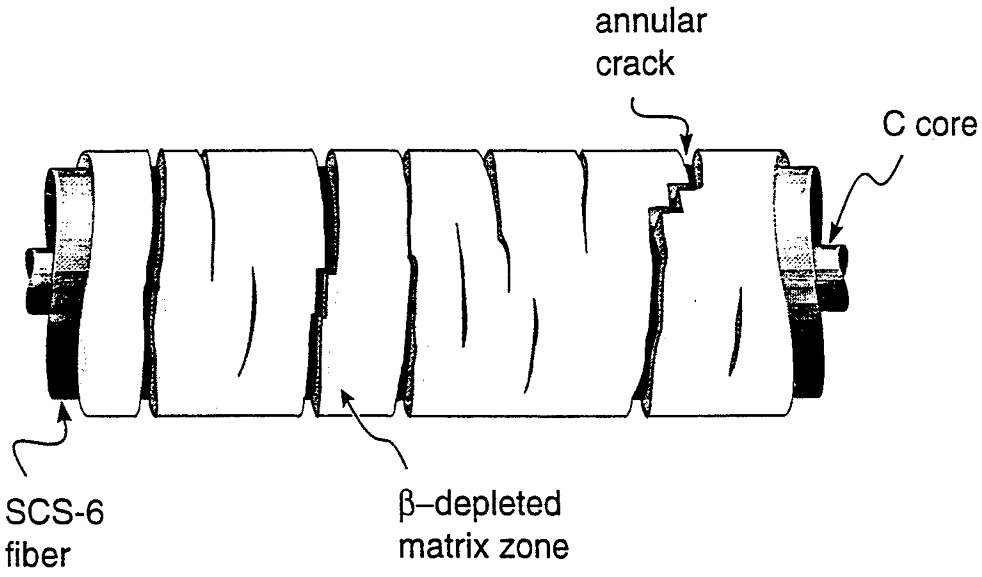
annular crack
C core
SCS-6 fiber
β–depleted matrix zone

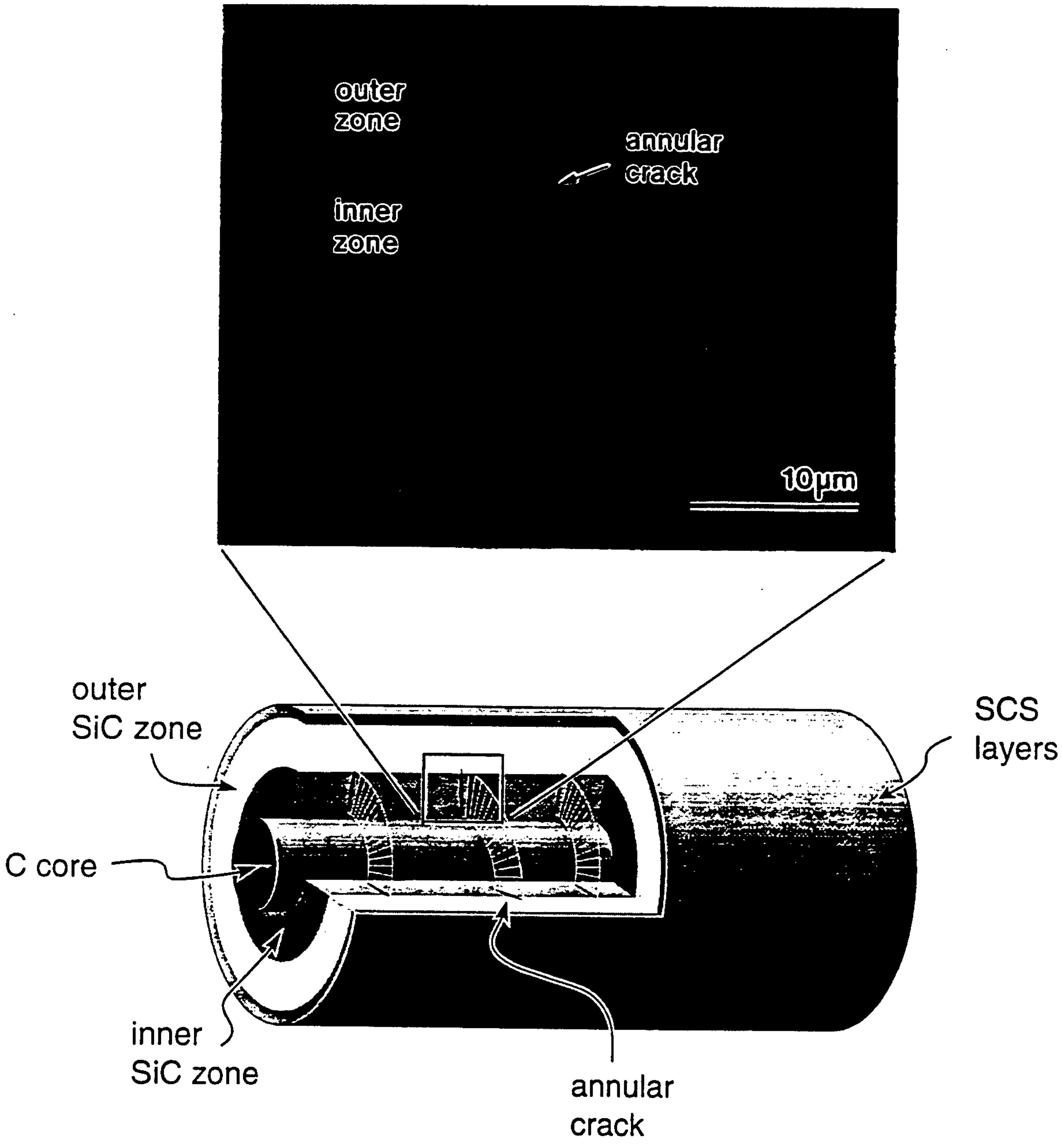
outer zone
annular crack
inner zone
10µm
outer SiC zone
SCS layers
C core
inner SiC zone
annular crack

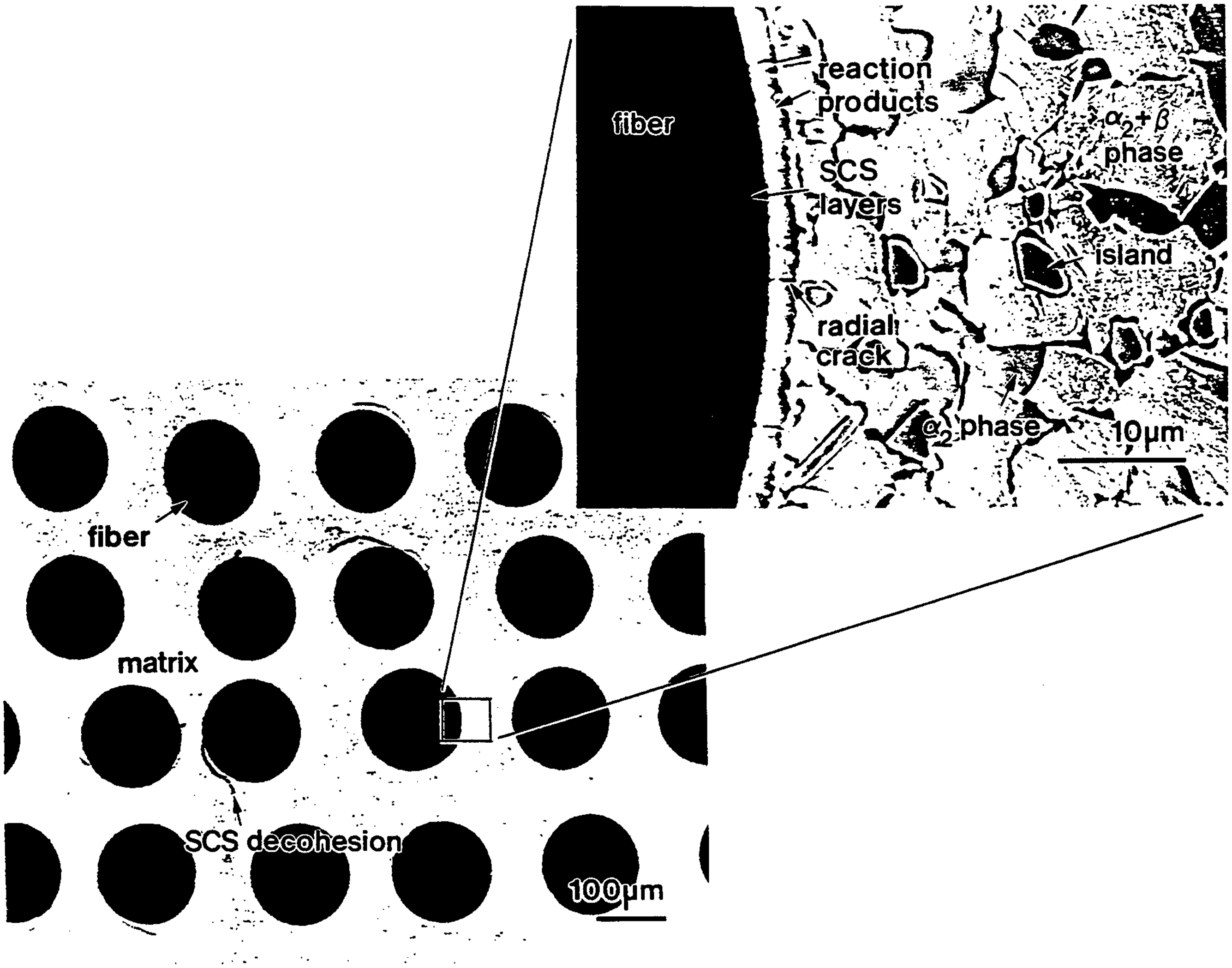
fiber
reaction products
SCS layers
radial crack
α_2 phase
$\alpha_2+\beta$ phase
island
10µm
fiber
matrix
SCS decohesion
100µm

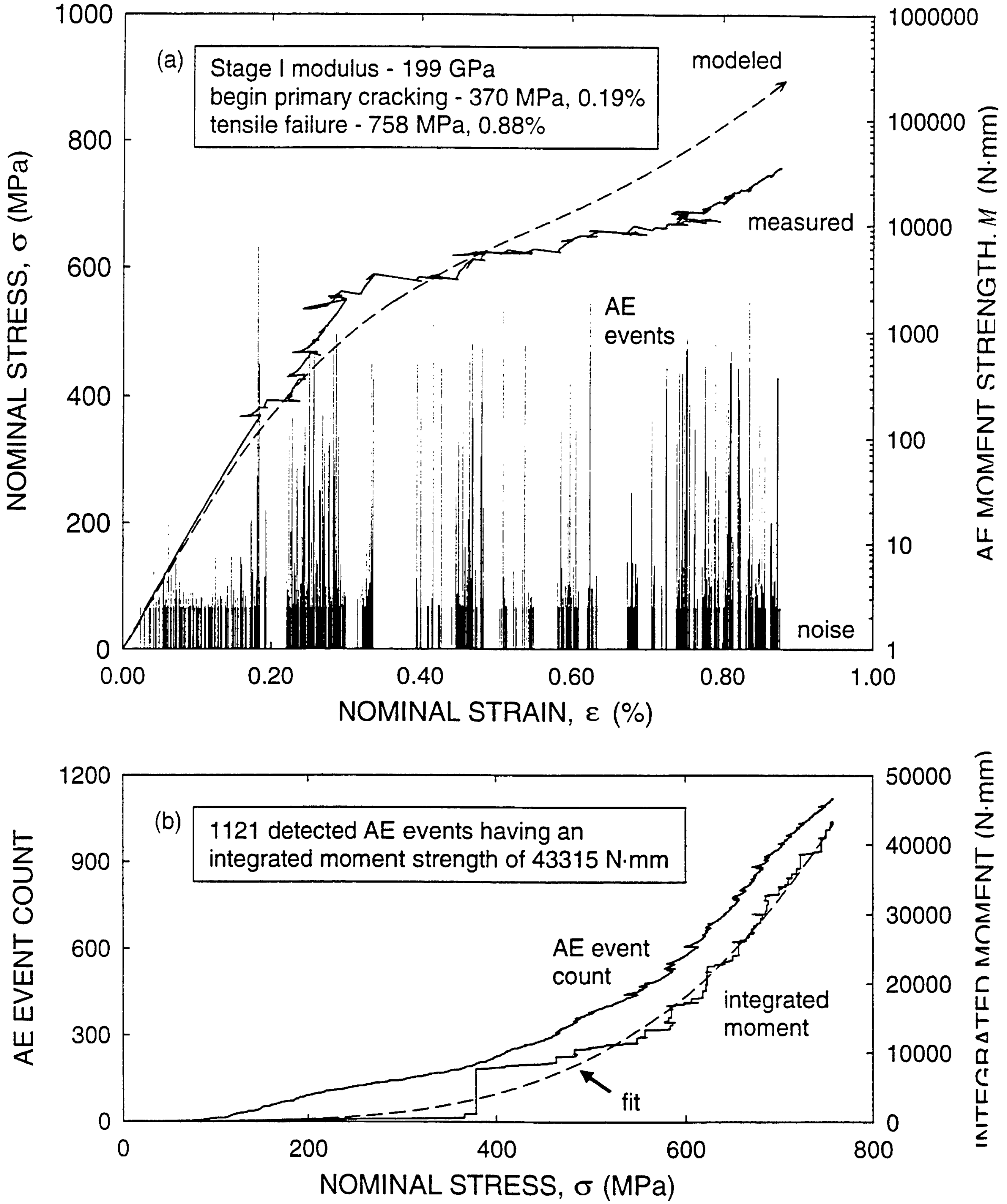
(a)
Stage I modulus - 199 GPa
begin primary cracking - 370 MPa, 0.19%
tensile failure - 758 MPa, 0.88%
modeled
measured
AE
events
noise
NOMINAL STRESS, σ (MPa)
AE MOMENT STRENGTH, M (N·mm)
NOMINAL STRAIN, ε (%)
0
200
400
600
800
1000
1
10
100
1000
10000
100000
1000000
0.00
0.20
0.40
0.60
0.80
1.00
(b)
1121 detected AE events having an
integrated moment strength of 43315 N·mm
AE event
count
integrated
moment
fit
AE EVENT COUNT
INTEGRATED MOMENT (N·mm)
NOMINAL STRESS, σ (MPa)
0
300
600
900
1200
0
10000
20000
30000
40000
50000
0
200
400
600
800

Fig. 3

(a)

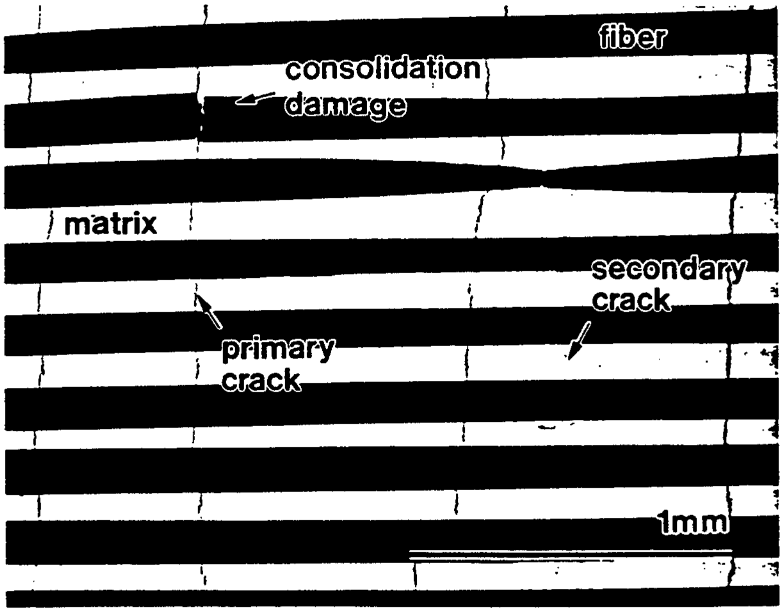
fiber
consolidation
damage
matrix
secondary
crack
primary
crack
1mm

(b)

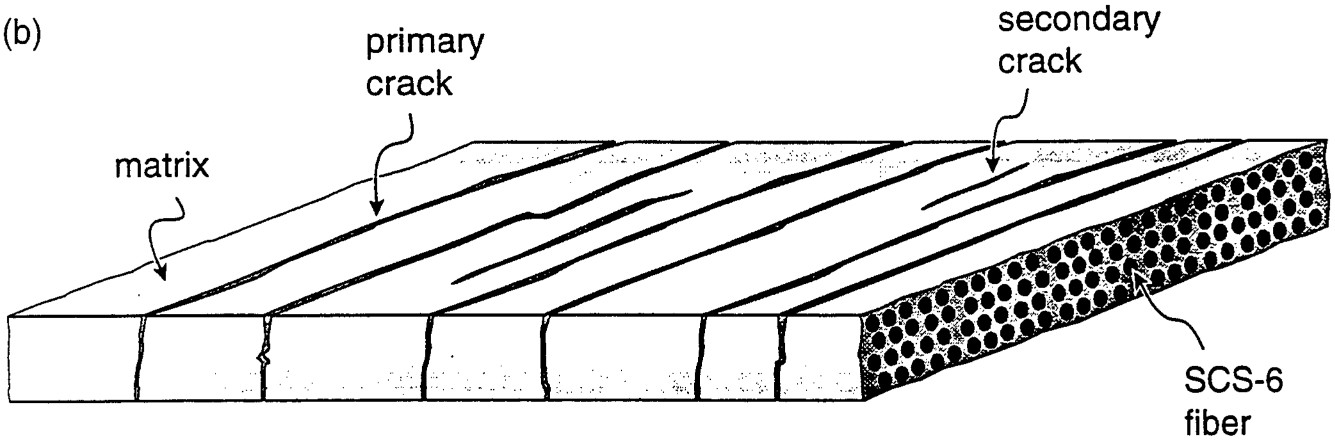
primary
crack
secondary
crack
matrix
SCS-6
fiber

Fig. 9

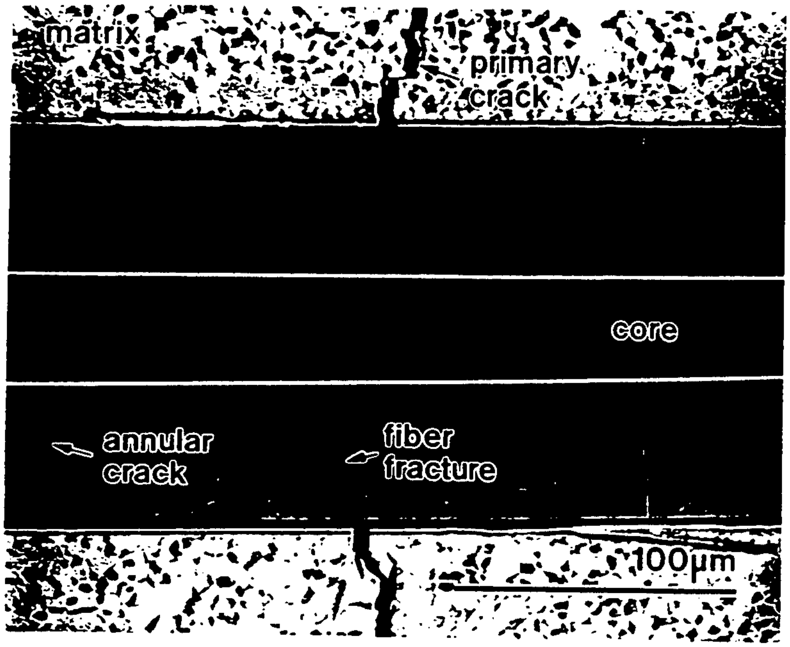
matrix
primary crack
core
annular crack
fiber fracture
100μm

Fig. 10

(a) $x' > l'$

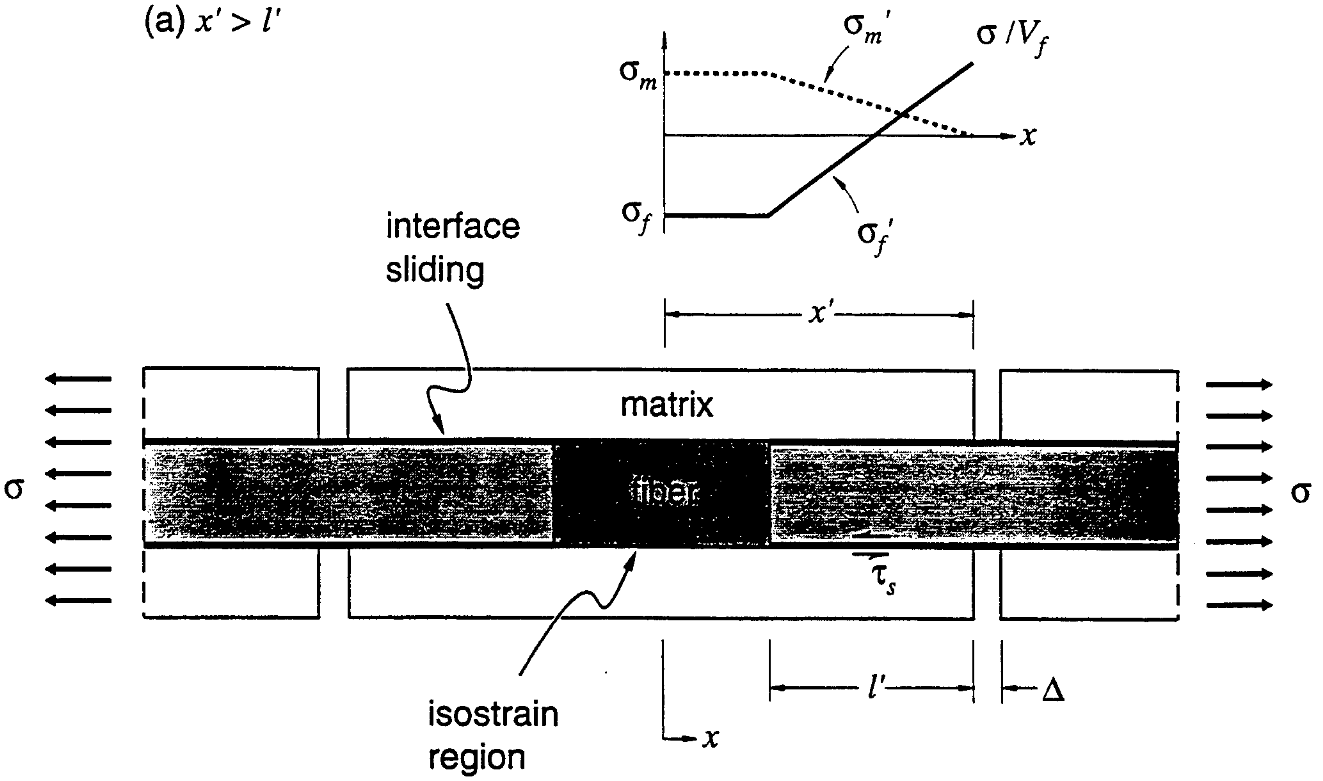
σ_m'
σ / V_f
σ_m
x
σ_f
σ_f'
interface sliding
x'
matrix
σ
fiber
σ
τ_s
isostrain region
l'
Δ
x

(b) $x' \leq l'$

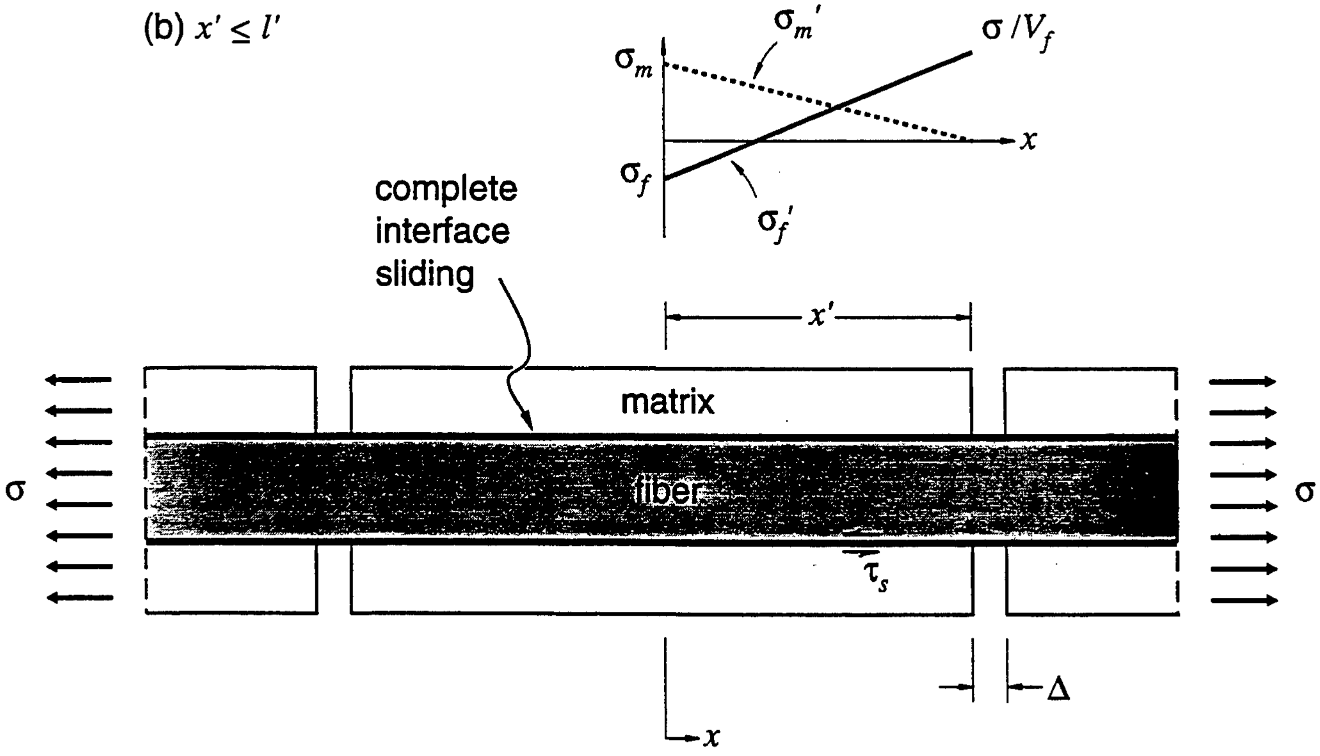
σ_m'
σ / V_f
σ_m
x
σ_f
σ_f'
complete interface sliding
x'
matrix
σ
fiber
σ
τ_s
Δ
x

Fig. 11

ACOUSTIC EMISSION ANALYSIS OF SCS-6 FIBER FRACTURE IN TITANIUM MATRIX COMPOSITES

David J. Sypeck and Haydn N.G. Wadley
School of Engineering and Applied Science
University of Virginia
Charlottesville, Virginia 22903

INTRODUCTION

One aspect of successful composite design involves development of a detailed knowledge of damage evolution. In metal matrix composites, cracking and/or plastic deformation of one or more constituents together with fiber-matrix interfacial debonding and sliding generally occur prior to catastrophic failure [1,2]. The nature and severity of these damage processes controls mechanical performance. In ductile matrix systems having a low fiber-matrix interfacial strength, the failure process can involve successive fragmentation of the fibers with increasing load. Broken fibers shed load (equally among the unbroken fibers in the case of global load sharing) until the fiber fracture density reaches some critical value and the sample catastrophically fails. Characterization of damage development has been slowed by a lack of NDE techniques. Here, the use of acoustic emission (AE) techniques is explored to further understand and quantify failure processes of this type.

Acoustic emission (i.e. detectable elastic waves) accompanies abrupt energetic microfailure events such as brittle fiber fracture. They contain information about the micromechanism from which they originate (i.e. crack area, location, orientation, opening displacement, dynamic behavior, etc.) [3,4]. Modern AE techniques seek to extract this information through remote measurement and analysis of the boundary displacements (i.e. AE signals) caused by the waves. Only the growing defects are sensed, potentially with 100% volume coverage. Previous studies [4,5] have shown the potential benefits of quantitative AE source analysis. Using models [6] originally developed for studying earthquakes and other geophysical disturbances, researchers have been able to relate measured AE signals to important characteristics of the sources causing them, thereby gaining quantitative insight into the fundamental mechanics of dynamic failure processes [4]. Here, these ideas are extended to investigate the micromechanics of fiber fracture in a fiber reinforced ductile matrix composite.

To facilitate analysis with wave propagation results for isotropic elastic plates [7], a titanium plate containing a single (longitudinally aligned) 140 μm diameter silicon carbide

Review of Progress in Quantitative Nondestructive Evaluation, Vol. 15
Edited by D.O. Thompson and D.E. Chimenti, Plenum Press, New York, 1996

fiber served as the test sample. Tensile loading in the fiber direction caused successive fragmentation of the brittle fiber and high fidelity piezoelectric sensors at eight point contact locations on the surface of the plate simultaneously captured the ensuing AE. Differences in first wave arrival times were used to locate the site of fracture and a micromechanical model for fiber fracture helped simulate the AE.

EXPERIMENTAL

To fabricate the single fiber tensile sample, -35 mesh PREP CP grade titanium powder (Nuclear Metals, Inc., Concord, Massachusetts) and a single centrally aligned SCS-6 (Textron Specialty Materials, Lowell, Massachusetts) silicon carbide fiber were electron beam sealed in an evacuated molybdenum foil lined steel canister. Hot isostatic pressing in an ABB Autoclave Systems Inc. (Erie, Pennsylvania) MiniHIPper at 100 MPa and 825°C for 4 hours resulted in microscopically complete consolidation. Upon removal from the steel canister, the sample was machined to a dogbone geometry, Figure 1.

Eight point contact miniature piezoelectric sensors [8] were spring loaded on the surface of the plate to measure boundary motion normal to the plate. Specific construction details and fidelity of the sensor are shown in Figure 2. A mixture of petroleum jelly and silver powder was used for acoustical and electrical coupling to the sample. Sensors were based on the broad band conical design [9] of the National Institute of Standards and Technology (NIST). To further reduce resonance, an acoustically lossy metallic alloy was cast into a brass cavity whose geometry was designed to reflect subsidiary waves away from the active piezoelectric element. When calibrated at NIST [8,10], the fidelity of the sensor's displacement response approached that of the original NIST design but in a much more compact size. Its frequency sensitivity and phase response showed no significant resonance in the 10 kHz to 2 MHz range.

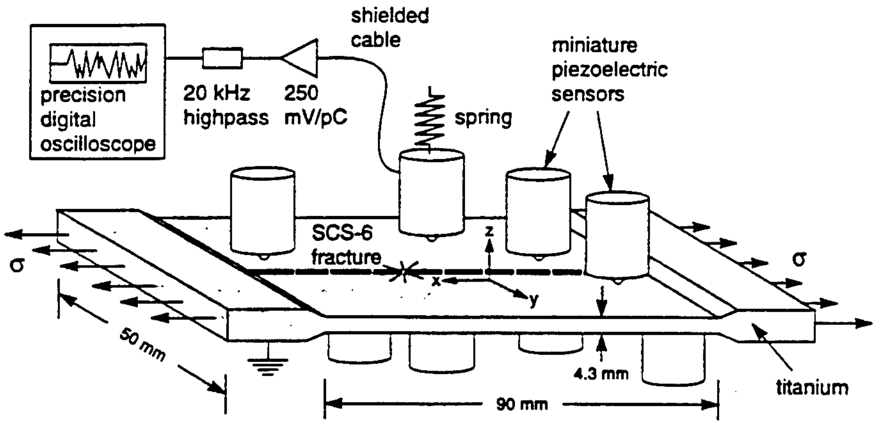

Figure 1. Experimental arrangement for fiber fragmentation.

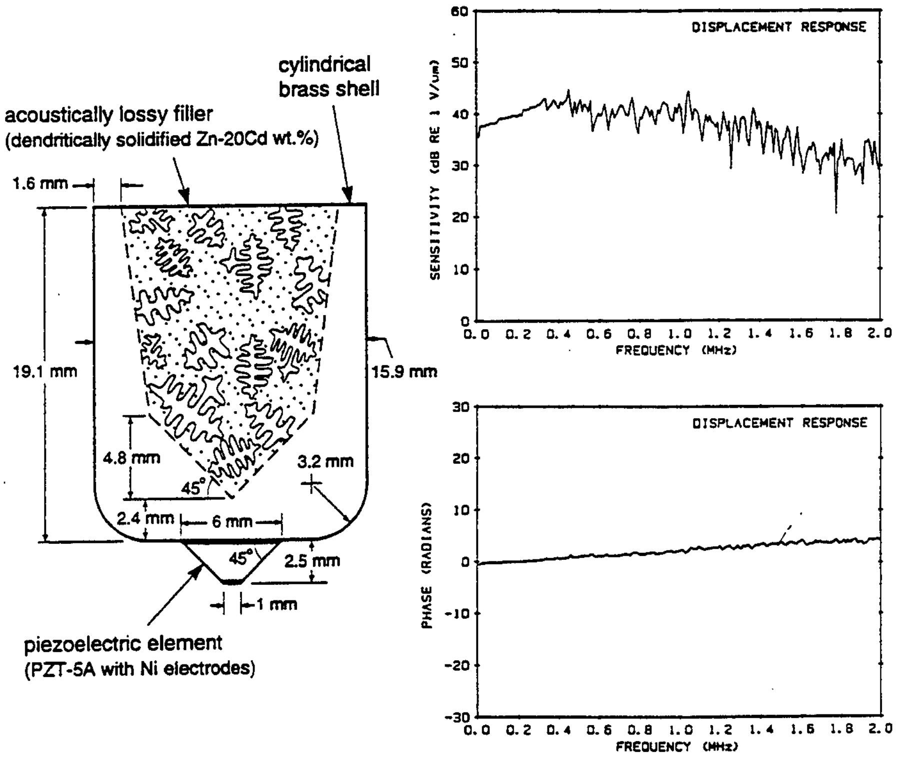

Figure 2. Construction details and typical calibration of the miniature sensor [8].

Short coaxial leads from the piezoelectric sensors were first directed through Cooknell Electronics (Weymouth, Dorset, England) CA6 charge amplifiers (model SU1 power supply unit) having a rated 250 mV/pC sensitivity and 10 kHz to 10 MHz bandwidth. Allen Avionics (Mineola, New York) 20 kHz high pass filters followed the charge amplifiers to eliminate unwanted environmental noise. The eight BNC leads directly connected to one of two LeCroy (Chestnut Ridge, New York) 7200 Precision Digital Oscilloscopes each having two 7242 plug-ins. AE signals were represented by 20,000 data points evenly distributed over a 50 µsec time interval (2.5 nsec per data point). A 300 kN capacity Instron (Canton, Massachusetts) 4208 electromechanical materials testing instrument equipped with a 300 kN loadcell (model 2518-114) and 250 kN serrated face wedge action grips (model A212-1022) was used to apply tensile load at a constant crosshead rate of 0.1 mm/min.

RESULTS

More than 40 individual AE events were observed during the test. The first at a plate tensile stress of 215 MPa and the last at 500 MPa. Shown in Figure 3 are measured AE signals from an event occurring at 484 MPa. Note the differences in first wave arrival times at the different sensor locations. The strength and high frequency content of the signals are indicative of an abrupt release of a relatively large amount of elastic energy.

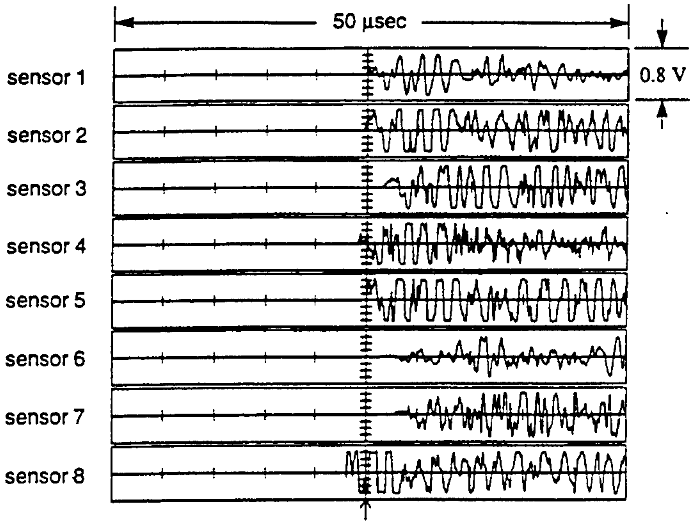

sensor	1	2	3	4	5	6	7	8
x (mm)	-6.2	24.3	-24.8	9.6	-12.5	27.2	-30.8	11.4
y (mm)	13.2	1.7	-4.5	-19.1	6.3	18.1	-14.1	-10.8
z (mm)	2.15	2.15	2.15	2.15	-2.15	-2.15	-2.15	-2.15
Δt_i (μsec)	1.87	1.71	3.52	1.22	1.86	3.58	4.70	0.00

Figure 3. Measured AE signals, sensor coordinates and time of flight differences.

SOURCE LOCATION

Suppose a cartesian coordinate system is located at the center of the sample, Figure 1. Let x', y' and z' be the unknown location of the source. The ith sensor located at x_i, y_i and z_i will experience a signal when

$$(x'-x_i)^2+(y'-y_i)^2+(z'-z_i)^2 = (c_p t_i)^2 \tag{1}$$

where t_i is the time required for the first compression wave to reach the sensor and c_p is its velocity. Since only differences in first wave arrival times can be obtained from the experimental data, let t_o be the travel time required to reach the closest sensor and Δt_i be the time difference between the closest and the ith sensor. Thus $t_i = t_o + \Delta t_i$. Location is accomplished by solving for unknowns x', y', z' and t_o using the measured Δt_i values. To linearize the problem, observe that subtracting any ith sensor equation from any jth provides one linear equation. If there are at least five sensors, four linearly independent equations can be formed via numerous routes. For an array of η sensors, there are a maximum $N = \eta(\eta-1)/2$ unique sensor equation subtractions which can be performed [8].

Time of flight differences in Figure 3 were found within approximately 20 nsec accuracy by determining when the AE signal magnitude first exceeded the background noise. The $N = 28$ linear equations (overdetermined and not linearly independent) were formed and then solved using a linear least squares algorithm. Using $c_p = 6.07$ mm/μsec for titanium, the returned source location was $x' = 5.5$ mm, $y' = -3.7$ mm, $z' = -2.9$ mm and $t_0 = 1.48$ μsec which was consistent with the source being near the plate centerline (i.e. x axis) and the approximate location of the fiber. We note that accuracy in z' is problematic for thin plates because the distance between a source and a sensor "far" from the source is not substantially affected by changes in z'.

ACOUSTIC EMISSION SIGNAL SIMULATION

Elastic radiation from an abrupt failure process like an earthquake or growing microcrack is induced by the release of elastic strain energy associated with a sudden creation of discontinuity in the displacement field or stress field across the surface of failure. In terms of fault characteristics, Burridge and Knopoff [6] arrive at a body force equivalent for the fault

$$\rho f_i(\mathbf{x}', t') = -\int_{\Sigma} v_l \{ [u_k](\xi, t') c_{klij}(\xi) \delta_{,j}(\mathbf{x}';\xi) + [u_{k,j}](\xi, t') c_{ilkj}(\xi) \delta(\mathbf{x}';\xi) \} d\Sigma \qquad (2)$$

where $\rho f_i(\mathbf{x}', t')$ is the body force per unit volume. The fault surface is represented by $\Sigma(\xi)$. $[u_k](\xi, t')$ and $[u_{k,j}](\xi, t')$ are the displacement discontinuity and its derivative (traction discontinuity) across the fault, $c_{klij}(\xi)$ are the elastic constants in the neighborhood of the fault, v_l is the unit normal to $\Sigma(\xi)$ and δ is the Dirac delta function.

Since internal sources must be self equilibrating, the traction discontinuity term in Equation (2) vanishes (i.e. $[u_{k,j}](\xi, t') = 0$) simplifying matters. For a point source centered at $\mathbf{x}'$, the seismic moment tensor (sometimes called the stress drop tensor or dipole tensor) is used to characterize the source [11].

$$M_{ij} = \int_{\Sigma} v_l [u_k](\xi) c_{klij}(\xi) d\Sigma \qquad (3)$$

The point displacement $u_i(\mathbf{x}, t)$ due to wave motion

$$u_i(\mathbf{x}, t) = M_{jk} \int_0^t G_{ij,k}(\mathbf{x};\mathbf{x}', t-t') f(t') dt' \qquad (4)$$

involves convolving the source time dependence $f(t')$ (i.e. source function) with spatial derivatives of the elastodynamic Green's tensor, $G_{ij,k}(\mathbf{x};\mathbf{x}', t-t')$. Each of its components represent the point response in the ith direction at x due to an impulsive (i.e. delta function) body force dipole concentrated at $\mathbf{x}'$. Subscripts j and k indicate the sense and separation direction of the dipole. Solutions to the response of a unit ramp are available [7]. In this case, Equation (4) takes the form

$$u_i(\mathbf{x}, t) = M_{jk} \int_0^t G^R_{ij,k}(\mathbf{x};\mathbf{x}, t-t') \ \ddot{f}(t') dt' \qquad (5)$$

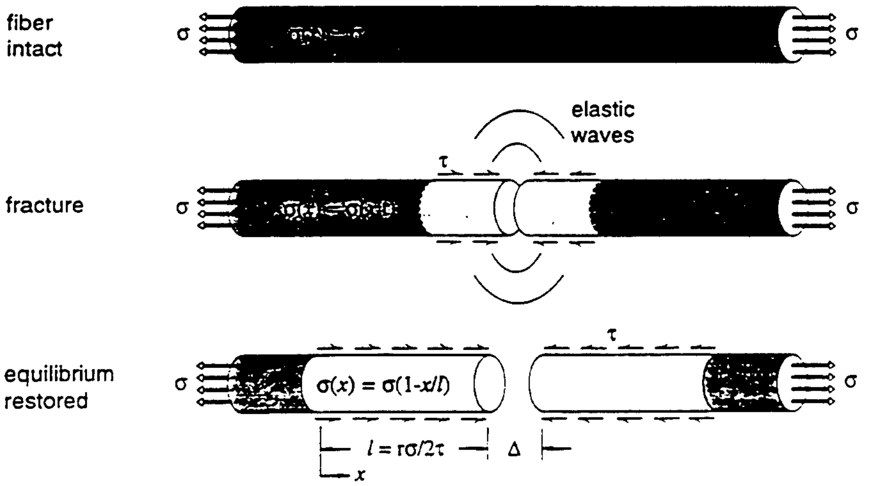

Figure 4. Micromechanics of fiber fracture.

where $G^R_{ij,k}(x;x', t-t')$ is the unit ramp response.

An estimate of the moment tensor for the fracture of a cylindrical fiber can be obtained by examination of Figure 4. Provided changes in radial and circumferential stresses are small, the analysis is simplified considerably by treating this as a one dimensional problem. The crack opening displacement Δ is given by

$$\Delta = \frac{r\sigma^2}{2E\tau} \tag{6}$$

where the shear recovery length $l = r\sigma/2\tau$ has been assumed. σ is the remote fiber tensile stress, τ the fiber-matrix interfacial shear stress, r the fiber radius and E its elastic modulus. For a matrix rigid in the x direction, debonding must occur along a length of at least l to satisfy equilibrium. In this manner, the crack opening is quantified as a function of remote fiber stress and interfacial shear stress. Symmetry simplifies Equation (3) (i.e. shear contributions cancel) and we arrive at the moment tensor

$$M_{ij} = \begin{bmatrix} \lambda+2\mu & 0 & 0 \\ 0 & \lambda & 0 \\ 0 & 0 & \lambda \end{bmatrix} \cdot \Delta\pi r^2 \tag{7}$$

in terms of the fiber Lamé constants $\lambda = \nu E/(1+\nu)(1-2\nu)$ and $\mu = E/2(1+\nu)$ where ν is the Poisson ratio.

To estimate the likely strength of a SCS-6 fracture source, let a fracture event occur at a fiber stress of $\sigma = 3500$ MPa. Take the interfacial shear stress to be $\tau = 140$ MPa while the radius and elastic moduli are $r = 70\ \mu m$, $E = 400$ GPa and $\nu = 0.14$ respectively. The crack opening is computed as $\Delta = 7.7\ \mu m$ and the moment tensor becomes:

$$M_{ij} = \begin{bmatrix} 49.4 & 0 & 0 \\ 0 & 8.0 & 0 \\ 0 & 0 & 8.0 \end{bmatrix} \text{N} \cdot \text{mm} \qquad (8)$$

The returned source location suggested that sensor 3 was oriented at an angle of approximately 1.5° with respect to the *x* axis of the selected source. We disregarded this small rotation and used Equation (8) directly. Unit ramp responses were computed for an infinite isotropic plate using a FORTRAN 77 code [7]. $x' = 5.5$ mm, $y' = -3.7$ mm and $z' = 0.0$ mm were the source coordinates we worked with. The properties of titanium were $\mu = 43.9$ GPa, $c_p = 6.07$ mm/μsec and $c_s = 3.13$ mm/μsec for the shear wave velocity. 450 data points beyond the first wave arrival and a 0.005 μsec step size resulted in 2.25 μsec of simulation data. This was enough to allow a reasonable comparison with the measured AE signal while avoiding reflections from the sides of the plate which were not accounted for (i.e. infinite plate) in the simulation. The convolution in Equation (5) was performed (discrete) using the second time derivative of a symmetrical parabolic ramp source function which had 0.38 μsec risetime. It first acted at $t = t' = 0$. We observe good agreement between the simulated and measured AE signal, Figure 5.

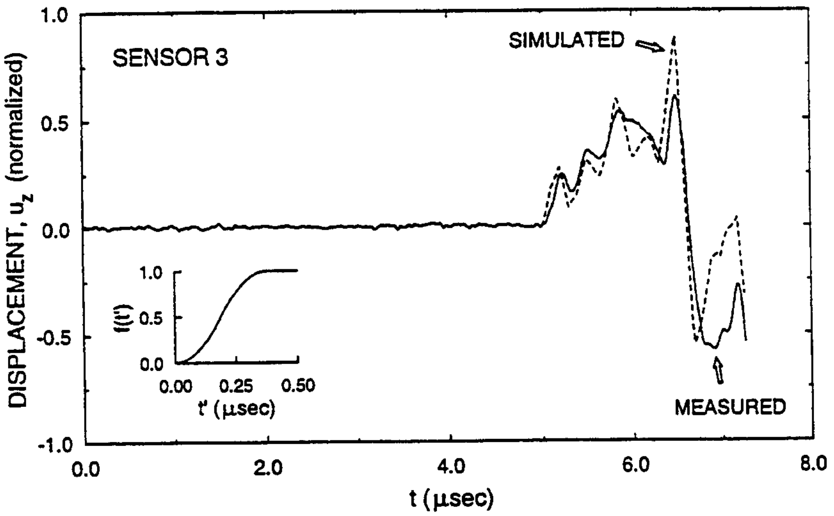

Figure 5. Comparison between experiment and theory.

CONCLUSION

A multichannel quantitative acoustic emission system has been developed and used to record acoustic emission associated with the successive fragmentation of a SCS-6 fiber in a titanium matrix plate. Three dimensional location of events has been accomplished and good agreement obtained between simulated and measured signals.

ACKNOWLEDGEMENTS

We wish to extend our appreciation to N. Hsu, F. Breckenridge and T. Proctor for their informative discussions and help. Funding for this work was provided by an ARPA-URI grant under contract No. N0014-86-K0753 (managed by S. Fishman and W. Coblenz) and a NASA-ARPA program (NAGW-1692, directed by W. Barker and R. Hayduk).

REFERENCES

1. Hashin, Z.,''Analysis of Composite Materials - A Survey'', Journal of Applied Mechanics, Vol. 50, pp. 481-505, 1983.
2. Kelly, A. and Macmillan, N.H., Strong Solids, Clarendon Press, Oxford, 1986.
3. Scruby, C., Wadley, H., and Sinclair, J.E., ''The origin of acoustic emission during deformation of aluminum and an aluminum-magnesium alloy'', Philosophical Magazine A, Vol. 44, No. 2, pp. 249-274, 1981.
4. Wadley, H.N.G., Scruby, C.B., and Shrimpton, G., ''Quantitative Acoustic Emission Source Characterisation During Low Temperature Cleavage and Intergranular Fracture'', Acta Metallurgica et Materialia, Vol. 29, pp. 399-414, 1981.
5. Kim, K.Y. and Sachse, W., ''Characteristics of an acoustic emission source from a thermal crack in glass'', International Journal of Fracture, Vol. 31, pp. 211-231, 1986.
6. Burridge, R. and Knopoff, L., ''Body Force Equivalents For Seismic Dislocations'', Bulletin of the Seismological Society of America, Vol. 54, No. 6, pp. 1875-1888, 1964.
7. Hsu, N. N., ''Dynamic Green's Functions of an Infinite Plate - A Computer Program'', NBSIR 85-3234, National Institute of Standards and Technology, Gaithersburg, Maryland, 1985.
8. Sypeck, D.J., Master of Science Thesis, University of Virginia, Charlottesville, Virginia, 1990.
9. Proctor, T.M. Jr., ''An improved piezoelectric acoustic emission transducer'', Journal of the Acoustical Society of America, Vol. 71, No. 5, pp. 1163-1168, 1982.
10. Hsu, N.N. and Breckenridge, F.R., ''Characterization and Calibration of Acoustic Emission Sensors'', Materials Evaluation, Vol. 39, pp. 60-68, 1981.
11. Aki, K. and Richards, P.G., Quantitative Seismology Theory and Methods, Volumes I and II, W.H. Freeman and Company, San Francisco, 1980.